Max-Planck-Institut für extraterrestrische Physik

RESEARCH 2013 – 2015

A Book of Abstracts

Observations – Measurements

Theory – Simulations

Experiments – Projects – Detector Developments

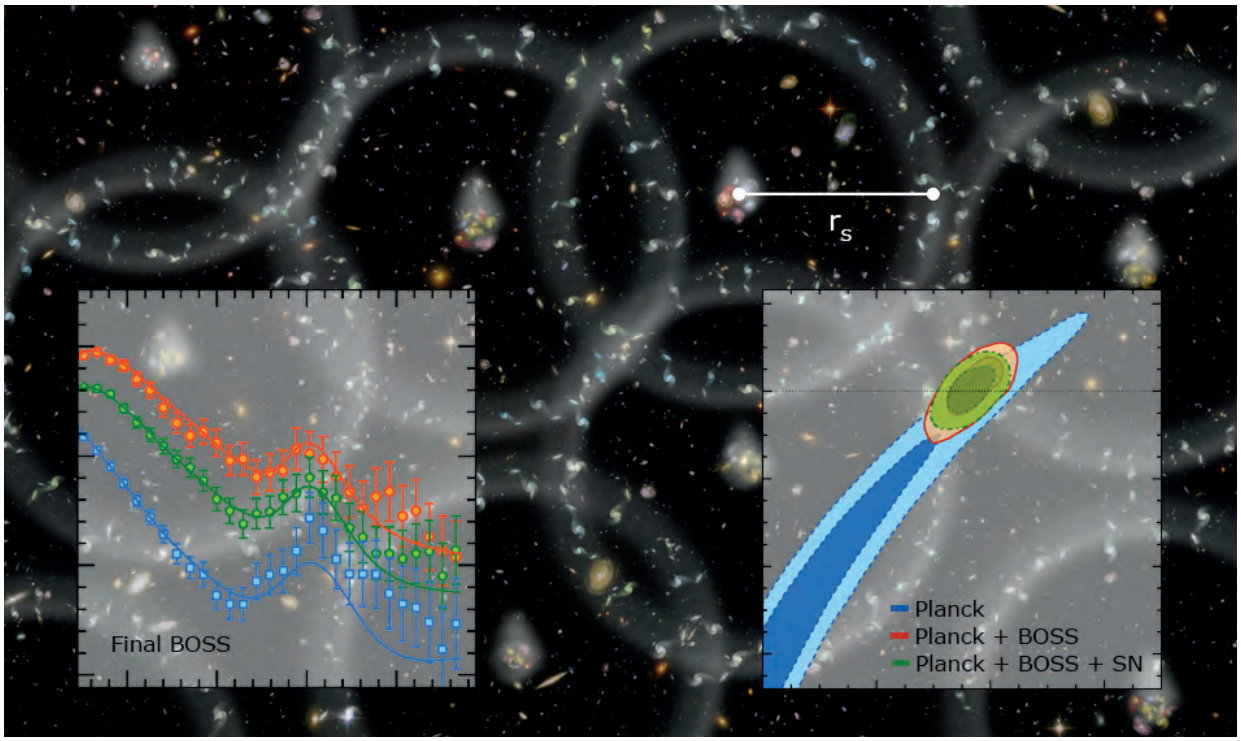

June 2016

Front Cover:
The grey spheres on the background panel image (credit: Zosia Rostomian, Lawrence Berkeley National Laboratory) illustrate the pattern of the "baryon acoustic oscillations" from the early Universe. Galaxies today have a slight tendency to be located on spheres whose radius is given by the sound horizon scale at recombination, r_s (the effect is greatly exaggerated in this illustration). This characteristic scale, imprinted in the galaxy distribution as measured from the Baryon Oscillation Spectroscopic Survey (BOSS), is seen as peaks in the correlation functions (left inset). The comparison of this scale with the predicted value can be used to constrain basic cosmological parameters, such as the matter density and the dark energy equation of state (right inset).

For details see the abstract at page 80.

Book of MPE Research/Experimental Highlights

This book of MPE research and experimental highlights for the years 2013 to 2015 was produced for the MPE Fachbeirat Meeting of June 27 to 29, 2016. Its goal is to provide a comprehensive overview as well as detailed information on science results, data analysis activities, ongoing experimental projects and detector developments in a fashion that is supplementary to the Science Report for these years. Scientists were encouraged to submit their highlight contribution for the three-years period as a one-page abstract. The authors of the abstracts are clearly identified and are solely responsible for their contents.

The contributions are sorted according to MPE groups (the main groups as well as sub-groups). They are also marked by different colors of their summaries. Inside the groups abstracts are sorted with respect to science or instrumental/hardware topics.

Edited by K. Nandra, W. Collmar

Table of Contents

Table of Contents

Table of Contents

Table of Contents

Table of Contents

I) Infrared / Submillimeter Astronomy

The KMOS^{3D} survey of spatially-resolved kinematics of high-redshift galaxies

The new KMOS multi-object near-IR integral field spectrograph at the ESO VLT, built by a consortium with MPE, is very powerful at exploring early galaxy evolution. The **KMOS^{3D} survey**, a highly successful 75-night guaranteed time program co-led by MPE/IR+OPINAS and begun in 2013, capitalizes on crucial synergies with multi-wavelength data, including the MPE/IR Herschel PEP survey, and the 3D-HST and CANDELS HST Treasury programs. KMOS^{3D} is 1) providing an unbiased census of spatially-resolved kinematics, star formation, outflows, excitation, and metallicity from a homogeneous sample of 600+ mass-selected ($\log[M_*/M_\odot] \gtrsim 9.5$) z~0.6-2.7 galaxies, spanning 5 Gyrs of cosmic time, 2) enabling the first reliable connection between these properties, stellar structure & populations, and environment, 3) constraining the mechanisms driving mass growth, feedback, and quenching. The survey strategy emphasizes **deep observations over a wide range of galaxy parameters** – uniquely enabling resolved measurements of faint line emission in individual objects and pushing IFU studies into new regimes, notably sub-main sequence galaxies in the process of quenching.

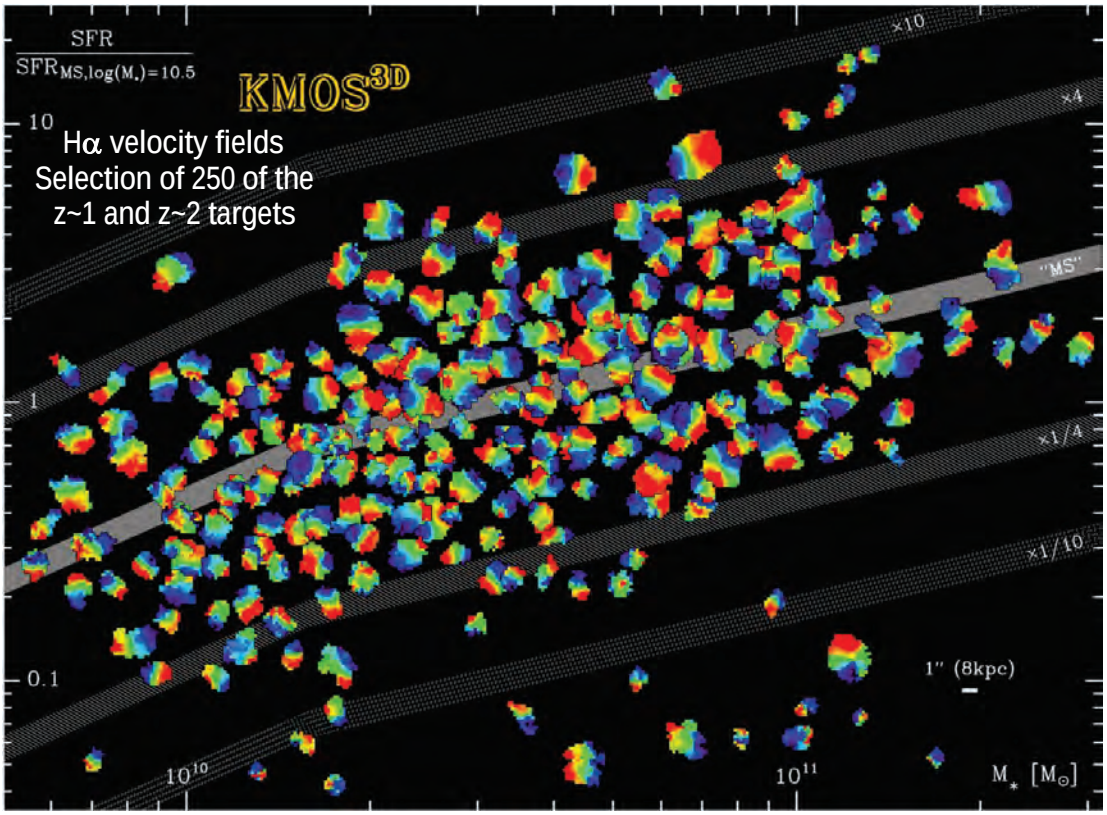

Hα velocity fields of 250 z~1 and z~2 galaxies in our current KMOS^{3D} sample of 536 objects. Galaxies are plotted at their location in the stellar mass vs star formation rate (SFR) plane. Blue to red colors show blueshifted to redshifted velocities relative to the systemic redshift of each galaxy.

The Hα kinematics from KMOS^{3D} confirm that ~70% of massive star-forming galaxies (SFGs) are rotationally supported disks, with intrinsic velocity dispersions increasing with redshift as $\sigma_0 \propto (1+z)$ in line with expectations for gas-rich disks and the observed evolution in cold gas fractions. The Hα detection rate is ~90% within ±0.6 dex in log(SFR) of the main sequence (MS) of SFGs, and ~15% at $\log(SFR/SFR_{MS})<0.6$ though the deep integrations of up to ~20h set stringent limits on line emission. Many of the detected sub-MS galaxies have unexpectedly strong Hα emission given their UV+IR luminosities, and are often spatially-resolved rotating disks at the ~4 kpc resolution of the KMOS data.

References: • Wisnioski, E., Förster Schreiber, N. M., Wuyts, E., et al. 2015, ApJ, 799, 209

N. M. Förster Schreiber, E. Wisnioski, D. Wilman & the KMOS^{3D} Team

The angular momentum distribution of star-forming galaxies at z ~ 1 – 3

The angular momentum links galaxies to their host dark matter halos and contains the imprint of their baryonic mass assembly history. Exploiting the high quality, spatially-resolved Hα kinematics of an unbiased sample of 360 $\log(M_*/M_\odot)$~9.3–11.8 z~1–3 galaxies from our KMOS^{3D} and SINS/zC-SINF surveys, obtained with the near-IR multi-object KMOS and AO-assisted single-object SINFONI integral field spectrographs at the VLT, we derive for the first time robustly the angular momentum distribution of massive star-forming galaxies around the peak epoch of cosmic star formation. The inferred halo scale angular momentum distribution of the galaxies is consistent with the theoretical prediction for their dark matter halos in terms of mean spin parameter $\langle\lambda\rangle$~0.037 and dispersion $\sigma(\log\lambda)$~0.2. Spin parameters correlate with disk size and stellar surface density but do not depend significantly on halo mass, stellar mass, or redshift. Our data support the long-standing assumption that, on average, the specific angular momentum of disks reflects that of their dark matter halos (j_d=j_{DM}). The weak correlation between $\lambda\times(j_d/j_{DM})$ and stellar surface density in the inner 1kpc suggests that internal processes lead to "compaction" and dense core formation inside massive high-z disks.

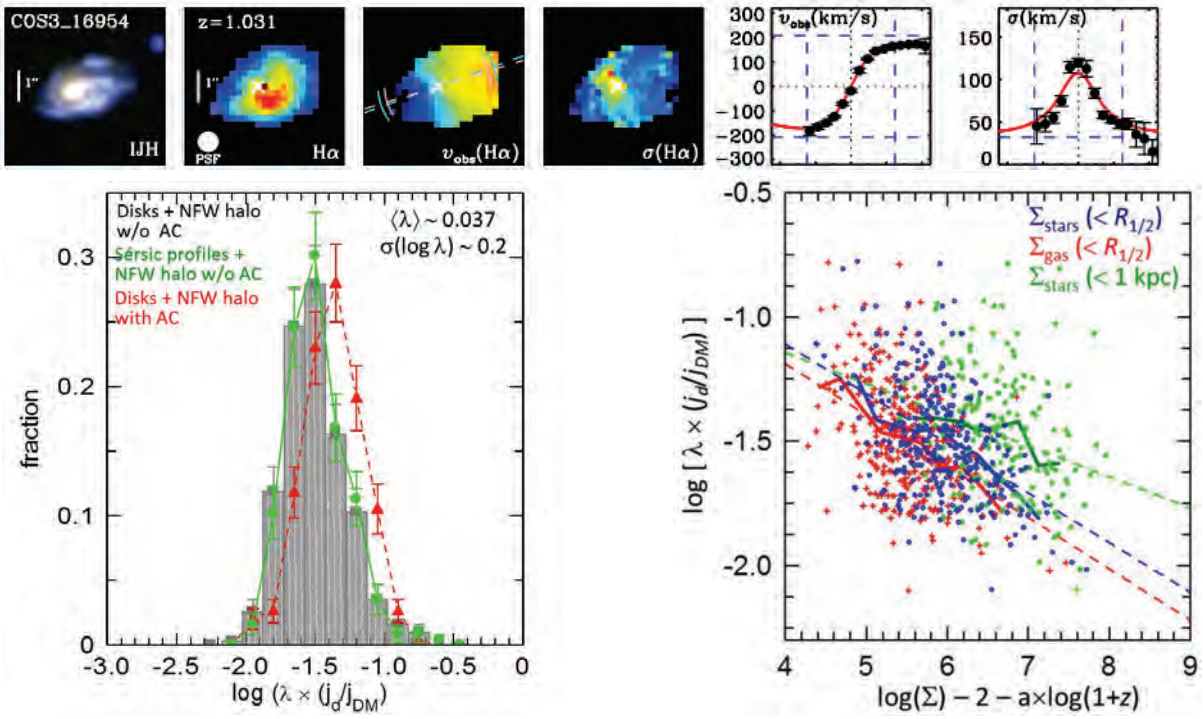

Top: Example of a *z*~1 galaxy observed in KMOS^{3D}: HST *IJH* bands color map, KMOS Hα flux, velocity, velocity dispersion maps, and major axis velocity and dispersion profiles. ***Bottom left:*** Angular momentum parameter distribution from modeling the data assuming exponential baryonic disks in NFW dark matter halos neglecting or accounting for adiabatic contraction (AC), and without AC but accounting for deviations from a pure disk profile for the galaxies. ***Bottom right:*** Angular momentum parameter versus stellar or gas mass surface density within the half-light radius corrected for redshift evolution of galaxy sizes, and with stellar mass surface density in the inner 1 kpc.

References: · Burkert, A., Förster Schreiber, N.M., Genzel, R., et al. 2016, ApJ, submitted (arXiv:1510.03262)

R. Genzel, A. Burkert, N. M. Förster Schreiber & the KMOS^{3D} + SINS/zC-SINF Teams

Outer rotation curves of high-redshift disks with KMOS^{3D} and SINS/zC-SINF

We exploit the deep Hα IFU kinematic data from the KMOS^{3D} and SINS/zC-SINF surveys to explore the so far unconstrained outer rotation curves of star-forming disk galaxies at high redshift. By stacking the signal of ~100 massive disks at $0.7 < z < 2.6$, we construct a representative rotation curve reaching out to several effective radii. Our stacked rotation curve exhibits a turnover with a steep falloff in the outer regions, significantly strengthening the tantalizing evidence previously hinted at only in a handful of individual disks among the sample with the deepest data.

This finding confirms the high baryon fractions found by comparing the stellar, gas and dynamical masses of high redshift galaxies independently of assumptions on the light-to-mass conversion and Initial stellar Mass Function (IMF). The rapid falloff of the stacked rotation curve is most naturally explained by the effects of pressure gradients, which are significant in the gas-rich, turbulent high-z disks and which would imply a possible pressure-driven truncation of the outer disk.

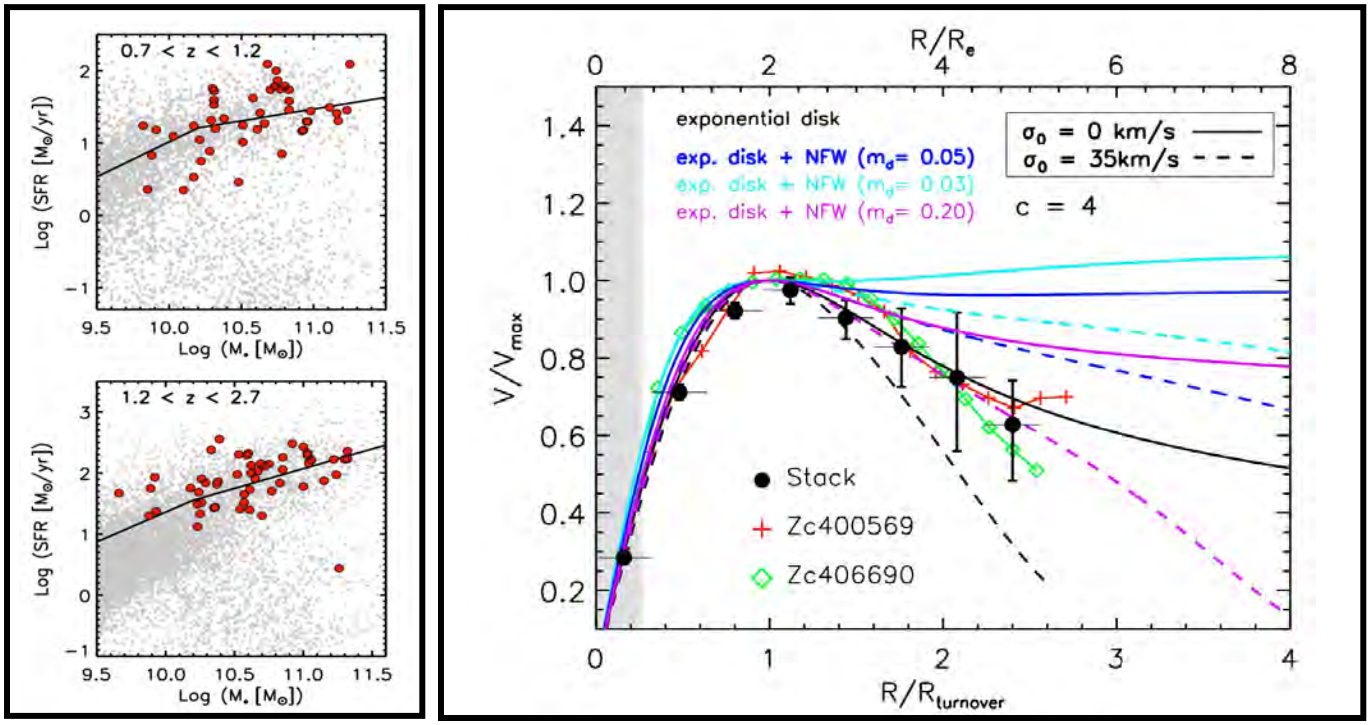

Left: Sample of stacked galaxies in the SFR-M_* plane with solid lines indicating the main sequence, grey points show the underlying 3D-HST population. **Right**: Stacked rotation curve in normalized coordinates, shown together with models representing a rotating exponential disk (black), and added dark matter NFW halos for different disk mass fractions m_d. The dashed (and solid) lines represent models with pressure support in the outer disk assuming $\sigma_0 = 35$ km/s (and with no pressure support, respectively). Rotation curves of galaxies with best S/N (Zc400569, Zc406690) are shown additionally. The grey area marks the HWHM of the average spatial PSF.

References:

- Förster Schreiber et al. 2009, ApJ, 706, 1364
- Mancini et al. 2011, ApJ, 743, 86
- Wisnioski et al. 2015, ApJ, 799, 209
- Burkert et al. 2015, ApJ, subm. (arXiv:1510.03262)

P. Lang, N. M. Förster Schreiber, R. Genzel, A. Burkert and the SINS/zC-SINF & KMOS^{3D} teams

KMOS^{3D} Rotating Compact SFGs: the precursors of passive spheroids

The representative selection and depth of **the KMOS^{3D} Survey** has allowed us to study, in unprecedented detail, rare galaxies at z~0.9-2.5 that may be in the process of quenching. The short timescales associated with the quenching process make it difficult to catch galaxies "in the act" of shutting down their star formation. Compact star-forming galaxies (SFGs), making-up ~7% of our sample, are selected to have properties aligned with already quenched galaxies at the same or lower redshifts, e.g. stellar mass, density, and sizes, but forming stars at rates 2-10x higher. We measure resolved kinematics of ~30 of these galaxies within the KMOS^{3D} survey. Our results, **the first resolved spectral data of such objects**, show that compact SFGs are rotationally-dominated systems, providing strong evidence that recently quenched galaxies at these epochs are likely to be "fast rotators". The majority of compact SFGs show evidence that they host an active galactic nucleus indicative of secular quenching processes.

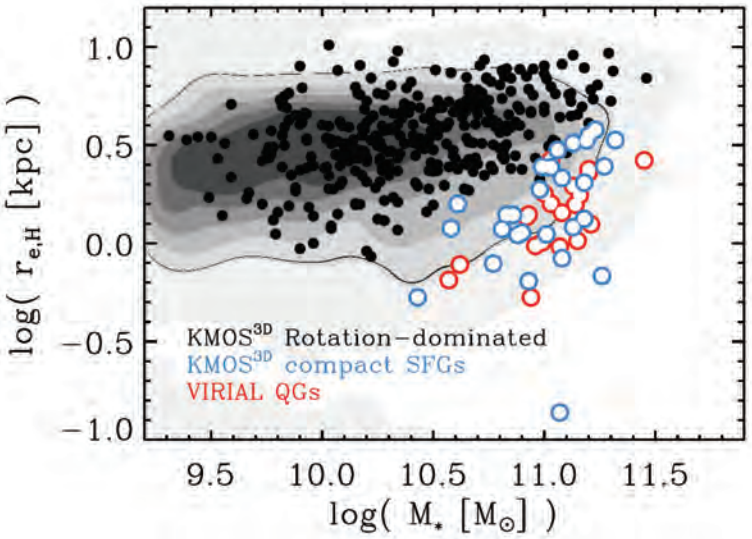

Figure 1: Galaxy size (r_e) vs. Mass (M_*) for 0.7<z<2.7 galaxies showing the underlying galaxy population (gray contours) extended (black) and compact (blue) KMOS^{3D} galaxies and quiescent VIRIAL galaxies (red; the GTO counterpart program targeting passive galaxies - see Mendel et al. poster). The compact SFGs are offset from the general SFG population to high masses at small sizes. They are more comparable to quiescent galaxies at z~1.4-2.0.

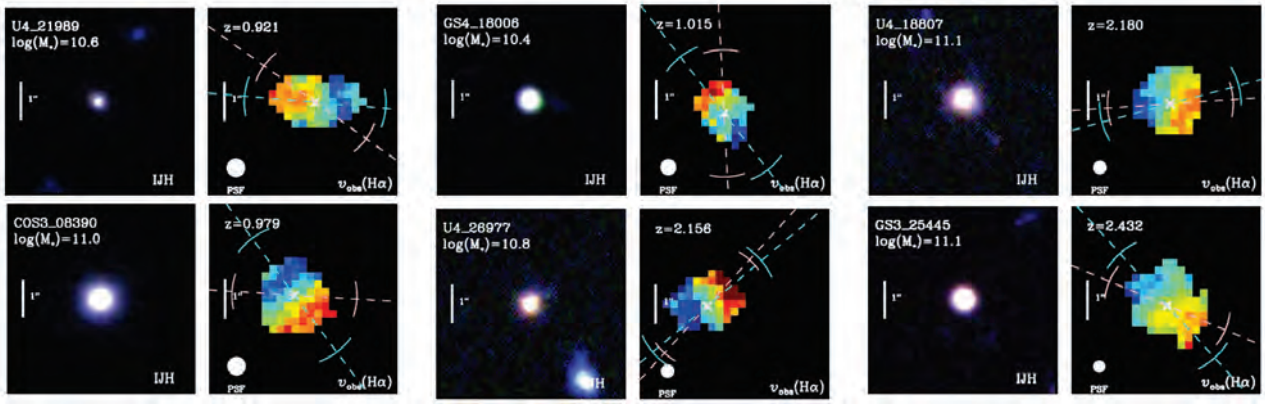

Figure 2: HST composite color images (left) and KMOS derived velocity fields (right) of 6 compact star forming galaxies dominated by rotational motions from z=0.9-2.5.

References: Wisnioski et al. 2015, ApJ, 799, 209; Barro et al. 2013, ApJ, 765, 104; Belli et al. 2015, ApJ, 799; Newman et al. 2015, ApJL, 813, 7; Emsellem et al. 2007, 379, 401; Mendel et al. 2015, ApJL, 804, 4.

E. Wisnioski, J. T. Mendel, N. M. Förster Schreiber, R. Genzel and the KMOS^{3D} Team

Deep Spectroscopy of High-Redshift Quiescent Galaxies

Our understanding of gas-poor quiescent galaxies relies on the study of absorption lines, which are much more difficult to observe than emission lines. In order to explore the quiescent population at high redshift, we collected deep Keck spectra for a large sample of passive galaxies at z > 1 and derived important constraints on their dynamics, stellar populations, and size evolution.

Taking advantage of the recent development in near-infrared detectors, we collected the largest sample of deep spectroscopic observations of quiescent galaxies at z > 1 using the Keck I telescope. Combining the wavelength coverage of the LRIS instrument with that of the new MOSFIRE spectrograph, we are able to target the same rest-frame spectral region for galaxies in the redshift range 1 < z < 2.5. These spectra show important features such as the 4000A break, Balmer and Calcium absorption lines. On the right, a few of the MOSFIRE spectra at z~2 are shown.

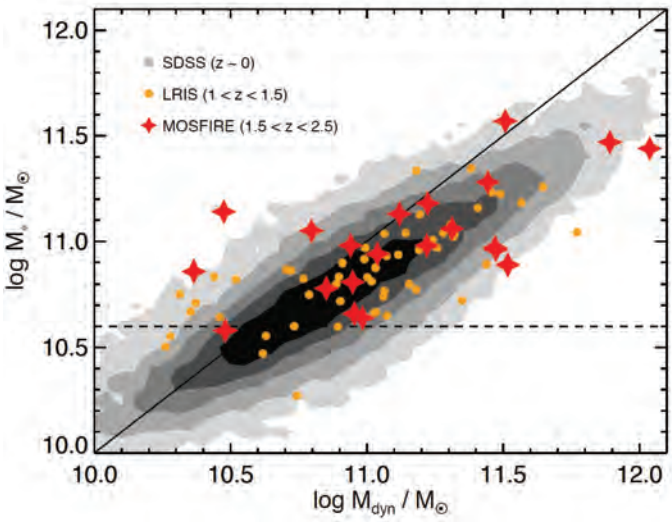

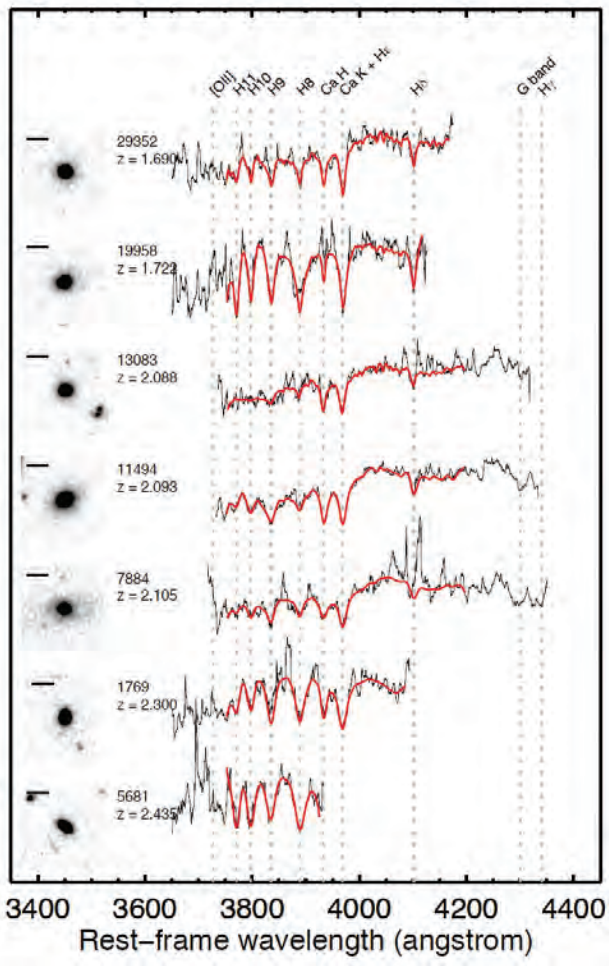

Such rich spectroscopic dataset allows us to derive important measurements, including the kinematics and stellar population properties. In particular, by measuring the velocity dispersions we can calculate the dynamical masses and compare them with the stellar masses derived from broad-band photometry (see figure on the left). Despite the fact that high redshift quiescent galaxies are significantly smaller than the local population, their dynamical and stellar masses are in excellent agreement with the values found at z~0. This represents an important constraint on the evolution of initial mass function, dark matter fraction, and galaxy structure. We also investigate the size evolution of quiescent galaxies and conclude that their growth is consistent with being caused by minor mergers.

References:

• Belli, S., Newman, A. B. & Ellis, R. S, in prep.
• Belli, S., Newman, A. B. & Ellis, R. S. 2015, ApJ, 799, 206
• Belli, S., et al. 2014, ApJL, 788, 29
• Belli, S., Newman, A. B. & Ellis, R. S. 2014, ApJ, 783, 117

S. Belli

The evolution of metallicity and metallicity gradients at z~0.6 – 2.7 from KMOS^{3D}

The metal content of galaxies and its spatial distribution provide important constraints on the interplay between gas accretion through cosmic inflow and mergers, star formation, and outflows driven by stellar and AGN feedback. We consistently use the [NII]λ6584/Hα ratio as probe of the gas-phase oxygen abundance over a wide redshift range z=0.6-2.7. We derive statistically robust mass-metallicity relationships using over 400 galaxies representative of the bulk of the star-forming population, from our KMOS^{3D} and SINS/zC-SINF surveys with KMOS and SINFONI at the VLT, and LUCI sample at the LBT. We find no significant dependence of the inferred metallicity on star formation rate (SFR) at fixed redshift and mass; this result, most significant for the *z*~1 sub-sample, is in contrast to findings at *z*~0 that led to the proposed "fundamental metallicity relation" whereby lower metallicities in high *z* galaxies would result naturally from their elevated SFRs. With the spatially-resolved KMOS^{3D} and SINS/zC-SINF data, we derived abundance gradients in ~200 galaxies, tripling current literature samples. The gradients are on average flat, with only ~10% of them having a slope significantly offset from zero even when accounting for beam smearing. Given that most of the galaxies show no sign of interaction/ merging, these results suggest efficient metal mixing mediated by strong outflows (as predicted by cosmological simulations, and observed in a majority of our sample); alternatively, shocks and ionization effects could contribute to mimick flat line ratio gradients.

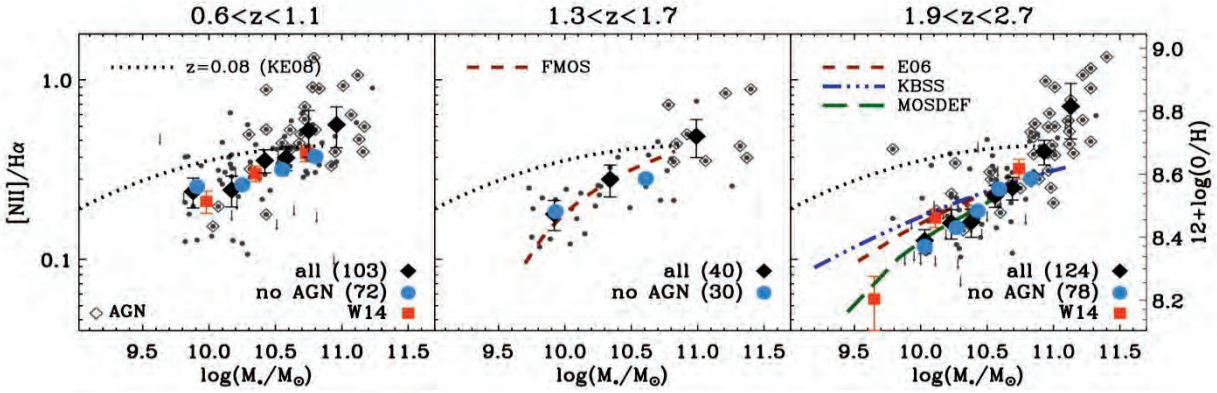

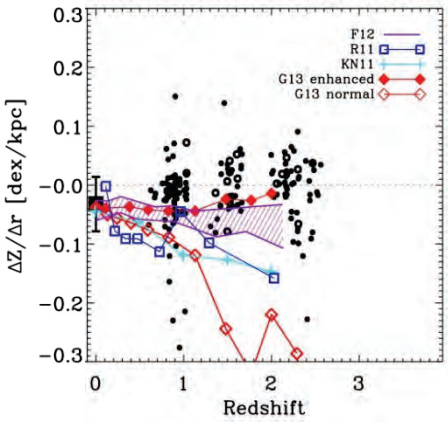

Top: Mass-metallicity relationship in three redshift bins from the integrated [NII]/Hα ratio of star-forming galaxies from KMOS^{3D} (black and blue symbols) and SINS/zC-SINF+LUCI (orange symbols); excluding galaxies with an AGN (shown with diamonds) reduces the sensitivity at high masses but otherwise results in similar relationships.
Left: Metallicity gradients from resolved [NII]/Hα radial profiles from KMOS^{3D} (black symbols) are on average flat (as found in previous studies with much smaller and more biased samples) and consistent with theoretical predictions (colored lines) from simulations when strong feedback is involved.

References: • Wuyts, E., et al. 2014, ApJ, 789, L40 • Wuyts, E., et al. 2016, ApJ, subm. (arXiv:1603.01139)

E. Wuyts, E. Wisnioski, N. M. Förster Schreiber
& the KMOS^{3D}+SINS/zC-SINF Teams

The mass budget in early star-forming disks

We exploit deep integral-field spectroscopic observations with KMOS/VLT of 240 star-forming disks at $0.6 < z < 2.6$ to dynamically constrain their mass budget. Our sample consists of massive ($\gtrsim 10^{9.8}$ $M_\odot$) galaxies with sizes $R_e \gtrsim 2$ kpc. By contrasting the observed velocity and velocity dispersion profiles to dynamical models, we find that on average the stellar content contributes a third, and the total (stellar + gas) baryonic content two thirds of the dynamical mass budget. Nearly all disks at $z > 2$ are strongly baryon-dominated within R_e. Substantial object-to-object variations in both stellar and baryonic mass fractions are observed, correlating most strongly with measures of surface density. Our findings can be interpreted as more extended disks probing further (and more compact disks probing less far) into the dark matter halos that host them.

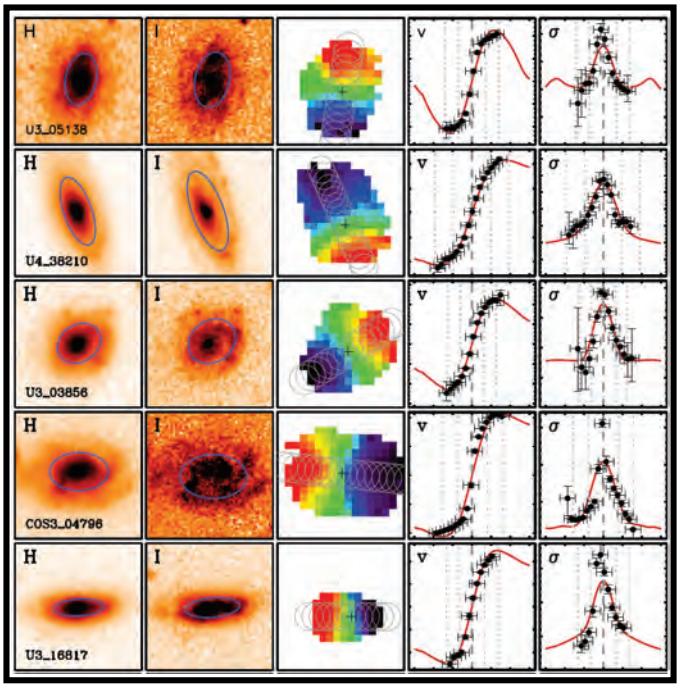

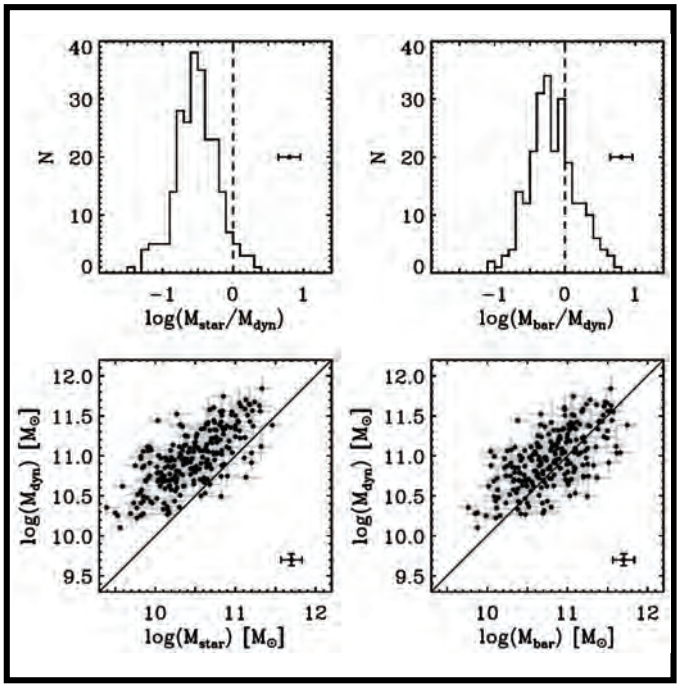

Left: HST postage stamps, KMOS velocity fields, velocity and velocity dispersion profiles for 5 galaxies in our sample. Using the structural information provided by HST, we carry out a forward modeling of the disk dynamics, accounting for pressure support, inclination and beam smearing, leaving the dynamical mass and floor of the dispersion profile as only free parameters.

Top right: Comparison of stellar and dynamical mass, and baryonic and dynamical mass. Here, the baryonic mass estimate accounts for the stellar content as well as molecular gas inferred from state-of-the-art scaling relations based on CO and dust observations.

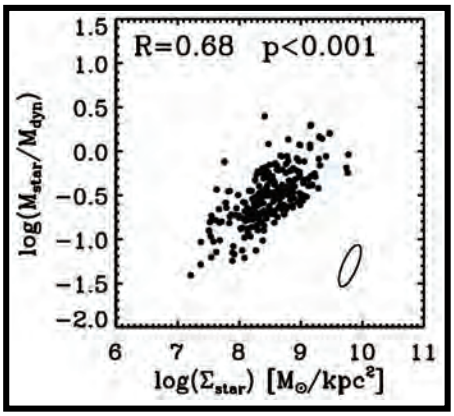

Bottom right: Stellar mass fractions correlate with stellar surface density. A qualitatively similar relation follows from the self-consistent modeling of stars, gas and dark matter in a ΛCDM context by the Illustris cosmological hydrodynamical simulation.

References:

• Wuyts, S., Förster Schreiber, N. M., Wisnioski, E., et al. 2016 (arXiv1603.03432)

S. Wuyts, N. M. Förster Schreiber, E. Wisnioski & KMOS^{3D} team

PHIBSS2: Evolution of Gas from z~2.5 - 0

PHIBSS2 is a comprehensive and systematic CO J=3-2 or 2-1 line survey of ~200 near "main sequence" star forming galaxies (SFGs) during the epochs that are associated with the rapid build-up (z>2), peak, and subsequent winding down (z<1) of star formation in the Universe. One important project from the survey is to develop the first molecular gas scaling relations of main sequence SFGs from z=0-3. Taking PHIBSS together with the low-z COLDGASS survey and other published high-z CO measurements, CO based gas mass estimates are available for >500 SFGs. We combine these data with gas masses derived from Herschel dust measurements in 512 galaxy stacks over the same stellar mass/redshift range to derive scaling relations of molecular gas depletion time (t_{depl}) and gas fraction (M_{molgas}/M_*) of SFGs near the 'main-sequence' with redshift, specific star formation rate (*sSFR*) and stellar mass (M_*) (see below). A steep redshift dependence of $M_{molgas}/M_* \propto (1+z)^3$ mirrors that of the *sSFR* and probably reflects the gas supply rate. Decreasing gas fractions at high M_* are driven by the flattening of the *SFR*-M_* relation. We find that t_{depl} scales as $(1+z)^{-0.3} \times (sSFR/sSFR(ms,z,M_*))^{-0.5}$, with little dependence on M_*. Throughout the redshift range probed a larger *sSFR* at constant M_* is due to a combination of an increasing gas fraction and a decreasing t_{depl}.

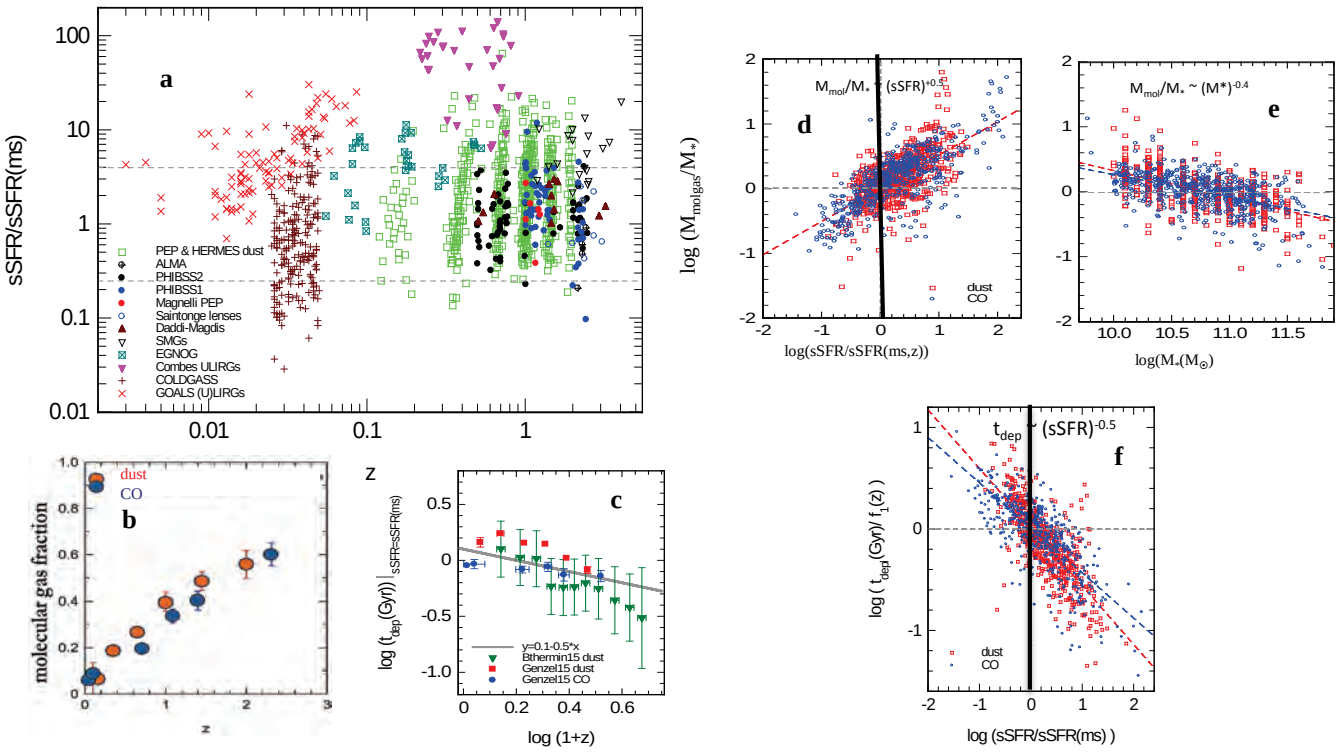

Fig1. **(a)** Distribution in the redshift –specific star formation rate plane of the >1000 SFGs CO- or dust-based gas mass estimates. Colors indicate the data sources. **(b) & (c)** Evolution of molecular gas fraction (b) and depletion time (c) with redshift for CO and dust based gas masses. **(d) & (e)** Scaling relations of M_{gas}/M_* with normalized sSFR (d) and stellar mass (e), after fitting for the redshift dependence, for CO and dust based gas masses. **(f)** The scaling relation of gas depletion time with normalized sSFR, after fitting for the redshift dependence, for CO and dust based gas masses. The black vertical line in (d) and (f) indicates the normalized main sequence mid-line.

References:

• Genzel, Tacconi, Lutz et al. 2015, ApJ, 800, 20

• Tacconi, Neri, Genzel et al. 2013, ApJ, 768, 74

L. Tacconi, R. Genzel, D. Lutz, S. Berta, M. Lippa and the PHIBSS2 team

The fuel of Star Formation in high redshift galaxies

We have derived gas masses of z=0-2.5 galaxies from dust masses based on the deepest *Herschel* extragalactic surveys (PEP, HerMES, GOODS-H), as well as from our largest collection of 500 CO detections (PHIBSS1/2, COLDGASS). Between these two methods, we find good consistency of the scaling relations of molecular gas depletion timescale (τ_{dep}) of star forming galaxies as a function of redshift (z), stellar mass (M^*) and specific star formation rate (sSFR). With Monte Carlo mock catalogs we explored the robustness of dust and gas mass estimates based on fitting far-infrared spectral energy distributions with state of the art Draine & Li (2007) dust models.

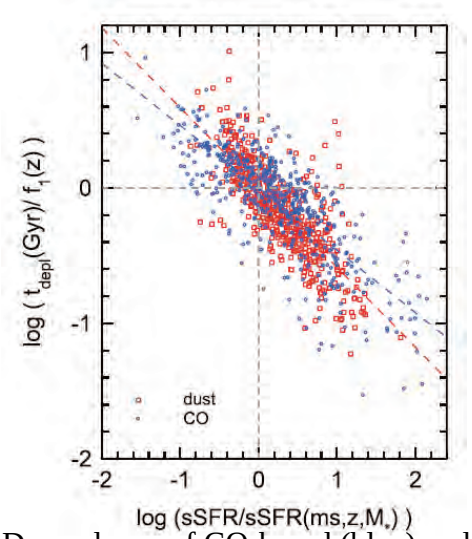

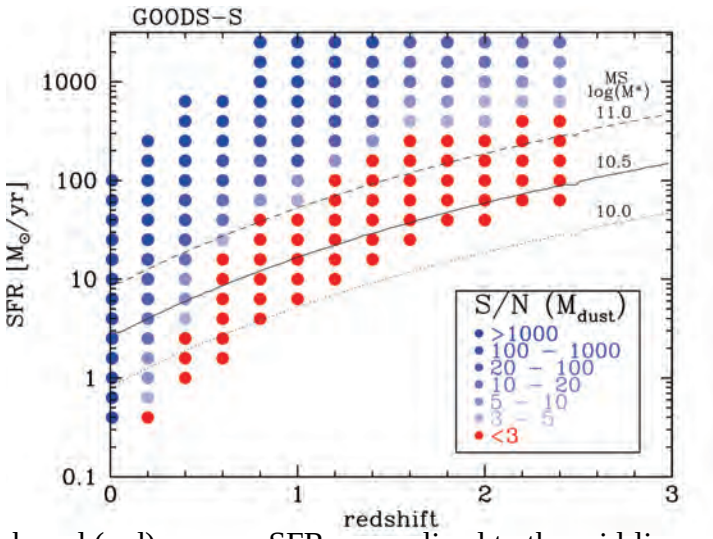

Left: Dependence of CO-based (blue) and dust-based (red) τ_{dep} on sSFR, normalized to the mid-line of the main sequence (MS) at each redshift. The slow redshift dependence of τ_{dep} has been removed. **Right:** signal to noise ratio of M_{dust} based on SED fitting to the deepest *Herschel* data.

In the (z, M*, sSFR) space, τ_{dep} can be expressed as the combination of three terms:

$$\log(\tau_{dep}) = 0.13 - 0.37 \times \log(1+z) - 0.43 \times \log(sSFR/sSFR_{MS}) + 0.10 \times (\log(M^*) - 10.5)$$

Gas masses are obtained either from scaling of SFR through τ_{dep}, or from SED-based M_{dust} scaled using the dependence of gas/dust mass ratio (δ_{GDR}) on metallicity. Our analysis showed that:

- Dust- and τ_{dep}-based M_{gas} determinations are consistent to each other and with CO-based estimates.
- The δ_{GDR} of z>1 star forming galaxies depends on metallicity in a similar way as for local galaxies.
- Far-IR SED fitting recovers dust mass to a >3σ accuracy and without systematics if the wavelength coverage offered by the data extends at least up to 160-200 μm (rest frame).
- Using mid- and far-IR data alone, M_{dust} is retrieved with a S/N>3 for z~1 galaxies on the MS only down to $M^* \sim 10^{11}\ M_\odot$, even in the deepest *Herschel* fields. Stacking allows to reach below the MS.
- Combining Herschel far-IR and ALMA sub-mm continuum observations it is possible to reduce the uncertainties on M_{dust} to <30% for virtually all *Herschel*-detected galaxies in GOODS-S up to z~2.

References:

•Berta et al., 2016, A&A, 587, A73. •Genzel et al., 2015, ApJ, 800, 20. •Tacconi et al., 2013, ApJ, 768, 74.
•Draine & Li, 2007, ApJ, 657, 810. •Magnelli et al., 2014, A&A, 561, A86.

S. Berta, R. Genzel, L. Tacconi, D. Lutz, PHIBSS Team, PEP Team

ALMA: Rapid formation of a central dense core in massive galaxies at z~2

We present 1 kpc resolution ALMA observations at 870 μm for 25 massive galaxies on the star formation main sequence at z~2. The 870 μm emission is preferentially detected in massive, actively star-forming galaxies and their rest-frame 850 μm luminosities are well correlated with gas masses derived from the scaling relation in the M_*-ΔSFR_{MS} plane at the given redshift (offset from the main-sequence). The high-resolution maps reveal that the dust continuum emission is mostly radiated from a single region close to the galaxy center rather than multiple components like star-forming clumps in disks. Exploiting the visibility data taken at large uv distances, we measure the half light radii of the rest-frame far-infrared emission and compare these with the sizes in WFC3/H_{160}-band and stellar mass maps derived from spatially resolved stellar population modeling. About half of the massive galaxies with log ($M_*/M_\odot$)>10.9 have compact dust emission with FWHM<0.3 arcsec (R_e~1.2 kpc), which is smaller by a factor of 2-3 than the rest-optical and the stellar size.

Given their extremely high SFR surface densities within a central 1 kpc radius, the compact starburst can rapidly build up a dense core with log ($\Sigma_{1kpc}/M_\odot$ kpc^{-2})>10 in only a few hundred Myr. Our results are consistent with an evolutionary scenario from extended star-forming disks to compact galaxies.

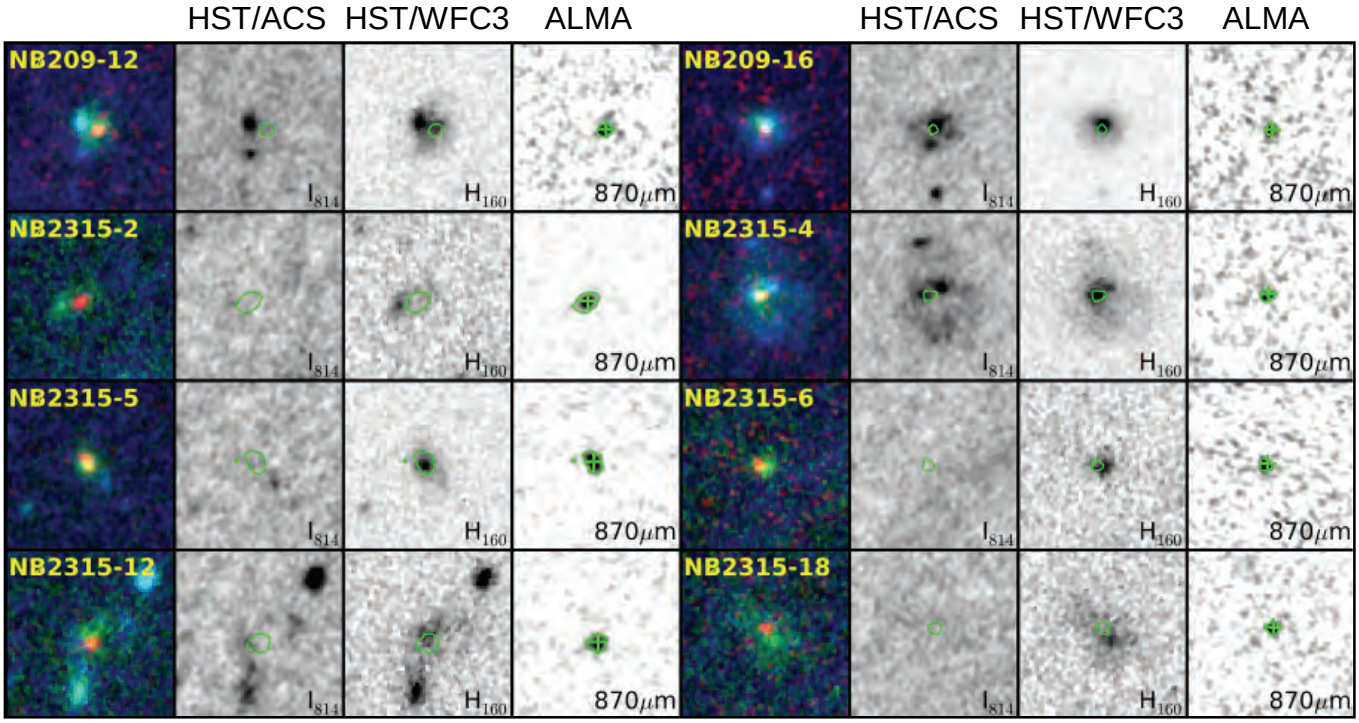

ALMA and HST color composite images for massive galaxies on/around the main-sequence at z~2. A green contour and cross indicate 4σ in ALMA/870μm maps and its center position, respectively.

References:
• Tadaki, K., et al. 2015, ApJ, 811, L3

K. Tadaki, R. Genzel, S. Wuyts, P. Lang and the KMOS^{3D}/PEP team

Spatially resolved molecular gas and stellar properties of massive SFGs at z≈1

We analyze spatially resolved observations of six massive star-forming galaxies (SFGs), namely CO-imaging spectroscopy from PHIBSS as a tracer of molecular gas and HST V-I-J-H photometry (rest-frame UV/optical/NIR) representing young and older stellar populations. This rich data set allows a unique insight into sub-galactic scales around the peak of cosmic star formation at redshifts z≈1. *One of our recent findings is that* ***fitting the stellar mass (M_*) distribution derived from the photometry recovers the position angle (PA) as determined from the CO kinematics*** *more reliably than fitting the individual HST brightness distributions.*

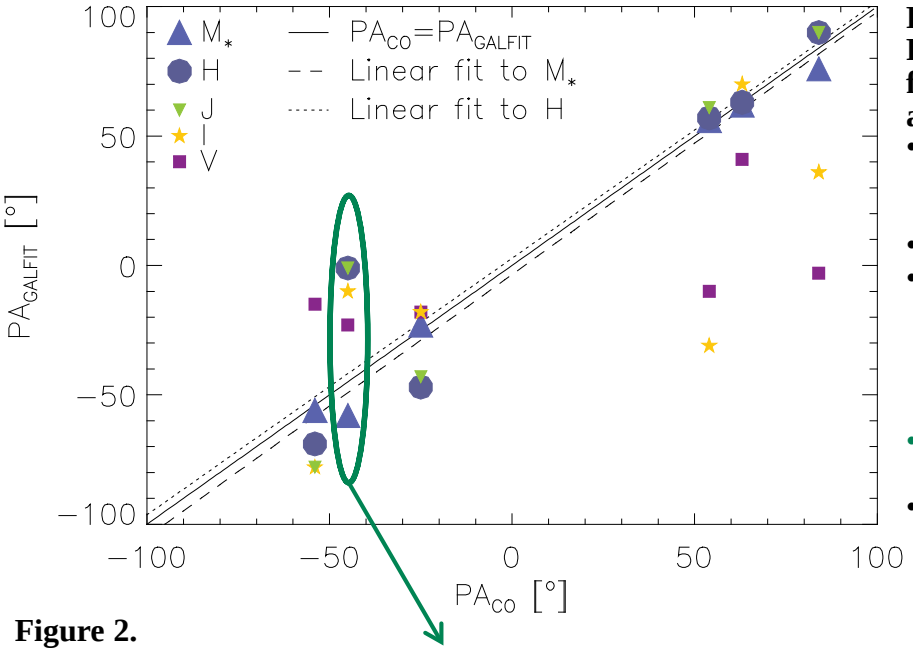

Figure 1.
PAs from exponential-disk fitting with GALFIT plotted against the kinematic PA_{CO}:

- on average PA_M and PA_H best proxies if no kinematic information available
- PA_J slightly worse than PA_H
- PA_V and PA_I bad because biased towards clumps of young star formation sites outside of the central stellar mass peak
- ***PA_M for individual objects never off by more than 13°***
- PA_H fails for the source EGS13004291 by 44° (details demonstrated below)

Figure 2.
"Worst-case" example of EGS13004291 at z=1.20 (from left to right):
CO 3-2 map with colors that show blue- to redshifted velocities, HST V-I-H photometry in blue-green-red and M_*-distribution in colors with the GALFIT model in white contours. The black crosses mark peaks of the underlying colored quantities and the lines correspond to the derived PAs.

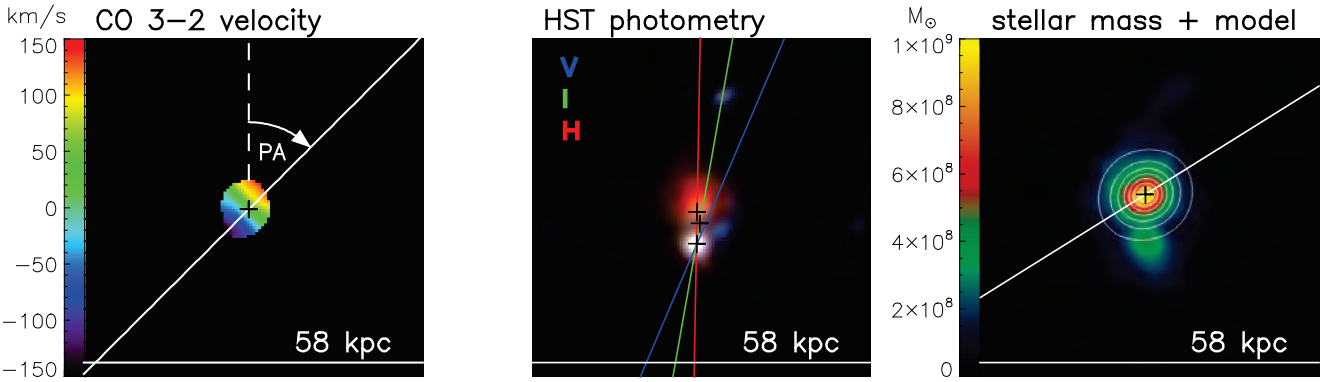

References:
- Tacconi et al. 2013, ApJ, 768, 74
- Genzel et al. 2013, ApJ, 773, 68
- Wuyts et al. 2013, ApJ, 779, 135

M. Lippa, L. Tacconi, R. Genzel, S. Wuyts, P. Lang and the PHIBSS team

High-z outflows with SINS/zC-SINF and KMOS^{3D}

Galactic outflows are known to play a critical role in the regulation of galaxy growth. The spatially resolved observations of star-forming galaxies at z ~ 1-3 from our SINS/zC-SINF and KMOS^{3D} surveys uncover the existence of nuclear outflows in the majority (2/3) of galaxies with stellar masses above $\log(M_*/M_\odot) \sim 10.8$. Whilst only about half of our sources are classified as AGN through independent diagnostics, the ubiquitous presence of broad emission in Hα, [NII], and [SII] with FWHMs of 500-2000 km/s and elevated [NII]/Hα ratios of ≥ 0.5 in the central few kpc of these massive galaxies indicates a high duty cycle that exceeds that of detectable AGN. Furthermore, we have been able to pin down the roots of star formation-driven outflows with mass loading factors around unity through the detection of broad Hα+[NII] emission (FWHM ~ 450 km/s) from star-forming clumps throughout the galactic disks at all galaxy masses. Our findings thus emphasize the importance of AGN as well as stellar feedback for the evolution of galaxies during the peak epoch of cosmic star formation history.

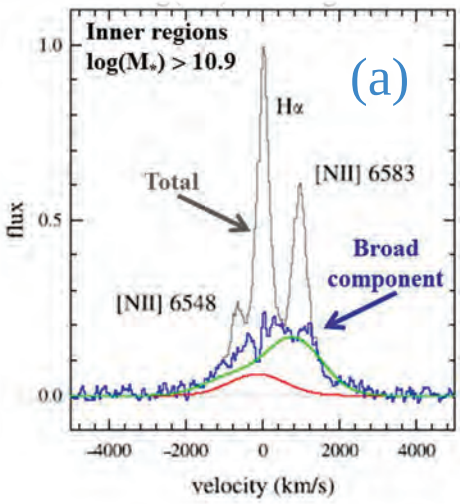

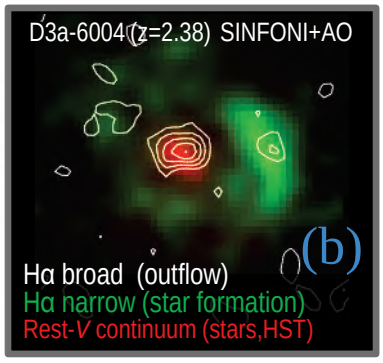

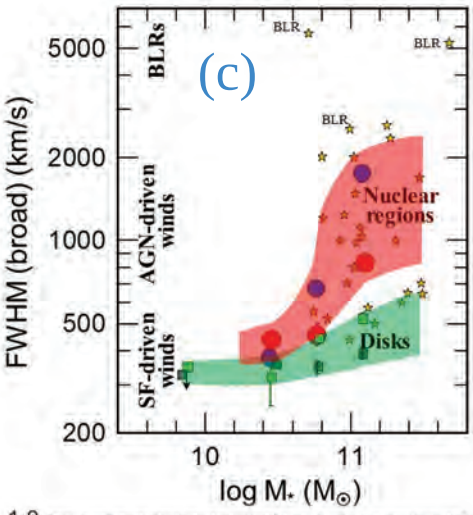

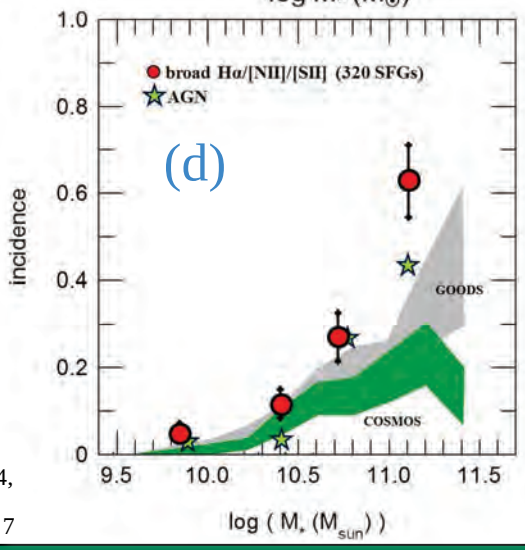

Broad nuclear emission is detected in **co-added** (a) as well as in **individual** (b) spectra of **massive galaxies**. The fairly **sharp onset** of broad nuclear emission with FWHMs of 500-2000 km/s **above $\log(M_*/M_\odot)$~10.8** (c, red region) is seen in 2/3 of our nuclear spectra (d). Broad emission with more modest velocity widths is **also detected in the outer disk spectra** (c, green region) at all galaxy masses.

References:

- Genzel, R., et al. 2011, ApJ, 733, 101
- Newman, S.F., et al. 2012a, ApJ, 752, 111
- Newman, S.F., et al. 2012b, ApJ, 761, 43
- Förster Schreiber, N.M., et al. 2014, ApJ, 787, 38
- Genzel, R., et al. 2014b, ApJ, 796, 7

H. Übler, R. Genzel, N. M. Förster Schreiber & the SINS/zC-SINF+KMOS^{3D} Teams

Unsynchronized coevolution of black hole accretion and star formation: Herschel results

We have combined the Herschel-PACS PEP far-infrared survey with X-ray surveys to study from different perspectives the relation of star formation and black hole accretion in galaxies up to z~2.5. On one hand, the average accretion in a galaxy population correlates well with star formation, even better than with stellar mass. On the other hand, there is little correlation of star formation with instantaneous accretion. While star formation and accretion seem to be connected and typically fed by the gas reservoir of main-sequence galaxies, this long term link is washed out by the rapid short term black hole accretion variations

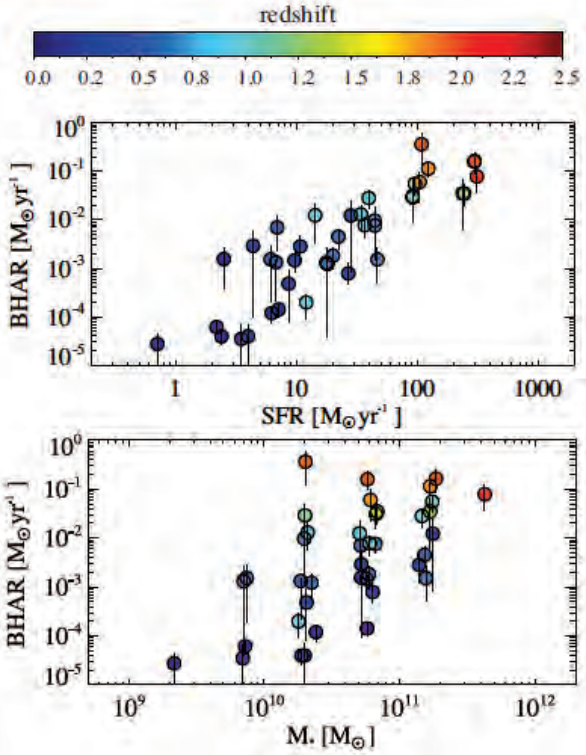

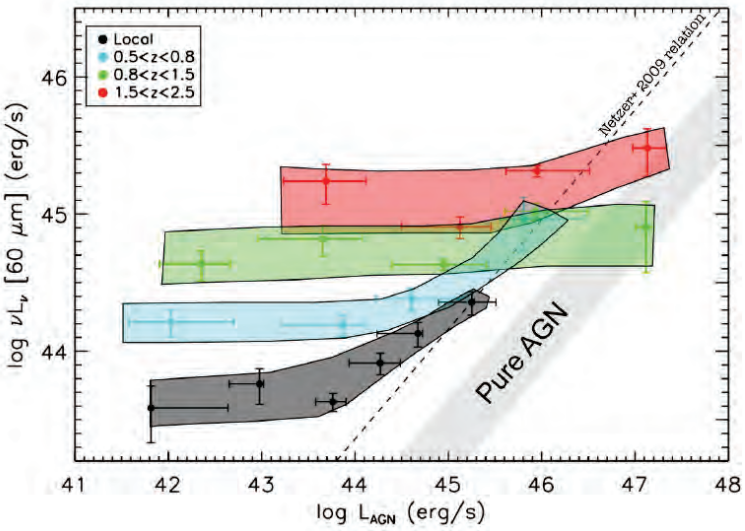

Left: **Average black hole accretion** for galaxy samples in bins defined by redshift, stellar mass, and SFR. Right: Average L_{IR}~SFR for galaxies of given **instantaneous black hole accretion**.

In a series of papers, we have used our deep Herschel-PACS PEP survey and Chandra and XMM surveys to shed light on the coevolution of AGN and their hosts. The main findings are:

- For samples of AGN hosts, there is little correlation between current AGN luminosity and average host SFR, with the exception of the most luminous AGN at z~0.
- Average SFRs of AGN hosts are similar to mass-matched main sequence galaxies at same redshift.
- About half of the hosts are individually detected in the deepest Herschel data reaching to the main sequence. The remainder may include slightly less star forming as well as truly quenched objects.
- Taking a reverse view, average accretion in bins of z, M*, SFR, is found to correlate with both SFR and M* (which are linked via the main sequence), with a somewhat tighter link to SFR.

This suggests that in the long term, both SFR and accretion are linked to the galaxy‘s cold gas supply, which is now independently measured to be larger at the z~1-2 „cosmic noon“. But the rapid variation of AGN accretion compared to the >Myr timescales sampled by star formation indicators obscures this link when analyzing instantaneous measurements – a situation of „unsynchronized coevolution“.

References:

• Rosario, D.J., Santini, P., Lutz, D., et al. 2012 A&A 545, A45
• Rosario, D.J., Santini, P., Lutz, D., et al. 2013 ApJ 771, 63
• Delvecchio, I., Lutz, D., Berta, S., Rosario, D.J. et al. 2015 MNRAS 449, 373

D. J. Rosario, D. Lutz, S. Berta, I. Delvecchio, PEP team

Stellar populations in the nuclei of AGN

The best current theoretical models for gas inflow to AGN on scales of 1-100pc suggest that star formation plays a key role on these scales: either by injecting turbulence which drives viscosity and hence inflow, or by the direct accretion of slow stellar winds in a post-starburst phase. Observationally the situation is far from clear. While there is some evidence supporting such a link, there are also indications that in some cases no recent star formation occurs in the central region. Our goal is to robustly test the models using our complete volume limited sample of local luminous AGN with matched inactive galaxies (the LLAMA project) by combining an analysis based on fitting stellar populations to high signal-to-noise and high resolution UV/optical Xshooter spectra, with estimates of the mass-to-light ratio from spatially resolved SINFONI data. We are generating fits similar to those below for the full sample.

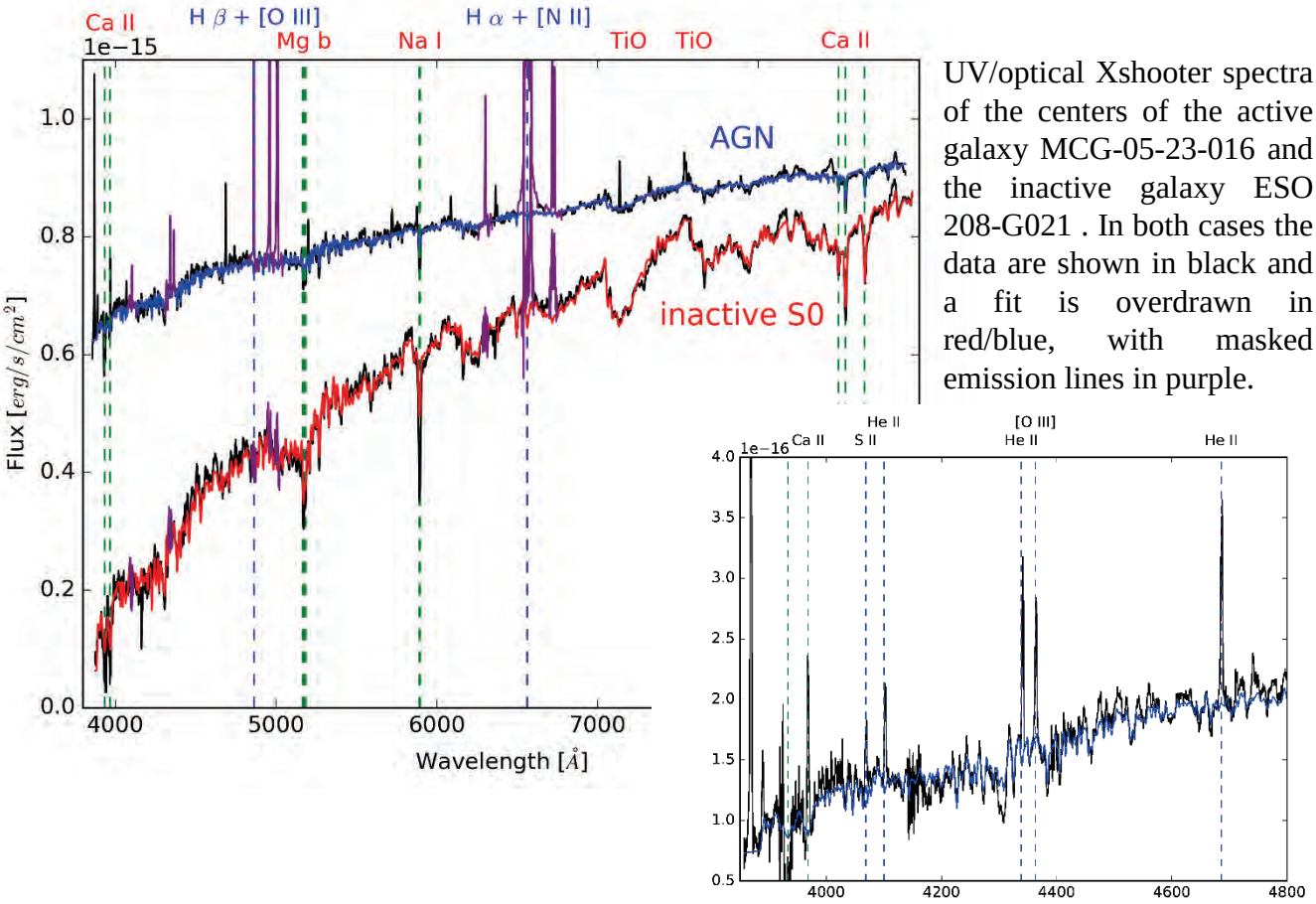

UV/optical Xshooter spectra of the centers of the active galaxy MCG-05-23-016 and the inactive galaxy ESO 208-G021 . In both cases the data are shown in black and a fit is overdrawn in red/blue, with masked emission lines in purple.

The insert of the AGN shows that the fit is a good match to the overall slope and shape, as well as to the exquisite detail of the stellar absorption features. And the high spectral resolution makes it easier to deblend the absorption and emission features. In the inactive galaxy, the entire stellar population is old. In the AGN, it is predominantly old, but there is a small contribution from a younger population.

References:
• Davies, R.I., Burtscher, L. et al., ApJ, 806, 127
• Burtscher, L., Davies, R.I., et al., in prep.

R. I. Davies, L. Burtscher, G. Orban de Xivry, D. Lutz, D. Rosario

Absorption and Obscuration in AGN

Using the largest sample of high-resolution integral field observations of local AGNs we calibrate the colour temperature in the near-infrared as a simple method to constrain the optical obscuration towards the hot dust located at the inner boundary of the dusty torus.

We then compare the optical extinction with X-ray absorption measurements as provided by multi-band multi-epoch spectral modelling including very hard X-ray Swift BAT data. We find that all objects either show a Galactic dust-to-gas ratio or higher. Many objects with relatively higher levels of X-ray absorption have variable absorption suggesting that the excess gas is dust-free neutral gas in the Broad Line Region (BLR) of the AGN.

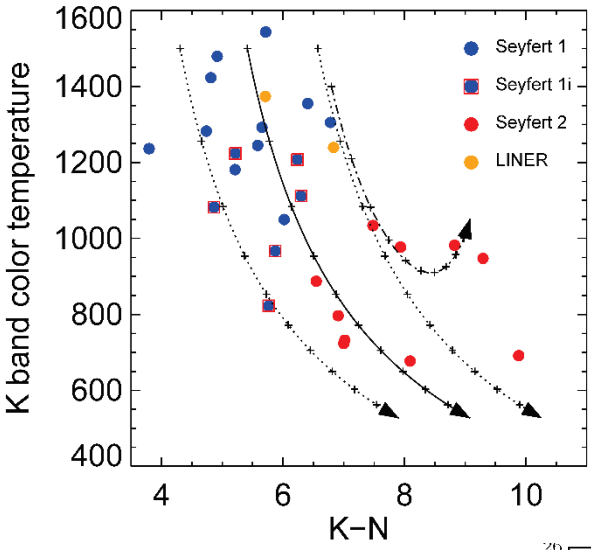

Observed K-band colour temperature versus near-to-mid-infrared colour. The K-band color temperature is derived from a spectral decomposition of the nuclear (~1 arcsec) near-IR light using a stellar template and a blackbody. The near-to-mid-IR colour is derived from sub-arcsecond photometry in the respective bands to isolate the nuclear emission. Unobscured Seyferts (type 1) exhibit high dust temperatures, while Seyferts with intermediate obscuration (type 1i) and those that are fully obscured (type 2) have cooler apparent temperatures and redder colours. This trend can be explained in terms of obscuration.

X-ray absorption vs. optical extinction for the same objects as above for which the X-ray absorption can be determined reliably. All objects have excess gas absorption compared to their optical extinctions (i.e. lie above the thick line representing the Galactic gas-to-dust ratio). This excess absorption is in several cases variable and can thus be attributed to the BLR. This analysis allows us to disentangle where absorption and obscuration occur.

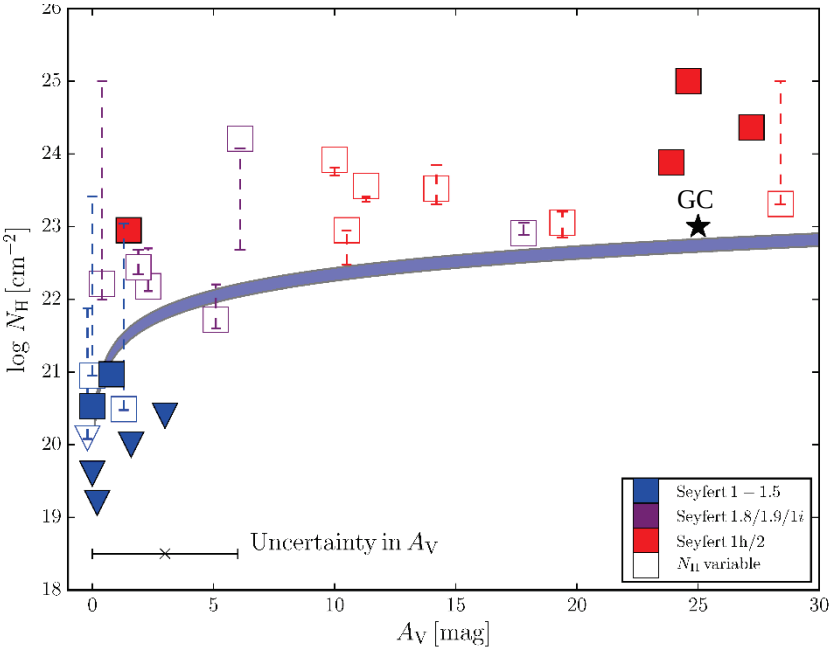

References:
• Burtscher, L., Orban de Xivry, G., Davies, R. et al., 2015, A&A, 578, A47
• Burtscher, L., Davies, R.I., et al., 2016, A&A, 586, A28

L. Burtscher, R. Davies, G. Orban de Xivry, D. Lutz, D. Rosario, et al.

Dense Gas in Seyferts: Disks and Outflows

Studying the dense molecular gas in the circumnuclear region is crucial to understand active galactic nuclei (AGN) and the co-evolution with their host galaxies. We now have 8 galaxies with 1" resolution HCN data tracing the kinematics of the dense gas structures on scales of <100 pc around nearby AGN. In 7 of these, the emission line kinematics imply there is a thick disk, suggesting such structures are a common occurrence. The relation between the inferred dynamical mass and observed HCN luminosity implies a constant gas fraction and HCN conversion factor. We also find a complex absorption system in NGC 3079, composed of self-absorption as well as narrow and broad continuum absorption. The broad absorption, with a blue wing extending to -350 km s^{-1}, likely traces a nuclear outflow.

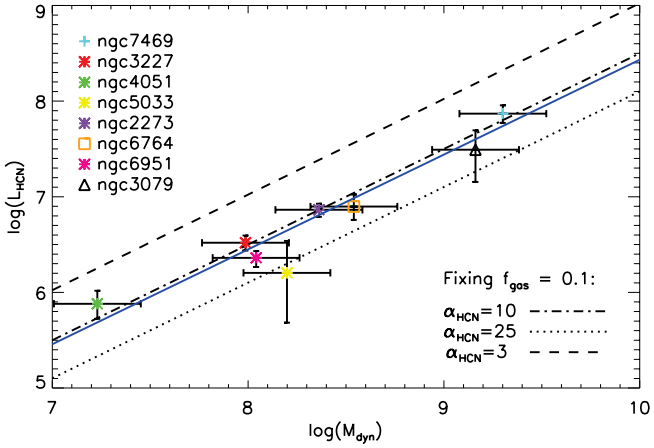

We created disk models to fit the kinematics of the observed data. These show that the nuclear disk is preferentially a **geometrically thick structure**. The inferred dynamical mass and observed HCN luminosity show a strong correlation that can be explained by f_{gas} ~ 0.1 and α_{HCN} ~ 10. The factor ~2 difference to values of α_{HCN} in the literature may imply the excitation close around AGN differs to other environments.

NGC 3079 exhibits complicated line profiles in different molecular species. We find not only line emission from a disk around AGN, but also at least three absorption components:

- Self-absorption in the centre due to gas at large radii in the edge-on disk;
- Narrow absorption due to the cold rotating material, which lies in front of the radio knots.
- Broad absorption induced by a **dense nuclear outflow** with maximum velocity of -350 km s^{-1}.

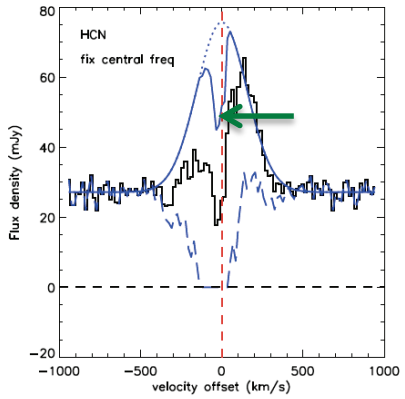

Self-absorption

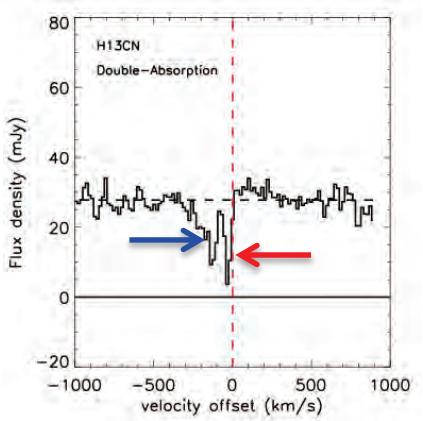

Narrow (nuclear) and
Broad (outflow) absorption

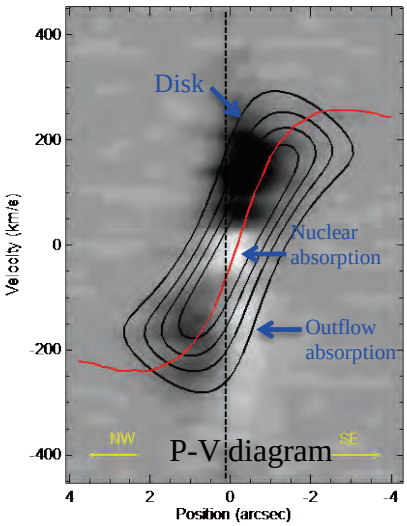

References:
• Lin, M.-Y. et al., 2016, MNRAS 458, 1375

M.-Y. Lin, R. Davies, L. Burtscher, A. Contursi, R. Genzel, J. Graciá-Carpio, D. Lutz, A. Janssen, G. Orban de Xivry, D. Rosario, A. Schnorr-Müller, E. Sturm, L. Tacconi

Massive Molecular Outflows and Feedback in ULIRGs and AGN

Following our discovery of ubiquitous AGN-driven molecular outflows in ultra-luminous galaxies via OH absorption (Sturm et al. 2011) we have been working towards a more holistic view of outflows. We have expanded our OH studies to a sample of ~45 ULIRGs and ~50 BAT AGN and augmented these by mm-observations with NOEMA and ALMA, spatially resolving the outflows in CO emission in ~10 objects. Our main emphasis is now on the multi-phase properties of the outflowing gas. A key aspect of this has been to show that broad wings of the FIR [CII] emission line correlate with the molecular outflows traced by OH in terms of velocity and mass, but also with Na I D in terms of velocity, suggesting that the atomic and molecular gas phases of the outflow are connected.

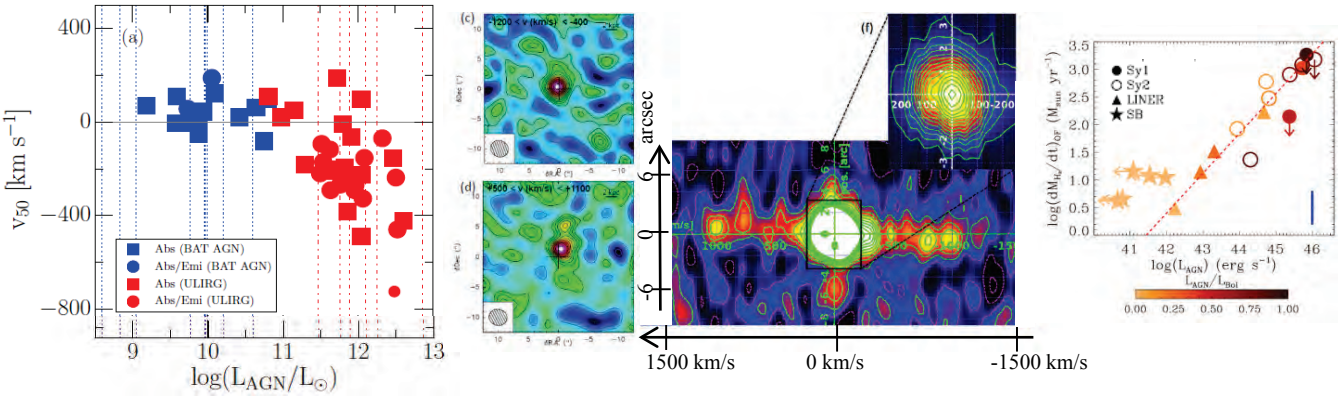

Left: outflow velocity (v_{50}) as a function of the AGN luminosity in a sample of ~100 ULIRGs and BAT AGN (Stone et al.); *Middle:* IRAM-PdBI maps and position–velocity diagram of the CO(1–0) emission line of IRASF08572+3915 (Cicone et al. 2014); *Right:* Outflow mass-loss rate as a function of the AGN bolometric luminosity (Cicone et al. 2014).

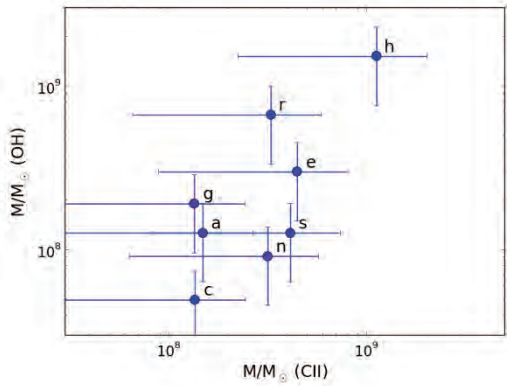

Total molecular outflow mass based on OH line modelling by Gonzalez-Alfonso (in prep.) on the y-axis, and atomic outflow mass based on the luminosity of the [CII] broad component on the x-axis. *Janssen et al.*

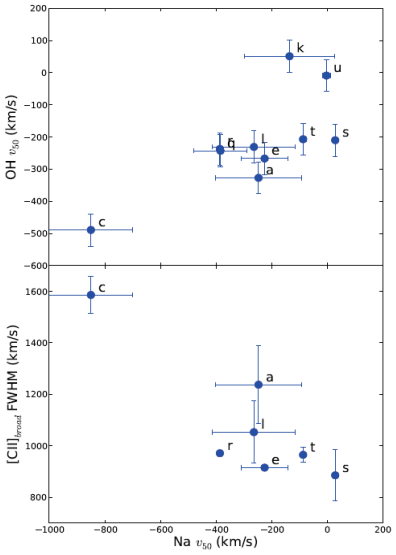

Na I D outflow velocity (v_{50}) compared to OH v_{50} (upper panel) and [CII] FHWM (lower panel). *Janssen et al.*,

References:

• Cicone et al. 2014, A&A, 562, 21 • Gonzalez-Alfonso et al., in preparation • Janssen et al., in press • Stone et al., submitted • Sturm et al. 2011, ApJ, 733, L16 • Veilleux et al. 2013, ApJ, 776, 27

E. Sturm, A. Janssen, A. Contursi, J. Graciá Carpio and the SHINING Team

Molecular outflows traced by broad [CII]

Molecular outflows in ULIRGs carry a lot of mass (~ 10^8 - 10^9 M_{solar} or 10^2 – 10^3 M_{solar}/year), and are therefore important for galaxy evolution. In order to understand how relevant molecular outflows are in normal galaxies and at higher redshifts, we need a good tracer of the outflow. OH outflows are observed in absorption and therefore require a FIR background. CO(1-0) is a good tracer in emission, but shifts out of the ALMA bands at z > 0.4. Broad [CII] wings could be a good alternative.

We study a sample of 22 local (z<1) Ultra Luminous InfraRed Galaxies, of which 16 have a molecular outflow as traced by the ground state transition of OH (119 μm). Most of these objects also show broad wings in the fine structure line [CII] (158 μm; Figure 1).

If the molecular outflows have a large opening angle and [CII] traces the outflow, a relation is expected between the broad [CII] FWHM and the blueshifted velocity of the OH absorption. Moreover, the best line fit to the velocities would go through (0, 0).

This is indeed observed (Figure 2). Moreover, the outflow masses derived from [CII] and OH119 are similar (within a factor 3). We conclude that the [CII] wings trace the molecular outflow.

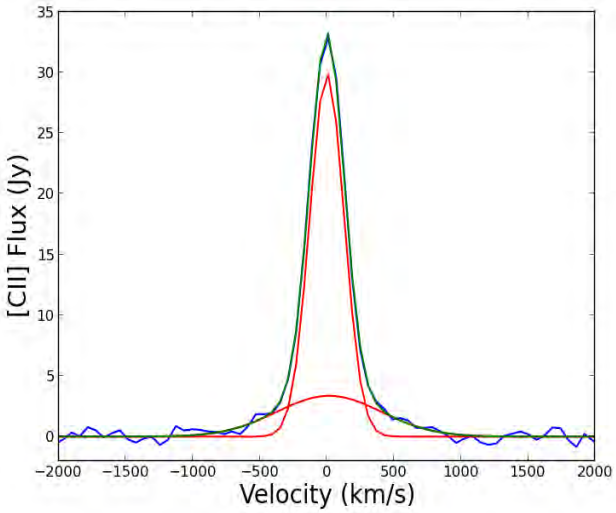

Figure 1: The [CII] line profile of the ULIRG IRAS 10565+2448 has broad wings extending up to ~1000 km/s.

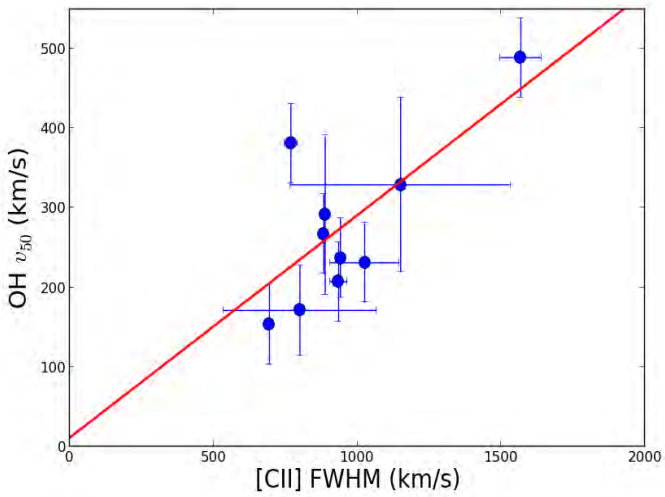

Figure 2: A velocity comparison for all objects with convincing outflows both in OH119 and [CII]. The best fit goes trough (0,0), as is expected if [CII] traces the molecular outflow.

References:
- Janssen et al. 2016 ApJ 822, 43
- Veilleux et al. 2013, ApJ, 776, 27
- Sturm et al. 2011, ApJ, 733, L16

A. Janssen, E. Sturm, N. Christopher, A. Contursi and the SHINING team

Fine structure lines in local infrared galaxies

We use the *Herschel*/PACS spectrometer to study the far-infrared (FIR) line emission of a large sample of local and high-z galaxies that includes star-forming systems, active-galactic nuclei (AGN) and luminous infrared galaxies selected from the SHINING sample (PI Sturm). The ionized carbon, oxygen and nitrogen FIR transitions included in this study allow us to probe the neutral and the ionized gas in the interstellar medium. We find an increasing number of galaxies (and regions within galaxies) with low line to FIR ratios as a function of increasing FIR luminosity (L_{FIR}), dust IR color, L_{FIR} to molecular gas mass ratio (L_{FIR}/M_{mol}), and FIR luminosity surface brightness (Σ_{FIR}). In the case of the [CII] 158 μm transition –a major coolant for the neutral atomic gas– the tightest line deficit relations are found as a function of L_{FIR}/M_{mol} and Σ_{FIR} (although for the latter case the sample is smaller), likely because these parameters are more closely related to the efficiency of the conversion of far-UV radiation into gas heating (Graciá-Carpio et al. 2011; Lutz et al. 2015; Herrera-Camus et al. in prep.).

[CII] line deficit (markers with black borders show the SHINING galaxies)

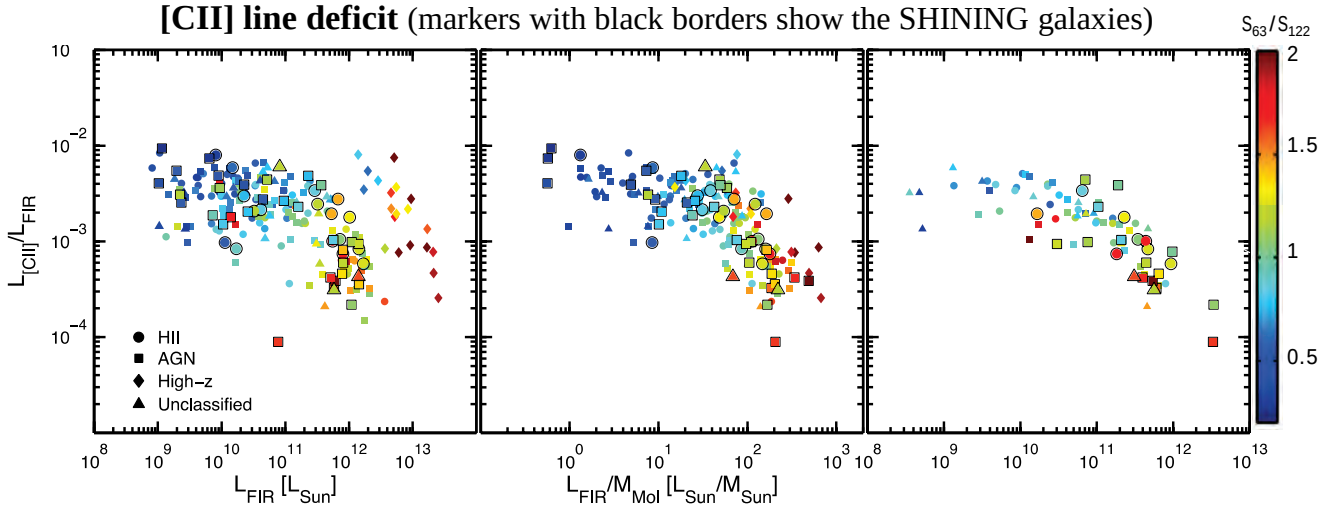

Spatially resolved FIR line deficit in SHINING star-forming (SF) and AGN galaxies

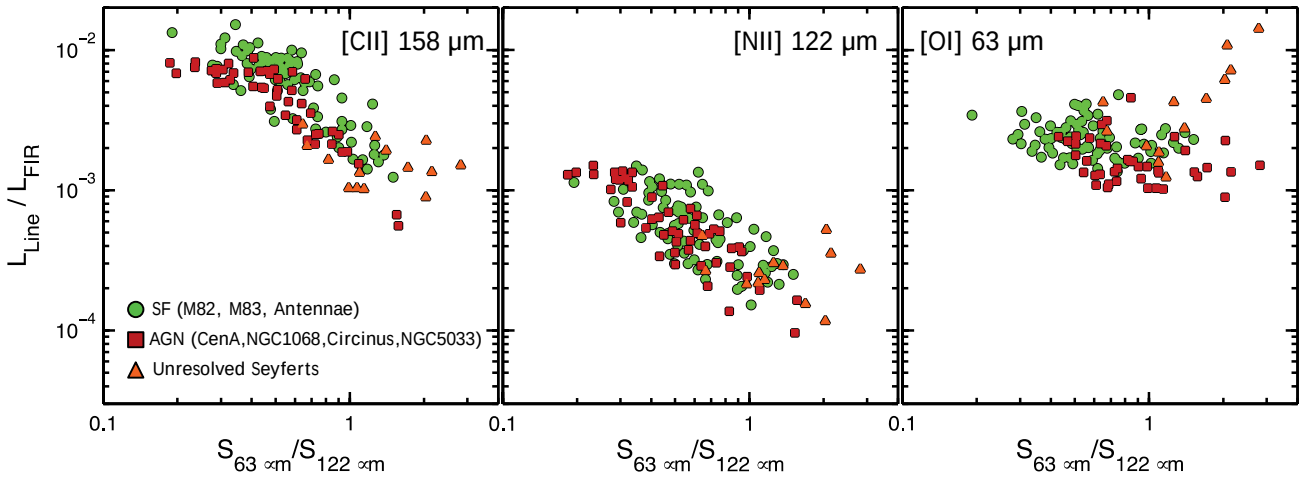

References: •Graciá-Carpio+ 2011, ApJ, 728 • Lutz+2015, arXiv: 1511.02075 • Sturm+. 2011, EAS, 52

R. Herrera-Camus, J. Graciá-Carpio, E. Sturm, D. Lutz, A. Contursi and the SHINING team

The far-infrared emitting region in galaxies and QSOs: Size and scalings

We have used Herschel/PACS data with excellent PSF stability to determine the size of the far-infrared emitting (i.e. star-forming) region in ~400 local galaxies and PG QSOs. FIR size and surface brightness scale with FIR luminosity, distance from the main sequence, and FIR color. Ultraluminous infrared galaxies far above the main sequence inevitably have small high surface brightness FIR emitting regions and can be close to optically thick at these wavelengths. Compared to these local relations, first ALMA sizes for the dust emitting region in high-z galaxies suggest larger size at same IR luminosity. We report a remarkably tight relation with 0.15dex scatter between FIR surface brightness and the [CII]/FIR ratio – the [CII] deficit is more closely linked to surface brightness than to luminosity or color. Hosts of local PG QSOs have similar FIR sizes as normal galaxies, supporting a star formation origin of that emission even in QSO hosts.

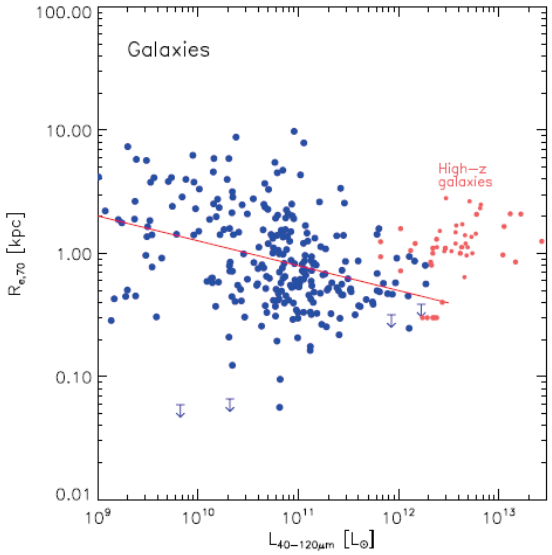

Scaling	Section
Scalings with L_{FIR}:	
$log(R_{e,70}) = 0.101 - 0.202 \times (log(L_{FIR}) - 10)$	4.1
$log(\Sigma_{FIR}) = 8.997 + 1.408 \times (log(L_{FIR}) - 10)$	4.1
$log(\Sigma_{SFR}) = -1.117 + 1.408 \times log(SFR)$	4.1
Scalings with main sequence offset:	
$log(R_{e,70}) = 0.19 - 0.39 \times log(sSFR/sSFR_{MS})$	4.1
$log(\Sigma_{FIR}) = 8.19 + 2.59 \times log(sSFR/sSFR_{MS})$	4.1
$log(\Sigma_{SFR}) = -1.53 + 2.59 \times log(sSFR/sSFR_{MS})$	4.1
Scalings with far-infrared color and dust temperature:	
$log(R_{e,70}) = -0.145 - 1.362 \times log(S_{70}/S_{160})$	4.1
$log(\Sigma_{FIR}) = 10.34 + 5.37 \times log(S_{70}/S_{160})$	4.1
$log(\Sigma_{SFR}) = 0.62 + 5.37 \times log(S_{70}/S_{160})$	4.1
$log(\Sigma_{FIR}) = -22.5 + 21.8 \times log(T_d)$	4.1
Scaling of [CII]/L_{FIR} with far-infrared surface brightness:	
$log(L_{[CII]}/L_{FIR}) = -11.7044 + 2.1676 \times log(\Sigma_{FIR}) - 0.1235 \times (log(\Sigma_{FIR}))^2$	4.3

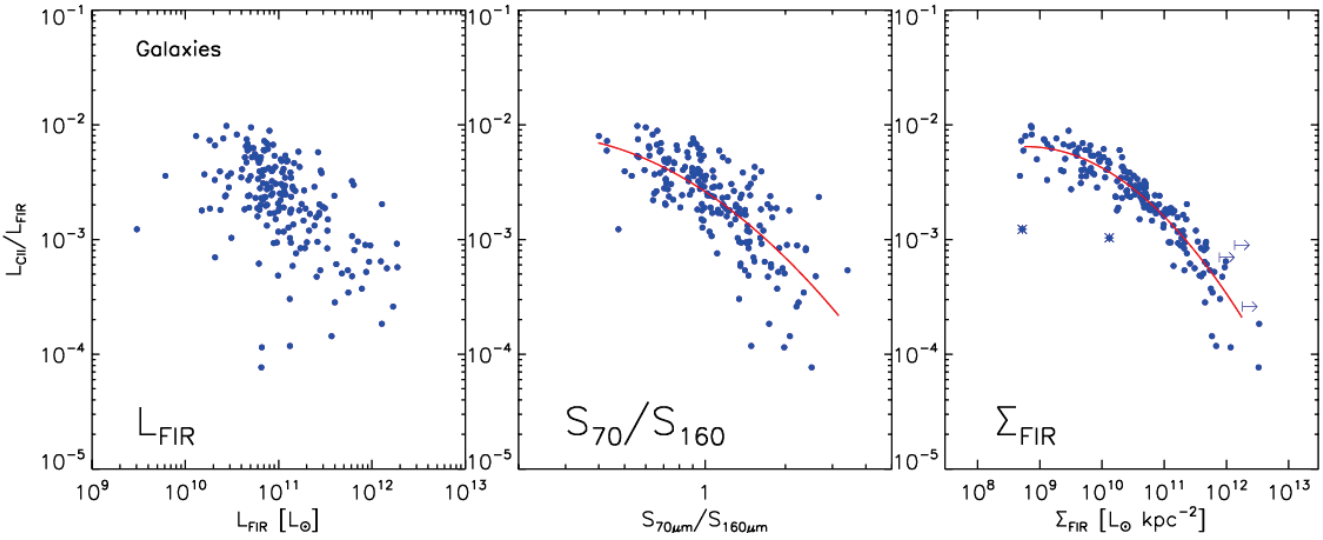

References:

• Lutz, D., et al. 2016 A&A in press (arXiv 1511.02075)

D. Lutz, S. Berta, A. Contursi, J. Gracia Carpio, R. Herrera Camus, E. Sturm, et al.

ISM properties of Lyman Break Analogs (LBAs)

We study the dust, atomic and molecular gas properties of a small sample of *z*~0.2 galaxies selected for being analogs of high redshift main sequence (MS) Star Forming Galaxies (SFGs). Our targets have $L_{IR} \sim 10^{11}\ L_{sol}$ but they have much higher L_{uv}/L_{IR} ratio than LIRGs. They lie above the local MS. However, their ISM properties are more similar to those of high *z* MS SFGs than to those of galaxies above the the local MS. This sample serves as reference for the upcoming [CII] ALMA observations of high z SFGs.

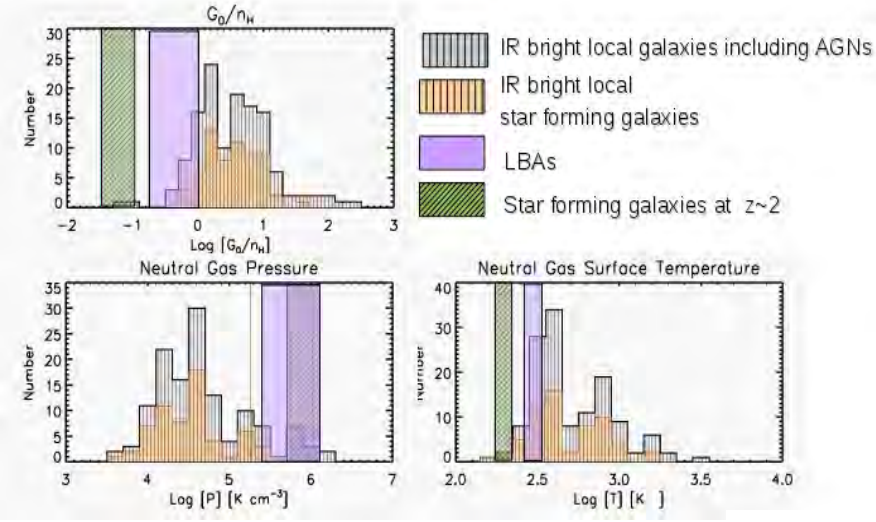

Figure 1

We model the [CII]], [OI] and the FIR continuum emission observed with ***Herschel-PACS***. We find that the atomic medium conditions in LBAs are extreme if compared with those of local SFGs: they have higher P, lower T_{gas}, and G_0/n_{gas} ratio. On the other hand, these values agree with those found in a sample of z~2 SFGs (Brisbin et al. 2015).

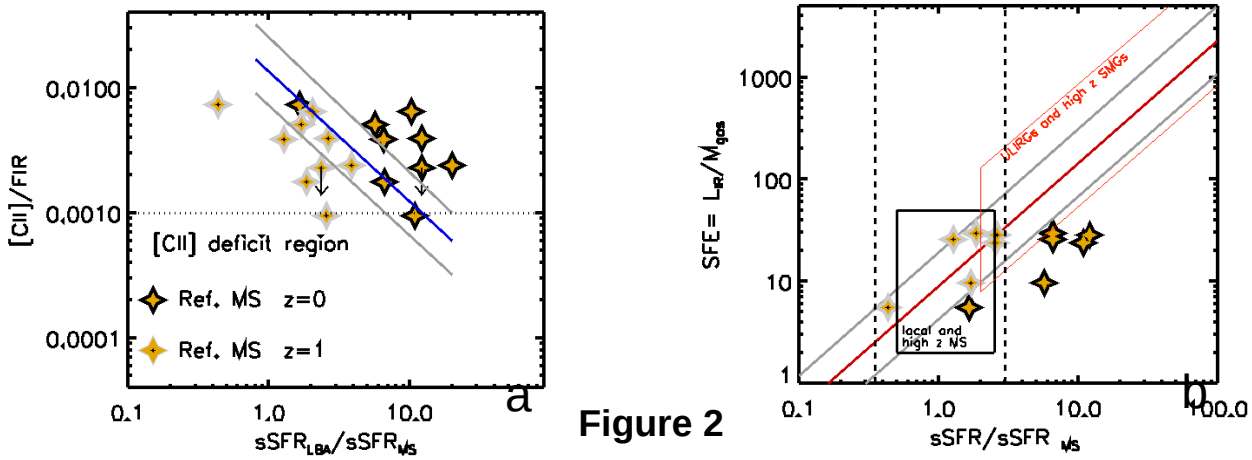

Figure 2

Panel a: the blue line shows the relation between the [CII]/FIR ratio and the distance from the local MS followed by a sample of local LIRGs (Magdis et al.) that matches the IR emission of LBAs. Symbols represent LBAs calculated w.r.t. the MS at *z*=0 and *z*=1. LBAs follow the LIRGs relation only when the MS at z=1 is considered.

Panel b: the star formation efficiency of LBAs as a function of their distance from the MS at z=0 and 1. When the local MS is considered, LBAs do not match any relation followed by local ULIRGs, distant submillimenter galaxies and local MS galaxies. The agreement is much better when the MS at *z*=1 is considered.

References:

- **Brisbin** et. al.2015, ApJ, 799,13; **Magdis** et al.2014,ApJ, 796,63

A. Contursi, S. Berta, D. Lutz, E. Sturm, et. al.

First Resolved View of the Structure of Molecular Clouds at Low Metallicity

To understand the physical process of star formation across cosmic times requires observations that resolve molecular clouds and probe low metallicity environments which resemble the early universe. With ALMA we have achieved such observations for the first time by targeting the Local Group dwarf galaxy NGC 6822. These ALMA CO(2-1) observations represent today`s finest view (2pc) on the structure of star-forming molecular clouds at low (~1/5 solar) metallicity. CO emission emerges from compact clumps of only a few parsec in size which are embedded in large (~100pc) complexes made of atomic (HI) and molecular (H_2) gas as traced by dust emission in the infrared. The low filling factor of CO-bright clumps is expected for low metallicity gas where higher gas columns are needed to attain sufficient attenuation of the dissociating radiation field and explain why pre-ALMA low-resolution CO observations repeatedly resulted in non-detections. For a sample of 150 CO-bright clumps we find their macroscopic properties (e.g., size, line width, density) to be similar to CO-bright clumps detected in the outer Milky Way and another dwarf galaxy, WLM (~1/8 solar metallicity). The dynamical state of these clumps is in agreement with kinetic and potential energy equipartition with additional confining pressure by the weight of the complex. The detected similarities in macroscopic properties of the dense clumps suggests that their dynamical evolution and thus the star formation process does not significantly change despite the 8x variation in metallicity.

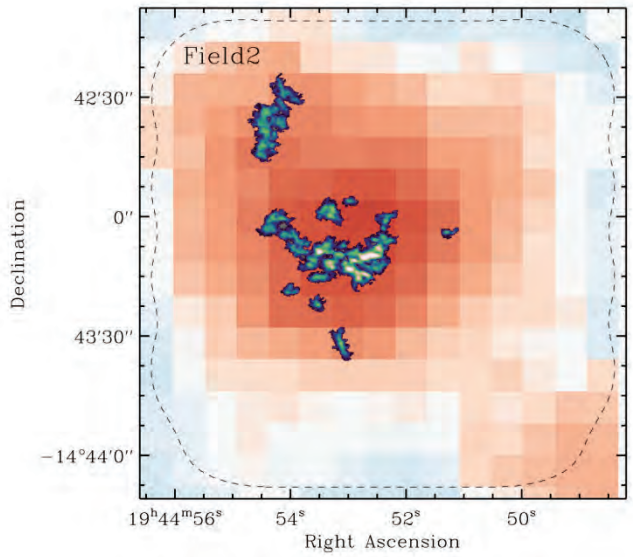

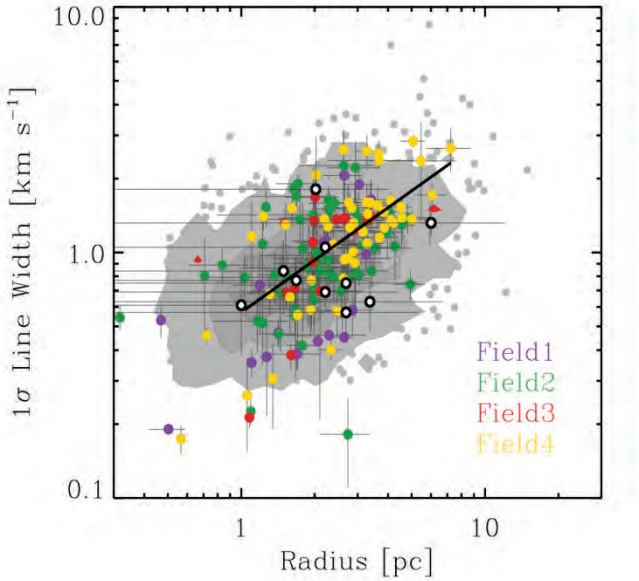

Left figure: ALMA CO(2-1) integrated intensity map at 2 parsec resolution (cubehelix color scheme) of an atomic-molecular complex in NGC 6822 with total mass M ~ 10^6 $M_\odot$ traced by low-resolution infrared dust modeling (red greyscale) over a 250 parsec field of view. The CO emission traces dense, well-shielded regions embedded in a more extended envelope of atomic and molecular gas. *Right figure:* size-line width relation of parsec-sized CO-bright dense clumps in NGC 6822 (color points), WLM (black-and-white points), and the outer Milky Way (grey contours of data density). All clumps share comparable line width (i.e. turbulence) at fixed size scale suggesting similar dynamical evolution and a uniform star formation process that is independent of the probed factor ~8 change in metallicity.

References: • Schruba, A. et al., 2016, AJ, subm; • Rubio et al. 2015, Nature, 525, 218; • Sternberg et al. 2014, ApJ, 790, 10; • Brunt et al. 2003, ApJS, 144, 47; • Heyer et al. 2001, ApJ, 551, 852

A. Schruba, E. van Dishoeck, L. Tacconi

The gas cloud G2 in the Galactic Center

G2 is a dusty, ionised gas cloud on a highly eccentric orbit around Sgr A*, which passed pericenter in spring 2014. During the past decade we have witnessed in beautiful detail how G2 has been tidally disrupted by the gravitational force of the massive black hole. We have been able to follow how the gas has swirled around the black hole, and according to simulations, the post-peri evolution should soon be dominated by hydrodynamic effects, observable as a spreading out of the gas and deviations from the originally Keplerian orbit.

While the nature of G2 is debated, it is undoubted that this constitutes the first case for which one was able to predict and follow a tidal disruption by a massive black hole. Our preferred model is that G2 is a dense knot in a much longer gas streamer. We see gas trailing behind along the same orbit, and we can connect the orbit of a second object, nicknamed G1, to the orbit of G2 by assuming that it runs 12 years ahead and that it was originally on the same orbit but then experienced a drag force during closest approach.

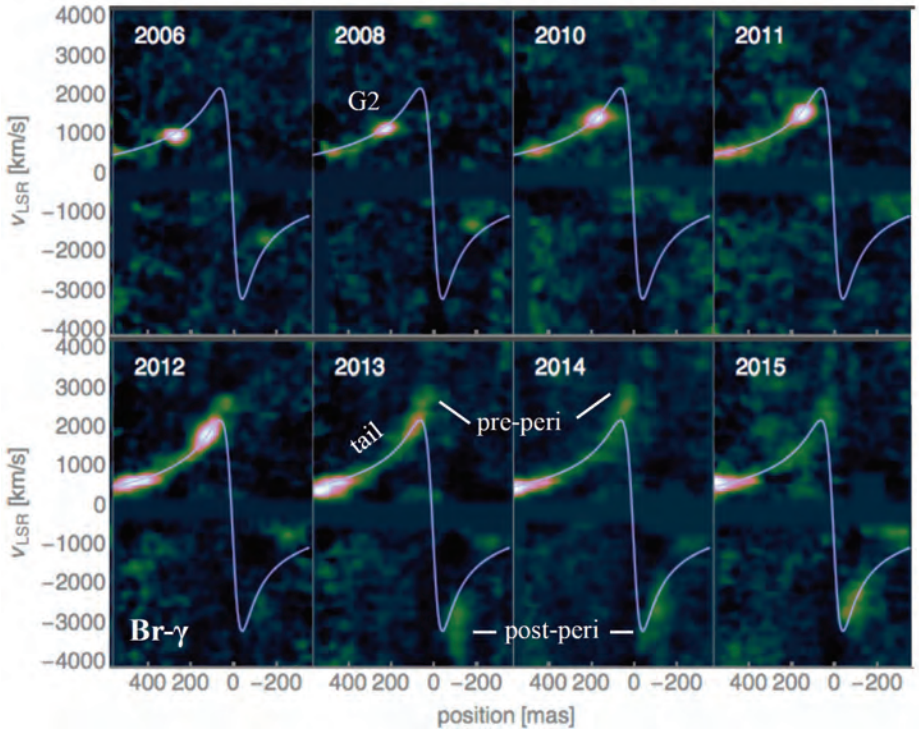

Figure 1: Time series of position-velocity diagrams obtained with SINFONI of the recombination line emission of G2. As the object accelerates to ever larger redshift along its orbit, it gets tidally stretched, until from 2013 to 2015 the gas swings around to the blue-shifted side.

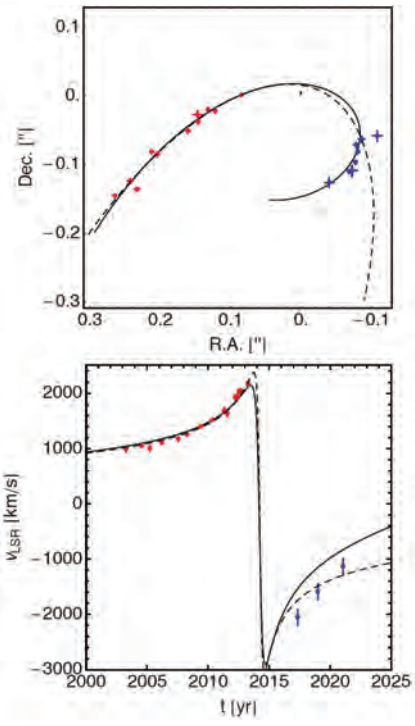

Figure 2: Drag-force orbit for the combined data from G2 (red) and G1 (blue). The motions of both objets can be described by assuming the G2 orbit and a drag force acting on G1 during pericenter passage.

References:

- Gillessen et al. 2012, Nature, 481, 51
- Gillessen et al. 2013, ApJ, 763, 78
- Gillessen et al. 2013, ApJ, 774, 44
- Pfuhl et al. 2015, ApJ, 798, 111

S. Gillessen, O. Pfuhl, P. Plewa, F. Eisenhauer, R. Genzel, T. Ott, M. Habibi, E. George, J. Dexter, I. Waisberg

The life of the S-stars in the Galactic Center from ultradeep spectroscopy

The central parsec of our Galaxy contains a large population of young massive stars. Their presence is puzzling given how inhospitable the region is for star formation. We present the result of 11 years (2004-2015) of high resolution spectroscopy within the central arc second of the Galactic center. By coadding the 50-100 hours of spectra we have obtained high signal/noise (50-400) H- and K-band spectra of a sample of 8 stars orbiting the central super massive black hole. Our deep spectra combined with model atmospheres can be used to constrain their stellar properties in order to investigate their true nature as massive young stars. We use these data to derive improved radial velocities and therefore improved 3d stellar orbits.

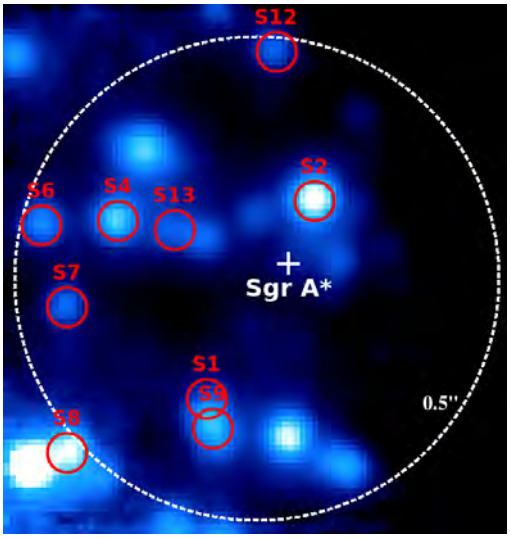

K-band image constructed from SINFONI observation in March 2013. S-stars which are analysed in this study are marked by a circle, along with their identification.

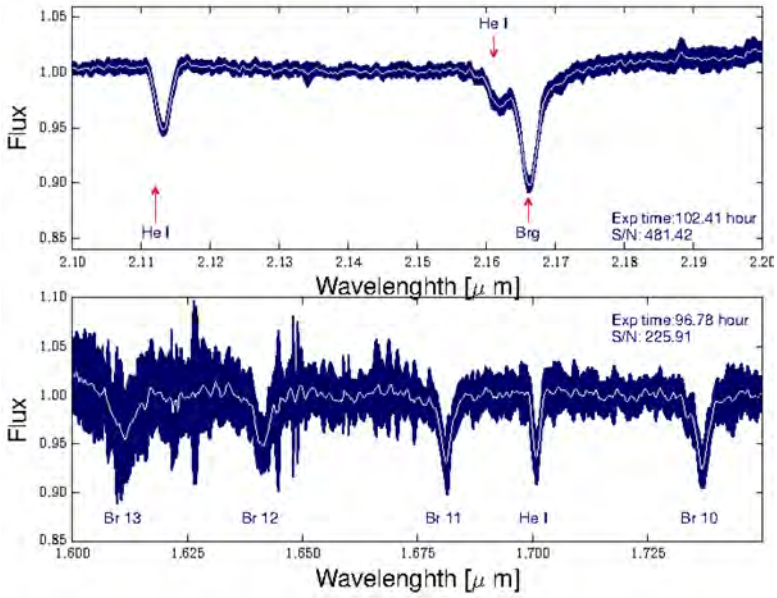

Combined S2 spectrum from the 2004–2015 SINFONI data. We see the Brackett series and some He I absorption lines, infrared characteristic of the early-type stars.

The red line indicate the ultra-deep spectrum while the other colors indicate the synthetic spectra. By comparing the observed ultra deep spectrum with model atmospheres we constrain the stellar properties like temperature, radius, and mass.

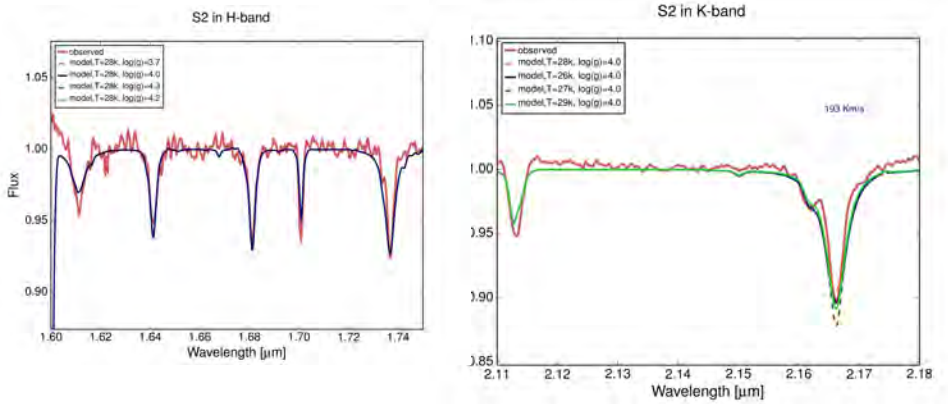

References:

- Habibi et al. 2015, in prep.
- Martins, F. et al. 2008, ApJ 672L,119
- M Hanson, M. M., et al. 2005, ApJS, 161, 154
- Eisenhauer, 2005, ApJ, 628, 246

M. Habibi, S. Gillessen, F. Eisenhauer, R. Genzel, P. Plewa, T. Ott, O. Pfuhl, E. George, J. Dexter, I. Waisberg

The mass and position of Sgr A*

The center of the Milky Way hosts a massive black hole. The observational evidence for its existence is overwhelming. The compact radio source Sgr A* has been associated with a black hole since its discovery. In the last decade, high-resolution, near-infrared measurements of individual stellar orbits in the innermost region of the Galactic Center have shown that at the position of Sgr A* (we pinpoint its position to 0.17 mas and its velocity to 0.07 mas/yr) a highly concentrated mass of 4.2×10^6 $M_\odot$ is located. Including our latest data, we now have orbital solutions for ~50 individual stars.

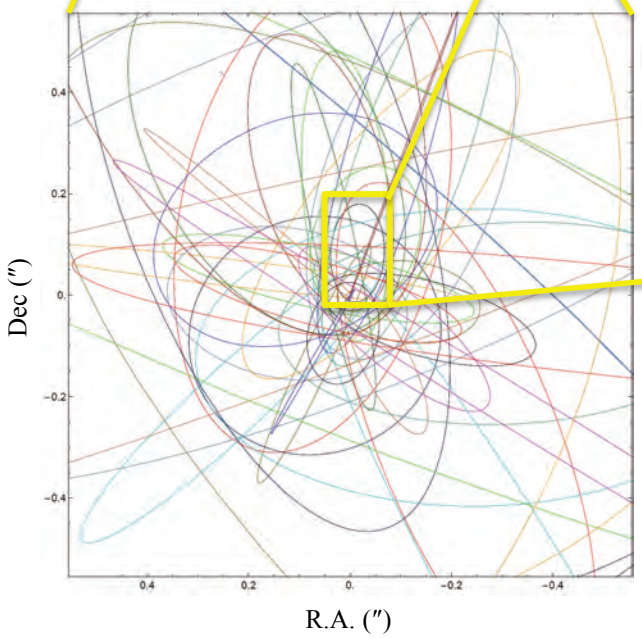

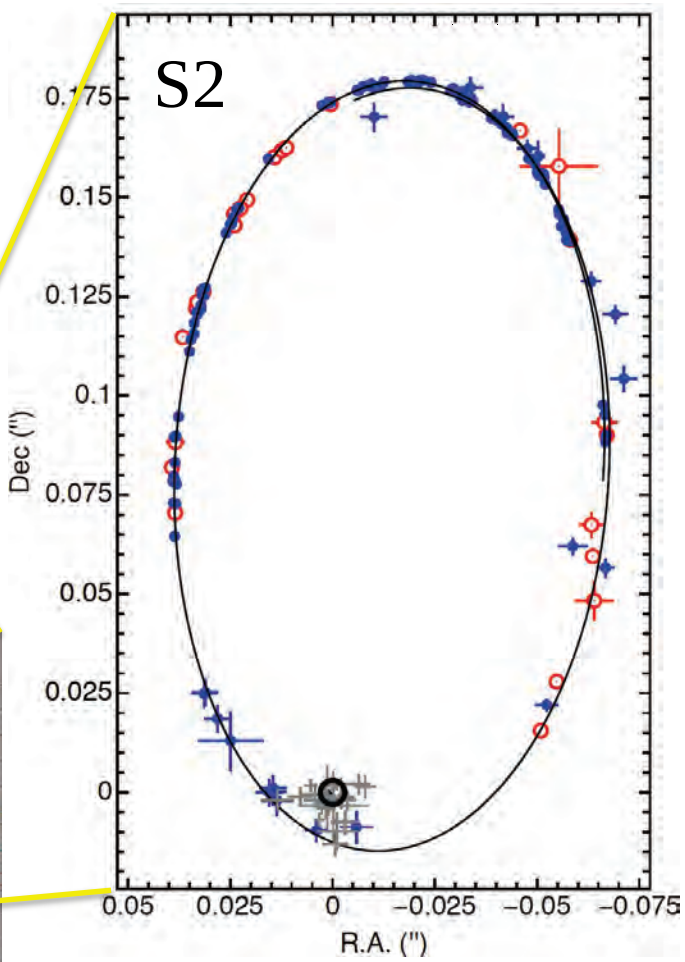

References:
- Schödel et al. 2002, Nature 419, 694
- Eisenhauer et al. 2003, ApJ 597, 121
- Eisenhauer et al. 2005, ApJ 628, 246
- Gillessen et al. 2009, ApJ 692, 1075
- Pfuhl et al. 2011, ApJ 741, 108
- Gillessen 2013, ASPC 467, 81
- Madigan et al. 2014, ApJ 784,23
- Plewa et al. 2015, MNRAS 453, 3234

T. Ott, S. Gillessen, O. Pfuhl, P. Plewa, F. Eisenhauer, R. Genzel, M. Habibi, L. George, J. Dexter, I. Waisberg

High-Precision Infrared Astrometry

A reliable astrometric reference frame is a fundamental requirement for our decade-long study of stellar motions in the Galactic Center. By modeling a spatially variable point spread function and correcting for optical image distortion, we have improved our ability to locate the radio source and massive black hole Sgr A* on our infrared images by a factor 5, to ~0.17 mas in position (in 2009) and ~0.07 mas/yr in velocity. A further improvement will follow future observations and facilitate the detection of relativistic effects on the orbits of short-period stars.

A typical distortion map for the S27 camera of the NACO/VLT imager.

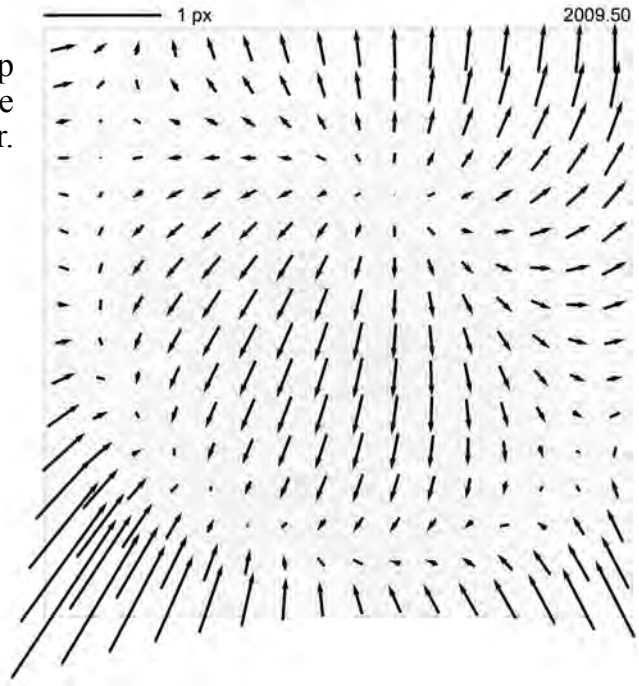

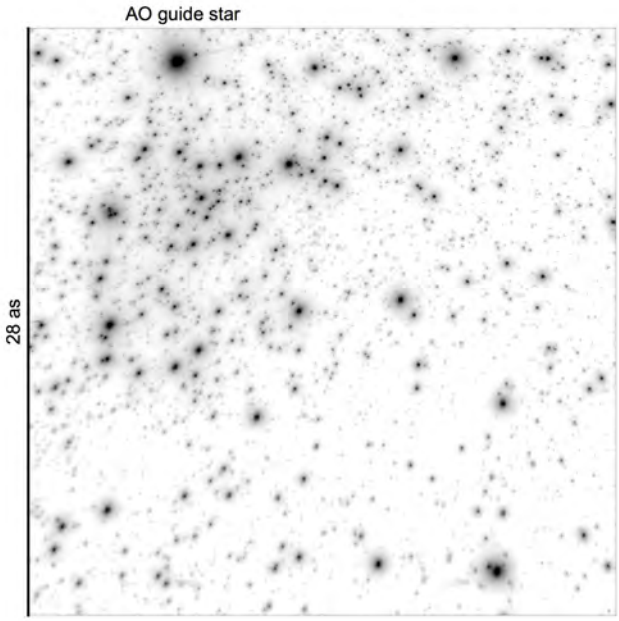

A typical image of the Galactic Center region used to set up the astrometric reference frame

A typical grid of point spread functions measured in different parts of the field of view.

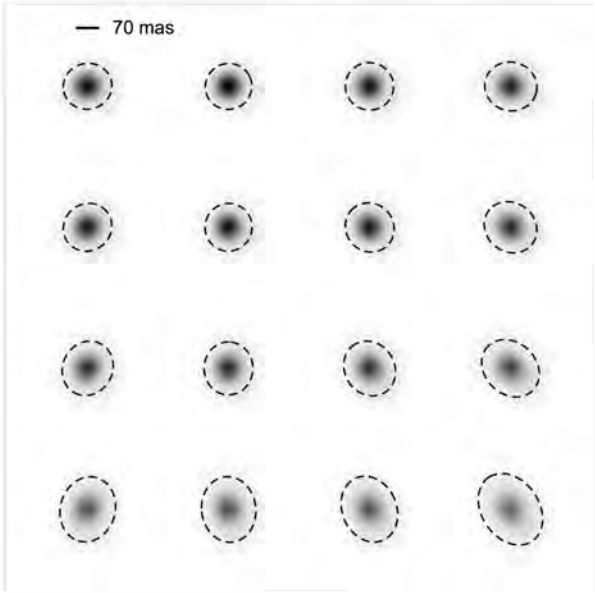

References:

- Plewa et al. 2015, MNRAS 453, 3234
- Fritz et al. 2010, MNRAS 401, 1177
- Gillessen et al. 2009, ApJ 692, 1075
- Trippe et al. 2008, A&A 492, 419

P. Plewa, S. Gillessen, F. Eisenhauer, R. Genzel, T. Ott, O. Pfuhl, E. George, M. Habibi, J. Dexter, I. Waisberg

Advanced deconvolution of data cubes

Within an advanced deconvolution framework, we try to enhance the SNR of spectroscopic SINFONI data cubes of the Galatic Center field, where we have bright sources, however a severe source crowding. The proposed methods range from semi/myopic deconvolution to full blind deconvolution. We investigate established methods and modify or extend them to meet our specific problem.

The image formation process can be modeled by convolving the true image **f** and the PSF **K**. Since convolution is a linear operation, we can substitute the convolution operator **K** by the matrix **A**. Consequently, the observed image **g** is the sum of a convolution and additive noise.

$$\mathbf{K} \star \mathbf{f} + \mathbf{n} = A\mathbf{f} + \mathbf{n} = \mathbf{g} \qquad \mathbf{f} \in R^{m \times n} \quad \mathbf{A} \in R^{(m \times n)^2}$$

Solving for **f** is usually a hard task, due to the ill-posedness of the inverse problem. However, under certain assumptions, an approximation of **f** can be found by the well known Lucy-Richardson iterative scheme [1]. Since the Lucy-Richardson iterative scheme is fully symmetric with respect to **A** and **f**, it can be also used to figure out **A**, essential in blind deconvolution [2].

$$\mathbf{f}^{k+1} = \mathbf{f}^k \circ A^T \frac{\mathbf{g}}{A\mathbf{f}^k + \mathbf{n}} \qquad A^{k+1} = A^k \circ \mathbf{f}^T \frac{\mathbf{g}}{A^k\mathbf{f} + \mathbf{n}}$$

One big drawback of the alternating LR algorithm is the need of an a priori stopping criterion, to avoid clustering or the trivial solution of a delta distribution for the PSF. It can be adressed by introducing regularization. We introduce regularization, to model gaussian noise of the sensor and a functional term to force sparsity. The latter preserves edges, but suppresses noise and is well suited for sparse astronomical objects [3]. Overall, these concepts can be modeled by a cost function **J**.

$$J(\mathbf{f}_j, A_j) = \sum_{j=1}^{N} \{\mathbf{g}_j \ln \frac{\mathbf{g}_j}{A_j\mathbf{f}_j + \mathbf{n}_j}\} + \mu_j \sum_{j=1}^{N} |A_j\mathbf{f}_j - (\mathbf{g}_j - \mathbf{n}_j)|_2^2 + \tau_j \sum_{j=1}^{N} |\mathbf{f}_j|_1$$

The first term represents data fidelity, degraded by poisson noise, the second detector noise and the third sparsity of the solution, characterised by the specific problem of sever source crowding. The parameters μ and τ define the relative weights of the different penalty terms, the index j covers the 3rd. dimension of the data cube. A necessary condition for optimality, of a differentiable cost function **J**, is a vanishing gradient.

$$\nabla_f J(\mathbf{f}, A) = 0$$

However, the difficulty lies in the non differentiability of the sparsity term. This can be addressed by using the isotropic total variation norm. Further modification, adjusting the weights in x, y, z are thinkable.

$$|\mathbf{f}_j| = \sqrt{(\nabla_x \mathbf{f}_j)^2 + (\nabla_y \mathbf{f}_j)^2 + (\nabla_z \mathbf{f}_j)^2}$$

The solution **f** cannot be figured out by a simple Lucy-Richardson algorithm anymore and has to be adressed by advanced iterative solving schemes. One of the most promising is the scaled gradient projection [4], since constraints on non negativity or flux conservation of **f** or **A** can be implemented cost efficiently.

References:

- [1] L.B. Lucy et al. (1974), J. Opt. Soc. 62, 1
- [2] D.A. Fish et al. (1995), J. Opt. Soc. 12, 1
- [3] Mugnier et al. (2004), J. Opt. Soc. 21, 10
- [4] S. Bonettini et al. (2015), SIAM J. of. Scientific Computing 37

S. Schmalzl, S. Gillessen, F. Eisenhauer, P. Plewa

Strong interstellar scattering towards the GC

Free electrons along the line of sight broaden the radio image of Sgr A*. For a long time, this strong interstellar scattering was thought to be local to the Galactic center, explaining the absence of pulsars (Cordes+2002). The observation of radio pulses from a recently detected magnetar near Sgr A* contradict this explanation (Spitler+2014).

We show that a single HII region 1.5-3.5 kpc away from Earth, with $n_e \sim$ 100-200 cm^{-3}, R ~ 3-5 pc, can explain the observed angular broadening and pulse time delay. For a magnetic field strength of 10-45 μG, the rotation measure, previously thought to come from hot gas in the Galactic center, can instead originate in a cloud along the line of sight. Furthermore, we predict that sources within ~10 pc should be scattered by this HII region, while other known GC pulsars at larger separations > 20 pc should not.

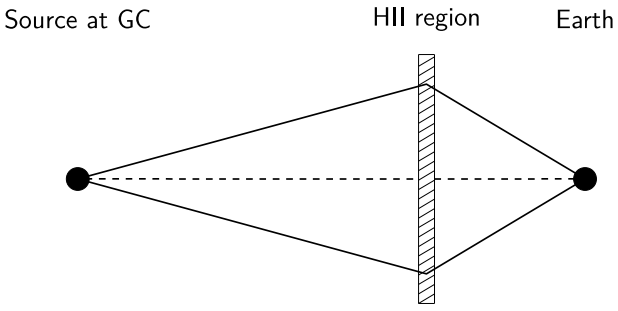

Figure 1: Sketch of the ray path from the source at the Galactic center (GC) to the observer, scattered by the HII region modeled here.

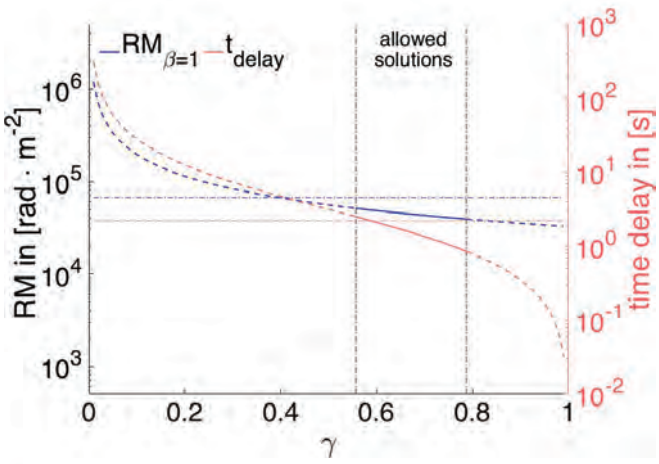

Figure 2: Rotation measure (RM) and pulse broadening versus the relative position of the HII region. Solid lines show the allowed solutions, which are far from the GC (γ = 0).

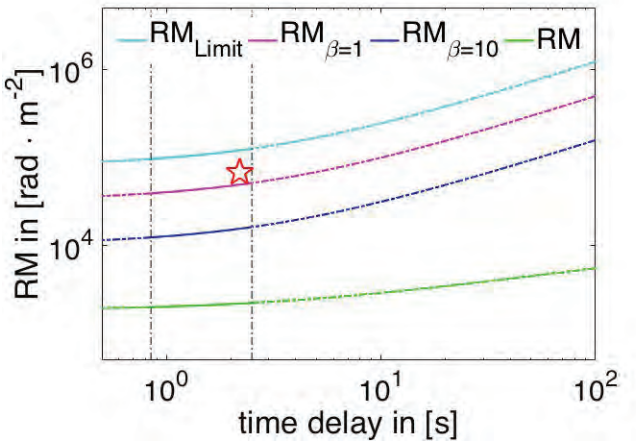

Figure 3: Rotation measure (RM) versus the pulse time delay. Strongly magnetized clouds (cyan and purple lines) can produce the observed RM (red star) which was previously thought to imply a dynamically important magnetic field in gas falling onto Sgr A* (Eatough+2013).

E. Sicheneder, J. Dexter, F. Eisenhauer

Event horizon scale emission from Sgr A*

Interferometric measurements in the submm (Event Horizon Telescope) and near-infrared (VLTI GRAVITY) are opening a new window into the study of black hole accretion physics and strong gravity by spatially resolving event horizon scales around Sgr A*.

One of the key science goals of our Sofja Kovalevskaja award group is to link the interferometric observables with theoretical models using radiative transfer calculations. Two recent examples are showing that i) non-thermal electrons add a diffuse halo of emission to black hole images (Mao+2016); and ii) the coherence of the polarization over the image is a sensitive probe of the intrinsic Faraday effects and plasma properties (Dexter 2016).

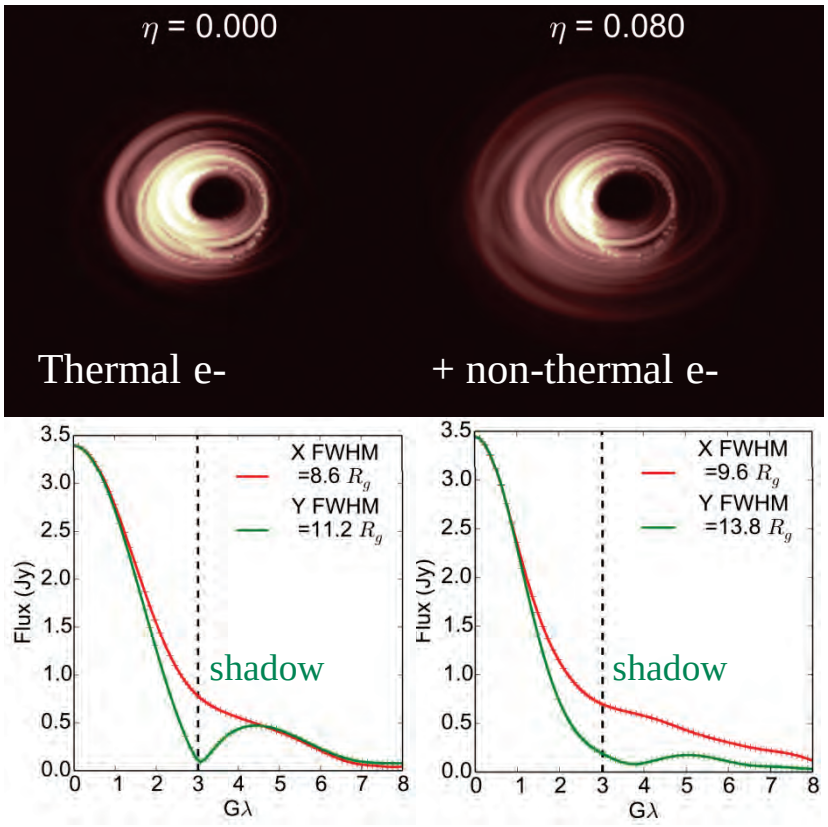

Fig. 1: False color model accretion flow images (top) and visibility amplitudes (bottom) of Sgr A* assuming purely thermal (left) and hybrid thermal/power law electron distribution functions. Including a small number of non-thermal electrons introduces a diffuse halo of emission. The observed EHT image size can constrain the flux in this halo and so the distribution function. The presence of this halo also changes the signature of the black hole shadow in the visibility amplitudes (dark region in middle of images and local minimum at 3 Gλ marked by dashed lines in visibilities).

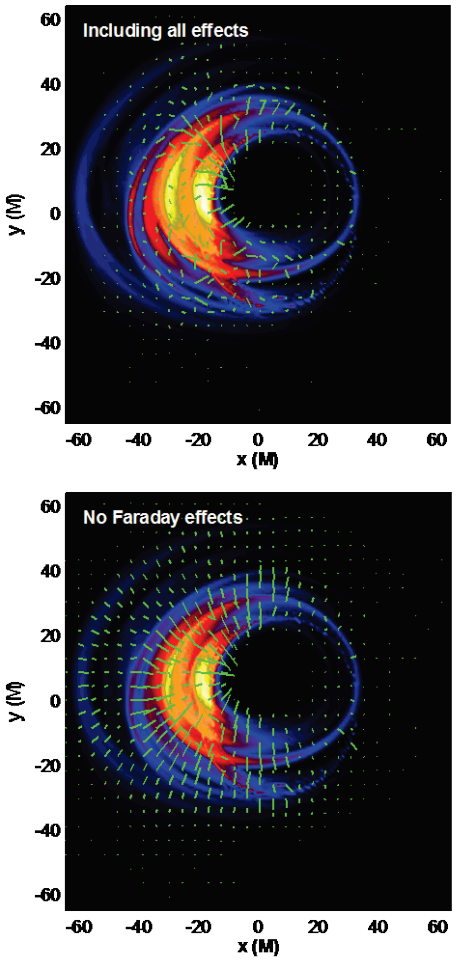

Fig. 2: Model images and polarization maps of Sgr A*. Faraday rotation intrinsic to the emission region scatters the polarization vectors (top) compared to when the effect is turned off (bottom). The observed degree of small scale polarization constrains the strength of this effect and the physical properties of the emitting electrons.

References:

• Mao, Dexter, Quataert 2016, to be submitted
• Dexter, J., 2016, arXiv:1602.03184

J. Dexter, et al.

Latest excitement on icy solar system bodies

Transneptunian Objects (TNOs) are believed to retain the most pristine and least altered material of the Solar System. In a Herschel photometric study "TNOs are Cool!“ (PI: T. Müller, MPE) we looked at a sample of more than 130 objects covering the major dynamical classes, including Centaurs and 2 satellites. The derived size and albedo information is crucial for testing Solar System formation and evolution scenarios. The constraints on thermal surface properties give deeper insights into surface processes in the outer Solar System. Analysis of more than 20 binary systems allow for an intriguing first-look at the density of TNOs as a function of size. The trans-Neptunian region harbors fascinating worlds: very special and diverse dwarf planets (Pluto, Eris, Haumea, Varuna, Makemake, Orcus, Quaoar, 2007 OR_{10}, ...), partially ice-covered, some with rings, super-comet candidates, multiple systems, very elongated bodies, indications for cryo-volcanism, and a water-ice dominated collisional family.

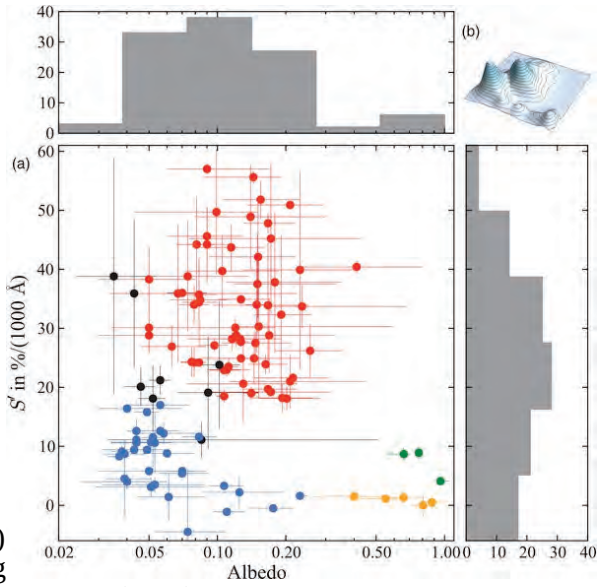

Color–albedo diagram for 109 TNOs showing two main clusters, one with dark neutral objects (blue points, p_V ~0.05 and S' ~ 10%), and another of bright red objects (red points, p_V ~0.15 and S' ~ 30%). This color-albedo separation is evidence for a compositional discontinuity in the young solar system (Lacerda et al. 2014).

Recent TNOs-are-Cool related references:

- Kiss et al.: A portrait of the extreme solar system object 2012 DR_{30}, A&A 555 (2013)
- Fornasier et al.: Combined Herschel PACS and SPIRE observ. of 9 bright targets at 70-500 µm, A&A 555 (2013)
- Perna et al.: Photometry and taxonomy of TNOs and Centaurs in support of a Herschel KP, A&A 554 (2013)
- Lellouch et al.: Thermal properties of KBOs and Centaurs from combined Herschel and Spitzer obs., A&A 557 (2013)
- Kiss et al.: Optimized Herschel/PACS photometer observing and data reduction strategies for moving solar system targets, ExA 37 (2014)
- Duffard et al.: A Herschel-PACS view of 16 Centaurs,A&A 564 (2014)
- Vilenius et al.: Analysis of classical KBOs from Herschel and Spitzer observations, A&A 564 (2014)
- Lacerda et al.: The albedo-color diversity of transneptunian objects, ApJL, 793 (2014)
- Böhnhardt et al.: Photometry of TNOs for the Herschel Key Program 'TNOs are Cool’, EM&P 114 (2014)
- Pál et al: Physical properties of the extreme centaur and super-comet candidate 2013 AZ_{60}, A&A 583 (2015)
- Grundy et al: The Mutual Orbit, Mass, and Density of the Large Transneptunian Binary System Varda and Ilmarë, Icarus 257 (2015)
- Marton et al.: Search for signatures of dust in the Pluto-Charon system using Herschel/PACS observations, A&A 579 (2015)
- Müller et al.: Herschel Survey of the Trans-Neptunian Population, IAUGA 29 (2015)
- Lellouch et al.: The long-wavelength thermal emission of the Pluto-Charon system from Herschel observations. Evidence for emissivity effects, A&A 588 (2016)
- Kiss et al.: Nereid from space: Rotation, size and shape analysis from Kepler/K2, Herschel and Spitzer observations, MNRAS 457 (2016)
- Pál et al: Large size and slow rotation of the trans-Neptunian object (225088) 2007 OR_{10} discovered from Herschel and K2 observations, AJ accepted (2016)
- Kiss et al.: The Eris-Dysnomia system as seen with the synergy of occultation and thermal emission measurements, A&A, submitted

T. G. Müller & the „TNOs-are-Cool!“ Team

GRAVITY opens up new horizons

Zooming in on the Galactic Center black hole is the main mission for our newly installed GRAVITY instrument at ESO's Very Large Telescope in Chile. During its first observations in November 2015, GRAVITY successfully combined starlight using all four Auxiliary Telescopes. The instrument has already achieved a number of notable firsts: for the first time in the history of long baseline optical interferometry, GRAVITY could make individual exposures of several minutes, more than a hundred times longer than previously possible. It was also the first time that four optical telescopes were co-phased with an off-axis reference star for the observations of a science object, which is too faint to stabilize the fringes otherwise. The commissioning with the four 8m Very Large Telescopes is foreseen in 2016.

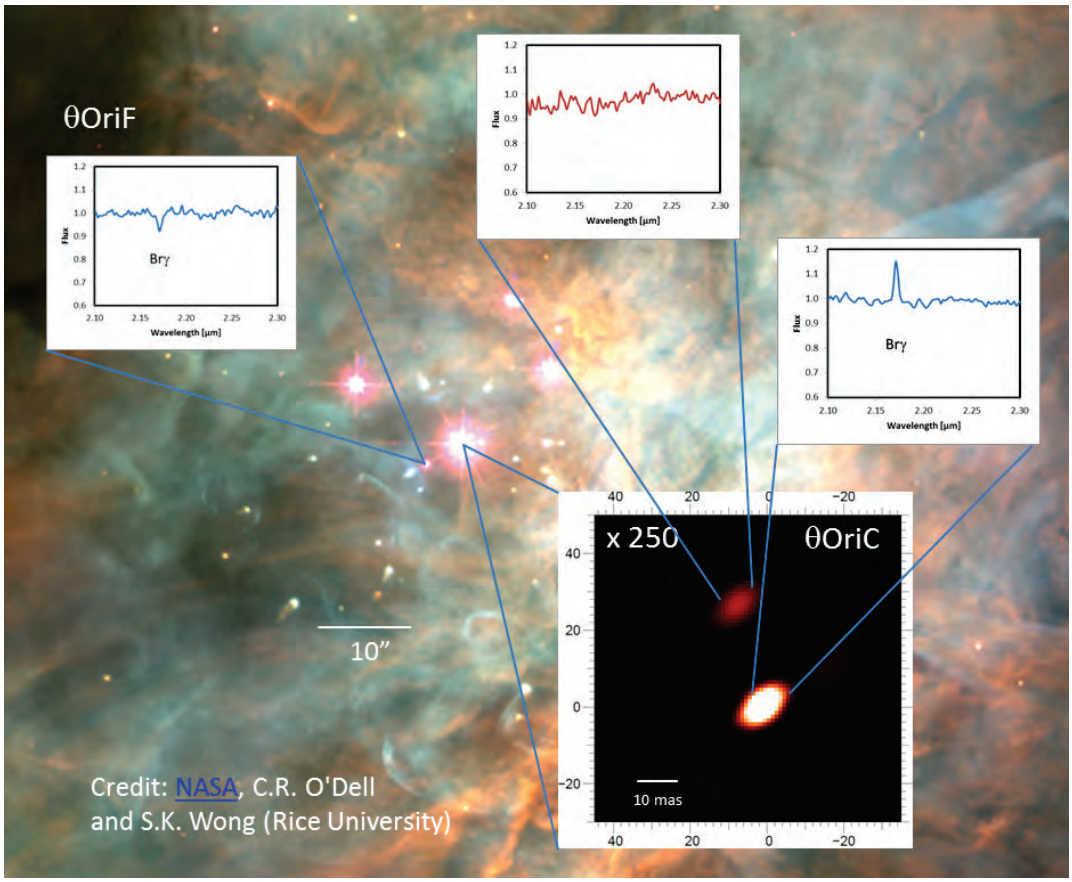

As part of the first observations GRAVITY looked closely at the bright, young stars known as the Trapezium Cluster. The bright binary star Theta Orion C is used to co-phase the four telescopes and to correct in real time the atmospheric phase fluctuation. This interferometric equivalent of adaptive optics is called fringe tracking and allows minute long, high spectral resolution observations of the faint, nearby B-star Theta Orion F. The same technique will be applied for the upcoming observations of the Galactic Center with the 8m Very Large Telescope, using IRS16 to stabilize the fringes for the observations of the fainter star S2 orbiting the Galactic Center black hole.

Reference: F. Eisenhauer et al. 2011, The Messenger, 143, 16

F. Eisenhauer, R. Genzel, S. Gillessen, O. Pfuhl, M. Haug, S. Kellner, E. Wieprecht, E. Sturm, F. Haußmann, T. Ott, M. Lippa, I. Waisberg, E. Wiezorrek, S. Yazici, O. Hans and the GRAVITY team

GRAVITY commissioning and instrument performance

The 2nd generation VLTI instrument GRAVITY has been developed to probe general relativity in the strong field of the supermassive black hole at the center of our Galaxy. This ambitious goal requires an unprecedented astrometric accuracy of 10 μas, a factor 20 better than what is possible with existing instruments. GRAVITY has been deployed at the telescopes in October 2015 and is currently being commissioned.

GRAVITY significantly enhances the capabilities of the VLTI. The instrument consists of two independent interferometers, one „fringe tracker“ and one R=20-4000 spectrometer. The first channel provides active fringe stabilization of four telescopes on a bright object. This allows long coherent integrations with the spectrometer on the same (single-field) or another nearby object (dual-field). The commissioning has been with the Auxiliary Telescopes in November 2015. The Unit Telescopes will be used together with GRAVITY for the first time in May 2016.

Some of the major milestones towards the final astrometric performance, which have been achieved until February 2016:

- Active fringe stabilization with 0.3 - 1kHz on stars as faint as m_K = 7.5 in single-field and m_K = 8.2 in dual-field mode.
- Fringe tracking residuals as low as 80nm RMS
- Field- and pupil stabilization of four telescopes
- Longest coherent integration (~300s) ever achieved in optical interferometry (100x deeper than previously possible)
- Dual-field interferometry, i.e. using fringe-stabilization on a bright object to integrate coherently on a second object.
- Spectro-interferometry (R=500 to 4000) of objects as faint as m_K = 8.5 (4 mag deeper than previous instruments)
- First astrometric measurements of binary stars with ~150 μas accuracy

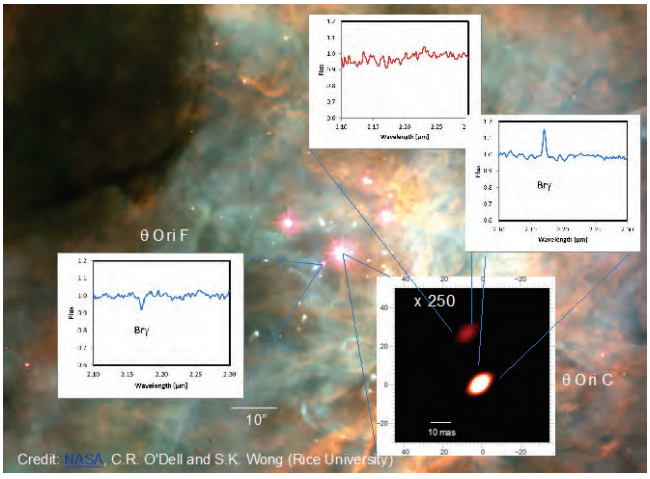

During the first commission run GRAVITY imaged two members of the Trapezium cluster, the binary θ^1 Ori C (20 mas separation, m_K~4.5) and θ^1 Ori F (m_K~8.5). θ^1 Ori F is one of the faintest objects ever observed with spectro-interferometry on the Auxiliary Telescopes.

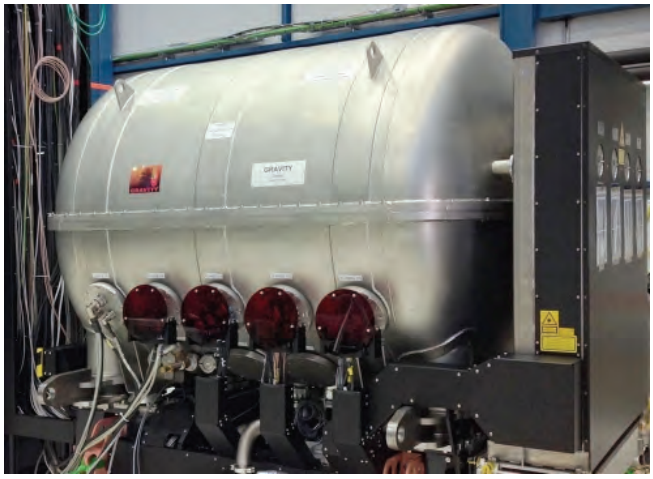

The GRAVITY cryostat in the integration hall at Paranal shortly after arrival. The instrument is cooled with liquid N_2 and sealed in a vacuum vessel. Isolated from ambient the instrument is extremely stable.

References:

• Eisenhauer, F. et al., GRAVITY: Observing the Universe in Motion, The Messenger, vol. 143, p. 16-24

O. Pfuhl for the GRAVITY consortium

GRAVITY Commissioning
Data Verification

We present preliminary results for the 4-beam VLT infrared interferometer GRAVITY, using data taken during the first two Commissioning Runs at the Auxiliary Telescopes (ATs). The three on-axis cases presented here demonstrate GRAVITY's basic interferometric and spectral capabilities, focusing on model fitting and image reconstruction of stellar and X-ray binaries.

A) Orion Trapezium Cluster

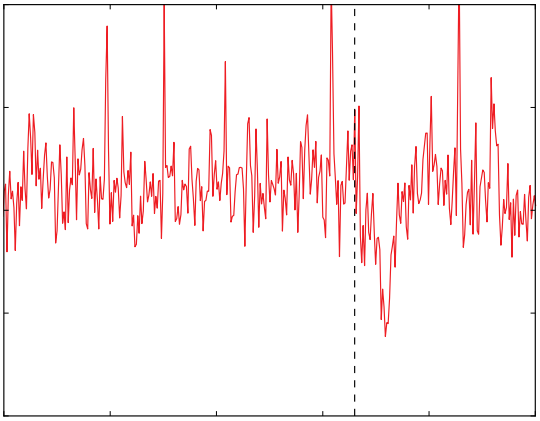

Binary Flux Ratio as a function of wavelength for Theta1 Orionis C (O7V/O5V, K=4.57). Note the prominent HI 2.166 μm line. Data taken in high-resolution mode (R=4,000) with DIT=30s exposures. This is consistent with the expected stronger absorption line for the cooler star.

B) High Mass X-Ray Binary Vela X-1

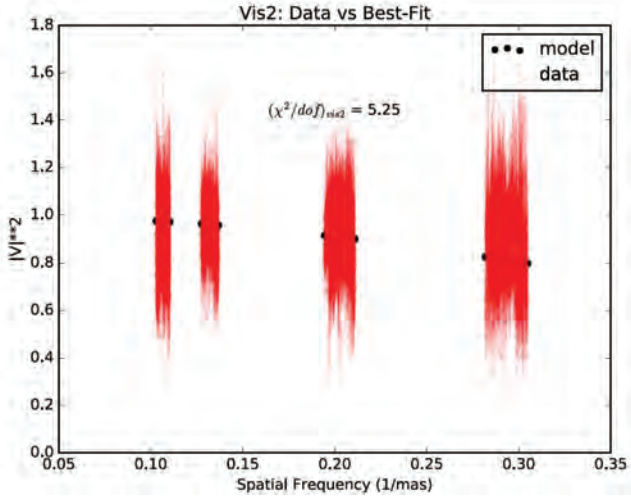

C) Symbiotic Star SS Lep

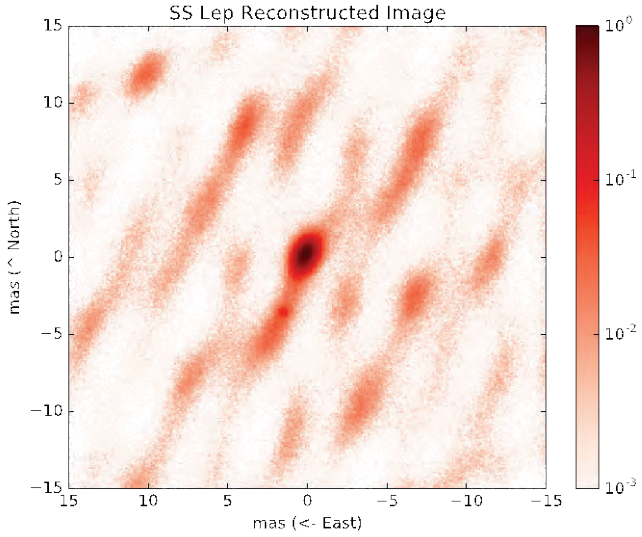

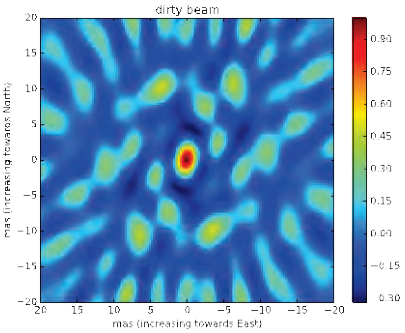

Up: Model-independent image reconstruction of SS Lep (A1V/M4V, K=1.62). Side: "Dirty beam" from 4 observations.

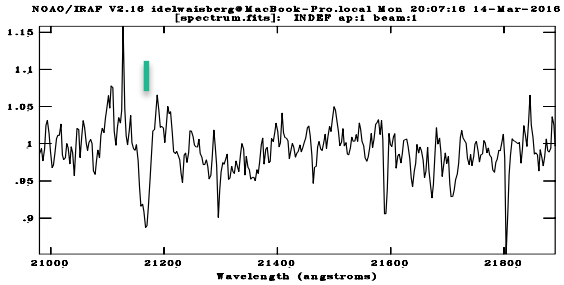

Left: Squared visibility vs. spatial frequency for Vela X-1 (B0.5I, K=5.596), with a best fit stellar diameter of ~ 1 mas. Data taken in high-resolution mode with DIT=100s exposures. Up: Vela X-1 spectrum as seen by GRAVITY. Note the prominent line HeI 2.113 μm marked in green.

I. Waisberg, F. Eisenhauer and the GRAVITY team

GRAVITY – System Overview

We delivered the Beam Combiner Instrument to the VLT Interferometer during summer 2015. The commissioning started in November 2015 with the Auxiliary Telescopes and will start with the Unit Telescopes in May 2016. Since February 2016 all sub-units are installed at the Paranal observatory.

The GRAVITY instrument consists of:

- four fiber coupler units
- four guiding receivers
- eight differential delay lines
- eight fibered polarization rotators
- one acquisition camera
- 3-channel laser metrology
- two spectrometers
- The calibration unit
- 32 metrology receivers
- 32 pupil tracking laser beacons
- eight tip-tilt laser beacons
- four IR wavefront sensors

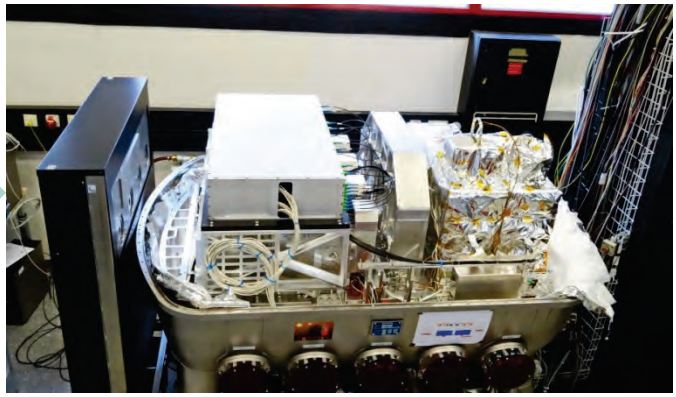

A LN_2 cryostat provides the operation temperature and stability for the beam combiner sub-units.

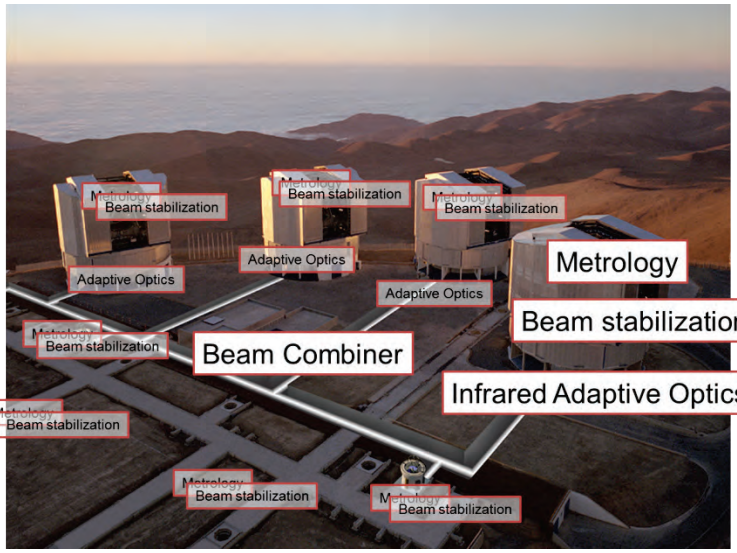

12 electronic cabinets host the control electronics.

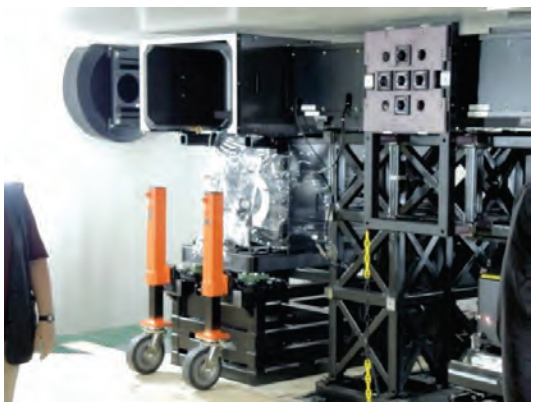

Infrared wavefront Sensors installed at all four UTs.

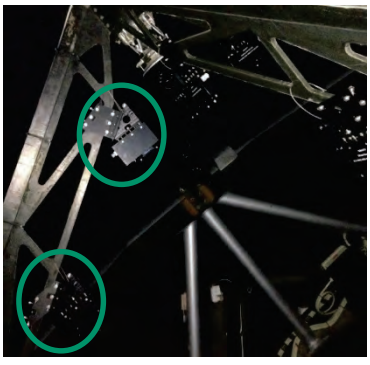

32 metrology receivers
32 pupil tracking laser beacons
installed at four UT's and four AT's

M. Haug, F. Haußmann, S. Kellner, F. Eisenhauer and the GRAVITY team

GRAVITY - Spectrometers

The spectrometers inside the beam combiner instrument of GRAVITY depict the two eyes of the Very Large Telescope Interferometer. The fringe tracker locks on the phase reference allowing the science spectrometer to take long exposures pushing to higher sensitivity on faint sources and increasing depth of the spectra in medium and high resolution on brighter sources.

The fringe tracking spectrometer provides a fixed low resolution of R=22, i.e. spectrally dispersing the astronomical K-band on 5 pixel, and thus allowing for group and phase delay tracking on the reference source, in combined and polarisation split configuration.

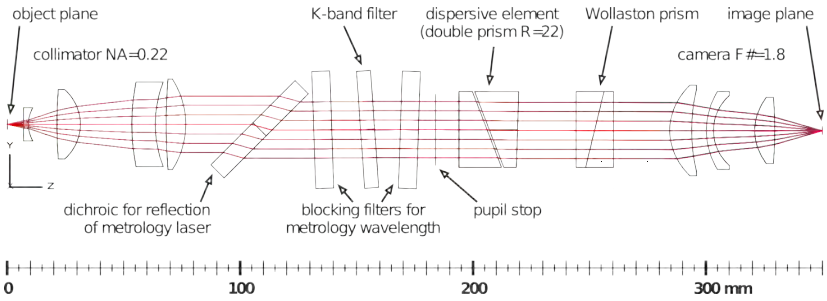

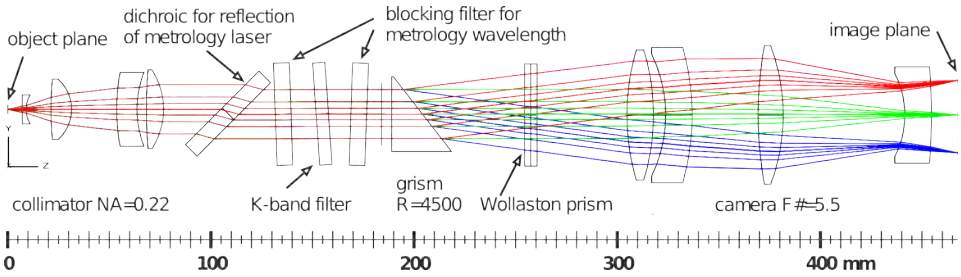

The science channel spectrometer provides three resolutions of R=22, 500 and 4500, all in polarisation split and combined mode.

The science channel spectrometers mechanical implementation including opto-mechanical devices such as the grism-wheel, Wollaston mechanism and detector focus stage. All mechanisms working at cryogenic temperatures.

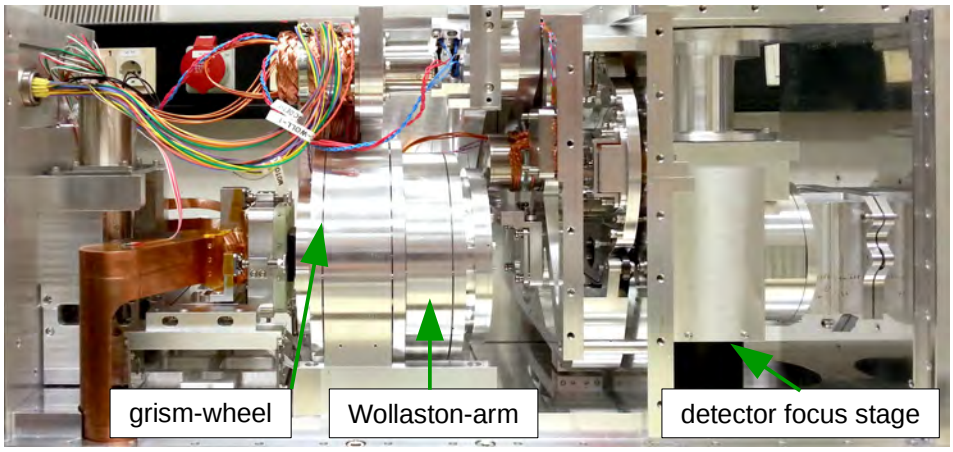

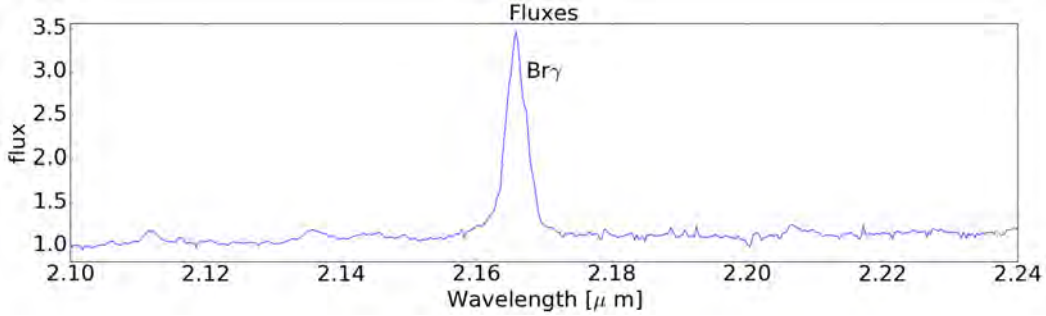

Pipeline processed total flux of all four telescopes in s-polarisation as an example of a spectrum taken on sky.

S. Yazici, F. Eisenhauer and the GRAVITY team

GRAVITY – The Metrology System

GRAVITY combines the beams from four Very Large Telescopes and provides phase-referenced imaging as well as narrow-angle astrometry by observing two celestial objects in dual-field mode. Their angular separation can be determined with 10µas-precision from their differential OPD (dOPD) when the internal dOPDs in the interferometer are known to a nanometer-level. *Here, we present the overview of the* ***novel three-beam metrology system*** *which performs these measurements.*

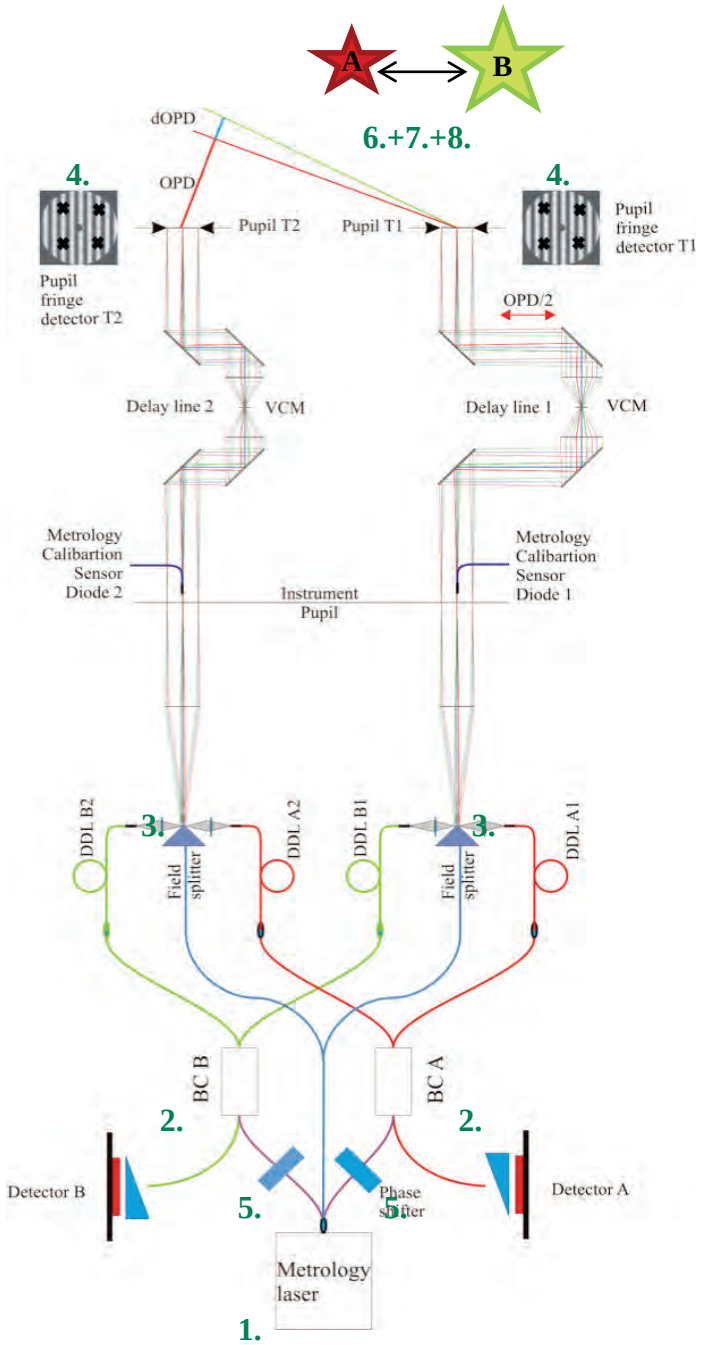

Working principle of the metrology system
(shown for two out of four telescopes)

1. Three-beam laser system:
Split laser light into two equally faint beams ($\approx 10^{-6}$) and one high-power "carrier" beam.

2. Injection of faint beams:
Inject faint beams backwards into the beam combiners (BC A and B) of the two observed objects A and B.

3. Injection of carrier beam:
Split and superimpose the carrier beam to enhance the faint signal for detection.

4. Three-beam interference:
Let the beams trace the optical paths of the astronomical light back to the telescopes T1 and T2 where they interfere.

5. Phase-shifting interferometry:
Phase-shift each faint beam with an individual frequency f_A and f_B.

6. Homodyne detection:
At each telescope disentangle the two fringe patterns between the faint beams and the carrier by coupling a lock-in amplifier to each of the frequencies.

7. Phase measurement:
Subtract the respective fringe phases from each other to cancel out the carrier phase and retrieve the actual fringe phase of interest between the faint beams (undetectably faint).

8. Internal dOPD:
Determine the dOPD within the interferometer from the phase difference between the two telescopes.

J. Weber, M. Lippa, S. Gillessen, N. Blind, Y. Kok, O. Pfuhl, M. Haug, S. Kellner, F. Haußmann, E. Wieprecht, T. Ott, F. Eisenhauer and the GRAVITY team

GRAVITY: Field, Pupil and Fringe Guiding

GRAVITY uses two infrared cameras to provide field, pupil and fringe guiding.The acquisition camera is used for both field and pupil tracking, the GRAVITY science detector is used in real-time for fringe tracking.

The acquisition camera field is split in four columns, one for each telescope, and four rows. The top row is used for pupil tracking, the second one displays the aberration sensor, the third one shows the image of the pupil and the last one is used for field tracking.

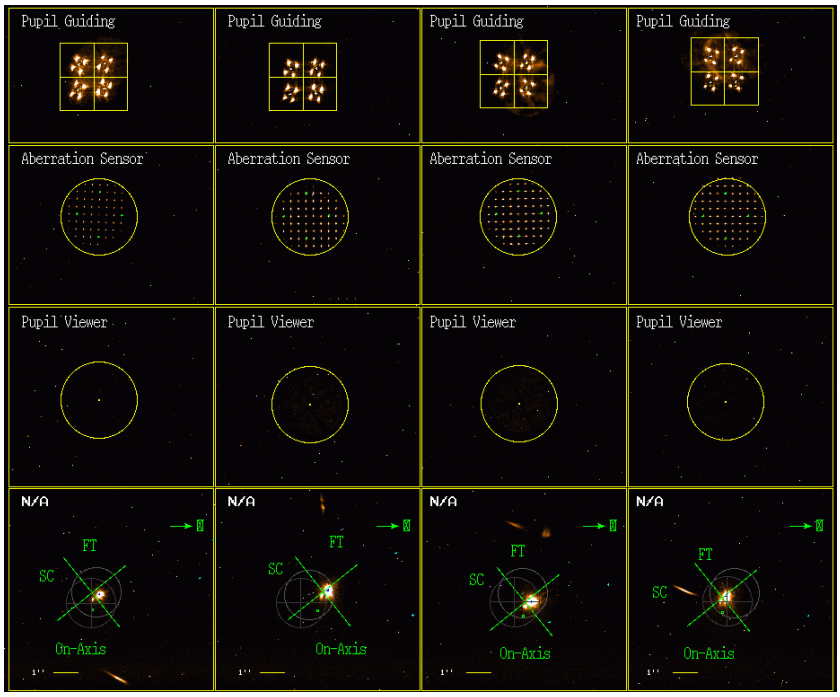

For the pupil guiding four laser diode beacons are placed at the telescope spiders of each telescope. The beacon light passes a 2x2 lenslet array providing four spots for each beacon.
Those spots allow lateral and longitudinal pupil tracking. Common shifts in x and y direction allow to measure the lateral pupil position, whereas a contraction or expansion of the four spot pattern is indicating a longitudinal shift.

For the field tracking the brightest object is detected and its position is used for stabilizing the light injection into the fibers.

The science detector is read out in real-time to detect fringes and to calculate the optical path difference (OPD) for each baseline. The fiber control unit of GRAVITY is used to minimize these OPDs by setting its optical path length for each telescope input.

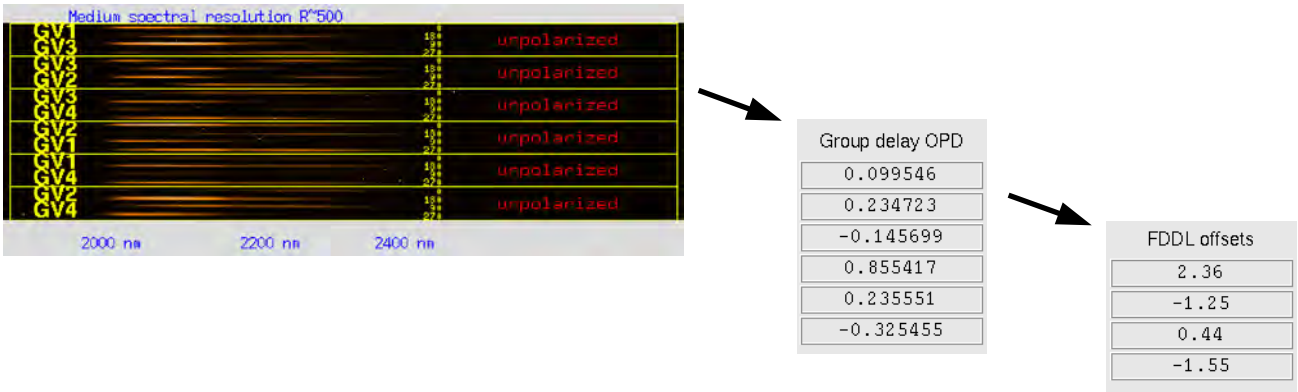

E. Wiezorrek, F. Eisenhauer, O. Pfuhl and the GRAVITY team

GRAVITY PLC based motor control & optimisation

GRAVITY is a highly precise performance instrument with a very sensitive metrology. Therefore vibrations caused by scientific actuator mechanisms must be reduced to a minimum. This requirement is achieved by the stepper motor control optimisation. PLC based stepper motor controllers from type Beckhoff ES7041 are defined as new ESO-Standard. GRAVITY is the first instrument following this standard on the Very Large Telescope (VLT).

The Stepper-Motor-Control-Unit, the Stepper-Motor-Breakoutbox and the Resolver-Readout-Box inclusive application were designed and built by MPE. All stepper-motor-mechanism optimisations were done by MPE and verified by the consortium partners afterwards.

GRAVITY-mechanisms with stepper motors

Name of mechanism	Units
Field Rotator	4
Half Wave Plate	4
Filter Slider	1
Polarizer	8
Wollaston	2
Focus Stage	2
GRISM-Wheel	1

Optimisation procedure

1. Check levels of motor- and feedback-signals with the oscilloscope using the breakoutbox.
2. Adjust motor-current-control-loop. Verification with current signal on oscilloscope.
3. Adjust motion-velocity-control-loop. Verification with the TwinCAT-Scope and the feedback of the Metrology-GUI from the Instrument Control Software (ICS)
4. Adjust the position-control-loop. Verification with the TwinCAT-Scope and Resolver-Readout-Box.
5. Final test with ICS and Metrology-GUI

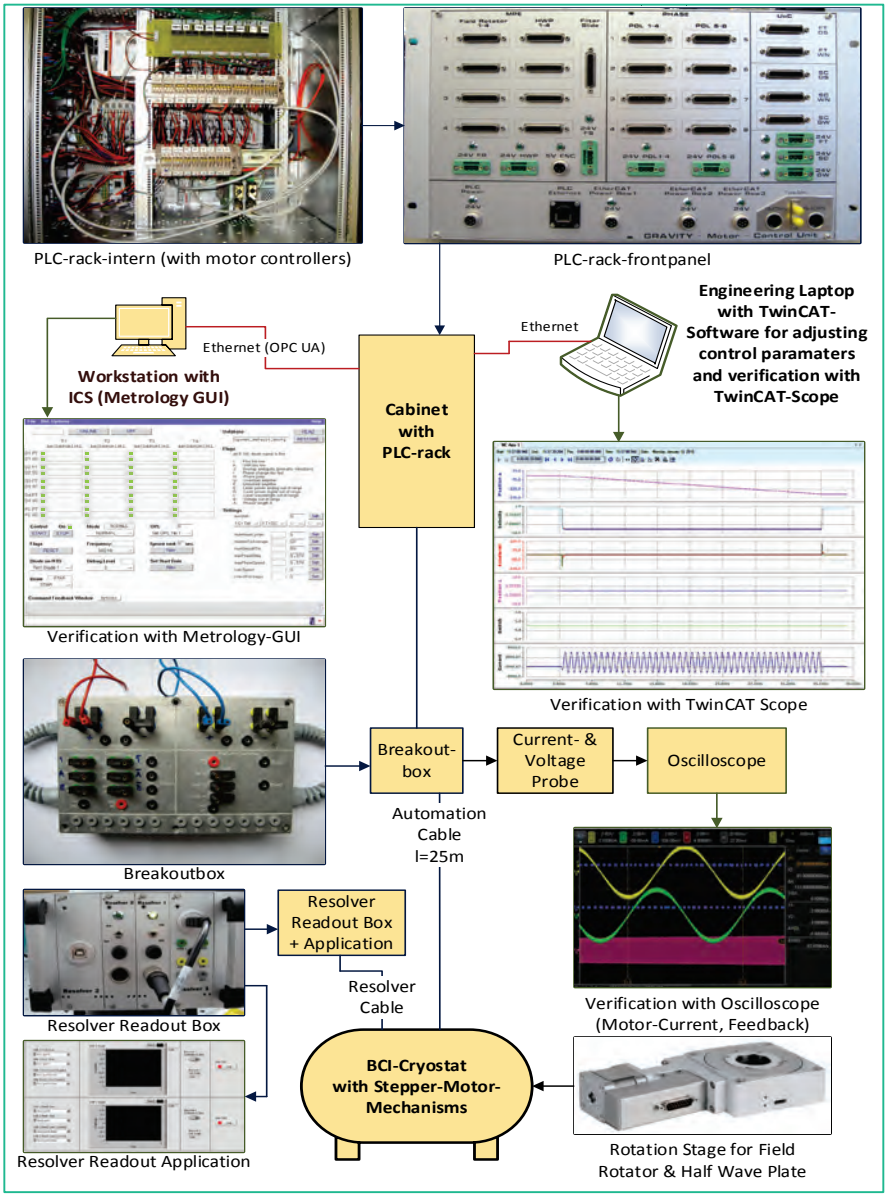

GRAVITY Stepper Motor Optimisation Scheme

C. Rau, S. Kellner, M. Plattner, F. Eisenhauer, E. Wieprecht, O. Pfuhl, T. Ott, S. Gillessen, S. Yazici, O. Hans, MPE-Workshops and the GRAVITY-Team

GRAVITY control electronics

The GRAVITY electronics consists of a multitude of systems, many of which are closed-loop control systems working at high speed and high accuracy. The motion systems use three different types of actuators: DC motors, stepper motors and piezo actuators. These operate at different, well-defined temperature levels, between 77K and room temperature.

A large part of the GRAVITY electronics was designed and manufactured at MPE.


GRAVITY: overview

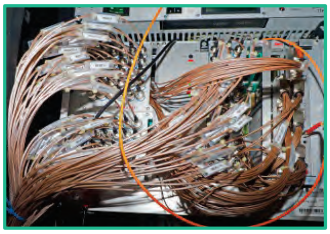
LCU cabling

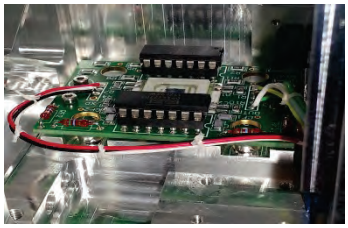
PSD controller (MPE)

The GRAVITY instrument is a fully remote controlled system since all functions are implemented in a cryogenic vessel.

The housekeeping control is done by a PLC and the system alarm is connected to the observatory's alarm system.

The main body of the instrument is located in the VLTI laboratory, while most of the electronic racks are in an adjacent room. Some of the electronics are placed at the UT and AT telescopes (metrology receivers and pupil beacons) or in the Coudé rooms (laser guiding electronics and wavefront sensors).
Because of the large number of components, the cabling is very complex with more than 700 cables with a total length of more than 6 km.

GRAVITY electronics in numbers	
Cabinets	6
DC motors	10
Stepper motors	21
Piezo actuators	46
Photo diodes	44
Computers	10
Temperature controllers	10
IR detectors	3
Shutters	12
Lock-In amplifiers	40
Frequency generators	3
PLC	2
Analog-in signals	132
Analog-out signals	60
Digital I/O signals	70

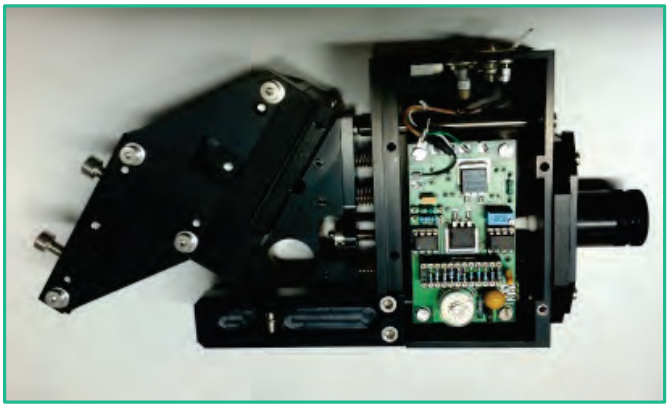
Metrology receiver (MPE)

S. Kellner, O. Hans, C. Rau, F. Eisenhauer, M. Haug, M. Plattner and the GRAVITY team

GRAVITY – Instrument Control Software

The GRAVITY Instrument Control Software has been successfully used during Instrument checkout and commissioning operations.
The software team is in the process of optimizing algorithms, performance and improving stabilization.

Instrument Control : Hardware Setup

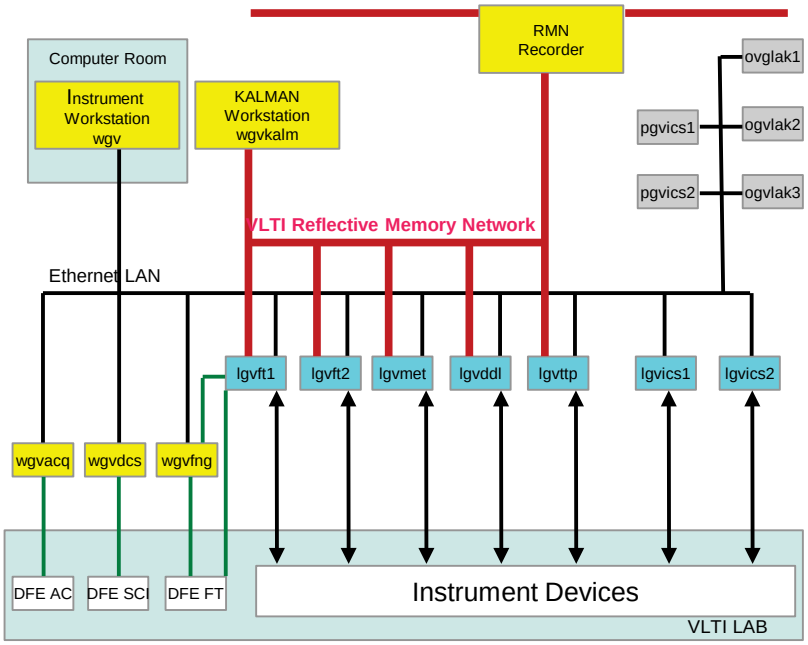

Operator Front End Panel

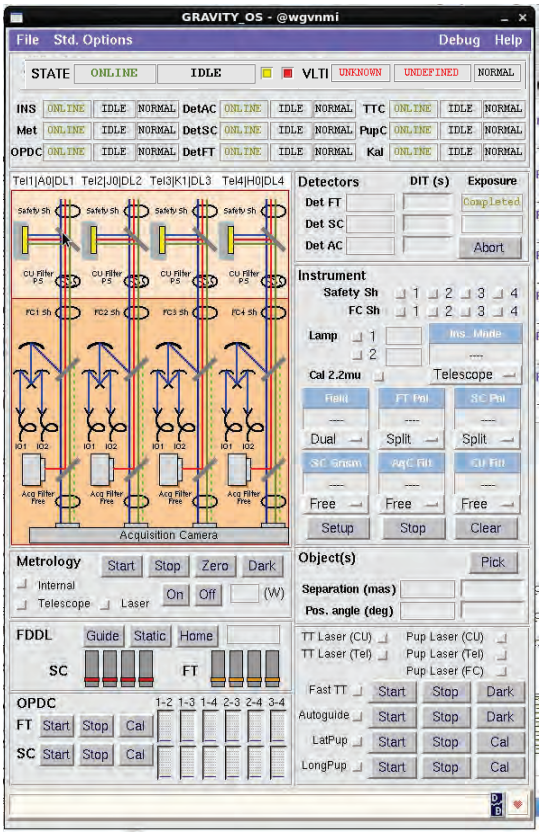

GRAVITY required the development of one of the most complex instrument software systems ever built for an ESO instrument.
Apart from its many interfaces and inter-dependencies, one of the most challenging aspects is the overall performance and stability of this system.
The three infrared detectors and the fast reflective memory network (RMN) recorder create a total data rate of up to 20 MiB/s, accumulating to a maximum of 250 GiB of data per night.
The detector workstations, the two instrument Local Control Units (LCUs), the five real-time LCUs running applications under TAC (Tools for Advanced Control) architecture and the Instrument and Kalman workstations, are interconnected with Gigabit Ethernet. RMN and other dedicated fiber connections ensure highest data-rates and low latencies.

E. Wieprecht, T. Ott, E. Wiezorrek, F. Eisenhauer and the GRAVITY team

GRAVITY Telescope Installations & Alignment

Each VLT Unit Telescope and each Auxiliary Telescope is equipped with four metrology receivers and four pupil tracking laser beacons. These units are clamped to the spider arms sustaining the M2 structure. The laser source for the beacons and the digitizer electronics for the metrology receivers are located in an electronics box at the center piece of the M1 cell.

During a pre-installation the four metrology receivers and the four laser beacons are mounted at the M2 spider armss within a radial precision of ± 15 mm. In a second step the final radial placement of ±1 mm is achieved by using a laser tracker system.

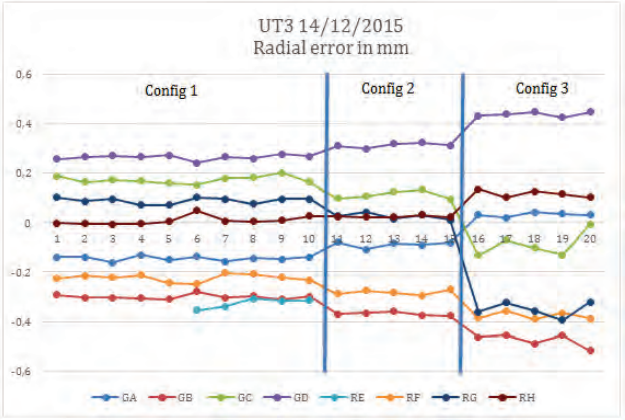

The measured radial positions of the units is at all altitude angles of the telescope within the specification of ±1mm.

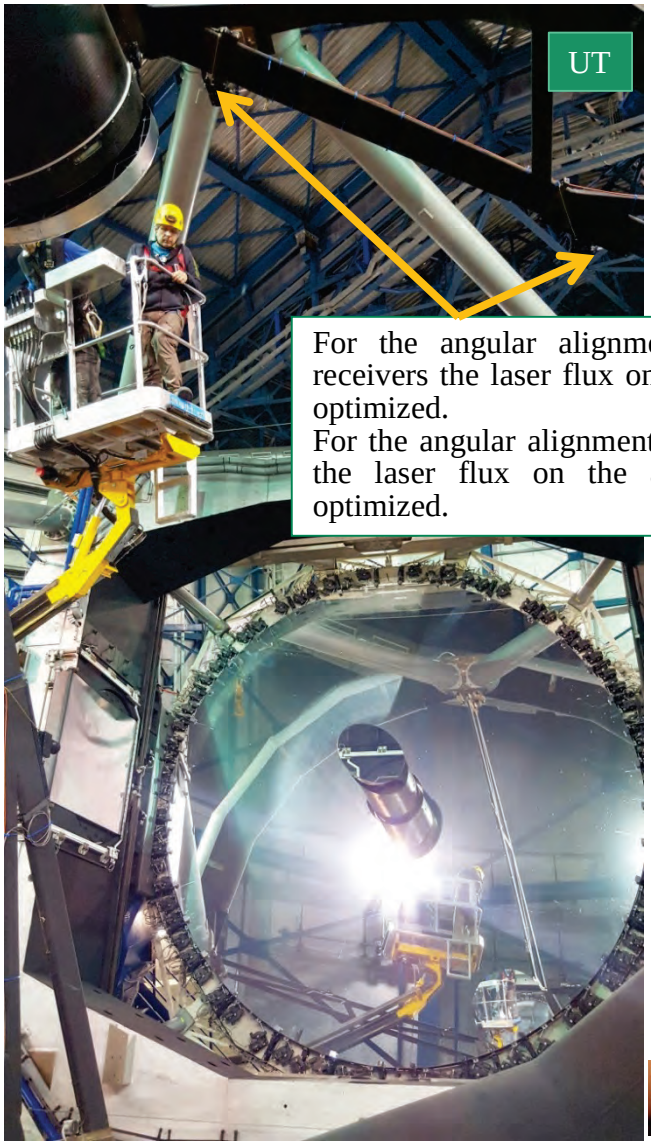

For the angular alignment of the metrology receivers the laser flux on **the receiver diode** is optimized.
For the angular alignment of **the pupil beacons** the laser flux on the acquisition camera is optimized.

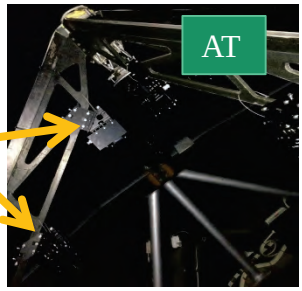

The **electronics box** placed at the center piece converts the analog metrology signal into a digital signal that can be transported with a fiber link. In addition, the fiber link is used to switch on the laser beacons and the metrology receivers.

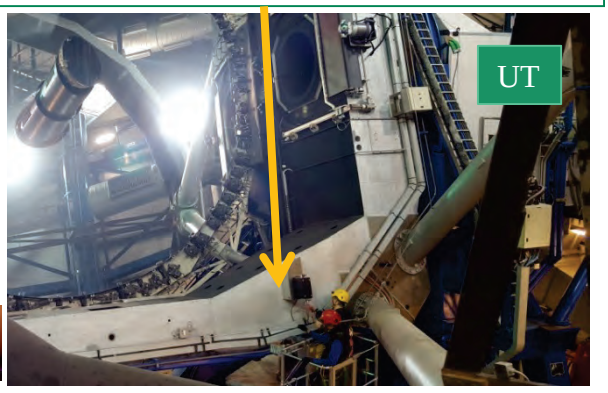

F. Haußmann, M. Haug, S. Gillessen, S. Kellner, M. Lippa, F. Eisenhauer, O. Pfuhl, Ş. Yazıcı, T. Ott

ARGOS

The ARGOS laser guide star facility has seen first light on sky and is currently undergoing commissioning at the large binocular telescope. With a Multi Laser Guide Star ground layer adaptive optics, ARGOS achieves first closed loop corrections on sky.

In a worldwide unique combination, ARGOS and the LUCI instruments at the LBT bring together an enhanced spatial resolution over a wide field of view, and a high multiplexing capability of the multi-object spectrographs. Amongst other scientific programs, high-z galaxy research will strongly benefit from the increased sensitivity, the spatially resolved spectroscopy and higher spectral resolution that can be achieved in that combination. Shrinking the PSF size towards a 'Hubble type' 0.2 to 0.3'' level, the signal to noise ratio of an observation can be increased by a factor 4 to 9, compared to seeing limited programs.

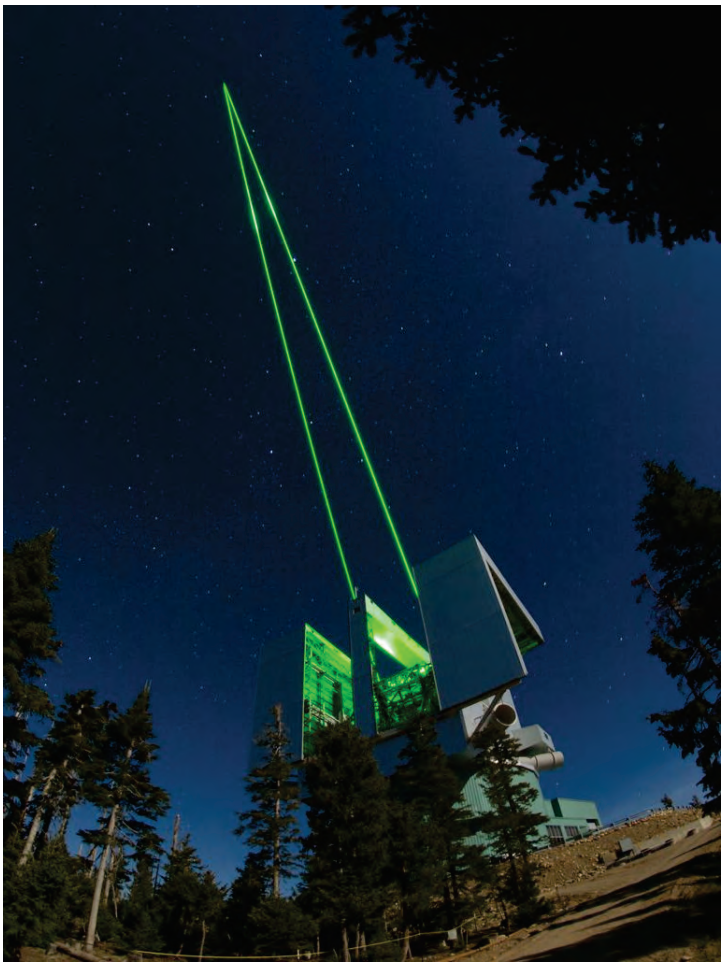

Argos is based on a pair of Rayleigh laser star constellations being launched into the sky above each of the LBTs 8.4m mirrors. A total of six powerful pulsed laser beams create a wide laser guide star constellation in the upper atmosphere. With detecting the scattered light in fast gated wavefront sensors, the atmospheric distortions of the atmospheric ground layers can be measured. Correcting these aberrations with LBTs adaptive secondary mirrors ARGOS achieves a uniform wide field correction. Both LUCI imagers and spectrographs can benefit from the enhanced image quality, resulting in increased point source sensitivity, higher spatial resolution and signal to noise.

http://www.mpe.mpg.de/ir/argos

S. Rabien, G. Orban de Xivry, J. Ziegleder and the ARGOS team

First On-sky Results with ARGOS

We present the first results of ARGOS, the multiple laser guide star and wavefront sensing facility for the Large Binocular Telescope. This system delivers an improvement by a factor of two in FWHM over the 4x4' field-of-view of both LUCI instruments. LUCI 1 and LUCI 2 are two near-infrared wide field imagers and multi-object spectrographs. Their capability and efficiency will be boosted by the increased resolution and encircled energy.

The first on-sky ground-layer adaptive optics loop closure with ARGOS has been achieved in Fall 2014 on the right eye of the Large Binocular Telescope.
Stable operations in closed-loop have been demonstrated in May 2015 with hour-long integrations and repeated good performances over several nights.
Since then, the commissioning has been proceeding with the installation of the left system and the beginning of the left on-sky operations in Fall 2015.

Fig. 1. shows a combined image of the galaxy Maffei1 obtained with ARGOS and LUCI2. Fig.2 illustrates the good uniformity of the correction provided by ARGOS on the same images with <0.3" PSF FWHM in all three bands. Fig. 3. presents a summary of the performances obtained so far with ARGOS in broad band near-infrared imaging.

Fig.1. 4'x4' imaging of Maffei 1 in J-, H-, Ks-band with LUCI2 and ARGOS.

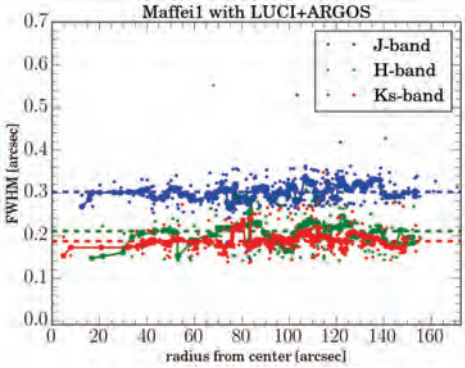

Fig.2. PSF FWHM as a function of radius from the center of the field.

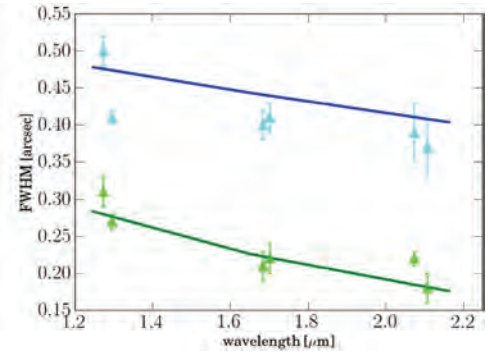

Fig.3. J-, H-, Ks-band PSF FWHM. (Blue) Open-loop seeing. (Green) Closed-loop PSF FWHM with the ARGOS correction. The curves show an early simulation of ARGOS for a seeing of 0.8". The points are data obtained during ARGOS commissioning.

References:

• Orban de Xivry G., Rabien S. et al. 2016,
"First Results of the Ground Layer Adaptive Optics System ARGOS", AO4ELT4 conference

G. Orban de Xivry, S. Rabien, J. Ziegleder and the ARGOS team

PACS Photometer: final calibration and processing

Processing and calibrating the superb PACS photometer data taken using Herschel observatory has entered the final stage: Legacy Products generation. The archives will provide users with fully calibrated and science ready maps as well as all the required files necessary for the users to reprocess the data according to her/his new science case.

The Herschel-PACS bolometers used a technology never flown before in space, but their excellent performance and stability have allowed the PACS Instrument Control Centre to achieve a calibration and processing quality to deliver science ready archive products. The flux calibration is accurate to 5-7% (dominated by uncertainties in the calibrator fluxes), reproducible to <3%, and linear over 5 orders of magnitude (Fig. 1). The calibration is consistent between three types of calibrators - stars, asteroids, and planets/satellites. Point spread functions have been fully characterised (Fig. 2), and recent improvements in the pointing reconstruction make them very stable. The significant 1/f noise of the PACS photometers led to a considerable effort of optimising and comparing mapmakers, and validating the archive products.

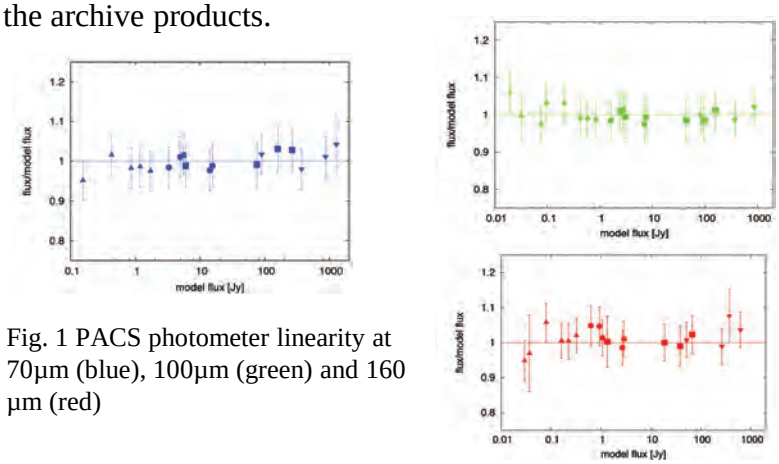

Fig. 1 PACS photometer linearity at 70µm (blue), 100µm (green) and 160 µm (red)

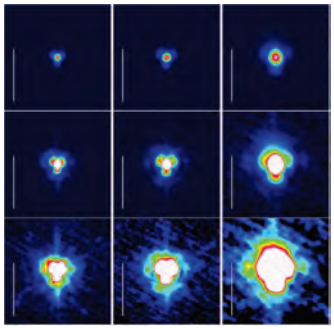

Fig. 2 Vesta PSF. left 70µm
middle: 100µm
right: 160µm

High quality and consistent results are now achieved on point and compact sources with chop/nod and high pass filtered scan observations, and for complex and extended structures the Jscanam and Unimap mappers have reached a high level of maturity. For scanned observations, JScanam maps will be available directly as standalone Browse products (top level download from the Herschel science archive), the others will be available as alternative mapping options.

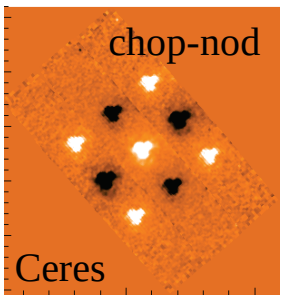

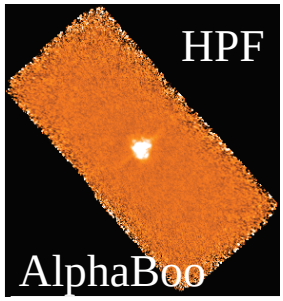

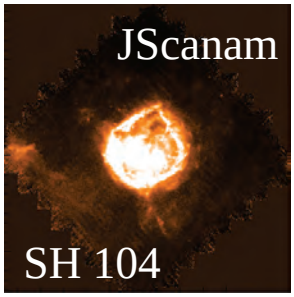

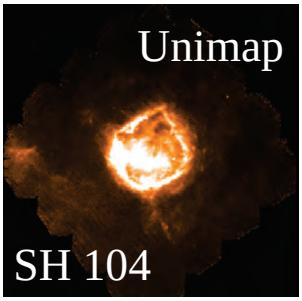

References:

1) Piazzo et al.: "UNIMAP: a generalized least-squares map maker for Herschel data", 2015 MNRAS, 446: 1471
2) Gracia-Carpio, et al. "The JScanam Map-Maker Method Applied to Herschel/PACS Photometer Observations", 2016 proceedings of ADASS XXV
3) Balog et al.: "The Herschel PACS photometer calibration: point sources flux calibration for scan maps" 2016, Exp Astron 37: 129 (Fig. 1, 2)
4) Mueller et al. 2016: arXiv 1502.05785

V. Doublier Pritchard, T. Müller, J. Gracia-Carpio, D. Lutz, S. Berta & PACS ICC

The JScanam Map-Maker

JScanam is the default map-maker for Herschel/PACS photometer observations. Making use of the redundant information from multiple passages on the sky with different scanning directions, JScanam is able to remove the 1/f noise that severely affects PACS far-infrared maps, preserving at the same time point sources and real extended emission. The JScanam pipeline has been designed to run automatically on all kind of maps and astronomical environments, from Galactic star-forming clouds to deep cosmological fields. Science users can download the results from the JScanam automatic pipeline from the Herschel Science Archive (http://www.cosmos.esa.int/web/herschel/science-archive) and the new ESA Sky interface (http://archives.esac.esa.int/esasky-beta).

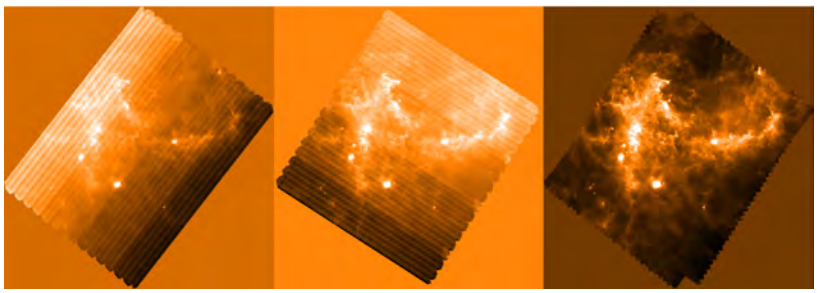

Maps of the scan (left panel) and cross-scan (central panel) observations of the Rosette cloud previous to any JScanam processing. Strong signal drifts are visible perpendicular to each scan direction. The right panel shows that the 1/f noise is removed after the JScanam automatic processing.

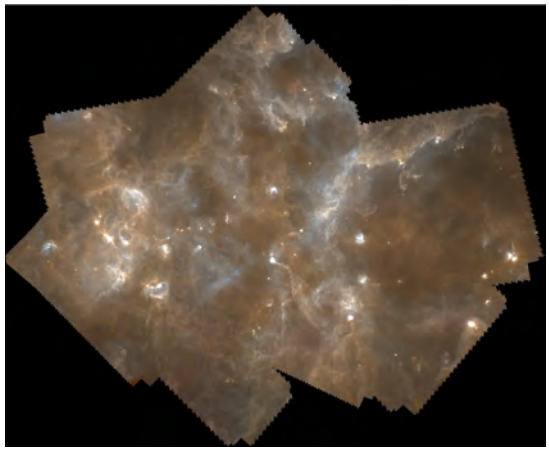

Composite map of the Cygnus-X massive star forming region (blue: 70µm, red: 160 µm). The map, 8.0 degrees wide and 6.6 degrees high, combines data from multiple Herschel programmes.

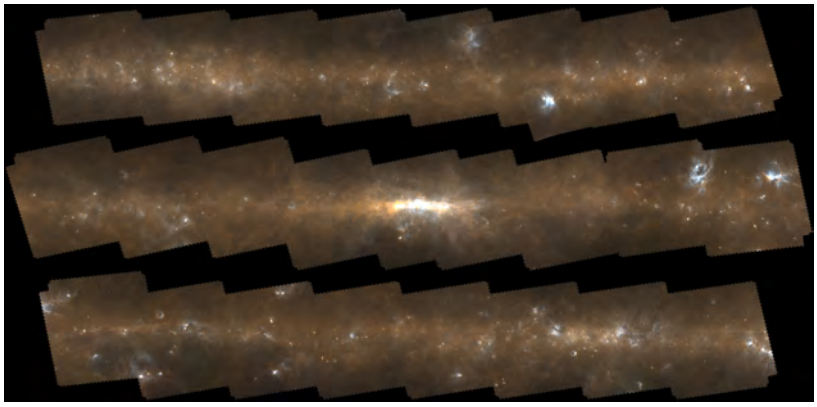

Colour maps of the central 50 degrees of the Milky Way (top image, blue: 70µm, red: 160 µm) and the Large Magellanic Cloud (right image, blue: 100µm, red: 160 µm). These kind of maps are currently being processed by the PACS ICC. The intention to make them available to the whole astronomical community in the form of Highly Processed Data Products.

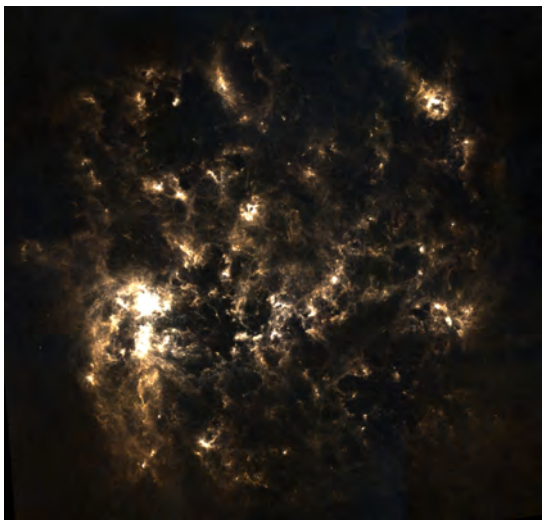

References: Graciá-Carpio, J., Wetzstein, M., Roussel, H., 2015 arXiv:1512.03252

J. Graciá Carpio, T. Müller, V. Doublier Pritchard, D. Lutz, S. Berta & PACS ICC

PACS Spectrometer: Final Calibration and Processing

After more than 10 years of instrument calibration and software development the PACS Instrument Control Center (ICC) is preparing the final bulk reprocessing of all 5180 PACS spectrometer observations with the pipeline to produce the legacy products for the Herschel Science Archive (HSA). We have completed all standard calibration algorithms and files for the flux, wavelength and spatial calibration and worked on tools to calibrate special cases like extended sources. Astronomers can use these tools in the Herschel Interactive Processing Environment (HIPE) to improve the calibration for specific science cases. Leftover work include some final calibration fixes, FITS header fixes, general bug fixes and documentation.

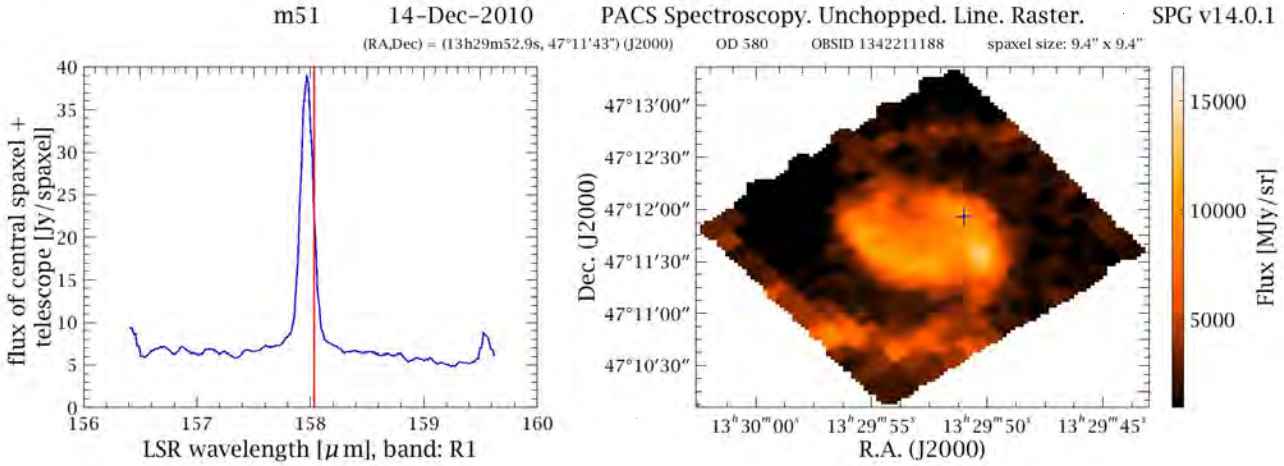

Figure 1: Example image from the HSA of an observation of M51. The right panel shows one layer (at the red line in the left panel) from a spectral cube and the left panel the spectrum at the cross.

One of the tools we offer deals with the flux calibration of extended sources. The standard flux calibration assumes that the source is a real point-source. It can be improved by computing the flux distribution on the IFU spaxels based on the instrumental PSF and a model of the morphology of the source. Fig. 2 shows how the additional correction depends on the size of the source. Further corrections which require manual interaction are offsets in the pointing (source not exactly on central spaxel), background contamination or very bright sources with saturation issues.

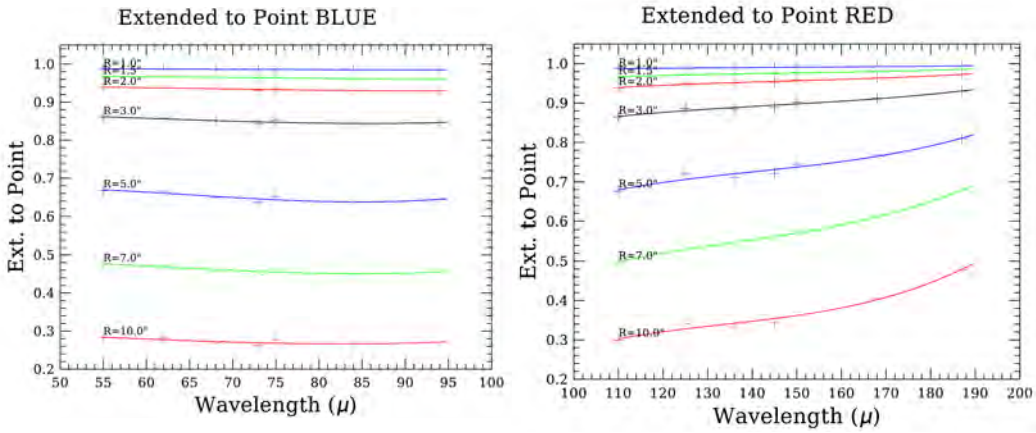

Figure 2: Corrections to the flux in the central spaxel of the PACS IFU relative to a point-source as a function of wavelength for a model disc source with a radius between 1.0 and 10.0 arcsec.

References:

- Poglitsch, A. et al., 2010, A&A 518, L2
- Schreiber, J. et al., 2009, Proceedings of ADASS XVIII, ASPC 411, 478
- Balm, P., 2012, Proceedings of ADASS XXI, ASPC 461, 733

J. de Jong, A. Contursi, H. Feuchtgruber, A. Poglitsch, E. Sturm and the PACS ICC

ERIS Project Overview

The MPE instrumentation project ERIS (**E**nhanced **R**esolution **I**mager and **S**pectrograph) for the Cassegrain focus of VLT UT4 has progressed to the preliminary design review. This instrument for the European Souther Observatory (ESO) combines diffraction limited near-IR integral field spectroscopic capabilities of the upgraded SPIFFI with a new 1-5µm imaging camera (NIX) and a new wavefront sensing sub-system for the ESO adaptive optics facility. In the course of 2014 the project has been reshaped from an ESO led project to a consortium project under leadership of MPE as the PI institute. ERIS will be used for a variety of science programs at MPE, including spatially resolved outflows in high redshift galaxies, and studies of stellar orbits and accretion events in the Galactic Centre.

The ERIS instrument design has evolved to the project preliminary design review:

- A simple optical design has been developed, maximizing throughput and image quality (Fig. 1)
- The mechanical design of the instrument has been consolidated to provide sufficient space for all sub-systems while at the same time remaining robust against flexures caused by the observing secenario in the Cassegrain focus of the VLT (Fig.2).
- Finite element analysis of the main structure showed compliance to the requirements regarding safety against earth quakes.
- All instrument budgets (mass, torque, volume, power, wavefront error, throughput, image motion) are compatible with specifications.

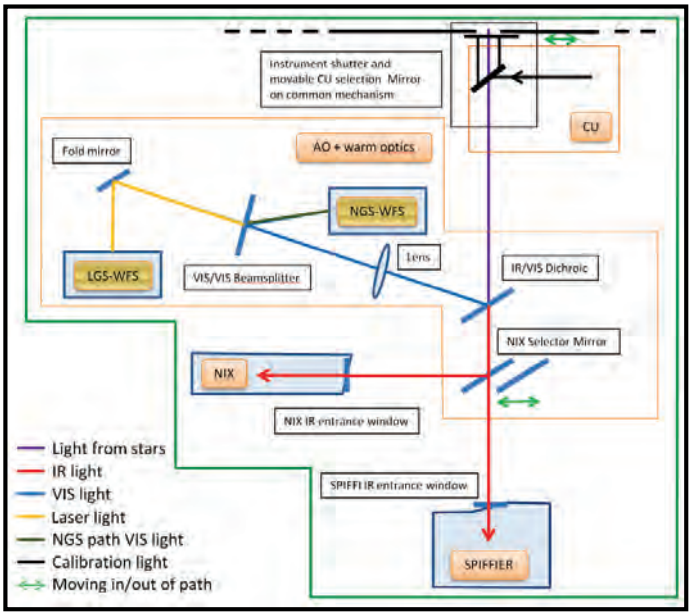

Fig.1: Optical concept of ERIS

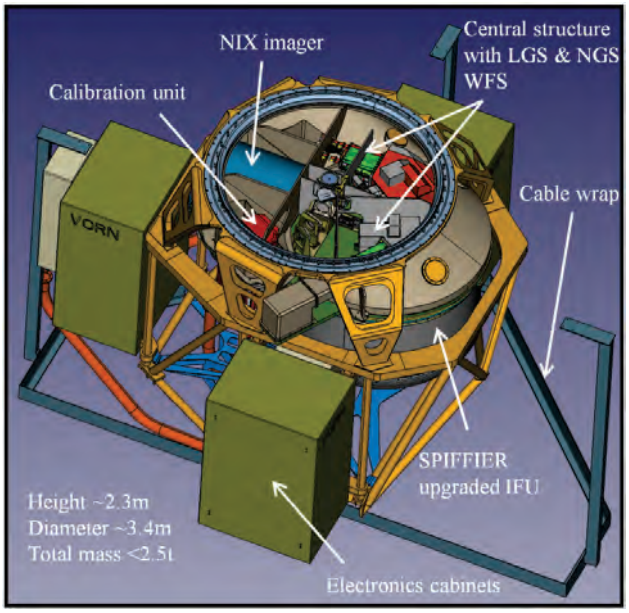

Fig.2: CAD overview of the preliminary design

The ERIS project and sub-systems are distributed among the following consortium partners:

- PI, project management, system engineering: MPE
- SPIFFI upgrade to SPIFFIER: MPE
- NIX: UK Astronomy Technology Centre in Edinburgh (ATC) and ETH-Zürich
- Central mechanical structure, system electronics and IR detectors: MPE
- Pipeline software: MPE (SPIFFIER), ATC (NIX)
- Adaptive optics and warm optics: INAF-Arcetri
- Calibration unit: INAF-Teramo
- WFS cameras, AO real time computer, detector procurement and testing: ESO
- Instrument control software: INAF-Padua (lead) with contributions from ATC and MPE

H. Feuchtgruber, A. Buron, R. Davies, F. Eisenhauer, E. George, D. Gräff, M. Hartl, H. Huber, M. Plattner, C. Rau, E. Sturm, E. Wiezorrek

Making SPIFFI SPIFFIER for use in ERIS

SPIFFI is an AO-fed integral field spectrograph operating as part of SINFONI on the VLT, which will be upgraded and reused as the subsystem SPIFFIER in the new VLT instrument ERIS. In January 2016, we used new technology developments to perform an early upgrade to some optical subsystems in the SPIFFI instrument, such that ongoing scientific programs can make use of enhanced performance before ERIS arrives in 2020. In the course of the early and late upgrades, optical components and the detector are replaced, resulting in substantial throughput and spectral resolution gains. These upgrades benefit all science cases, but in particular will benefit our groups' work on spatially resolved spectra of high redshift star-forming galaxies and our studies of the galactic center. Additionally, upgrades to the electronics and motors ensure that this scientifically prodigious instrument remains operational for the lifetime of ERIS.

Figure 1: Labeled interior of the SPIFFI cryostat from the original commissioning. Many components are changed in SPIFFIER for enhanced performance and reliability.

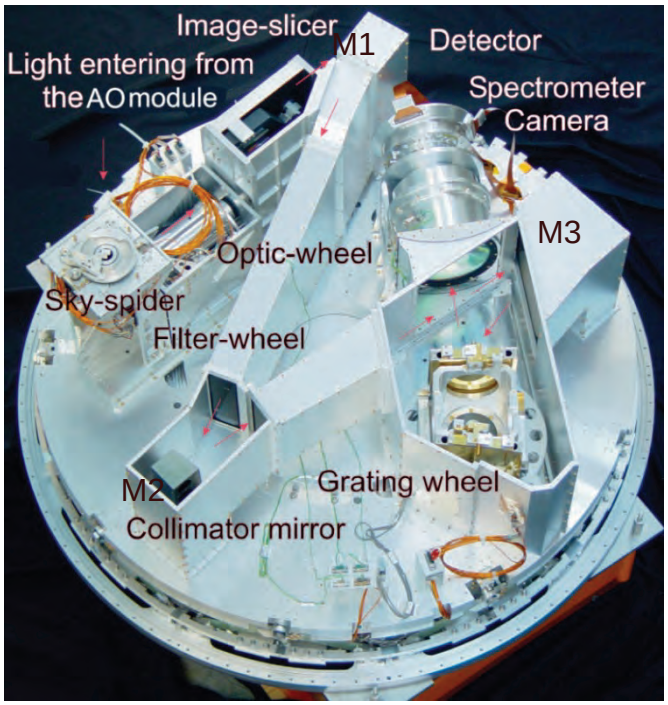

The early upgrade included replacing:

- Entrance field stop
- pre-optics collimator
- Pre-optics in all pixel scales (25, 100, 250 mas) and pupil imager
- J, H, and K – band Filters
- Spectrograph collimator mirrors (M1, M2, and M3)

Table 1: Performance increase results from the early upgrade.

Band	Throughput Gain	Resolution Gain (25, 100, 250) mas
J	+10-50%	+(4, 18, 14)%
H	+8%	+(2, 19, 12)%
K	+10%	+(11, 41, 15)%
H+K	--	+(0, 36, 23)%

Figure 2: Plot of New/Old thoughput in J-band.

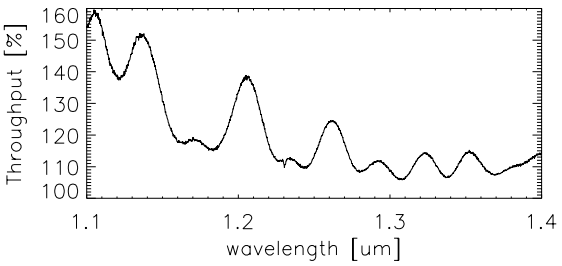

The full upgrade will include:

- New cryogenic motors and grating drive
- Upgrading electronics to PLC control
- Replacing H+K grating by high-resolution grating operating in J, H, and K bands.
- New order sorting filters
- New detector with higher quantum efficiency.
- New cryostat cover with new entrance window and cold finger for thermal background suppression in NIX.

E. George, A. Buron, R. Davies, F. Eisenhauer, H. Feuchtgruber, D. Gräff, M. Hartl, H. Huber, M. Plattner, C. Rau, E. Sturm, E. Wiezorrek

Analysis of diamond turned mirrors for SPIFFI

The upgrade of SPIFFI, which is the integral field spectrograph of the SINFONI instrument on the VLT, is part of the ERIS instrument project. The main goals of this upgrade in January 2016 were to improve the image quality, contrast and throughput. Therefore the three spectrometer collimator mirrors in SPIFFI have been replaced during the upgrade.

The collimator optics of the SPIFFI spectrometer is a three-mirror-anastigmat working in a wavelength range of J, H, and K band (1.0 – 2.5 µm). It consists of one spherical (M1) and two off-axis prolate elliptical (M2 and M3) mirrors which are made out of gold coated aluminum.

Why did we exchange the mirrors?

The old mirrors were manufactured ~15 years ago and show a circular shaped texture from the diamond turning process of the aluminum (fig.1, left). This leads to worse image quality. The applied post-polishing at that time could only partly cure the surface quality of M1 and M3.

What is the difference between the new and the old mirrors?

Old mirrors: nickel-plated aluminum with unprotected gold layer
New mirrors: no nickel layer, but SiO_2 protection layer on the gold surface
Current diamond turning machines can be controlled more accurately, resulting in turning marks which are a factor of 20 smaller (fig.1, right).

Figure 1: M3 mirror wavefront deviation from nominal. Left: Old M3. Right: New M3.

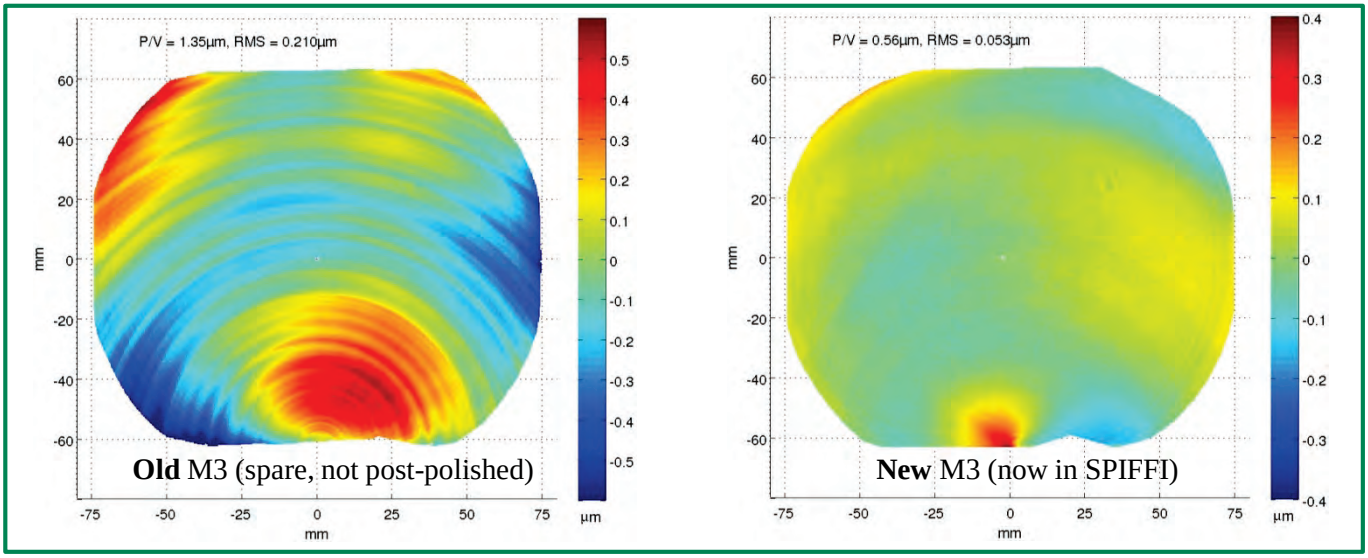

How do we measure mirror surfaces?

We look at the surface of the mirrors with an interferometer in single and combined setups. The wavefront distortion on the M3 mirror is shown in microns on the scale on the right of figure 1.

What do we expect from the new mirrors?

Better PSFs from the collimator (figure 2), corresponding to higher spectral resolution in the spectrometer.

Figure 2: PSF from the combined 3 collimator mirrors using 633nm laser [scale in mm]. Left: Old. Right: New.

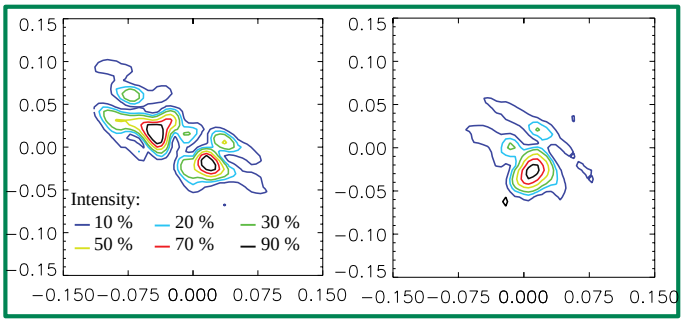

D. Gräff, H. Feuchtgruber, E. George, M. Hartl

MICADO – Multi-AO Imaging Camera for the E-ELT

MICADO is the Multi-Adaptive Optics Imaging Camera for Deep Observations. It will provide diffraction limited imaging at near-infrared wavelengths as an E-ELT first light instrument, with an additional focus on precision astrometry, as well as high contrast imaging and long-slit spectroscopic modes. The Agreement with ESO for the design and construction of MICADO was signed in September 2015, and MPE is leading the consortium which includes institutes in 5 European countries.

MICADO is optimised to work with a ~1' field of view at the Nasmyth port of the European Extremely Large Telescope (E-ELT), corrected by a natural guide star single-conjugate adaptive optics (SCAO) and a laser guide star multi-conjugate adaptive optics module (MAORY). It will provide two diffraction limited imaging modes with pixel scales of 4 mas and 1.5 mas and an astrometric accuracy of 50 µas, as well as a long-slit spectroscopic mode with a resolution of ~8000 for wavelengths from 0.8 µm to 2.4 µm. High-contrast imaging will be implemented via a classical focal plane coronograph with Lyot stop.

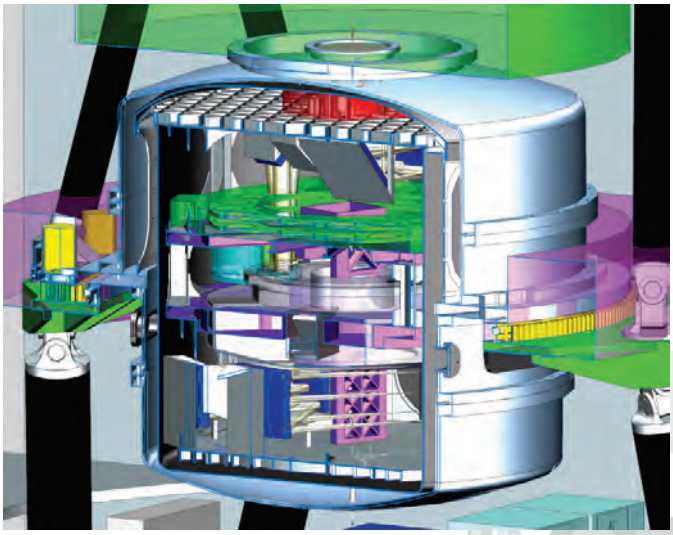

MICADO opto-mechanical design.

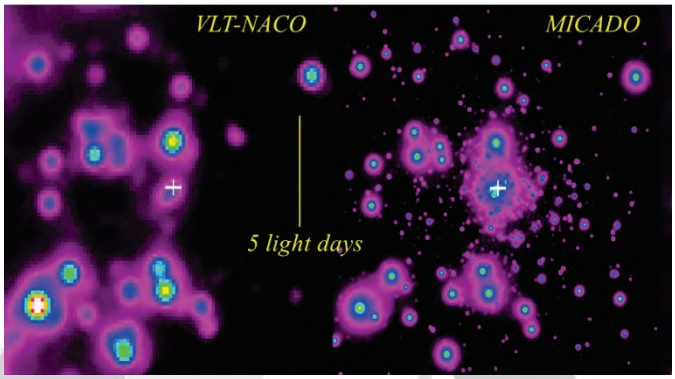

Galactic centre as seen by the current VLT-NACO camera compared to a simulated image by MICADO with ~5 times higher resolution.

The key science cases addressed by MICADO, and which impose a variety of technical challenges on it, are:

Imaging: Cosmic star formation history: resolved stellar populations; structure of high-z galaxies on 100 pc scales; nuclei of nearby galaxies (stellar cusps, star formation, black holes).

Astrometric imaging: Stellar motions within light hours of Sgr A*; IMBHs in stellar clusters and dwarf galaxies; Milky Way formation: proper motion of clusters and dwarf galaxies.

Spectroscopy: Ages, metallicities, masses of first elliptical galaxies at z=2-3; spectra of first supernovae at z=1-6; redshifts, velocities, metallicities of SFGs at z = 4-6.

High-contrast imaging: Giant/massive planets at a few AU around nearby stars; direct detection of planets discovered via RV measurements.

Time resolved astronomy: Pulsars and magnetars; accreting white dwarfs; compact binary systems transits and occultations.

R. Davies, M. Hartl, M. Haug, V. Hörmann, J. Schubert, E. Sturm and MICADO team

I.1) Group: Prof. Ewine F. van Dishoeck

ALMA reveals planet construction sites

Transitional disks around young stars with large dust cavities are prime targets to search for young embedded planets. Models of planet-disk interaction predict that young planets clear a gap in the gas while trapping dust at larger radii. To test these models, high spatial resolution ALMA data of ^{13}CO and C^{18}O lines of four transitional disks with large dust cavities have been obtained. Using the DALI code, the gas surface density profiles have been quantified.

Gas cavities are found to be up to three times smaller than those of the dust, whereas the gas surface density inside the gas cavities decreases by a factor of 100-10^4 compared with that derived for the outer disk. Gas viscosities are likely low, α=10^{-4}-10^{-3}. These resolved measurements of the gas and dust rule out alternative scenarios and strongly suggest the presence of giant planetary companions inside the cavities, at orbital radii smaller than indicated by the dust images alone.

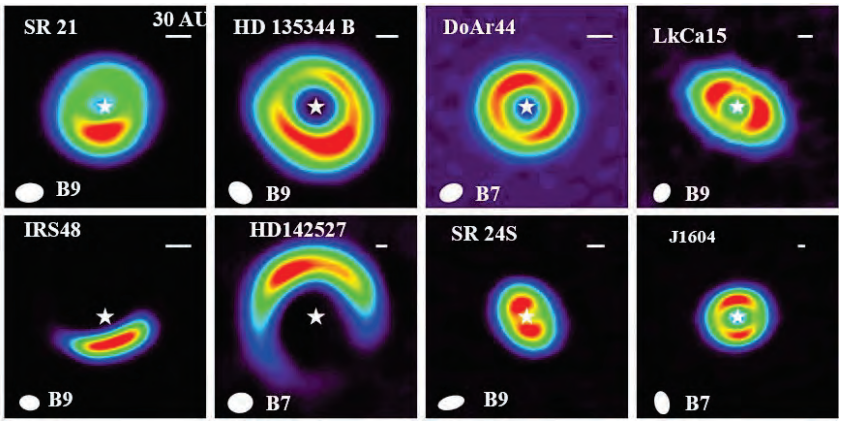

Fig. 1: Gallery of ALMA mm continuum images of transitional disks from our and other programs, illustrating the variety of dust structures . Both radial and azimuthal dust traps are seen (van Dishoeck et al. 2015).

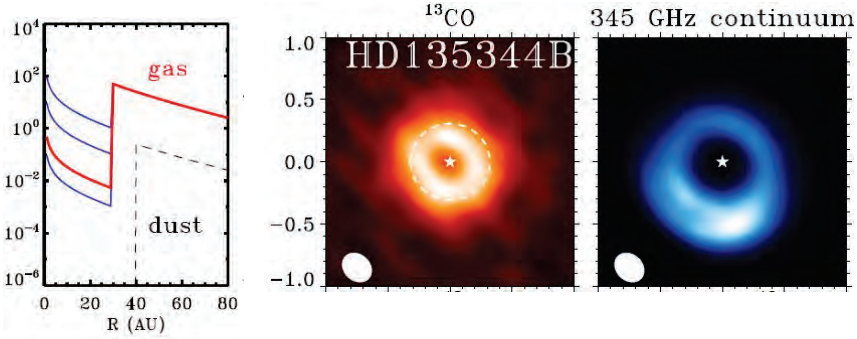

Fig. 2. ALMA images of dust (mm continuum, blue) and gas (^{13}CO 3-2 , orange) of the HD 135344B disk. The gas cavity is clearly smaller than that of the dust. Left: Inferred gas and dust surface density profiles in gr cm^{-2}; the red line indicates the best-fitting model (van der Marel et al. 2016).

References:

• Bruderer 2013, A&A 559, A46
• van der Marel, van Dishoeck, Bruderer et al. 2016, A&A 585, A58
• van Dishoeck et al. 2015, ASP conf series, vol. 499, ed. D. Iono et al., p. 281

E. F. van Dishoeck, S. Bruderer

Vortices and spirals in protoplanetary disks: millimeter vs. scattered light

In recent years spiral structures and asymmetric dust traps have been observed in protoplanetary disks and linked with the presence of planets. Spirals have so far been observed in scattered light, and dust traps in millimeter dust emission.
We present ALMA Band 7 (335 GHz or 0.89 mm) continuum observations of the disk around HD135344B at unprecedented spatial resolution of 0.16'' (22 AU). The data show an inner dust ring and an outer structure, cospatial with a spiral arm observed in scattered light. However we demonstrate that the millimeter dust feature itself is not consistent with a spiral arm due to its coradiance. Modelling of the morphology of our ALMA image shows that a single planet is sufficient to explain all observed millimeter features and one of the spiral arms observed in scattered light. The second spiral arm is instead triggered by the outer dust trap.

Left: 335 GHz ALMA continuum emission of HD 135344B. The white dashed ellipse indicates the 45 AU radius. The newly resolved features are labeled F1 and F2. **Right:** Overlay of the scattered light image of Garufi et al. (2013) (black contours) on top of the ALMA continuum emission. The spirals as identified by Muto et al. (2012) are labeled as S1 and S2.

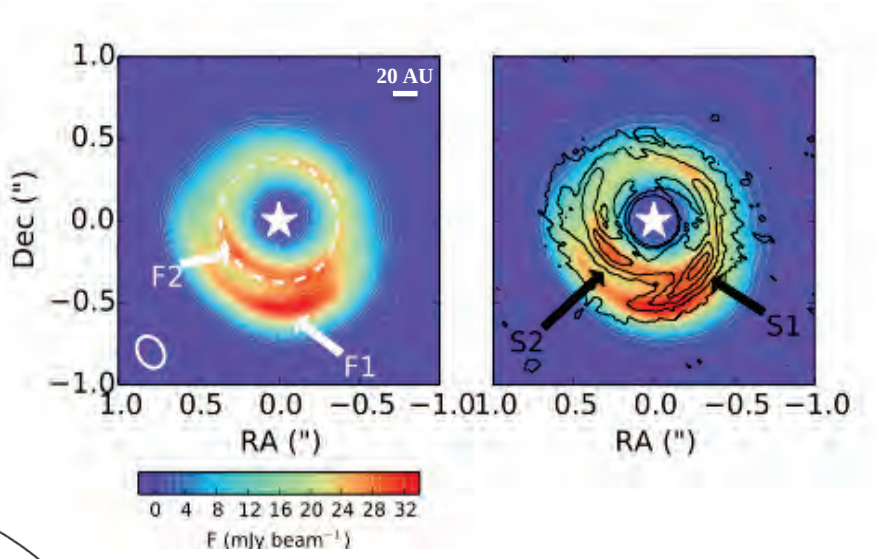

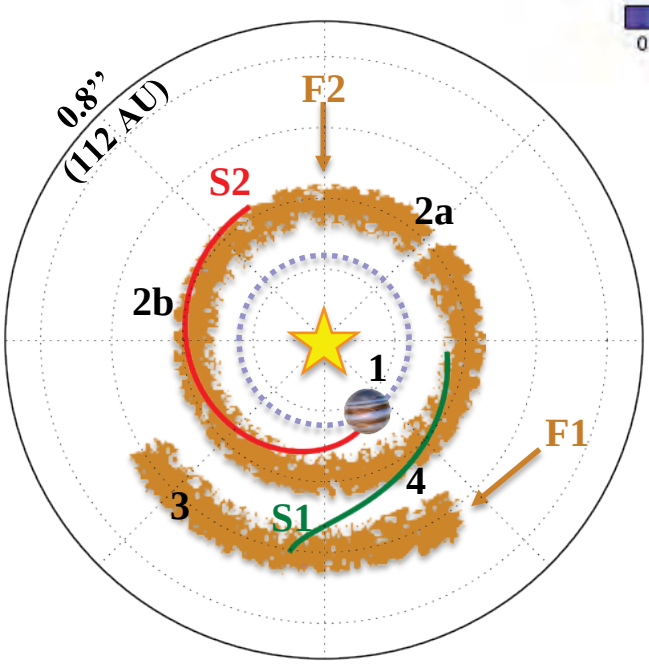

We propose the following scenario as an explanation:

1. A massive planet is formed at 30 AU radius.

2a. The planet triggers an inner dust trap F2

2b. The planet launches a first spiral arm S2

3. The inner ring triggers the formation of a second generation dust trap F1 (e.g. Lobo Gomes et al. 2015)

4. F1 acts like a planet and launches a second spiral arm S1 directed inward

References:
• Muto et al. 2012, ApJ, 748, L22; van der Marel et al. 2013, Science, 340, 1199; Garufi et al. 2013, A&A, 560, A105; Lobo Gomes et al. 2015, ApJ, 810, 94; van der Marel, Cazzoletti et al. submitted

P. Cazzoletti, E. F. van Dishoeck, et al.

The interplay of dust evolution and gas chemistry in protoplanetary disks

Thanks to new observational facilities, we have entered the era where both gas and dust properties of protoplanetary disks can be obtained simultaneously via high spatial and spectral resolution observations. In particular, ALMA has shown that large dust grains are systematically well segregated in the inner regions of protoplanetary disks, whereas gas tracers like CO emit from much larger radii as well.

We have coupled grain growth and dust segregation mechanisms with the thermo-chemical code DALI. We find that mm continuum and CO observations of well studied disks can be reproduced with a self-consistent model, when dust segregation is properly taken into account. Vertical settling of dust grains can significantly affect the thermal and chemical structure of the disk, and thus modify the most prominent emission lines. We conclude that both gas and dust need to be modeled simultaneously. By doing so, we can probe the thermal structure and the dust-to-gas ratio in disks, which are key parameters in planet formation theories.

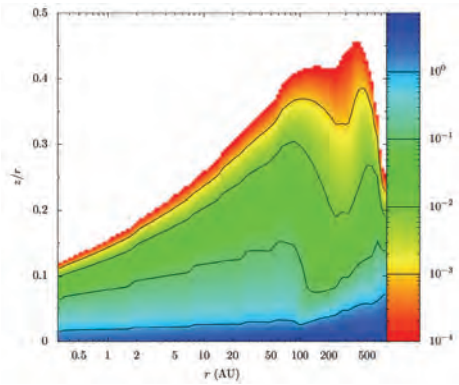

Figure 1. *Dust-to-gas ratio multiplied by a factor 100. The dust is settled in the disk midplane.*

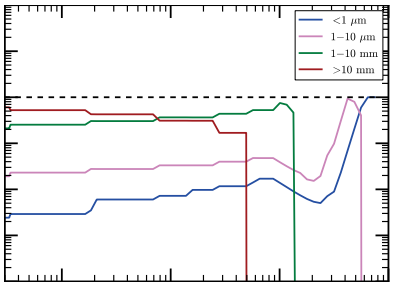

Figure 2. *Dust-to-gas ratio for different grain size bins, including dust evolution (cf. Birnstiel+15).*

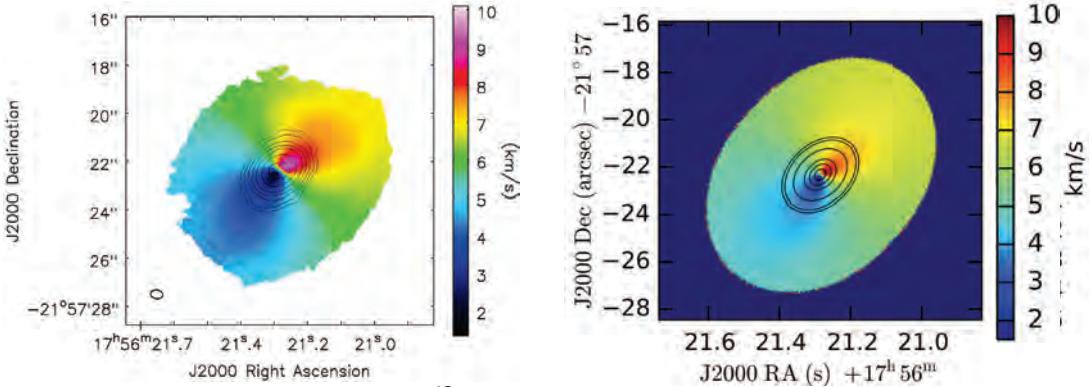

Figure 3. *Left panel: ALMA moment 1 map of ^{12}CO (3-2) of HD163296 (de Gregorio-Monsalvo+13); contours show continuum emission at 850 μm. Right panel: synthetic observation of a model of the system including dust evolution. Contours are shown at the same absolute flux values as the observations.*

References:
- de Gregorio-Monsalvo et al. (2013), A&A, 557, A133
- Bruderer (2013), A&A, 559, A46
- Birnstiel et al. (2015), ApJ, 813, 14
- Facchini et al. (2016), in prep.

S. Facchini, E. F. van Dishoeck

The role of cosmic rays in tracing molecular gas in galaxies

Molecular hydrogen (H_2) clouds are the dominant sites for star formation in galaxies. H_2 is not readily observable by radiotelescopes, so CO is widely used as a tracer. However, there is growing evidence that the standard CO-to-H_2 method may not be applicable to extragalactic objects. This evidence is supported by the recent discovery of CO destruction due to cosmic rays (CR) which has the potential of leaving vast amounts of H_2-rich gas undetectable in CO but traceable alternatively with CI. Understanding the role played by CRs is of great importance in energetic environments such as ULIRGs and starburst galaxies. Using 3D-PDR (Bisbas et al. 2012) we post-process a hydrodynamical snapshot of a 4000$M_\odot$ fractal GMC. We calculate the abundance distribution when the cloud is embedded in different CR energy densities and examine the behaviour of both CO-to-H_2 and CI-to-H_2 methods.

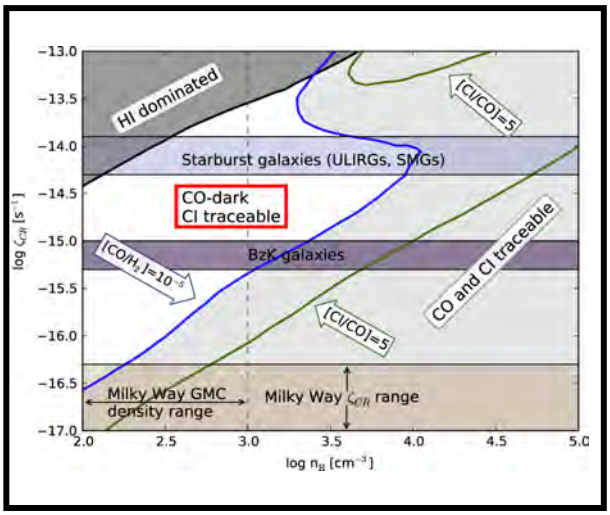

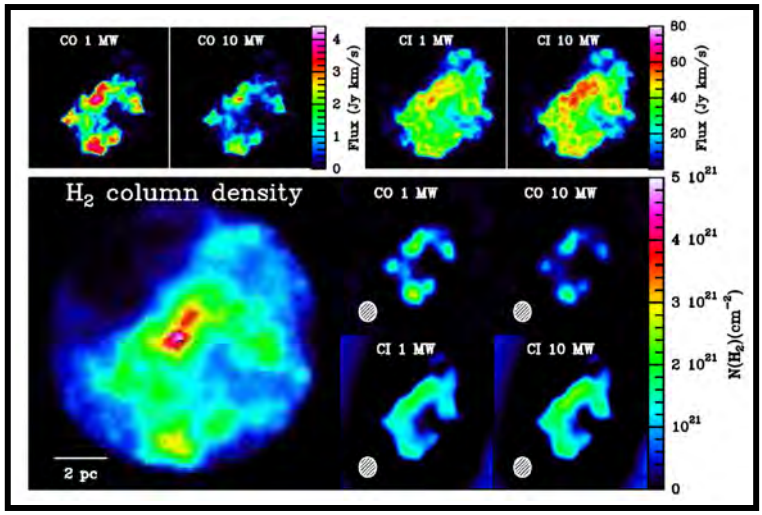

Left figure: The Bisbas et al. (2015) parameter plot showing the traceability of H_2 using CO and CI versus the H-nucleus number density, n_H, and the CR ionization rate, ζ_{CR}.

Right figure: Synthetic ALMA observations of lines emitted from a typical Milky Way (MW) cloud exposed to standard FUV and inundated by CRs with ionization rates 1 and 10 times the average MW ($\zeta = 10^{-17}$ s^{-1}). The top row shows emission lines using RADMC-3D. The bottom four panels show the inferred N(H_2) using the standard CO-to-H_2 (upper pair) and CI-to-H_2 (lower pair) methods (Bisbas et al. 2016). CI traces the original model cloud much better than CO.

Results:

- High CR ionization rates destroy CO very effectively but not H_2 while increasing the CI abundance
- Destruction of CO favours using CI-to-H_2 conversion in estimating the molecular gas mass

Predictions:

- H_2-rich galactic disks inundated by high CR ionization rates may appear clumpy in low-*J* CO lines
- CI observations may reveal smoother H_2 gas distributions in CR-permeated galactic disks

References

- Bisbas, T.G., Bell, T.A., Viti, S., Yates, J., Barlow, M.J., 2012, MNRAS, 427, 2100
- Bisbas, T.G., Papadopoulos, P.P., Viti S., 2015, ApJ, 803, 37
- Bisbas, T.G., Szűcs, L., Zhang, Z., van Dishoeck, E.F., Papadopoulos, P.P., 2016, *in prep.*

T.G. Bisbas, L. Szűcs, E.F. van Dishoeck, et al.

II) Optical & Interpretative Astronomy

Central rotation of globular clusters

Globular clusters (GCs) have historically been viewed as simple systems that are dominated by their stellar velocity dispersion and, whilst rotation has been observed in the outskirts of a handful of systems, it was thought to play little role within their core radii. Moreover, most Milky Way GCs exhibit some degree of flattening; clusters closer to the bulge tend to be more flattened than those in the halo. How much of this flattening is due to the Galactic tidal field or to the cluster rotation is still under debate. We have constructed a survey of the central regions of 30 Galactic GCs using the optical, high-spectral resolution Integral Field Unit instrument VIRUS-W mounted at the 2.7m McDonald telescope, aimed to study their formation and dynamical evolution.

We used the VIRUS-W data to derive the radial velocity fields on scales of about one to two core radii for the GCs in our sample, to which we fitted a plane to obtain a velocity gradient and kinematic position angle.

We detect central rotation in 27 of the 28 GCs analyzed so far (Fig. 1), suggesting that a large majority of Galactic GCs rotate.

This result is at odds with theory that predicts that central rotation should be lost on a few dynamical time scales and shows a clear need for theoretical models to produce and to sustain rotation on scales comparable to the core radius.

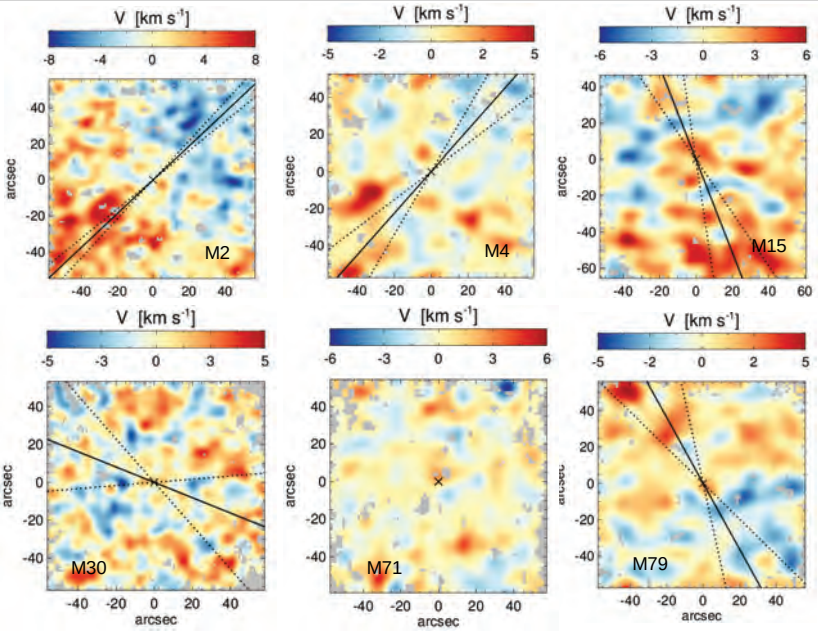

Fig. 1: Central velocity fields for 6 of the 30 GCs in our sample.

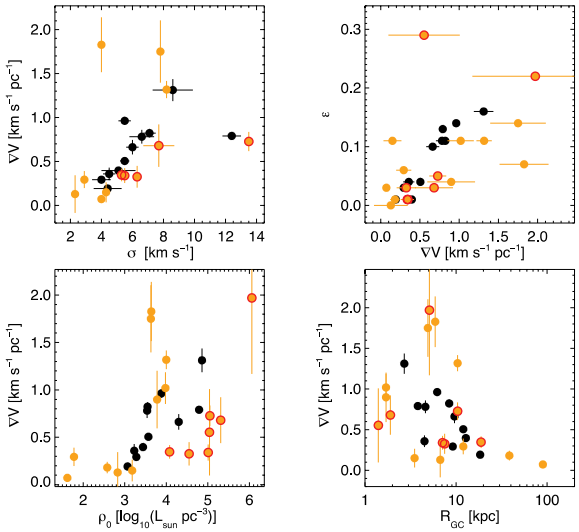

Fig. 2: Relation between the velocity gradients and other published parameters.

We compared the values of the central velocity gradients with published values of the velocity dispersion (σ), outer ellipticity (ε), central luminosity density (ρ_0) and distance to the Galactic center (Fig. 2).

The central rotation correlates very well with the velocity dispersion and the outer ellipticity, with the exception of a few outliers. While the first relation could be a consequence of the dispersion measurements not being corrected for rotation, the relation between the central rotation and the outer ellipticity is most likely physical.

We find only mild rotation in the clusters at large distances from the Galactic center, consistent with the rotation being produced by the Galactic tidal field.

References:

• Fabricius et al. 2014, ApJL, 787, L26

X. Mazzalay, M. Fabricius, R. Saglia, R. Bender, U. Hopp, J. Thomas, et al.

Kinematics, dynamics and stellar populations in M31

We observed the nearby spiral galaxy M31 with the integral field unit spectrograph VIRUS-W [1] mounted on the 2.7m telescope at the McDonald Observatory. We covered the whole bulge and sampled the disk along six different directions. We derive stellar line-of-sight velocity distribution maps by fitting the absorption line spectra, and gas velocity and velocity dispersion maps by fitting the emission lines Hβ, [OIII] and [NI]. From our data, we produce kinematical maps of unprecedented detail. The stellar kinematics is relatively regular with minor asymmetries that hint at the existence of a stellar bar. The gas emission lines in a large fraction of our covered region show double peaks, pointing to two kinematically distinct gas components. We also fit the stellar populations, which are predominantly old in the bulge region and more metal-rich towards the center. Based on the kinematics, a detailed three-dimensional mass model of M31 will be constructed. This will help in the interpretation of the micro-lensing events we are collecting in the Pandromeda project [2] and allow us to better understand the nature of the massive compact dark halo objects (MACHOs).

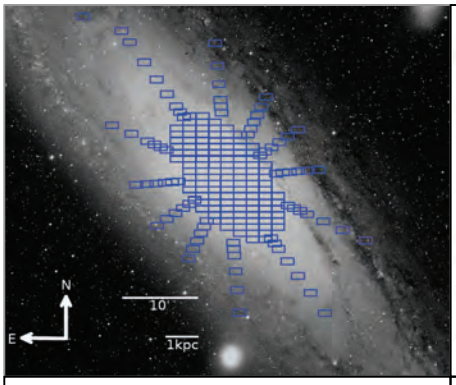

Fig. 1: Observed VIRUS-W pointings on a V-band image of M31

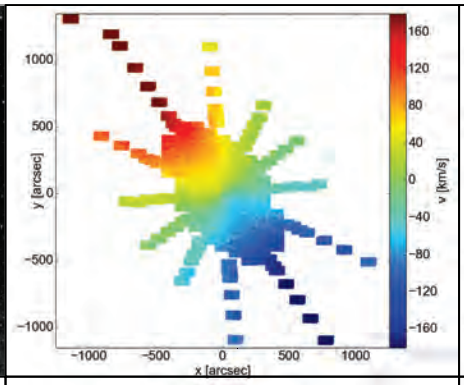

Fig. 2: Stellar velocity field derived with pPXF

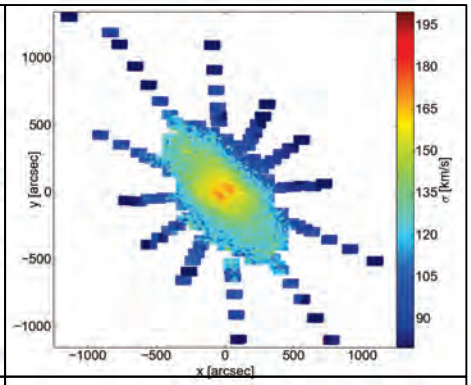

Fig. 3: Stellar velocity dispersion

The positions of the observed pointings are shown in Fig. 1. The data reduction resulted in approximately 50,000 individual spectra, which were rebinned into 7563 bins using a Voronoi tesselation code [3]. Stellar and gas kinematics were fitted using pPXF [4] and GANDALF [5]. The resulting maps for v and σ of the stars are shown in Figs. 2 and 3. We also measured stellar populations by comparing absorption line indices with simple stellar population models [6,7,8]. The age is plotted in Fig. 4, the populations are predominantly old in the bulge region and only become younger in the disk. The metallicity in Fig. 5 shows a gradient with higher values towards the center, whereas the α/Fe overabundance in Fig. 6 is relatively constant in the bulge region. This appearance of the stellar populations cannot be explained by a superposition of a slowly rotating bulge and a fast rotating disk.

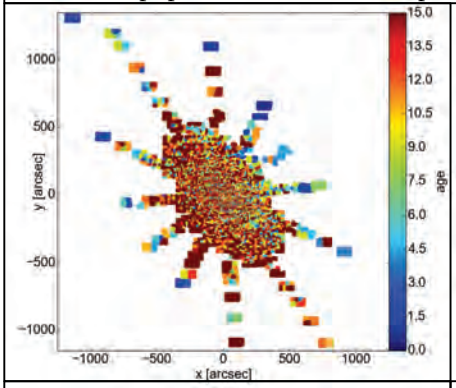

Fig. 4: Age [Gyr]

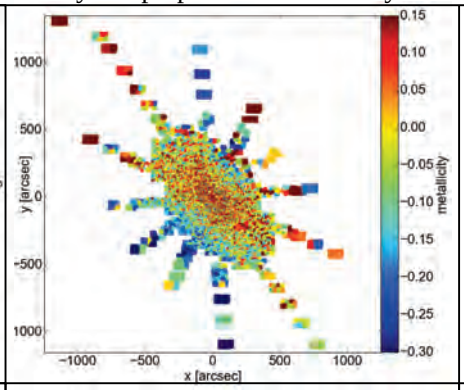

Fig. 5: Metallicity [Z/H]

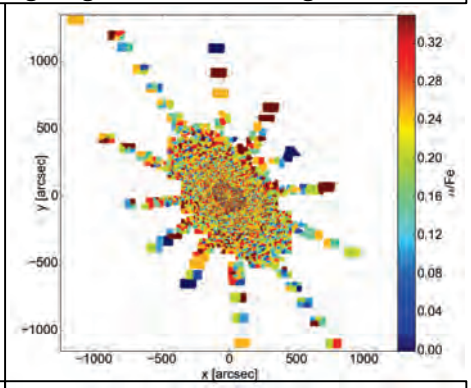

Fig. 6: α-elements overabundance [α/Fe]

References:
[1] Fabricius M.H. et al., 2012, SPIE, 8446, 84465K
[2] Lee C.-H. et al., 2015, ApJ, 806, 161
[3] Cappellari M. & Copin Y., 2003, MNRAS, 342, 345
[4] Cappellari M. & Emsellem E., 2004, PASP, 116, 138
[5] Sarzi M. et al., 2006, MNRAS, 366, 1151
[6] Maraston, 1998, MNRAS, 300, 872
[7] Maraston, 2005, MNRAS, 362, 799
[8] Thomas et al., 2003, MNRAS, 339, 897

M. Opitsch, R. Saglia, M. Fabricius, M. Blaña, O. Gerhard, R. Bender

Structure and formation of cD galaxies: NGC 6166 in Abell 2199

We investigate the morphological and dynamical structure of the prototypical cD galaxy NGC 6166. Our HET spectroscopy shows that the velocity dispersion of NGC 6166 rises from σ ≃ 300 km/s in the inner r ∼ 10″ to σ = 865 ± 58 km/s at r ∼ 100″ in the cD halo, reaching the cluster velocity dispersion of ~820 km/s. This supports our picture that cD halos consist of stars that were stripped from individual cluster galaxies by fast tidal encounters. However, our photometry does not confirm the widespread view that cD halos are identifiable as an extra, low- surface-brightness component that is photometrically distinct from the inner, steep-Sérsic-function main body of an otherwise-normal giant elliptical galaxy. Instead, all of the brightness profile of NGC 6166 outside its core is described to ±0.037 Vmag/arcsec^2 by a single Sérsic function with index n ≃ 8.3. A mass model based on published cluster dynamics and X-ray observations fits our observations if the tangential stellar dispersion is larger than the radial dispersion at r≃20″-60″, also consistent with halo formation from stripped stars.

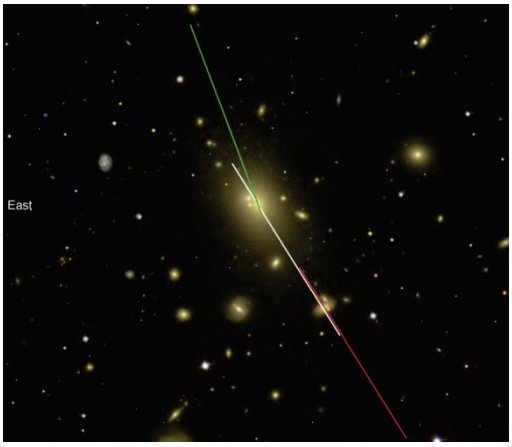

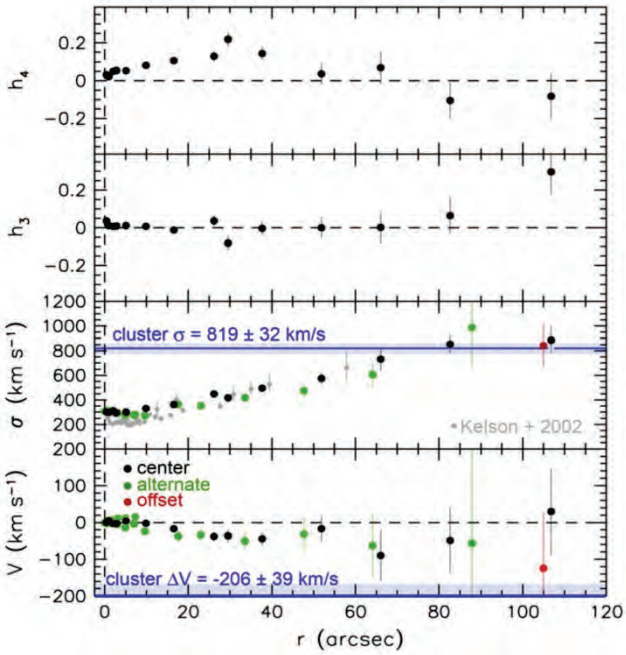

Top: NGC 6166 image with HET slit positions superimposed. Top right: corresponding kinematic measurements. Bottom right: surface brightness profile. Bottom: simple spherical dynamical model using mass contraints from X-rays, cluster dynamics and plausible stellar M/L.

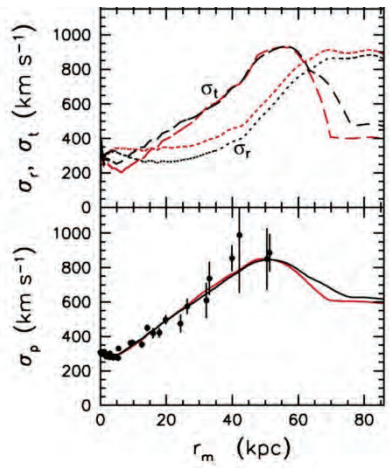

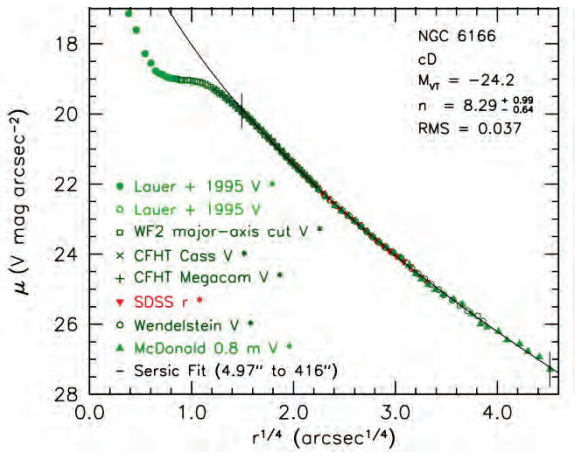

Reference: Bender, R, Kormendy, J, Cornell, M.E., Fisher, D.B.: 2015, Astrophys. J. 807, p56-80

R. Bender, J. Kormendy, et al.

Photometry and kinematics of cD galaxies

Deep imaging of galaxy clusters has revealed a faint and extended intracluster light (ICL) component in many objects. This contribution is due to of stars associated with the cluster potential and accounts for 5 - 50% of the clusters' stellar masses [1]. Its exact origin is not well understood, partly because observational constraints are missing. Our ongoing survey of cD galaxies with the new Wide Field Imager (OPINAS/USM) at the 2m Fraunhofer Telescope at Mt. Wendelstein aims at measuring the surface brightness (SB) profiles of a large sample of local ($z < 0.15$) brightest cluster galaxies in the g and r bands with a precision down to $< 1/1000^{th}$ of the night sky brightness. Together with kinematical data these new observations will allow to distinguish between different formation models of cD galaxies.

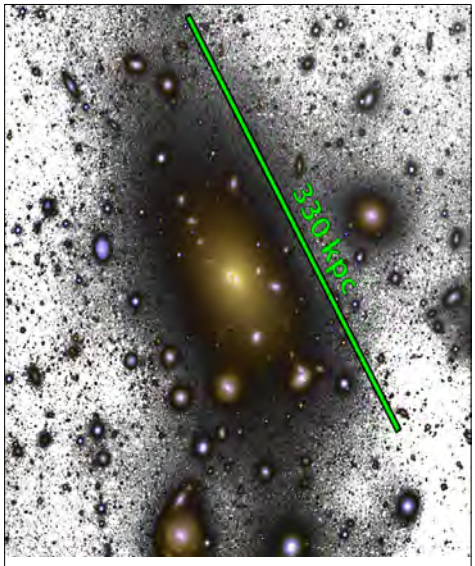

Fig. 1: u-g-r image of Abell 2199 with the deep g-band image inverted

Definition of "cD galaxy":

The historical galaxy type "cD" describes a massive elliptical galaxy that is located at its associated galaxy cluster centre (BCG = brightest cluster galaxy) and is embedded in a sea of ICL. Our new results suggest that whether or not a BCG qualifies as a cD galaxy can only be inferred from a combination of photometric and kinematic data.

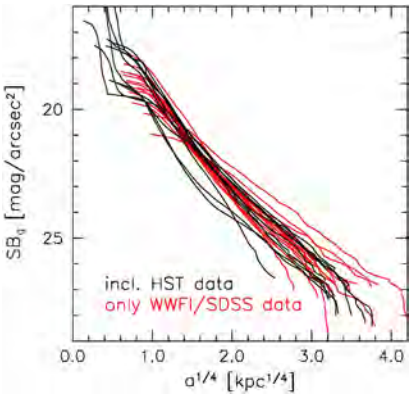

Fig. 2: Major axis SB profiles of 26 BCGs

Preliminary results:

- 20 out of 26 BCGs examined have similar radial SB profiles which differ by no more than ~1 mag between 1 - 80 kpc radius. Sérsic fits are in very good agreement with the SB profiles throughout at least 90% of the measured radius range.
- 16 out of 26 BCGs are very well fitted (rms < 0.053 mag) by a single Sérsic law. The transition from BCG to ICL is smooth. This is surprising because at least one of the considered BCGs (NGC 6166) shows a clear change in its stellar kinematics between the BCG and ICL regions [2].
- 10 out of 26 BCGs need two coadded Sérsic profiles to account for their outer excess light.

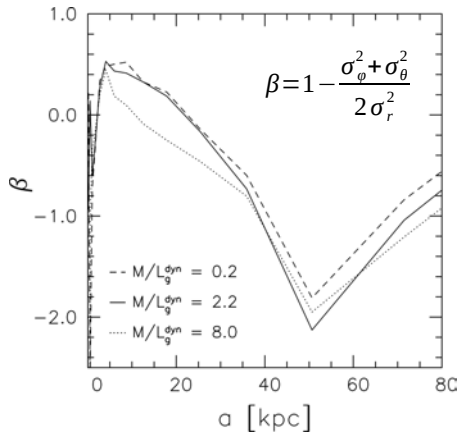

Fig. 3: Anisotropy β of the stellar velocity dispersion σ

Kinematic modelling can disentangle the ICL component from the BCG. A dynamical model of a first cD, NGC 6166 in Abell 2199, has been obtained using the orbit superposition technique [3]. It is constrained by our SB profile and fitted to the stellar kinematics measured with the Hobby-Eberly Telescope [2] along the galaxy's major axis *a*.
The tangential velocity dispersion of the stars is larger than the radial dispersion (classical anisotropy parameter $\beta < 0$) for $a > 20$ kpc. This is in contrast to normal boxy-core-nonrotating elliptical galaxies, for which the dispersion remains radially anisotropic outwards ($\beta > 0$). This behaviour points towards a different formation scenario for the halo than for the BCGs' main body.

References:

- [1] Lin & Mohr (2004)
- [2] Bender et al. (2015)
- [3] Thomas et al. (2004)

M. Kluge, R. Bender, J. Thomas

The MASSIVE survey

Massive early-type galaxies represent the modern day remnants of the earliest major star formation episodes in the history of the universe. These galaxies are central to our understanding of the evolution of cosmic structure, stellar populations and supermassive black holes: the most massive galaxies populate the richest galaxy structures and are supposed to have the most extreme IMFs and most massive black holes. Yet the details of their complex formation histories remain uncertain. To address this situation we have initiated the MASSIVE survey, a volume-limited, multi-wavelength, integral-field spectroscopic and photometric survey of the structure and dynamics of the ~100 most massive (above $10^{11.5}$ M_{sun} stellar mass) early-type galaxies within a distance of 108 Mpc.

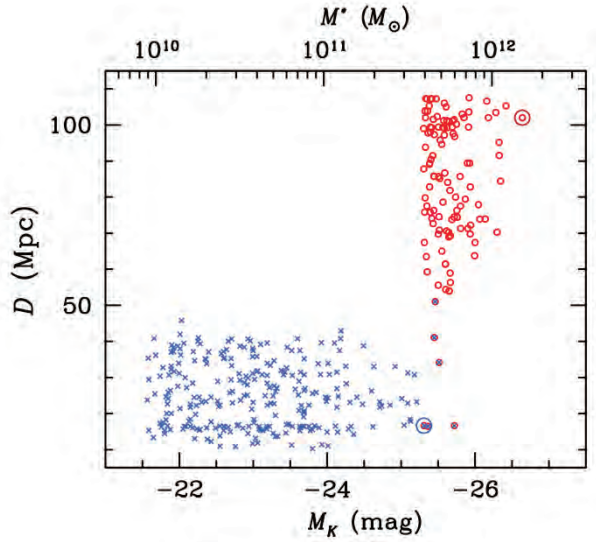

Fig. 1: The MASSIVE survey

- all E/S0 galaxies within D < 108 Mpc brigther than M_K<-25.3 mag (dec>-6 deg, A_V<0.6), red circles
- this mass regime hasn‘t been studied systematically yet: only 6 galaxies are in common with ATLAS^{3D} (blue crosses), the rest lie beyond the ATLAS^{3D} distance cut of 42 Mpc (big circles: M87 and NGC 4889 in Coma)
- integral-field spectroscopy out to ~$2r_{eff}$ using the Mitchell spectrograph at the McDonald observatory (→ stellar kinematics & stellar populations)
- high-resolution spectroscopy (~100 pc resolution) for BH mass measurements for a subsample of ~25 galaxies (GMOS, NIFS)
- multi-wavelength: CO gas observations (NOEMA, VLA) and X-ray halo measurements (CHANDRA) under way

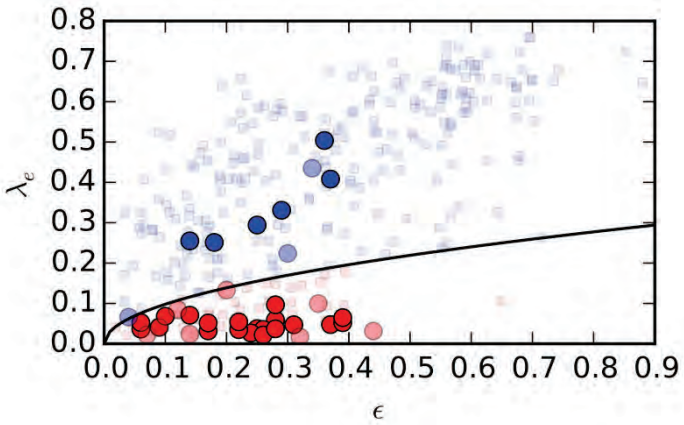

Fig. 2: Stellar kinematics

- the 42 brightest galaxies (M_K<-25.69) are predominantly slow rotators (red circles), but even in this high-mass subsample we find ~25% fast rotators (blue circles, galaxies with the highest S/N are highlighted; squares show the ATLAS^{3D} sample for comparison)

Moreover, we find that many galaxies reveal dispersion profiles that rise towards the centre and towards large radii, probably indicating massive BHs and dark-matter halos. Also, we detect peaked line-of-sight velocity distributions in the outer parts (h_4>0), that probably indicate radially anisotropic stellar orbits and may be a relic of the late assembly of stellar mass.

References:

- Ma et al., 2014, ApJ 795, 158
- Greene et al., 2015, ApJ 807, 11
- Davis et al. 2016, MNRAS 455, 214
- Goulding et al., submitted
- Thomas et al., Nature (in press)

J. Thomas and the MASSIVE team

Triaxial modeling of massive ellipticals

The brightest early-type galaxies (ETGs) are supposed to host the most massive black holes (BHs) and the most extreme dwarf-dominated initial mass functions. Moreover they are often triaxial. Axisymmetric models of the biggest ETGs are suspected to underestimate the BH mass and to be biased towards viewing angles corresponding to edge-on inclinations. To obtain reliable BH masses and stellar and dark matter mass distributions of the most massive ETGs (e.g. MASSIVE survey), we developed a triaxial implementation of the orbit-based Schwarzschild method.

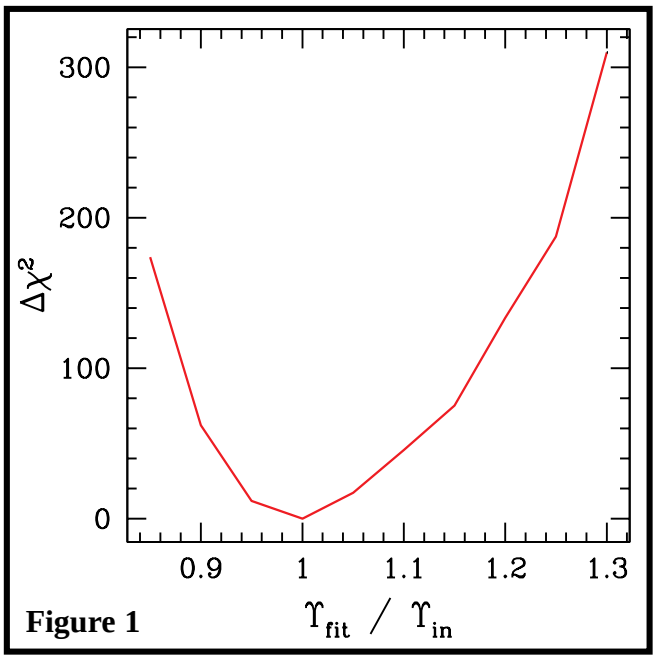

Figure 1

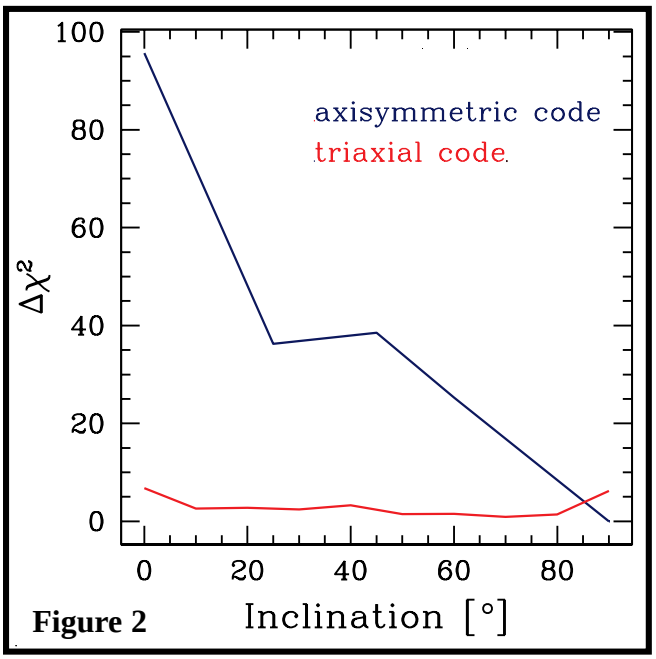

Figure 2

Axisymmetric models recover well the stellar masses of ETGs. As an initial consistency check, we test the newly developed triaxial code on a self-consistent isotropic Hernquist sphere and verify the mass reconstruction.

- We probe different mass-to-light ratios Υ for a fixed viewing direction;
- We compute libraries of 2 x 112560 orbits;
- As shown in Figure 1, the best fitting model corresponds to a mass-to-light ratio that equals the input mass.

As a first application we tackle a suspected bias in the viewing direction, which is specified by one inclination angle in the axisymmetric case.

- We consider a self-consistent isotropic Hernquist sphere and produce mock line-of-sight velocity distributions (LOSVDs) with simulated noise;
- We apply the axisymmetric and triaxial codes to these LOSVDs, probing diverse viewing directions;
- While the axisymmetric code fits the data better with edge-on inclinations, the triaxial code fits equally well for all viewing directions, which is expected for a spherical system (Figure 2);
- This is because the triaxial code obeys less symmetries and hence the degrees of freedom depend less on the viewing direction.

References:

• Thomas J. et al, 2004, MNRAS, 353, 391
• Thomas J. et al, 2007, MNRAS, 381, 1672
• Van den Bosch et al, 2010, MNRAS, 401, 1770
• Ma C.P. et al, 2014, ApJ, 795, 158
• Finozzi F. et al, in preparation

F. Finozzi, J. Thomas, R. Saglia

NGC 1600, diffuse cores & big BHs

Quasar activity implies that black holes (BHs) with 10^{10} M_{sun} already existed 13 billion years ago. Two possible present-day descendants of these BHs have been found in NGC 3842 and NGC 4889 at the centres of the Leo and Coma galaxy clusters, which together form the central region of the Great Wall, the largest local structure of galaxies. The most luminous quasars, however, are not confined to the highest density regions of the early universe; yet similarly massive BHs outside of modern-day rich clusters have not been hitherto found. We observed the stellar velocity distribution in NGC 1600, a relatively isolated elliptical galaxy near the centre of a galaxy group. We measure a BH mass of (1.7 +/- 0.15) 10^{10} M_{sun}. The spatial distribution of stars near the centre of NGC 1600 is rather diffuse. We find that the region of depleted stellar density in massive elliptical galaxies extends over the same radius as the gravitational sphere of influence of the central black hole.

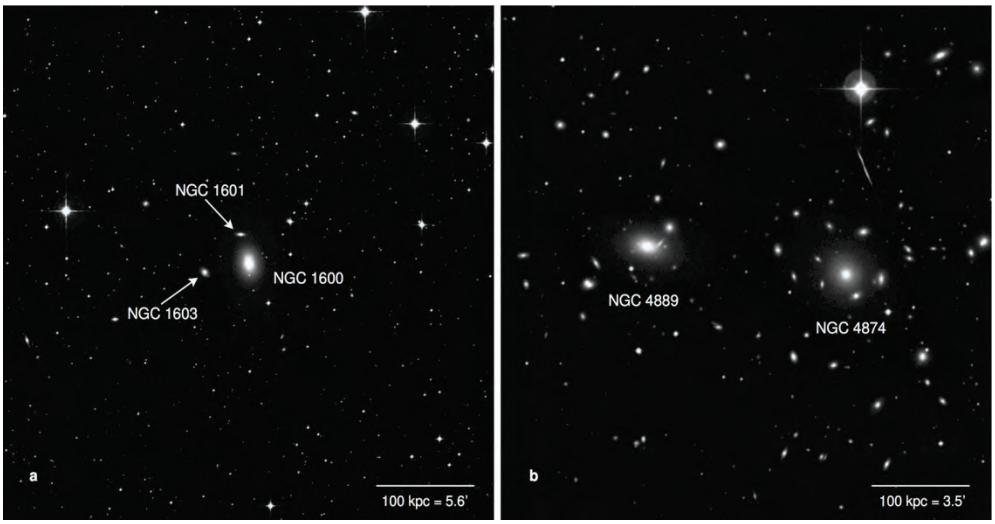

Fig. 1: Environment of NGC 1600 (left) versus NGC 4889 (at the center of the Coma cluster). NGC 1600 is the first galaxy outside of a rich galaxy cluster with a very massive BH. The BH in NGC 1600 is ~10 times more massive than predicted by the galaxy velocity dispersion, but consistent with the galaxy's large depleted stellar core.

Fig. 2: The new correlation between the size r_b of the depleted stellar core in massive ellipticals and the radius of the gravitational sphere of influence of the central BH, r_{SOI}. *The two radii are statistically identical* (dotted: one-to-one relation; red: best-fit linear correlation). The scatter in this relation (0.17 dex) is a factor of two smaller than that of the known scaling relations between BH mass and galaxy properties. The r_b-r_{SOI} relation strengthens the conclusion that depleted galaxy cores are a dynamical imprint of the central black holes. NGC 1600 has the faintest known core among all galaxies with dynamical M_{BH} (inset: galaxies from Lauer et al. 2007, D<100 Mpc; NGC 1600 and the central/brightest galaxies of the Virgo, Coma and Leo clusters are highlighted).

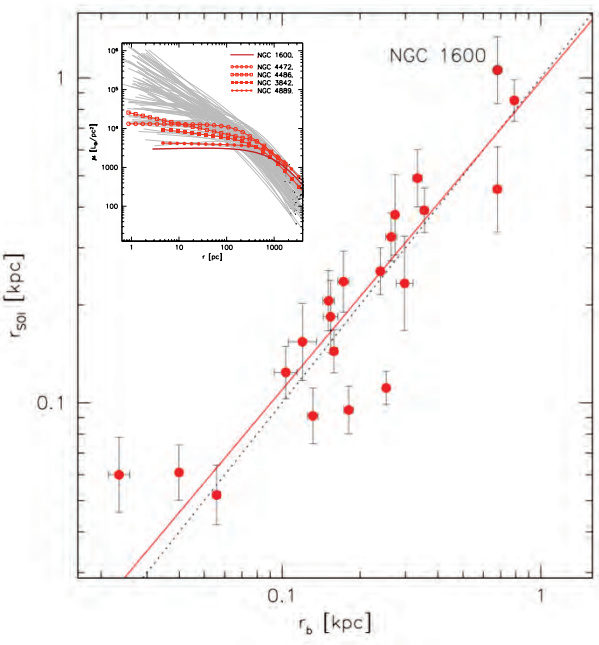

References:

• Thomas et al, Nature (in press)

J. Thomas and the MASSIVE team

Supermassive black hole and double nucleus of the core elliptical NGC 5419

We obtained high spatial resolution IFU SINFONI observations of the central regions of the giant elliptical galaxy NGC5419. HST and SINFONI images show a point source located at the galaxy's photocenter and a second nucleus, off-centered by ≈ 70 pc. We use orbit-based dynamical models to measure the black hole mass (M_{BH}) of NGC 5419 from the kinematical data outside of the double nuclear structure. The models reveal M_{BH} = 7.2 x 10^9 $M_\odot$, consistent with the size of the depleted stellar core. While the nature of the double nucleus in NGC 5419 is certainly puzzling, our observations suggest that this galaxy might host two supermassive black holes at its center, separated by only ~ 70 pc. Our measured M_{BH} likely corresponds to the larger of the two black holes, located at the galaxy's photocenter.

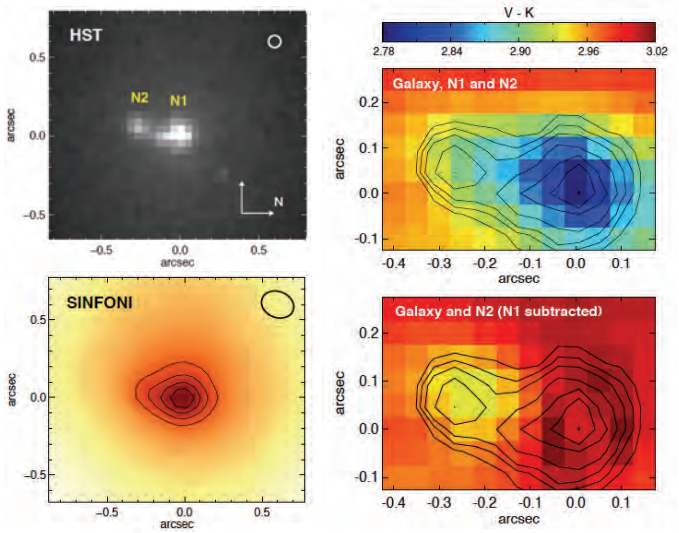

The double nucleus

HST image of the central region (410 x 410 pc) of NGC 5419 (*upper-left panel*) shows the two resolved nuclei, N1 and N2. These are also seen in our lower spatial-resolution SINFONI K-band image (*lower-left panel*).

Right panels: V – K color maps of the region around the two nuclei. While the galaxy has a color typical of an old stellar population (V – K ≈ 3), the *intrinsic* colors of the nuclei N1 and N2 are much bluer. We obtained V – K = 1.13 for N1, consistent with the low-luminosity AGN present in NGC 5419, and V – K = 1.68 for N2, indicative of a metal poor ~ 2 Gyr old stellar population.

Stellar kinematics

The kinematics derived from our data show that NGC 5419 is a dispersion-dominated galaxy (*upper panels*). While the rotational velocity does not exceed 50 km s^{-1}, a clear rotational pattern is observed, revealing a counter-rotating core in the inner few arcseconds.

Outside of the central double nucleus, we measure an almost constant velocity dispersion of about 350 km s^{-1}. In the region where the double nucleus is located, the dispersion rises steeply to a peak value of ~ 420 km s^{-1} (*lower-left panel*).

Dynamical modelling

The best-fitting dynamical model is indicated with gray lines in the *upper panels*. Data points inside r < 0.35 arcsec were omitted in the fit. The dotted lines show the inward extrapolation of the best-fit model. *Lower-right panel*: $\Delta\chi^2$ as a function of M_{BH} and best-fit model M_{BH}.

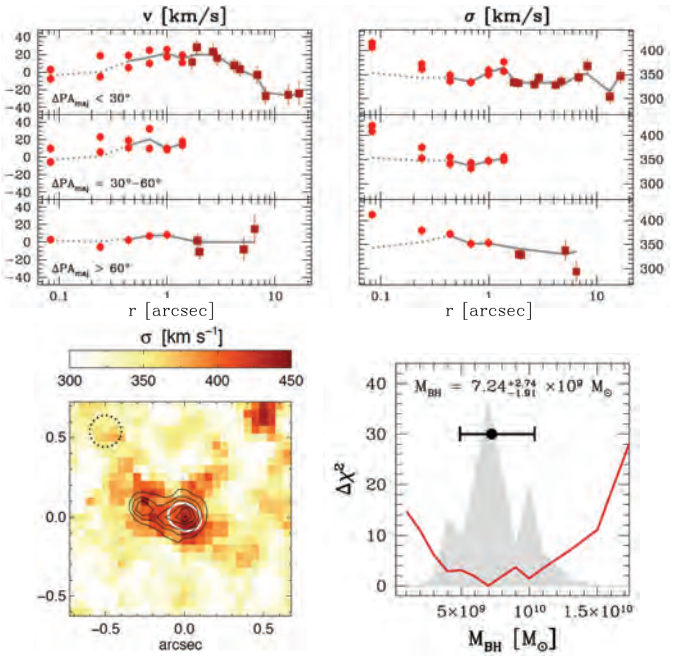

References: Mazzalay et al., submitted to MNRAS

X. Mazzalay, J. Thomas, R. Saglia, R. Bender, P. Erwin, M. Fabricius, et al.

The Black-Hole Fundamental Plane revisited

We investigate the correlations between the black hole (BH) mass M_{BH}, the velocity dispersion σ, the bulge mass M_{Bu}, the bulge density ρ_h and its half-mass radius r_h using a sample of 97 galaxies, 25 of which were observed during our recent SINFONI BH survey. We establish five significant bivariate correlations (M_{BH}-σ-ρ_h, M_{BH}-σ-r_h, M_{BH}-M_{Bu}-σ, M_{BH}-M_{bu}-ρ_h, M_{BH}-M_{bu}-r_h), taking into account for the first time the full error covariance matrix. They predict M_{BH} of core and power-law ellipticals and classical bulges with intrinsic scatter as low as 0.26 dex. In contrast, pseudo-bulges have systematically lower MBH but approach the predictions of the above relations at densities $\varrho_h \geq 10^{10} M_\odot kpc^{-3}$. The bivariate correlations point to a link between BH mass and $M_{Bu}^{0.5}\sigma^2$, as proposed by Hopkins et al. (2007a,b, ApJ, 669, 45 & 67) or the bulge kinetic energy $M_{Bu}\sigma^2$, as first suggested by Feoli & Mele (2005, IJMPD, 14, 1861).

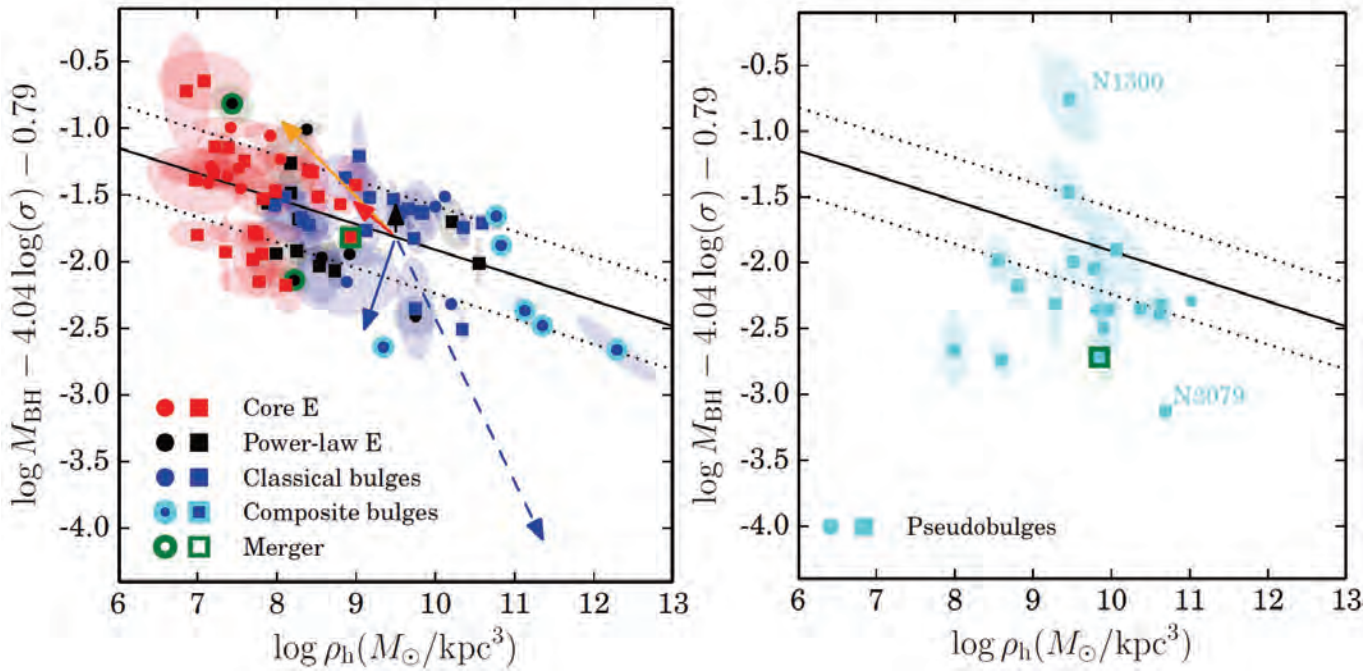

The bivariate correlation M_{BH}-σ-ρ for core and power-law ellipticals and classical bulges (left) and pseudo bulges (right). The solid lines show the best-fit relation for the sample of galaxies of the left plot, with dotted lines showing the estimated intrinsic scatter.

BH and classical bulge masses coevolve: core ellipticals are the result of dry mergers of power-law bulges (red and orange arrows); power-law ellipticals and bulges are the result of (early) gas-rich mergers of disk galaxies (blue arrows). BHs grow through accretion and merging (black line), producing feedback that locks them to the bulge mass. In contrast, the (secular) growth of BHs is decoupled from the growth of their pseudobulge hosts, except when (gas) densities are high enough to trigger the same feedback mechanism valid for classical bulges.

References:

• R. Saglia et al. 2016, ApJ, 818: 47

R. Saglia, M. Opitsch, P. Erwin, J. Thomas, A. Beifiori, X. Mazzalay, R. Bender

Constraining the galaxy mass content of clusters' core using Strong Lensing

We demonstrate an innovative Strong Lensing (SL) analysis of cluster cores, in which we use galaxies' velocity dispersion measurements (σ_{sp}) as a proxy for masses of cluster members. As lensing probes the overall projected cluster mass, we aim to disentangle the galaxy from the large scale dark matter halo (DH) cluster mass components. The use of cluster members' σ_{sp} in the SL analysis allows us to break inherent mass degeneracies and refine the constraints on the galaxy mass component and, as a result, on the cluster DH, a high-end goal of lens modelling.

We perform SL analysis of two galaxy clusters, Abell 383 (A383, Fig.1) and Abell 611 (A611, Fig.2), using the software GLEE (Suyu & Halkola 2010). We use photometry and spectroscopy from the Cluster Lensing and Supernovae with Hubble (CLASH, Postman et al. 2012) and CLASH-VLT (Rosati et al. 2014) surveys, combined with σ_{sp} from the Hectospec survey (Geller et al. 2014).

For A383 (see Monna et al. 2015), the use of σ_{sp} in the SL analysis improves the constraints on the cluster DH mass parameters by ~10%, while for the galaxy component, the mass parameters are refined by ~50%. F**or A611** (see Monna et al. 2016)**,** the improvements on the parameters describing the galaxies are less significant.

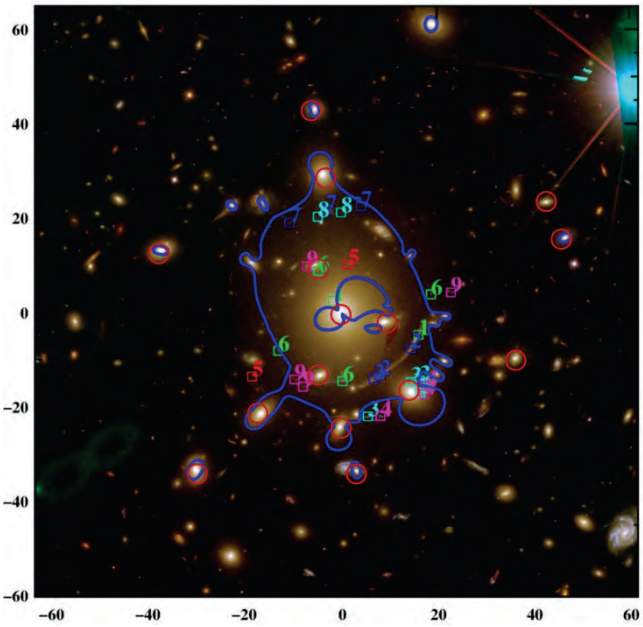

Fig.1 *HST color composite image of A383. Multiple images are labeled with numbers, cluster members with measured σ_{sp} are labelled with red circles, and critical lines for a source at redshift z_s = 2 are shown in blue. Axis are in arcseconds with respect to the BCG.*

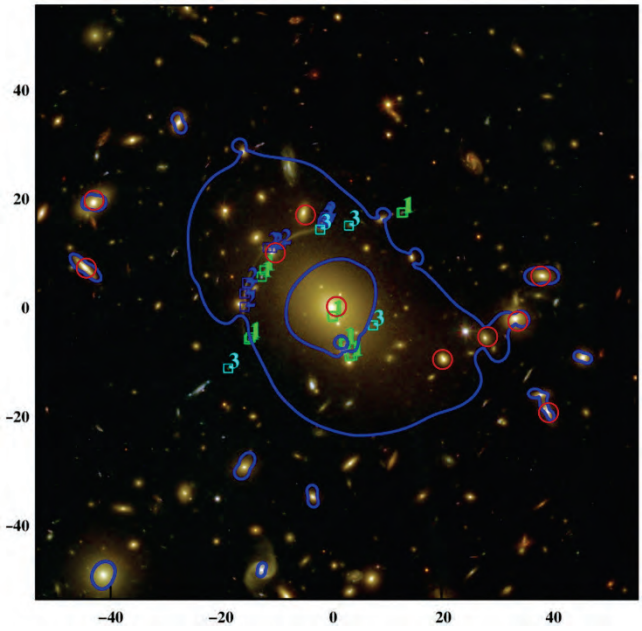

Fig.2 *HST color composite image of A611, multiple images, galaxies and critical lines are labelled as in Fig.1*

The different improvements on the galaxy mass parameters obtained in the two clusters derive directly from the available set of lensed features and of cluster members with measured σ_{sp}. Indeed these are different for the two clusters (see Fig.1 and 2): A383 has ~10 galaxies with σ_{sp} within and close to the cluster critical lines, which define the region robustly probed by SL, while A611 has only 5 galaxies with σ_{sp} inside this region. Furthermore, A611 has only 3 systems of multiple images used to constrain the mass in the cluster core, whereas A383 has 10. However by using σ_{sp} in the SL analysis we still improve the determination of the galaxy mass component also for A611. Indeed without using the galaxies' σ_{sp}, we would overestimate their mass by a factor of ~1.5, and consequently the mass of the large scale dark matter would be underestimated by ~5%.

References:

• Geller, M. J., et al., 2014, ApJ, 783, 52 • Monna, A., et al. 2015, MNRAS, 447, 1225 • Monna, A., et al. 2016, Arxiv eprint,1602.08491 • Postman, M., et al., 2012, ApJs, 199, 25 • Rosati, P., et al., 2014, Msngr, 158, 48R

A. Monna, S. Seitz, et al.

Lensing around Galaxy Troughs

Trough lensing is an innovative probe that provides high signal-to-noise measurements of gravitational light deflection in the underdense universe. As such, it is not only independent of the physics at the high density tail of the matter distribution but also potentially sensitive to the effects of modified gravity theories.

There is increasing interest in studying the low density universe, both because it is sensitive to the effects of modified gravity theories and because low density regions can be understood more easily on the theory side. It is, however, a difficult task to obtain high signal-to-noise measurements of signals from underdense regions. In Gruen, Friedrich et al. (2016) we have presented a new cosmological probe that measures the radial alignment of background sources around underdense lines of sight (troughs). We define these troughs as a certain percentile of the most underdense lines of sight in the foreground galaxy field, where the latter is smoothed by a scale which we call the trough radius.

We have measured the lensing around troughs in early data of the Dark Energy Survey (DES) and found a highly significant radial alignment. Also, we have developed a model for the trough lensing signal and demonstrated that the alignment around troughs can be understood from minimal cosmological principles.

The final, 5-year DES data (DES-Y5) will allow for a measurement of trough lensing that has about 30 times the signal-to-noise of our measurement in early DES data. This provides a number of challenges and opportunities for future analyses of this effect. On the one hand, the Gaussian model we have developed so far will most likely fail to describe such a significant measurement.

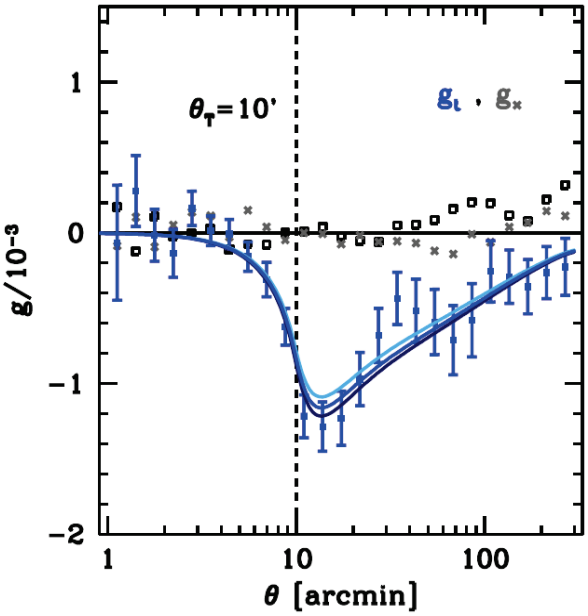

Measurement of radial alignment around troughs with a radius of 10 arcminutes. The blue lines indicate our model for different values of the galaxy bias (see Gruen at al. 2016).

On the other hand, understanding the details of lensing around galaxy troughs might shed light on interesting open questions of cosmology such as the possible existence of deviations from General Relativity in underdense environments. In Friedrich, Gruen et al. (in prep) we are taking the first step towards a better understanding of trough lensing by developing a log-normal model for it and investigating the cosmology dependence of that model. We found that the signal significantly depends on the late time non-Gaussian features of the matter and convergence field. If these features are well understood, the trough lensing signal of DES-Y5 can provide significant constraints on cosmological parameters stemming from low density regions only.

References:
Gruen, Friedrich et al. 2016, MNRAS, 455, 4301.

D. Gruen, O. Friedrich, S. Seitz and the DES Collaboration

Photometric Redshift Estimation

Photometric redshifts have recently become a major challenge for large area photometric surveys like the Dark Energy Survey or Euclid. We investigate how cosmological observables are biased by misestimated photometric redshifts and develop methods to alleviate these biases.

The estimation of accurate photometric redshift distributions is important in order to use photometric samples to **constrain cosmological parameters** with, for example, angular correlation function measurements in tomographic bins. **Machine Learning** methods have been shown to provide **highly accurate** photometric redshift estimates, often outperforming template fitting method, that fit analytical templates to the photometry (e. g. Sánchez et al. 2014). As the redshift cannot be perfectly recovered by photometry alone, accurate estimation of the **photometric redshift uncertainty** is important to constrain cosmology and **avoid systematic biases**.
In the advent of petascale astronomy, redshift information for **billions of objects** has to be **accurately** estimated and **efficiently** distributed.
In Rau et al. 2015 we developed an **efficient method** to estimate photometric redshift distributions of samples of objects. For each photometric object a **single floating point number** is predicted such that their distribution resembles the true spectroscopic sample. This estimate **reduces the bias** in cosmological observables compared with traditional Machine Learning predictions like the Neural Network code ‚ANNz'. ANNz can produce either a single photometric redshift for each object or a Gaussian distribution for each object, that includes the error in the photometric redshift as its standard deviation. We can obtain the redshift distribution of the photometric sample by either directly estimating the distribution from the ANNz photometric redshifts (‚ANNz') or we can add the Gaussians estimated for each object (‚ANNz-stack'). Our method outperforms ANNz in both cases.

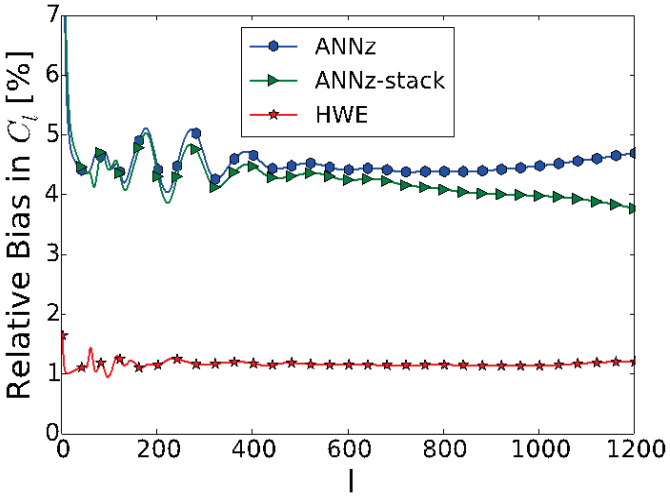

Bias in the angular correlation power spectrum by the inaccurate estimation of the photometric redshift distribution. We compare the neural network code ANNz with the more accurate reconstruction using the Highest Weight Element (HWE) estimate proposed in Rau et al. 2015.

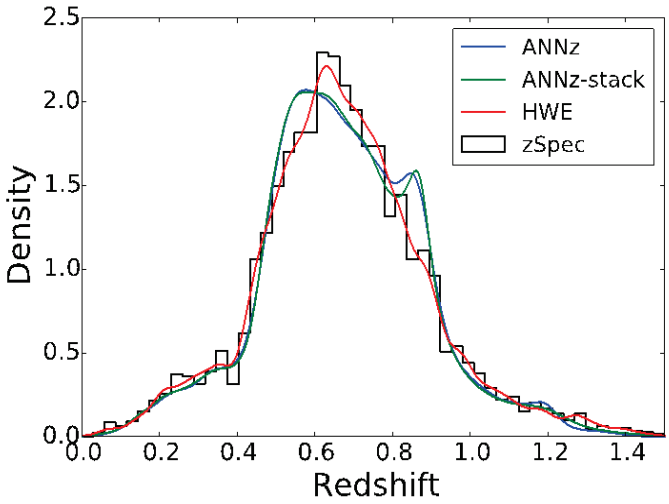

Redshift distribution of the CFHTLS data corresponding to the plot shown on the left. The redshift distribution is estimated using both the neural network code ANNz and the method (HWE) proposed in our work. The true spectroscopic redshift distribution is shown for comparison.

Photometric redshift estimation using Machine Learning and template fitting methods require **spectroscopic samples** to validate and calibrate the obtained results. These spectra are often not available for faint objects and this **spectroscopic incompleteness** can bias photometric redshifts.
In Hoyle et al. 2015 we proposed a method to augment the spectroscopic calibration data using a combination of simulations and synthetical spectra to extrapolate into regions of color-magnitude space where no spectra are available. We show that, in the presence of spectroscopic incompleteness, data augmentation can **reduce** the number of **misestimated photometric redshifts** by up to **80%**, for SDSS DR 8.

References:

• Rau, Seitz, et al. 2015, MNRAS, 452, 3710-3725
• Hoyle, Rau, et al. 2015, MNRAS, 450, 305-316
• Sánchez, et al. 2014, MNRAS, 445, 1482-1506

M. M. Rau, S. Seitz, et al.

Variability of XMM-COSMOS AGN and photometric redshifts

We probe the optical variability of active galactic nuclei (AGN) for a large sample of X-ray selected AGNs in the XMM-COSMOS field, using the multi-epoch light curves (LCs) provided by the Pan-STARRS1 (PS1) 3π and Medium Deep Field (MDF) surveys. PS1 3π LCs are enough to flag sources that vary by at least 3%. Colors obtained minimizing the interval in observing time provide the best photometric redshifts.

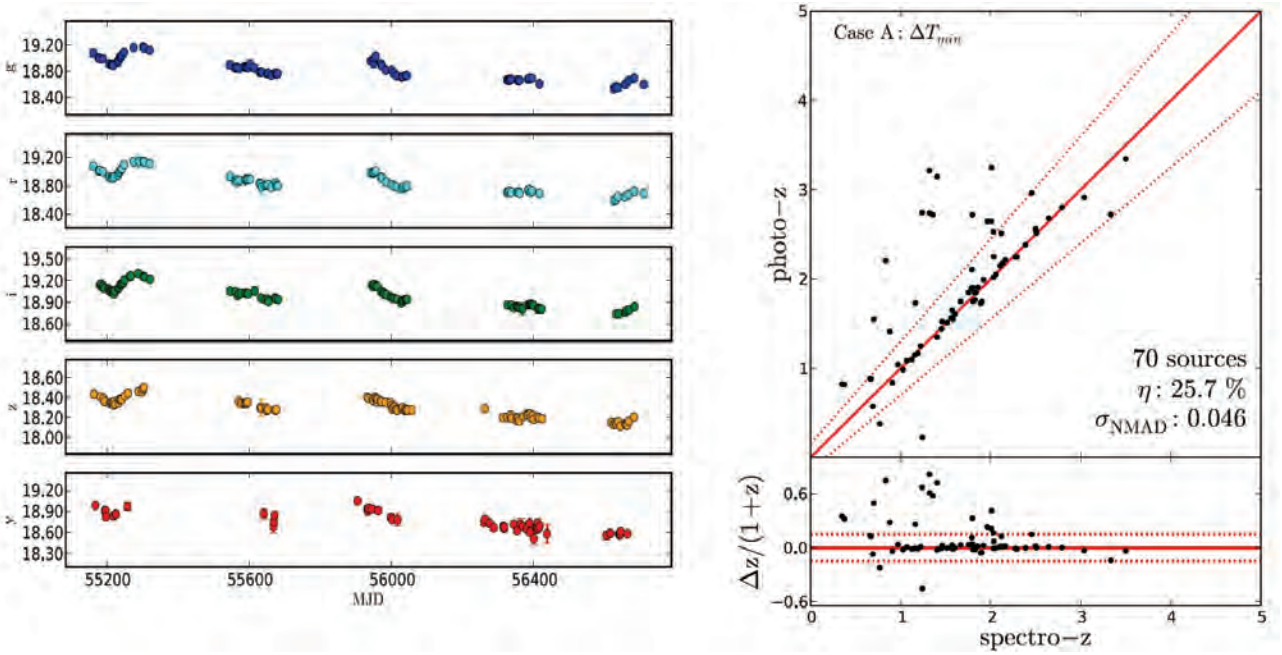

Left: the grizy light-curves of the AGN XID1. Right: comparison of the photometric and spectroscopic redshifts derived using quasi-simultaneous colors.

The identification of variable sources such as AGNs is important in view of the science goals of the Euclid missions, where accurate photometric redshifts are of vital importance. The PS1 3π survey covers ¾ of the sky, observed 12 times in 5 bands over a time span of 3.5 years. Additionally10 MDF have been observed several hundreds of times. The LCs derived from the MDF4 dataset, allow us to assess the possibility to detect AGNs based on their optical variability. We find that almost all of the XMM X-ray selected AGNs in the COSMOS field (covered by the MDF4 of PS1) are flagged as optically variable using the MDF LCs. Approximately half of these objects (the ones that vary by more than 3%) are also detected using just the 3π data.

Variability impacts on the precision of the photometric redshifts of AGNs. The best result in terms of accuracy (σ_{NMAD}=5%) and percentage of outliers (η=26%) is obtained when considering colors derived simultaneously as much as possible and adding GALEX and IRAC bands. We conclude that in view of the Euclid survey AGNs should be flagged (using all possible means, including variability) and excluded from the standard photometric redshift analysis.

References:

• Simm, T., Saglia, R., Salvato, M., Bender, R. et al. 2015, A&A, 584, A106

R. Saglia, T. Simm, M. Salvato, R. Bender

Cl J0217-05: A large-scale structure at z = 0.65 in UDS

We report the confirmation of a large-scale structure of galaxies, Cl J0217-05, at z = 0.65 in the UKIDSS/UDS field. A number of clusters at z~0.65 were reported in the field. However they were not identified as a unique structure entity. We assessed the clustering at z ~ 0.65 in UDS by means of a cluster search and found >30 cluster and group candidates within UKIDSS spread across >10 Mpc. We conducted a spectroscopic follow-up of with VLT/VIMOS which provided redshifts for ~650 sources in the field and confirmed the physical association of 16 groups and clusters including five with mass estimates $M_{200} > 10^{14} M_{\odot}$. Its richness, number of subgroups and spatial extent makes Cl J0217-05 one of the most prominent structures identified to date which serves as a unique laboratory to study the dependence of properties with environment. A series of on-going studies are investigating star-formation distribution, quenching mechanisms, massive galaxy formation and morphological transformation across the structure.

CL J0217-05

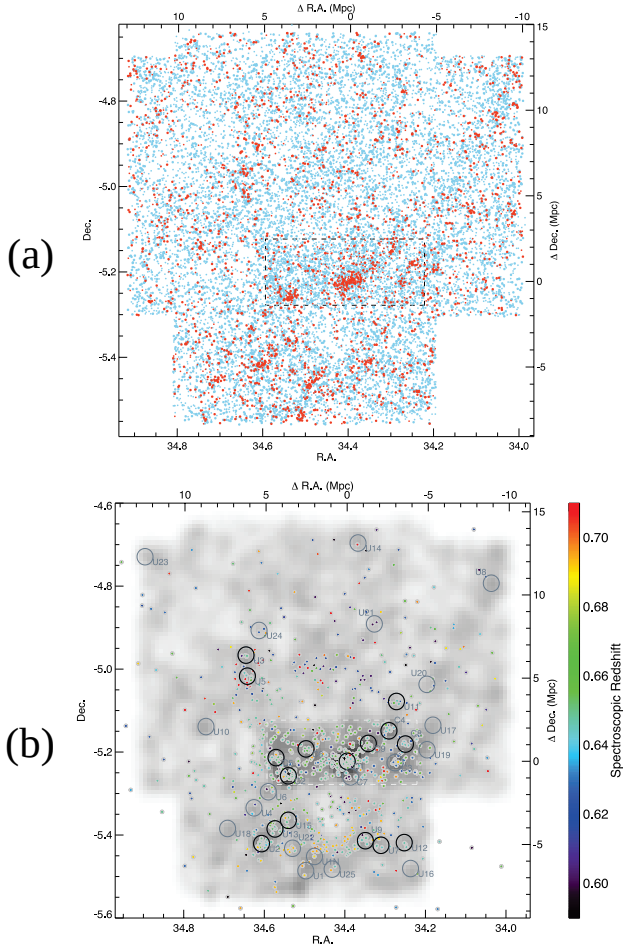

Fig. 1: Cl J0217-05 (a) Distribution of sources at z_{phot}~0.65 in the UKIDSS/UDS field. Passive galaxies (selected by restframe colors and Sérsic index) are marked in red, star-forming in blue. The rectangle indicates the CANDELS HST footprint. (b) Distribution of spectroscopic redshifts in UDS including 650 new z_{spec} from our VIMOS follow-up on top of the density map derived from Fig a. Cluster candidates and associated members identified by our 3D search are shown in gray. 16 clusters (in black) are confirmed to be part of the structure at z=0.65.

Structure dynamical analysis

Redshift were assigned to 21 structures including 16 at z~0.65. Velocity dispersions were derived (for clusters with sufficient statistics; 7 clusters) using bi-weight estimators (Beers et al. 1990). We derive R_{200} and mass based on Carlberg et al. 1997. 5 clusters were found with $M_{200}>10^{14} M_{\odot}$.

Quenching of star-formation along filaments

The birth of structures relies on the formation of clusters through the accretion of groups that join the denser regions along filaments. If it is clear that galaxies reaching clusters undergo a transformation compared to isolated ones, the influence of filaments on star formation and its quenching is hard to quantify. We are studying the pockets of star formation across the structure using SFR from MIPS, SED fitting and the [OII] emission line from our VLT/VIMOS spectra.

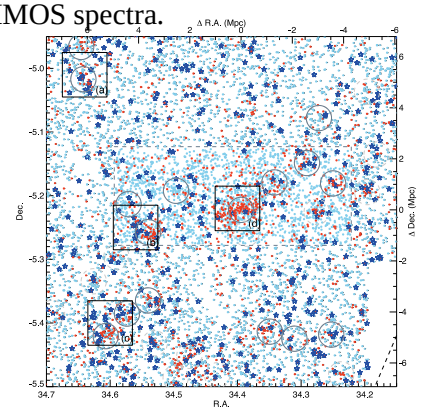

Fig. 2: Distribution of galaxies detected in MIPS 24μm on top of the distribution of sources from Fig 1-a. Confirmed clusters are marked in gray. (a), (b) and (c) show active pockets of star formation (d) indicates the more massive cluster whose members are mainly passive galaxies.

A. Galametz

Sizes, colour gradients and resolved stellar mass distributions in XMMUJ2235-2557

We analyse the sizes, colour gradients, and resolved stellar mass distributions for 36 massive, passive galaxies in the cluster XMMUJ2235-2557 at z=1.39, as part of our KMOS Cluster Survey (KCS), using optical and near-IR Hubble Space Telescope (HST) imaging. We generate spatially resolved stellar mass maps using an empirical relationship between stellar mass-to-light ratio (M_*/L) and colour and derive mass-weighted Sérsic fits for individual galaxies: the mass-weighted sizes are ~41% smaller than their rest-frame r-band counterparts compared with an average of ~12% at z~0. We attribute this change to the evolution in colour (or equivalently M_*/L) gradients, which are mostly negative and are twice the local value. We find that this evolution implies the presence of an age gradient, while the survival of weaker colour gradients in local passive galaxies requires also the presence of a metallicity gradient. This favours a gradual mass growth mechanism for these passive galaxies at high redshift, such as minor mergers.

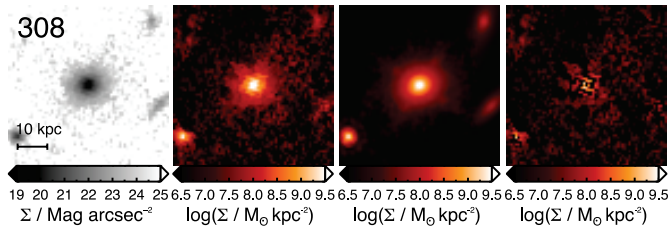

Figure 1. From left to right: HST Wide Field Camera 3 (WFC3) H_{160} image, stellar mass map, best-fit Sérsic model with GALFIT and residual in mass of a galaxy in our sample. We extract sizes from both HST images (light-weighted) and mass maps (mass-weighted).

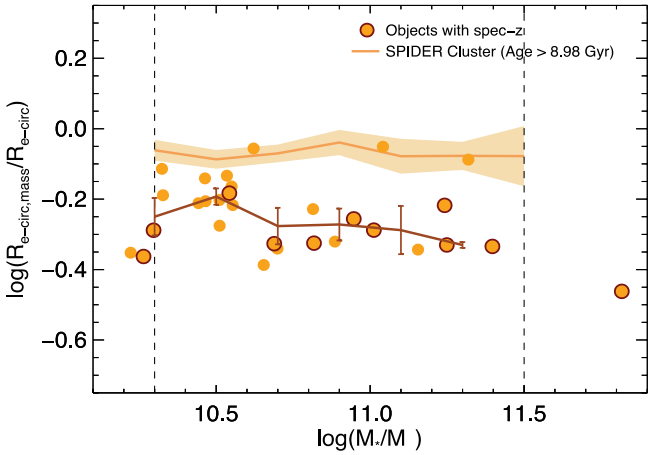

Figure 2. Comparison of the ratio of mass-weighted to light-weighted sizes vs. stellar mass at different redshifts, including the local size ratios from the progenitor bias corrected (age > 8.98 Gyr) SPIDER cluster sample (La Barbera et al. 2010). The light brown line and shaded region correspond to the median size ratio and ±1σ error on the median for the local sample.

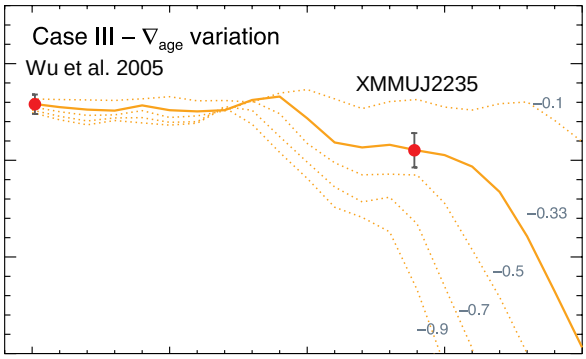

Figure 3. Evolution of (U-R) colour gradient over redshift. The solid line shows the colour gradient evolution of simple stellar population (SSP) models (Bruzual & Charlot 2003) assuming a formation redshift z_{form}= 3.0, an initial age gradient of ∇_{age} = −0.33 (at z=1.39) and a metallicity gradient of ∇_Z = −0.2. Dotted lines show the evolution with different age gradients.

References:
• Bruzual G., Charlot S., 2003, MNRAS, 344, 1000
• Chan J.C.C, Beifiori A., Mendel J.T., Saglia R.P. et al., 2016, arXiv:1603.00468, MNRAS, in press
• La Barbera F., de Carvalho R. R., de La Rosa I. G. et al., 2010b, MNRAS, 408, 1313
• Wu H., Shao Z., Mo H. J., Xia X., Deng Z., 2005, ApJ, 622, 244

J. C. C. Chan, A. Beifiori, J. T. Mendel, R. P. Saglia and KMOS Cluster Team

Hα disk sizes across 85% of cosmic time

To understand where stars are forming within galaxies, we utilize spatially resolved observations of the Hα emission line from KMOS^{3D} and HAGGIS (H-Alpha Galaxy Group Imaging Survey), tracing star formation rates (SFR) over ~85% of cosmic time (z~2.6-0). In the local Universe, we find that in galaxies with less total ongoing star formation than is normal for their stellar mass, star formation is restricted to the galaxies' inner parts, a phenomenon which appears to be more common in the satellites of massive galaxy groups. In contrast, at the peak of cosmic star formation, the star forming disks of KMOS^{3D} galaxies are more extended than the old stars, indicative of a growth in size as well as mass, but with high intrinsic scatter to be explored.

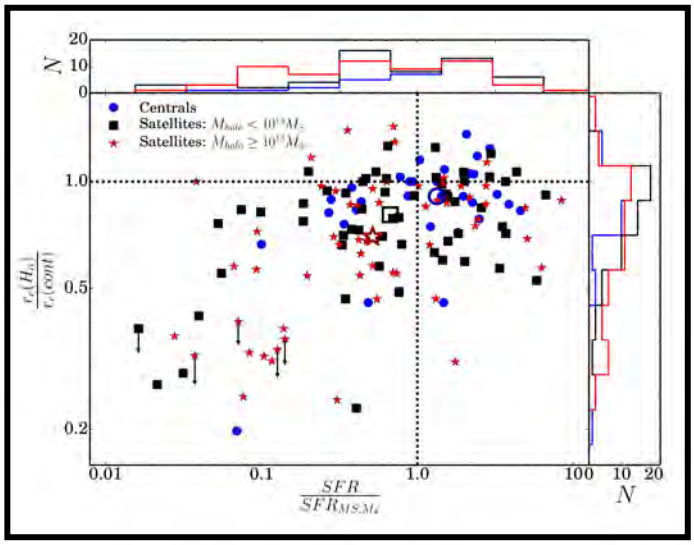

Left: Our HAGGIS survey at z~0 (Kulkarni, PhD Thesis) shows that in galaxies with normal SFR for their stellar mass, the ratio of Hα size tracing star formation to continuum size tracing the old stellar population is close to 1. In contrast, the star formation in galaxies with lower global star formation rates is more spatially compact than that of their stars. These low SFR, compact Hα galaxies are more common among the satellite population of groups than among central galaxies, suggesting their star forming outer gas disks may have been removed. This picture is supported by Fossati et al., 2013 who find that HI-poor galaxies host compact Hα disks.

Right: a) KMOS^{3D} has sufficient depth and resolution to measure the Hα profiles of individual, normally star forming galaxies at z~0.7-2.6. Most galaxies at both high and low environmental density have larger Hα sizes than their stellar size, suggesting size growth via star formation. Typical error bars are small (box/dotted lines show typical 1 and 2-σ errors), and the large scatter is mostly intrinsic. **b)** This contrasts to the situation in the local Universe for which satellites tend to be host more compact star forming disks.

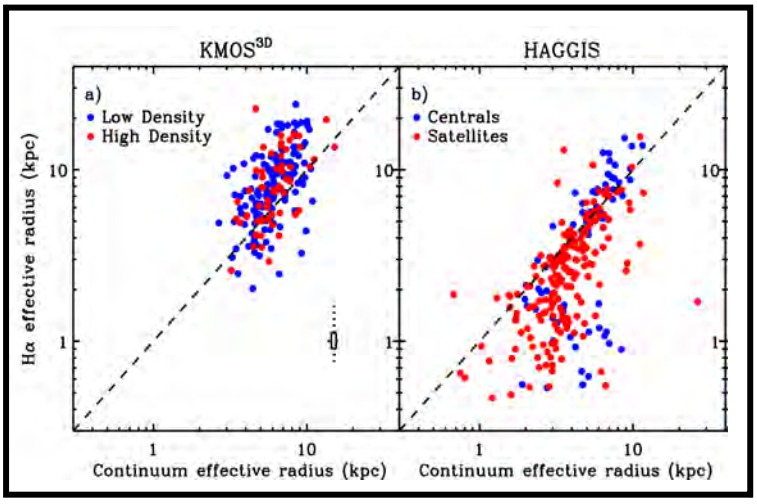

References:

- Fossati, M. et al, 2013, A&A, 553A, 91
- Kulkarni, S., PhD Thesis, https://edoc.ub.uni-muenchen.de/18818/1/Kulkarni_Sandesh.pdf

D. Wilman, M. Fossati, S. Kulkarni, P. Erwin, KMOS^{3D} and HAGGIS Teams

Quiescent galaxies at the peak of cosmic star formation

The latest generation of ground- and space-based photometric surveys have demonstrated that the population of massive quiescent galaxies starts to emerge even at z~2-3, when cosmic star formation activity is at its peak. With deep near-infrared spectra obtained using KMOS we are now able to study detailed properties of quiescent galaxies at this critical epoch, including not only their kinematic properties, but also details of their star-formation histories.

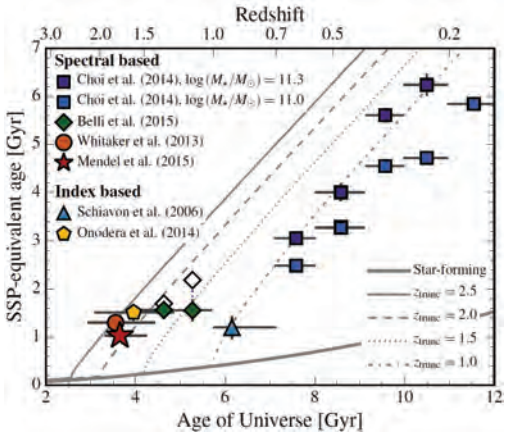

Timing the evolution of massive, passive galaxies

At $z > 1$ we observe that the age of massive galaxies plateaus at ~1 Gyr, suggesting that the quiescent population is being "kept young" by the constant addition of recently quenched galaxies.

At $z < 1$ galaxies' stellar populations appear to evolve passively, with additional growth occurring through the assembly of existing stellar mass, rather than star formation.

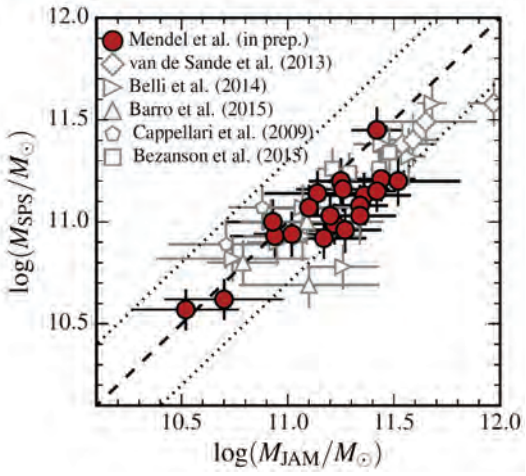

We find a good correlation between galaxies' total dynamical masses and their stellar masses derived from broadband photometry, suggesting that there is relatively little dark matter in the cores of massive galaxies at $1.5 < z < 2$.

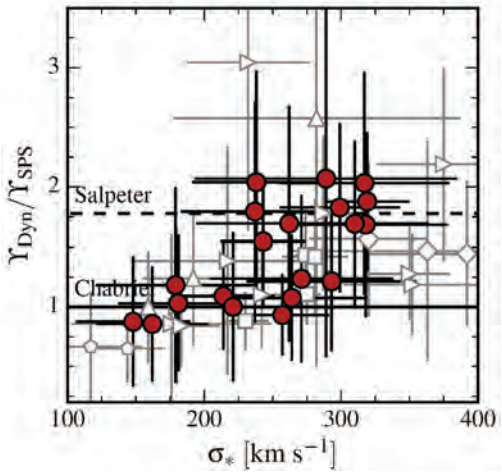

Comparing the dynamical mass-to-light ratio with that predicted for a Milky Way like stellar initial mass function (IMF), we find evidence for an increase in the IMF normalization with stellar velocity dispersion, consistent with the results of local galaxy studies.

References:
•Mendel et al. 2015, ApJL, 804, L4; Mendel et al. in preparation

J. T. Mendel, R. Saglia, A. Beifiori, R. Bender, D. Wilman, et al.

The fundamental plane of passive galaxies at z~1.5 from the KMOS Cluster Survey

We present the KMOS Cluster Survey (KCS), a 30 nights guaranteed time program led jointly by MPE and the University of Oxford (PIs: R. Bender & R. Davies) that is using the K-band Multi-Object Spectrograph (KMOS) on the ESO/VLT. KCS obtained deep (~20 hrs on source) absorption line spectroscopy for > 80 galaxies in four high-z clusters with the aim of studying the evolution of kinematics and stellar populations of galaxies in dense environments at redshift 1.4 < z < 2, a crucial time during which the galaxy population undergoes a transition from star-forming to passive. The combination of existing Hubble Space Telescope (HST) imaging, our HST Cycle 22 Wide Field Camera 3 (WFC3) data and our KMOS spectroscopy allowed us to study **the fundamental plane (FP) of passive galaxies in dense environments** at the time when the Universe was less than 5 Gyrs old.

KCS allowed us to measure stellar velocity dispersions for one of the largest homogeneous samples of galaxies – with $\log(M_\star/M_\odot)>10.4$ - in dense environments at z > 1.4

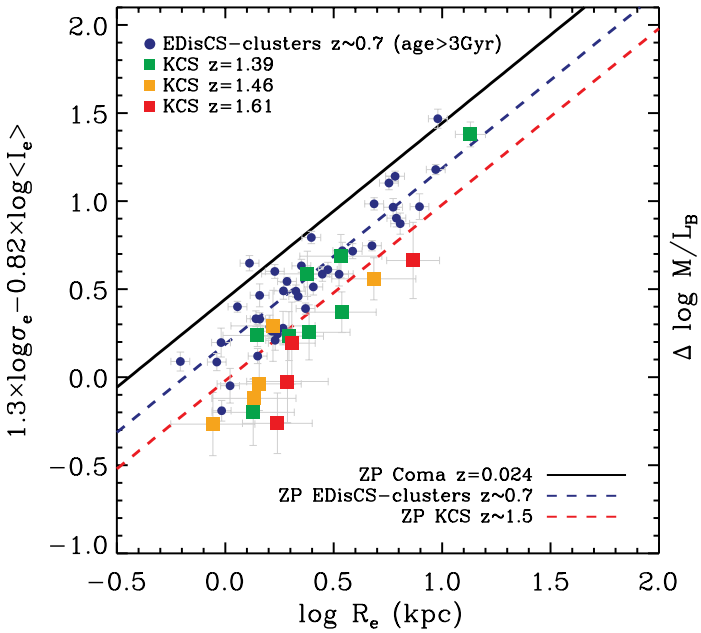

Edge-on projection of the FP for our KCS sample, relating galaxy's surface brightness, size, and velocity dispersion. Our results confirmed previous findings at z < 1.2 that the zero-point of the edge-on projection of the FP evolves with redshift.

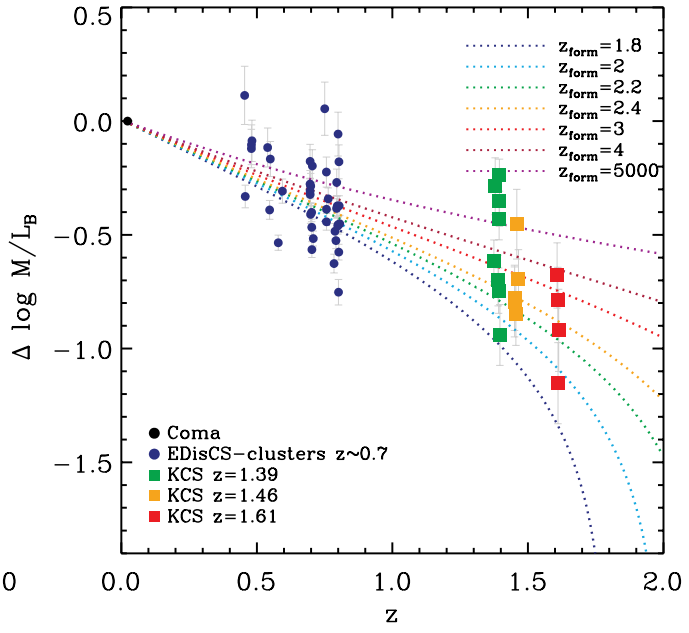

Evolution of the mass-to-light ratio $\Delta\log M/L_B$ of KCS galaxies compared to the intermediate and local samples. From the evolution of the M/L we derived the age of the last star formation episode and found that cluster galaxies are ~0.5-1 Gyr older than those found stacking passive galaxies in the field at similar redshifts (e.g., Mendel et al. 2015).

References:

- Beifiori et al, in prep.
- Mendel et al., 2015, ApJ, 804,4

A. Beifiori, J. T. Mendel, R. P. Saglia, J. Chan, R. Bender, A. Galametz, D. Wilman & UK-KCS team

Calibrating galaxy environment in the 3D-HST deep fields

We quantified the environment in which galaxies reside in three deep fields (COSMOS, GOODS-S, UDS). A careful and meaningful calibration of galaxies' environments has, until now, been difficult if not impossible at high-z due to incomplete and biased spectroscopic coverage of deep fields. This situation has changed with 3D-HST, which provides accurate redshifts for all galaxies in these fields up to z ~ 3. We derived local densities, halo masses and determined whether a galaxy is a central or a satellite of its halo. Combined with multi-wavelength photometry and resolved spectroscopy from KMOS^{3D}, we will explore the co-evolution of galaxies with their environment.

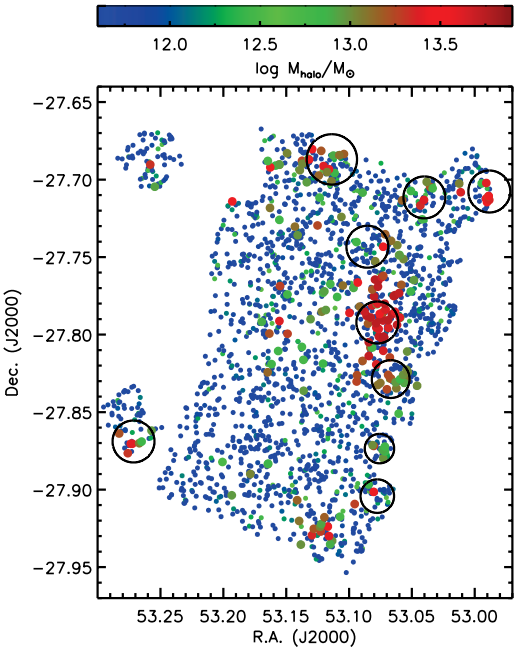

Left: The spatial distribution of galaxies in a narrow redshift slice (0.7 < z < 0.9), color coded by their halo mass. The figure clearly shows the large dynamic range in environment that we find in the deep fields, spanning from the low density field to massive groups or clusters. The black circles highlight known X-Ray groups which confirm the quality of our method (The size of the circle corresponds to the virial radius of the group) .

We devised and characterized an observationally motivated quantification of the local environment based on galaxy counts in fixed cylinders. We applied the 3D-HST selection function and redshift accuracy to mock galaxy catalogues. The combination of multi-scale environmental information in the observations and in the models allows us to link observed to physical quantities (e.g. halo mass), of fundamental importance for the interpretation of observational trends. We use the rank in stellar mass within a stellar-mass dependent aperture to distinguish between the central galaxies of their halo and satellite galaxies orbiting in the potential of other (more massive) galaxies.

Bottom right: The distribution of the ratio of stellar to halo mass in bins of increasing halo mass, separately for centrals and satellites. In low mass haloes central galaxies are distributed in a narrow peak, i.e. their halo mass is tightly correlated with their stellar mass. Satellite galaxies are by definition less massive, and the range of stellar to halo mass ratios is limited by the stellar mass limit of the sample. Going to higher halo masses we find satellites over an ever increasing range of stellar mass. This means that high-mass haloes are well populated by satellite galaxies which are much less massive than their centrals. This unique dataset and our accurate characterization of the environment will allow us to disentangle internal and external processes acting on galaxies at the epoch of the peak of the cosmic star formation activity.

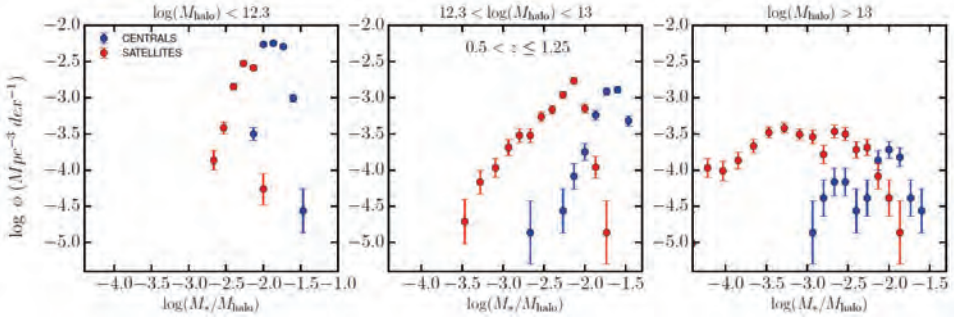

References:
- Fossati et al. 2015
- Fossati et al., in prep.

M. Fossati, D. J. Wilman, J. T. Mendel, A. Beifiori, R. Saglia, et al.

Anisotropic Galaxy clustering in the final BOSS

We explore the cosmological implications of anisotropic galaxy clustering measurements in configuration space of the final data release of the SDSS-III Baryon Oscillation Spectroscopic Survey (BOSS). The large volume and number density of this galaxy sample make it ideally suited for the analysis of the large-scale structure of the Universe. We implement a new detailed model of the effects of non-linear evolution, bias and redshift-space distortions to extract cosmological information from our clustering measurements. We combine this information with the latest cosmic microwave background (CMB) and Type Ia supernovae (SN) data to obtain cosmological constraints, with an emphasis on the properties of dark energy and the detection of deviations from the predictions of general relativity.

We use the clustering wedges statistic defined by Kazin et al. (2012), which is computed by averaging the two-dimensional correlation function, $\xi(\mu, s)$, over wide bins in the line-of-sight parameter μ.

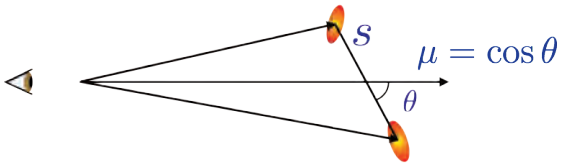

The figure on the left shows the measurements of three wedges in the directions transverse (orange), intermediate (green) and parallel (blue) to the line of sight using data from BOSS for $0.5 < z < 0.75$ (Sánchez et al. in prep). The BAO signal can be clearly seen in all wedges. The differences in amplitude and shape between the wedges are caused by redshift-space distortions. The information encoded in these measurements can be used to probe the expansion history of the Universe and the growth-rate of cosmic structure.

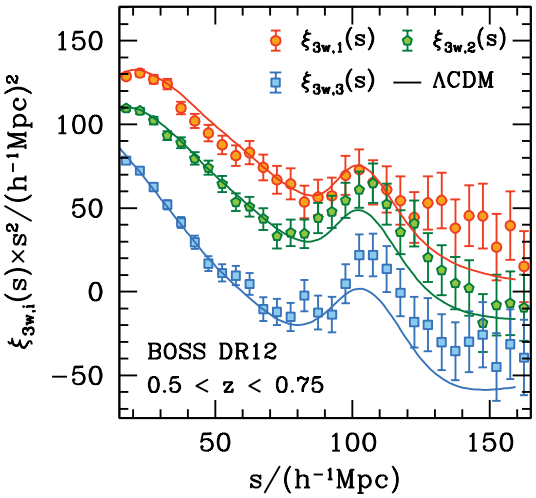

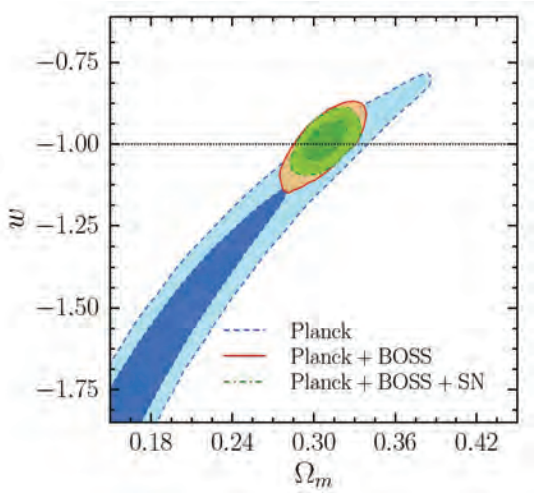

As an example, the figure on the right shows the joint 68% and 95% confidence levels in the $\Omega_m - w$ parameter plane inferred from Planck data alone (blue) and its combination with BOSS (orange). The CMB-only constraints show a strong degeneracy, which is broken by the inclusion of BOSS data. Additionally including SN information (green) leads to a final constraint of $w = -0.998 \pm 0.041$, in complete agreement with a cosmological constant. We also explore the constraints on the growth-rate of structures in the Universe assuming $f(z) = \Omega_m(z)^g$ and obtain $g = 0.601 \pm 0.079$, consistent with the predictions of general relativity of $g = 0.55$.

References:

• Kazin E., Sánchez, A.G. & Blanton M., 2012, MNRAS, 419, 3223
• Sánchez, A.G. in prep

A. G. Sánchez, J. N. Grieb, S. Salazar-Albornoz, M. Lippich & the BOSS collaboration

Cosmological implications of the BOSS DR12 Fourier space wedges

We extract the cosmological information from the full shape of the redshift-space two-point statistics measured from the final BOSS sample [1] by extending the definition of *clustering wedges* [2] to Fourier space [3]. Using novel approaches for the modelling of our clustering measurements, we are able to derive tighter cosmological constraints than in previous analyses. The constraints obtained from the combination of the BOSS Fourier-space wedges with cosmic microwave background (CMB) and Type Ia supernovae (SN) data are in perfect agreement with the standard ΛCDM model, which is thus further consolidated by our analysis.

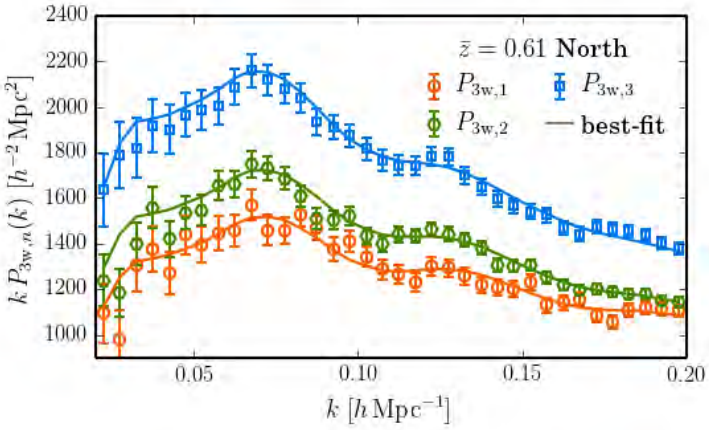

For three redshift bins of the BOSS sample, we measure three wedges, $P_{3w}(k)$, computed by averaging the 2D power spectrum, $P(\mu,k)$, over wide bins in the line-of-sight parameter μ. On the left, the results for the case of the highest z-bin and the Northern Galactic Cap are shown. The best-fit predictions of our new model of non-linearities, bias, and redshift-space distortions are drawn as solid line in the same plot.

For all three bins, we determine the angular diameter distance, $D_M(z_{eff})(r_d^{fid}/r_d)$, the Hubble parameter, $H(z_{eff})(r_d/r_d^{fid})$, and the growth rate, $f\sigma_8(z_{eff})$. r_d is the sound horizon scale. The constraints on D_M and $f\sigma_8$ for the lowest redshift bin are shown on the right (green contours). The obtained results are consistent with the ΛCDM predictions from the latest CMB observations (Planck 2015; blue contours) for all parameter combinations and redshift bins.

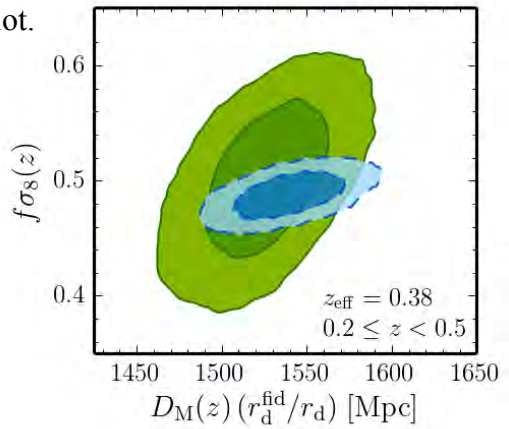

Besides probing the expansion history and the growth of structure, we derive cosmological constraints from our full-shape measurements. Here we highlight one result: the redshift evolution of the dark energy equation of state parameter, $w_{DE}(z)$, derived assuming the CPL parametrization [4]. The plot on the right shows the constraints obtained from CMB data alone (blue) and successively adding the BOSS (green) and SN data (orange). The combination of all data sets shows no signature of a deviation from a cosmological constant.

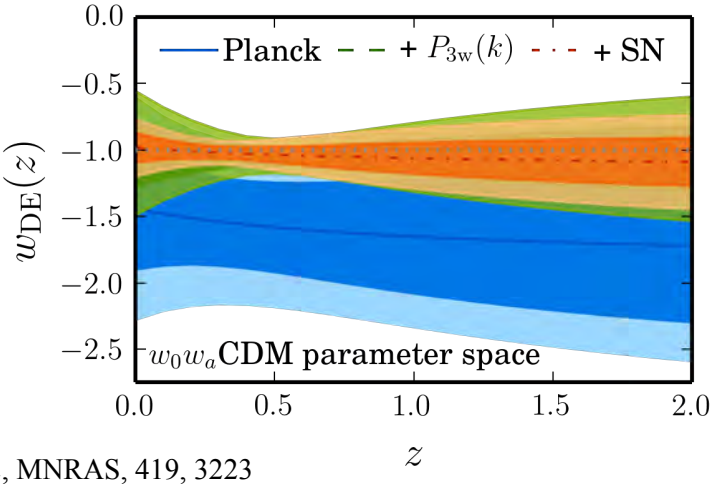

References:

- [1] Grieb, J. N. et al., in prep.
- [2] Reid, B. A. et al. 2016, MNRAS, 455, 1553
- [3] Kazin E., Sánchez, A. G. & Blanton M., 2012, MNRAS, 419, 3223
- [4] Chevallier, M. & Polarski, D., 2001, Int.J.Mod.Phys. D10, 213; Linder, E. V., 2003, PRL 90, 091301

J. N. Grieb, A. G. Sánchez, S. Salazar-Albornoz, & the BOSS Collaboration

Clustering Tomography on BOSS

As part of the analysis of the final SDSS-III BOSS (DR12) galaxy sample [1], we perform a tomographic clustering analysis by means of angular auto- and cross-correlation functions measured in thin redshift-bins [2], following the methodology presented in Salazar-Albornoz et al. (2014) [3]. Modelling the redshift evolution of the angular clustering signal we are able to trace the expansion history of the Universe and put constraints on cosmological parameters for a number of different cosmological models. Unlike the traditional analysis of the galaxy-clustering signal that uses the 3D positions of galaxies, this methodology has the advantage of using cosmology-independent measurements, as well as being able to include light-cone effects in the analysis. Here we present measurements of the redshift evolution of the linear galaxy-bias, which cannot be obtained by the traditional 3D analysis.

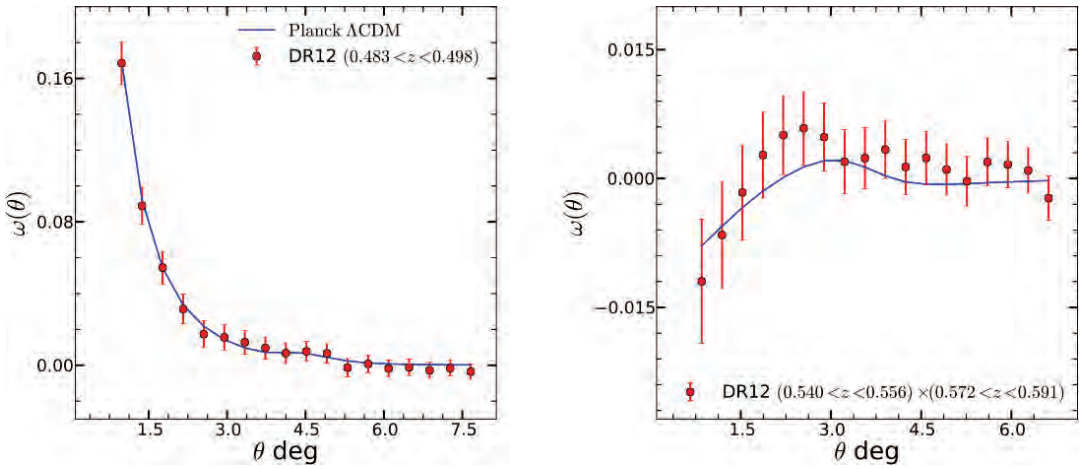

Figure 1. An auto-correlation function (left) and a cross-correlation function (right) between different redshift bins (see key) from the final BOSS galaxy sample. Measurements are shown by red symbols, while the blue line shows the prediction of our model for the clustering signal, assuming the best-fitting ΛCDM cosmology from the cosmic microwave background (CMB) temperature-anisotropy power spectrum as measured by the *Planck* satellite.

Figure 2. Redshift evolution of the linear galaxy bias. Red symbols show individual fits to 18 angular auto-correlation function measurements, in redshift bins, obtained using BOSS data. The green band shows the result of performing the same exercise on the mean of 1000 MD-Patchy BOSS mock catalogues [4]. The dashed lines show the 68% and 95% confidence intervals obtained by fitting all clustering measurements simultaneously (excluding the three highest-redshift ones, see [2]) with a linear bias model given by

$$b_1(z) = b^* + b'(z - 0.5).$$

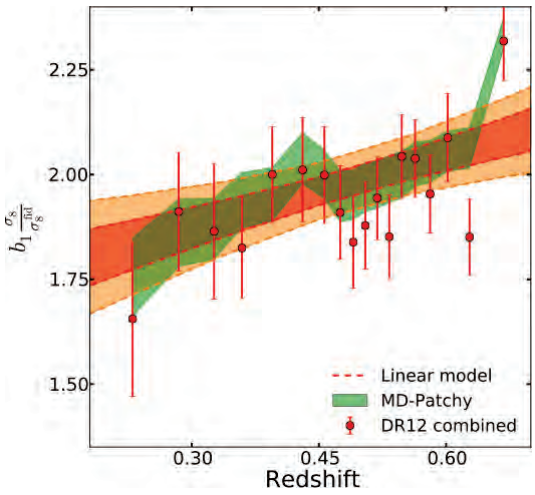

References:

- [1] Reid B. et al., 2016, MNRAS, 455, 1553
- [2] Salazar-Albornoz S. et al., in prep.
- [3] Salazar-Albornoz S. et al., 2014, MNRAS, 443, 3612
- [4] Kitaura F. et al., 2016, MNRAS, 456, 4156

S. Salazar-Albornoz, A. G. Sánchez, J. N. Grieb & the BOSS collaboration

Inverse bias weighting for redshift-space distortion measurements

The bias of galaxies depends on their luminosity. If not accounted for, this effect can introduce an artificial scale-dependence on clustering measurements. In order to avoid this, it has been proposed to weight each galaxy by its inverse bias [1]. We explore the impact of using such a correction on Redshift-Space Distortion (RSD) measurements, which represent a powerful tool to probe the growth of cosmic structure. Our results show that the technique of inverse bias weighting is not suitable for RSD measurements. This can present a complication for magnitude-limited surveys. For surveys that behave as volume-limited samples, such as the Baryon Oscillation Spectroscopic Survey (BOSS) [2], it is possible to perform an accurate RSD analysis without inverse bias weighting.

Our analysis was conducted on synthetic halo catalogues from the *Minerva* N-body simulations [3]. We measure the clustering of halos, using mass as a proxy for luminosity; and derive the mass dependence of halo bias. A "weighted" correlation function, $\xi_w(s)$, is obtained by weighting each halo by the inverse of its bias.

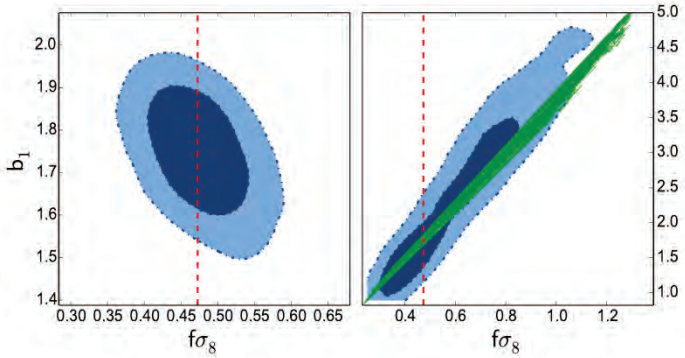

The growth rate factor, f(z), can then be constrained by fitting a model for the full shape of $\xi(s)$, including the effect of nonlinear evolution, bias and RSD. The figure on the left shows the resulting constraints on the parameter combination, $f\sigma_8$, and the linear bias parameter, b_1. The blue dashed lines represent the 68 and 95 percent confidence levels. The red dashed lines indicate the correct value of $f\sigma_8$. For the unweighted case (left panel) the correct value of $f\sigma_8$ is recovered.

However, for the weighted case (right panel) $f\sigma_8$ is inaccurately constrained. This is caused by a degeneracy between $f\sigma_8$ and b_1 that follows a constant $\beta = f\sigma_8 / (b_1\sigma_8)$, here shown by the green locus. It is not an exact line, because non-linearities introduce small deviations from the linear-theory relationship. This implies that when using the weighted correlation function we loose the information about σ_8 and only β, but not $f\sigma_8$ can be measured.

The figure on the right shows a comparison between the constraints on $f\sigma_8$ (upper panel) and β (lower panel) obtained with and without inverse bias weighting as a function of halo mass. The dashed lines indicate the expected parameter values. For all mass bins $f\sigma_8$ can only be accurately constrained without inverse bias weighting. Expressing the constraints in terms of β leads to similar results for both cases.

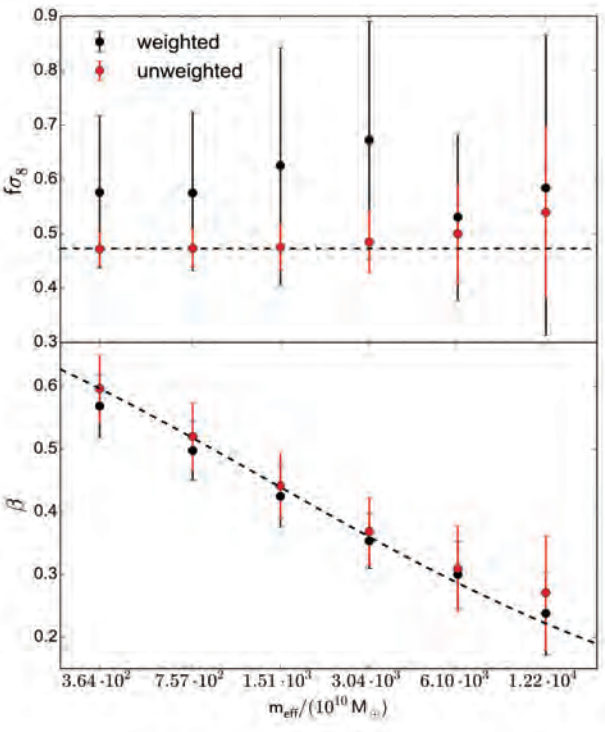

References:
- [1] W. Percival et al., 2004, MNRAS, 347, 645
- [2] B. Reid et al., 2016, MNRAS, 455, 1553
- [3] J.N. Grieb et al., 2016, MNRAS, 457,1577

M. Lippich, A. G. Sánchez, J. N. Grieb, S. Salazar-Albornoz

Projected Galaxy Clustering in GAMA

We measure the 2-point correlation function of galaxies (2PCF) in the 180 deg^2 GAMA II galaxy redshift survey, in several redshift slices in the range 0.0<z<0.5. We find more clustering in samples with higher luminosities, larger stellar masses and redder colours. Red galaxies also have steeper small-scale 2PCFs. We compare our results to the semi-analytic models of Lacey et al. (2015; L15) and Gonzalez-Perez et al. (2014; G14). The models reproduce the increase of galaxy clustering with mass, but not the sharp increase in clustering past L*. The models also show disagreements with the GAMA 2PCF on small scales, particularly under-predicting the small-scale clustering of blue galaxies. This poster highlights two problems with the models, these and other results are presented in Farrow et al. (2015).

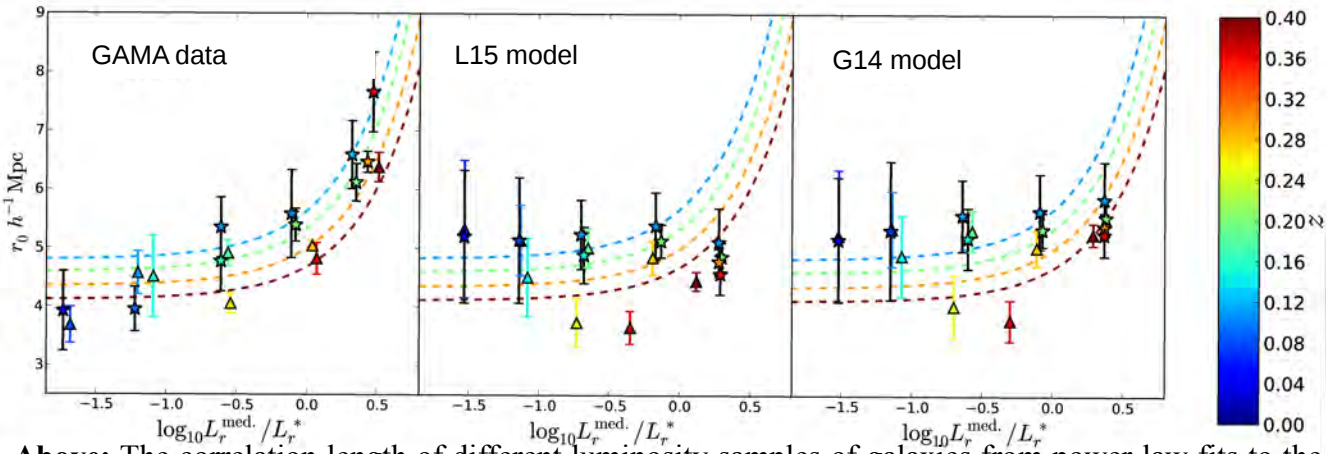

Above: The correlation length of different luminosity samples of galaxies from power-law fits to the 2PCF. Stars represent volume-limited samples. The flux limited samples (triangles) have been produced in the models by applying the GAMA selection-function. Colours show the median redshift. Dashed lines are computed from an empirical bias fitting formula for volume-limited SDSS galaxies (Zehavi et al. 2006), evolved to a range of redshifts using the Fry (1996) model for the passive evolution of the galaxy bias. They allow us to see if the galaxy distribution is co-evolving with the dark matter.

Right: The 2PCF of galaxies split into red and blue rest frame (g-r) colours, divided by a reference power law. We only show one of our redshift slices here: 0.24<z<0.35. Red galaxies are more strongly clustered in both the model and the data. However, both models under predict the clustering of blue galaxies at smaller scales.

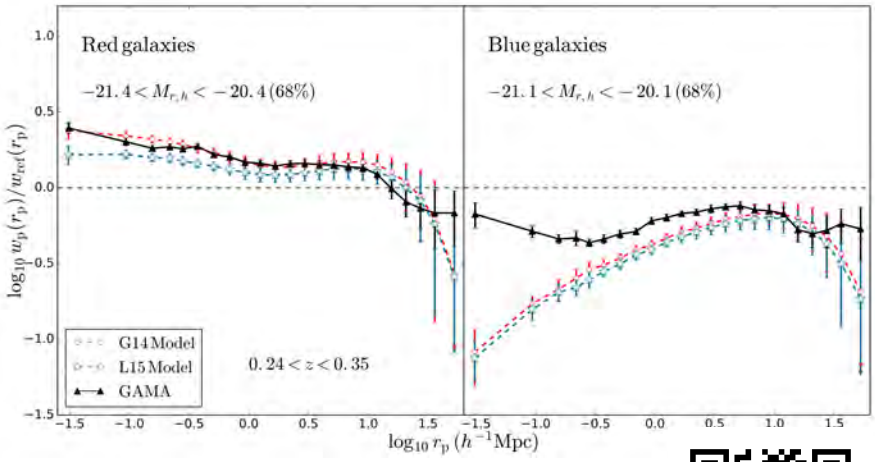

References:

- Farrow D. J., Cole S., Norberg P. et al., 2015, MNRAS, 454, 2120
- Fry J. N., 1996, ApJ, 461, L65
- Gonzalez-Perez V., Lacey C. G., Baugh C. M. et al., 2014, MNRAS, 439, 264 (G14)
- Lacey C. G., Baugh C. M., Frenk C. S. et al., 2015, MNRAS submitted (L15)
- Zehavi I. et al, 2011, ApJ, 736, 59

D. J. Farrow and the GAMA team

Search for giant planets in M67

We present the results of a 7 year radial velocity survey of a sample of 88 main sequence (MS) and evolved stars to reveal signatures of Jupiter-mass planets in the solar age and solar metallicity Open Cluster (OC) M67. We aimed to perform a long-term study on giant planet formation in open clusters and determine how it depends on stellar mass, chemical composition and birth environment. Five new extrasolar planets have been discovered in this survey: three new Hot-Jupiters (HJ) in orbit around three G dwarfs and two giant planets around two evolved stars. Remarkably, one of the G planet-hosts is a perfect solar-twin. In contrast with early reports, our results show an excess of HJs in dense OCs and a total planets frequency compatible with that around field stars.

Method: Radial Velocity (RV) Spectroscopy is an indirect method, based on the Doppler effect measurements, used to determine periodic RV changes in the stars that can attributed to the gravitational influence of one or more planets or to intrinsic pulsation of the stellar surface. We analysed precise RV measurements obtained with five different telescopes and spectrographs combinations: HARPS at the ESO3.6m (La Silla), SOPHIE at the OHP (France), HRS at the Hobby-Eberly Telescope (USA), HARPS-N at the TNG (La Palma) and CORALIE at the Eulerian Swiss Telescope (La Silla). We have performed a total of 1149 single observations with a precision as good as ~10m/s.

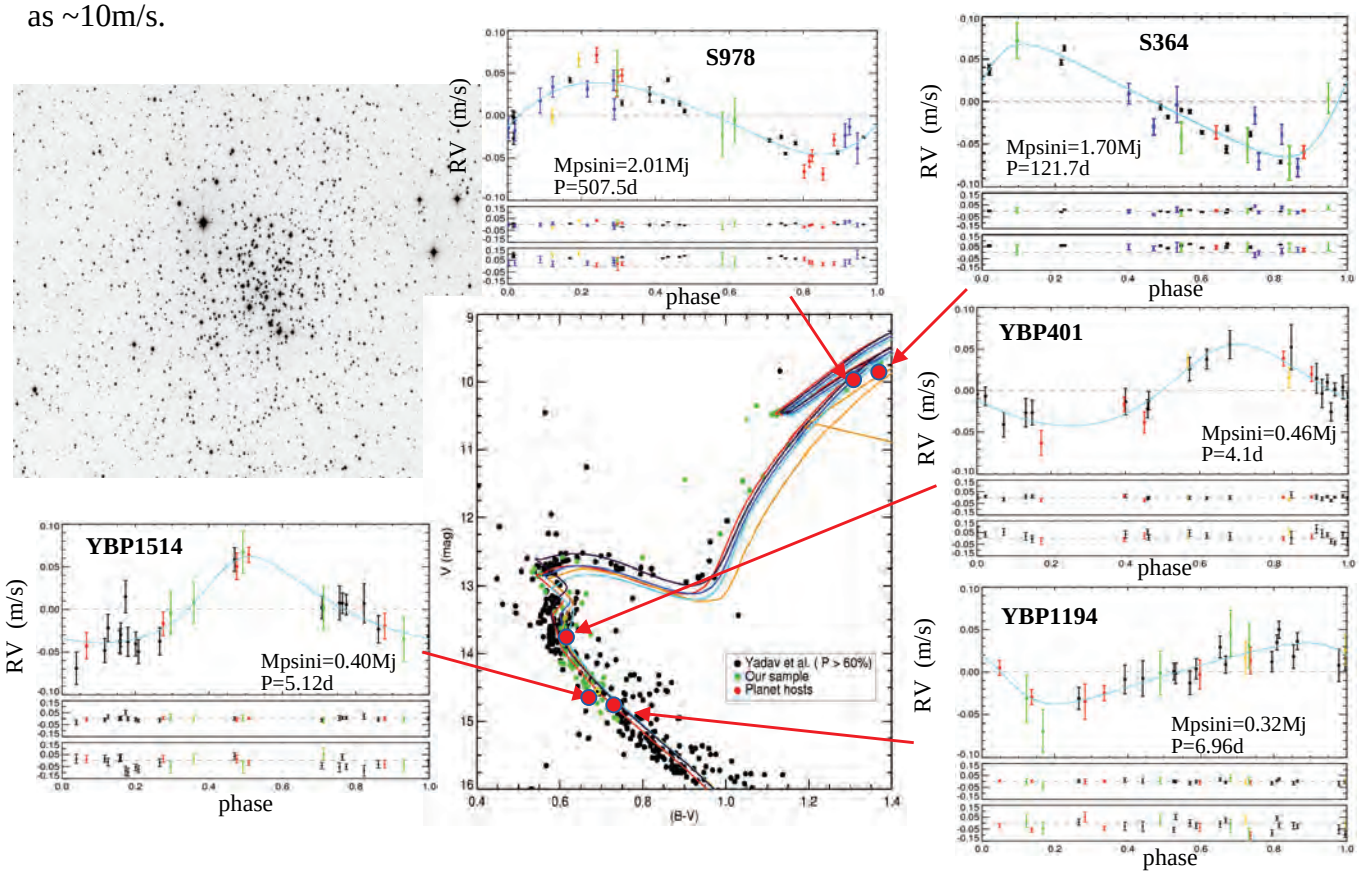

Figure: Central panel: CMD of open cluster M67. Green points: RV sample. Red points: planet-host stars connected to each respective plot of the phased RV measurements and the best Keplerian Fit. Top Left: Image of the open cluster M67.

References:

•Brucalassi, A., Koppenhoefer, J., Saglia, R. P. et al. 2016, A&A, submitted
•Brucalassi, A., Pasquini, L., Saglia, R. P. et al. 2014, A&A, 561, L9

A. Brucalassi, R. P. Saglia, J. Koppenhoefer, et al.

Pan-Planets - Searching for hot Jupiters around cool stars

Hot Jupiters, in many ways remarkable planets, can be used as a laboratory to study different planet formation models. There is an ongoing debate whether the discs surrounding M dwarfs during formation contain enough building material to create such a gas giant. Previous surveys did not have a sufficiently high number of M dwarfs to tackle this question. The Pan-Planets survey was created to give a statistical assessment of the occurrence rate of such hot Jupiters.

The Pan-Planets survey is based on data from the Pan-STARRS1 telescope, located in Hawaii. Over the course of three years, between 1500 and 6000 data points (depending on the region) were collected for 4 million sources with magnitudes $13 < i' < 18$. We achieve a precision of 5mmag at the bright end which is sufficient to detect hot Jupiter transits for M, K and G stars. The large FOV (42 sq. deg.) means that Pan-Planets has one of the largest M-dwarf samples to date with 65000 estimated targets. The large number makes spectroscopic characterization unfeasible. To improve upon simple colour cuts, we implemented SED fitting with iterative dust fitting, using a 3D dust map (Green et al. 2015, ApJ, 810, 25), and proper motion cuts as additional constraints.

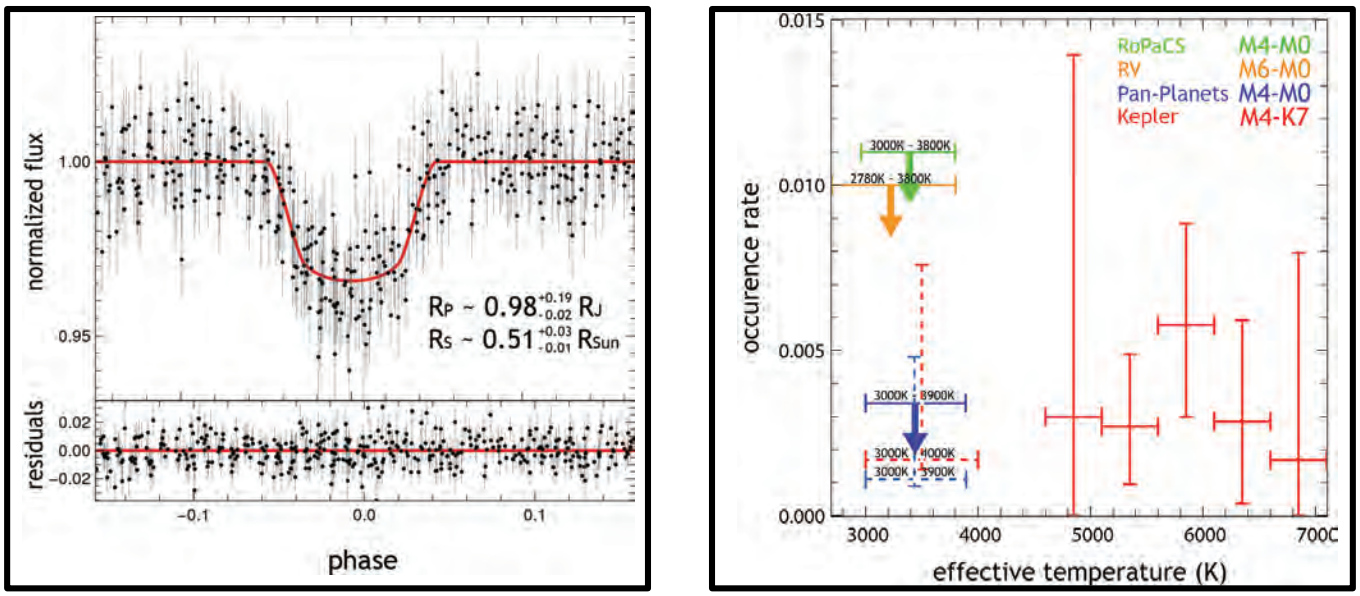

Left: folded light curve of the high-priority target PP403-05317, centered around the transit. The best-fitting MCMC transit model is indicated as a red line, with residuals below. Right: Estimated hot Jupiter planet occurrence rates or upper limits for different effective temperatesand surveys. In case of one detection, we estimate an occurrence rate of 0.17%.

We performed extensive Monte-Carlo simulations by injecting transit signals into the real light curves and then attempting to recover the signal with the Pan-Planets detection pipeline. Using these results, we could determine the detection efficiency of this project. We set new limits to the occurrence rate of hot Jupiters around M dwarfs, depending on the final amount of planet detections. We are in the process of following up several high-priority targets with high-resolution spectroscopy.
Based on these results, we can neither refute nor confirm the theoretical assumption that hot Jupiters are less frequent around M dwarfs. However, their occurrence rate seems to be on par with that of hotter stars.

References:

- Obermeier et al. 2016, A&A, 587, id.A49, 15 pp.

C. Obermeier, J. Koppenhoefer, R. Saglia, A. Riffeser, M. Kodric, R. Bender

The M31 Near-Infrared Cepheid Period-Luminosity Relation

We derive a sample of 371 Cepheids in the Andromeda galaxy (M31) with near-infrared photometry from the Hubble Space Telescope (HST) Panchromatic Hubble Andromeda Treasury (PHAT) program. The obtained period-luminosity relations (PLRs) have a very small dispersion, i.e. 0.155 mag in F160W (see Fig. 1), despite using random phased observations. This remarkably small dispersion allows us to determine that the PLRs are significantly better described by a broken slope at ten days than a linear slope. The use of our sample as an anchor to determine the Hubble constant H_0 gives a 3.2% larger Hubble value compared to the Riess et al. 2012 sample.

For a subsample of Cepheids we published in Kodric et al. 2013 we obtain near-infrared photometry from the HST PHAT program (Dalcanton et al. 2012). Our data reduction pipeline takes the HST and PanSTARRS difference images of Andromeda into account in order to identify the correct source in the PHAT data. We obtain a sample of 371 Cepheids with random-phased F110W and F160W photometry. The sample consists of 319 fundamental mode (FM), 16 first overtone (FO) and 36 type II Cepheids. 110 FM Cepheids have periods of 10 days or more.

The PLRs we derive have a very small dispersion (see Fig. 1 for the F160W PLRs) which allows us to investigate the broken slope hypothesis. We find that a broken slope describes the data significantly better than a linear slope. Fig. 2 shows that the 3σ contour lines of the bootstraping of the broken slope fit, with a common suspension point y_0 at 10 days, do not overlap.

An estimation of the effect of our PLRs on H_0 shows that our sample gives a 3.2% larger H_0 than the Riess et al. 2012 sample. Since the Riess et al. Cepheids are largely a subsample of our Cepheids, the offset between the two PLRs points to a sample selection bias that might significantly impact the error budget of H_0.

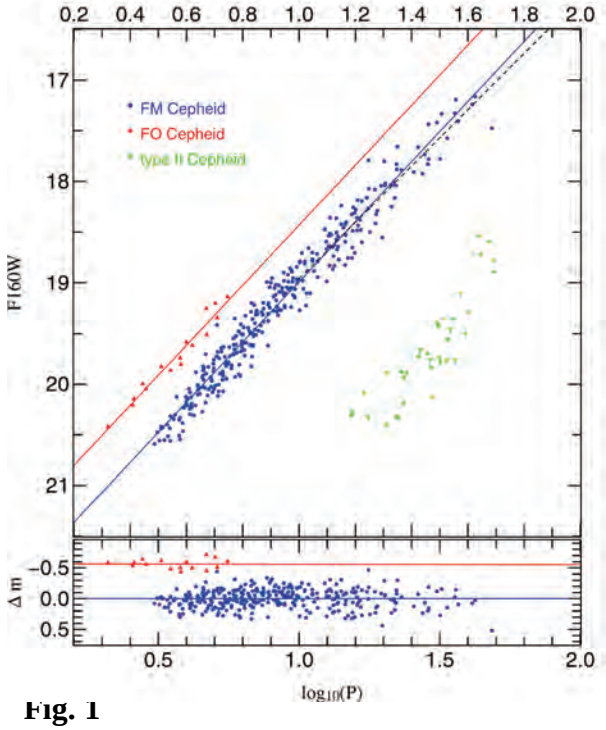

Fig. 1

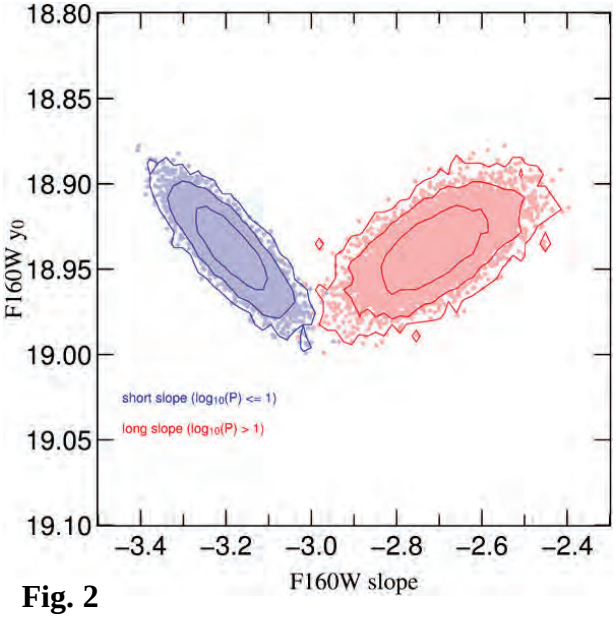

Fig. 2

References:

- Kodric et al. 2013, AJ, 145, 106
- Kodric et al. 2015, ApJ, 799, 144

M. Kodric, A. Riffeser, S. Seitz, J. Snigula, U. Hopp, C. Goessl, R. Bender, et al.

The Hobby-Eberly Telescope Dark Energy Experiment

The Hobby-Eberly Telescope Dark Energy Experiment (HETDEX) is a blind, fibre-fed spectroscopic survey designed to map about 800.000 Lyman-α (Lyα) emitting galaxies at 1.9<z<3.8 over 420 deg². HETDEX will measure the Hubble parameter, H, and the angular diameter distance, D_A, with about 1.3% accuracy. MPE has a primary role in the development of the data analysis software, the understanding of the Lyα selection function and the cosmological analysis.

The HETDEX instrument consists of 78 integral field spectrographs, called VIRUS. Each one is composed of:

- a bundle of 448 optical fibres, covering about 50" x 50";
- a pair of spectrographs with a wavelength coverage 350-550 nm and a resolution of about 0.5 nm.

The survey will start late 2016 and in the next 3 years will scan 420 deg² measuring about 2.5 million spectra. Around 0.8 million of them will be Lyα emitters at 1.9 < z < 3.8. They will sample the matter distribution in a volume of about 9 Gpc³ and will allow us to constrain H and D_A with 1.2% and 1.3% accuracy respectively. It will also provide competitive results on neutrino masses and inflation models.

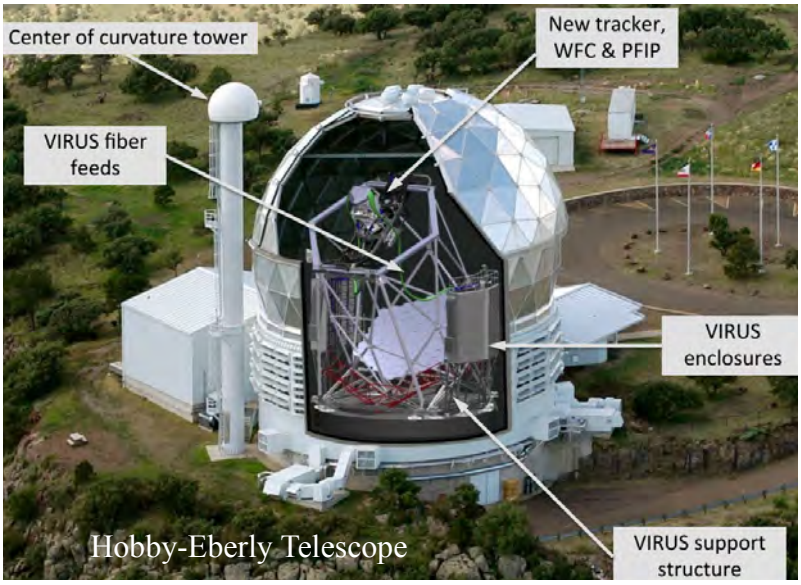

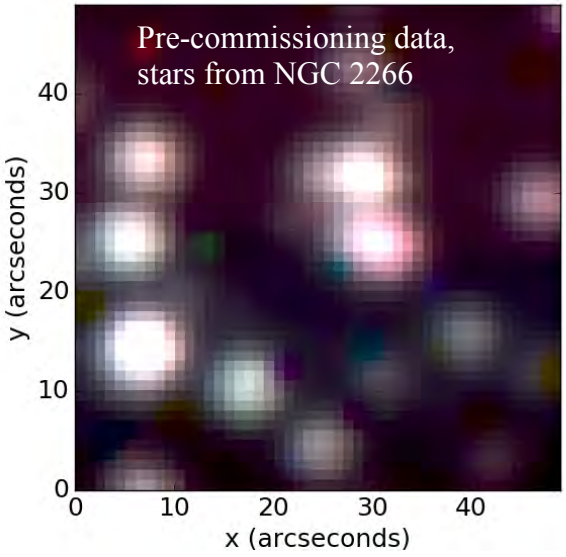

Current status:

- ✔ IFU bundles commissioned.
- ✔ Wide Field Corrector (WFC) and Prime Focus Instrument Package (PFIP) mounted and tested.
- ✔ Half of the VIRUS spectrographs assembled; lab tests ongoing.
- ✔ First spectrograph deployed to test the telescope software and begin training the scientists and the pipeline. The figure on the left shows a false colour image reconstructed from pre-commissioning data.
- ☐ 24 spectrographs to be selected and sent to the telescope by April 2016.
- ☐ First fibre bundle shipped at the beginning of April
- ☐ Start commissioning by the end of April with 24 VIRUS units
- • Start science observations on late 2016

References: ● Hill G., 2014 ● Takanada M., 2006

F. Montesano, R. Bender, D. Farrow, U. Hopp, A. G. Sánchez, J. Snigula and the HETDEX team

Upgrade of the Hobby-Eberly Telescope primary mirror control system

With its segmented 11-meter mirror, the Hobby-Eberly Telescope (HET) is one of the world's largest optical telescopes. It's strength is its queue scheduling system which allows fast reaction to time critical observations and transient alerts as well as efficient large area surveying.[1] The HET primary consists of 91 mirrors which requires a Segment Control System (SCS) that actively controls the primary's shape. The SCS will be upgraded to SCS2 using the latest technology based on OPINAS/USM's DECANIC* system. SCS2 will improve and speed up the HET primary mirror control and reduce waste heat significantly, thus leading to better overall performance and image quality.

The primary mirror alignment is maintained by feedback loops between the diagnostic system and the SCS. Movement is achieved by stepper-motor driven actuators on three axes per segment. Due to their age, the current SCS controllers are not anymore maintainable. For the new SCS2, we adapted the OPINAS/USM developed general DECANIC* system to the specific needs of the HET to address the current system's weak points[2]:

1. Reconfiguration time: SCS only moves half of the 273 axes at a time, SCS2 drives them all at once.
   => This reduces the actual alignment time in half and yields a closer to ideal primary shape.

2. Communication time: Change from SCS's RS232 to the latest industry standard CAN bus control.
   => This reduces the communication time to negligible 120 ms for the whole array with its 273 axes.

1. Dome seeing: In contrast to the current SCS, SCS2 works remotely without on-segment controllers.
   => This eliminates the dominant heat source from under the primary which will reduce dome seeing.

The new Segment-Motion-Controller (SMOCO) can drive up to 12 axes (4 segments) in parallel, so we need just 23 controllers (of 10cm x 16cm size each) to drive all axes simultaneously. SCS needed 138 controllers and dissipated 1,3 KW while the SMOCO array dissipates less than 30W for all 273 axes.

The new SCS2 meets the following alignment accuracy requirements:

$$\Delta tip_{max} = 24 \text{ mas} \qquad \Delta tilt_{max} = 14 \text{ mas} \qquad \Delta piston_{max} = 18 \text{ nm}$$

*DECANIC = *decentralized CAN-based instrument control-system*

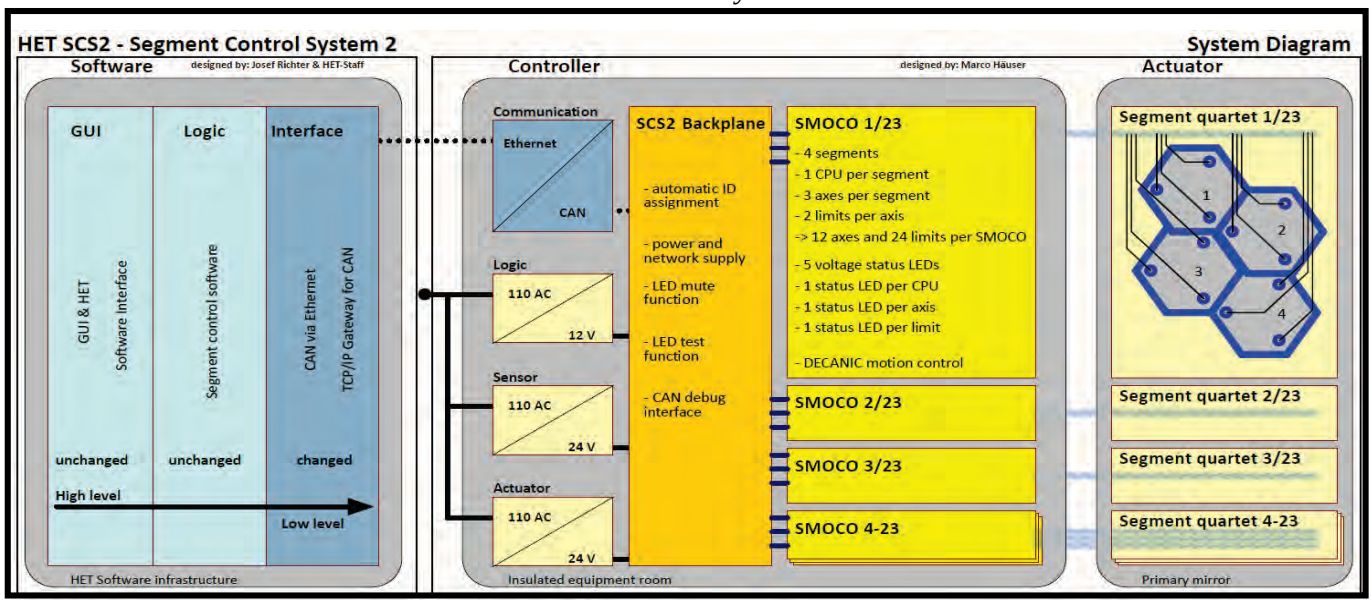

References: **[1]** Shetrone et al., 2007 PASP 118,556 **[2]** Marco Haeuser et al., 2016, SPIE Conf. (in preparation)

M. Haeuser, J. Richter, U. Hopp, R. Bender and HET-Staff

Virus Data Analysis Tool
Virus Health Check

MPE is a major player in the development and maintenance of the data analysis pipeline for the Hobby-Eberly Telescope Dark Energy Experiment (HETDEX). The main software products are cure/cure-WISE, the official automatic pipeline (see “cure” poster for more details), the Virus Data Analysis Tool (VDAT), a visualisation and reduction program with a graphical interface, and the Virus Health Check (VHC), an automatic data validation system.

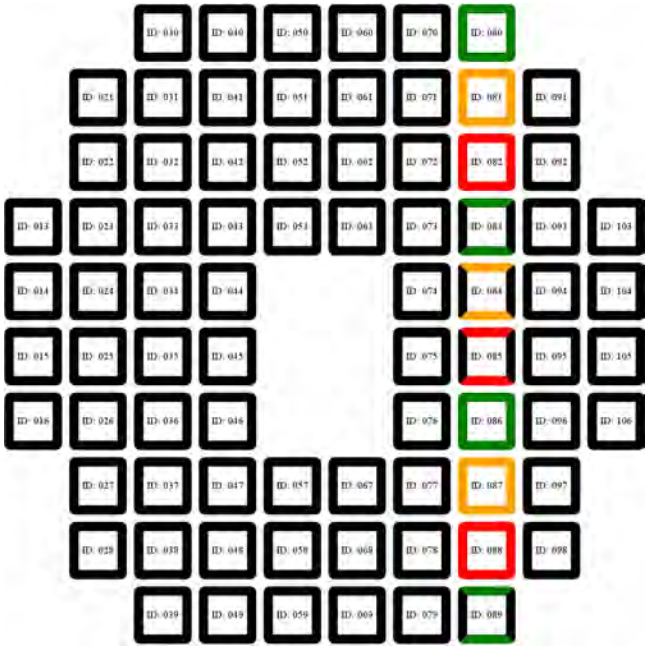

VHC

- Validate data right after CCD readout.
- Collect all the fits files from a single HETDEX observation.
- Run a set of predefined or user-provided tests. The tests are designed to check if the files are within specifications.
- Write execution and error logs.
- Create a HTML visualisation document that recaps the status of the observation. An example can be seen in the figure on the left. Each box represents an IFU and can be clicked to visualise the test results.

VDAT

- Select a set of files to be reduced on the left hand side tree.
- Visualise the fits files and other reduction results.
- Expand a single IFU for inspection by double clicking on it.
- Select one or more IFUs for the data reduction
- Execute the desired action(s) on the selected IFUs by button-click
- VDAT is highly customizable: type of files to display, buttons name/action and reduction commands are stored in configuration files.

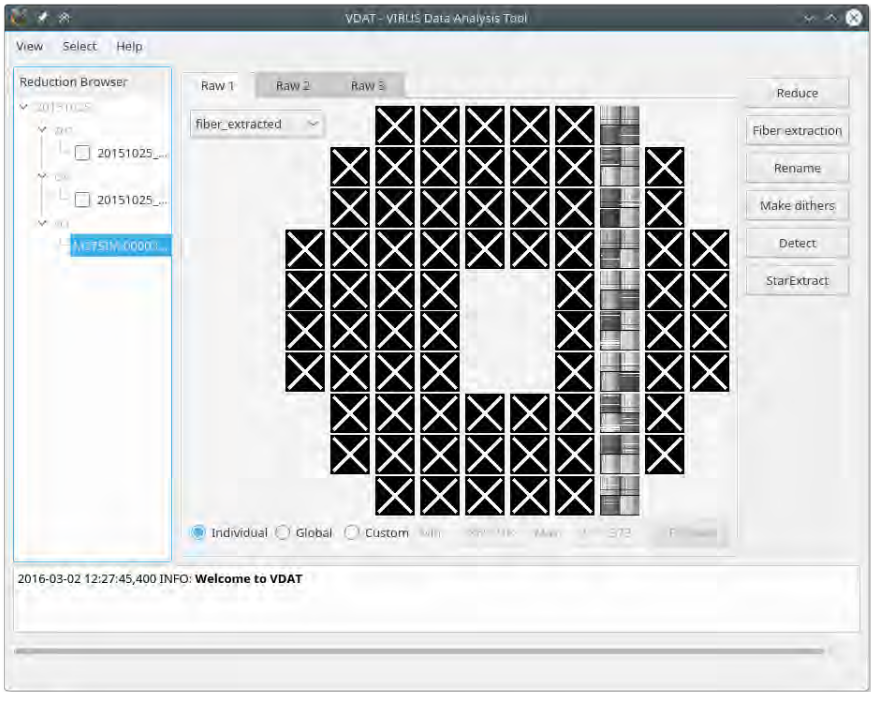

F. Montesano, D. Farrow, J. Snigula and the HETDEX collaboration

Cure – The HETDEX data reduction pipeline

The VIRUS instrument used by the Hobby-Eberly Telescope Dark Energy Experiment (HETDEX) will, with every exposure, generate almost 35000 individual fibre spectra, most of them of empty sky regions. To analyse these, we developed a reduction pipeline for the fast, reliable automated detection and classification of emission line and continuum spectra.

Cure is the data reduction and object classification pipeline for HETDEX. It is designed to reduce the raw images, subtract the sky background, extract spectra from the images, classify the spectra and find the Lyα emitters. All operations support full Gaussian error propagation for every image pixel. It provides the data reduction backend for VDAT (see poster) and cure-WISE. Additionally we developed a simulation framework for HETDEX data. The simulated data allow us to estimate the completeness of the source detections, test the correctness of flux recovery and sky subtraction schemes and to stress-test the whole data reduction pipeline.

Cure provides:

- Basic image reduction, bias subtraction and removal of pixel to pixel sensitivity variations.
- Detection and tracing of individual fibre spectra along the dispersion direction.
- Fitting of the cross dispersion fibre profile of the individual spectra
- Wavelength calibration for each spectrum using calibration lamp images.
- Sky subtraction with sky spectra extracted from the same integral field unit (IFU), or from a different IFU for extended objects.
- Detection of emission lines using the information from all three dithers to eliminate contamination from cosmic ray events.
- Detection of continuum spectra.
- Extraction of rectified spectra
- Tools for visualisation and quality control of calibration products and detected sources.
- Image reconstruction from a complete dithered set of observations.
- Quality control routines for Virus Health Check (VHC).
- A simulation package for a full end to end simulation of the HETDEX survey.

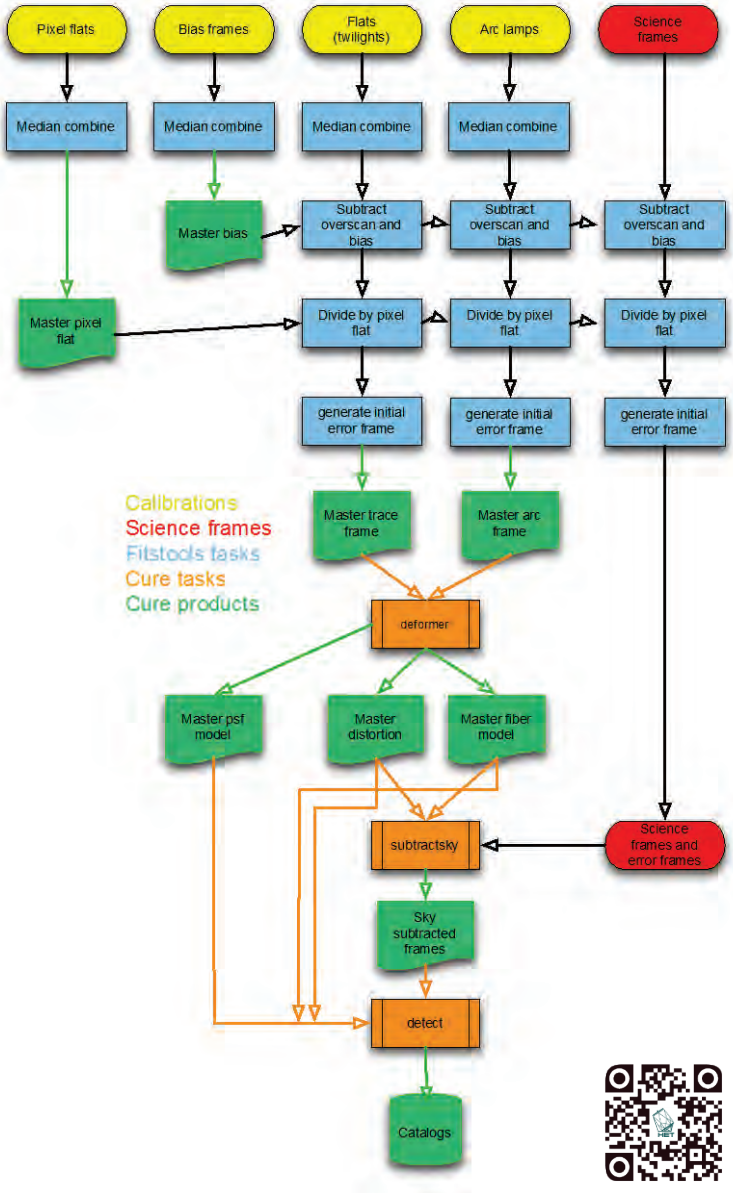

J. Snigula, F. Montesano, D. Farrow, N. Drory and the HETDEX team

Cure-WISE – HETDEX data reduction with Astro-WISE

During its three (five with extension) years of observations, we expect the Hobby-Eberly Telescope Dark Energy Experiment (HETDEX) to produce almost 34000 individual FITS images on a typical night. To analyse and catalogue this data volume we implemented the CURE pipeline within the Astro-WISE system[1,2] (Astronomical Wide- field Imaging System for Europe).

The Cure-WISE pipeline provides:

- automated parallel reduction of all the images from a 78 IFU VIRUS exposure.
- a database backend for the data management.
- full dependency tracking for all the data reduction steps.
- bookkeeping of the observed data.
- quality control for every reduction step.
- trend analysis for various parameters, e.g. chip degradation over time.
- organization of the detected sources.
- storage for the additional imaging data and aperture photometry for every spectrum in various optical and NIR pass-bands.
- user and project management
- access to the database and data reduction facilities for all HETDEX consortium members through its federated structure.

Cure is the data reduction and object detection pipeline for HETDEX. We created python wrappers for all the reduction steps in cure (cure-WISE), encapsulating it in the Astro-WISE environment. The wrappers give us access to the Astro-WISE batch system control for parallel data reduction of all IFUs at once. The system includes automated quality control checks at various steps in the pipeline. First tests with mock HETDEX data have shown that we will be able to reduce the observations in real time, with enough capacity to re-reduce older data as we improve the underlying pipeline. Since Astro-WISE is designed to be used with many instruments, it enables us to store the accompanying imaging survey. From these images we will create catalogues to match against our emission line detections, and to measure aperture photometry at the position of the Lyα detection.
Cure-WISE is written in python making it easy to expand and to further analyse the sources detected by cure.

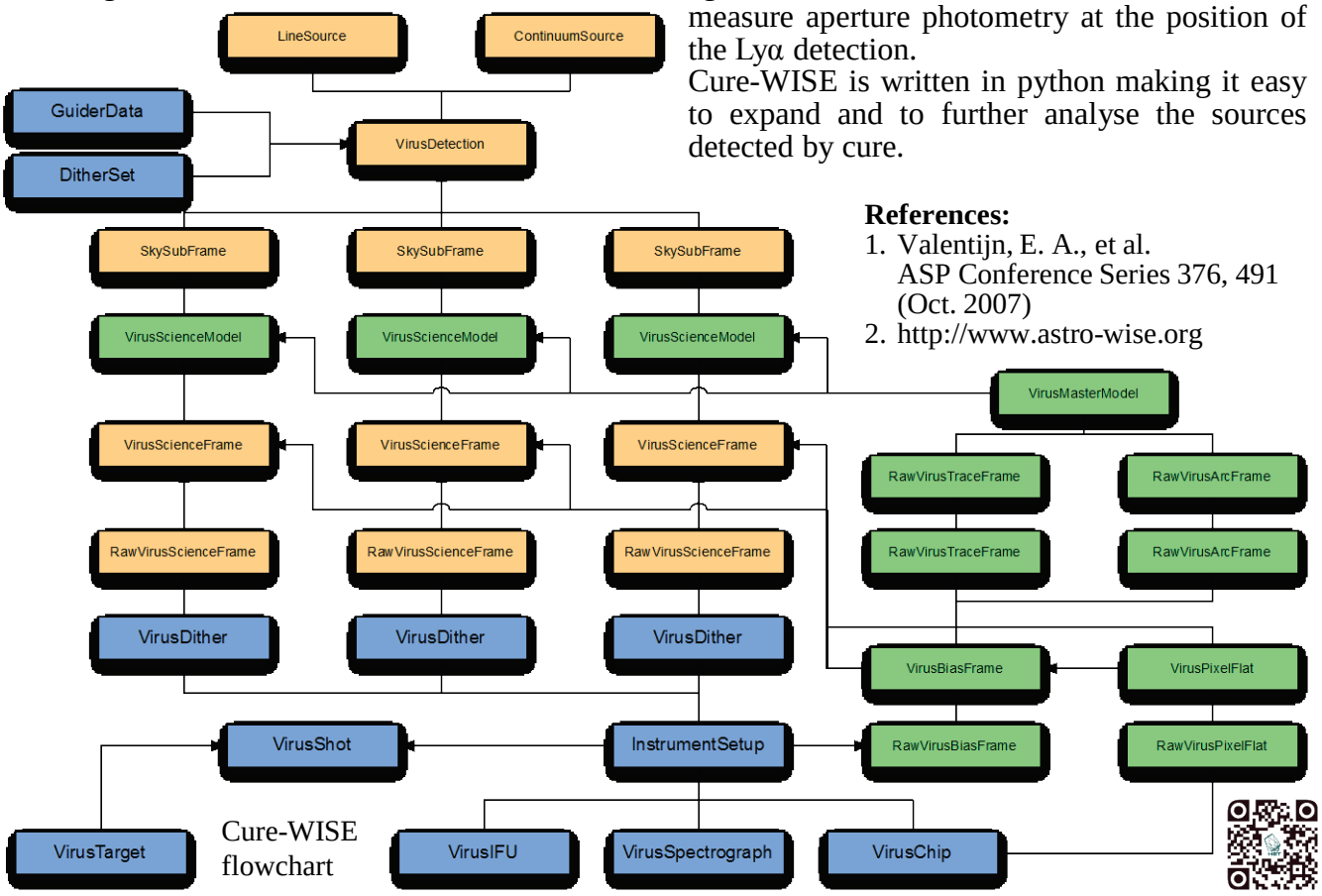

Cure-WISE flowchart

References:

1. Valentijn, E. A., et al. ASP Conference Series 376, 491 (Oct. 2007)
2. http://www.astro-wise.org

J. Snigula, F. Montesano, D. Farrow and the HETDEX team

Science with Euclid

Euclid is an ESA satellite dedicated to the investigation of the nature of Dark Energy, which will be launched 2020. Euclid will image the 15,000 square degrees of the extragalactic sky with high spatial resolution in one optical and three near-infrared bands. This will allow to analyze the evolution of large scale clustering out to redshifts of ~2 using the cosmological weak lensing (WL) signal of ~10^9 galaxies. In addition, slit-less spectroscopy will be employed to probe the characteristic scale of the Baryonic Acoustic Oscillations (BAO) and the galaxy clustering as a function of redshift.

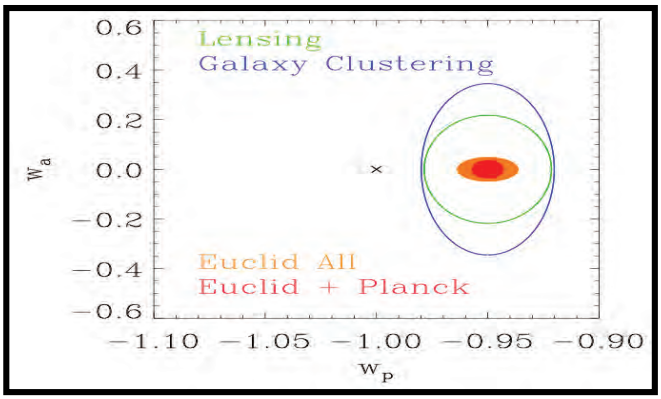

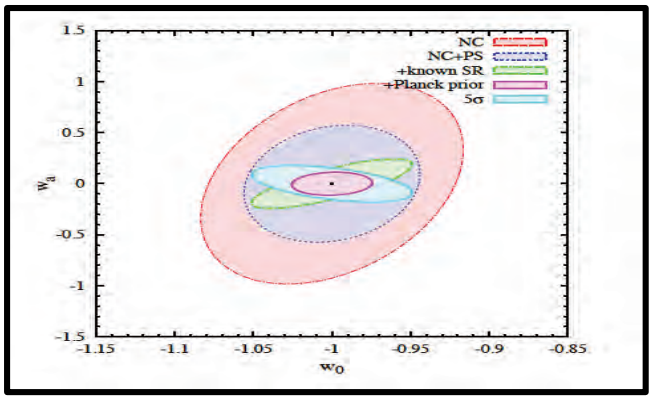

The properties of dark energy relevant for cosmology can be parameterized by the equation of state factor "w", which is the ratio of pressure to density of the dark energy fluid. A cosmological constant would correspond to a constant w=-1. It is common to parameterize this evolution with the value of w today (w_0) and at early times (w_0+w_a). The quality of the experiment to constrain dark energy can hence be estimated by the errors in the w_0-w_a plane (left). We show forecasts for Euclid WL only (green), Euclid BAO only (blue), all the Euclid probes (orange) and all Euclid with Planck CMB constraints (red). An additional test for cosmological models can be performed with the redshift and spatial distribution of galaxy clusters from Euclid. On the right we show how this probe performs. The different colors indicate different information and different assumptions about the relation of the cluster mass to the observable. MPE together with its partners at the University Observatory (USM) is prominently represented in Euclid at the various levels, Ralf Bender is member of the Euclid Board, Jochen Weller is co-lead of the clusters of galaxies science working group, Frank Grupp is the chief optical architect for the mission and responsible for the optical design of NISP, several more MPE/USM scientists are represented in the various science working groups. Moreover, MPE is hosting the German Science Data Center, lead by Max Fabricius, and provides the optics including mounts for the NISP instrument.

References:

• "Euclid Definition Study Report", R. Laureijs et al., ESA/SRE(2011)12, arXiv:1110.3193
• "Constraints from the Euclid Galaxy Cluster Survey", B. Sartoris et al., arXiv: 1505.02165

J. Weller, R. Bender, M. Fabricius, A. Galametz, F. Grupp, B. Hoyle, F. Raison, R. Saglia, A. Sanchez, S. Seitz

EUCLID near infrared optical system

Understanding the nature of dark matter and dark energy are the key science goals of the *ESA Cosmic Vision Program* mission EUCLID. In collaboration with industrial partners the MPE is developing optics, opto-mechanics and alignment procedures for the near infrared optical assembly NI-OA.

A 12kg heavy and ≈ 170mm aperture 4 lens system has been designed and is currently being implemented for the Euclid 1.2m space telescope mission. With its close to diffraction limit performance requirement the system puts extreme demands on manu-facturing and post launch and cooldown alignment of the optics.
These largest ever flown lenses, in combination with the stringent requirements in both manufacturing and assembling require the development of new and unique techniques. Computer generated holograms have been proven to be a great tool for both lens manufacturing and optical system alignment.

Basic parameters and specification:
Field of view: ≈ 0.5 sq.deg
Spectral bands: Y, J, H + 2 spectro. bands
Spectral resolution: R ≈ 500
Photometric limiting magnitude: 24.5 mag

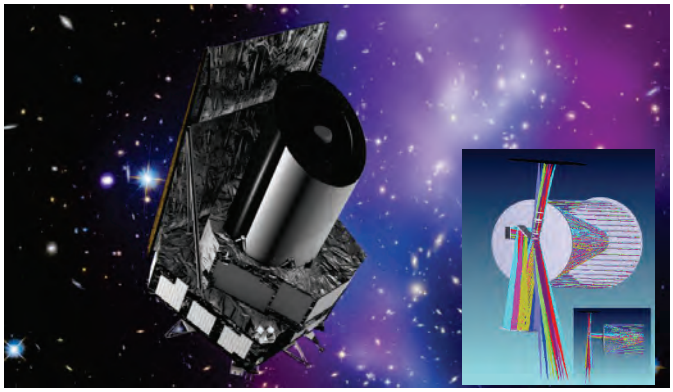

An artist's view on the Euclid spacecraft in the outer Lagrange point L2. **Lower left:** Euclid optical design. The MPE contributes the near infrared optics design and opto-mechanical implementation.

The mechanical design of NI-OA was driven by the interplay of optical performance and launch load survival on the one hand, and unit weight on the other. To achieve this balance most modern techniques of dynamic material growth (like bones in the body) have been applied.

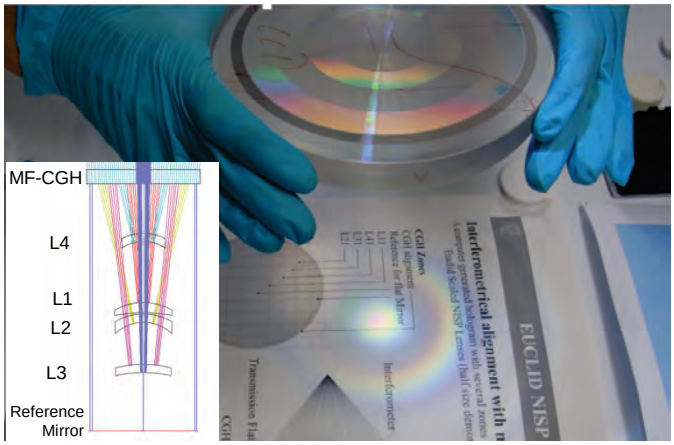

A computer generated hologram CGH with 6 annular zones. Four of them producing spots of different focal length, each of them fitting in auto-collimation to one of the 4 lenses of NI-OA. This allows lens centration with one micron sensitivity.

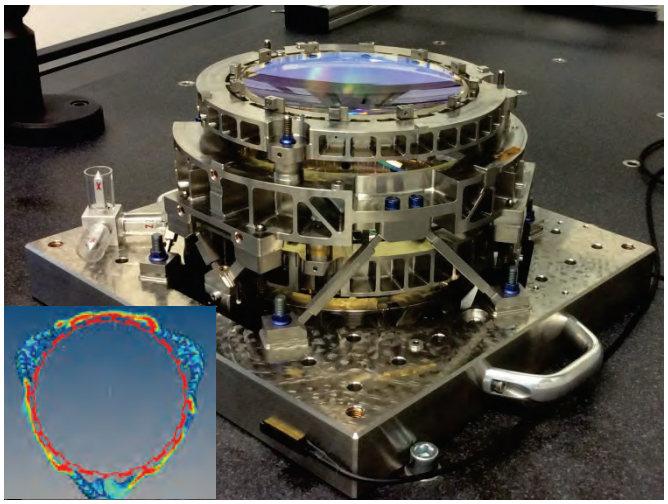

NI-OA as a real scale model on the coordinate measuring machine. **Lower right:** A visualization of the applied dynamic material growth model.

References:

•Laureijs, R.; Amiaux, J.; Arduini, S. and 216 co authors, 2011, Euclid definition study report, ESA
•Grupp, F.; Prieto, E.; Spano, P.; et.al., 2011, SPIE, 8146, 283
•Grupp. F.; Prieto, E.; Geis, N.; et.al.,2014, SPIE, 9143, 2

F. Grupp, R. Bender, A. Bode, C. Bodendorf, N. Geis, R. Katterloher, J. Snigula, C. Wimmer, D. Penka, O. Goldenbogen, I. Hartung

Recipes for *Euclid* Template-fitting Algorithm

The *Euclid* mission will characterize the nature of dark energy through cosmological probes such as weak lensing that require accurate photometric redshift estimates. The use of photometric redshifts is crucial in light of the number of sources observed simultaneously in wide-field surveys and the lack of complete spectroscopic coverage. Although the success of surveys such as *Euclid* rely on the accurate knowledge of source position, current photometric redshift codes do no reach the required precision for cosmological studies. One technique commonly used to estimate photometric redshifts is `template-fitting', which relies on modeling the observed multi-wavelength photometry with templates. A new template-fitting code is currently implemented for the *Euclid* mission. We are exploring new avenues of investigation in order to reach *Euclid* requirements on photometric redshift accuracy.

The Euclid Template-fitting algorithm

The method consists in building a library of SED templates to be compared to the observed photometry in order to derive a source redshift and physical parameters. A new template-fitting algorithm is being implemented within the *Euclid* Ground Segment pipeline. It is also a stand-alone code (Phosphoros) to be released for a broader use to the astronomical community by mid-2016.

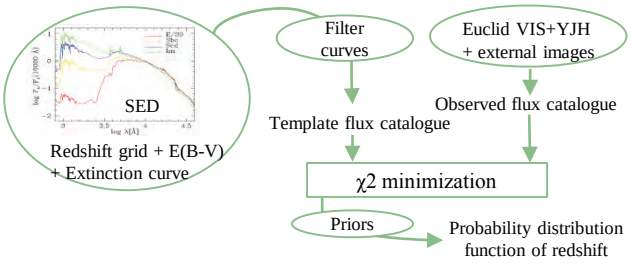

New recipes for template-fitting methods

We are exploring new recipes to improve current photometric redshift techniques: new prescriptions of the galactic and intergalactic medium absorption, the addition of nebular emission to the models and use of (luminosity) priors.

Galactic extinction: The interstellar medium of our galaxy is composed of dust which contaminates the flux of extragalactic sources. The flux is an integral over a filter of the source SED, the line-of-sight reddening E(B-V) and the extinction curve of the MW k_λ. In a wide-band filter, the galactic extinction thus depends on the SED. This dependence is usually neglected since the source type is not known *a-priori*; the de-reddening is usually adopted as E(B-V) × k_p (k_p the value of the MW curve at the filter pivot).

There exists a linear relation between the dust column density D and reddening p×D. Studies have tried to derive p from the color excesses of sources with known SED. They however adopt prescriptions of the MW curve calibrated with stars and neglect the band-pass corrections required to consider the SED dependence. We estimate that these corrections bias the measure of p and thus of the reddening by up to 10% (see Figure 1). The non-consideration of these effects causes large errors on galactic extinction estimates, up to 0.1 mag in u- and g-band for line-of-sight reddening of mild E(B-V) = 0.1, which can produce dramatic errors on photometric redshift estimates (see Fig. 2). Within Phosphoros, the galactic extinction recipe is implemented at the template library level to take these band-pass corrections into account.

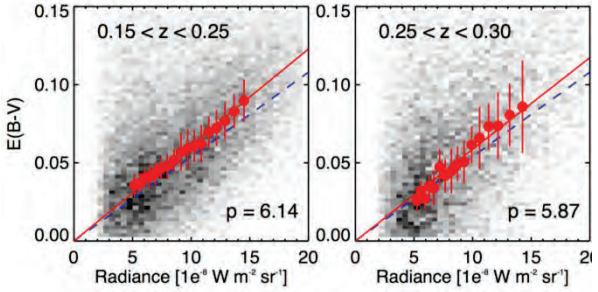

Fig. 1: Galactic reddening of a sample of SDSS passive galaxies versus radiance along their line-of-sight (Planck). The linear rescaling factor p was derived from sources in different redshift bins, and thus different mean SED. We note that p depends on the type of sources used for the calibration. (Galametz et al. in prep.) p derived by Planck from a sample of SDSS quasars is shown in blue.

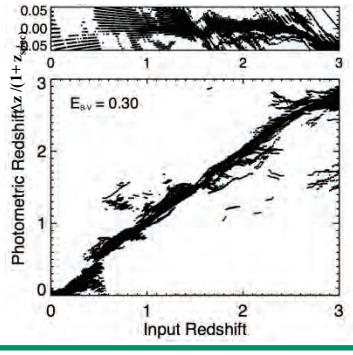

*Fig. 2: Discrepancies between the input redshift of a grid of models to which we apply a galactic reddening along the-line-of-sight of E(B-V)=0.3 and the output photometric redshifts from Phosphoros derived after correcting the fluxes by the classically adopted constant galactic extinction correction E(B-V) * k_{pivot}.*

A. Galametz, R. Saglia, R. Bender, B. Hoyle, M. Rau, S. Seitz

The German Euclid Science Data Center

The **German Euclid Science Data Center (SDC-DE)** is one of nine data centers of the ESA's Euclid space mission. The main responsibility of the SDC-DE is the processing and storage of large **external data** sets such as the Dark Energy Survey (DES) and Kilo Degree Survey (KiDS) before they are **merged** with the **satellite data**. The computer hardware is set-up at the Rechenzentrum of the Max Planck Society in Garching (MPCDF). The SDC-DE collaborates mostly with the Euclid groups at the Ludwig Maximilians University in Munich (LMU), the Argelander Institute for Astronomy in Bonn (AIfA), the Max Planck Institute for Astronomy in Heidelberg (MPIA) and the Kapteyn Astronomical Institute in the Netherlands.

The **Euclid space mission** has passed successfully the Mission Preliminary Design Review (M-PDR) in October 2015. The satellite is expected to be launched in 2020. The main goal of the mission is to study the nature of dark energy and dark matter using several complementary cosmological probes. The Euclid satellite will be equipped with an optical imager (VIS) and a near infra-red imager (NIR) and spectrograph (NISP). During its six year mission, Euclid will collect 300 TByte of raw data that will be processed by the ESA Science Operations Center (SOC) and the nine national Science Data Centers (SDCs) of the Euclid Consortium. All results will be stored in a centrally organized Euclid Archive System (EAS).

External data will provide broad band photometry in optical bands and are really important for the success of the mission. Together with the Euclid NIR measurements they will allow to derive precise photometric redshifts of all galaxies in the Euclid sample. The KiDS processing pipeline has been recently fully integrated at SDC-DE and DES processing pipeline integration is underway in close collaboration with the Euclid team at the LMU.

As mentioned, an important task of the Euclid ground segment will consist in **merging the satellite data and the external data**. SDC-DE is involved in the implementation and the integration of this part of the processing (MER).

Thanks to its know-how, SDC-DE is also **contributing to the Euclid science ground segment** (SGS). For example, an infrastructure has been provided to monitor and control the status of the ground segment processing services.

SDC-DE is offering a leadership in the **organization of the software testing** and taking part in the testing itself. SDC-DE is also **training** the developers of the consortium to master the development environment.

Finally, the storage and processing of these large data sets requires huge investments in computer hardware. This hardware in return allows us to test and optimize our processing pipelines and to refine our data management strategies. SDC-DE cluster computing power is now reaching 816 cores. A new procurement phase is starting in order to renew the current cluster to be decommissioned in the next years.

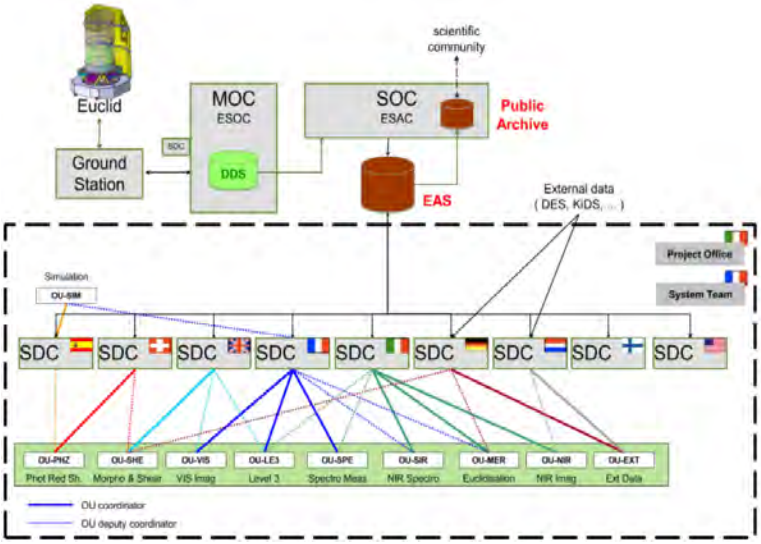

Fig. 1: Overview of the SGS and main components. *Courtesy Euclid Consortium/ESA/SGS Team.*

F. Raison, J. Koppenhoefer, A. Piemonte, M. Wetzstein, R. Bender, A. Bohnet, R. P. Saglia, J. Snigula

MICADO – Multi-AO Imaging Camera for Deep Observations

MICADO is one of the selected first light instruments for the European Extremely Large Telescope (E-ELT) ESO started to build on Cerro Armazones in Chile. Combined with the Adaptive Optics Module MAORY, MICADO will be able to deliver diffraction limited images in two different resolutions (1.5 and 4 mas/px). MICADO also provides a medium resolution spectrograph R~4000 (goal R~8000) covering a broad Wavelength range (J-K Band) and a high contrast imaging mode, used for the discovery and characterization of planets. The OPINAS/USM group is responsible for control electronics, control software and the design and implementation of a selection mechanism to switch between the different observing modes

The MICADO Instrument is located on one of the Nasmyth Platforms of the E-ELT. To guarantee maximum stability for astrometry, the instrument is mounted in a gravity invariant way beneath the Adaptive Optics Module MAORY. The OPINAS/USM group is responsible for the following tasks:

- Implement the selection mechanism (see Figure 3) which inserts different optical elements between the fixed collimator and camera optic.
- Control Electronics (see Figure 1)
- Control Software (see Figure 2)

The MPE infrared group will present a science report (R. Davies et al.), and a poster describing the optical design (M. Hartl et al.).

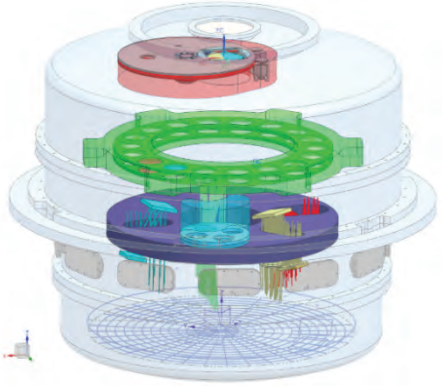

Figure 3 MICADO Cryostat and mechanisms: *Mechanisms inside the cryostat provide the elements needed for the different observing modes (Imaging, spectroscopy, coronagraphy). The OPINAS/USM group is responsible implementing the selection mechanism (purple) incl. the optics and mounts for the spectrometer (reflective echelle + cross disperser grism) and the 4mas imager (2x plane mirrors) mode.*

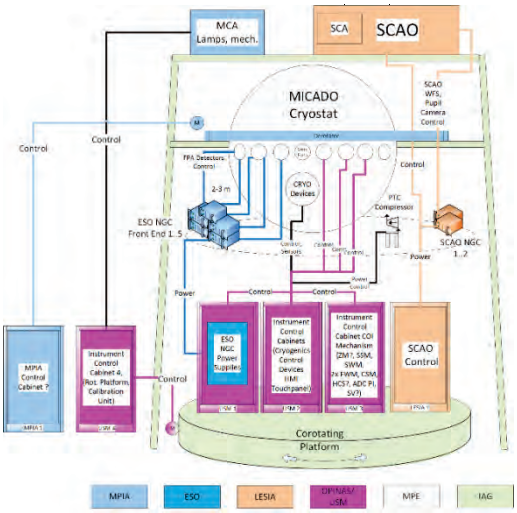

Figure 1: Current design of the MICADO control electronics. *Cabinets controlling elements attached to or inside the cryostat are mounted on a co-rotating platform underneath the instrument. All other non-rotating cabinets are located on the Nasmyth platform*

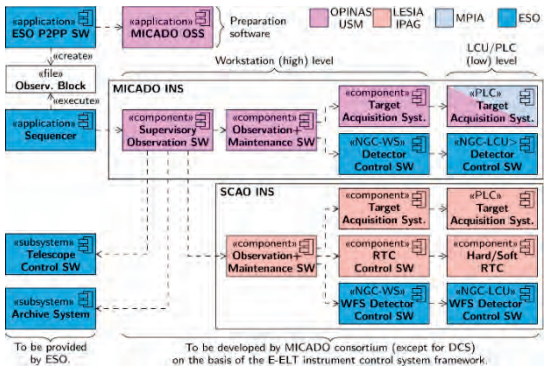

Figure 2: Overview of the MICADO control software architecture. *The software is divided in three blocks. The OPINAS/USM group is responsible for all high/low level software to control the MICADO instrument (mechanisms, housekeeping, cryogenic control, etc). The software package also includes a preparation tool for observation planning (guide star selection, dither patterns etc.).*

References:

- MPE infared group Poster Hartl, M. et al.
- MPE infrared group science report Davies, R. et al.
- Davies, R. et al.: MICADO: the E-ELT adaptive optics imaging camera; 2010, SPIE 7735, 2A

F. Lang-Bardl, R. Bender, M. Haeuser, H.-J. Hess, U. Hopp, H. Kravcar, A. Monna, J. Richter, J. Schlichter, J. Thomas, M. Wegner

3KK- The Fraunhofer telescope 3-channel imager

The 3 channel imager was built in collaboration with the University Observatory Munich, the Institute for Astronomy in Hawaii and the Excellence Cluster Universe for the new 2m Fraunhofer telescope on Mt. Wendelstein in the Bavarian Alps. It is optimized for fast multi-wavelength follow-up of targets of opportunity (e.g. Gamma-Ray-bursts, SNe) or efficient photometric redshift determination of galaxy clusters identified in optical (PanSTARRS), SZ (Planck) or X-ray (eROSITA) surveys. The 3KK was installed at the Fraunhofer telescope at the end of 2015 and is the second instrument available to gather scientific data.

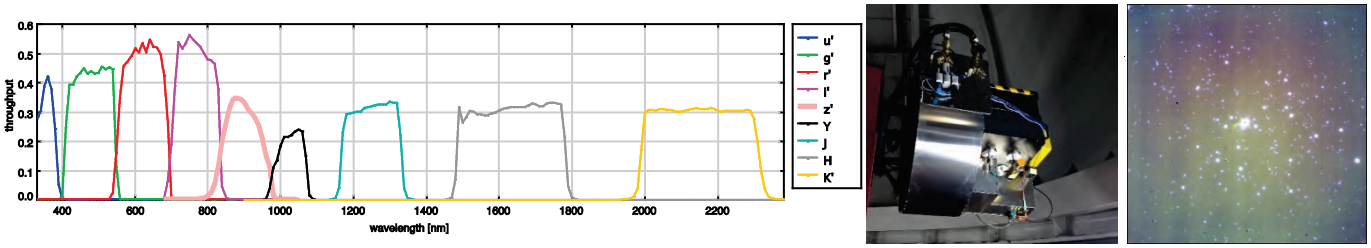

Figure 1: [left] *Efficiency of the 3KK based on lab measurements in the different broadband filter passbands. Some narrow band filters are also available* ***[middle]*** *3KK mounted on the telescope* ***[right]*** *1st light image stack WNIR (J,H,Ks) of M37*

The 3KK mounting structure is divided into the following three sections (see figure 2):

- **First Ring section:** A preliminary 1st ring is now employed which will host the fiber pick-off optics for the FOCES spectrograph, that is located in the basement of the observatory. The final 1st ring will also provide calibration sources, a wave front sensor and a guide camera module.
- **Optical channels section:** Contains the beam splitter system and the two optical channels, each built from customized Apogee ALTA F3041 cameras, equipped with 60 mm Bonn Shutters and a 7-position filter wheel. Both channels are mounted on linear stages for differential Focusing with respect to the fixed WNIR camera.
- **WNIR and auxiliaries section:** Contains the WNIR camera cryostat and the cooled electronics cabinet, that provides all necessary power supplies, control electronics and interfaces to the observatory network. Because of the nearby BR broadcasting station all electronics have to be EMV shielded to get stable operating conditions. The power line entering the cabinet is filtered. Fiber links are used to connect to the Jade2 Card and the observatory network.

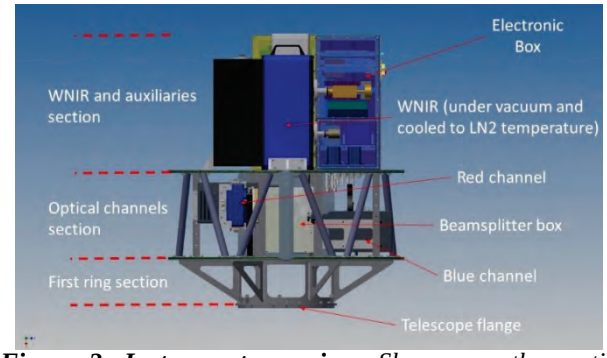

Figure 2: Instrument overview: *Shown are the sections with the different elements.*

	Blue Channel	Red Channel	NIR Channel
Filter	u', g', r', [OI], Hα, [SII]	i', z'	Y, J, H, Ks, H_2, Br_γ
Pixel scale	0.2 ˝/px	0.2 ˝/px	0.24 ˝/px
WL [nm]	340 – 695	695 – 970	970 – 2310
FoV	6.8 ‘	6.8 ‘	8.2 ‘

Status: 3KK entered the commissioning phase at the beginning of this year. We are now in the process of analyzing the image quality of the system on sky and determining the zero points for the used filter passbands.

References: Lang-Bardl, F. et al:, 2010, SPIE 7735-133

Acknowledgement: Financial support by Excellence Cluster Universe
and MPE

F. Lang-Bardl, R. Bender, C. Goessl, F. Grupp, H.-J. Hess, U. Hopp, H. Kravcar, A. Monna, W. Mitsch, J. Schlichter, M. Wegner, et al.

FOCES: a planet hunter for Wendelstein

The FOCES échelle spectrograph is intended to be operated at the 2.0m Fraunhofer Telescope at the Wendelstein Observatory. Primary science case of this instrument is the detection and the characterization of extra-solar planetary systems. We aim to obtain a regime of <1m/s in radial velocity (RV) accuracy by means of intense environment stabilization, a re-newed high level fiber link between the spectrograph and the telescope and by using an astro-frequency comb as new revolutionary calibration source.

Radial Velocity surveys for exoplanets require high-precision spectrograph and long term stability to detect tiny RV variations in the m/s domain, corresponding to super-earth planet signals around a solar type star. This signal is equivalent to a physical shift of 1/3000 pixel on a typical high resolution échelle spectrograph. Crucial points to achieve such high RV accuracy are:

- Coupling stability (Fig.1)
- Pressure and temperature stability (Fig. 2)
- Calibration stability (Fig. 3)

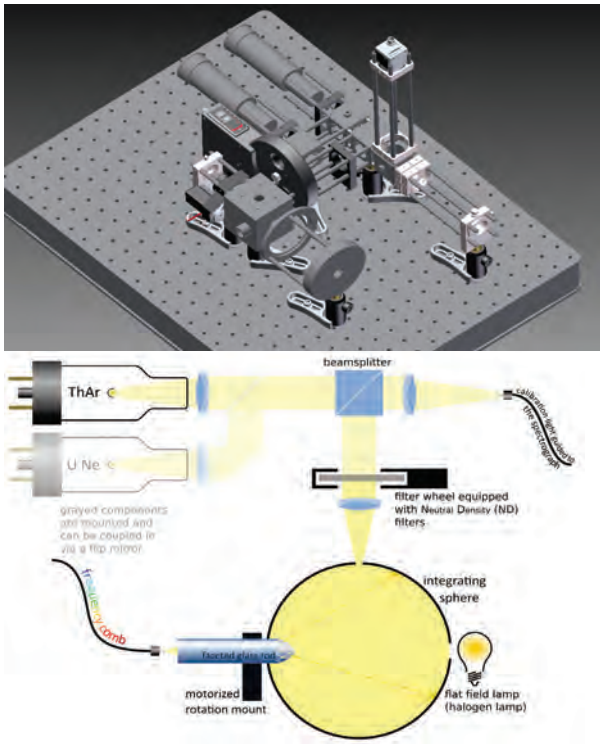

Fig.1: Assembly *design and model view of the new calibration unit.* *A versatile and compact solution allows a multi-selection of different calibration sources: ThAr lamp, UNe lamp, flat-field, and astro-frequency comb light.*

Basic parameters and specification:
Resolution: R=λ/Δλ=70000
Spectrograph Stability: < 0.001px (averaged)
Temperature Stability: < 0.01 K
Pressure Stability: <0.01 hPa
Radial velocity accuracy: ≤ 1 m/s

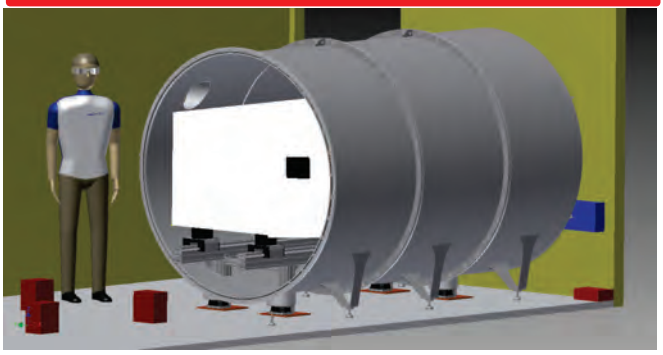

Fig.2: *Design for the FOCES environment stability.* *The temperature and pressure stabilization are obtained by a two-layer thermal solution (internal box and external tank) and one-layer pressure control (external tank).*

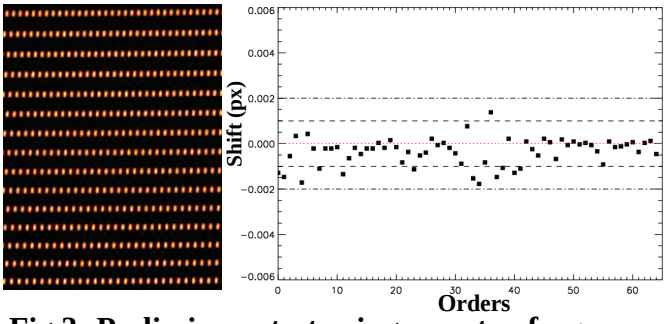

Fig.3: Preliminary test using an astro-frequency-comb as calibration source. *Left:Comb spectrum acquired with FOCES. Right: Movement of the échelle orders within 30 min period. Un-calibrated drift is already down 1/2000 px for many orders.*

References

Kellermann H., Grupp F. et al. , 2015, SPIE 9605
Brucalassi A., Feger T. et al., 2012, SPIE 8446,2
Grupp F., Udem T. et al., 2010, SPIE 7735, 232

F. Grupp, A. Brucalassi, H. Kellermann, L. Wang, F. Lang-Bardl, T. Pfleger, S. M. Hu, U. Hopp, R. Bender

MCP – The Master Control Program for the Wendelstein Observatory

The observatory on Mt. Wendelstein supports a multitude of different hardware. This includes the 2m telescope[1] with a wide field camera[2], a 3 channel optical/NIR camera[3] (3KK, see poster), two fibre coupled spectrographs[4,5], a 40cm telescope with instruments, the domes, and various environment sensors. We developed the "Master Control Program" (MCP) to provide a consistent interface to the different scientific instruments and related hardware. It is implemented as a multi-threaded Python daemon, for easy extensibility as hardware is replaced. The MCP has been built to enable complex automated observation schemes. It supplies meta data for scientific data containers (i.e. FITS keys) and can be used to trigger simple quicklook, calibration, or even full-fledged data reduction.

Observatory operations require the support of a variety of hardware, usually with different communication protocols. For the Wendelstein observatory we encapsulate every device with a program translating the device specific commands to a common human readable interface language.

- The MCP provides a consistent interface to the various hardware devices, unifying the different control interfaces, a middle layer for complex operations involving several devices, e.g. dithered observations with guiding.
- It is implemented in Python for quick development and easy debugging. The individual device modules can be configured, started and stopped through the user interface for easy reconfiguration and adding/removal of different device modules.
- The device structure is hierarchical. A scientific instrument can be a top-level device (e.g. `wwfi`), its individual elements are then sub-devices (e.g. `wwfi.guider.camred`). Empty devices can be added to reflect the logical structure of the parts of an instrument.
- The configuration is stored in a simple file based database. During start-up the MCP loads the individual device modules, loads the configuration and starts the device, and then recursively all configured sub-devices.
- The Python implementation of MCP allows us to automatically alter the device classes during setup, and add functionality (e.g. external commands to get/set parameters), making it easy to expand the MCP quickly and add new device modules.
- The system is multithreaded, so all device modules can run in parallel.
- An extensive logging system helps debugging possible errors.
- All the connections, external ones to the users, and internal ones to the device programs are managed in a separate thread by the central ConnectionManager.

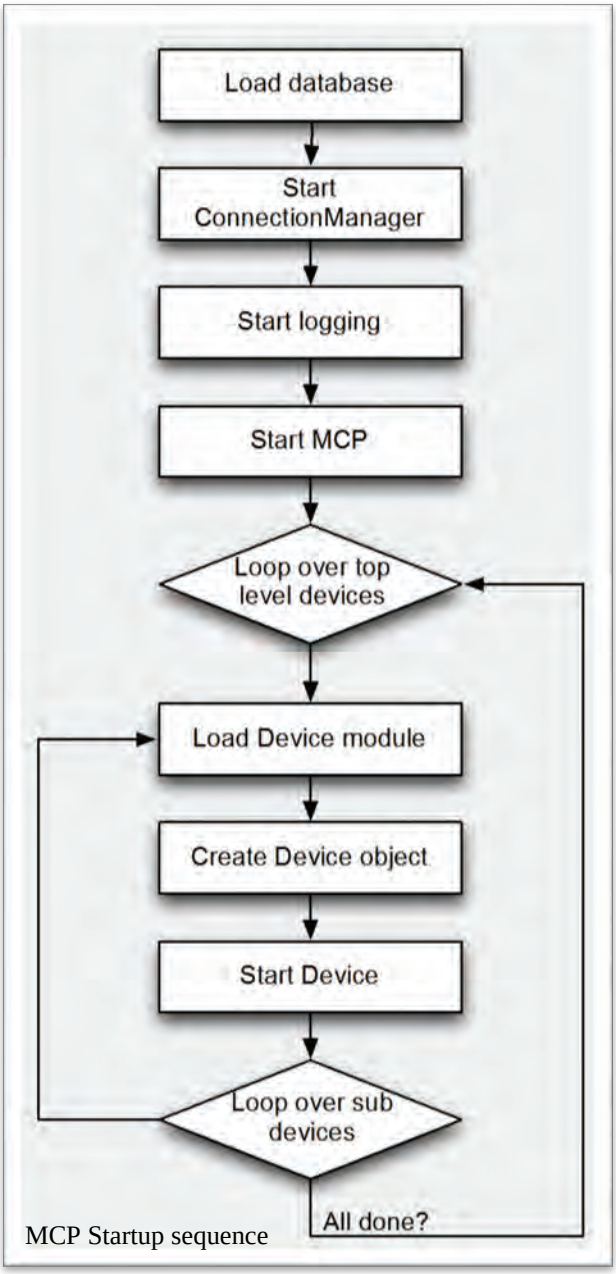

MCP Startup sequence

References:
1. Proc. SPIE 7733, 8444, 9145
2. Proc. SPIE 7735, 8446
3. Proc. SPIE 7735
4. Proc SPIE 7735, 8446
5. Proc. SPIE 7014, 8446

J. Snigula, C. Gössl, J. Schlichter, M. Wegner

II.1) Group: Prof. Ortwin Gerhard

The structure of the central Milky Way

Using Red Clump Giant stars (RCGs) as standard candles we have reconstructed the shape and structure of the central 5kpc of the Milky Way. We find the bar has half length 5.0±0.2kpc and lies between (28–33)° to our line of sight, aligned to the barred bulge. The thinner bar outside the bulge appears naturally connected to the barred bulge in a similar way to external galaxies and N-body simulations where the central region of bars buckles to form a box/peanut bulge.

RCGs are core Helium burning stars which are a standard candle with $\sigma(M_K) \approx 0.18$ and therefore from their distribution we can infer the shape of the Galaxy. On the right we show RCG identification and slices of their distribution in the inner Galaxy. We combine the VVV, UKIDSS, 2MASS and GLIMPSE surveys to gain the most robust and wide view of the central Milky Way.

Unlike some earlier works we find that the bar outside the bulge is closely aligned with the 3D barred bulge, and the scale height smoothly transitions between the two. This suggests that the Galactic Bulge/Bar are one connected structure.

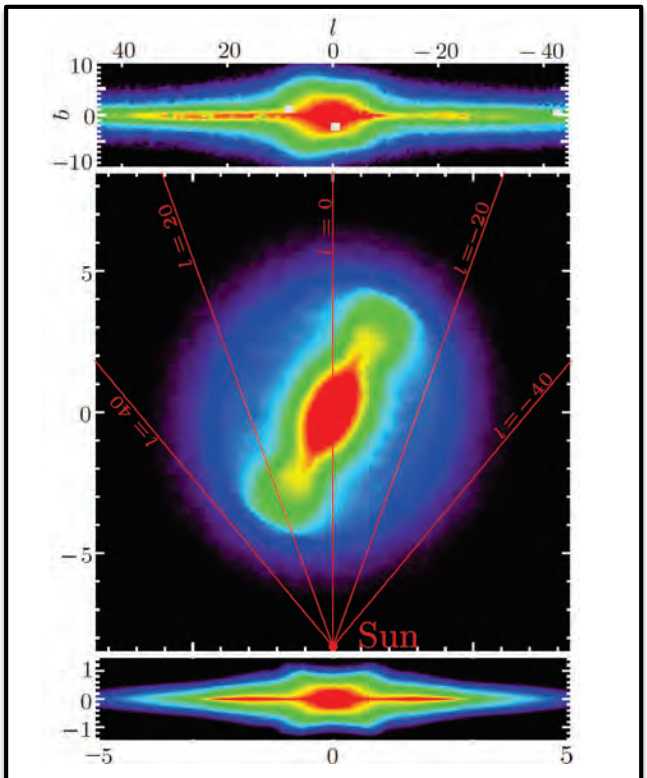

Top panel:The extinction corrected number of bright giants as seen from the Sun. Outside the bulge the bar is thinner ending near $l \approx 30°$

Lower panels: Top view and side view of best fitting model density.

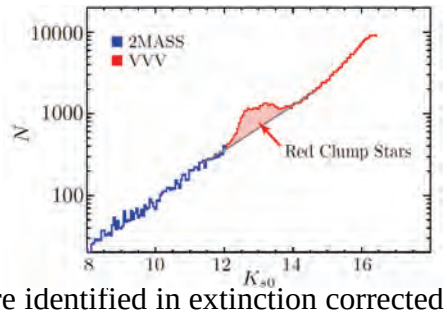

RCGs are identified in extinction corrected NIR magnitude distributions

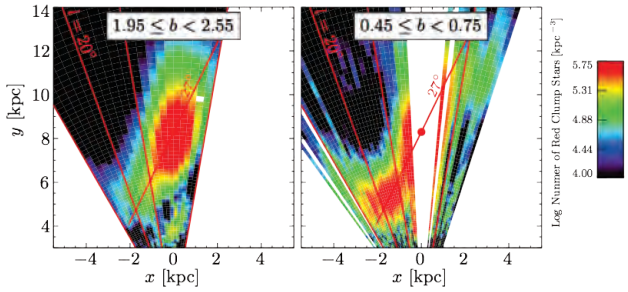

Latitude slices though the identified RCGs. That the bar is aligned with the bulge is evident and is confirmed by simulated data and detailed modelling.

We have convolved model densities with a luminosity function and adjusted them to fit the RCG magnitude distributions. On the left we show a view from above and the side of one of our best fitting densities. The fitted bar is aligned with the barred bulge within 2° and has a length (5.0±0.2) kpc.

Two components are seen in the vertical profile of the bar outside the bulge: a 180pc thin bar reminiscent of the old thin disk, and a 45pc 'super-thin bar' which is dominant towards the bar end and is probably related to more recent star formation.

Because only stellar matter microlenses, the stellar to dark matter degeneracy can be broken in a way unique to the Milky Way. We have constrained our models using MOA-II survey data and find a low dark matter fraction and a maximal disk is required [submitted to MNRAS].

References:

• Wegg, Gerhard & Portail, MNRAS, 450, 4050 (2015)

C. Wegg, O. Gerhard, M. Portail

Dynamical modelling of the Galactic bulge

We construct a set of dynamical models of the Galactic bulge in different dark matter halos using the Made-to-Measure method. We constrain the models to match the Box/Peanut (B/P) bulge density measured from Red Clump Giants (RCGs), together with the stellar kinematics from the BRAVA survey. This requires that the total mass (stellar + dark matter) of the Galactic bulge is 1.84 x 10^{10} $M_{\odot}$ with <5% uncertainty. Using the bulge IMF, this implies that the bulge stellar mass is between 1.4 and 1.7 x 10^{10} $M_{\odot}$ and the dark matter fraction between 10 and 25%. By studying the orbital structure of our models we find that their B/P shape is supported by a new "brezel" orbital family, different from the traditionally assumed banana orbits.

The Galactic bulge as traced by RCGs shows a very prominent B/P shape, similar to bulges formed in N-body models by the buckling of an unstable stellar bar. Starting from an initial N-body model of an evolved barred stellar disk we slowly adapt the weights of the N-body particles to reproduce the observed 3D density and kinematics of the Galactic bulge.
We fit the data to five N-body models that differ in their dark matter fraction in the bulge. For each model we can recover from the modelling the bulge stellar mass required to match the data, in a given dark matter halo. Fig. 1 show that the total mass of the bulge is in all cases within 5% of 1.84 x 10^{10} $M_{\odot}$.

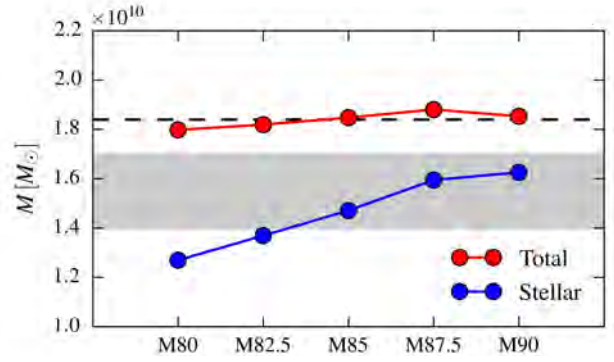

Fig 1. Stellar and total mass of the bulge models with different dark matter fraction. Grey area shows consistency with the bulge IMF measured by Calamida et al. (2015, ApJ, 810, 8)

We classify the N-body orbits of our bulge models by frequency analysis. We find that B/P shaped bulges can be seen as the superposition of several B/P shapes embedded one into another. Most of the mass is on orbits of classes B and C related to what we call "brezel orbits". B/P shaped bulges are therefore not necessarily supported by banana orbits (class F) as commonly assumed.

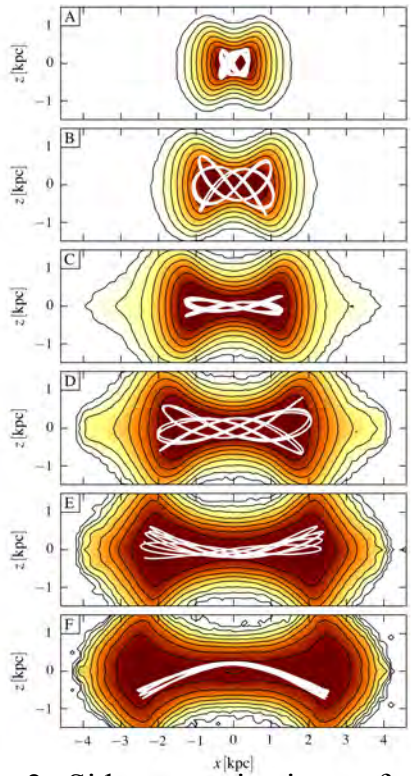

Fig 2. Side-on projections of the different orbital classes.

References:

- Wegg C., Gerhard O., 2013, MNRAS, 435, 1874
- Portail M., Wegg C., Gerhard O., Martinez-Valpuesta I., 2015, MNRAS, 448, 713
- Portail M., Wegg C., Gerhard O., 2015, MNRAS, 450, L66

M. Portail, C. Wegg, O. Gerhard, I. Martinez-Valpuesta

Inner Stellar Halo in the Milky Way: Predicted Shape and Kinematics

The metal-poor stellar halo is the oldest component of the Milky Way made. In its innermost region, it overlaps with the Galactic box/peanut bulge. Here we use N-body simulations to investigate how its shape and kinematics evolve during the formation and evolution of the Galactic bar and B/P bulge.

We model the metal-poor stellar halo as an oblate component with axial ratio c/a=0.6 and a single power-law density profile, $\rho \sim r^{\alpha}$. Observations of RR Lyrae stars both near the Sun (Sesar et al. 2013) and in the inner region of the Galaxy (Pietrukowicz et al. 2015) indicate $\alpha \approx -3$, and with this α the density normalisations approximately match. We use model M85 from Portail et al. (2015) to follow the halo evolution. At t=0 we use the dark matter halo particles from the model to determine weights such that they represent our stellar halo model. After the model has evolved through bar formation (t=1.6 Gyr) and bar buckling (t=2.9 Gyr) to its final time (t=5.2 Gyr), we take these particle weights to reconstruct the stellar halo at the final time.

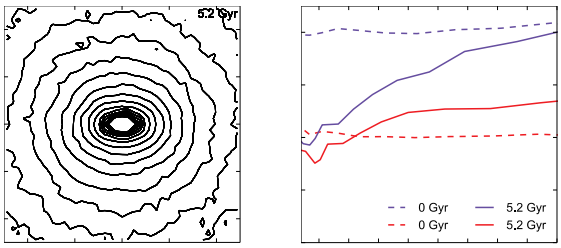

Fig 1. Left: face-on projection of the stellar halo density at the final time. Right: Axes ratio (b/a and c/a) of the stellar halo before bar formation (dashed lines) and at 5.2 Gyr (solid lines).

Figure 1 shows the face-on projection of the density contours at the final stage and how the shape of the stellar halo evolves from an oblate to a triaxial component. This evolution in the shape of the stellar halo is related to the gravitational influence of the Galactic bar and B/P bulge.

Figure 2 shows predicted kinematic maps for the same two snapshots presented in Figure 1: t=0 (top panels), and t=5.2 Gyr (bottom panels). Before the bar formation, the mean radial velocity is zero, the dispersion is between 70 to 130 km/s depending on galactic longitude and latitude, (l,b). After the bar and B/P bulge formation, the maximum radial velocity is ~|25| km/s and the dispersion is ~120 km/s in $|l|=30^{o}$ and $|b|=15^{o}$. This rotation measured in the later stages of the N-body simulation is due to the angular momentum transfer during the bar formation (Saha et al. 2012).

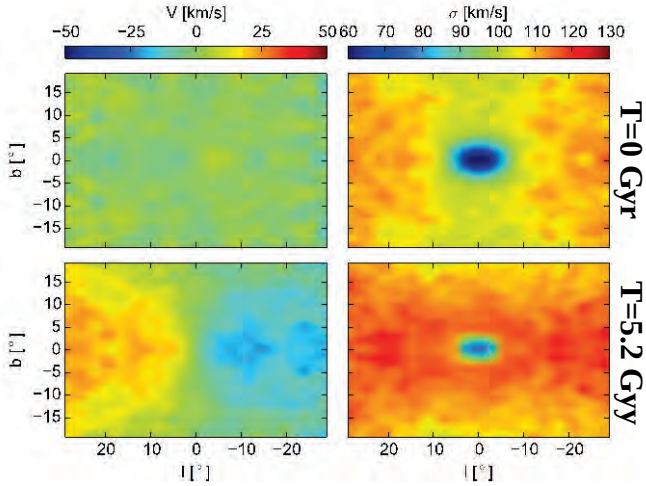

Fig 2. Kinematic predictions of the stellar halo at the initial final time of the simulation. Left panels show the mean radial velocity and right panels show velocity dispersion.

References:
• Pietrukowicz, P., Kozlowski, S., Skowron, J., et al. 2015, ApJ, 811,113
• Portail, M., Wegg, C., Gerhard, O. & Martinez-Valpuesta, I., 2015, MNRAS, 448, 713
• Saha, K., Martinez-Valpuesta, I., & Gerhard, O. 2012, MNRAS, 421, 333
• Sesar, B., Ivezić, Ž., Stuart, J. S., et al. 2013, AJ, 146, 21

A. Pérez-Villegas, M. Portail, O. Gerhard

Dynamical Models for M31 Bulge & Bar

We analyze the nature of M31's triaxial bulge with an extensive set of N-body bulge models, which include Box/Peanut (B/P) bulges as well as initial classical bulges (ICBs). Comparing with the IRAC 3.6μm data, only one model finally matches simultaneously all the properties of M31's bulge, and requires a B/P bulge with ~2/3 the total mass of the bulge.

Motivation: Due to its proximity M31 is one of the best cases to study in great detail the properties of bulges in spiral galaxies. Bulges are present in most spirals and are classified in two major groups, classical bulges and pseudo-bulges among which we can find B/P bulges.

Simulations: we explore the parameter space with models that are built with a dark matter halo and a disk that secularly evolves to form a bar and a B/P bulge. 72 of these models include an ICB component, each with a different initial mass and scale length. We then measure photometric properties with ELLIPSE in all models and compare them with M31 converging to one best model (Fig. 1 to 3).

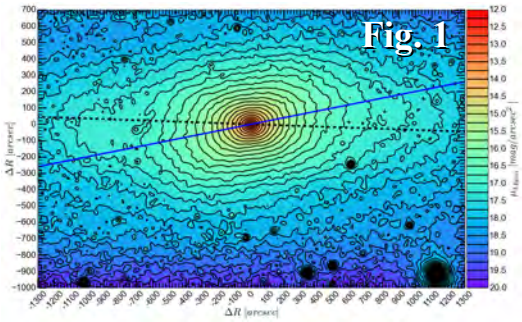

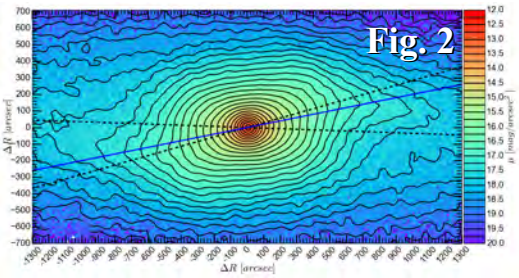

Surface-brightness images with isophotes for M31(Fig.1 IRAC3.6μm [1]) and for the best model (Fig.2). Lines trace the major axis of the B/P bulge (dashed) and the disk (solid).

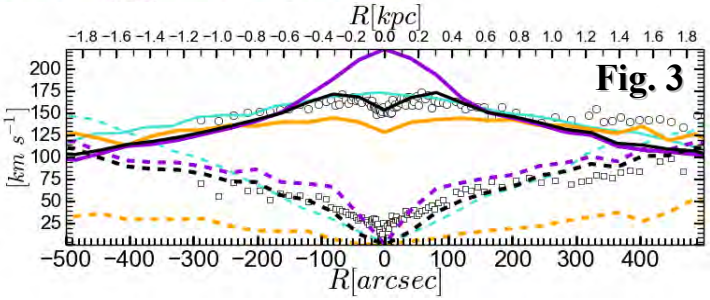

Fig.3: Major axis profiles of velocity (dashed lines) and dispersion (solid lines) of the best model compared to M31 velocity (squares) and dispersion (circles) [2]. The colors identify the ICB(orange), the B/P bulge (purple) and the combined structure (black). Cyan lines correspond to a pure B/P bulge model.

CONCLUSIONS: we find that M31's bulge consists of a massive Box/Peanut structure dominating in the outer bulge and a classical component dominating in the central region, with the properties:

- The mass of M31's classical bulge is ~1/3 of the total mass of the bulge, while the B/P bulge has ~2/3 of the total.
- The B/P bulge dominates the dynamics within 3.0-0.3 kpc, while the ICB dominates within 300 pc.
- The B/P bulge and bar angle is θ_{bar}=55° (if θ_{bar}=0° the bar would be align with the disk's major axis).

On-going work: improve the best model using a Made-to-Measure method implemented in NMAGIC, using the IRAC 3.6μm image as a fitting target.

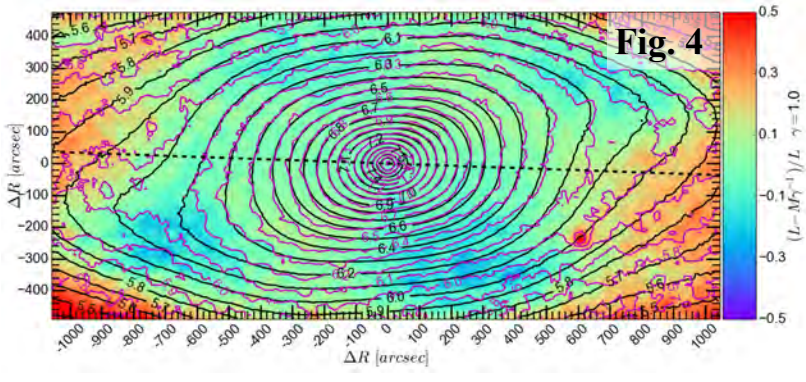

Fig.4: Luminosity contours in log units for M31 (magenta) compared to the improved best model (black). The difference is quantified by the colored map in linear units.

Future work: include kinematics of M31 from VIRUS-W observations [3] to better constrain the masses of each component

References: [1] Barmby et al. 2006, ApJ 655, L61; [2] Saglia et al 2010 A&A, 509, A61; [3] Opitsch et al, in prep.

M. Blana, C. Wegg, O. Gerhard, P. Erwin, M. Portail, M. Opitsch, R. Saglia, R. Bender

Dynamical Modelling of NGC 4278

NGC 4278, a low luminosity elliptical galaxy in the Coma I group, has an uncharacteristic flat Vrms profile, more typical of high mass ellipticals. Investigating this, we have modelled the potential and anisotropy of NGC 4278 using Jeans equations. We use kinematics data from SAURON for the inner region (<0.5 Re) and planetary nebulae (PNe) data for the outer region of the galaxy up to 6 Re. Our models show that NGC 4278 has a M/L higher than predicted for a Salpeter IMF. This together with the nearly flat circular velocity curve suggested by the models is again uncharacteristic of a low-luminosity elliptical galaxy.

We computed several illustrative, mostly isotropic, models, whose Vrms is shown in Figure 1 and circular velocity in Figure 2 together with the measured data. The circular velocity, and therefore potential, is partially constrained by the deprojected HI data from Morganti et al. (2006). The power-law model uses a potential with a density slope of 2.1. The constant models use a potential with constant circular velocity of 300 km/s. The stellar model uses the photometry with a Mass-to-Light Ratio (M/L) to calculate a potential. The Navarro-Frenk-White (1997) (NFW) and NFW + Constant Model use the stellar potential combined with analytic dark matter halos.

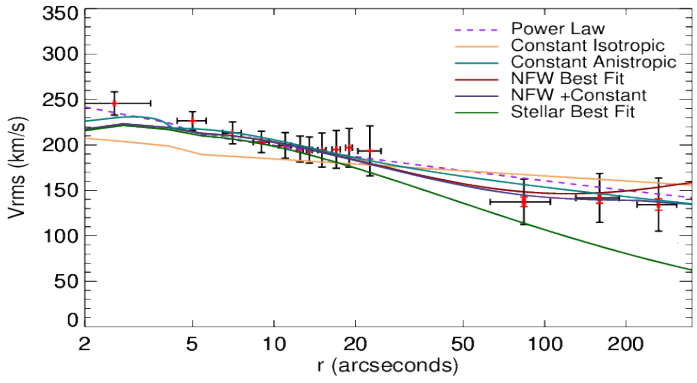

Figure 1. Vrms profiles from SAURON and PNe data. Coloured lines show various models and different potentials.

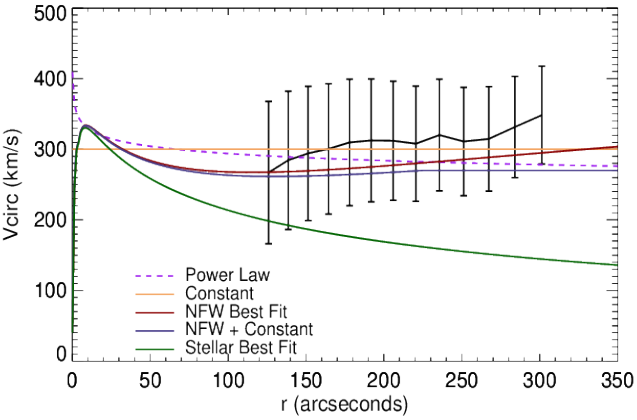

Figure 2. HI circular velocity data from Morganti (2006). Coloured lines show the same models as in Figure 1.

We found that invoking the stellar component only is not able to explain the high Vrms at the outer radii (r > 50”). Comparing the stellar model to the NFW and NFW + Constant models suggests that dark matter is needed at large radii to fit the Vrms and circular velocity data. The NFW + Constant, constant, and power law models all provide better fits to the SAURON and PNe data than the stellar and NFW models, and resemble the flat circular velocity curves suggested by the HI data.

Low-mass early-type galaxies usually have more slowly rising dark matter profiles, and falling velocity curves while massive ellipticals have more isothermal total mass profiles and flat circular velocity curves (Gerhard 2013, Wu et al. 2013). Intriguingly, the stellar, NFW, and NFW + Constant models of NGC 4278 all favour a M/L slightly higher than the M/L predicted with Salpeter IMF by Cappellari et al. (2006), which is unusual for a low-mass early-type galaxy. In addition, the flat circular velocity curve, as well as constant outer Vrms profile are also uncharacteristic for a low-luminosity elliptical such as NGC 4278.

References: Cappellari, M., et al. 2006, MNRAS, 366, 1126; Morganti, R., et al. 2006, MNRAS,371,157; Gerhard O. 2013 in IAU Symp. 295, Cambridge Univ. Press; Wu, X., et al. 2014, MNRAS,438, 2701; Navarro, J., Frenk, C., White, S., 1997, ApJ, 490, 907

I. Söldner-Rembold, O. Gerhard, M. Arnaboldi and PN.S Team

Halo kinematics unveiling the nature of early type galaxies

We have analyzed the velocity fields in the halos of 33 early-type galaxies (ETGs), reaching radii of up to ~8 Re with planetary nebulae (PNe) as tracers. The sample comprises 25 galaxies from the PN.S ETG survey and 8 further galaxies with extended PN velocity data from the literature [1]. The catalogues from these 33 ETGs provide astrometric positions and heliocentric line-of-sight velocities for a total of 8354 extragalactic Bona Fide planetary nebulae. All these catalogues are treated homogenously for the identification of kinematic outliers. We studied the rotation velocities, position angle twists, and triaxiality for these halo velocity fields, separating between slow rotators, fast rotators, and mergers. We found examples of both slow rotators and fast rotators with triaxial halo velocity fields, questioning the current picture of the fast rotators as disky galaxies [2].

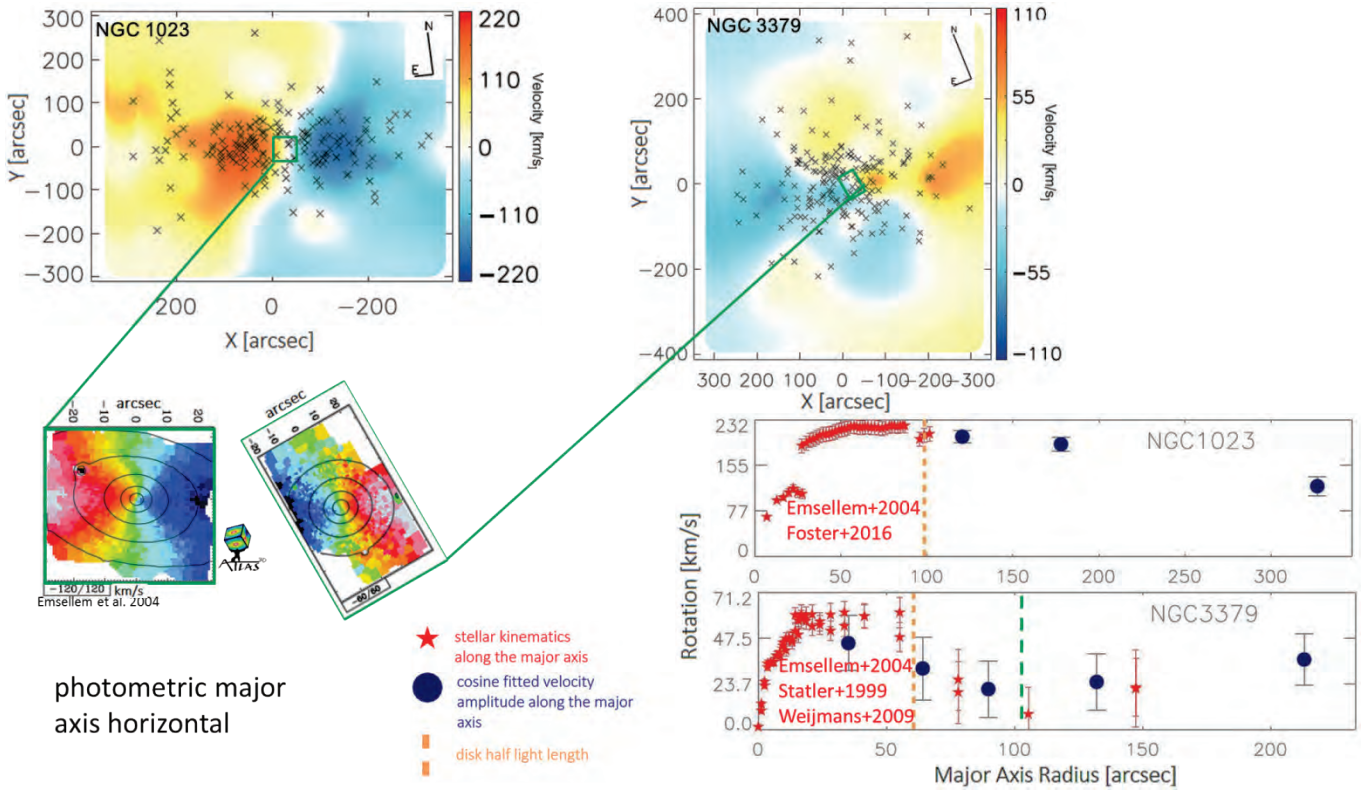

Figure 1. Kinematics of the fast rotators NGC 1023 and NGC 3379. Although the kinematics in the innermost regions appears to be similar, the halos unveil differences in the orbital distribution and in the shape of the gravitational potential. The disk structure (orange dashed line [3,4]) fades in the outer more dispersion dominated spheroidal component, as can be noticed in the drop of the rotation velocity profile. While the body of NGC 1023 still rotates fast also in the outskirts and does not show any twist in the kinematic position angle, NGC 3379 has weak or no rotation at ~100 arcsec. Beyond this "transition radius" (the green dashed line), the outermost regions appear to rotate both along the major axis and along the minor axis, revealing the intrinsic triaxial shape of the halo.

References:
[1] Arnaboldi et al. 2016, in preparation
[2] Emsellem et al. 2011, MNRAS, 414, 888
[3] Krajnovic et al 2013, MNRAS, 414, 2923
[4] Cortesi et al. 2013, MNRAS, 432, 1010

C. Pulsoni, O. Gerhard, M. Arnaboldi and the PNS team

II.2) Group: Prof. Hans Böhringer

Multi-scale cosmic matter distribution

We study the cosmic structure and its growth from sub-Mpc scales to the largest observable mass assemblies using our well-defined REFLEX sample. While substurctures in clusters visible through X-ray emitting intracluster medium provide insights into cluster formation, the concentration of clusters into superclusters outlines the largest cosmic stuctures and provides an outlook to the most massive objects to expect in the future.

The X-ray emitting intracluster medium traces cluster dynamical evolution. The merger history of RXCJ2359-6042 in Fig.1 can be unveiled by a study of the spectrally determined temperature and metallicity as well as the surface brightness distribution. A compact yet extended small galaxy group falls into a large gravitational potential well of the main system with a speed little more than Mach number of unity. The stripped cold gas of the small system, which survived the fall seen in the middle of the figure, is a peculiar feature. The location of the shock front induced by the merger is located on the left edge of the main cluster as expected. As interesting as they are, dynamically disturbed clusters make it more difficult to determine their total mass, consequently cluster scaling relations. They are currently the largest systematics for the determination of precise cosmological constraints with cluster number counts. Since we rely on simulations to calibrate mass, they must, in turn, correctly reproduce small scale gas physics in observations. One of the properties that we compared between observations and simulations is the degree of substructures, quantified by centre shifts and power ratios as shown in Fig 2. We see that clusters in hydro simulations with AGN feedback are much more substructured (larger values in both parameters) than in observations despite the fact that the same simulations reproduced the observed cluster scaling relation closely.

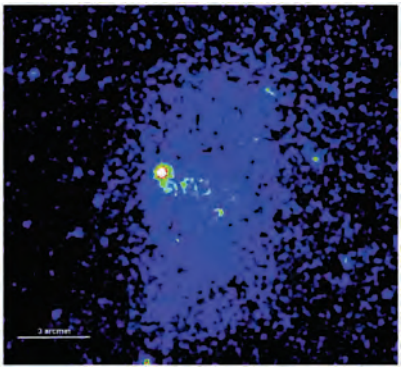

Fig.1 Surface brightness map of RXCJ2359-6042 from XMM-Newton observations.

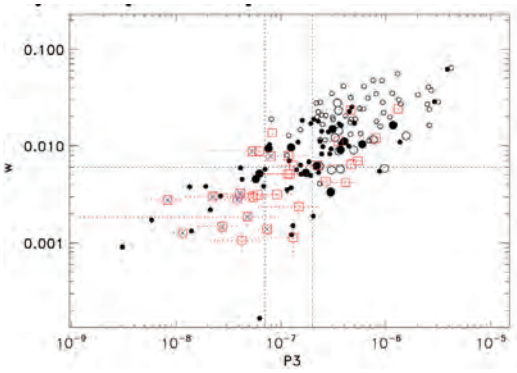

Fig.2 Comparison of substructures between X-ray observations (squares) and hydro simulations (circles).

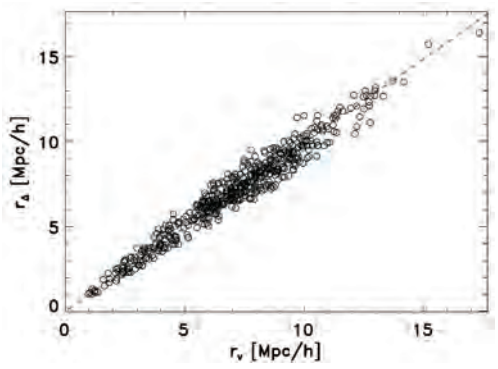

Fig.3 Comparison of the sizes of collapsing structures given by dynamical and overdensity criteria.

Completing the spectroscopic follow-up of our all-sky X-ray cluster survey with a well-understood selection function, we can address the large-scale distribution of matter in a quantitative way by, for example, constructing the first X-ray supercluster catalogue. Our approach is new as we consider only those structures that will survive the expansion of the Universe using a friends-of-friends algorithm. The linking length is constrained by the overdensity solutions to Friedmann equations for a spherical collapse model in a flat ΛCDM cosmology. With this physically motivated definition of large structures, coined as superstes-clusters, we study their properties with N-body simulations. Fig.3 show that the sizes of superstes-clusters built with an overdensity threshold matches well to the expected sizes from a dynamical infall criterion from the underlying dark matter field.

References:

• Chon, G., Böhringer, H., A&A 567, 144 (2014), A&A 575 L14 (2015)
• Chon, G., Böhringer, H., Zaroubi, S., A&A 574, 132 (2015), Chon, G., et al., submitted

G. Chon, H. Böhringer

Dynamical state of massive galaxy clusters

We use a sample of ten X-ray-selected massive galaxy clusters at redshifts z~0.21-0.45 to study the dynamics of the intra-cluster gas and of their galaxies. In addition we look for correlations of the cluster substructures with the large-scale cluster environment.

The sample of clusters was observed in X-ray with the XMM-Newton satellite. The X-ray luminous intra-cluster medium traces the gravitational potential of the cluster's mass distribution and the spectroscopic temperature distribution gives insight into the cluster's thermodynamic history. These results are compared to the dynamics of the galaxy population, which is inferred from spectroscopic data taken by the VIMOS instrument. An optical follow-up was also performed with the wide-field imager, WFI, allowing us to characterize the large-scale environment of the clusters. We outline here the methodology employed to assess the dynamical state of the clusters from the galaxy population.

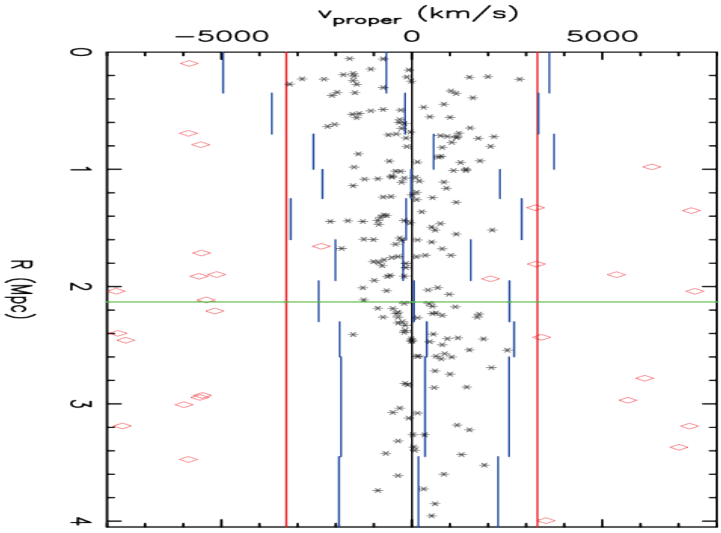

The reduction of the spectroscopic data and the redshifts estimation were done with the standard tools, VIPGI and EZ. With three VIMOS pointings extending in east/west direction, we obtained redshifts from the clusters' core to several Mpc, well beyond their virial radius. The selection of the cluster members was performed with a 3σ-clipping scheme in the projected phase space (PPS). An example is presented on the left, where black stars are confirmed cluster members, blue and red lines show the local and global $3\sigma_v$, and the green line traces the estimated virial radius.

With between 100-300 members per cluster, we are able to analyze their dynamical state with various tests. We look in redshift space for departures from gaussianity, e.g. skewness and kurtosis of the velocity distribution. In the PPS, we search for gradients in the velocity dispersion profile $\sigma_v(R)$, which could arise from the presence of substructures. The combination of the spatial and redshift distribution is used to highlight local departures from the global dynamics. On the right is an example of a velocity map, which reveals substructures, where the color code runs from positive (blue) to negative (yellow) velocities.

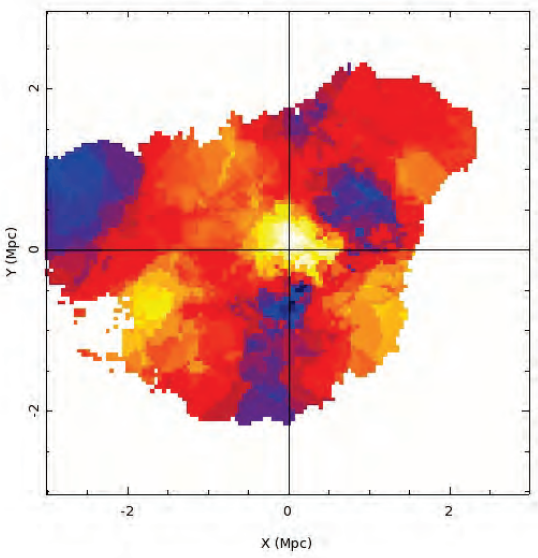

References:
- Foëx, G., Böhringer, H. & Chon, G., in preparation
- Scodeggio, M., Franzetti, P., Garilli, B., et al., 2005, PASP, 117, 1284

G. Foëx, H. Böhringer, G. Chon

Cosmological studies with galaxy clusters

We used our recently completed flux-limited redshift survey of X-ray luminous galaxy clusters to test cosmological models by means of the cluster X-ray luminosity function and to perform cosmographical studies with the spatial distribution of the clusters. We obtain tight constraints on cosmological parameters and an indication for the existence of massive neutrinos. We also find a significant underdense region in the southern sky, which has important implications for local measurements of cosmological parameters.

With the completion of our survey of X-ray luminous galaxy clusters based on the ROSAT survey in the region outside the galactic band, within our REFLEX and NORAS projects, we have now assembled a flux-limited sample comprising 1747 clusters with a very well characterised selection function. This is now by far the largest well defined X-ray galaxy cluster sample, well suited for a number of interesting cosmological studies.

Comparing the cluster X-ray luminosity function with predictions from cosmological models allows us to get constraints on important cosmological parameters, in particular, the cosmic matter density parameter, Ω_m, and the amplitude of the density fluctuations, σ_8, as shown in Fig. 1. In the Figure we also compare the results to those from the Planck mission. We find a good agreement with the results for Planck detected clusters, but a discrepancy with the results from the Planck CMB analysis. The discrepancy could be explained with a sum of the mass of all three neutrino species in the range 0.17 – 0.7 eV. The precision of these results is mostly limited by the uncertainty of the mass measurement of the galaxy clusters in the sample. Therefore we are currently undertaking large efforts to improve our knowledge of the galaxy cluster structure and the methods of mass determination.

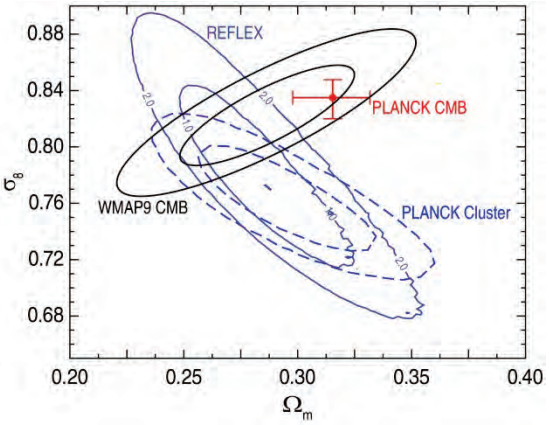

Fig. 1 Constraints on the cosmological parameters Ω_m and σ_8 from the REFLEX, the Planck, and the WMAP survey.

Studying the spatial density distribution of the clusters in the survey, we note a significant underdense region in the nearby southern sky out to a distance of about 170 Mpc. This is shown in Fig 2 with the relative cluster density as a function of radius. The density deficit is detected with a significance larger than 3.6σ. The underdensity is most pronounced around the South Galactic Pole, where it has also been traced in galaxy surveys.This finding has important consequences for the interpretation of measurements of cosmological parameters in this region. For example we estimate that the Hubble constant could be about 3% higher in the local underdensity compared to the global mean.

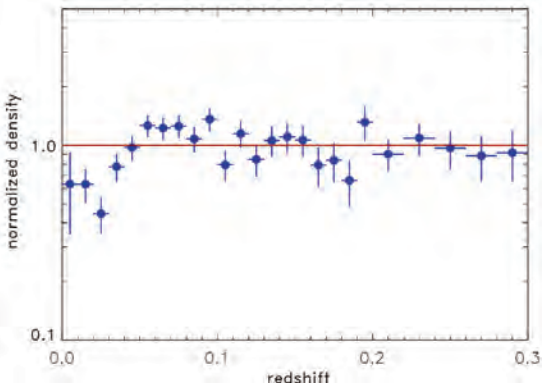

Fig. 2 Relative density distribution of the galaxy clusters in the REFLEX survey as a function of redshift with a clear underdense region at z < 0.04.

References:
Böhringer et al. 2013, A&A, 555, A30, Chon & Böhringer 2012, A&A, 538, A35, Böhringer et al., 2014, A&A, 570, A31, Böhringer et al. 2015, A&A, 574, A26, Böhringer & Chon A&A, 574, L8

H. Böhringer, G. Chon

III) High-Energy Astrophysics

The second ROSAT all-sky survey catalogue

We present the second ROSAT all-sky survey source catalogue (2RXS). This is the second publicly released ROSAT catalogue of point-like sources and is a revised and extended version of the combined Bright and Faint Source Catalogues (Voges et al. 1999, 2000). 2RXS provides the deepest and cleanest X-ray all-sky survey catalogue in advance of eROSITA.

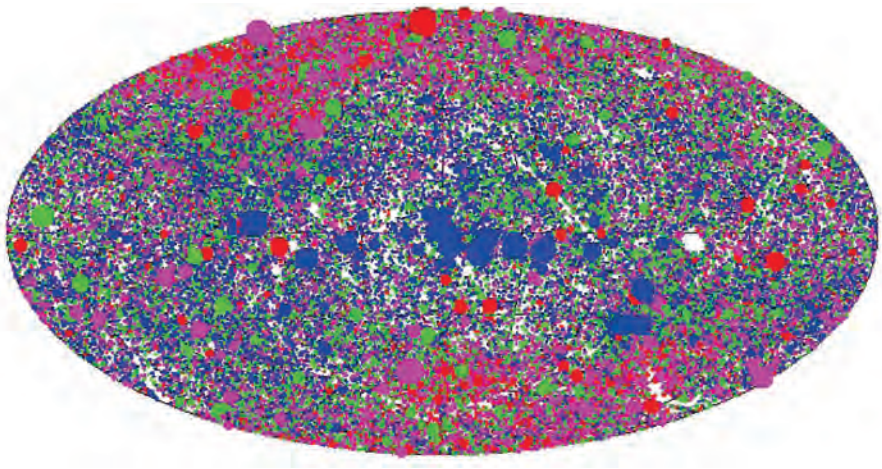

Aitoff projection in Galactic coordinates of the sky distribution of 2RXS sources. The size of the symbols scales with source count rate and the colours represent different spectral characteristics (increasing hardness ratio from red to blue).

We have re-analysed the photon event files from the ROSAT all-sky survey. The main goal was to create a catalogue of point-like sources, more reliable than the 1RXS catalogue (Voges et al. 1999, 2000). We have improved the reliability of detections by an advanced detection algorithm and a complete screening process. Photon event files with corrected astrometry (RASS-3.1 processing) were made available in FITS format.

We obtained about 135,000 X-ray detections in the 0.1-2.4 keV energy band down to a likelihood threshold of 6.5. Our simulations show that the expected spurious content of the catalogue is a strong function of the detection likelihood, and the full catalogue is expected to contain about 30% spurious detections. Above a likelihood of 9 the catalogue contains about 71,000 detections with a 5% spurious fraction.

Intra-day variability in the X-ray light curves was quantified based on the normalized excess variance and a maximum amplitude variability analysis. X-ray spectral fits were performed using three basic models, a power law, a thermal plasma emission model, and black–body emission. X-ray images and overlaid X-ray contour lines provide an additional product to evaluate the detections visually. Thirty-two large extended regions with diffuse emission and embedded point source were identified and excluded form the present analysis.

With the publication of the 2RXS catalogue and its data products, a detailed science specific exploration will now be possible for the astrophysical community. With 2RXS, the deepest and most reliable X-ray all-sky survey catalogue became available before the launch of eROSITA. The experience gained by the HE group at MPE in creating the new catalogue will be incorporated into the data reduction analysis and scientific exploration of the forthcoming eROSITA all-sky survey.

References:

• Boller, Th., Freyberg, M., Trümper, J., Haberl, F., Voges, W., Nandra, K., A&A 568, A103, 2016
• Voges, W., Aschenbach, B., Boller, Th. et al., A&A, 349, 389, 1999
• Voges, W., Aschenbach, B., Boller, Th. et al., IAU Circ., 7432, 3, 2000

T. Boller, M. J. Freyberg, J. Trümper, F. Haberl, W. Voges, K. Nandra

N-Way: A bayesian approach to multi-λ association and its application to ROSAT

The landscape of photometric surveys has increased significantly over the last decade, but when pairing them, complications arise from different positional accuracies, spatial resolutions (in particular at X-ray, UV and MIR wavelengths) and depths that do not match each other. Here we present a new approach and apply it to the new 2RXS ROSAT point source catalog.

Historically, the Maximum Likelihood Ratio technique (e.g. [1],[2]) is adopted for pairing an X-ray detection to its multi-wavelength counterparts. In the basic MLR incarnation, for a given source the ratio between the probability of being either the counterpart or a background source is computed and when the ratio is above a certain assumed value, the counterpart is accepted. When catalogs at different wavelengths are available, the procedure is repeated and the counterpart common to all the applications is assumed to be the right one. For the remainder cases in which the different wavelengths provide different counterparts, visual inspection and subjective decision are necessary. **This is not only unmanageable for wide and deep area surveys, but the method also totally neglects the effects of SEDs and redshift on the galaxy distribution, assigning the same strength to the various catalogs.**

For these reasons we have developed [3] a new Bayesian code, N-way, that similarly to [4], can work simultaneously on various catalogs but unlike [4] it correctly considers the case when a source is present in a catalog and not in the other. In addition, our code can work simultaneously on a different combination of different type of priors. We tested the code on XMM-COSMOS (where counterparts are confirmed also by Chandra), using a simultaneous prior on the "i", K and IRAC[3.6] bands. We then applied the code for finding the counterparts to the ROSAT sources in the 2RXS catalog [5]. The prior was built by comparing the distribution in WISE bands W1-W2 versus W2 for about 1000 3XMM sources with X-ray flux similar to ROSAT, to the distribution of normal galaxies in the field (Fig.1; left). The power of simultaneously combining color and magnitude distribution in disentangling an X-ray counterpart (either star, galaxy, AGN and QSO) from the background population appears obvious when comparing it to a prior based on pure magnitude distribution, e.g. W2 (Fig.1; right).

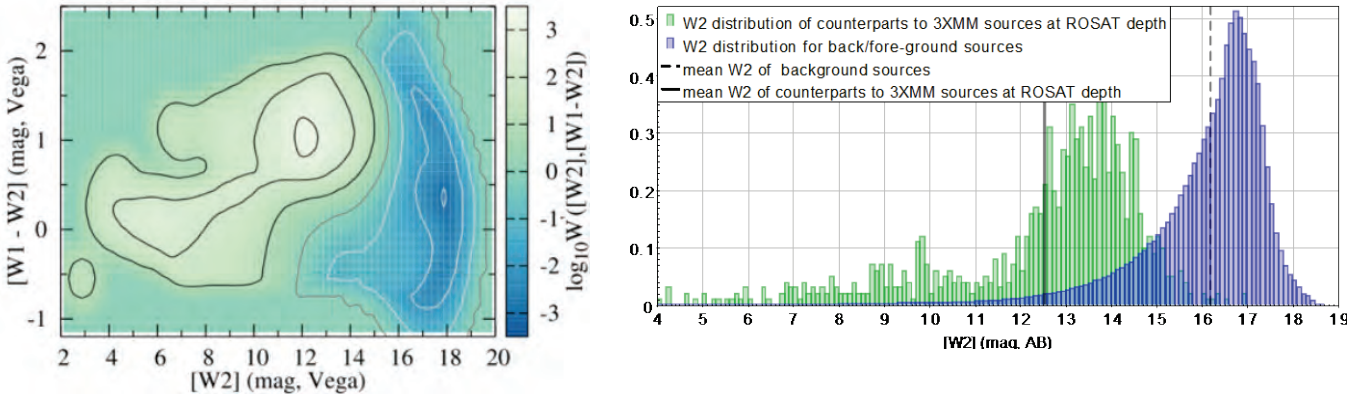

Results: A pure magnitude prior tends to select brighter counterparts (meanW2=12.56) than using a combined color-magnitude prior (meanW2=12.62). The counterparts found using the two methods is the same only for 77% of the ~108.000 ROSAT sources. However, when compared with SDSS-DR12, the fraction of AGN/QSO confirmed via spectroscopy is higher for the color-magnitude prior than for the magnitude prior alone. Similarly, the chance association (obtained by searching a counterpart to random positions in the sky) is much lower when using the color-mag prior than when using the magnitude prior alone. These facts suggest the color-magnitude being more reliable. Similarly to the MLR method, N-way can be used when searching for example, the counterparts to radio sources.

References:
[1] Ciliegi et al 2005; [2] Brusa et al 2007; [3] Salvato et al. in prep; [4] Budavari and Szalay 2008;
[5] Boller et al. 2016

M. Salvato, J. Buchner, T. Dwelly, A. Merloni, et al.

SPIDERS – Wide area X-ray AGN survey

SPIDERS (SPectroscopic IDentification of eROSITA Sources) is an SDSS-IV project running in parallel with the eBOSS and TDSS surveys. SPIDERS will obtain optical spectroscopy for 1000s of X-ray selected AGN and galaxy cluster members detected in eROSITA, XMM-Newton and ROSAT surveys. Before the launch of eROSITA we have targeted two classes of X-ray selected AGN candidates: sources detected in i) the ROSAT all sky survey, and ii) the XMM-Newton Slew survey. Here we describe this survey, and present initial results.

The first step towards exploiting the information content of an X-ray survey is almost always to associate each X-ray detection with a longer wavelength counterpart (or counterparts). The correct selection of counterparts is often a non-trivial task because of the relatively large positional uncertainties for most sources found in all-sky X-ray surveys. After choosing counterparts, the next step is to obtain redshift information, ideally through spectroscopy. Redshift information from optical spectroscopy is of particular importance for extragalactic science programs that, for example, seek to chart the demographics of the X-ray selected AGN population, or to constrain cosmological parameters through identification of X-ray selected clusters.

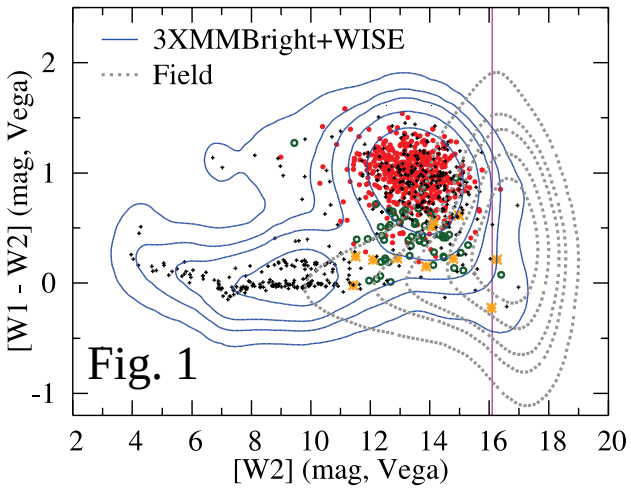

We start with a sample of ~35000 X-ray detections taken from the ROSAT All Sky [1] and XMM Slew surveys [2]. Exploiting a novel Bayesian cross-matching algorithm, and guided by priors based on mid-infrared (mid-IR) colour-magnitude information from the WISE [3] all sky survey (see Fig. 1), we select the most probable optical (SDSS) counterpart to each X-ray detection (for more details of the algorithm see [4]). The high fidelity of our counterpart selection method is confirmed using reference samples of bright X-ray sources from the XMM-Newton, Chandra and Swift-XRT serendipitous catalogues. In over 94% of cases our method chooses the correct optical counterpart despite the poor positional uncertainty (typically >30") of the ROSAT detections.

After putting aside the 13000 X-ray sources with redshift information from SDSS-DR12 ([5], see Fig. 2), and selecting only targets with 17<r<22.5, we have submitted nearly 10000 targets for observation in SDSS-IV (currently on-going).

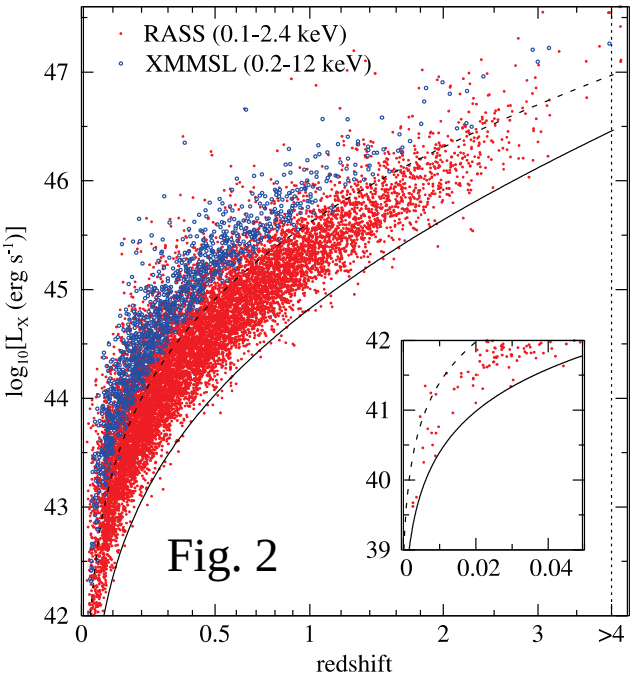

On completion of the SPIDERS ROSAT/XMM slew follow-up program we expect to have collected spectroscopic redshifts and classifications for >85% of the X-ray sources having counterparts fainter than r_{AB}=17. The pre-eROSITA SPIDERS program will result in a large and highly complete sample of X-ray bright AGN suitable for statistical studies of AGN evolution and clustering.

References:

[1] Voges et al. (1999, 2000); [2] Saxton et al. (2008); [3] Cutri et al. (2013); [4] Salvato et al (2016); [5] Alam et al. (2015).

T. Dwelly for the SPIDERS team

The Relation between X-ray and UV Emission in Quasars

As part of the SPIDERS program, a sample of ROSAT X-ray selected quasars have been assigned counterparts via their WISE infrared colours, and have optical spectra available from the Sloan Digital Sky Survey. These sources were then matched to GALEX UV counterparts, which resulted in a catalogue of 5500 sources in the redshift range $0 \leq z \leq 2$. This sample is currently being used to investigate the relationship between the UV and X-ray emission in quasars. The possibility of standardising quasar luminosities, such that they can be used as standard candles, will also be investigated.

Disk - Corona Interaction: The correlation between the UV and X-ray luminosity for the ROSAT selected sample of quasars is shown in Fig. 1 below. The slope of this relation is typically found to be less than one, indicating that the relative energy distribution between the UV and X-ray emitting regions is luminosity dependent. The slope of the relation shown in Fig. 1, 0.70 ± 0.02, is consistent with that found by Vignali et al. 2003. The relative contribution of the UV accretion disk emission and the X-ray emission from the surrounding corona, is usually characterised by the UV to X-ray spectral index, α_{OX}. Using the ROSAT selected sample of quasars, the anti-correlation between α_{OX} and UV luminosity is confirmed, with a slope -0.119 ± 0.008, in agreement with previous work (e.g. Young et al. 2010). This anti-correlation suggests that increasing UV luminosity diminishes coronal emission in quasars.

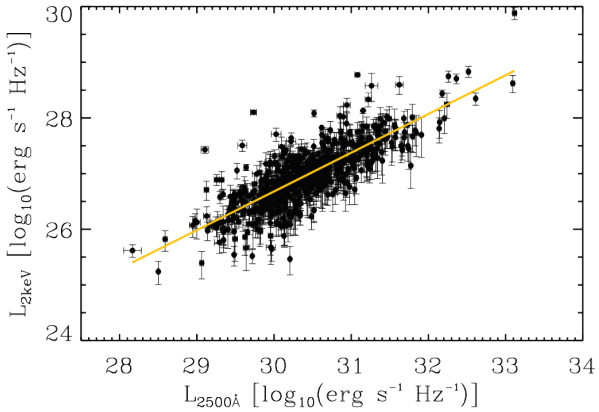

Fig. 1. Monochromatic 2 keV versus 2500Å luminosity for a subsample of 627 sources with well constrained luminosity measurements.

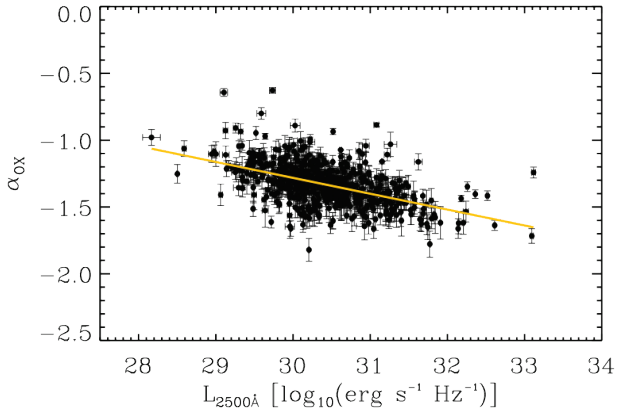

Fig. 2. UV to X-ray spectral index versus rest frame monochromatic UV luminosity for the same subsample as in Fig. 1.

Further work: The UV and X-ray luminosity relation has recently been used to include quasars as standard candles in a Hubble diagram in order to estimate the cosmological parameters Ω_M and Ω_Λ (Risaliti and Lusso 2015). This sample may also provide a large number of sources which can be added to the Hubble diagram in the redshift range currently populated by type 1a supernovae ($z \leq 1.4$). This will allow the cosmological parameter results obtained from quasars to be compared directly with those obtained from supernovae.

References:
•Risaliti, G., & Lusso, E. 2015, ApJ, 815, 33
•Vignali, C., Brandt, W. N., & Schneider, D. P. 2003, AJ, 125, 433
•Young, M., Elvis, M., & Risaliti, G. 2010, ApJ, 708, 1388

D. Coffey, M. Salvato, T. Boller, A. Merloni, K. Nandra

A Spectroscopic Survey of X-ray selected AGN in the XMM-XXL

We present a survey of X-ray selected active galactic nuclei (AGN) in the equatorial XMM-XXL north field. The sample is matched to optical (SDSS) and infrared (WISE) counterparts and has been subject to a spectroscopic follow-up with the BOSS spectrograph. The survey allows for a prediction of AGN populations in future eROSITA follow-up programmes (SPIDERS) and a comparison of different AGN selection critera. The results of this work have been published in Menzel et al. 2016.

Introduction to the Spectroscopic Survey: Our dataset consists of 8445 point-like X-ray sources detected by XMM-Newton ($F(0.5\text{-}10\ keV) > 10^{-15}$ erg/s/cm^2) in an 18 deg^2 area. We followed up 3042 sources ($r < 22.5$ mag) with the SDSS BOSS spectrograph and yielded a reliable redshift measurement for 2578 objects ($z = 0.02 - 5.0$), with 0.5-2 keV luminosities ranging from 10^{39}-10^{46} erg/s. This is currently the largest published spectroscopic sample of X-ray selected AGN in a contiguous area and benefits from coverages in many multi-wavelengths bands.

A) AGN Population in the XMM-XXL

The bimodal distribution of optical line widths allows an efficient separation between broad- and narrow-emission line AGN. The broadline AGN dominate our sample due to the relatively bright X-ray flux limit and the optical BOSS magnitude limit (70 per cent, $0 < z < 5$). We classify the narrow emission line AGN by using standard BPT diagnostics (22 per cent, $0 < z < 1.5$). A small number of objects exhibit the typical narrow line ratios of star-forming galaxies (SFG), or only have absorption lines (ALG) in their spectra. We term the latter two classes 'elusive' AGN, which would not be easy to identify correctly without their X-ray emission (8 per cent, $0 < z < 1$).

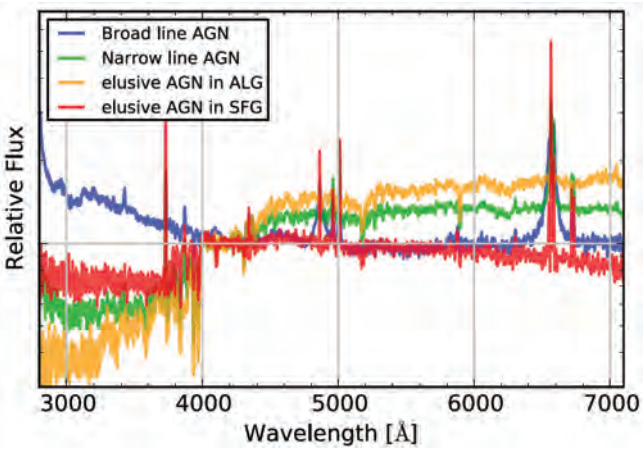

Fig 1: Stacked BOSS spectra representing the AGN population in the XMM-XXL north survey.

B) Comparison of AGN Selection Criteria

We compare X-ray (grey circle, XMM-Newton), optical color (blue circle, SDSS, Bovy et al. 2011), and infrared color (red circle, WISE, Assef et al. 2013) AGN selections in the XMM-XXL field. X-ray observations reveal, by far, the largest number of AGN. The overlap between the selections, which is a strong function of the imaging depth in a given band, is also remarkably small. We show using spectral stacking that a large fraction of the X-ray AGN would not be selectable via optical or IR colours due to host galaxy contamination. A substantial fraction of AGN may therefore be missed by these longer-wavelength selection methods.

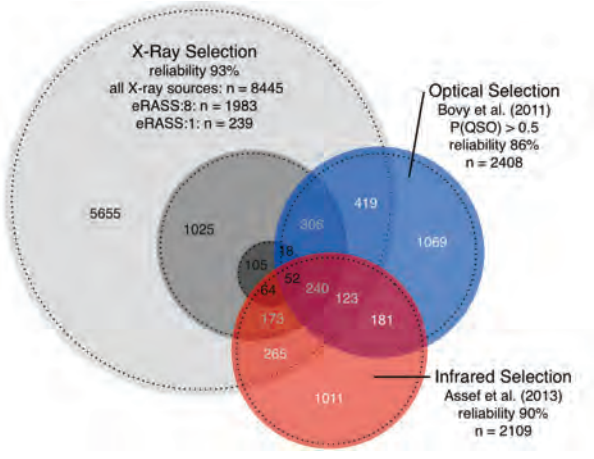

Fig 2: Venn diagram of X-ray, optical and infrared AGN selection criteria applied to the XMM-XXL north.

References:

• Bovy, J., Hennawi, J. F., Hogg, D. W., et al. 2011, ApJ, 729, 141; Assef, R. J., Stern, D., Kochanek, C. S., et al. 2013, ApJ, 772, 26; Menzel, M.-L., Merloni A., Georgakakis A. et al., 2016, MNRS, 457, 110

M.-L. Menzel, A. Merloni, A. Georgakakis, M. Salvato, K. Nandra

Constraining the contribution of AGN to the reionisation of the Universe

Deep and shallow/wide-area X-ray surveys are combined to determine the luminosity function of X-ray selected AGN at redshifts z>3 and constrain their contribution to the UV photon field necessary to re-ionise the Universe at high redshifts. It is found that the space density of X-ray AGN drops rapidly with redshift at z>3, and therefore these systems are only a minor component of the reionisation of the Universe at *z*>4.

The luminosity function of AGN at high redshifts, z>3, provides constraints on both the formation history of the first Supermassive Black Holes and the role of Active Nuclei in the re-ionisation of the Universe. Selection at X-ray wavelengths allows estimates of the AGN space density to much fainter accretion luminosity levels compared to e.g. UV/optical studies. In Georgakakis et al. (2015) one of the largest samples of high redshift (z=3-5) X-ray selected AGN has been assembled by combining both pencil-beam/deep (AEGIS, COSMOS, CDFN, CDFS) and wide-area/shallow surveys (XMM-XXL) fields. This allowed constraints on the AGN space density over a luminosity baseline of more than 3 orders of magnitude (see Fig. 1-left). A Bayesian methodology has been developed to provide robust constraints on the AGN space density by propagating into the analysis uncertainties in the determination of both the redshift (e.g. photometric redshift errors) and the accretion luminosity of individual sources. It was found that the AGN space density decreases rapidly in the redshift interval *z*=3-5. As a result the contribution of X-ray AGN to the ionising UV photon-rate density needed to keep the Universe ionised at *z*>4 is small.

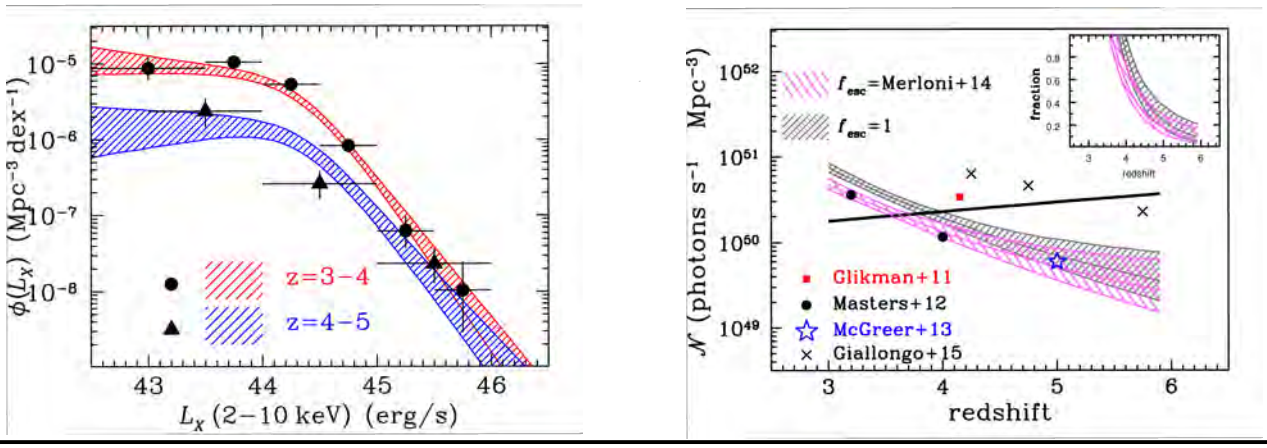

Left: Space density of AGN in two redshift intervals *z*=3-4 (filled circles and red regions) and *z*=4-5 (filled triangles and blue regions). The data points show non-parametric estimates of the AGN space density, while the shaded regions show a particular parametrisation for the luminosity function of AGN and its evolution with redshift. Datapoint errorbars and the extent of the shaded regions correspond to the 68% confidence intervals. **Right:** Hydrogen ionising photon rate density as a function of redshift. The shaded regions are the constraints from the X-ray luminosity functions shown on the left under different assumptions on the escape fraction of AGN photons. The grey-shaded region assumes an escaping fraction of unity, i.e. ignoring obscuration effects close to the supermassive black hole. The pink-shaded region assumes the luminosity-dependent Type-1 AGN fraction of Merloni et al. (2014). The data points are results in literature. The thick black line in the plot shows the photon rate density required to keep the Universe ionised at any given redshift. The ratio between the shaded regions and the black line are presented in the inset plot. Even in the extreme case of unity escape fraction the photon rate density produce by the declining X-ray AGN population is insufficient to keep the Universe ionised at *z*>4.

References: Georgakakis et al., 2015, MNRAS, 453, 1946; Giallongo E., et al., 2015, A&A 578, A83; Glikman E., et al., 2011, ApJ, 728, L26; Masters D., et al., 2012, ApJ, 755, 169; Merloni A., et al., 2014, MNRAS, 437, 3550; McGreer I. D., et al., 2013, ApJ, 768

A. Georgakakis

Heavily-obscured black hole accretion in the high redshift Universe

Coupling X-ray and multi-wavelength studies of AGN, such as in the infrared band where the effects of obscuration are small, can help unveiling the most obscured active galactic (AGN) population. Indeed, the study of a sample of mid-infrared (MIR) luminous quasars, i.e. the most powerful AGN, at redshift z~2 in the Chandra Deep Fields, has shown that the vast majority (~80%) of these quasars are obscured in the X-ray band, and a significant fraction (~30%) is undetected even in the deepest X-ray data. Unprecedented insights on the heavily-obscured AGN population and its contribution to the Cosmic X-ray background (CXB) are also provided by hard X-ray studies (E>10 keV) with NuSTAR, which allows a full characterisation of the intrinsic spectral properties of AGN up to high energies, especially at E~20–30 keV, where the CXB peaks.

Current X-ray surveys have proved to be essential for the identification and study of active galactic nuclei (AGN) across cosmic time. However, as most of the accretion onto supermassive black holes (SMBHs) occurs in obscured environments, even the deepest X-ray surveys can fail to identify the most heavily-obscured, Compton-thick (CT) AGN. These sources are a key ingredient to explain the observed spectrum of the cosmic X-ray background (CXB), and might also represent a particularly active and dusty phase of SMBHs and galaxy evolution.
However, our models of the CXB still suffer from degeneracies in the parameters, which prevent us from securely constrain the fraction of CT AGN in the Universe (e.g., [1], [4]). NuSTAR can directly provide the constraints needed to improve our understanding of the CXB composition, of the space density of CT AGN, and thus, of their role in the SMBH-galaxy evolution.

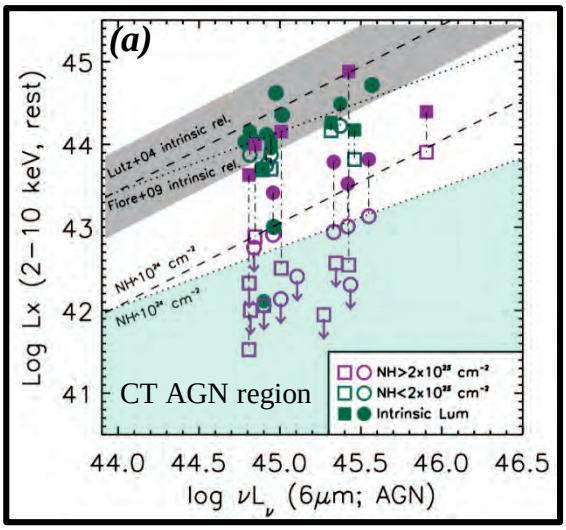

Fig. 1 (a) *- MIR 6 micron (intrinsic) AGN luminosity vs. observed X-ray 2-10 keV luminosity (open symbols) for a sample of MIR selected quasars at z~2 ([3]): ~30% are X-ray undetected, yielding a fraction of CT AGN candidates up to ~48%.* ***(b)*** *- The derived CT AGN space density is consistent with models.*

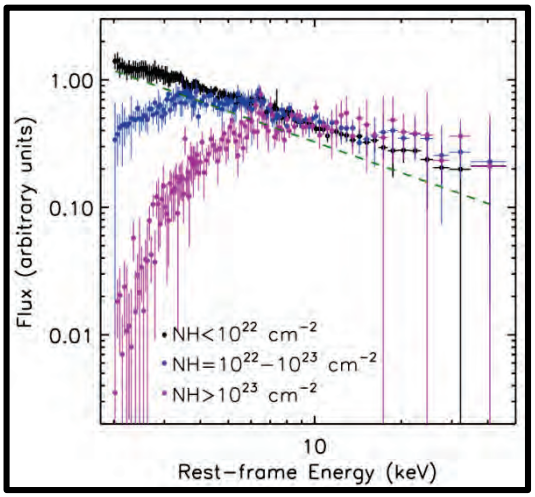

Fig. 2 *- Composite 2-40 keV Chandra+NuSTAR spectra for unobscured (black), moderately obscured (blue) and heavily obscured (magenta) AGN. NuSTAR directly probes the energies where the CXB peaks (20-30 keV) and therefore provides essential constraints on the intrinsic spectral properties of AGN (e.g., [2]), which help us braking existing degeneracies on the parameters on which the synthesis models of the CXB and X-ray luminosity functions rely (e.g., [1], [4]).*

References: • [1] Aird, J., et al. 2015, ApJ, 815, 66 • [2] Del Moro, A., et al. 2014, ApJ, 786, 16 • [3] Del Moro, A., et al. 2016, MNRAS, 456, 2105 •[4] Treister, E., et al. 2009, ApJ, 696, 110

A. Del Moro, et al.

PSD analysis of AGN light curves

Although optical variability of AGN has been observed for many decades, its physical origin is still debated. The shape of the power spectral density (PSD) of a time series potentially allows gaining insight into the underlying processes connected to variability. In this work we used a novel method applying continuous-time autoregressive moving average (CARMA) models (Kelly et al. 2014), which allows us to derive the PSD even for irregularly sampled light curves. Our studies are based on a large sample of ~100 variable X-ray selected AGN from the XMM-COSMOS catalog (Brusa et al. 2010), with optical light curves provided by the Pan-STARRS1 (PS1) MDF survey (Kaiser et al. 2010). We find that the optical PSD can be described by a broken power law exhibiting a characteristic bend at rest-frame timescales ranging between 100 and 300 days. The low-frequency slope of the PSD is consistent with a value of -1 for most of our objects, the high-frequency slope shows a broad distribution of values between -2 and -4. Moreover we observe that the PSD amplitude is strongly anticorrelated with bolometric luminosity and Eddington ratio, whereas there is no correlation with black hole mass and redshift.

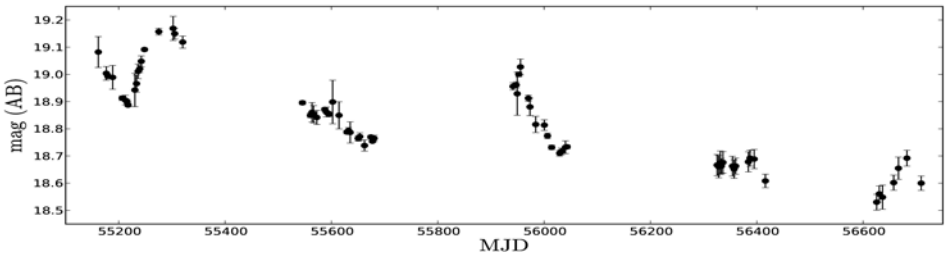

Fig.1: PS1 MDF light curve (g band) for one of our sources showing strong variability.

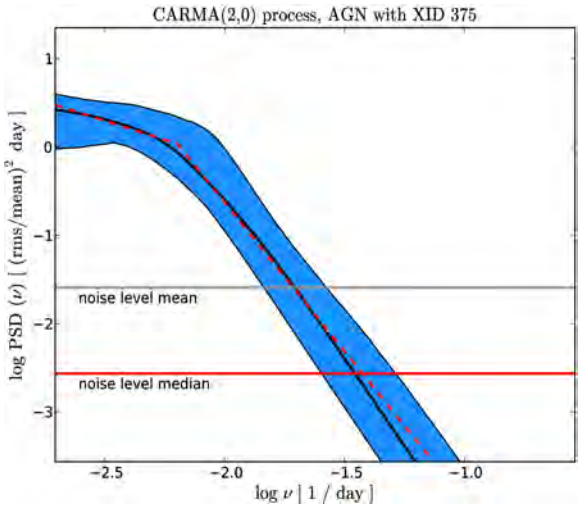

Fig. 2: CARMA model estimate of the PSD for one of our AGN with 95% error regions shown in blue. The red dashed line is the best-fit broken power law. The break occurs at a timescale of 158 days.

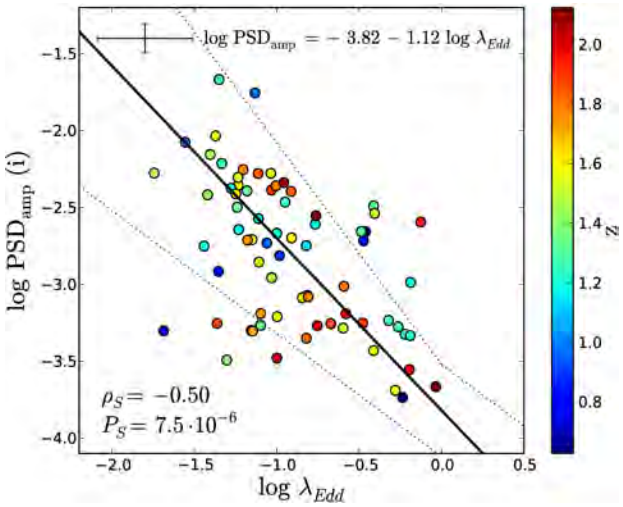

Fig. 3: PSD amplitude (i band) versus Eddington ratio. The redshift is given as a color bar. The relation is present for all PS1 bands and can be described by a power law with slope of ~-1. The same slope is observed for the anticorrelation with bolometric luminosity.

References:

- Kelly, B., et al. 2014, ApJ, 788,33
- Brusa, M., et al. 2010, ApJ, 716,348
- Kaiser, N., et al. 2010, Proc.SPIE, 7733

T. Simm, M. Salvato, R. Saglia, G. Ponti, G. Lanzuisi, B. Trakhtenbrot, K. Nandra, R. Bender

Relativistic Reflection in a sample of Sefyert 1

Broad iron lines are expected, and observed, to be a widespread feature in bright AGN. However, a significant fraction of objects misses a disk line component. We extracted from the sample of all Seyfert 1 galaxies the ones with no detection of a broad Fe Kα line, to investigate the physical cause of this absence. We analysed all archival Suzaku observations that, thanks to the broad energy band, allow us to investigate the connection between broad Fe Kα line and reflection continuum. Our analysis shows that relativistic FeKα lines are ubiquitous features in the spectra of Seyfert galaxies, but are often difficult to detect without very high quality data. We also investigate the relation between the Fe Kα line and the reflection continuum. For most of the sample, the strength of the reflection component is consistent with that of the line.

We first focused our attention on IC 4329A, the brightest object of the sample. The five Suzaku observations were fitted with a model which includes a neutral absorber at the redshift of the source, a cut-off power law together with reflection continuum and a narrow FeKα component. We then added to the previous model a relativistic FeKα component and fitted each single spectrum. A relativistic Fe Kα line is detected with high significance only when all the observations are combined and the S/N ratio increases. The combined data to model ratio, where only the continuum and the narrow Fe Kα component are fitted, are plotted in Figure 1. Residuals above 5 keV indicate the presence of a broad relativistic line. This demonstrates that high statistic is a fundamental key to reveal broad Fe Kα lines (Mantovani et al., 2014).

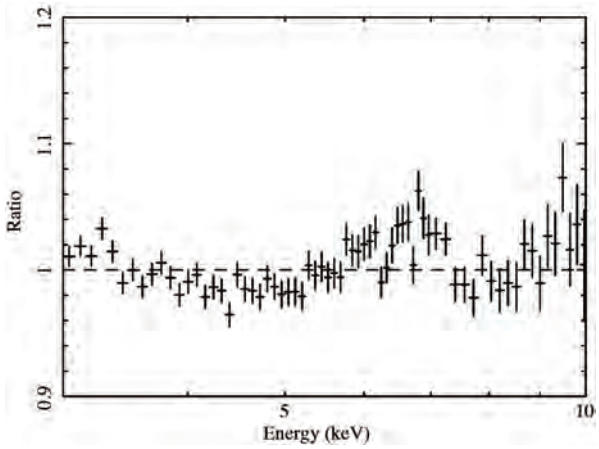

Figure 1: Ratio of data/model between 3-10 keV when only the continuum and the narrow Fe Kα component are fitted.

We then fitted the spectra with the self-consistent model *pexmon* (Nandra et al., 2007), which links the emission of the FeKα line and the Compton reflection component. The data in our sample are consistent with both the narrow and broad Fe line tracing the emission at high energies. This result confirms that they are features of the same reflection spectrum.

We then extended this analysis to a sample of Seyfert 1 galaxied where the broad component was not detected in previous XMM-Newton observations (Nandra et al. 2007). Figure 2 presents the results of this work. The relativistic FeKα line is detected only in the observations where the statistics in the 5-7 keV energy band is sufficiently high in order to disentangle this feature from the underlying continuum (Mantovani et al. 2016, submitted).

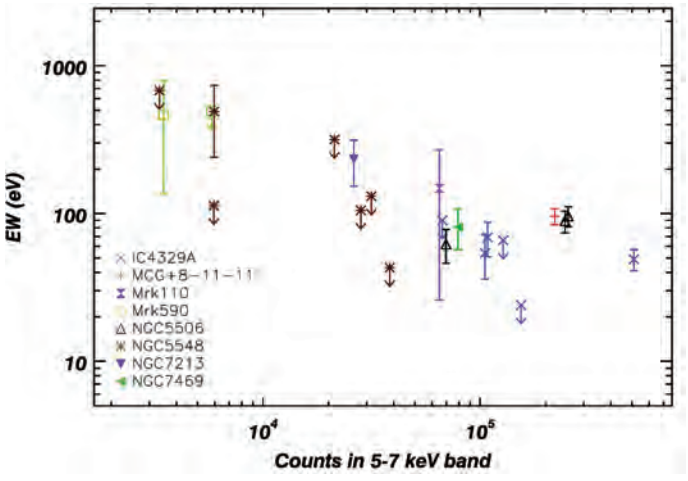

Figure 2: Relativistic Fe line Equivalent Width as a function of the counts in the 5-7 keV band.

References:

• Nandra K., O'Neill P.M., Geroge I.M., Reeves J.N., 2007, MNRAS, 382, 194
• Mantovani G., Nandra K., Ponti G., 2014, MNRAS, 442, L95
• Mantovani G., Nandra K., Ponti G., 2016, MNRAS, submitted

G. Mantovani, K. Nandra, G. Ponti

A tidal disruption flare in a massive galaxy?

During the preparation for the targeting of the SDSS-IV/SPIDERS survey, we recently discovered a massive SDSS galaxy that underwent a rapid increase in the X-ray and optical/UV luminosity, followed by a steady decay, associated to a dramatic change of its optical spectrum, over a ten year timescale, changing from a typical type-1 AGN to a galaxy-dominated state. In Merloni et al. (2105), we offered an interpretation of this event as a tidal disruption flare. Future X-ray and optical surveys will help us revealing the overall role of stellar tidal disruptions for SMBH triggering, and may shed new light on mysterious classes of sources, such as elusive, X-ray bright and optically normal, and changing look AGN.

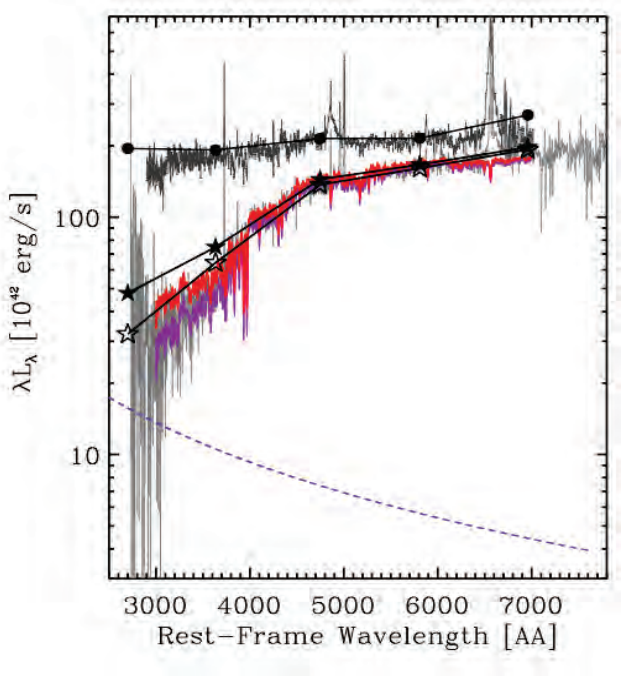

Figure 1: SDSS J0159+0033 was observed twice by SDSS. The two grey lines show the calibrated spectra from the year 2000 (upper curve) and from 2010 (lower curve). Superimposed are the u'g'r'i'z' photometric data points from near the outburst peak (2000, black solid circles), and from 2007 (black solid stars). The red solid line is the best-fit model to the continuum emission of the 2010 spectrum, which is the sum of the host galaxy spectrum (solid purple line) plus a power-law continuum (dashed line). The observed spectral changes can ascribed entirely to the strong decrease of the power-law component and the broad emission lines.

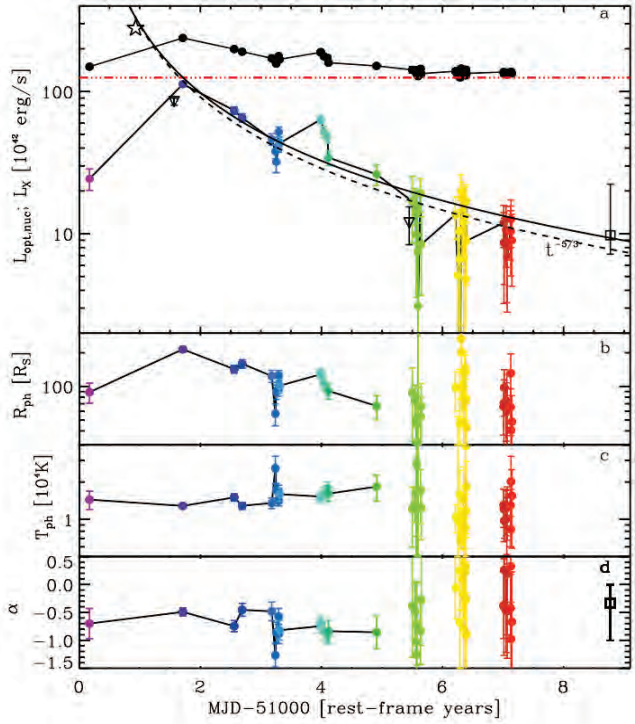

Figure 2: Panel a: the time evolution of the nuclear luminosity is shown with the colored circles. The black circles are the total optical luminosity of SDSS J0159+0033, shown here for reference, together with the estimated (constant) luminosity of the host galaxy (red horizontal dot-dashed line). The empty triangles show the X-ray (2–10 keV) luminosity measured by XMM-Newton (first epoch) and Chandra (second epoch). The black solid line is the best fit power-law evolution of the flare decay, including all data points. The dashed line, which is not a fit to the data, shows the $t^{-5/3}$ long-term decline expected in most TDE models. Panel b and c show the evolution of the best fit photospheric radius and temperature (filled circles). Panel d shows the best-fit power-law slope α, where $L_\lambda \propto \lambda^{-2+\alpha}$. Such almost 'achromatic' evolution has been observed in many other TDE candidates.

References:

• LaMassa, S., et al., 2015, ApJ, 800, 144

• Merloni, A., et al., 2015, MNRAS, 452, 69

A. Merloni, T. Dwelly, M. Salvato, A. Georgakakis, J. Greiner, G. Ponti, A. Rau

A very deep Chandra view of the Centaurus cluster of galaxies

We examine very deep Chandra X-ray observations of the Centaurus cluster of galaxies. Applying an edge-detection filter to the data shows a wealth of structure on scales from 100pc to 10s of kpc. We see signatures of the intracluster medium sloshing in the potential well on larger scales, highlighted by multiple surface brightness edges (which are also seen in temperature and metallicity). The western cold front edge has indentations consistent with Kelvin-Helmholtz instabilities. The edge filtering reveals multiple flat surface brightness regions around the core of the cluster, some of which are associated with radio emission. If these are AGN-generated cavities, they indicate the AGN has been repeatedly active on 5-10 Myr timescales. This is in agreement with the ~3.5 Myr age of a central shock found around the AGN. We also confirm the presence of linear ripple-like structures, which could be sound waves generated by the AGN with 6 Myr periods.

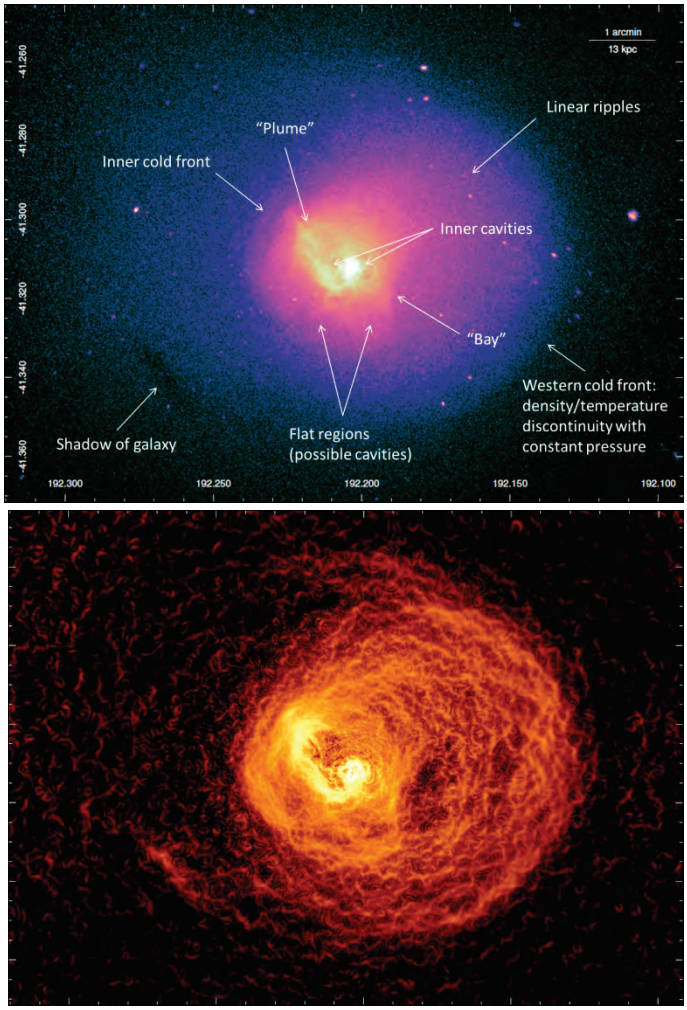

Fig 1 (above): Original X-ray image (top) and Gaussian gradient-magnitude-filtered X-ray image.

We use for the first time the Gaussian gradient magnitude filter to an X-ray image of a galaxy cluster (*Fig 1*). The filtering is done on multiple scales and combined to show edges in the X-ray surface brightness over the region. On larger scales the overall morphology is dominated by sloshing, where the potential well has likely been affected by a perturber. The cold front edges (temperature and density discontinuities, continuous in pressure) are a signature of this.

The central region is dominated by AGN activity (*Fig 2*), seen as multiple (up to 9) X-ray surface brightness depressions. There is a central shock around the nucleus and shocks around the inner cavities. A soft filamentary plume is seen, likely cool material dragged from the core due to AGN activity. The coolest X-ray emitting material is offset from the X-ray faint central nucleus.

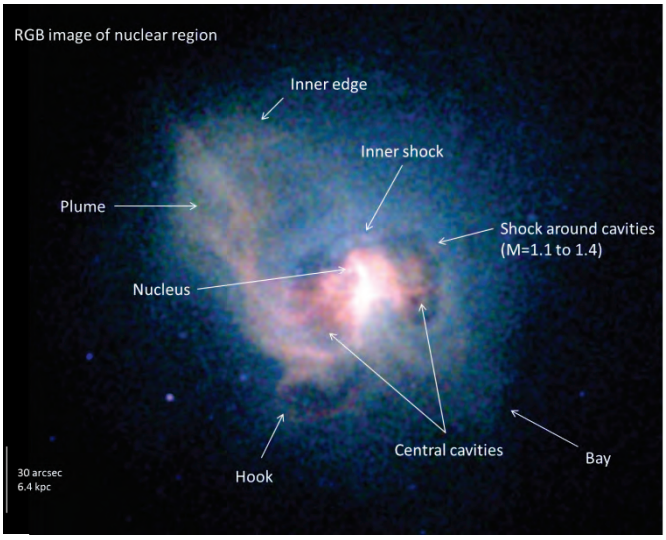

Fig 2 (right): RGB image of the nuclear region.

Reference:

• Sanders et al., 2016, MNRAS, 457, 82

J. S. Sanders, et al.

Thermodynamic perturbations in galaxy clusters

In high resolution X-ray observations of the hot plasma in clusters of galaxies significant substructure caused by AGN feedback, mergers and turbulence can be detected. Using archival data taken with the Chandra ACIS instrument our aim was to study the substructures in thermodynamic properties of the X-ray emission from clusters of galaxies and to apply this to better understand the thermodynamic and dynamic state of the intra-cluster medium. We analyzed deep observations for a sample of 33 clusters with more than 100 ks of Chandra exposure each at distances between redshift 0.025 and 0.45. The combined exposure of the sample is 8 Ms. We mapped thermodynamic properties of the intra-cluster medium and investigated deviations from radial symmetry around the cluster centers. The relation of asymmetries in different parameters can be used as an indicator for turbulence. This study provides detailed asymmetry measurements for a large sample of clusters which will be used to make predictions for future X-ray missions like eROSITA (Merloni et al. 2012).

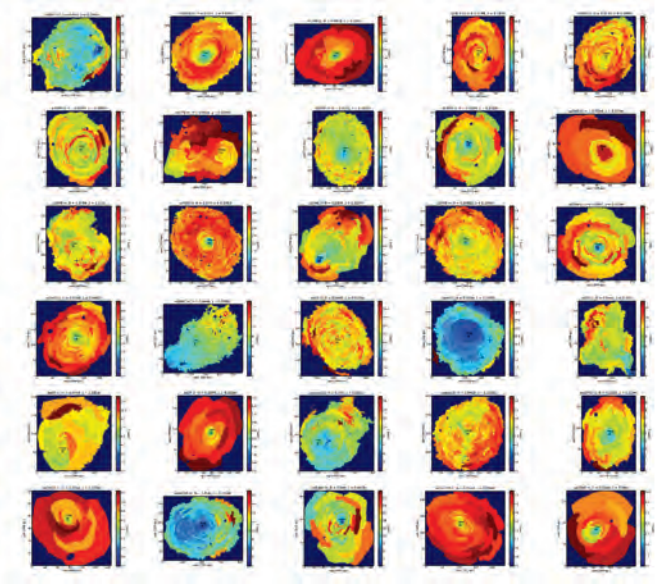

Fig. 1: Temperature maps of 30 clusters in the >100 ks Chandra Cluster Sample. Binned with a signal-to-noise of 50 (using the *CONTBIN* method by Sanders 2006). Temperatures in keV.

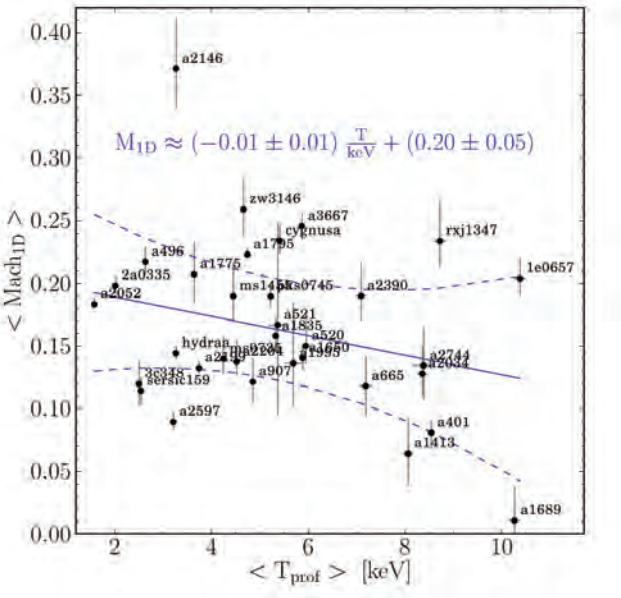

Fig. 2: Relation between the average cluster temperature and the 1D Mach number. The solid and dashed lines represent the best linear correlation and its 1σ scatter.

We measured the fractional spread of temperature, density, pressure, and entropy in concentric annuli around the cluster center using the thermodynamic maps of the clusters (see Fig. 1). Comparing the results to high-resolution 3D hydrodynamic simulations of the intra-cluster medium by Gaspari et al. 2014 we were able to constrain the average 1D Mach number of the cluster sample to **$\mathrm{Mach_{1D}} \sim 0.16 \pm 0.07$** (see Fig. 2). This would suggest that turbulence energy in this sample of clusters is on average only four per cent of the thermal energy in the systems implying a small non-thermal pressure support and only four per cent bias in hydrostatical cluster mass estimates.

References:

- F. Hofmann, J. S. Sanders, K. Nandra et al. 2016, A&A, Vol. 585, Article A130
- M. Gaspari, E. Churazov, D. Nagai et al. 2014, A&A, Vol. 569, Article A67.
- J. S. Sanders 2006, MNRAS, Vol. 371, pp. 829.
- A. Merloni, P. Predehl, W. Becker et al. 2012, eROSITA science book, arXiv:1209.3114.

F. Hofmann, J. S. Sanders, K. Nandra, N. Clerc, et al.

Ultra-fast Galaxy Assembly in the Densest Cluster Environment at z~1.6

The X-ray selected galaxy cluster XDCP J0044.0-2033 at z=1.58 is the most distant confirmed system from the XMM-Newton Distant Cluster Project (XDCP) survey (Fassbender et al. 2011) and constitutes the densest environment currently known at this redshift. With a hydrostatic mass estimate of M_{200}=4.4x10^{14} M_{sun} and an ICM temperature of T_X=$6.7_{-0.9}^{+1.7}$ keV based on a 380ksec Chandra observation (Tozzi et al. 2015) this cluster offers now the possibility to study structure and galaxy formation processes at work in the most extreme environment at a lookback time of 9.5 Gyrs. This extreme is reflected in an unprecedentedly high cluster star formation activity with at least 4500 M_{sun}/year based on Herschel measurements (Santos et al. 2015). Moreover, a comprehensive multi-wavelength galaxy population study of XDCP J0044.0-2033 (Fassbender et al. 2014) has shown evidence for an ultra-fast galaxy assembly process based on merger activity in the cluster core featuring a red-sequence still in formation. The latest HST imaging of the cluster confirms this picture by revealing the details of the complex ongoing assembly activity of the massive cluster galaxies.

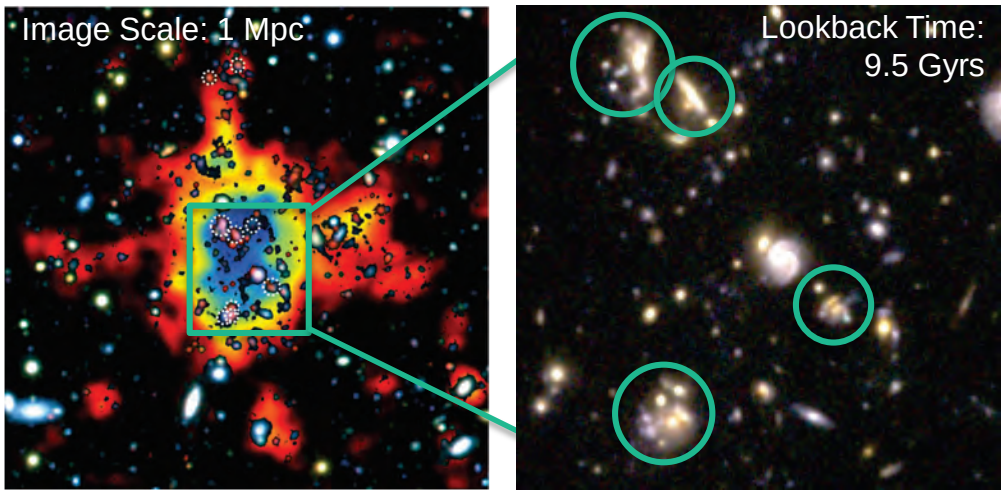

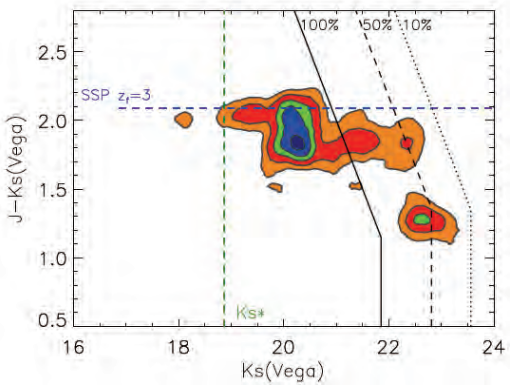

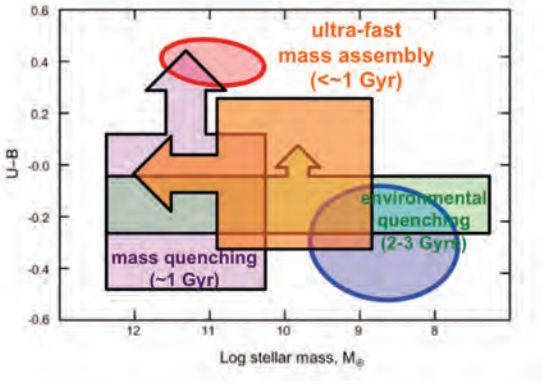

Fig.1 (top left): 2´x2´ V+i+JK color composite of the cluster environment with the extended ICM X-ray emission shown by the colored background.
Fig.2 (top right): HST NIR view of the cluster core with a high degree of mass assembly activity among the confirmed members (circles).
Fig.3 (bottom left): Color-magnitude-diagram of galaxy densities showing the cluster red sequence still in formation.
Fig.4 (bottom right): Schematic view of galaxy formation processes and timescales at work in the cluster in color-galaxy mass space.

References:

- Fassbender, R. et al., 2011, N.J.P. 13, 125014
- Fassbender et al., 2014, A&A, 568, A5
- Tozzi et al., 2015, ApJ, 799, 93
- Santos et al., 2015, MNRAS, 447,L65
- Hayden, Perlmutter et al. 2015

R. Fassbender

Spectroscopic follow-up of large samples of X-ray galaxy clusters

The distribution of galaxy clusters puts stringent and independent constraints on cosmological models and on the formation of large-scale structure across cosmic times. Observations of wide sky areas in the X-ray band provide the large samples necessary to studying the population of halos as a function of their mass, in space and in time. We present the results obtained from the confirmation of a sample of 230 clusters detected in X-ray data (ROSAT All-Sky Survey) and followed-up by multi-object spectroscopic observations with BOSS on the SDSS telescope. Optical spectroscopy of their member galaxies confirms the nature of these systems, their location in space and provides independent information on their mass distribution.

SPIDERS is a survey part of the SDSS-IV project and performs optical spectroscopy of X-ray selected, massive (~10^{14} to 10^{15} M_{sun}) galaxy clusters discovered in ROSAT and XMM-Newton data (Clerc et al. 2016), before data from the *eROSITA* all-sky survey are available (Merloni et al. 2012). The main aims are the confirmation and the determination of precise ($\Delta z \sim 0.001$) redshifts for 4,000 to 5,000 of these systems out to z~0.6 in the Northern hemisphere. A pilot study covering 300 deg^2 led to the confirmation of 230 objects using spectroscopic redshifts of their galaxy members.

The analysis procedure required innovative developments. They consist in several steps :

1. ***Data reduction:*** performed within the SDSS/BOSS collaboration, it led to pipeline-determined redshifts based on 2D fiber spectra.
2. ***Redshift collection****:* these observations raised the number of spectroscopically observed red-sequence members from 2 to 10 in each individual system.
3. ***Membership confirmation:*** a pipeline identified likely members by analysing the clustering of galaxies in redshift space. When more than 3 galaxies were found with consistent redshifts in the red-sequence of a cluster, a systemic redshift was assigned to the cluster.
4. ***Visual screening:*** clusters went through individual screening in order to resolve complex cases (line-of-sight superpositions, exceptional cases, etc.) and to confirm the nature of the objects.
5. ***Catalogue production****:* the newly calculated redshifts were used to compute accurate X-ray luminosities (Fig. 1) and virial radii estimates for the confirmed systems. Velocity dispersions were estimated as a proxy for the dynamical mass of the systems, which scales with the X-ray luminosity of the hot gas (Fig. 2).

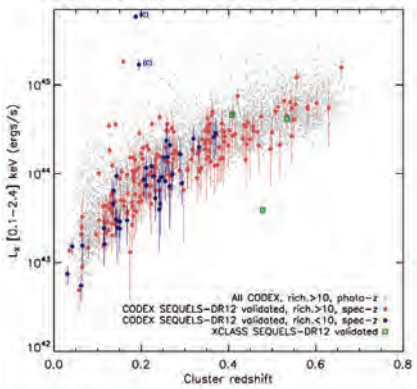

The luminosity-redshift distribution of the 230 systems confirmed as part of the pilot sample (colored points)

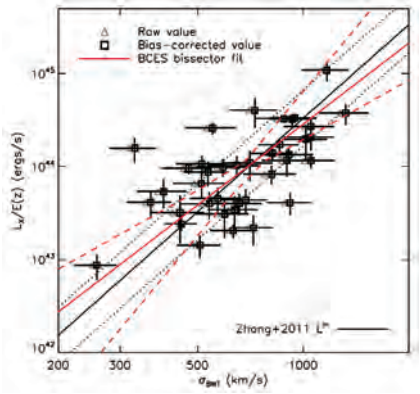

Scaling between velocity dispersion and luminosity for the richest clusters.

References:
• Merloni, A. et al. 2012, eRosita science book, arXiv 1209:3114
• Clerc et al., submitted to MNRAS

N. Clerc, A. Merloni, A. Finoguenov, T. Dwelly, K. Nandra, J. Ridl, M. Salvato

Optical follow-up of X-CLASS galaxy clusters with GROND

Galaxy clusters are the most massive gravitationally bound structures in the Universe. The number density of clusters as a function of mass and redshift depends strongly on fundamental cosmological parameters such as Ω_m and σ_8 and as such, large cluster surveys provide a powerful probe of these parameters. The X-ray emission of clusters can be translated into mass related properties, provided an accurate redshift is available. Thus, in order to fully exploit the cosmological signal of such cluster surveys, X-ray and optical data must be combined.

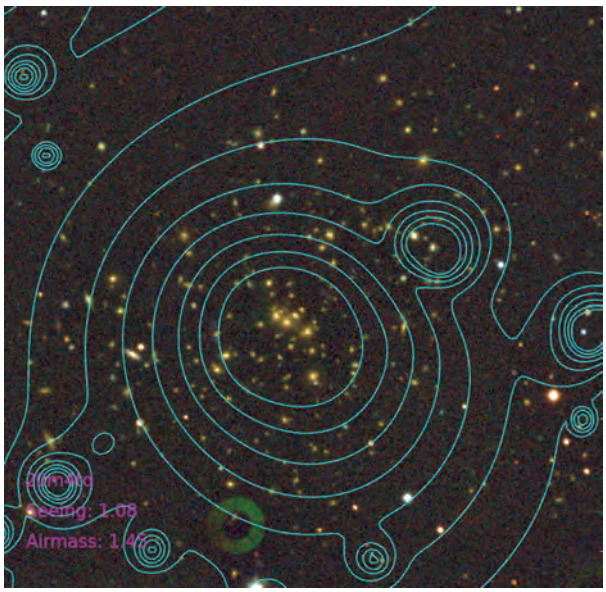

Figure 1: A *gri* composite image of a typical XCLASS cluster. The cyan contours represent the X-ray emission of the cluster

The XMM Cluster Archive Super Survey is a serendipitous, X-ray selected catalogue of galaxy clusters, containing 850 clusters extracted from 2774 archival XMM pointings, following the methodology of the XMM-LSS/XXL. A high signal-to-noise subset of the catalogue of 260 clusters have been followed up by GROND, a simultaneous, seven-channel (*grizJHK*) imager, mounted on the MPG/ESO 2.2m telescope at La Silla. These clusters form the Southern part of the extended X-CLASS cosmological sample, which benefits from a uniquely well controlled selection function of 90 deg^2. The GROND photometry allows for the easy identification of red sequence member galaxies and thus provides an efficient tool for the determination of cluster photometric redshifts. This in turn allows for the characterisation of the X-ray properties of the clusters to be used in cosmological analyses.

An extensive observing campaign has been completed. Clusters were targeted with standard GROND observing blocks with integration times determined by a rough classification based on the DSS. A photometric data analysis pipeline has been set up and optimised for use on galaxy clusters and once calibrated photometry has been obtained, galaxy colours are fed into a photo-z calculation algorithm, designed specifically for dealing with GROND observations. Where possible, the resulting photo-z is compared to spectroscopic redshift from various sources in literature (see Figure 2). Once this catalogue is finalised, a full cosmological analysis using the CR-HR-z method [Clerc el al. 2012a,b] will be performed. These methods will be useful in the context of eROSITA.

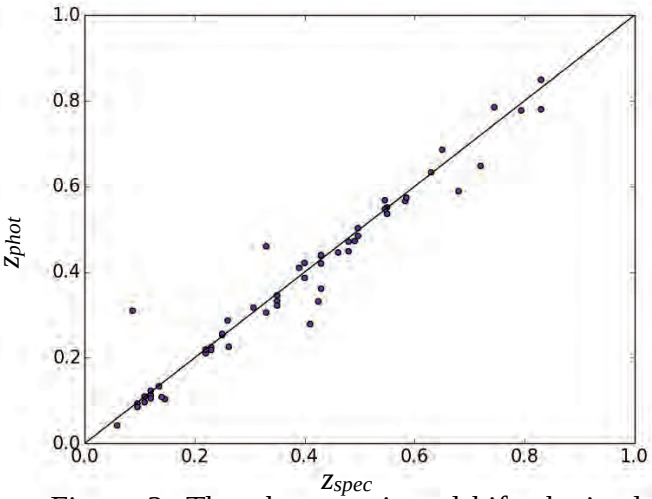

Figure 2: The photometric redshift obtained from GROND is compared with spectroscopic redshifts from literature. The agreement is at the 2-3% level

References:

• Clerc et al. 2012, MNRAS 423, 3545
• Clerc et al. 2012, MNRAS 423, 3561

J. Ridl, N. Clerc

The deepest X-ray catalog of galaxy groups

Ultra-deep observations of ECDF-S with Chandra and XMM-Newton enable a search for extended X-ray emission down to an unprecedented flux of 2 x 10^{-16} ergs/s/cm^2. By using simulations and comparing them with the Chandra and XMM data, we show that it is feasible to probe extended sources of this flux level, which is 10,000 times fainter than the first X-ray group catalogs of the ROSAT all sky survey. Extensive spectroscopic surveys at the VLT and Magellan have been completed, providing spectroscopic identification of galaxy groups to high redshifts. Furthermore, available HST imaging enables a weak-lensing calibration of the group masses.

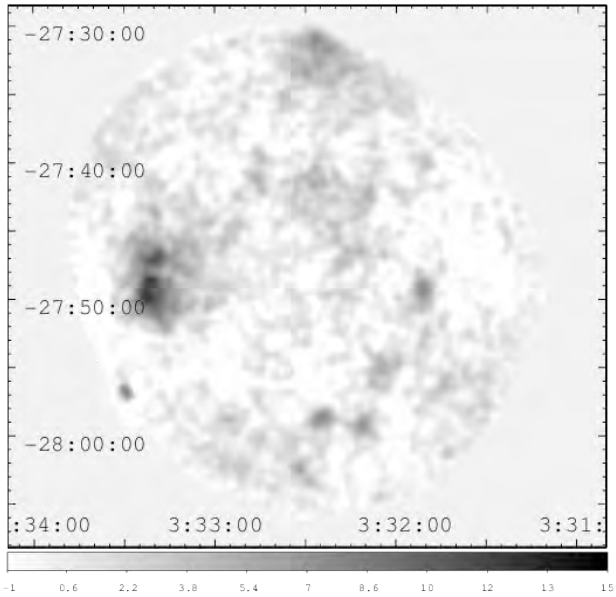

Signal-to-noise of the XMM data after point source removal and smoothing with a 16" Gaussian kernel. The color bar shows the correspondence between the color and the significance of the emission, starting with white for -1 sigma.

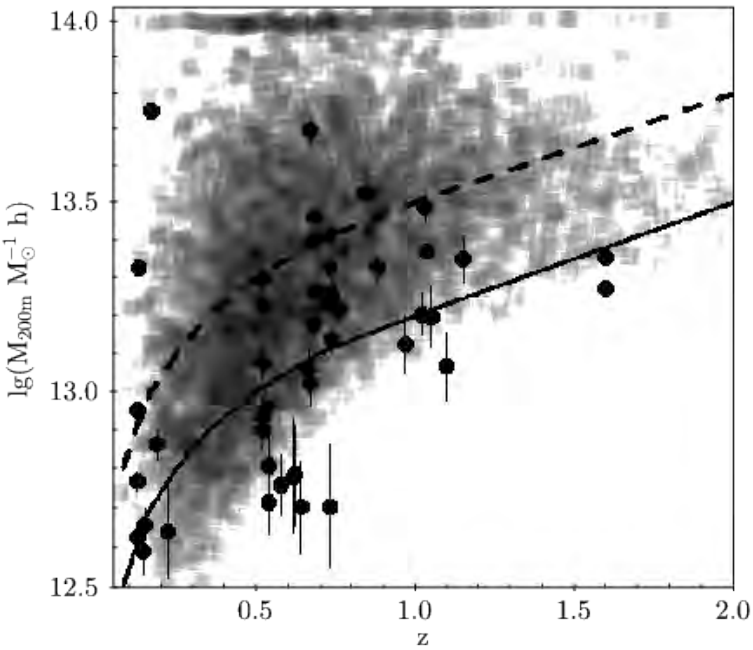

Mass-redshift sampling in the ECDF-S. Grey shadowing indicate the density of detected groups in simulations, with Planck+BAO cosmological parameters and the weak lensing calibrated scaling relations. Solid circles show the parameters of ECDF-S groups. The dashed and solid lines show the location of 90% and 50% detection completeness level.

We present the search for the extended emission on spatial scales of 32" in both Chandra and XMM data, covering 0.3 square degrees and model the extended emission on scales of arcminutes. We present a catalog of 46 spectroscopically identified groups, reaching a redshift of 1.6. We show that the statistical properties of ECDF-S, such as logN-logS and X-ray luminosity function are broadly consistent with LCDM. We present one and two point statistics of the galaxy groups as well as weak-lensing analysis to show that the detected low-luminosity systems are indeed low-mass systems. We verify the applicability of the scaling relations between the X-ray luminosity and the total mass of the group, derived for the COSMOS survey to lower masses and higher redshifts probed by ECDF-S by means of stacked weak lensing and clustering analysis, constraining any possible departures to be within 30% in mass.

References:

• Finoguenov et al. 2015, A&A, 576, 130

A. Finoguenov, et al.

Iron in the hot gas around groups & clusters

We present an analysis of the iron abundance (*Z*) in the high-temperature (*T*) gas surrounding galaxy groups and clusters. To do this, we first compile and homogenise a large dataset of 79 low-redshift systems (159 individual measurements) from the literature. We then compare this dataset to groups and clusters in the Munich galaxy evolution model, *L-Galaxies*.

Our observational dataset reveals a tight *T-Z* relation for clusters (Fig. 1), with a scatter in *Z* of only 0.10 dex and a slight negative gradient. After examining potential measurement biases, we conclude that at least some of this negative gradient has a physical origin. Our galaxy evolution model suggests greater accretion of hydrogen in the hottest systems, via stripping of gas from infalling satellites, as a cause. At lower *T*, *L-Galaxies* over-estimates *Z*, indicating that metal-rich gas removal (via e.g. AGN feedback) is required in galaxy groups.

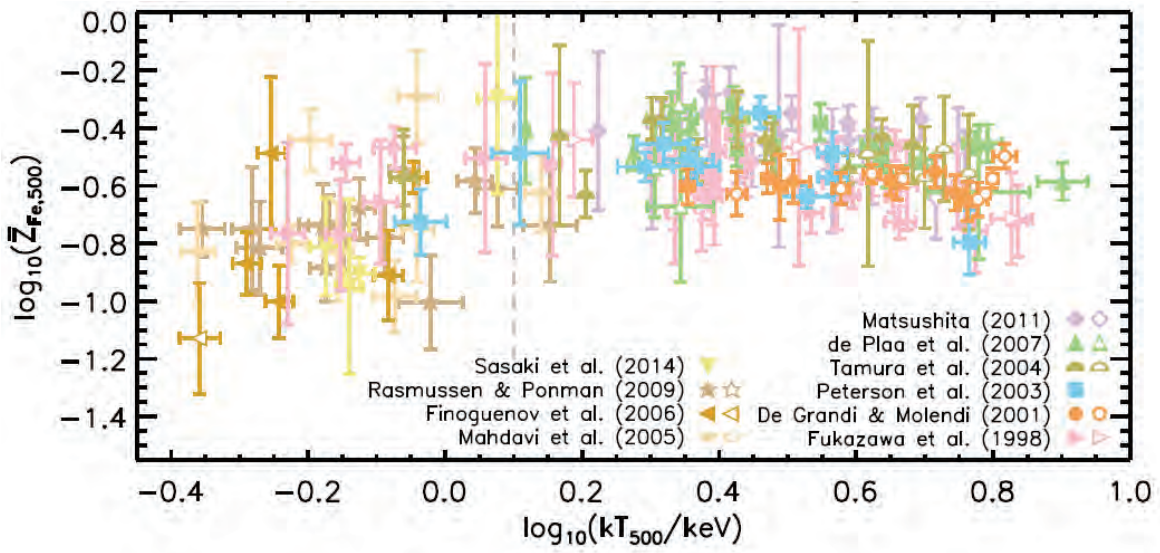

Fig. 1: *The T-Z relation for our observational dataset.*

Our analysis accounts for differences in aperture size, solar abundance, and cosmology, and scales all measurements using customised radial profiles for the temperature, gas density, and iron abundance. This allows us to accurately scale the iron abundances for any systems with X-ray spectra.

In *L-Galaxies*, the iron abundance in clusters at redshift 1 (~7.6 billion years ago) is 79% that seen today.

Our model therefore shows that a significant amount of the metallicity evolution in clusters is complete by redshift 1, as suggested by a number of observational studies.

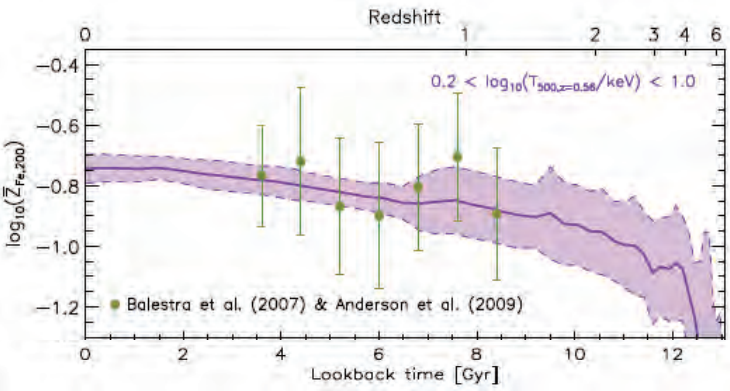

Fig. 2: *Evolution of the iron abundance with time. Green points are observations, purple line represents model clusters.*

Reference:
Yates, Thomas & Henriques, 2016, arXiv: 1602.04858

R. Yates, et al.

Universal accretion on all scales

The central engines of disc-accreting stellar-mass black holes appear to be scaled down versions of the supermassive black holes that power active galactic nuclei. However, if the physics of accretion is universal, it should also be possible to extend this scaling to other types of accreting systems, irrespective of accretor mass, size, or type. We examined new high-time resolution observations, obtained with the space-based mission *Kepler/K2* and ground-based ULTRACAM instrument, of accreting white dwarfs and young stellar objects. Every object in the sample displays the same linear correlation between the brightness of the source and its amplitude of variability (rms-flux relation) and obeys the same quantitative scaling relation as stellar-mass black holes and active galactic nuclei. We show that the most important parameter in this scaling relation is the physical size of the accreting object, rather than its mass as previously thought. This establishes the universality of accretion physics from proto-stars still in the star-forming process to the supermassive black holes at the centers of galaxies.

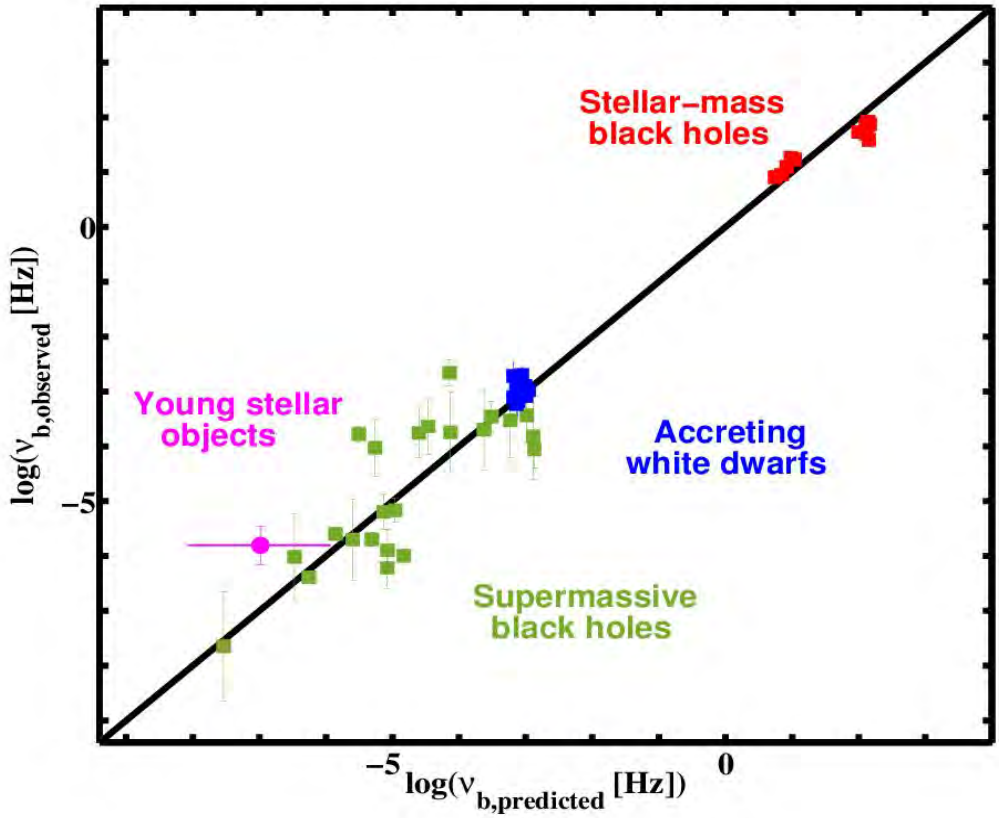

The accretion variability plane showing the observed characteristic bend frequencies in the power spectral densities of accreting systems versus the predicted ones. The predicted values are derived by inserting the observed masses, radii, and mass accretion rates into the best-fit relationship obtained by combining supermassive black holes, stellar-mass black holes, and accreting white dwarfs. If the predicted and observed bend frequencies are identical, then an object will exactly lie on the black line. Additionally shown is the position of the young-stellar object V866 Sco with the filled magenta circle. This demonstrates that the variability plane of accreting systems extends from supermassive black holes all the way to young-stellar objects.

References:

- Scaringi et al. 2015, *Science Advances*, e1500686

S. Scaringi, et al.

X-ray Reverberation around Accreting Black Hole Systems

Comptonized X-ray emission from accreting black hole (BH) systems shows strong, aperiodic variability on a wide range of time scales. This variable primary X-ray radiation, produced in an optically thin plasma of unknown geometry (corona), interacts with any surrounding matter, including the accretion disc. Light travel time delays are expected between the primary and the reprocessed emission in the disc. Hence, these reverberation lags can be used to map the inner regions of the accretion flow. Following our discovery of a relation between X-ray reverberation lags and BH mass in active galactic nuclei (AGN), we used this powerful diagnostic tool to study the geometry of smaller size BH-accreting systems. We obtained the first significant detection of reverberation in an ultra luminous X-ray source (ULX), confirmed the presence of reverberation lags in black hole X-ray binaries (BHXRBs), and revealed the existence of a trend of reverberation lag amplitude with luminosity in the hard state. The latter gives indirect evidence of evolving disc geometry during the outburst.

We detected a soft X-ray reverberation lag of ~5 s in the ULX NGC 5408 X-1 (De Marco et al. 2013b). This suggests that reverberation lags are a common feature of accreting systems. The lag implies a distance of the primary-to-reprocessed emission regions of 10–100 r_g if the central object is an intermediate mass BH of $10^{3\text{-}4}$ $M_\odot$ accreting below the Eddington limit (disc reverberation, Fig. 1).

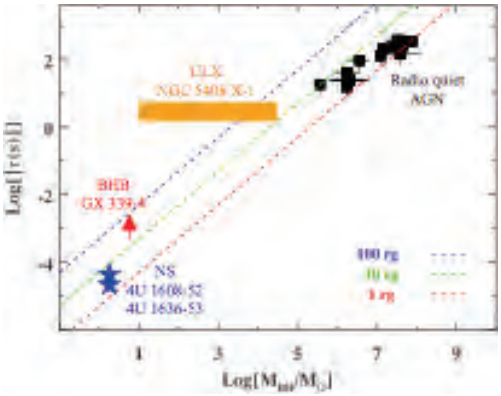

Fig. 1: *Soft X-ray time lags as a function of BH mass for several accreting systems: a sample of radio quiet AGN (De Marco et al. 2013a), two neutron stars (NS de Avellar et al. 2013), and a BHXRB (Uttley et al. 2011; De Marco et al. 2015a).*

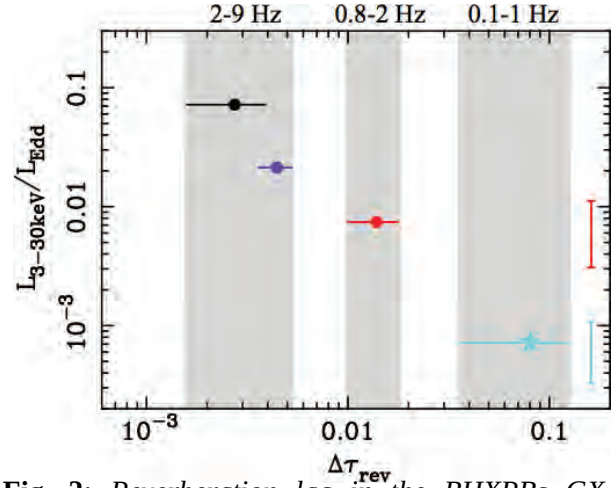

Fig. 2: *Reverberation lag in the BHXRBs GX 339-4 (black, blue, and red dots) and H1743-322 (light blue star) as a function of luminosity. The error bars take into account the uncertainties on the distance and BH mass.*

We systematically studied X-ray lags in a sample of BHXRBs (De Marco et al. 2015a). The XMM-Newton soft X-ray response allowed us to detail the disc variability (De Marco et al. 2015b). A soft reverberation lag ascribable to disc thermal reprocessing is always detected in the hard state, whenever the quality of the data is sufficiently high. The intrinsic amplitude of the reverberation lag decreases as the source luminosity and the disc fraction increase (Fig. 2). This suggests that the distance between the X-ray source and the optically thick disc decreases as the source rises in luminosity throughout the hard state, e.g. as a consequence of reduced disc truncation (De Marco et al. 2015a).

References:

• De Marco B., et al., 2013a, MNRAS, 431, 2441
• De Marco B., et al., 2013b, MNRAS, 436, 3782
• De Marco B., et al., 2015a, ApJ, 814, 50
• De Marco B., et al., 2015b, MNRAS, 454, 2360
• de Avellar, et al., 2013, MNRAS, 433, 3453
• Uttley, et al., 2011, MNRAS, 414, L60

B. De Marco, G. Ponti, K. Nandra

GROND Campaign on MAXI J1305-704

Galactic black hole binaries are predominantly found close the Milky Way disk where strong attenuation prevents their observations at UV/optical wavelengths. Being located in a region with a low Galactic foreground reddening of $E_{(B-V)}$~0.3mag the 2012 outburst of MAXI J1305-704 offered the very rare opportunity for an in-depth view at the UV/optical/NIR evolution of a Low Mass X-ray Binary during its decline from maximum to quiescence.
We provide a glimpse at the wealth of information gathered in a >1 year long monitoring campaign of the transient with the Gamma-Ray burst Optical Near-ir Detector (GROND,[1]) and Swift/UVOT.

The source was discovered as an X-ray transient by MAXI/GSC on 2012 April 9th [2] and its optical/NIR counterpart was identified by us with GROND and Swift/UVOT observations two days later [3]. GROND monitored the target in >300 observations simultaneously in each of the seven filters providing >4000 individual photometric data points (Fig 1.).
The initial brightness of the target allowed mapping the early evolution of the spectral energy distribution (SED) with a time resolution of ~1min revealing a plethora of temporal and spectral variability on different time scales (Fig 2., top) . Spectral template fitting to the GROND SED revealed that the outburst emission was dominated by an accretion disk component with a small (~4% in the i'-band) contribution from a ~4400K donor star (Fig. 3).

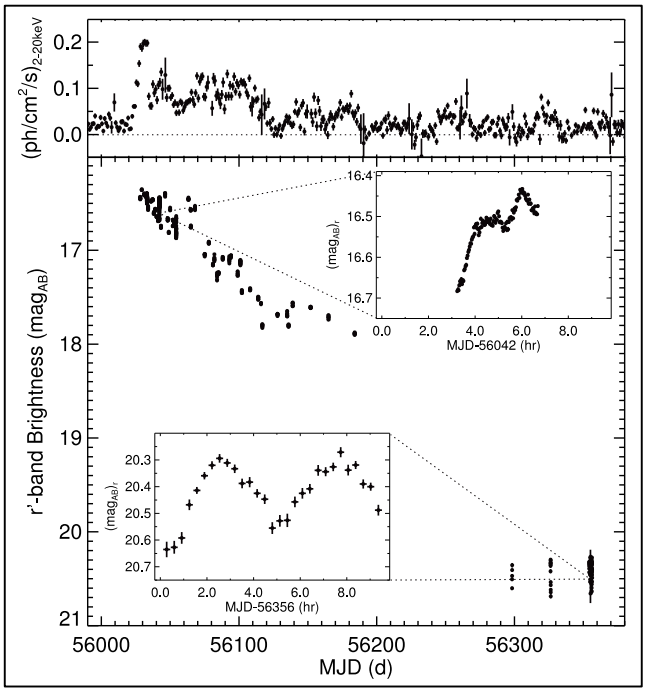

Fig. 1: MAXI/GSC 2-20keV (top) and GROND r'-band (bottom) light curves. Strong short-time variability during the decline from outburst and at late times is demonstrated in the insets.

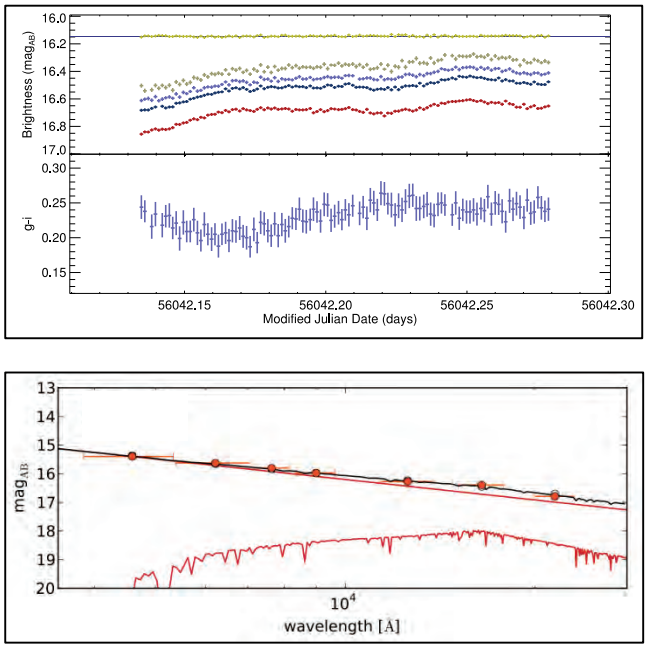

Fig. 2: (Top:) Detailed view at the GROND g'r'i'z' photometry and the g'-i' colour evolution of the top right inset of Fig.1. (Bottom:) Early time spectral energy distribution decomposed in accretion disk component and donor star emission.

Observations during quiescence revealed a clear sinusoidal signature from which an orbital period of 9.45hr was estimated. Comparing the ellipsoidal brightness variations with binary template light curves generated in XRBinary [4] further constrained the orbit inclination to ~81deg [5]. The short orbital period suggests a small binary separation explaining the small absorption radius and high gas densities found in Chandra outburst spectra.
A VLT spectroscopic campaign is scheduled for March 2016 to measure the mass of the accreting black hole from the radial velocity variations of the donor star emission.

References:
1) Greiner et al., 2008, PASP, 120, 405
2) Sato et al. 2012, ATel, 4024
3) Greiner, Rau, Schady, 2012, ATel, 4030
4) Robinson, http://www.as.utexas.edu/~elr/Robinson/XRbinary.pdf
5) Schiegg, 2013, Bachelor Thesis

A. Rau, F. Schiegg, J. Greiner for the GROND Team

Dust Scattering Halo from an Eclipsing X-ray Binary at 1.5 arcmin from Sgr A⋆

AX J1745.6-2901 is an eclipsing neutron star low mass X-ray binary. This source is bright in X-rays and it has a high column density of absorbing gas along the line of sight, showcasing a strong dust scattering halo. Moreover, the dust scattering halo shows time evolution during the eclipsing phase. The combination of these phenomena can provide important information about the location of the neutron star and the dust properties along the line of sight. In this research project, we show that based on a large set of XMM-Newton and Chandra data, we can conduct, for the first time, a powerful combined analysis of the radial profile of the dust scattering halo and the time evolution of the halo during the eclipsing phase. Our study can put constraints on the location of the source, the distribution and composition of the dust, and the metal abundance towards the source. Due to the proximity of the source to the super-massive black hole Sgr A⋆ in the Galactic centre, these properties are highly relevant to the dust in the Galactic centre, and especially relevant to the dust on the line of sight towards Sgr A⋆.

We extract the radial profile of AX J 1745.6-2901 during its eclipsing period and compare it with the radial profile in the normal period (figure on the left below). The result clearly suggests that there should be multiple dust components on the line of sight to the binary system.

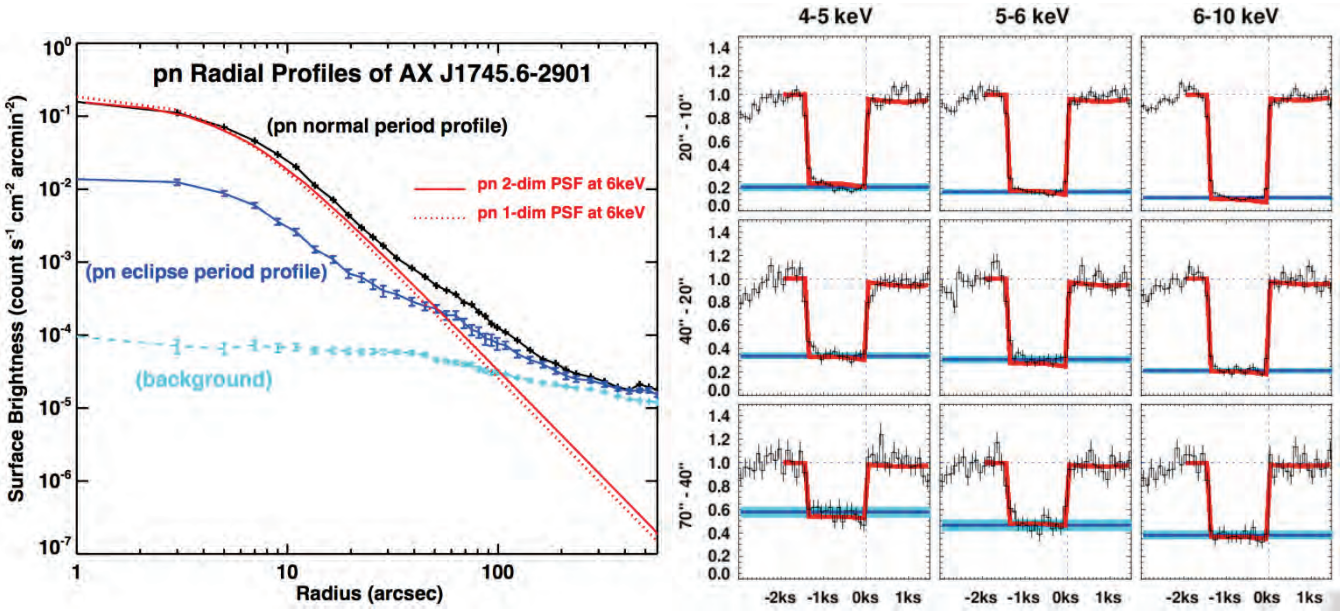

A rare phenomenon in AX J1745.6-2901 is the residual flux during its eclipsing phase. The mechanism of this flux was speculated to be dust scattering. Based on the dust models constrained by the radial profile, we can simulate the response of the dust scattering to any specific eclipsing signal. The right figure above shows the eclipsing shape of the source at various energy bands and radial distances, overlaid by the result of our simulation. It is the first time that a dust scattering model can reproduce not only the observed radial profile, but also the eclipsing phenomena in the dust scattering halo. Combining the real data and simulation, we are able to obtain strong constraints on the location of the source and the distribution and composition of the dust on the line of sight towards the Galactic center, and especially towards the Sgr A⋆ – the super massive black hole in the center of our Milky Way.

References:

• Hyodo et al., 2009, PASJ, 61, 99 • Ponti et al., 2015, MNRAS, 446, 1536 (2015) • Smith, 2008, ApJ, 681, 343
• Mathis & Lee,1991, ApJ, 376, 490 • Ponti et al., 2015, MNRAS, (arXiv:151102855)

C. Jin, G. Ponti, F. Haberl

LS 5039 – the Counterpart of the Unidentified MeV Source GRO J1823-12

MPE's COMPTEL aboard CGRO observed the soft gamma-ray sky (0.75 - 30 MeV) for more than 9 years. COMPTEL detected many gamma-ray sources, among them an unidentified one labeled GRO J1823-12, positional consistent with the prominent gamma-ray binary LS 5039. A recent reanalysis of the COMPTEL data identified GRO J1823-12 as being the MeV counterpart of LS 5039 via its orbital variability of 3.9 days. The COMPTEL fluxes, put into multifrequency perspective, provide new constraints on the SED modelling (X-rays to TeV gamma-rays) of the peculiar high-energy emission pattern of LS 5039.

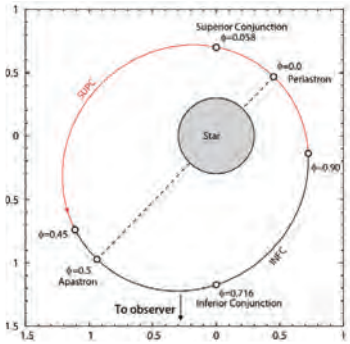

The unidentified COMPTEL MeV source, GRO J1823-12, is positional consistent with the prominent γ-ray binary LS 5039. LS 5039, a high-mass X-ray binary system, was established as a γ-ray source at TeV energies by HESS (Aharonian et al. 2005) and at GeV energies by Fermi/LAT (Abdo et al. 2009) during recent years, whose γ-radiation is modulated along its binary orbit (Fig. left). Given this new information we reanalysed the COMPTEL data of GRO J1823-12 including orbital resolved analyses.

The COMPTEL results (Collmar et al. 2014) show a significant MeV source (lower Figs., upper left), which is positional consistent with LS 5039, but also with other close-by Fermi/LAT sources. The orbit-resolved analysis shows that the MeV flux of GRO J1823-12 is modulated along the binary orbit of 3.9 days of LS 3059 (lower Figs., lower left), proving its binary nature. At MeV energies the source is brighter at the orbital part around inferior conjunction than at the part of the superior conjunction. So, it is in phase with X-rays and TeV γ-rays, but in anti-phase with GeV γ-rays. The high-energy SED (lower Figs., right) from X-rays to TeV γ-rays shows the high-energy emission maximum of LS 5039 to be at MeV energies, i.e. showing a spectral turnover there. The inclusion of the COMPTEL fluxes into the SED provides severe new constraints on the modelling of the peculiar high-energy emission pattern of the γ-binary LS 5039, which is not yet understood.

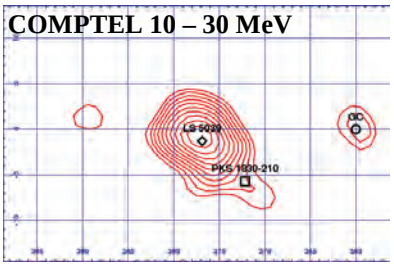

b

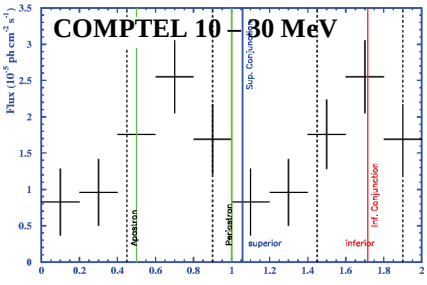

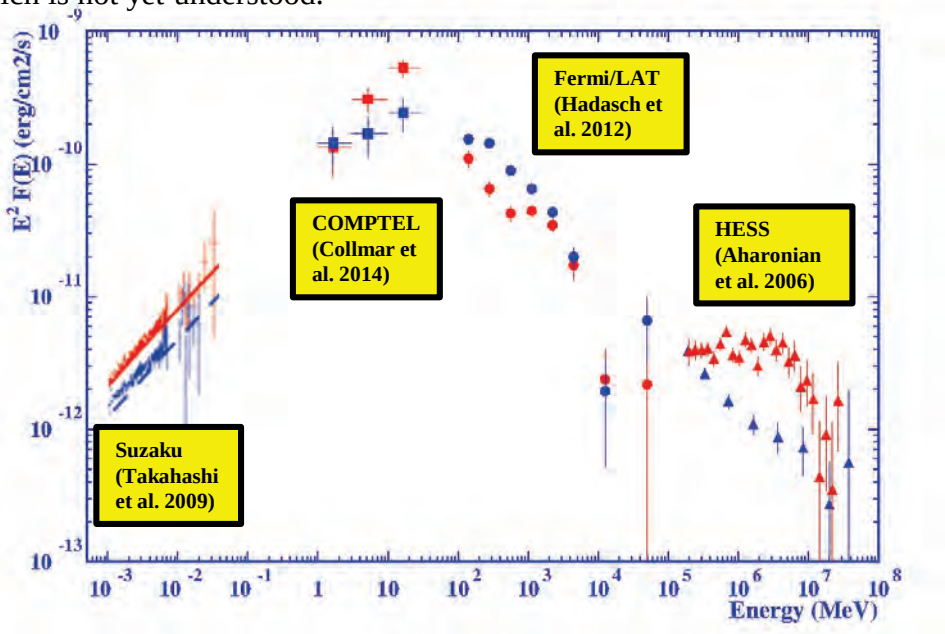

References:

● Aharonian et al. 2005, Science 309, 746 ● Abdo et al. 2009, ApJ 706, L56 ● Collmar et al. 2014, A&A 565, A38

W. Collmar, et al.

Gamma-ray source populations in the Galaxy

The Fermi-LAT gamma-ray instrument has detected over 3000 sources, about 260 of which are Galactic, many others are unidentified. However the Galaxy contains tens of thousands of sources, most of which are below the Fermi detection threshold, but which contribute to the Galactic 'diffuse' emission. Our population synthesis studies address this subject.

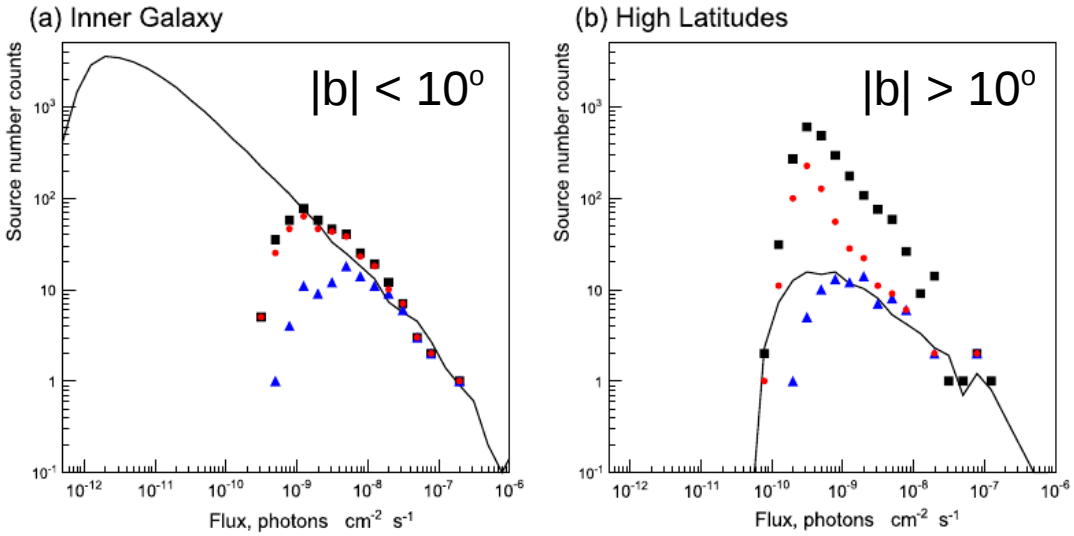

Gamma-ray source number counts (per 0.2 dex) as a function of flux S > 1 GeV.
a) inner Galaxy, b) high latitudes. Curve: model.
Data: *3FGL*: blue: Galactic sources, red: Galactic + unidentified sources,
Black: all sources including extragalactic. From Acero et al. (2015).

The 3rd Fermi-LAT gamma-ray source catalogue (*3FGL*) includes about 260 Galactic and many unidentified sources, out of a total of over 3000 sources; however the Galaxy surely contains many thousands of sources below the LAT detection threshold. These contribute to the Galactic 'diffuse' emission, most of which is interstellar, from interactions of cosmic rays with gas and radiation. Studying the unresolved populations is therefore important both for the source content of the Galaxy and to account for in interstellar work. It also helps reveal the nature of the unidentified sources.

A gamma-ray source population synthesis code has been developed, computing the sources for a given luminosity function and spatial distribution; these are broadly based on those observed for pulsars but are not restricted to those. Comparing the model gamma-ray source differential number counts *N(S)* with those observed in *3FGL* puts significant constraints on the possible parameters of the populations. In particular, low latitude *N(S)* constrains the high-luminosity, low space-density sources, while high latitude *N(S)* constrains the low-luminosity, high space-density sources, as shown in the figure.

A typical model consistent with *3FGL* has a power-law luminosity function with index -1.8 and a luminosity range 10^{32}-10^{37} erg s^{-1} above 1 GeV, and a space density of 100 kpc^{-3}. The total source content of the Galaxy is ~30000. Using this model, it is estimated that 3-5% of the Galactic diffuse emission originates in unresolved sources, but this is strongly energy-dependent.

References:

- Strong. A.W. , 2007, Ap.Sp.Sci. **309**, 35
- Acero, F., et al., (Fermi-LAT Collaboration, *3FGL)*, 2015, Ap.J.Supp. **218**, 23

A. Strong

The high mass X-ray binary population of the Large Magellanic Cloud

We present an overview of our investigation of the high-mass X-ray binary (HMXB) population in the Large Magellanic Cloud (LMC). Using multi-wavelength observations we have expanded the sample of previously known HMXB systems of the LMC. The updated catalog consists of ~18 confirmed HMXB pulsars and 45 candidate systems. Using this up-to-date HMXB census we derived the statistical properties of the population, like the spin period and orbital period distributions.

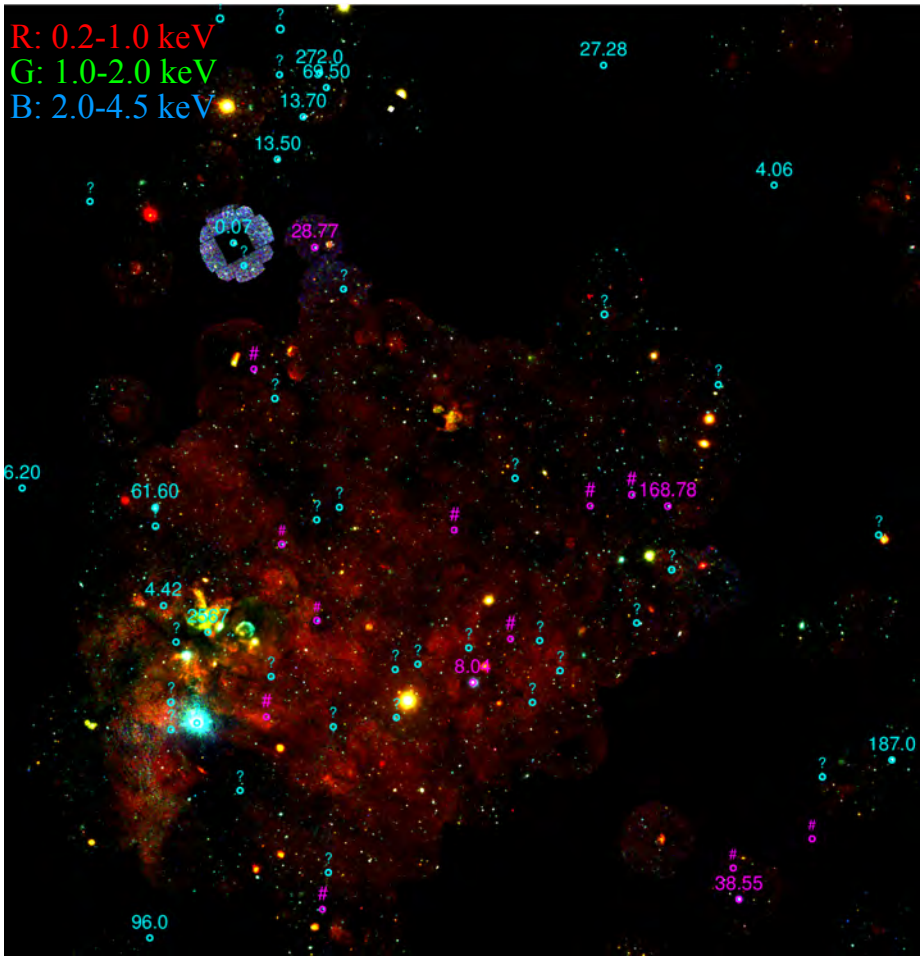

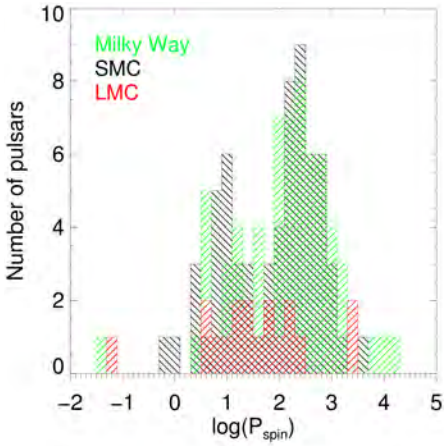

Left: XMM-Newton mosaic of the LMC, composed of archival observations plus 70 pointings from the VLP survey program (PI: F. Haberl). The survey pointings added the discovery of 4 confirmed BeXRB pulsars [1,2,3,4,5] and 11 good candidate systems (magenta points). Cyan points indicate confirmed and candidate systems prior to the LMC survey.

Up-Right: Spin period distribution of HMXB pulsars in the LMC, SMC and Milky Way.

The selection of the HMXB systems was based on the X-ray and optical properties of the detected sources and their optical counterpart, i.e. hard X-ray sources correlated with early type stars. To support our initial classification we performed follow-up observations in optical, infra-red and X-ray wavelengths. All the new HMXB candidates display either (i) long-term X-ray variability, (ii) moderate H_{alpha} emission, (iii) periodic behaviour in their optical light-curve.

We further monitored the strongest candidates in the X-rays searching for possible X-ray outbursts using *Swift* space observatory. For systems for which the X-ray luminosity exceeded 10^{36} erg/s we triggered XMM-Newton ToO observations. These ToO observations revealed intriguing characteristics in the X-ray spectra of the systems (e.g. emission lines from hot plasma, strong variability with spin phase), while resulting in successfully measuring the spin period of the neutron star of the HMXB system.

References:

- 1: Maggi et al. 2013 A&A 554A,1M
- 2: Vasilopoulos et al. 2013, A&A 558A,74V
- 3: Vasilopoulos et al. 2014, A&A 567A,129V
- 4: Vasilopoulos et al. 2016, submitted to MNRAS
- 5: Vasilopoulos et al. 2016, submitted to A&A

G. Vasilopoulos, F. Haberl, P. Maggi

High-mass X-ray binaries in the Small Magellanic Cloud

The large population of high-mass X-ray binaries (HMXBs) in the Small Magellanic Cloud (SMC), in particular Be/X-ray binaries (BeXRBs), provides the largest homogeneous sample of such systems in any nearby galaxy for statistical population studies. After our survey of the SMC with XMM-Newton, which revealed 45 new HMXB candidates, we investigated the multi-wavelength properties of 148 confirmed and candidate HMXBs, to shed light on the real nature of the X-ray sources. Our final catalogue comprises 121 relatively high-confidence HMXBs (the vast majority with Be companion stars). For about half of the objects X-ray pulsations are not detected yet.

Based on the sample of well-established and optically identified HMXB pulsars (63 are known in the SMC today, see Fig. 1), we investigated which observed properties are most appropriate for a reliable classification of such systems. We defined different levels of confidence for a genuine HMXB based on spectral and temporal characteristics of the X-ray sources and colour-magnitude diagrams from the optical to the infrared of their likely counterparts. E.g. using U, B and V colours of the optical counterparts we find a significant difference of the derived Q-parameter distribution for class I (clearly identified BeXRB pulsars) and class VI (low confidence BeXRB candidates) as shown in Fig. 2.
The infra-red excess, which is seen from BeXRBs as emission from the circum-stellar disc, can be characterized using Spitzer IRAC and 2MASS fluxes. We finally identify 27 objects that probably are misidentified because they lack the infrared excess of the proposed counterpart.

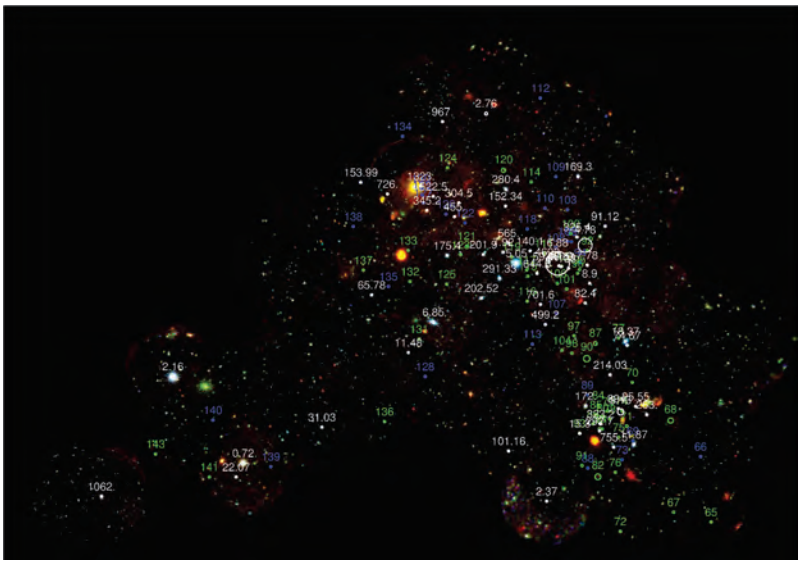

Fig. 1: Distribution of high-mass X-ray binaries in the SMC. Pulsars are marked in white with their pulse periods in seconds. Green and blue colours indicate candidate systems with high and lower levels of confidence for a HMXB nature. The colour image represents the combined EPIC mosaic image obtained from the XMM-Newton survey of the SMC.

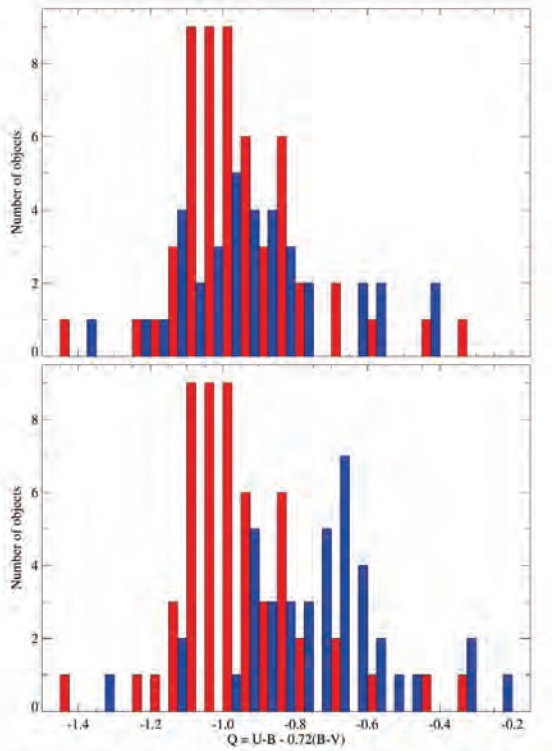

Fig. 2: Distribution of the reddening-free Q parameter for different HMXB confidence classes. The top panel compares the pulsars (class I) with identified optical counterpart (red) with objects from classes II to V (blue), while in the bottom panel the comparison with class VI is shown.

References:

• Sturm R., Haberl F., Pietsch W., et al., 2013, A&A 558, A3
• Haberl F. & Sturm R., 2016, A&A 586, A81

F. Haberl, R. Sturm

Studying magnetic CVs using GROND

A project to improve our knowledge on the spatial distribution of magnetic cataclysmic variables (mCVs) in our galaxy has been set up. For this project we use MPEs 7 channel (g, r, i, z, J, H, K) imager GROND that is mounted on the ESO/MPI 2.2m telescope in La Silla Chile which allows us to obtain time resolved light curves of the individual objects in our sample. Using the data taken in 7 bands simultaneously enables us to put constraints on the system geometry, determine the distance to the objects from the K band brightness of the secondary star obtained during eclipses of the WD and in the faint - low accretion state, as well as improve the ephemerides of the objects to better relate the optical data to observations taken at different times using space telescopes.

Currently there is a discrepancy between the standard model for the population of CVs that predicts a vast number of short- period systems, Porb < 2 h, and a high space density of $\sim 10^{-5}$–10^{-4} pc^{-3} and the observed CV population, with an estimated space density of $\sim 6\times10^{-6}$ pc^{-3}, or 5×10^{-7} pc^{-3} for polars (Pretorius et al. 2013). The main reason for this difference is that theoretical predictions are selection effects such as flux limitation. As long as trigonometric parallaxes do not become available also for the fainter CVs, infrared photometry is the only way to get the distance to magnetic CVs using the relationship between the distance and K-band surface brightness of the secondary star, its radius and the observed K-band color as given in Ramseyer 1994. Below first results from observations using GROND (see Fig. 1 and 2) that will provide us with improved distances to the mCVs are shown.

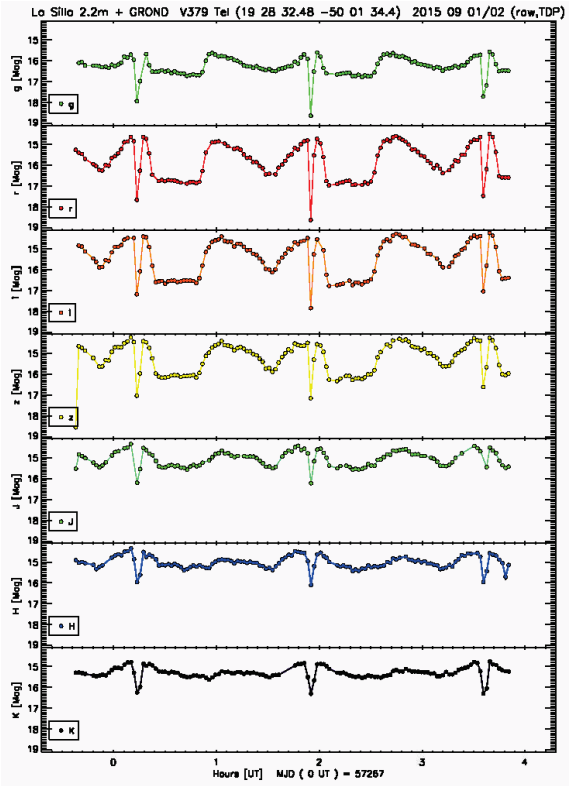

Fig. 1: GROND light curve of the eclipsing polar V378 Tel obtained in May and September 2015: Note that the eclipses are clearly visible in the IR.

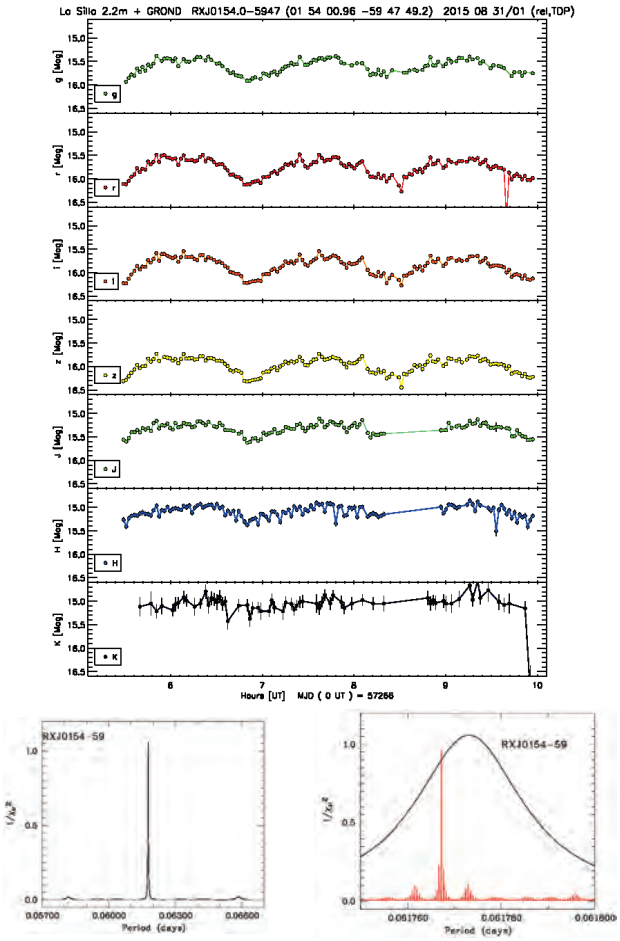

Fig. 2: (top) RX JO152-59 GROND Sept. 2015 Lightcurve. (bottom, left) Periodogram using just the Aug/Sep 2015 GROND and WFI r-band data. (bottom,right) 2015 data combined with data from light curves going back to 1993.

References:

•Kolb, U., 1993, A&A, 271, 149K
•Pretorius, M.L. et al., 2013, MNRAS, 432, 570P
•Ramseyer, T.D., 1994, ApJ, 425, 243R

V. Burwitz, J. Greiner, D. Z. Camurdan

The population of supernova remnants in the Large Magellanic Cloud

Supernova remnants (SNRs) release tremendous amounts of kinetic energy and freshly-produced heavy elements into the interstellar medium (ISM), and accelerate cosmic-rays. They are a key component of the chemical and thermodynamical evolution of the ISM in galaxies. Surveyed recently with an XMM-Newton Very Large Programme (VLP), the Large Magellanic Cloud (LMC) offers an ideal laboratory for the study of a complete population of SNRs. We showcase results from the first systematic X-ray analysis of the LMC SNR population.

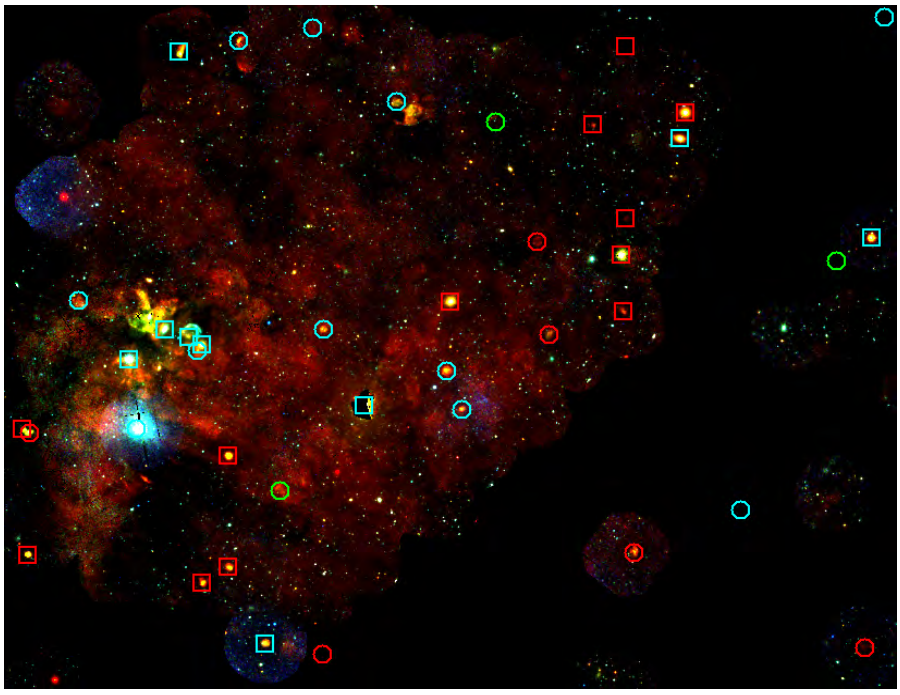

Fig. 1: The XMM-Newton mosaic of the LMC (RGB: 0.2-1 keV, 1-2 keV, 2-4.5 keV). We combined all archival observations with the 70 pointings from the VLP survey (PI: F. Haberl), providing a homogeneous covering of the central region. Our collaboration increased the number of SNRs in the LMC to 59: Five sources were discovered serendipitously in the VLP survey (Maggi et al. 2012, 2014), and seven candidates were confirmed (e.g. Bozzetto et al. 2014, Kavanagh et al. 2013, 2015). The locations of SNRs are marked: In red, those originating in a type Ia supernova (SN); in cyan, the remnants of core-collapse SNe. A square is used if the classification is secure, a circle if it is only tentative (unknown origin in green).

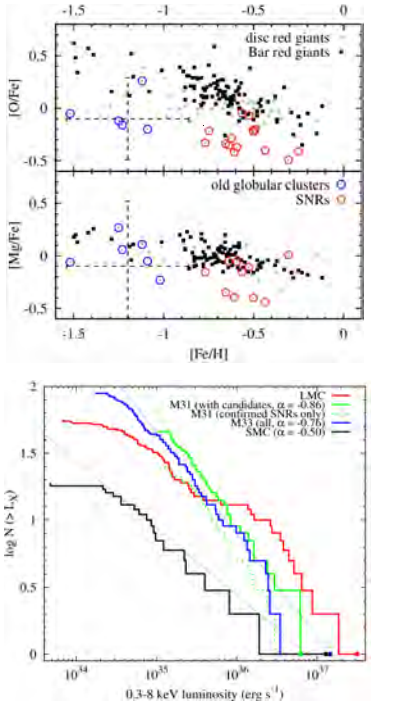

Fig. 2: Top: LMC abundance ratios of O and Fe as a function of metallicity, for populations of various ages. **Bottom:** Cumulative X-ray luminosity functions of SNRs in Local Group galaxies. The LMC stands out with an excess of bright SNRs and a significant flattening at the faint end.

The homogeneous analysis of X-ray spectra of the entire population (Maggi et al. 2016) allows for the first time meaningful comparisons of temperature, chemical composition, and luminosity of LMC SNRs. We measured chemical abundances in the hot phase of the LMC using SNRs. Compared to older populations, the SNR-derived abundances ratios reflect the continued iron enrichment by type Ia Sne (Fig. 2, top). We devised a new method to tentatively type all SNRs, based on their local stellar environment. Thus, we can constrain the ratio of core-collapse to type Ia SN rates to N_{CC}/N_{Ia}=1.35 (-0.24/+0.11). The relatively high type Ia rate is attributed to the specific star formation history of the LMC. Finally, we compared SNRs in the LMC to other Local Group galaxies with different metallicities and star formation properties (Fig. 2, bottom).

References:

- Maggi, P., et al. 2012, A&A 546, A109
- Maggi, P., et al. 2014, A&A 561, A76
- Maggi, P., et al. 2016, A&A 585, A162
- Bozzetto, L. M., et al. 2014, MNRAS 439, 1110
- Kavanagh, P. J., et al. 2013, A&A 549, A99
- Kavanagh, P. J., et al. 2015, A&A 573, A73

P. Maggi, F. Haberl, G. Vasilopoulos, W. Pietsch, J. Greiner

Supernova remnants in the Milky Way

High-mass stars strongly influence and shape the interstellar medium (ISM) in their vicinity. Stellar winds and supernova explosions form cavities around stellar groups enclosed by shells which mainly consist of neutral hydrogen (HI). The size of these shells can reach several 100 pc for massive stellar populations. In our work we search for HI shells in the Milky Way using the new Effelsberg Bonn HI Survey (EBHIS) and the Galactic All-Sky Survey (GASS) which trace the galactic distribution of 21 cm line emission of HI. We use a new method based on the assumption that shells are not necessarily closed but can be composed of arclike structures. An edge detection algorithm is applied in order to find circle- or arclike structures in individual spectral channels of the HI data. Nearby circles within consecutive channels are connected representing expanding shells. The result is a catalogue of HI shells from EBHIS+GASS. As an interim result the detected shells from the old Leiden Argentine Bonn (LAB) HI survey are plotted in Fig. 1 on top of the total HI column density of the Milky Way. A total amount of 432 shell candidates are identified in the range of -100 km/s < V_{LSR} < +100 km/s.

Figure 1

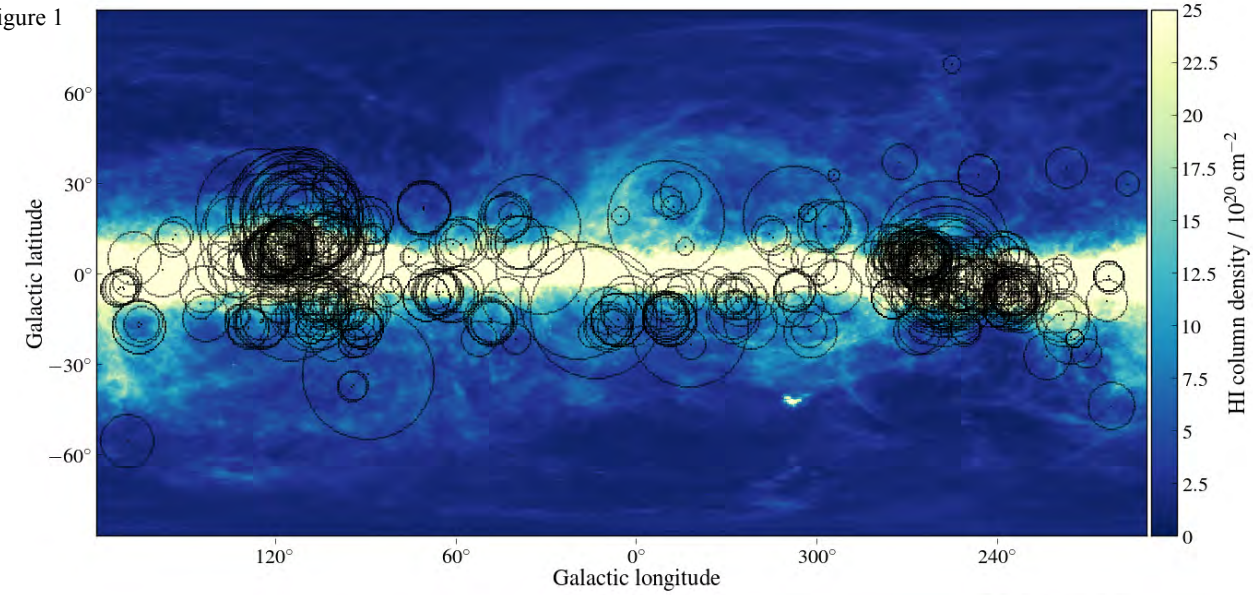

The ISM in the vicinity of the Scorpius Centaurus OB association (fig. 2) especially around the Upper-Sco subgroup is investigated in more detail. Sodium absorption line data, together with a parametrisation of a homogeneous expanding spherical shell model are fitted to the data in order to get additional information about the parameters of the shell which are the distance, the expansion velocity, the center velocity, the density, the coordinates of the center in galactic longitude and latitude, the inner radius and the thickness. These parameters are fitted to the data using a Markov Chain Monte Carlo algorithm. The results are listed below.

D_0 = (138±26 pc), V_{exp} = (7.1±1.1) km/s, V_0 = (8±0.9) km/s,
ρ = (6±2) HI/cm^3, l_0 = (347±0.5)°, b_0 = (25±0.5)°,
R_{in} = (12.33±0.69)°, Δr = (2.73±0.32)°

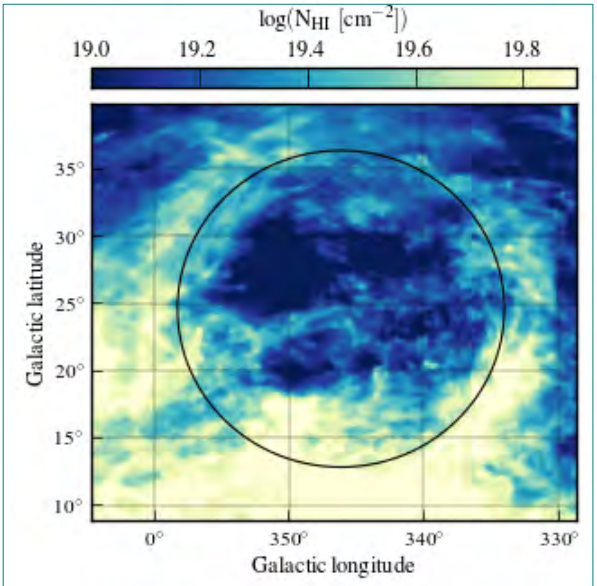

Fig.2 Channelmap of the ISM in the vicinity of the Upper Scorpius region. The shell is indicated by the black circle.

References:

- Winkel, B., Kerp, J., Flöer, L., et al. 2016, A&A, 585, A41
- Kalberla, P. M. W. & Haud, U. 2015, A&A, 578, A78
- Pöppel, W. G. L. et al.. 2010, A&A, 512, A83

D. Kröll, R. Diehl, J. Kerp, T. Siegert

Interplanetary GPS Using Pulsar Signals

With an ever increasing number of Earth satellites and deep space probes, autonomous methods of spacecraft navigation are getting more and more important. An external reference system suitable for deep space navigation can be defined by millisecond pulsars. They have timing stabilities comparable to atomic clocks and provide characteristic temporal signatures that can be used as natural navigation beacons, quite similar to the use of GPS satellites for navigation on Earth. A spacecraft that carries the means to detect and analyse the periodic pulsar signals can determine its position and velocity by comparing pulse arrival times measured on-board with those predicted at a reference location. Position accuracies of the order of 30-300 m are possible. In contrast to standard navigation methods based on radio tracking, pulsar-based navigation can operate autonomously. This is particularly interesting for space missions that require a higher degree of autonomy, e.g. exploration of the outer solar system or manned missions to Mars, but can also be beneficial as augmentation of existing space technologies, such as GPS and Galileo.

Range difference along the line of sight to the pulsar:

$$\Delta x \approx cP(\Delta\phi + n)$$

Phase Shift

Pulse Period

$n = 0, \pm1, \pm2\ldots$ (multiple solutions)

For 3D position at least 3 pulsars have to be observed. More pulsars are needed, if multiple solutions occur.

Position determination in space:

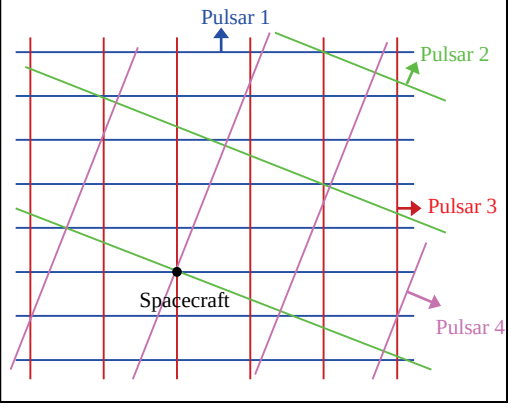

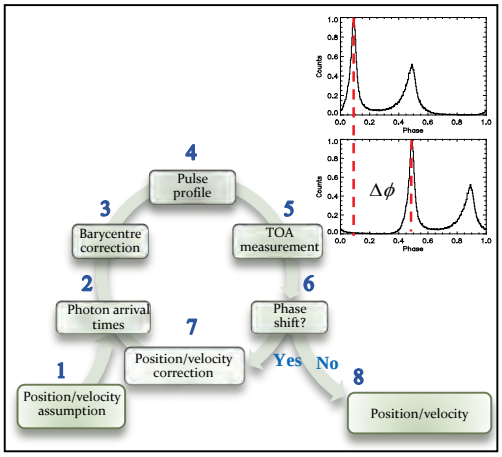

As pulsars emit broadband electromagnetic radiation from radio to X- and γ-rays, a pulsar-based navigation system can be designed for any energy band that is optimal in terms of pulsar characteristics (luminosity, pulse shape, pulse period etc.), hardware specifications (type and collecting power of the antenna, temporal resolution of the detector etc.) as well as boundary conditions given by the spacecraft (size, weight, power consumption etc.).

We have been analysing the performance of pulsar-based navigation systems as a function of these parameters by simulating pulse profiles as measured by an arbitrarily moving virtual observer. According to our studies, an implementation of this novel technology seems particularly promising in the light of new telescope and detector developments, such as low-mass X-ray mirrors and active pixel detectors developed e.g. for the Athena mission. Our research project aims at proposing telescope/detector configurations feasible for application in future pulsar-based navigation systems.

Most recent reference:

W. Becker, M. G. Bernhardt, A. Jessner, 2015. Interplanetary GPS Using Pulsar Signals. Astron. Nachr., Vol 336, Issue 8/9, pp.749-761

W. Becker, M. G. Bernhardt

Accreting Magnetars

We assume that the quiescent emission of magnetars (i.e. soft gamma-ray repeaters (SGRs) and anomalous X-ray pulsar (AXPs)) is produced by accretion from a fall-back disk. This model requires „normal“ dipole fields (10^{12} – 10^{13} G) of the neutron star and explains the super-Eddington bursts by explosions in multipole magnetic fields. The quiescent emission of these sources consists of two distinct spectral components: (1) a hard X-ray emission (10-150 keV) which is produced by thermal and bulk Comptonization in the accretion shock and forms a fan beam, and (2) a soft component (0.5-10 keV) emitted by the polar cap which is heated by the fan beam (Fig. 1). Following earlier work (FBR 2013) we present here the results of an analysis of the broad band X-ray spectra of 5 AXPs and SGRs observed by RXTE, Integral ISGRI and Suzaku (Figs. 2-6), which show that our model spectra provide good fits to the observed data, providing further evidence that AXPs and SGRs are accreting pulsars.

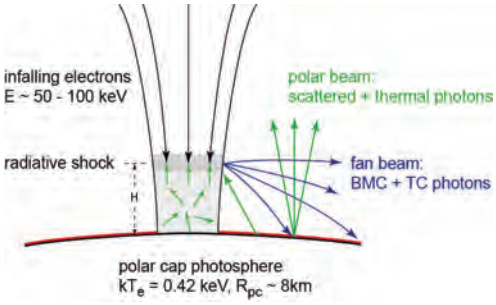

Fig.1

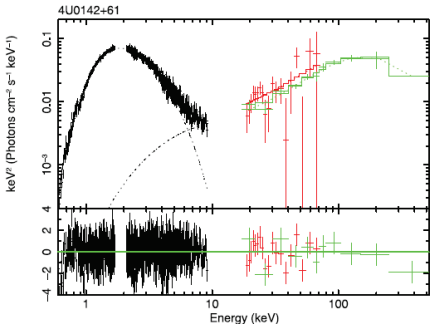

Fig.2

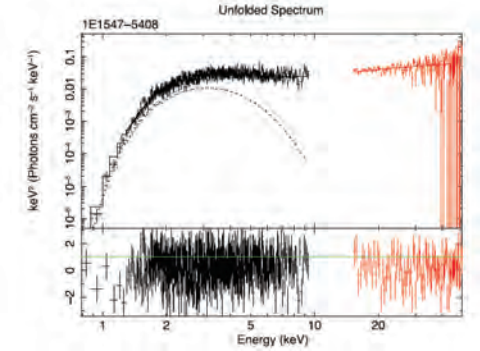

Fig.3

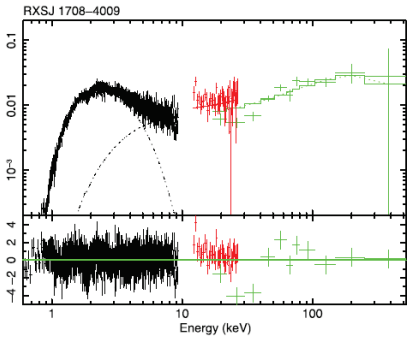

Fig.4

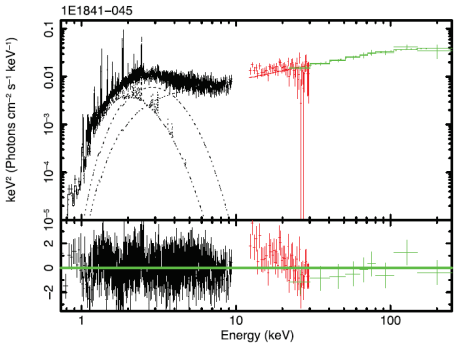

Fig.5

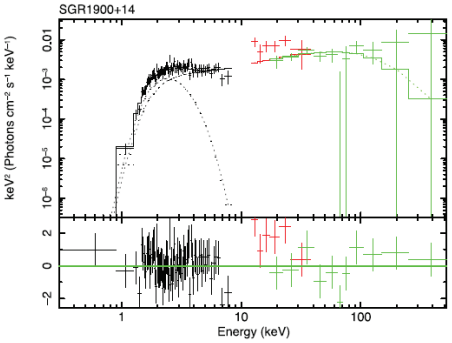

Fig.6

Figs 2-6: Broad band spectra from Suzaku XIS (black) and HXD (red), as well as Integral ISGRI (green), along with the best fitting spectral models

References: Zezas, A., Trümper, J.E. & Kylafis, N.D., 2015, MNRAS 454, 3366-3375
Kylafis, N.D., Trümper, J.E. & Ertan, Ü., 2014, A&A 502, A62

A. Zezas, J. E .Trümper, N. D. Kylafis

A very luminous magnetar-powered Supernova associated with an ultra-long Gamma-Ray Burst

The combination of very high luminosity and very blue spectrum of the supernova (2011kl) related to the ultra-long GRB 111209A cannot be explained with powering through ^{56}Ni-decay. This opens interesting connections to superluminous supernovae and magnetars.

A new class of ultra-long-duration (>10 ks) gamma-ray bursts (GRB) has recently been suggested. It was speculated that they originate in the explosion of stars with much larger radii than those producing normal long-duration GRBs or in the tidal disruption of a star. With GROND we found a supernova (SN 2011kl) associated with the ultra-long-duration GRB 111209A, at a redshift z =0.677. This SN is more than three times more luminous than type Ic SNe associated with long-duration GRBs, and its spectrum is distinctly different. The slope of the continuum resembles those of super-luminous SN, but extends further down into the rest-frame ultraviolet implying a low metal content. This combination of high luminosity and low metal-line opacity cannot be reconciled with typical type Ic SN (powered by Nickel decay), but can be reproduced by a model where extra energy is injected by a strongly magnetized neutron star (a magnetar), which has also been proposed as the explanation for super-luminous SNe.

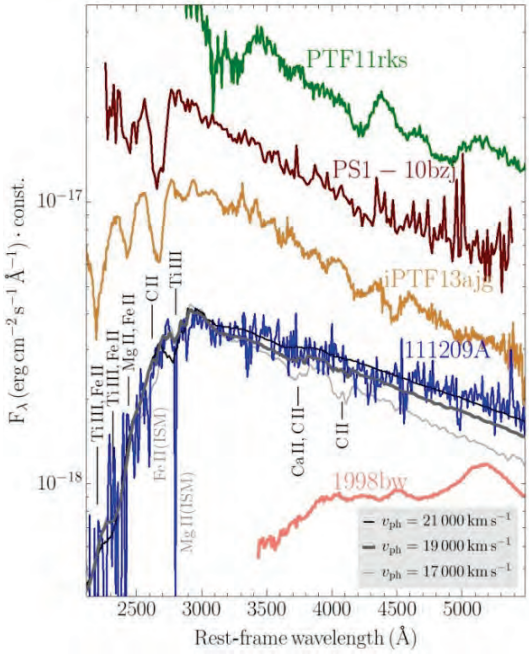

Fig. 2: VLT/X-shooter spectrum of SN 2011kl compared to other SLSNe. The blue spectrum suggests little ejecta, incompatible with the light curve modelling (Fig. 3)

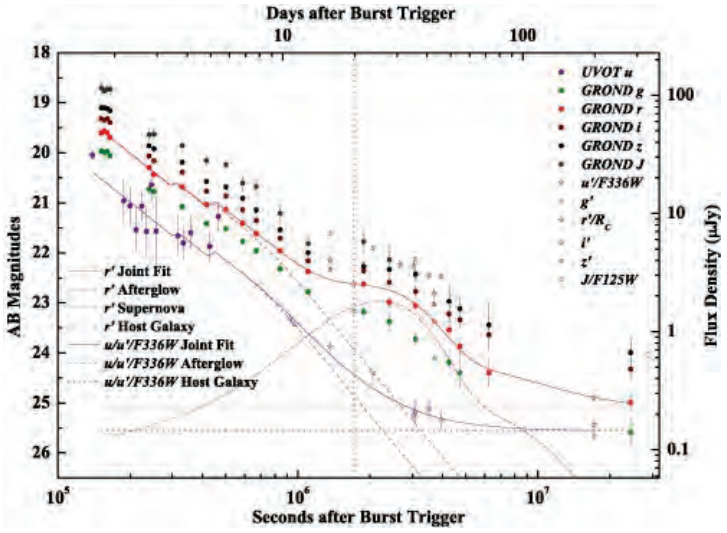

Fig. 1: GROND light curve of the GRB 111209A afterglow and the related supernova SN 2011kl.

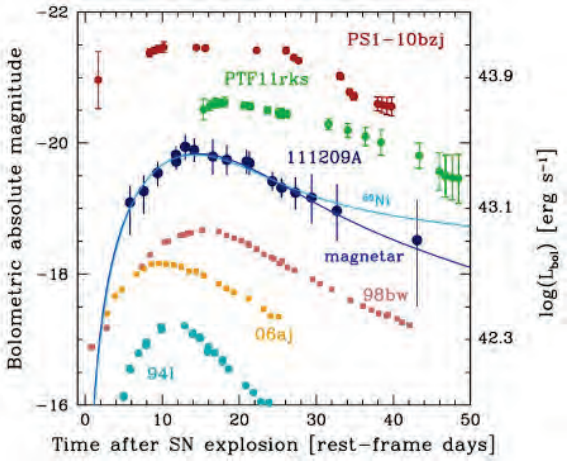

Fig. 3: Bolometric light curve of SN 2011kl compared to other GRB-SNe and SLSNe. SN 2011kl requires 3±1 $M_\odot$ ejecta mass and 1.0±0.1 $M_\odot$ Ni mass.

References: J. Greiner, P.A. Mazzali, D.A. Kann, T. Krühler, E. Pian, S. Prentice, F. Olivares E., A. Rossi, S. Klose, S. Taubenberger, F. Knust, P.M. J. Afonso, C. Ashall, J. Bolmer, C. Delvaux, R. Diehl, J. Elliott, R. Filgas, J.P.U. Fynbo, J. F. Graham, A. Nicuesa Guelbenzu, S. Kobayashi, G. Leloudas, S. Savaglio, P. Schady, S. Schmidl, T. Schweyer, V. Sudilovsky, M. Tanga, A. C. Updike, H. van Eerten, K. Varela, 2015, Nature 523, 189

J. Greiner for the GROND/GRB Team

A Superluminous Supernova OGLE15qz followed by GROND, VLT and large surveys

An extremely bright and rare supernova, OGLE15qz, was discovered by the untargeted OGLE wide-field survey. PESSTO spectroscopic survey classified it as a Type Ic superluminous supernova around maximum light. This supernova, at redshift z = 0.6, provides a unique opportunity to get the best rest frame UV spectra to date that will be an invaluable reference point for future work. The cause of the extreme luminosities of superluminous supernovae remains unknown, a pair-instability SN or a magnetar are two competing theoretical models. We have used VLT X-SHOOTER to acquire a UV spectrum in the photospheric phase, in order to accurately measure the velocity of ejecta, which together with the peak luminosity, provides an estimate of the ejected mass. We combine spectroscopy with our well-covered photometry data from GROND, OGLE and PESSTO to investigate the nature of these bright explosions.

The UV spectrum of OGLE15qz will undoubtably be an essential reference point for the SLSN field for many years to come. In the era of medium to high cadence sky searches, such as the Dark Energy Survey, Subaru Hyper Suprime-Cam and eventually LSST, it is more critical than ever to have a good understanding of the rest frame UV spectral characteristics of superluminous supernovae to allow them to be recognised photometrically at high redshift.

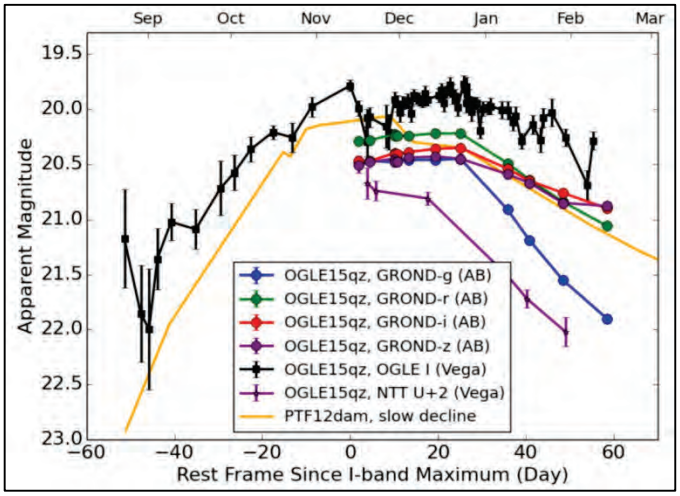

Light curves of OGLE15qz.
The GROND light curve shows this supernova is similar to PTF12dam (Nicholl et al. 2013, Chen et al. 2015). No colour changes around the peak, and evolves bluer from the peak to +50 days.

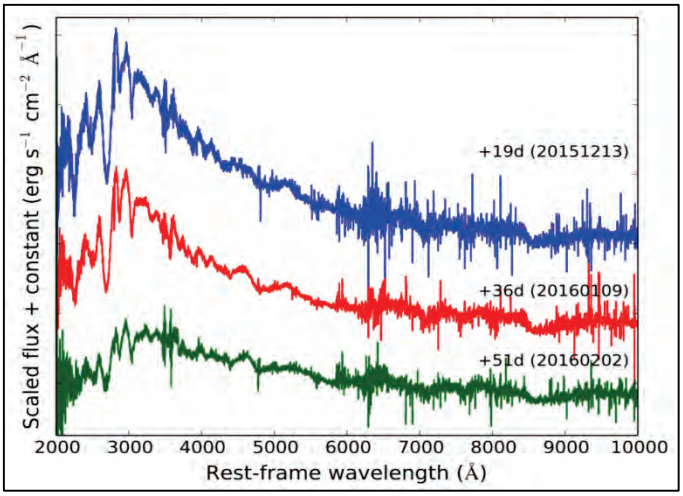

VLT+X-SHOOTER spectra of OGLE15qz.
The typical O II features shown at +19d spectrum and the blackbody temperature fitting of 15000K. Some metal lines appear at +36d and +51d spectra, they are Mg II + Fe II, Mg I], Si II, O I and Ca.

References:

• Nicholl et al. 2013, Nature, 502, 346
• Chen et al. 2015, MNRAS, 452, 1567

T.-W. Chen, J. Greiner, T. Krühler, J. Bolmer, P. Schady, J. Graham
on behalf of the GROND Team and a larger collaboration

The *Fermi*/GBM Gamma-Ray Burst and Spectral Catalogs

The Fermi Gamma-ray Burst Monitor (GBM) has triggered on 1770 cosmic gamma-ray bursts (GRBs) until the end of 2015. The second of a series of catalogs of GRBs observed with the *Fermi*/GBM are summarizing the basic characteristics of the triggered GRBs, like sky location, duration, peak flux, fluences and spectral properties. The first time resolved spectral catalog presents 1,491spectral fits from the 81 brightest bursts of the first four years.

The **second GRB catalog** extends the first two-year catalog by two more years, resulting in an overall list of 953 GBM triggered GRBs. It is providing information on the most important observables of the GBM detected GRBs, the location and main characteristics of the prompt emission, the duration, peak flux and fluence. Furthermore, information is given on the settings and modifications of the triggering criteria and exceptional operational conditions during years three and four in the mission.

The **second spectral catalog** is presenting an updated set of spectral analyses of gamma-ray bursts (GRBs) detected by the Fermi Gamma-Ray Burst Monitor during its first four years of operation. It contains two types of spectra, time-integrated spectral fits and spectral fits at the brightest time bin, from 943 triggered GRBs. Four different spectral models were fitted to the data, resulting in a compendium of more than 7500 spectra. All 487 GRBs from the first two years have been re-fitted using the same methodology as that of the 456 GRBs in years three and four. The analysis procedure and criteria are described in detail and the results are presented in form of parameter distributions for the observer-frame and rest-frame quantities.

The **first time-resolved spectral catalog** is presenting 1,491 spectra from the 81 brightest bursts of the first four years with high spectral and temporal resolution. Distributions of parameters, statistics of the parameter populations, parameter-parameter and parameter-uncertainty correlations, and their exact values are obtained and presented as main results in this catalog. A criterion is reported that is robust enough to automatically distinguish between different spectral evolutionary trends between bursts. A search for plausible blackbody emission components was performed which shows that only 3 bursts (36 spectra in total) show evidence of a pure Planck function. It is observed that the averaged time-resolved low-energy power-law index and peak energy are slightly harder than the time-integrated values.

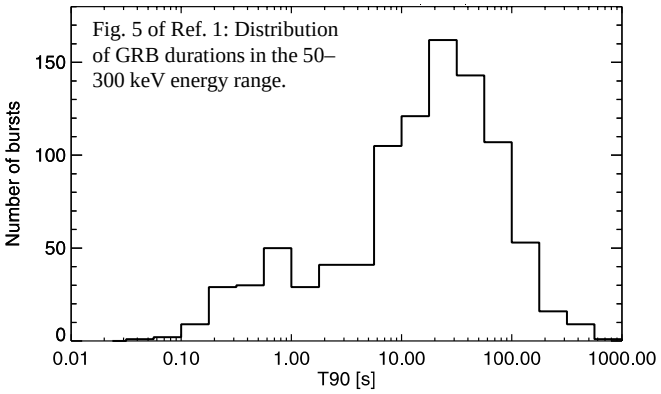

Fig. 5 of Ref. 1: Distribution of GRB durations in the 50–300 keV energy range.

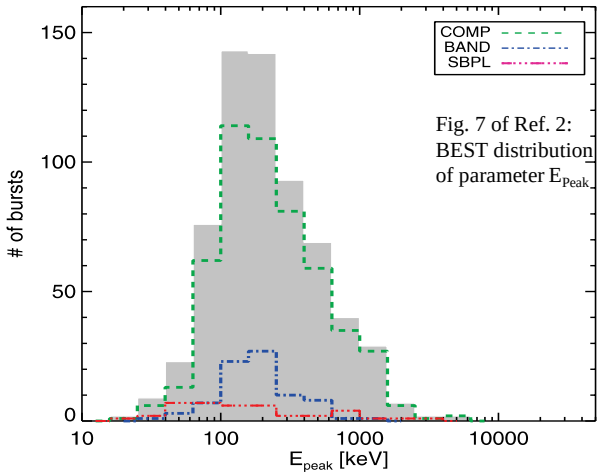

Fig. 7 of Ref. 2: BEST distribution of parameter E_{Peak}

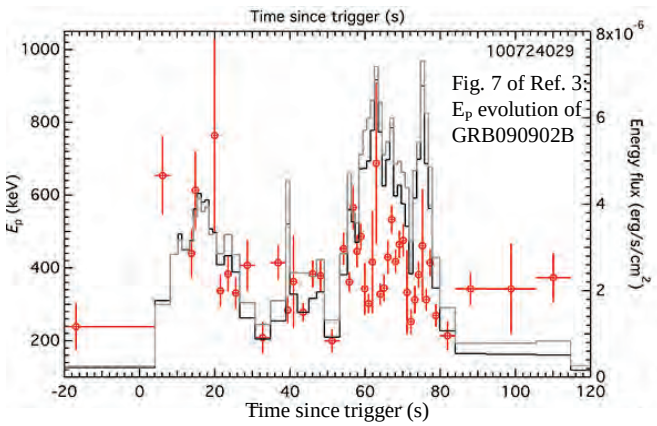

Fig. 7 of Ref. 3: E_p evolution of GRB090902B

References:

• A. von Kienlin et al. 2014, ApJS, 211, 13
• D. Gruber et al. 2014, ApJS, 211, 12
• H.-F. Yu et al. 2016, A&A submitted

A. von Kienlin, D. Gruber, H.-F. Yu, et al.

GRB hosts through cosmic time

We present data and initial results from VLT/X-shooter emission line spectroscopy of 96 galaxies selected by long γ-ray bursts (GRBs) at $0.1 < z < 3.6$ detected by *Swift*. This is the largest sample of GRB host spectra available to date. We find a strong change in the typical properties of GRB-selected galaxies with redshift. With increasing redshift, they have higher star-formation rates and ionization parameters. Typical metallicities of GRB hosts are 12+log(O/H) = 8.5 (or two thirds of the solar value). The fraction of galaxies with super solar metallicities is 20% at $z < 1$. This is much higher than originally thought, but much lower than the fraction of star-formation in similar environments. This shows, that a very high metallicity efficiently suppresses the formation of a GRB.

We have used the largest and most comprehensive sample of GRB host spectroscopy available to date to trace the evolution of galaxies selected by GRBs through cosmic time.

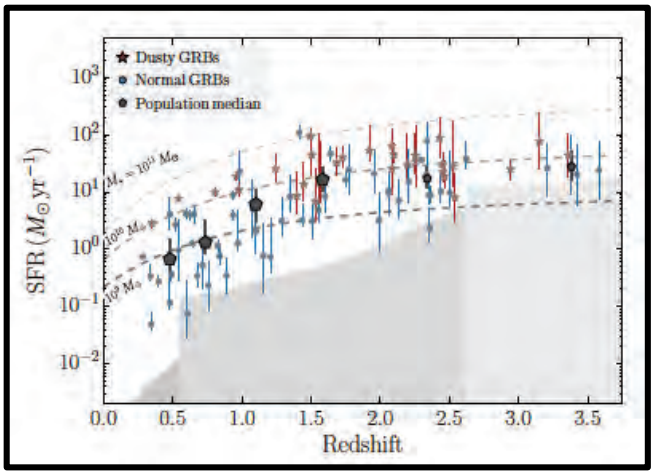

Figure 1 to the left shows the evolution of the star-formation rates of our galaxies. The blue and red data denote normal and dusty GRB hosts, respectively. Dusty GRBs are more abundant at higher redshift, and are typically hosted by galaxies with a higher SFR. Bigger symbols show the population median, which increases by a factor of 20 from 0.6 $M_\odot$/yr at $z \sim 0.5$ to 15 $M_\odot$/yr at $z \sim 2$. The evolution of field galaxies is indicated by the dashed grey lines for galaxies with different stellar mass. The grey areas are the sensitivity limits of our observations, constraining our measurements at the highest redshifts.

Figure 2 to the right shows the distribution of oxygen abundances from the sample of $z < 1$ GRB hosts. The black histogram shows the raw data on which we have applied a completeness and selection function correction (blue data). Most GRB hosts have a metallicity between 12+log(O/H) = 8.2 and 8.6, corresponding to 20% and 80% of the solar value. The red line is the expectation from the galaxy mass function at a similar redshift if GRBs would show no preference for a specific type of environment. It is clear, that GRBs avoid galaxies that have a very high metallicity.

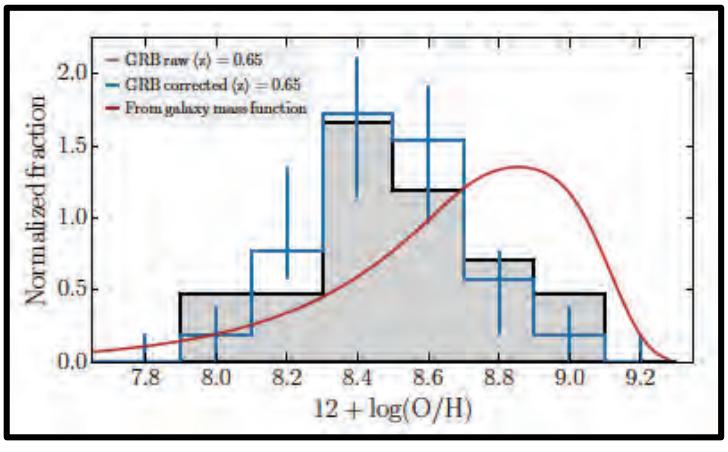

These properties of GRB hosts and their evolution with redshift can be understood in the context of cosmic evolution of galaxies and star-formation and a picture in which the hosts' properties at low redshift are influenced by the tendency to avoid the most metal-rich environments.

References:

• Krühler et al., 2015, A&A, 581, 125

T. Krühler for the X-shooter GRB collaboration

Energy injection in gamma-ray burst blast waves and large-sample correlations

With the launch of the Swift satellite, capable of quickly slewing to the source and starting X-ray / optical measurements of gamma-ray bursts very early on, a new challenge to the standard model arose: at early times the emission holds more steady than the decline associated with a decelerating relativistic blast wave. Such steady plateaus of emission require either long-lasting input from the source or, in the standard black hole model ('collapsar' scenario) a shell embedded in a slower moving ('cocoon') component.

These afterglow plateau stages can be modelled from hydrodynamical simulations and self-similar mathematical descriptions of outflows from sources with long-lasting luminosity, approaches that can be generalized to any relativistic source. In addition, reported correlations between observables in afterglow light curves (e.g. plateau duration and flux level) can be shown to rule out the basic collapsar model with slower moving component, but support the magnetar scenario or a more complex collapsar model where ejecta have a spread in velocities.

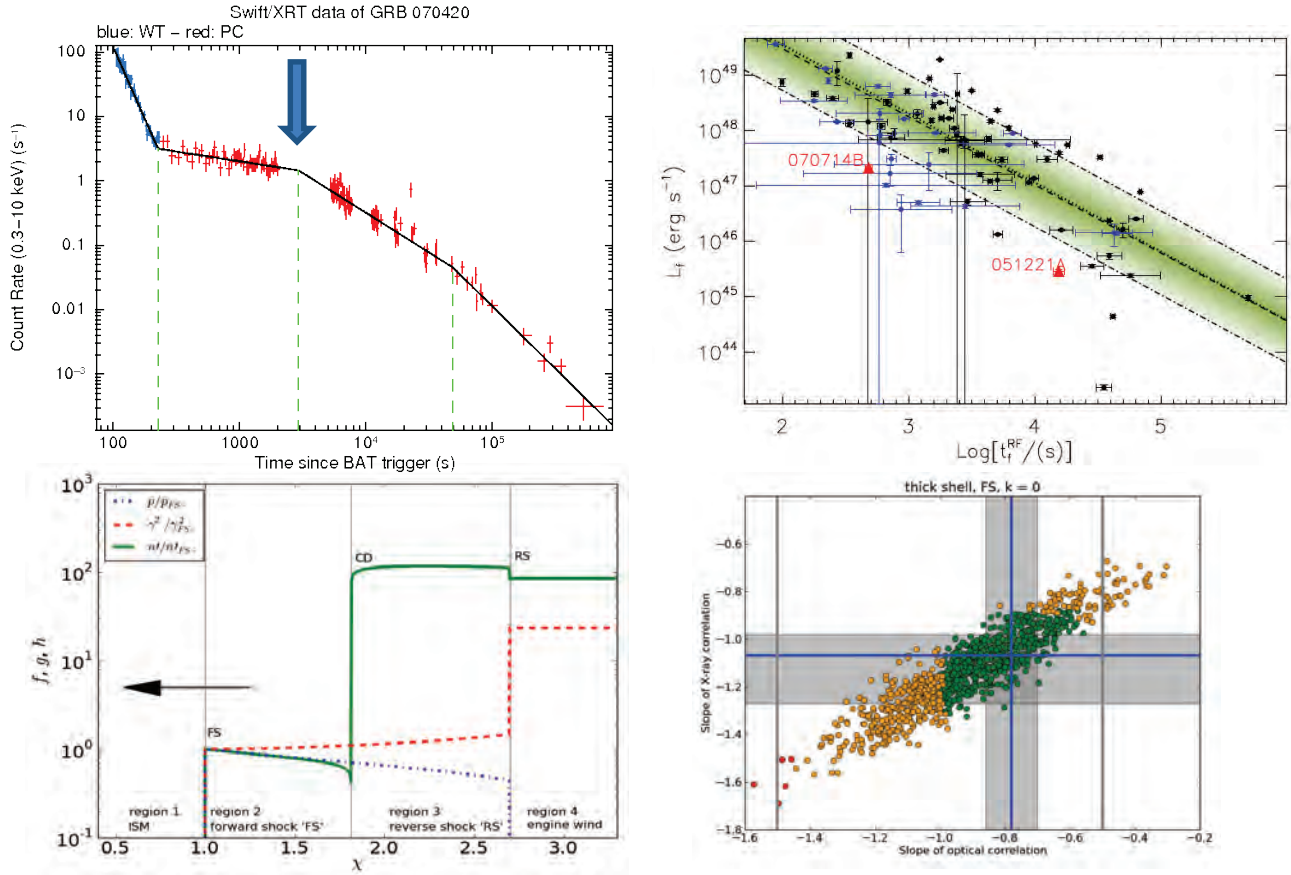

Top left figure shows a typical Swift X-ray afterglow light curve with the plateau end marked with an arrow. Top right shows the reported large-sample correlation between plateau end time and X-ray luminosity from Margutti et al. 2013. Bottom left shows a self-similar blast wave moving left. The profile and post-injection transition were confirmed by simulations. Bottom right shows a successful reproduction of both X-ray and optical plateau correlations, using a Monte Carlo approach to generate self-similar blast waves. Steady energy injection is found to be required.

References:
- HJvE 2014, MNRAS 442, 3495
- HJvE 2014, MNRAS 445, 2414

H. J. van Eerten

First GRB afterglow multi-band fits based on hydrodynamical simulations

For the first time we fit a model based on numerical 2d hydrodynamical simulations to multi-band data. In this example we use GROND photometric data, Swift/UVOT photometric data and Swift/XRT spectra of GRB 081121A, which allow us to constrain all standard fireball parameters using a Bayesian approach.

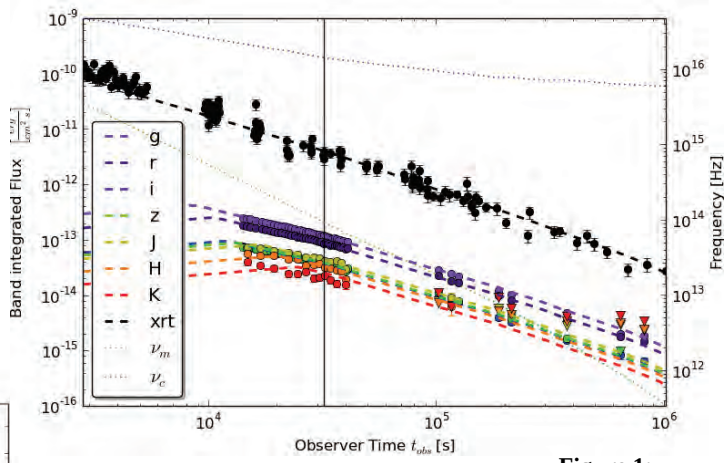

Figure 1: Light curve with data and model

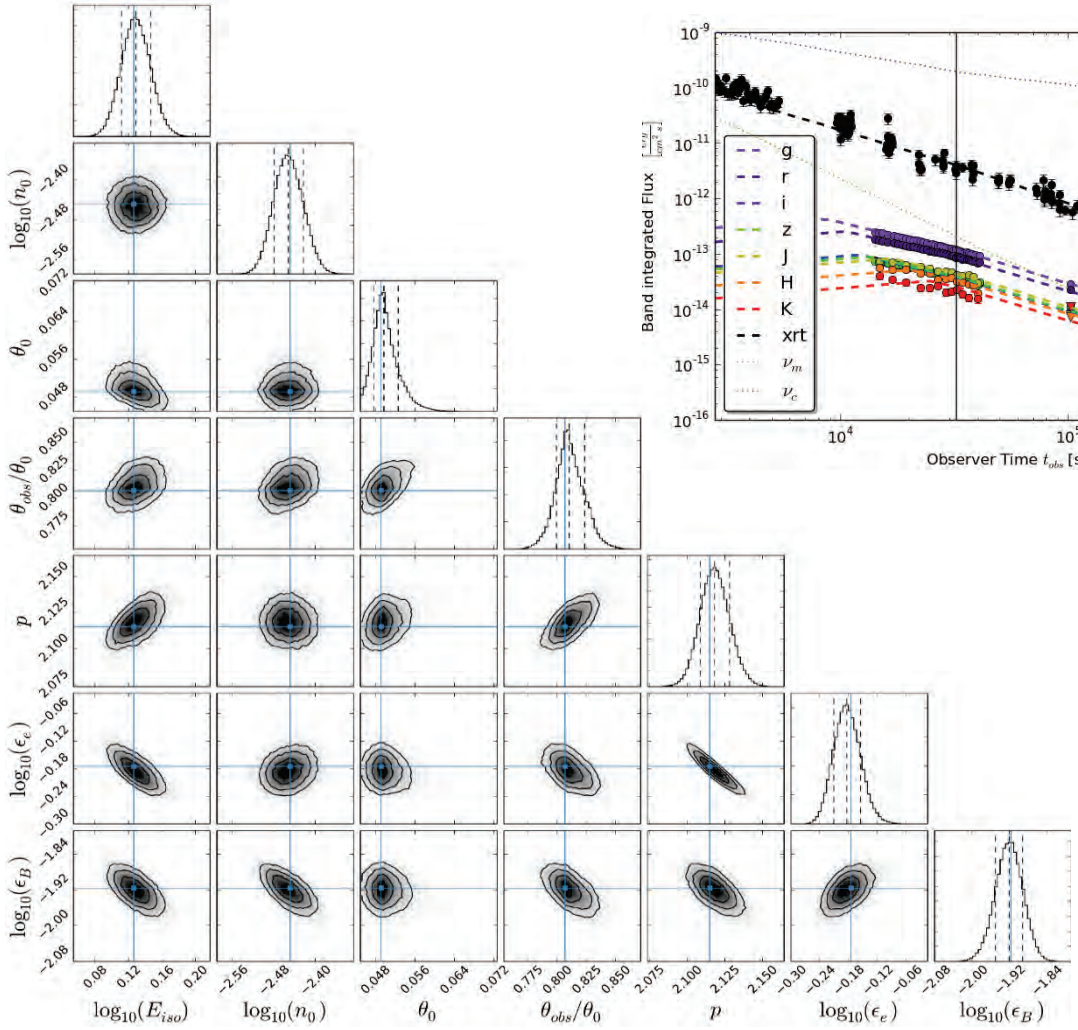

Figure 2: PDF of the fireball parameters

In our model the dynamics of the relativistic jet of the GRB is given by simulations (Van Eeerten+ 2010a,b). They are more detailed than standard analytical approaches and allow us to constrain all fireball parameters. Moreover it opens the new possibility to determine the observer angle and the jet opening angle without a clear jet break.

We fit the whole SED evolution and therefore have no need for time synchronous data gathering (or extrapolations). The light curve (Fig. 1) shows the model (dashed lines for the fluxes, dotted lines for the temporal evolution of the characteristic frequencies) and the data.

The applied Markov Chain Monte Carlo (MCMC) fitting method (Ryan+2015) allows us to sample the whole Posterior Distribution Function (PDF) of the fireball parameters (Fig. 2), and is very robust towards degenerate parameters and multi modal behavior of the PDF.

References:

- van Eerten et al.2010a, ApJ, 722, 235
- van Eerten et al. 2010b, MNRAS, 403, 300
- Ryan, G. et al. 2015, ApJ, 799, 3

F. Knust, H. J. van Eerten, J. Greiner

Microphysics and dynamics of the Gamma-Ray Burst 121024A

We analysed the afterglow of GRB 121024A and showed that the multi-wavelength data enable the afterglow spectra and temporal parameters to be measured to a high degree of accuracy, which sets strong constraints on the micro-physics in the shock region and on the dynamics of the jet.

In the standard afterglow model, the dominant emission process during the afterglow phase is associated to synchrotron emission from shock accelerated electrons. Broadband observations from X-ray to radio allow a detailed analysis of the characteristic properties of the synchrotron spectrum. We combine a temporal (Fig. 1) and spectral analyses (Fig. 2 and 3) of the multi-epoch broadband observations of GRB 121024A afterglow to study the dynamics of the outflow and the microphysics in the shock region during the afterglow phase.

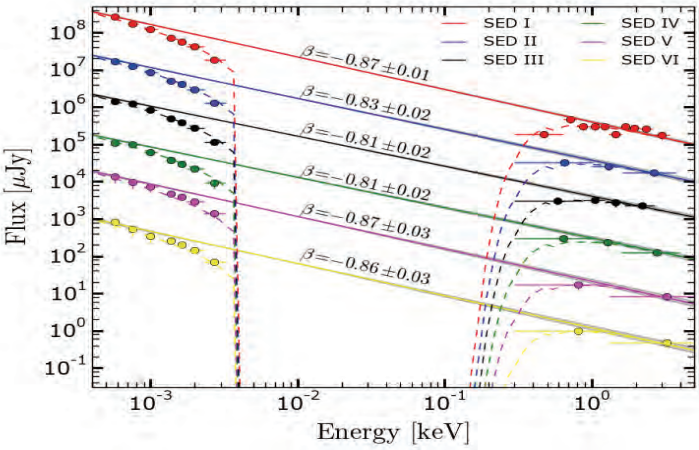

Fig. 2: The combined GROND and XRT data allowed us to determine the spectral slope in this energy regime with high accuracy, and therefore we were able to measure the electron index p .

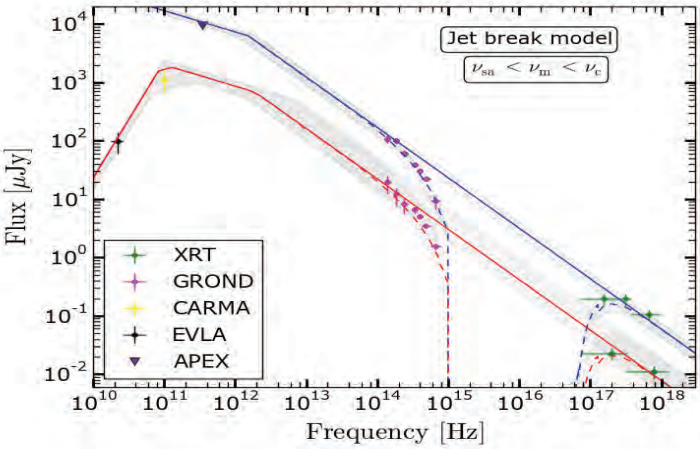

Fig. 3: Broadband SEDs of the afterglow of GRB 121024A from the radio to the X-ray regime. Blue line: SED at t = 21 ks. Red line: SED at t = 109 ks. The dashed lines represent the absorbed model, the solid lines the unabsorbed model. The grey-shaded regions corresponds to the 1-sigma limits of the model.

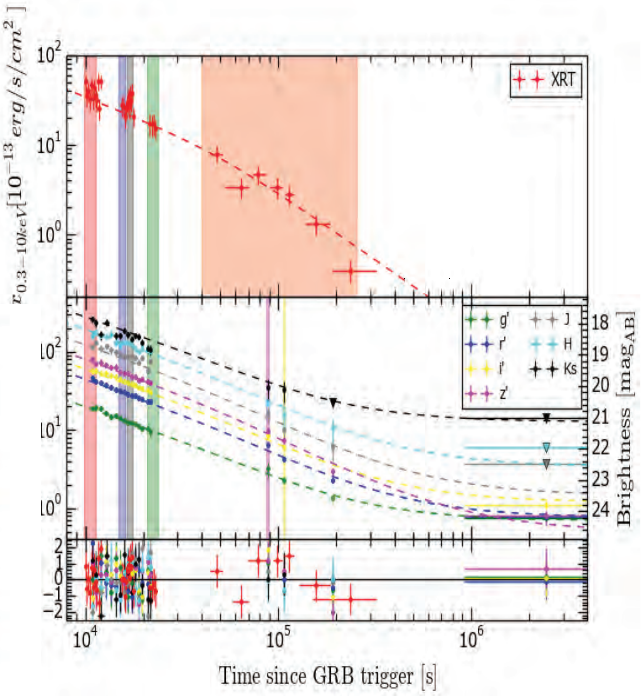

Fig. 1: Light curve of the afterglow of GRB 121024A. Top : XRT light curve from the XRT repository. Bottom : GROND light curve. The best fit for the combined light curve (optical/NIR and X-ray data) is a smoothly broken power law with host contribution, shown with dashed lines. The epochs used for the spectral analysis are highlighted with the vertical bars. The break time tb = 49.8 ks.

We showed that the observations can not be explained by the basic standard afterglow model, and therefore requires additional components. As a result, we modeled our complete set of observations using two different physical interpretations: a jet-break model with a hard-electron spectrum and a prolonged energy-injection model. In light of the extreme microphysical parameters required by the energy injection model, we favour a jet break scenario to explain the observations. This scenario gives physically meaningful microphysical parameters, and it also naturally explains the reported detection of linear and circular polarisation.

References:

• K. Varela, H. van Eerten, J. Greiner, P. Schady, et. al. 2016, A&A (in press.)

K. Varela for the GROND team

Sharpness of GRB Prompt Emission Spectra

We take the large sample of spectra obtained from the *Fermi* GBM GRB time-resolved spectral catalog (Yu *et al.* 2016) and compute the sharpness angle around the spectral peaks or breaks. We compare this new measured quantity to values obtained from various representative emission models: blackbody, single-electron synchrotron, synchrotron emission from a Maxwellian or power-law electron distribution. We conclude that more than 91% of the high temporally and spectrally resolved spectra are inconsistent with any kind of optically thin synchrotron emission model alone. It is found that the limiting case, a single temperature Maxwellian synchrotron function, can only contribute up to 58^{+23}_{-18}% of the peak flux. We also show that even the sharpest but non-realistic case, the single-electron synchrotron function, cannot explain a large fraction of the observed spectra. Since any combination of physically possible synchrotron spectra added together will always further broaden the spectrum, emission mechanisms other than optically thin synchrotron radiation are likely required for a full explanation of the spectral peaks or breaks of the GRB prompt emission phase.

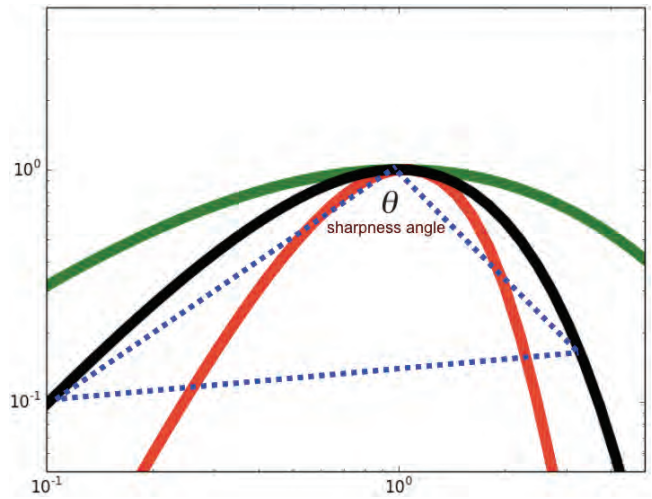

Fig. 1: Comparison between the sharpness of the observed spectrum (black) and that of theoretical predictions (green for Maxwellian synchrotron, red for blackbody). The sharpness angle is defined in normalized energy flux versus energy space using the spectral peak position (E_p).

Even the mathematical limit of single-electron synchrotron is much broader than 35% of our sample. Such inconsistency cannot be accounted for by the statistical uncertainty of the observed spectra. Monte Carlo simulations have been performed using an uniform probability function on the best-fit parameters of the fit functions (black curve in Fig. 1). It is found that the angle uncertainty distribution peaks at about four degrees. Thus we can shift the vertical limits in Fig. 2 leftward by four degrees and our conclusion remains unchanged. We also fit the Maxwellian function (green curve in Fig. 1) under the best-fit function and found that it can only contribute up to 58^{+23}_{-18}% of the peak flux.

We obtained 1,491 time-resolved spectra of gamma-ray bursts (GRBs) detected by *Fermi* Gamma-ray Burst Monitor (GBM). This sample is extracted from the 81 brightest bursts observed during *Fermi*'s first four years of mission (Yu *et al.* 2016). By measuring a novel quantity, the sharpness angle (Fig. 1, Yu *et al.* 2015), we can directly compare the observed shape around the spectral peaks or breaks to theoretical predictions from various emission models. This comparison is done in normalized energy flux versus energy space using the peak position, therefore the redshift dependence of the spectral shape is removed. In Fig. 2 the cumulative distribution function indicates there is a 91% inconsistency between the physically sharpest case among all optically thin synchrotron emission model, the Maxwellian synchrotron.

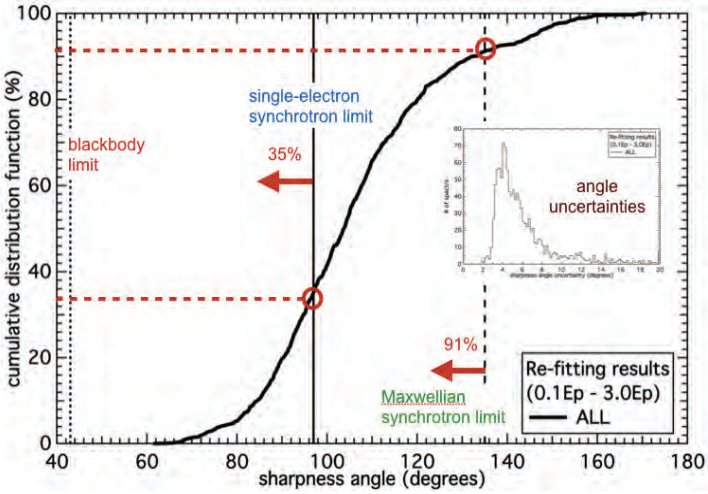

Fig. 2: Cumulative distribution function of all spectra used versus the sharpness angle. Vertical lines indicate limits predicted from theoretical emission models. Inset shows the error distribution of the sharpness angles by performing Monte Carlo simulations.

Reference: Yu, H.-F., van Eerten, H., Greiner, J., *et al.* 2015, A&A, 583, A129
Yu, H.-F., Preece, R. D., Greiner, J., *et al.* 2016, A&A, 588, A135

H.-F. Yu, H. van Eerten, J. Greiner

The Relative and Absolute Rates of LGRB Formation as a Function of Metallicity

By comparing the rate of LGRB formation as a function of metallicity with that of star-formation we find that per unit star-formation an LGRB occurs about 30 times more often at metallicities below 8.3 on the KK04 scale than above. Using this information we compare the cosmic star-formation history with the observed LGRB rate corrected for instrumental selection to find that an aligned LGRB occurs approximately every 4000 ± 2000 low metallicity broad-lined Type Ic Supernovae, for a total LGRB rate of approximately one every 40 broad-lined Type Ic Supernovae.

There is now strong evidence that Long-duration Gamma-Ray Bursts (LGRBs) have an intrinsic preference for low-metallicity environments despite the existence of some exceptions to this trend (Graham & Fruchter 2013). Here I present a pair of results expanding on this work. First, in Graham & Fruchter 2015, we will use the sample from Graham and Fruchter 2013 to give a quantitative answer to the fundamental question: How much more likely is an LGRB to form at one metallicity to another? By dividing metallicity distribution of LGRB by the metallicity distribution of star forming galaxies, we thus directly determine the relative rate of LGRB formation as a function of metallicity in the low-redshift Universe. In particular, we find that per unit star-formation an LGRB occurs about 30 times more often at metallicities below 8.3 on the KK04 scale than above. Then, in Graham & Schady 2015, we employ this result to relate the LGRB rate as a function of redshift to the cosmic star-formation rate via an approach patterned loosely off the Drake equation. Beginning with the cosmic star-formation history, we consider the expected number of broad-line Type Ic events (the SNe type associated with LGRBs) that are in low metallicity host environments adjusted by the contribution of high metallicity host environments at a much reduced rate. We then compare this estimate to the observed LGRB rate corrected for instrumental selection effects to provide a combined estimate of the efficiency fraction of these progenitors to produce LGRBs and the fraction of which are beamed in our direction. We estimate that an aligned LGRB occurs approximately every 4000 ± 2000 low metallicity broad-lined Type Ic SNe. Assuming a semi-nominal LGRB beaming factor of 100, in low-metallicity environments one LGRB occur approximately every 40 broad-lined Type Ic SNe.

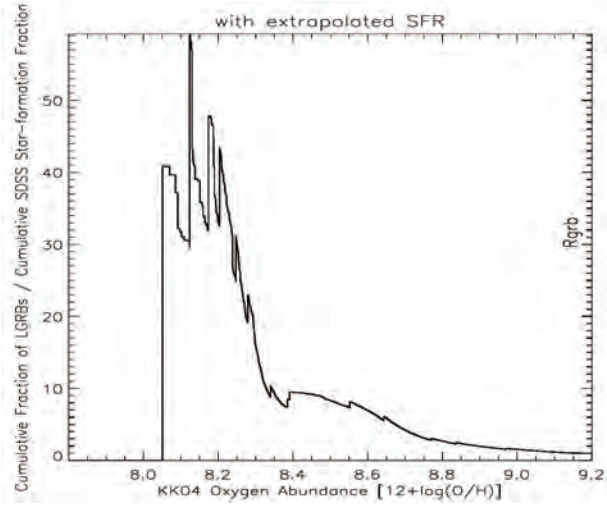

Relative LGRB rate per unit SFR calculated by dividing the cumulative fraction of LGRBs by the cumulative SDSS star-formation fraction.

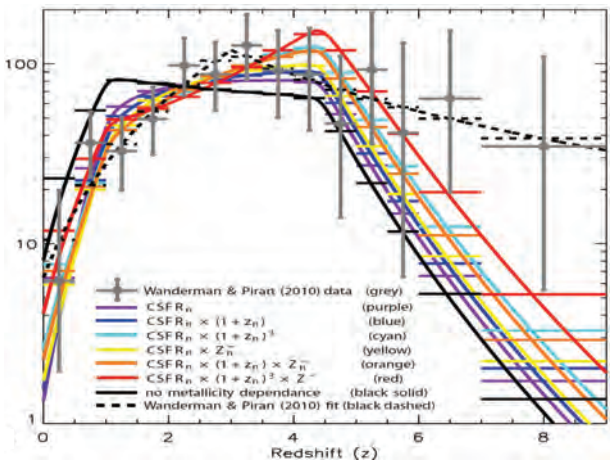

Predicted LGRB distribution as a function of redshift for various low metallicity CSFRH models (colored lines), and the CSFRH (black solid line) without metal dependence. The measured LGRB distribution is shown in the grey data points.

References:

• Graham & Schady 2015, Astro-ph: 1511.01466, ApJ in press
• Graham & Fruchter 2015, Astro-ph: 1511.01079, ApJ in press
• Graham & Fruchter 2013, ApJ, 774, 119

J. Graham, P. Schady, et al.

The super-solar metallicity host galaxy of the ultra-long GRB130925A

The progenitors of long gamma-ray bursts (GRBs) remain uncertain, and a newly identified class of ultra-long GRBs has fuelled further speculation on current models. Our X-shooter data reveal that the host galaxy of the ultra-long GRB130925A [1] has a super-solar metallicity at the galaxy nucleus, where the GRB occurred, and at an outer star-forming region. Such homogenous high metal enrichment raises challenges for progenitor models of both long and ultra-long GRBs, and further spatially resolved spectral observations of GRB hosts is essential to shed light on this apparent dichotomy.

In X-shooter observations of the host galaxy of the ultra-long GRB130925A [2], we resolve emission from the GRB exposition sight (SF1) as well as a star forming region 6 kpc away (SF2), located in the outskirts of the galaxy (Fig. 1&2). Both regions have a super-solar metallicity that places the galaxy within the 10-20% most metal-rich GRB hosts detected [3]. This is in apparent conflict with the 0.3-0.5$Z_{\odot}$ upper limits placed by standard models of both long duration GRBs and ultra-long GRBs.

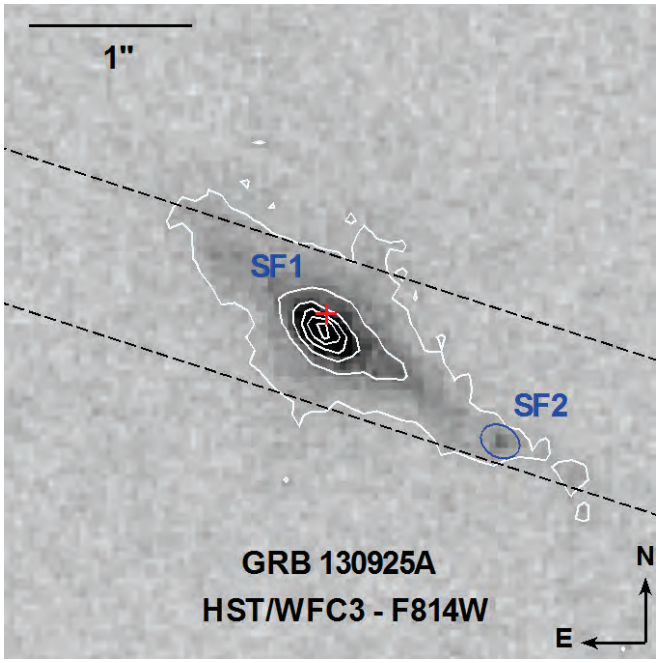

Fig. 1: HST/F814W image of the host galaxy of GRB130925A. The position of the X-shooter slit (dashed black lines) and the GRB afterglow (red cross) is overlaid. Regions SF1 and SF2 are resolved in our X-shooter data.

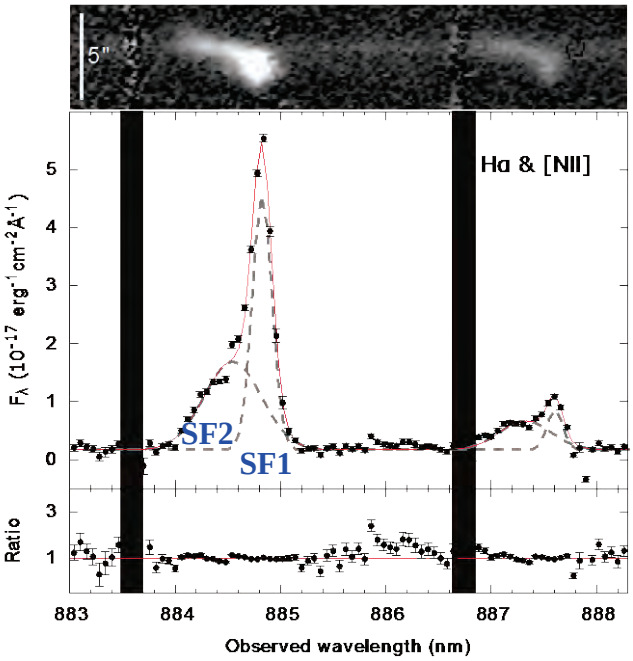

Fig. 2: A zoom-in of the X-shooter 2D (top) and 1D (middle) spectra, and residuals from our two-component fit (bottom).

These data of GRB130925A are only the second example of spatially resolved spectroscopic observations of a super-solar GRB host galaxy, and they are the first for an ultra-long GRB. The edge-on orientation of the host galaxy and the sightline to the GRB through the galaxy disk raise the possibility that GRB130925A occurred within a metal-poor region within the host galaxy. Nevertheless this is not supported by the metal-rich star-forming region at the outskirts of the galaxy. Ultimately, further spatially resolved spectral observations of metal-rich GRB host galaxies are required to place statistical constraints on the frequency of metal-poor pockets within metal-rich hosts.

References:
[1] Greiner, J., et al., 2014, A&A, 568, 75
[2] Schady, P., et al. 2015, A&A, 579, 126
[3] Krühler, T,, et al., 2015, A&A, 581, 125

P. Schady, T. Krühler, J. Greiner and the GROND team

Dust in the high redshift ISM: Comparing depletion and extinction in GRB afterglows

Measures of dust-depletion in gamma-ray burst (GRB) afterglow spectra tend to conflict with the amount of dust inferred from reddening of the SEDs. We compute the dust-to-metals ratio (DTM) in a new way for a sample of 20 GRBs to attempt to reconcile the two.

Reddening (Av) caused by dust in the line of sight to GRBs can be measured by modelling the optical/near infra-red to X-ray spectral energy distribution (SED) of the afterglow. It can also be inferred from the DTM, measured from column densities of metal absorption lines in the afterglow [1]. However, when both are measured simultaneously, there is a systematic over-estimation of Av by the DTM method [2].

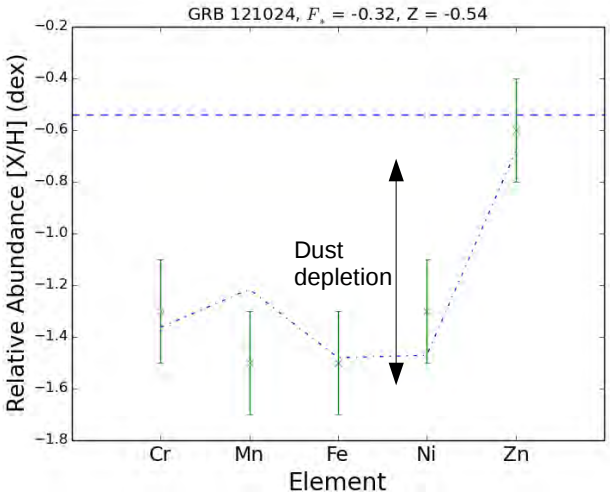

Fig. 1: Depletion model (dashed) fit to relative abundances (points) measured in the spectrum of GRB 121024A. The horizontal dashed line is the best fit metallicity

Metal column density measurements from afterglow spectra are not fully representative of the intrinsic column density – some of the metal is *depleted* onto dust grains and not seen. By modelling the observed 'missing' fraction of metals (Fig. 1) using known depletion sequences [3], we calculated the dust-depletion strength factor F* [4], for 20 GRBs, and DTM. We compare this to the Av measured from the broadband SED (Fig. 2), finding no strong trend between the two, suggesting these effects trace distinct properties of the dust.

Our method also provides the most accurate measures of metallicity, and our results imply a correlation between this and the DTM, suggesting grain growth in the ISM as favourable over supernovae as the dominant dust-production mechanism in GRB host galaxies.

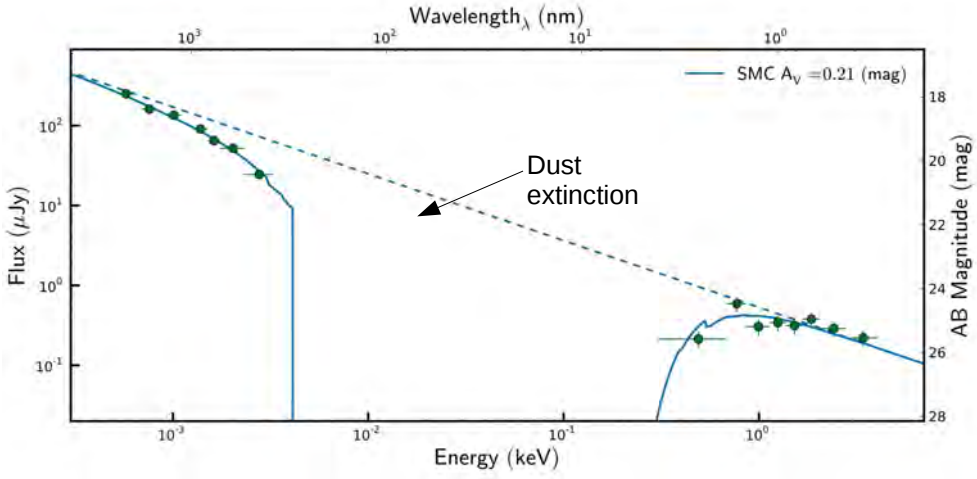

Fig. 2: The broadband SED of GRB 121024A from GROND (visible bands, left) and Swift/XRT (X-ray band, right) data. The dotted line shows the unabsorbed power-law spectrum, while the solid line plots the best fit model to dust and metal absorption.

References:
[1] D'Elia, V., Fynbo, J. P. U. , Goldoni, P et al., 2014, A&A, 564, A38
[2] Savaglio, S., Fall, S. M., & Fiore, F. 2003, ApJ, 585, 638
[3] De Cia, A. et al. 2016, A&A, *submitted*
[4] Jenkins, E. B. 2009, ApJ, 700, 1299

P. Wiseman, J. Bolmer, T. Krühler, P. Schady and the GROND/GRB Team

Soft X-ray absorption excess in GRB-afterglow spectra: Absorption by turbulent ISM

Two thirds of long duration gamma-ray bursts (GRBs) show soft X-ray absorption in excess of the Milky Way and the column densities of metals inferred from UV/optical spectra and from soft X-ray spectra differ, at times by an order of magnitude, with the latter being higher. While the UV/optical photons probe the neutral gas in the interstellar medium (ISM) the X-rays are absorbed by the total gas column along the line of sight, with C V, N VI and O VII ions being the primary absorbers. This suggests that an undetected reservoir of highly ionised gas exists along the line of sight. We investigate using simulations of turbulent-collisionally ionised ISM (Gatto et al. 2016), a typical feature of star forming galaxies such as GRB hosts, the absorption imprint of the ISM on the GRB optical and X-ray afterglow. We use simulations with densities 1 cm^{-3} and 3 cm^{-3}, pass 100 random line of sight through them and track the various ionisation states of C, N and O. The soft X-ray absorption excess is estimated as a fraction of total oxygen column density to neutral column density (N_{OX}/N_{OI}).

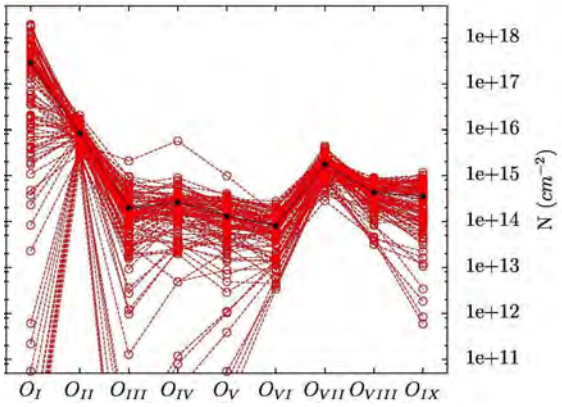

Fig. 1: Column densities of O ions for 100 sightlines passed through our ISM data cube with density 3 cm^{-3}. The black points indicate the average ion column densities for our 100 sightlines.

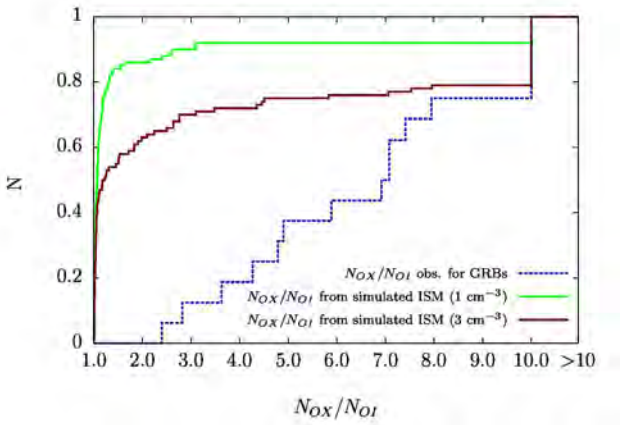

Fig. 2: Green and brown lines show the cumulative distribution of N_{OX}/N_{OI} for 100 sightlines crossed through our ISM data cubes with densities 1 cm^{-3} and 3 cm^{-3} respectively, and the blue dashed line shows the observed cumulative distribution of N_{OX}/N_{OI} for a sample of 16 GRBs.

ISM with density 3 cm^{-3} can produce total and neutral O column densities that show N_{OX}/N_{OI} > 10 but the column densities for such sightlines are 2-3 orders of magnitude lower in comparison to the GRB afterglow spectra. Furthermore, the column densities of molecular hydrogen in GRB host ISM are insufficient to account for the soft X-ray excess. Thus an additional X-ray absorber either within the circumburst medium and/or the warm-hot intergalactic medium is required to explain the soft X-ray absorption excess.

Species like C V, N VI and O VII ions are undetected in the GRB afterglow spectra and we predict high column densities of such ions and these could potentially be detected by future generation X-ray telescopes such as Athena.

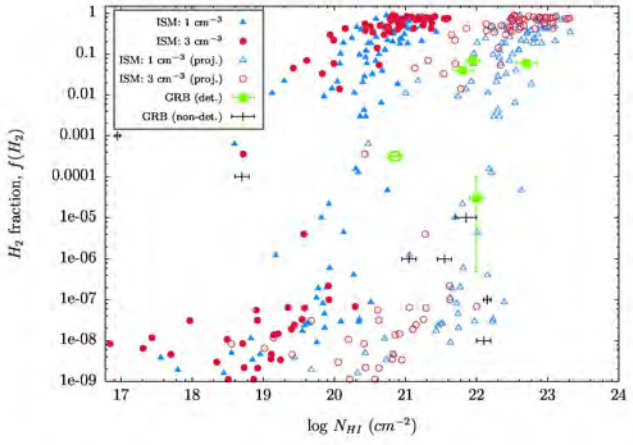

Fig. 3: Apart from metals, molecular hydrogen can absorb X-rays. The H_2 fraction ($f(H_2)$ = $[2.85N_{H_2}+ N_{HI}]/N_{HI}$) required to cause significant soft X-ray excess > 0.5. No GRB afterglow spectra shows $f(H_2) > 0.1$ and thus H_2 cannot be the source of soft X-ray absorption.

References:
1. Tanga, M., et al. 2016, accepted A&A.
2. Gatto, A., et al. 2015, MNRAS, 449, 1057
3. Schady, P., et al. 2011, A&A, 525, A113

M. Tanga, P. Schady, J. Greiner, M. G. H. Krause, R. Diehl

X-ray emission from the Galactic Center

We produced the deepest X-ray maps of the central few degrees of the Galactic center (GC), allowing us to discover several new features such as supernova remnants, superbubbles and X-ray filaments. We compiled an atlas of extended features within ±1 degree of Sgr A*, deriving a supernova rate of 3.5-15×10^{-4} yr^{-1}, that implies a kinetic energy input higher than 10^{40} erg s^{-1}. We also discovered a new candidate super-bubble,peaking around G0.1−0.1, likely associated with the Quintuplet cluster. We investigated Sgr A's bipolar lobes and suggest they originate from energy release at the GC. We also discovered warm plasma at high Galactic latitude, likely associated with an inhomogeneous hot 'atmosphere' over the GC, perhaps fed by continuous or episodic outflows of mass and energy from the central few parsecs.

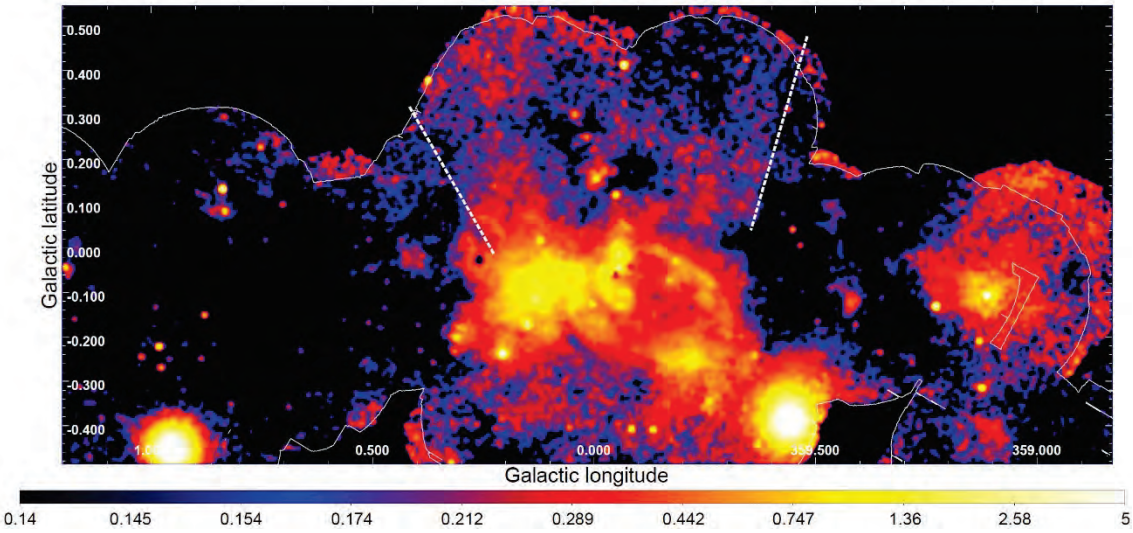

Top panel: Map of the normalization of the soft thermal plasma component (in units of 10^{-4} times the APEC normalization). The white lines indicate the extent of the survey having more than 7.2 ks exposure. The intensity of the soft thermal plasma peaks at the position of Sgr A*, the Sgr A's bipolar lobes and the two nearby super-bubbles. The white dashed lines show the position of the two sharp edges in the distribution of the high-latitude plasma. Some bright point sources (i.e. 1E1743.1−2843, AXJ1745.6−2901, 1E1740.7−2942, GRS1741.9−2853) have been removed, thereby producing artificial holes in the maps at their respective locations.

Right panel: Zoom into the central 100 light years of the Milky Way. Red: Si-S + S xv; green S-Ar + Sxv + Ar xvii; blue: Ar-Ca + Ca xiv. Sgr A* is located at l~359.9, b~-0.05 deg (Ponti et al. 2015b), surrounded by the emission of the supernova remnant Sgr A East, while at ~1.5 arc min is the bright X-ray binary AX J1745.6 2901 (Ponti et al.2015c). North and South of Sgr A* are the Sgr A's bipolar lobes. The bright X-ray emission at G0.1-0.1 is a superbubble candidate.

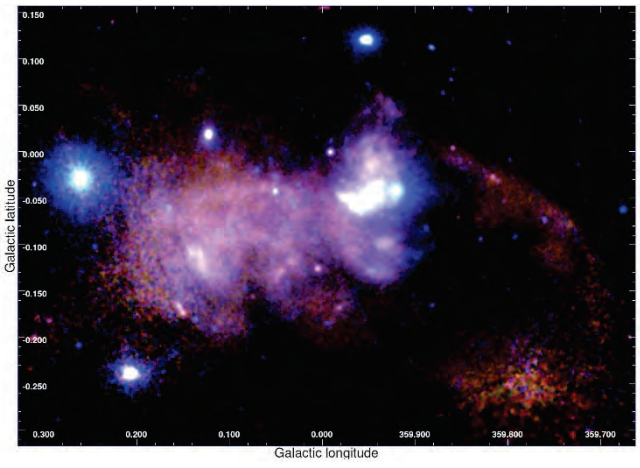

References:

* Ponti et al. 2015a MNRAS 453 172; * 2015b MNRAS 454 1525; * 2015c MNRAS 446 1536.

G. Ponti, F. Haberl, R. Sturm, P. Predehl, K. Nandra, et al.

SN2014J: Discovery of ^{56}Ni decay γ-ray lines

SN2014J was a type Ia supernova, exploding at a relatively nearby location at ~3.5 Mpc distance. This allowed us to search for gamma ray lines from the ^{56}Ni decay chain with INTEGRAL's spectrometer. We discovered both the expected lines from ^{56}Co decay with its ~3 months radioactive decay time, but also, surprisingly, lines from ^{56}Ni decay with 9 days radioactive decay time. A 40-year old dream of astrophysicists has come true: Direct detection of the source of SN Ia light. Upon a closer look, the explosion might have been triggered by an explosion in matter accreted from the companion star, and deviate from spherical symmetry.

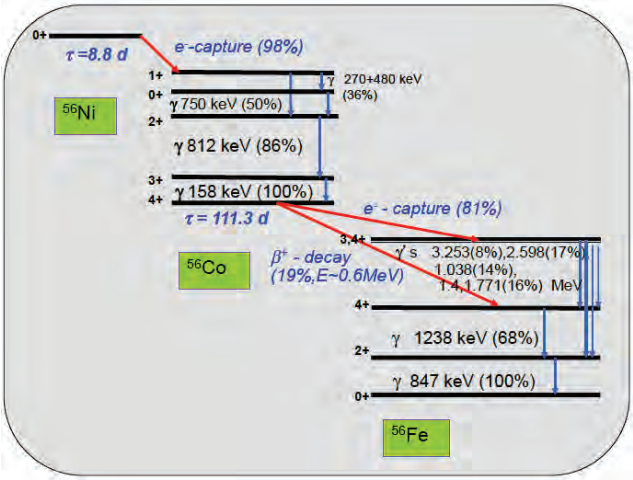

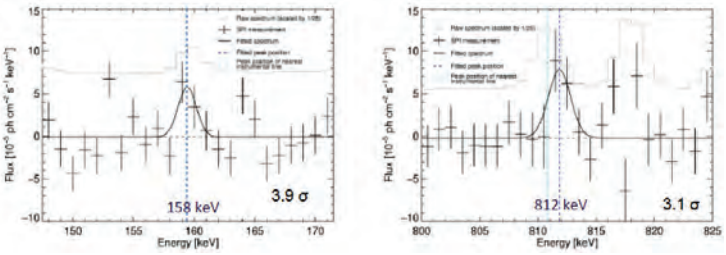

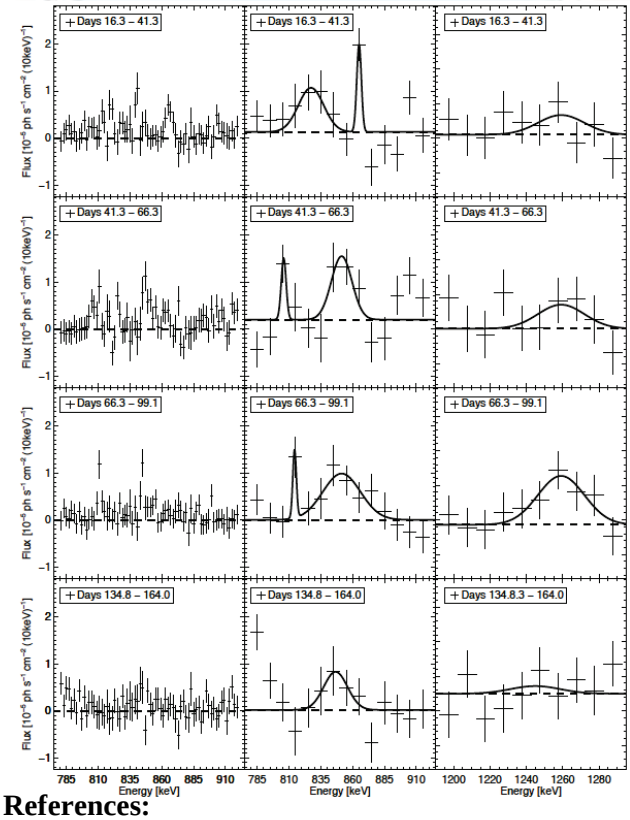

^{56}Ni is the main product of nuclear fusion reactions, when a white dwarf star ignites Carbon fusion reactions, and is disrupted in the thermonuclear runaway. The nuclear flame propagates faster than white dwarf matter can lift degeneracy and expand. Only outer regions of the white dwarf are expected to escape complete nuclear burning, to produce partially burnt or unburnt leftovers of the original white dwarf star composed of C and O, mainly.

We discovered (Figures above on the right) the gamma-rays which characterise the decay of ^{56}Ni (see decay scheme Figure on the top left) in ist first decay stage with 8.8 days characteristic lifetime. This implies that some ^{56}Ni must have been close to the surface of the exploding white dwarf, contrasting the above expectations of inside-out nuclear burning. Several scenarios have been proposed, such as collisions of two white dwarf stars, or a build-up of helium from accretion on the surface, which detonates in a helium flash, thus igniting the white dwarf from the outside. From the narrowness of the detected lines, large velocities along the line of sight are excluded, which suggests a face-on viewing geometry, and a He belt as triggering explosion.

From the lines emitted in the second decay stage towards the ^{56}Fe daughter nucleus, the typical velocities of a SN Ia explosion of 4000-7000 km s^{-1} are seen in the Doppler broadened lines. However, when we exploit our high spectral resolution (Figure on the left), we recognise that with gradually increasing transparency of the supernova, not all of the ejecta are revealed homogeneously, but emission may originate from individual clumps of ejecta.

References:

• Diehl R., et al., Astron. & Astroph., 574, A72 (2015)
• Diehl R., et al., Science 345, 1162 (2014)

R. Diehl, T. Siegert, J. Greiner, M. Krause, X. Zhang

Positron Annihilation in the Milky Way

The γ-ray signal originating in the annihilation of electrons and positrons in the ISM has been well measured with the coded-mask telescope SPI aboard INTEGRAL. When electrons and positrons annihilate, their rest masses are converted into γ-ray photons of 511 keV energy. This annihilation radiation is the strongest persistent γ-ray line-signal in the Milky Way, but its spatial morphology is still not understood: Unlike at any other wavelength, the emission is concentrated towards the centre of the Galaxy, while the disk is very faint in 511 keV radiation. An explanation where all the positrons are continually created is still not found. Among candidate sources are massive stars, supernovae, and X-ray binaries.

With eleven years of INTEGRAL data, it was possible to disentangle different annihilation sites in bulge and disk, and to constrain the size of the low surface-brightness disk. The total positron annihilation budget suggests that one source type alone may not be sufficient to explain the entire galactic signal. Positron propagation through the ISM is found to be a crucial factor in explaining the emission morphology, being different to any source population.

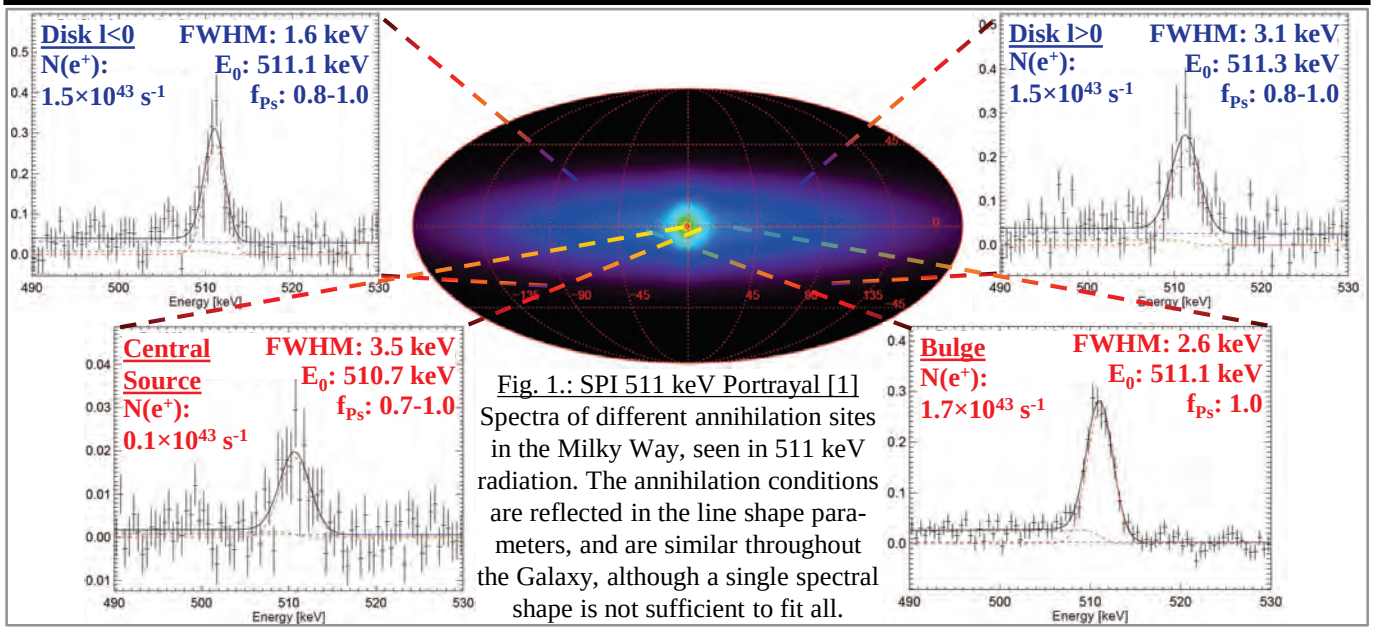

Fig. 1.: SPI 511 keV Portrayal [1] Spectra of different annihilation sites in the Milky Way, seen in 511 keV radiation. The annihilation conditions are reflected in the line shape parameters, and are similar throughout the Galaxy, although a single spectral shape is not sufficient to fit all.

• The total positron budget (production ≙ annihilation) in the Galaxy, $N(e^+) = 3.5\text{-}6.0\times10^{43}$ s^{-1}, cannot be sustained by a single source type population. Massive stars and radioactive decay positrons may account for 0.7×10^{43} s^{-1}, type Ia SNe up to 2×10^{43} s^{-1}, and microquasars of the order 10^{43} s^{-1} [2,3].
• The newly identified source in the centre of the Galaxy shows a broadened and red-shifted gamma-ray line which might be an indication for the super-massive black hole Sgr A* and its surroundings. The PSF of SPI covers a physical region of 400 pc at 8.5 kpc distance which is reminiscent of the central molecular zone with its turbulent medium, being able to also produce a broadened line.
• The longitudinal and latitudinal extent of the disk has been determined to be $\sigma_l = 60°\pm10°$, and $\sigma_b = 10°\pm2°$, respectively, for a bulge-to-disk luminosity ratio ≤ 1. The latitude extent suggests a vertical scale-height of about 1 kpc. None of the prominent source candidates are distributed that spaciously, implying that positrons have to propagate several hundred pc to match the measured morphology.

References:
[1] Siegert, T., Diehl, R., Khachatryan, G., et al. 2016, A&A, 586, A84
[2] Prantzos, N., Boehm, C., Bykov, A. M., et al. 2011, Rev. Mod. Phys., 83, 1001
[3] Siegert, T., Diehl, R., Greiner, J., et al. 2016, Nature, accepted

T. Siegert, R. Diehl, et al.

Superbubbles and Stellar Feedback

How long do massive star ejecta take to get into the next generation of stars, and which route do they take? Our ^{26}Al-1.8 MeV-line observations with INTEGRAL combined with superbubble simulations place the bulk in large, hot superbubbles. Massive star clusters differ.

Each generation of stars enhances the metallicity in a galaxy by nucleosynthesis in stellar interiors. How the freshly synthesised nuclei get into the next generation of stars is an interesting problem. Probably cycling through interstellar and intergalactic medium as evidenced by their high metallicities plays a role, as well as immediate recycling as witnessed by short-lived radionuclides in the early solar system. We have combined the results of our superbubble simulations with observations to constrain the transport of massive star ejecta on star cluster and galactic scales. On galactic scale, the bulk of the massive star ejecta are in hot gas in superbubbles (Fig. 1). Gas expulsion via superbubbles does not happen in massive star clusters known to dump the bulk of massive star ejecta into low mass stars directly. How this exactly happens is still a puzzle, but our results rule out popular models in which the stellar mass was initially much higher (Fig 2.).

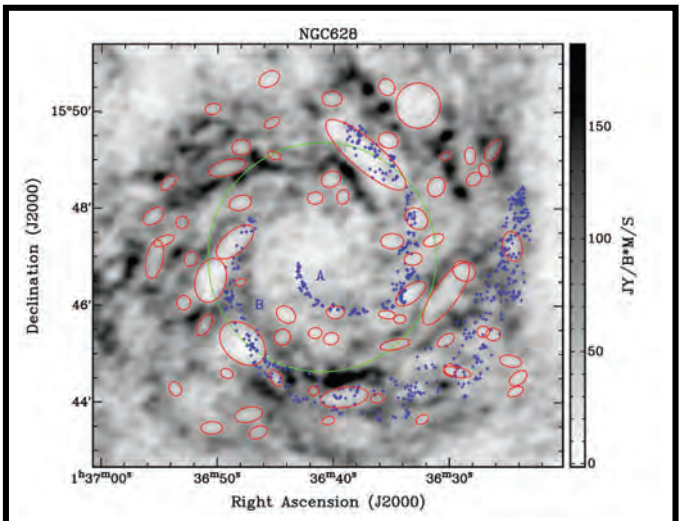

Fig.1: HI image of a nearby galaxy visualising our results for the Milky Way. The blue symbols mark star forming regions from Hα. We find that inside corotation (green circle) winds and supernovae lead to a spiral arm outflow into large old interarm superbubbles (red ellipses), we measure the velocity of the outflow (~200 km/s) by Doppler shifts of the ^{26}Al line and reproduce it in 3D simulations of merging superbubbles[1].

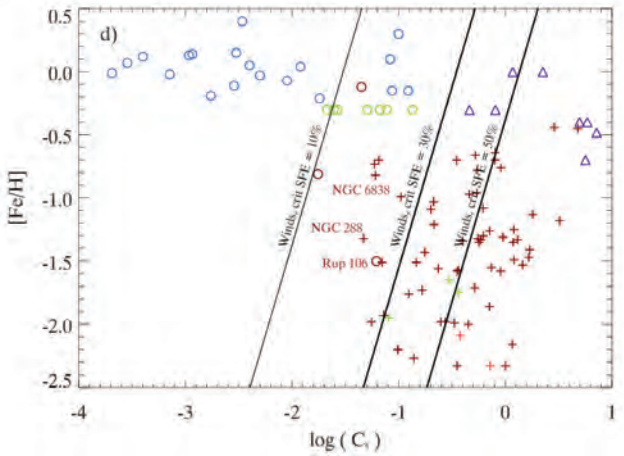

Fig.2: Metallicity over compactness index C_5 (stellar mass of a cluster in units of 10^5 solar masses over its half-mass radius in pc) for observed star clusters. Plus-symbols are star clusters which have dumped the bulk of their massive star ejecta into low-mass stars locally. The ones with open circles did not do this. For the triangles we do not know. Colours code different samples. The solid lines divide the parameter space into regions where superbubbles can (left) or cannot (right) expel the residual gas from formation at the indicated star formation efficiency (SFE, 10, 30, 50 %). Gas expulsion with strong loss of stars best works for 30% SFE. Even without secular mass loss, clusters to the right of the rightmost line cannot have lost many stars by gas expulsion[2].

References:

- Krause, Diehl, Bagetakos, Brinks, Burkert, Gerhard, Greiner, Kretschmer & Siegert, 2015, A&A 578, A113
- Krause, Charbonnel, Bastian & Diehl, 2016, A&A 587, A53

M. Krause, R. Diehl

eROSITA - Telescope

eROSITA is the main instrument on board of the Russian/German „Spectrum-Roentgen-Gamma“ (SRG) mission. The primary mission goal is to perform an X-ray all-sky survey lasting four years. eROSITA consists of 7 identical telescopes, each equipped with nested Wolter-I mirror modules + pnCCD-cameras. The design of the instrument is driven by the goal to detect 100.000 clusters of galaxies in order to constrain cosmological parameters including Dark Energy. MPE is responsible for the design, development and integration of the instrument. Furthermore, also the software development for the data analysis is led by MPE.

Status: All components and subsystems are in place. All Mirror Modules and Cameras have been calibrated; their performances are well within or at least quite close to the original specification. We are now integrating the telescope and prepare for the final tests before delivery to Russia. The launch is planned now for September 2017.

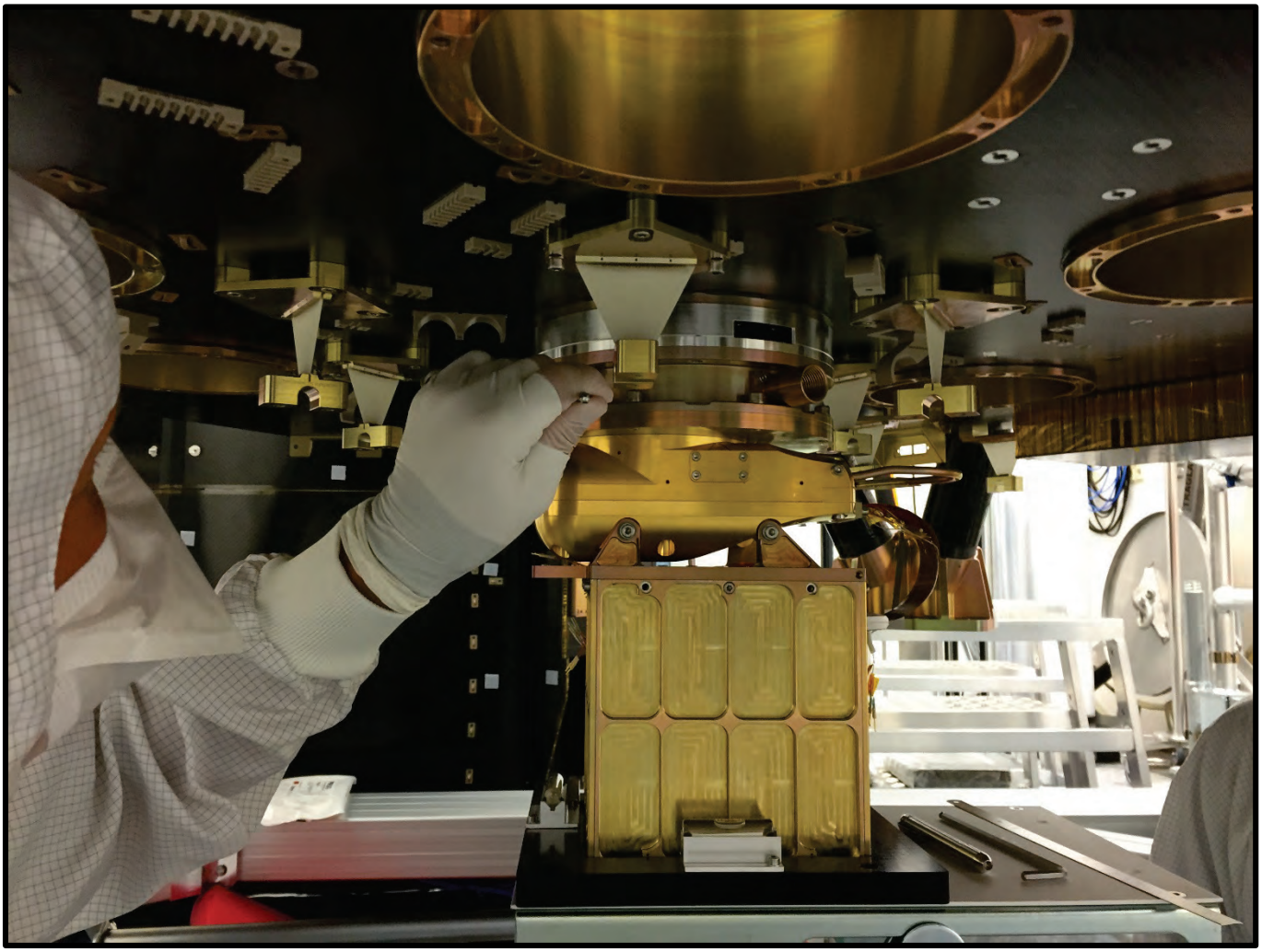

The integration of Mirror Modules and Camera Assemblies (shown here) requires an extreme accuracy: The individual focal length (1600mm) of each pair has to be matched within 50µm. The metrology has been developed at MPE.

P. Predehl on behalf of the eROSITA Team

The eROSITA PNCCD Cameras

The eROSITA X-ray observatory is a scientific payload on the Russian research satellite SRG. The instrument comprises an array of 7 identical and parallel aligned telescopes. Each of the seven focal plane cameras is equipped with a PNCCD detector, an enhanced type of the XMM-Newton focal plane detector. This instrumentation permits spectroscopy and imaging of X-rays in the energy band from 0.3 keV to 10 keV with improved performance compared to the XMM-Newton EPIC PN camera. All seven eROSITA CCD detectors have been successfully tested after integration.

The key component of each camera is the PNCCD chip, a back-illuminated, fully depleted and column-parallel type of charge coupled device (Fig.1). The image area of the 450 micron thick frame-transfer CCD comprises an array of 384x384 pixels, each with a size of 75x75 micron^2. Readout of the signal charge that is generated by an incident X-ray photon in the CCD is accomplished by the so-called eROSITA CAMEX ASIC. The read noise of this system is equivalent to a noise charge of about 2.5 electrons rms, a factor of 2 better compared to the XMM-Newton PNCCD camera. The camera shows excellent energy resolution over the entire energy range, e.g. FWHM(277eV)=49eV, FWHM(1.5eV)=76eV, FWHM(6.4keV)=139eV, and FWHM(9.7keV) = 177eV. Nearly no pixel defects (bright, noisy, dead) occur a the nominal operating temperature of -95°C. Radiation hardness tests showed that no substantial radiation damage will arise during the mission time of 7.5years. The eROSITA QM camera (Fig.2) passed all qualification tests successfully.

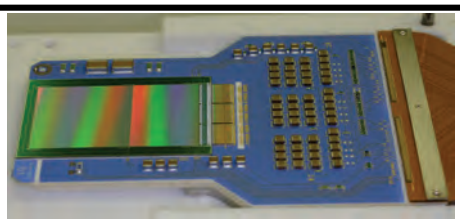

Fig. 1: eROSITA PNCCD detector consisting of the detector board (blue color), eROSITA PNCCD (on the left), three CAMEX ASICs (center) and rigid flex printed board as electrical interface (on the right).

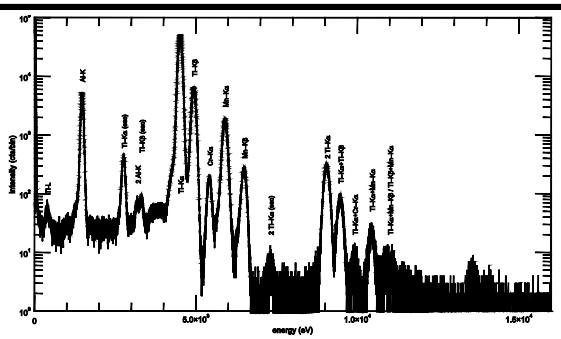

Fig. 3: Spectrum of the eROSITA onboard calibration source, which emits several lines at energies between 1.5keV and 6.5keV.

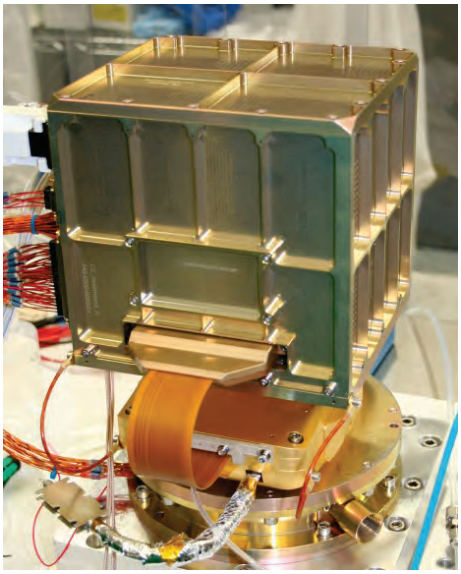

Fig. 2: eROSITA camera assembly with camera electronics box above and filter wheel below the camera head.

The flight cameras will be integrated to the eROSITA instrument after all acceptance tests and calibrations are finished (Fig.3). All so far obtained results confirm the camera design and meet the requirements of the eROSITA project.

References:

• Meidinger, N., et al., 2014, Proc. Of SPIE, 9144, 1W-1
• Meidinger, N., et al., 2010, NIM A, 624, 321
• Predehl, P., et al., Proc. of SPIE, 9144, 1T-1

N. Meidinger on behalf of the eROSITA team

Acceptance Tests and Calibration of the eROSITA Mirror Modules

The integration of all eight eROSITA flight mirror modules – including the flight spare module – was completed in November 2013. From the acceptance tests performed in our X-ray test facility PANTER we learned that all modules have a very good performance including a low energy on-axis resolution of 16" HEW. Then, each mirror assembly was completed with an X-ray baffle protecting the cameras against stray light. In February 2014 all mirror assemblies were ready for calibration. The setup for calibration in PANTER, which includes a precise measurement of the focal length (> 0.1 mm), was thoroughly checked and subsequently modified and improved. The calibration has started in 2015 and will continue til early 2016.

eROSITA's X-ray telescope consists of 7 co-aligned mirror assemblies, each with 54 nested Wolter-1 electro-formed mirror shells and an X-ray baffle made of concentric invar foils. The optical performance of each mirror module was tested in MPE's X-ray test facility PANTER (s. table below). After these acceptance tests the mirror modules were equipped with X-ray baffles that were precisely aligned; this was done under optical control in a dedicated baffle mounting and alignment stand that was improved after tests with the QM and finally reached an accuracy of 20 µm. A new vacuum proof gauge with optical distance sensors for the focal length measurement had been designed, built and tested and is now in use for the calibration. It will be also needed for the adjustment of the cameras to the telescope's optical bench.

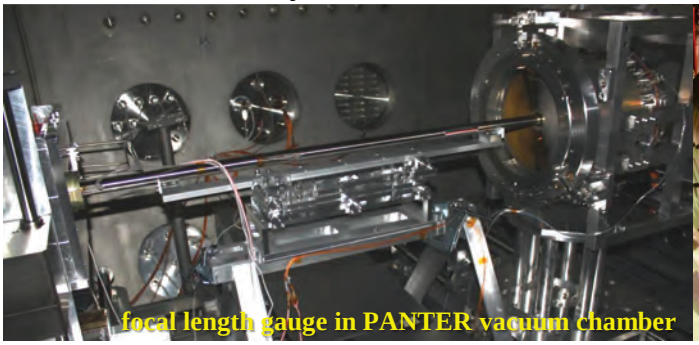
focal length gauge in PANTER vacuum chamber

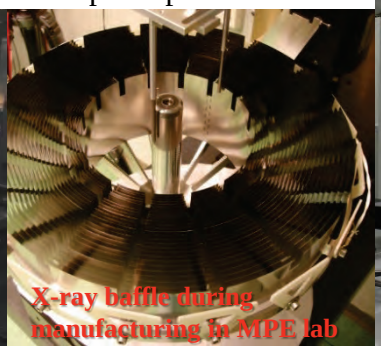
X-ray baffle during manufacturing in MPE lab

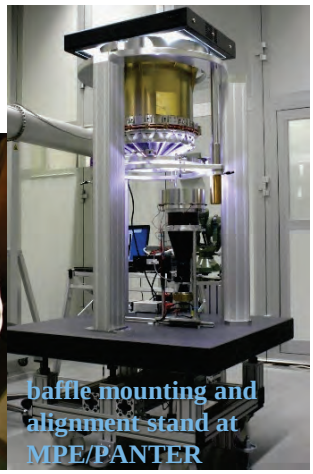
baffle mounting and alignment stand at MPE/PANTER

	Specification		Acceptance Test							
	Orbit	Derived for PANTER	FM 1	FM 2	FM 3	FM 4	FM 5	FM 6	FM 7	FM 8
			Dec 2012 / Jan 2013	Mar 2013	May 2013	Sep 2013 / Oct 2013	Sep 2013	Dec 2013	Dec 2013	Jun 2013
HEW Al-K (1.49 keV)	< 15''	< 15''	16.1±0.2''	16.8±0.3''	15.7±0.3''	16.0±0.3''	16.2±0.2''	16.3±0.3''	15.6±0.3''	17.1±0.3''
HEW Cu-K (8.04 keV)	< 20''	< 20''	15.2±0.1''	15.4±0.3''	16.7±0.4''	16.4±0.3''	16.2±0.3''	16.2±0.3''	16.6±0.3''	18.4±0.4''
W90 C-K (0.28 keV)	< 90''	< 90''	~89.8''	~106.5''	~107.9''	~106.7''	~119.6''	~127.3''	~107.9''	~123.6''
Eff. Area Al-K	> 350 cm^2	> 363.6 cm^2	391.9±16.1 cm^2	391.1±20.6 cm^2	392.6±15.5 cm^2	369.4±24.8 cm^2	387.9±19.2 cm^2	378.4±19.2 cm^2	391.6±24.8 cm^2	389.6±20.5 cm^2
Eff. Area Cu-K	> 20 cm^2	> 21.0 cm^2	24.8±0.8 cm^2	24.8±1.1 cm^2	25.1±1.2 cm^2	23.8±0.9 cm^2	24.1±0.6 cm^2	25.1±1.1 cm^2	25.0 ±0.9 cm^2	24.2±1.0 cm^2
Micro-roughness	< 0.5 nm	Scattering Cu-K < 15.7%	Scattering Cu-K 10.8%	Scattering Cu-K 11.2%	Scattering Cu-K 10.7%	Scattering Cu-K 12.0%	Scattering Cu-K 13.3%	Scattering Cu-K 11.3%	Scattering Cu-K 11.7%	Scattering Cu-K 11.4%

References:

- Burwitz, V. et al., "The calibration and testing of the eROSITA X-ray mirror assemblies", SPIE 9144, 91441X (2014)
- Meidinger et al., "Report on the eROSITA Camera System", Proceedings SPIE 9144, 91441W (2014)
- Dennerl, K. et al., „Determination of the eROSITA mirror half energy width (HEW) with subpixel resolution", SPIE 8443, 844350 (2012)
- Menz, B. et al., "Alignment of eROSITA like mirrors at the PANTER X-ray test facility", SPIE 8861, 88611I (2013)
- Friedrich, P. et al., "The eROSITA X-Ray Baffle", SPIE 9144, 91444R (2014)

P. Friedrich on behalf of the eROSITA team and the PANTER team

Environmental Tests of eROSITA Camera

For the qualification model of the eROSITA cameras a multitude of tests have been carried out. These include vibration, thermal-vacuum, electromagnetic compatibility (EMC) and numerous functional and performance tests. The data that is acquired from the PNCCD detector module during these tests is analyzed in order to verify that no degradation of the detector performance has occurred during the qualification procedure.

Space equipment must be able to withstand all environmental conditions that can occur during launch and the operation in orbit. The dynamic loads and the vibrations generated by the launcher are simulated in the vibration test by mounting the camera on a shaker. In addition to the damage control by optical inspection and measuring of eigenfrequencies, the performance of the camera was checked directly before and after the test by a special test procedure which allows us to operate the camera at atmospheric pressure and room temperature.

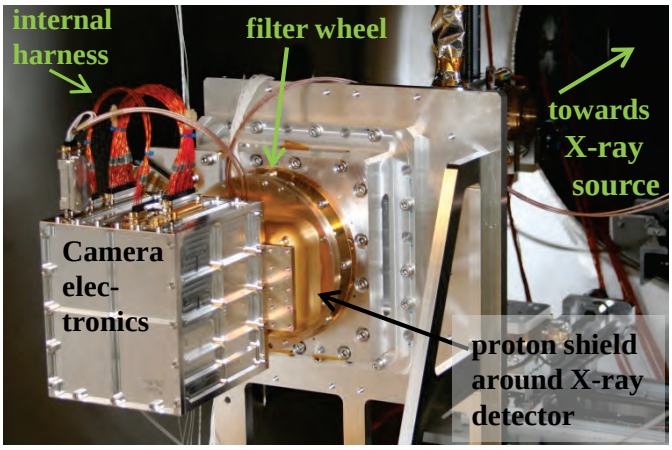

Figure 1: eROSITA camera assembly in the vacuum tank of the PUMA test facility

Figure 2: RF anechoic chamber for testing electromagnetic compatibility

After launch the cameras cannot be switched on instantaneously which leads to a rapid decrease in temperature. Thus switch on at low temperatures is critical for the reliability of the instrument. In the thermal vacuum test a startup of the camera at -52°C has been demonstrated. Figure 1 shows the setup for this test in the PUMA test facility. The camera electronics and the detector module were exposed to eight temperature cycles inside this vacuum chamber. The temperature range for the electronics and the detector module was -25°C to +30°C and -105°C to +23°C, respectively. Data were acquired during all cycles, the analysis showed a small dependence of the gain on the temperature of the electronics and of the detector but no evidence for an evolution in the course of the test.
For the conducted EMC test disturbances in the range from 1 kHz to 30 MHz are applied on the 27 V supply voltage of the camera. For all frequencies and for 10Hz spikes with ± 27V amplitude the readout noise of the detector of 2.5 electrons ENC was unaffected (within ±0.5%).
Radiated EMC was performed in an anechoic chamber at IABG (Fig 2). Electric fields with frequencies ranging from 10 kHz to 9 GHz and a field strength of 2 V/m were used as well as magnetic fields with frequencies from 1 kHz up to 300 kHz and a field strength of 0.1 A/m. A susceptibility of the camera was found at frequencies around 60 MHz which led to an increase of the mean noise of 8%. This can however be mitigated by a design change of the internal harness that has meanwhile been tested and showed only a noise increase of less than 1% in the critical frequency range. The performance of the eROSITA QM camera was unaffected after all environmental tests. Thus the instrument has proven to be reliable for the 7 year long SRG mission.

References:

• N. Meidinger, R. Andritschke, V. Emberger et al., Proc. SPIE , 9144

V. Emberger

eROSITA in-flight calibration programme

The German eROSITA telescope aboard the Spectrum-Roentgen-Gamma (SRG) mission will be placed into a halo orbit around the Sun-Earth Lagrangian Point L2, and perform, during its nominal 7.5 years lifetime, 8 all-sky surveys followed by a pointed observation programme. On the 15 weeks-long way to L2, the telescope will be commissioned and calibrated (accompanied by scientific performance verification observations). The celestial targets for the calibration phase have been carefully selected taking specifically into account the instrument capabilities (and also the limitations), visibility constraints, scientific priorities, as well as cross-calibration prospects with current and future missions.

Mission Timeline: After SRG launch and major orbit correction maneuvers the telescope door and the filter wheels will be opened for outgassing, along with initial check-out. After about 4 weeks the 7 cameras will be cooled. The commissioning of the first camera is expected to be finished after another week, the other cameras following at a rate of two per week, such that the full eROSITA telescope shall be operational with optimized set-up after about 8 weeks.

Calibration plan: The remaining time before reaching L2 shall be spent on in-flight calibration (4 weeks) and performance verification (3 weeks). While the targets for the latter phase will be selected based mainly on scientific value and instrumental capabilities, the calibration targets have been chosen to fit best certain calibration subjects. These include:

1. Plate scale and boresight of the modules
2. Gain and CTI calibration and monitoring
3. Optical light blocking filter integrity and performance
4. Soft X-ray response and contamination monitoring
5. Power-law type spectra for cross-calibration
6. Effective area, vignetting, and flat-fielding
7. PSF on-axis and off-axis for survey applications
8. X-ray baffle for stray-light reduction of sources with off-axis angles of 30-190 arcmin
9. Absolute and relative timing
10. XUV response below nominal threshold

Monitoring of background and CTI will be done with only one camera at a time, to avoid dark regions in the survey maps. After each all-sky survey several celestial sources shall be observed for further monitoring. Prior to the pointed programme an additional dedicated calibration campaign is planned to update and extend the initial calibration.

The corresponding celestial targets and/or target classes for the above listed calibration subjects are: (1) fields with many sources with well-known positions like Hyades, Pleiades, NGC 2516, etc.; (2) thermal supernova remnants like 1E 0102-72, Vela, Puppis-A, 3C58, in addition to on-board Fe-55 calibration source; (3) objects with extended optical emission, like the globular clusters Omega Cen, M4, M22, 47 Tuc, etc.; optical loading via X-ray dark star like alpha Cen; (4) non-variable soft sources like isolated neutron stars; (5) Mkn 3, PKS 0558-504, MS 0419.3+1943, MS 0317.0+1834, MS 0737.9+7441; (6) supernova remnants and clusters of galaxies, but also the survey itself, similar to creating the ROSAT PSPC detector maps; (7) due to pile-up restrictions only moderately bright X-ray sources can be observed: the baseline is to observe a few selected sources in the 3-10 cts/s regime from the 3XMM catalogue and in addition using the first eROSITA survey catalogue of point-like sources to construct off-axis dependent PSF, with wings from brighter sources like Cen X-3,Mkn 766, Mkn 205, 3C273; (8) scans or full great circles like the ROSAT mini-survey over Sco X-1 or other very bright point-like source; (9) pulsars like PSR J1119-6127, scans over X-ray sources in different directions to determine time-delays; (10) white dwarfs like HZ43, GD 153, PG 1658+441, PG 0136+251.

M. Freyberg on behalf of the eROSITA Consortium

Synergies in the XMM and eROSITA calibration

The eROSITA RMF was computed by fitting empirical mathematical functions which describe the shapes of various components and their energy dependence to X-ray spectra taken at the BESSY II synchrotron. The same technique was then applied to derive an empirical mathematical description of the already existing XMM/EPIC pn RMF. This made it possible to gain control of RMF fine structures which were not accessible before, and to let the RMF get automatically improved by passing this control to a program which adjusts the RMF by minimizing the residuals which result from simultaneous fits of fiducial X-ray spectra. This pioniering technique might also be of interest to future X-ray missions, like Athena.

The knowledge of the Redistribution Matrix File (RMF) is essential for the interpretation of measured astrophysical spectra. Unfortunately the RMF is often not known with the desirable accuracy, and it may change with time. This causes systematic errors in spectral fits which show up as increased residuals or may lead to wrong results. In order to improve this situation, we applied a method, which was originally developed for the determination of the eROSITA RMF, to XMM-Newton/EPIC-pn.

We tested it on the SNR 1E0102, which exhibits a rich and well known emission line spectrum, and could improve the spectral fit substantially. In order to minimize the risk that the RMF is adjusted to only one individual spectrum, we have now included simultaneous fits of complementary spectra into the optimization process.

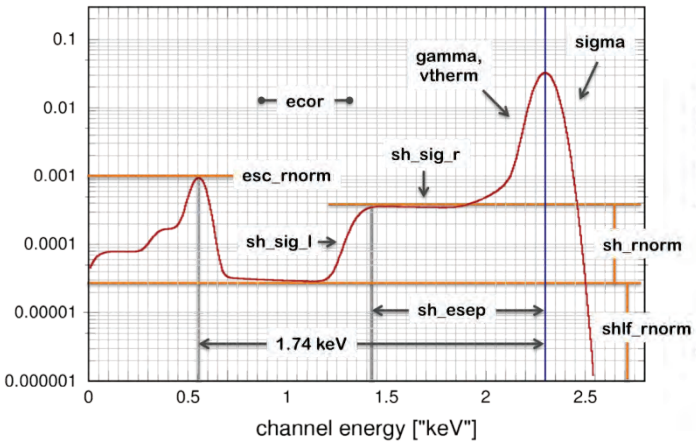

Fig. 1: Empirical parametrization of the XMM/EPIC pn RMF

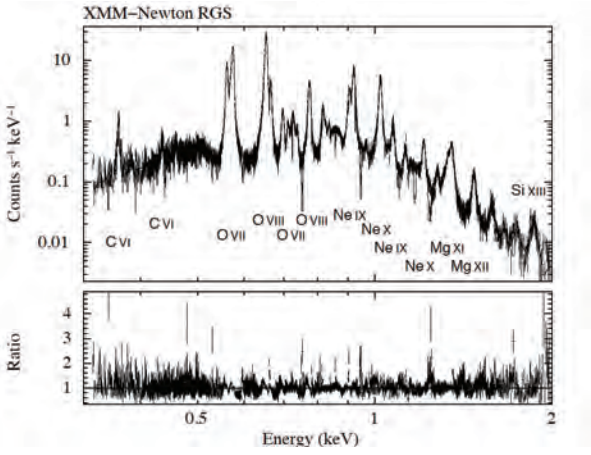

Fig. 2: XMM/RGS spectrum of the SNR 1E0102

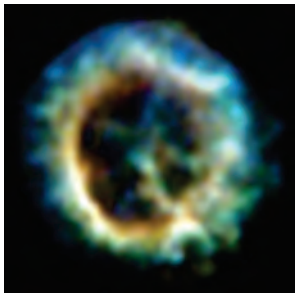

Fig. 3: Chandra image of the SNR 1E0102

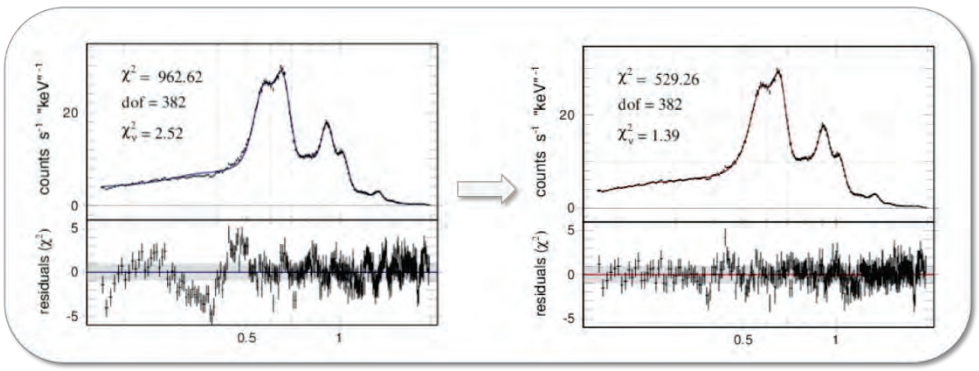

Fig. 4: EPIC pn best fit spectra of 1E0102 before and after the RMF refinement

K. Dennerl, F. Haberl

The eROSITA ground segment: preparing for in-orbit operations

As we are approaching the in-orbit phase of the eROSITA mission, the focus of the ground segment activities has shifted to integrating and testing the eSASS data analysis pipeline and to establishing interfaces and procedures with our Russian partners. Since mid 2014 an interactive version of the eSASS eROSITA data analysis software package is available to the eROSITA user community, which supports the analysis of simulated eROSITA data. Feedback from users, from internal testing by the software team, as well as from the eROSITA ground calibration activities, are fed into upgrades and improvements of the data analysis software.

eSASS Interactive Analysis

EVTOOL	SRCTOOL
FLAREGTI	
EXPMAP	ERBACKMAP
ERMASK	ERSENSMAP
ERBOX	ERMLDET
TIMECORR	BARYCORR
PATTERN	ENERGY
EVATT	RADEC2XY

Left: The eSASS software package provides interactive data analysis tools for **event filtering and binning**, **map creation**, **source detection**, **time correction**, and **event calibration** (color coding as in figure). Software tools printed in black are currently in use; tools printed in grey are still in development.

Bottom: The eSASS data analysis pipeline is set up to process data received during each daily ground contact within hours of reception at MPE. It is organized into processing chains for event calibration (TEL), exposure creation (EXP), source detection (DET), and source products (SOU), supporting the parallel execution of 200+ processing chains and of several pipeline configurations. All-sky survey (S), pointing (P) and calibration (C) data are separated into different data streams. Testing of the pipeline is conducted by feeding mock mission planning data through the SIXTE event simulator. The projection of all-sky survey scans, pointings and of slews between pointings into sky fields is shown.

eSASS Pipeline Processing

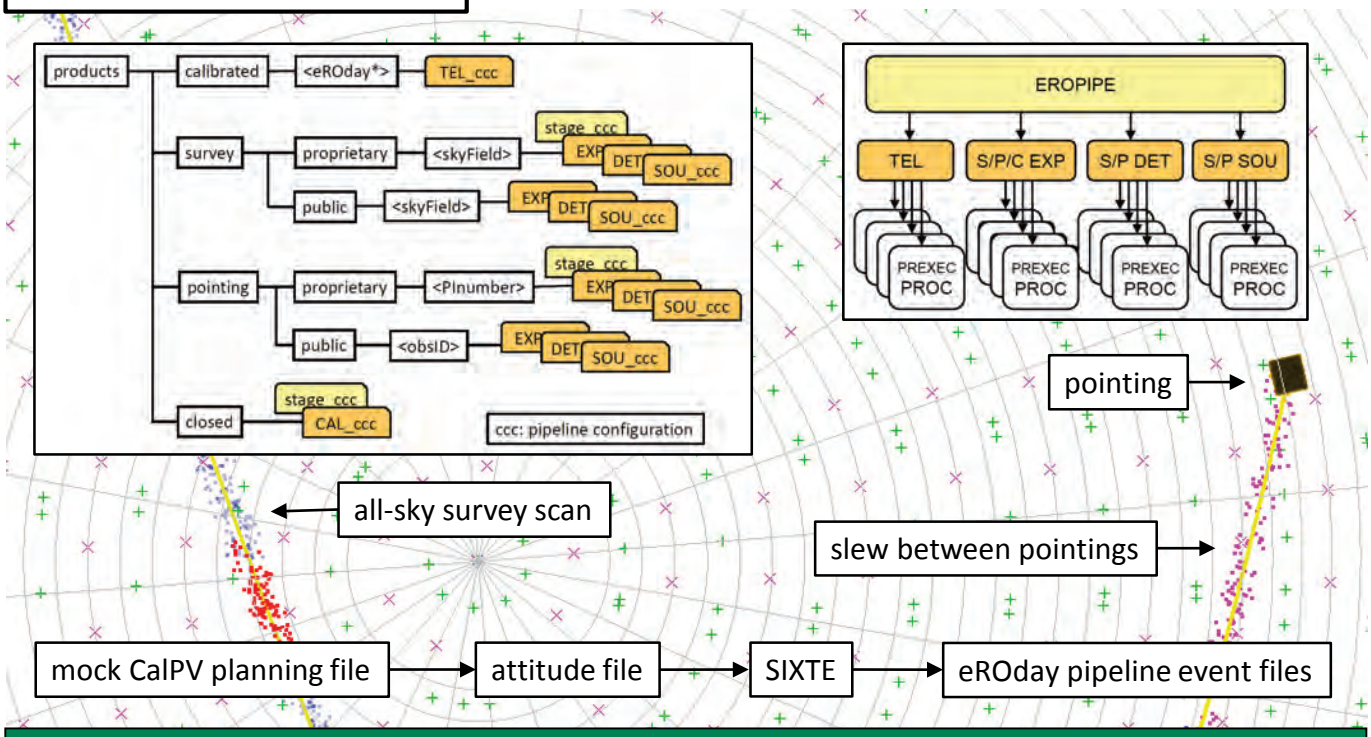

H. Brunner and the eROSITA ground software team

The eROSITA data analysis software: Events, Source Catalogs, Data Access

One of the crucial aspects for the upcoming eROSITA mission is to manage a large number of data products - more than 3 million sources are expected to be detected - and make them accessible to the scientists. Many different software tasks were created to accomplish this, some of which are highlighted here. For instance, task evtool creates merged and filtered eventlists as well as images. Task catprep produces self-updating source catalogs by identifying sources with previous detection runs and in overlapping skyfields. Finally task datool collects and prepares requested data products and makes them available to the user.

1 ... N event files

ID	RA	DEC
1	92.14	66.21
2	88.73	65.98
3	91.33	66.74
4	89.71	67.17
5	90.87	65.49
6	88.61	66.28
7	88.90	65.81
8	89.23	64.97

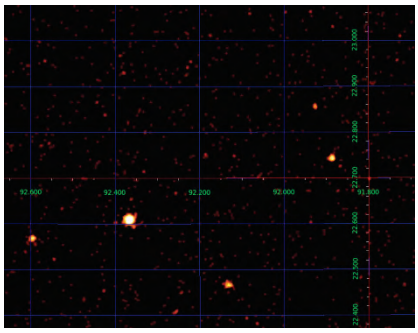

Evtool example: Multiple simulated eventlists (input catalog: RASS) were merged and region filtered. The image shows only a small part of the skyfield region. Events have been binned and smoothed with a Gaussian kernel for display purposes.

Catprep: Skyfields are processed individually. Sources are associated with the skyfield they were first detected in. More complex scenarios:

a) Source position is outside its respective skyfield (positional error). A boarder region (blue) for each skyfield is used to avoid missing this source, in the event that it is not detected in skyfield A and skyfield B.
b) Source is detected in two skyfields. Identification to avoid registering two sources instead of one.
c) Identify sources after each revolution.

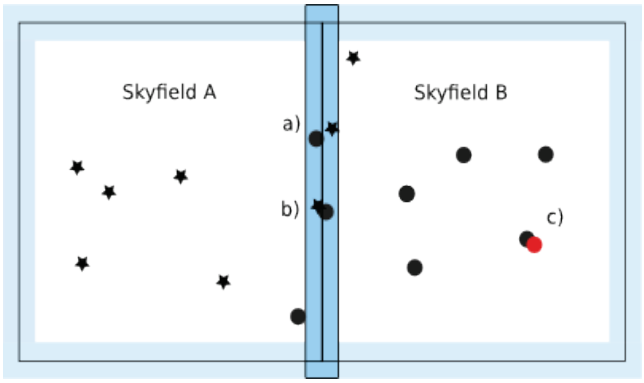

Datool: A data request is issued on a website. Datool will then collect all the files from the appropriate archive directories and prepare them according to the request.

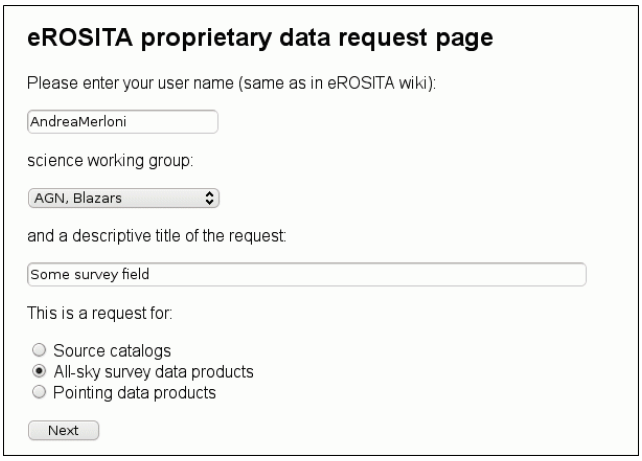

C. Grossberger, H. Brunner, T. Dwelly and the Bamberg eROSITA team

The Wide Field Imager for Athena

The WFI (Wide Field Imager) instrument is planned to be one of two complementary focal plane cameras on ESA's next L-class X-ray observatory Athena. It combines unprecedented survey power through its large field of view of 40x40 amin^2 together with excellent count-rate capability (<1% pile-up at 1 Crab). The energy resolution of the silicon sensor is state-of-the-art in the energy band of interest from 0.2 keV to 15 keV, e.g. the full width at half maximum of a line at 7 keV will be ≤170 eV until the end of life. This performance is accomplished by using DEPFET active pixel sensors with a pixel size of 130x130 µm^2 well suited to the on-axis angular resolution of 5 asec HEW of the mirror system.

Parameter	Value
Energy Range	0.2-15 keV
Field of View	40' x 40'
Angular Resolution Pixel Size	PSF=5`` (on-axis) 130 x 130 µm$^2$ (2.2``)
Large DEPFET detector	1024 x 1024 pixel
Fast DEPFET detector	2 x (32 x 64 pixel)
Quantum efficiency on-chip + external filter	20% @ 277 eV 80% @ 1 keV 90% @ 10 keV
Energy Resolution (end of life)	FWHM(7keV) ≤ 170 eV
Time Resolution full frame Fast detector Large detector	 80 µs <5 ms
Count Rate Capability @ 1 Crab	>80% throughput <1% pile-up
Particle Background (L2 orbit)	< 5 × 10^{-3} cts cm^{-2} s^{-1} keV^{-1}

Tab. 1: Key requirements and characteristics of WFI

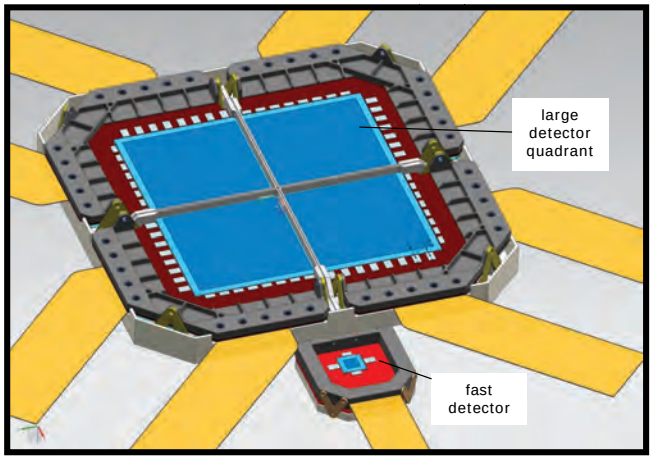

Fig. 1: Focal plane design of the WFI instrument: The large-area detector consists of four quadrants. The high count rate capable detector (shown at the bottom) has a format of only 64x64 pixels and is read out in split full frame mode to achieve the high time resolution of 80µs.

The main subsystems of the WFI instrument are the camera head with the detectors (see fig.1), a filter wheel with optical stray light baffle mounted in front of it, six detector electronics boxes dedicated to the detector units, and an instrument control and power distribution unit. The detector and electronics will be cooled in a passive way by large-area radiators. The volume of WFI is approx. 1.2x0.8x1.0 m^3, its mass is 227 kg, and has an average power consumption of 683W.

In the present technology development activity phase of Athena, prototype DEPFET sensors are developed in cooperation with the semiconductor laboratory of the Max-Planck-Society. They serve for a study about optimum transistor design and fabrication technology. Furthermore, a breadboard model of the detector with electronics will be developed for a test of performance and readout speed.

MPE is the lead institute for the WFI development (PI and project office) within the instrument consortium that comprises seven countries.

References:

• Meidinger, N., et al., 2015, Proc. SPIE, 9601, 0H-1
• Meidinger, N., et al., 2015, JATIS, 1,1, 014006-1
• Nandra, K., et al., 2013, 'The Hot and Energetic Universe' white paper, arXiv:1306.2307
• Rau, A., et al., 2013, 'The Hot and Energetic Universe' supporting paper, arXiv:1308.6785

N. Meidinger on behalf of the Athena WFI team

Thermal analysis of the WFI on ATHENA

The Wide-Field Imager (WFI) is one out of two instruments on the ATHENA observatory.

A large DEPFET detector for a field of view of 40'x40' requires a relatively high power consumption of the electronics. Both, the detector size and the power consumption, are challenging not only for the thermal control system.

Sensors as well as front-end electronics and electronics boxes have to be cooled. In order to reduce the necessary radiator area, three separate cooling chains with three different temperature levels have been foreseen.

After first estimations of heat loads and radiator areas, a more detailed model of the camera head was used to further improve and optimize the design of the instrument.

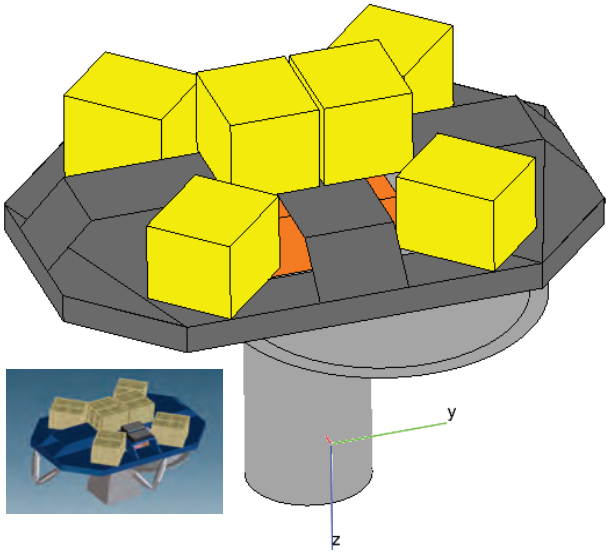

Fig. 1: Reduced thermal model of the WFI (small: CAD-model)

Simultaneously, the camera head has been evaluated in detail to optimize the mechanical design.
The CAD geometry is directly used for thermal analysis to get as accurate results as possible for the identification of possible bottlenecks with respect to heat flows.

Due to the low minimum operating temperature of the detector (-80°C), gradients are regarded particularly critical with respect to cooling power.

Step by step, the design has been improved and the result is a reasonable starting position for development tests.

The overall thermal behaviour is important for specifying the necessary boundary conditions such as required radiator area and thermal interaction with the other instrument and the spacecraft, respectively.

Therefore, a thermal model has been developed that has simplified but representative dimensions and contains the main power consumers and thermal couplings, taken from the detailed analysis as described below.

The result is a thermal budget with three interface points to the spacecraft, each with different heat loads at a certain temperature level that guarantee optimum operating conditions for the instrument.

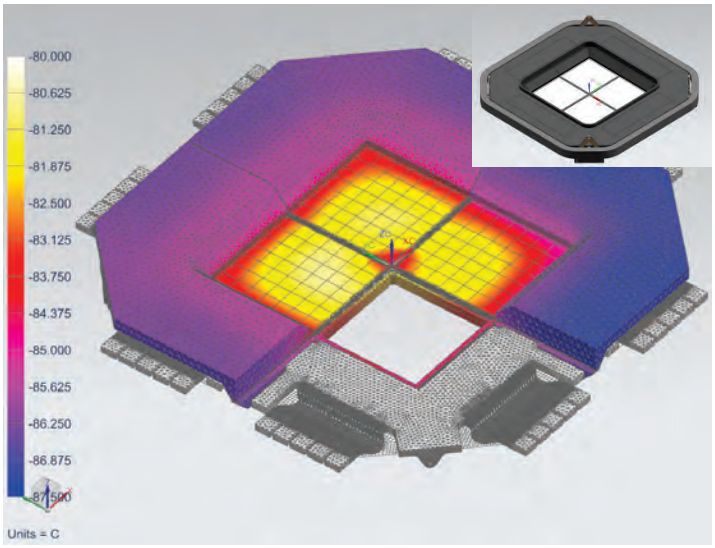

Fig. 2: Detailed temperature distribution of the WFI camera head (small: CAD-model)

M. Fürmetz for the ATHENA WFI team

WFI Detector Electronics and On-Board Data Processing

The Wide Field Imager is one of the two instrument on-board ESA's next generation X-ray observatory ATHENA. Active-pixel sensors are read-out with front-end ASICs. Data pre-processing is performed on-board using an FPGA-based frame processor.

The WFI focal plane inside the Camera Head consists of a detector array with five DEPFET sensors. Four large sensors, each at a size of 512x512 pixels, form an array to achieve the wide field of view of 40 arcmin squared. One fast sensor (64x64 pixels) is read-out in two halves and thereby provides high count rate capability with a frame rate of 12.5 kHz. The Control Frontend Electronics (CFE) is controlled by the Sequencer module of the Detector Electronics. The Analog Frontend Electronics (AFE) consists of 34 VERITAS readout ASICs generating an analog data stream of 260 MPixels per second.

This analog data stream is guided to six Detector Electronics units, each of which processes one quadrant of the large sensor array respectively one half of the fast sensor. In order to perform event recognition, the data stream needs to be processed. First, offset maps have to be generated by calculating each pixel's baseline level averaged over some hundreds of dark frames. Second, noise maps are calculated that provide the fluctuations for each pixel. With the use of the generated maps, offset subtraction is performed for all pixels of the frame while the common mode is corrected row-wise. Event filtering is then performed by selection of the signals with an amplitude higher than the lower event threshold but not exceeding an upper threshold. Invalid events that are e.g. due to MIPs (minimally ionizing particles) are rejected by algorithms. This pre-processing effectively performs data reduction which is necessary to be performed on-board in order to not exceed the feasible telemetry data rate from the satellite to the ground station. Further algorithms for loss-less data compression are performed in the Instrument Control and Power-distribution System. The following figure shows the data processing architecture of the WFI instrument.

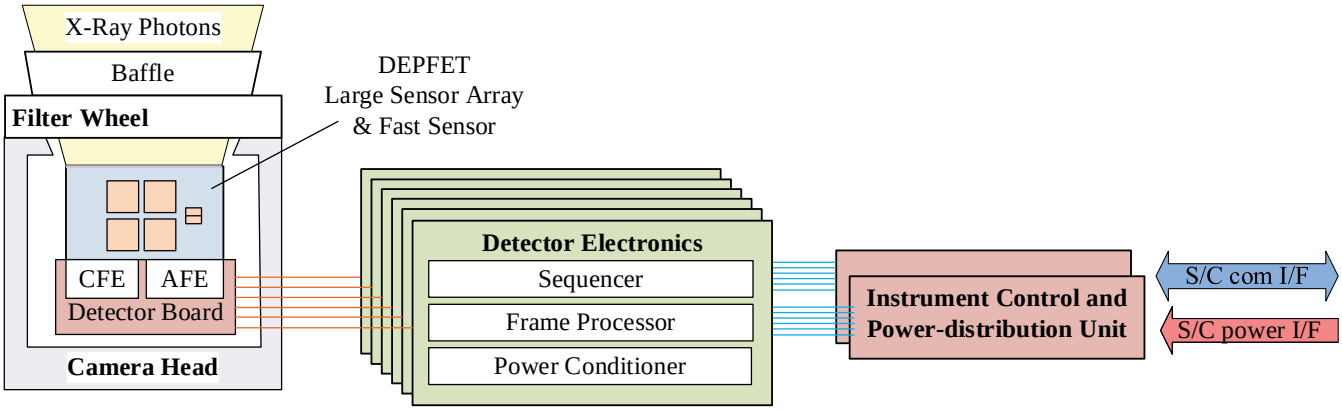

Various DEPFET devices are being designed and manufactured in the semiconductor laboratory of MPG. A modular and flexible test setup is currently being developed that allows testing of sensor devices in relevant environment. This laboratory setup serves as basis for the development of the WFI Detector Electronics development model which has to be built in the course of the WFI model philosophy.

M. Plattner on behalf of WFI Electronics Development Team at MPE

New evaluation concept of the ATHENA WFI camera system by emulation of X-ray DEPFET detectors

The Wide Field Imager (WFI) is an X-ray camera for the future observatory Athena, an ESA L-class mission. The signal processing chain of the WFI reaches from the sensing of incoming photons to the telemetry transmission to the spacecraft. Up to now the signal processing chain is verified with measurements of X-ray sources, thus only limited test scenarios are possible.

We present a new concept for evaluating the X-ray camera system. Therefore a new end-to-end evaluation is proposed, which makes use of a programmable real-time emulator of the WFI DEPFET detector system including front-end electronics.

This evaluation method is a powerful tool to support the development of the WFI camera setup not only in the early stage, but also to analyze problems occurring when the WFI is in orbit.

Figure 1 shows the end-to-end evaluation method schematically. The DEPFET detector with front-end electronics is replaced by the emulator which is connected to the Detector Electronics. With a variation of the input data and the emulator parameters different output data can be obtained. Specific image processing algorithms allow a comparison of the known input data with the output data. This helps to obtain more information about the system characteristics and further evaluate, debug and optimize the processing system of the WFI camera.
The proposed emulator has to be modular and flexible to incorporate all features and characteristics of the WFI detectors. For example different pixel structures, readout modes and timing characteristics can be emulated and effects like noise, pile-up, misfits, offset drift or disturbances can be generated.

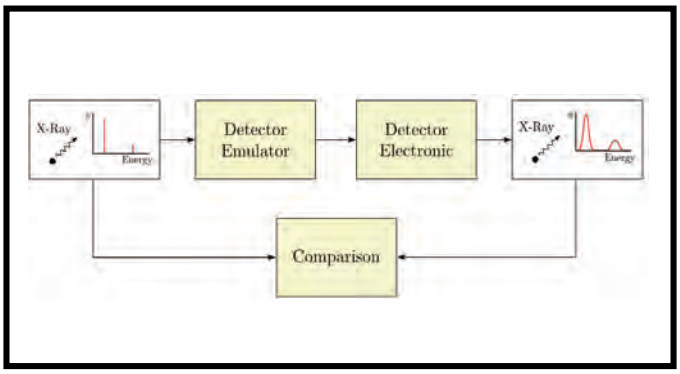

Fig. 1: Overview of the end-to-end evaluation method. The detector is replaced by an emulator system. The input can be set by the user. With a parametrization of the emulator and a comparison of input and output data, the method is a powerful tool to evaluate the WFI camera system from end-to-end.

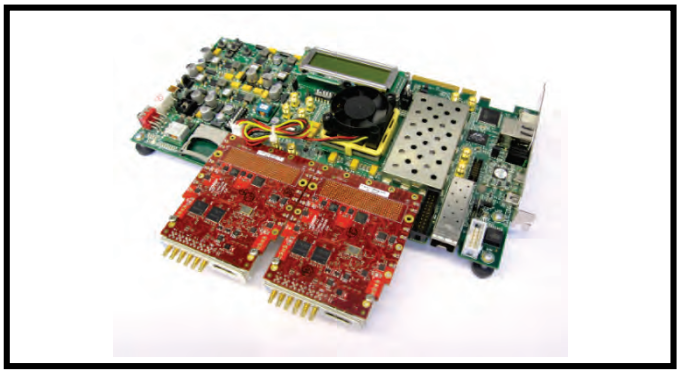

Fig. 2: Picture of the emulator hardware which consists of a XILINX Virtex 7 board equipped with two fast Digital-to-Analog converter cards providing up to eight channels.

In figure 2 a picture of the emulator hardware system is shown. The output signal is generated by a field programmable logic device to guarantee real-time behavior. Digital-to-analog-converters are connected to the FPGA. They provide eight simultaneous sampling channels with a resolution of 16 bit per sample and a sample rate of up to 400 MSample/s to generate eight output signals as needed for the large area detector with 512 pixels per row. A data rate of 6.4 Gbyte/s is needed to emulate the analog output of the WFI camera head in real-time.

S. Ott

Data Acquisition and Online Analysis software for ATHENA DEPFET detectors

For the development of the Wide Field Imager (WFI) within the ATHENA (Advanced Telescope for High-Energy Astrophysics) project, detectors equipped with various prototypes of DEPFET sensors need to be built, tested, optimized and qualified. Several test setups are currently used for this purpose, the so-called lab systems. In parallel to the development of a new DAQ (Data acquisition) system, a corresponding DAQ software has been developed. First measurements which use these DAQ components, have successfully started. Furthermore, existing Online Analysis software is being extended with new algorithms to investigate the new types of X-ray sensors.

The large detector array of the WFI consists of 4 DEPFET sensors with 512x512 pixels each. The MPG semi-conductor laboratory is expected to complete the production of another batch of DEPFET sensor prototypes in varying sizes in the second half of this year. The previous lab system could not handle this diversity in sensor sizes, especially the large sensor size with up to 8 readout-ASICs. The new lab system hardware under development suits these needs. Parallel to the development of DAQ hardware, matching DAQ software is required and the Online Analysis software has to be extended.

DEPFET lab-system with MicroTCA rack

The DAQ hardware components, such as ADC (Analog to Digital Converters) and sequencer, are based on the MicroTCA standard and use Gigabit Ethernet connections. The software which communicates with the MicroTCA system is running on a Linux machine.
It is responsible for configuring and controlling the ADCs and for configuring and programming the sequencer. The sequencer itself does program the readout ASICs and controls various detector components such as the switcher units. The software receives and processes data from the ADCs. A control GUI (Graphical User Interface) is included. The software includes a complete basic set of functionalities to operate the DAQ. Measurements with these components and their software have successfully started.

The Online Analysis software allows monitoring the detector performance in real-time. The existing software is well-tried with eROSITA detectors, but needs adaptations for DEPFET detectors. New algorithms are being developed, to allow the investigation of various types of X-ray sensors.

G. Hauser

Semiconductor Device Simulations for the Wide Field Imager of Athena

The Wide Field Imager (WFI) aboard Athena will use the DEPFET as base cell for its pixelated sensors. The DEPFET is a field effect transistor built on high resistive silicon substrate. A deep-n implantation below the transistor's external gate forms a potential minimum for electrons. Charge generated in the bulk by incident radiation is collected in this minimum, modulates the transistor's channel conductivity and can thus be detected.
Currently the prototype production for Athena's WFI sensor is fabricated at the Semiconductor-Laboratory of the Max-Planck-Society. The production includes several variations of transistor design and fabrication technology. To optimize these devices, an ongoing simulation study is conducted.

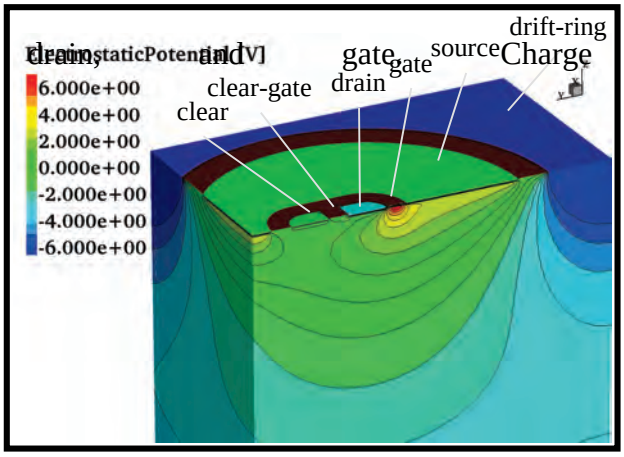

The DEPFET is a MOS-transistor formed by source, drain and gate. Charge generated in the bulk is collected in a potential minimum below the transistor gate, modulates the current-flow between source and drain and can thus be detected. A reset of the device is possible through the adjacent clear and clear-gate.
An example for a three dimensional simulation of the electrostatic potential of a DEPFET is shown left. Here, the DEPFET structure is embedded in a so-called drift ring. The most positive potential, the "internal gate", is formed below the transistor gate. As the isopotential-lines indicate, charges generated in the bulk are collected there.
While three dimensional simulations are mandatory to evaluate the complete functionality of a device, several optimizations can be done using two dimensional cuts through the device. A cut through the DEPFET's drain, gate, and source is shown below. With that simplified geometry, the properties of the MOS-transistor as transfer-characteristic, output-characteristic, transconductance, and charge gain as well as the influence of different technologies can be studied. Those simulations can be used to predict the optimum operational voltages for a given device and to estimate its performance.
The prototype fabrication of the WFI devices includes two main technology branches, that are primarily distinguished by their oxide thickness. The thick-oxide technology is well tested and currently the standard for spectroscopic applications. The thin-oxide technology provides a fully aligned production process that is less susceptible to alignment errors and offers a more homogeneous device performance. In addition, the thinner oxide is intrinsically more tolerant to radiation damages of the silicon dioxide insulator. However, these improvements are related to a decreased device amplification and higher electrical fields. Both technology branches were studied using two and three dimensional simulations.
For the thin oxide technology, an adaption of the implantation procedure that should reduce the electrical fields in the device and simultaneously increase the device gain was found. Overall, the device performance should improve. Two of the twelve prototype wafers are fabricated using that technology variant. The prototype production will be finished in the middle of this year.

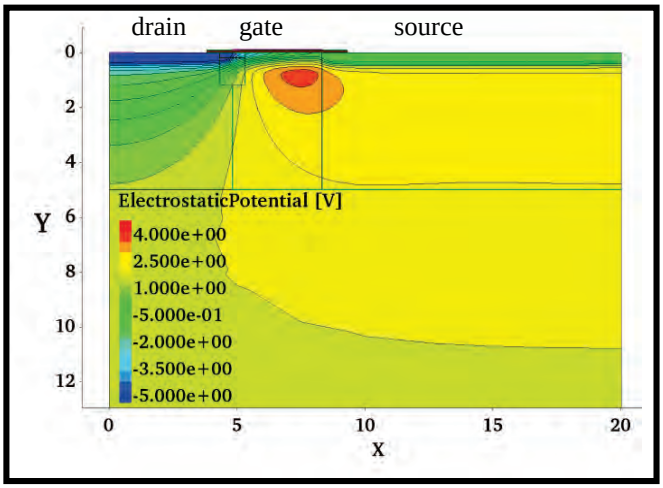

A. Bähr

High speed data acquisition system for the readout of the Athena DEPFET prototype sensors

The heart of the Athena camera is formed by a set of DEPFET (DEpleted P-channel Field Effect Transistor) active pixel sensors. In order to specify the characteristics of the different DEPFET prototype sensors, several preliminary investigations have to be done in the laboratory. The Semiconductor Laboratory (MPG HLL) will deliver a wide range of sensors. The sensors differs in size (64x64, 256x256, 512x64, 128x512 pixel) and readout modes (drain current & source follower readout). Therefore the lab system has to be flexible and modular. This lab system consists of up to eight fast ADCs (analog-to-digital converters) in combination with an FPGA, a multichannel sequencer system and a power supply for the front end electronics. This system is fast enough for the acquisition of raw sensor data. Therefore a µTCA (Micro Telecommunications Computing Architecture) based lab system is developed.

Fig. 1: µTCA data acquisition System (Rack)

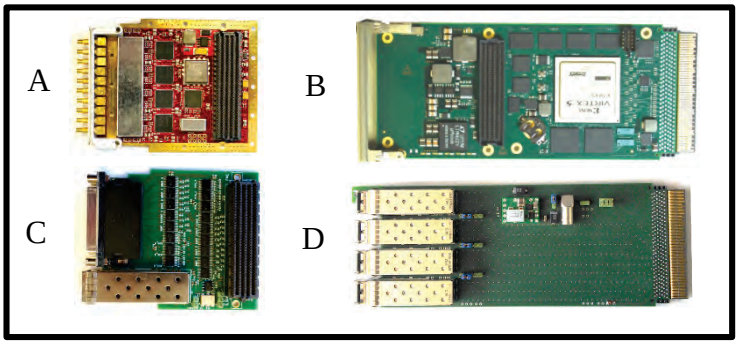

Fig. 2: µTCA Components: A: ADC card, B: FPGA card, C: sequencer interface, D: data interface (SFP)

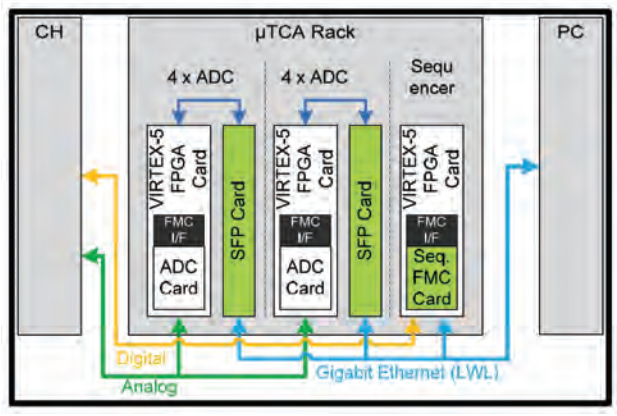

Fig. 3: DAQ-System (block diagram of the µTCA Rack)

The data acquisition system includes a sequencer in order to synchronize and control the ASICs (VERITAS & SWITCHER) and the ADCs. The sequencer consists of an FPGA card and a sequencer interface. Analog signals which are read out by the ASICs of the camera head (CH) are converted by two ADC cards (4 channels each) in combination with two FPGA cards. The Gigabit Ethernet interface with fiber optics performs the transmission of the frame data to the measurement computer. In order to minimize the data overhead the transmission is based on UDP (*User Datagram Protocol*).

Technical Data	Value
Frame Data Interface	8 x Gigabit Ethernet (SFP optical fiber)
ADC Channels	8 Channels
ADC Resolution	14 bit / 160 MSPS (ADC card is interchangeable)
FPGA	3 x VIRTEX 5
Sequencer Interface	66 x LVDS (for controlling & synchronizing the ASICs & ADCs)

J. Reiffers

Studies of prototype DEPFET sensors for the Wide Field Imager of Athena

The WFI camera of ATHENA will combine an excellent spectroscopic performance and high count rate capability with a large field of view. The large field of view will be covered by four DEPFET active pixel arrays. Each large array consists of 512x512 pixels. The requirement for the time resolution is defined to be smaller than 5 ms. Two readout possibilities are evaluated, in order to achieve a fast readout in combination with a good spectral performance.

One significant feature of DEPFET sensors is their ability to intrinsically amplify detected signals in order to enable a high speed and low noise operation. For this purpose charge, which is generated inside the silicon bulk is collected in a potential minimum below the P-channel MOSFET transistor gate (G). Each collected electron modulates the channel conductivity. After the channel conductivity has been measured the transistor is reset to its ground state by an N-channel MOSFET, which moves the collected charge through the clear gate (CG) to the clear contact (C). For the readout the gate of each pixel is switched on, the channel becomes conductive and an electrical current generates. The current consists of an offset fraction and a signal fraction. These current fractions can be separated by two readout methods. In the source follower (SF) configuration, the drain (DR) potential is fixed and a constant current is imposed through the channel. This results in a modification of the source (SRC) potential. In contrast, all potentials are fixed at the drain current (DC) readout, the offset current is compensated and changes of the drain currents - due to collected signal charge - are measured.

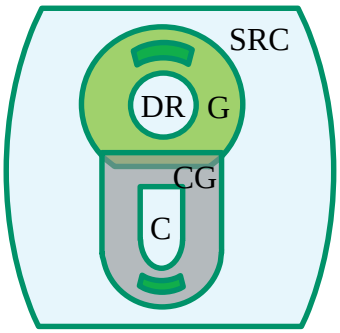

For the operation of large sensor devices, the two methods offer different advantages and disadvantages. The **source follower** readout mode allows easy coping with non homogeneities of the pixel matrix due to the AC coupled signal. On the other hand, it presents a relatively long settling time of the source potential, which is proportional to the load capacitance of the sensor. The **drain current** readout hardly requires any settling time but is sensitive on local variations of the transistor current due to the globally applied current compensation.

To evaluate the different readout methods, two similar 64x64 pixel sensors of circular cut gate devices have been illuminated in vacuum with a ^{55}Fe source at -50°C. The spectra of all pixel are considered to calculate the energy resolution at the Mn-K_α peak of 5894 eV for different readout timings. In both measurements, the VERITAS-2 readout ASIC, which can be operated in SF and DC configurations was used.

The readout time consists of a clearing period of 850 ns, a current integration and a settling period. The minimal required settling time was determined for both modes. Different readout times were applied by varying the integration time. For the 64x64 pixel device the methods deliver comparable results, although the drain current readout is better suited for short readout times.

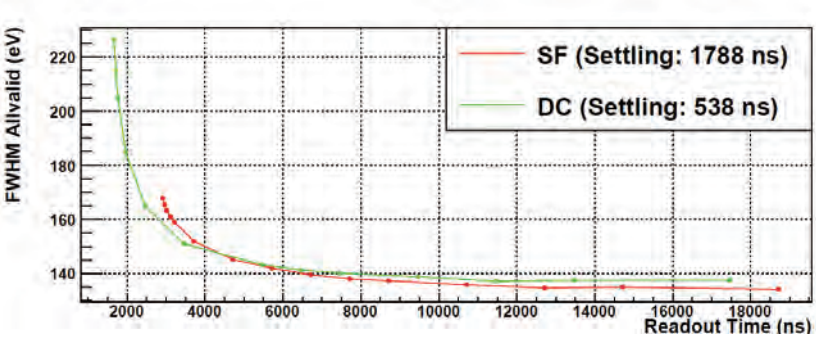

References:
• N. Meidinger, et al., *JATIS*, 1, 1, 014006 (2015)
• J. Treis, et al., IEEE Trans. Nucl. Sci., vol. 52, no. 4 (2005)
• M. Porro, et al., Proc. of SPIE Vol. 9144 91445N-1 (2014)

W. Treberspurg

Active Pixel Sensor Prototypes for Fast X-Ray Detectors

While the DEPFET types planned for the WFI of Athena show worse spectral response for very fast timings, the so-called Infinipix has been developed that mitigates this effect. It allows the spatial separation of the collection and the readout of the charges. This is realized by using two DEPFETs per pixel. One DEPFET collects the charge while the other one is read out. In the next frame the tasks of the two sub-pixels are interchanged. The current implementations of the Infinipix arrays already show excellent spectroscopic results. The energy resolution at 6 keV expressed as FWHM is 133.5 eV with a peak-to-valley ratio of 3500 for a readout speed of 2.5 µs per row and even 129.0 eV (peak-to-valley ratio of 4300) for a slower 5 µs readout.

In the depleted p-channel field-effect transistor (DEPFET) sensor concept (Kemmer and Lutz 1987), the signal charges generated by a X-ray photon in the fully depleted silicon bulk are stored in an internal gate that is implemented underneath a transistor. The collected charges influence the transistor current proportional to their number. That allows the generated charge to be measured directly in the pixel without destruction.
For the development of the Infinipix DEPFETs, three different layout variants were produced as 32 x 32 pixel arrays with a pixel size of 150 x 150 µm². They vary in the gate width and the design of the clear contacts which remove the collected charge after they are measured (Fig. 1).

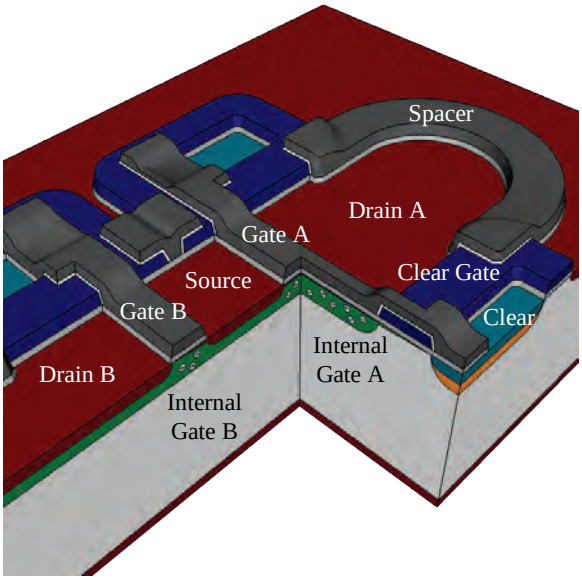

Fig. 1: Cut through a 3D outline of an Infinipix DEPFET with its two subpixels in the upper right and the lower left. The shared source is the readout node for the pixel. The collected charges are removed from the internal gates via the clear transistors.

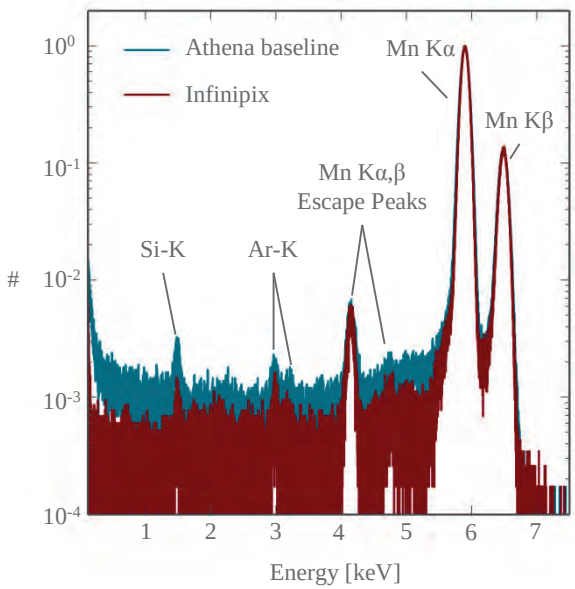

Fig. 2: Spectra (normalised to the Mn-Kα peak of a Fe55 source) of the DEPFET used as baseline for Athena and of an Infinipix. Even for moderate timings the difference in the background generated by the sensor during readout is visible.

The Infinipix shows its full potential for very fast timings. To achieve these, the next step would be a full parallel readout as that is one of the advantages of an active pixel sensor. At the moment the prototypes are designed and read out in a rolling shutter mode. With parallel readout the frame time and therewith the time resolution is reduced to the current readout time per row of a few microseconds.

References:

- Kemmer, J. and Lutz, G., 1987, Nucl. Instr. and Meth., A253, 365
- Bähr, A., et al., 2014, Proc. of SPIE, Vol. 9144, 914411-1

J. Müller-Seidlitz

Characterization of the readout ASIC VERITAS-2 for Athena's Wide Field Imager

For Athena's WFI a multi-channel ASIC is being developed at the Max-Planck-Institute for Extraterrestrial Physics. The VERITAS-2 ASIC will be used to readout DEPFET sensor matrices. It has been designed to operate in drain readout mode which permits a higher readout speed comparing to previous readout ASICs. Furthermore, it is the first ASIC to be fully differential, making it much less sensitive to induced noise. The development of the VERITAS-2 for the Athena project is an iterative process, where insights from previous versions are considered in the design of the subsequent one.

Several test setups were developed to enable a large range of measurements either on the VERITAS-2 alone or in combination with DEPFET devices and SWITCHER ASICs controlling the DEPFETs. A series of measurements, such as linearity, crosstalk, readout speed and noise were performed on the newest VERITAS version, the VERITAS-2.1. The measured characteristics will serve as a tool to identify necessary design adjustments and performance comparison for the final flight ASICs.

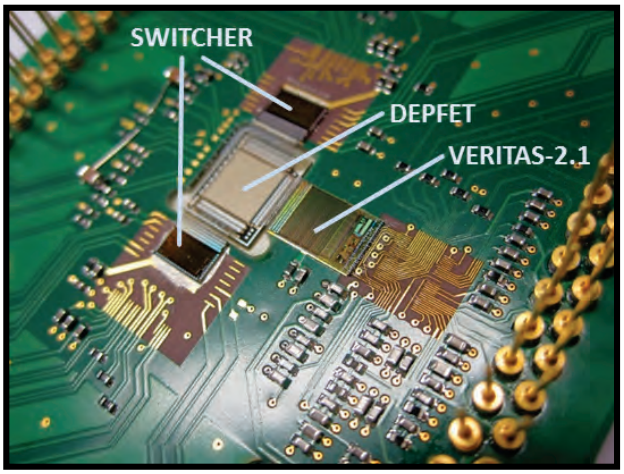

Fig. 1: Photograph of the hybrid used for first spectroscopic measurements with a VERITAS-2.1 readout ASIC, two SWITCHER ASICs and a 64x64 DEFET prototype matrix.

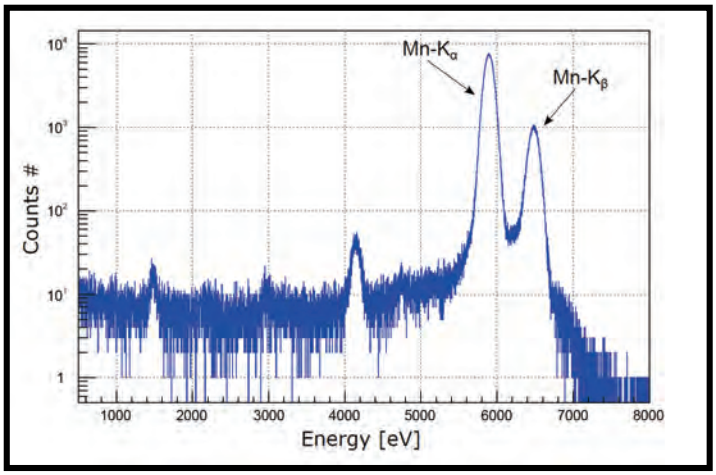

Fig. 2: Spectrum of a ^{55}Fe calibration source. Measured in drain readout with the VERITAS-2.1 ASIC.

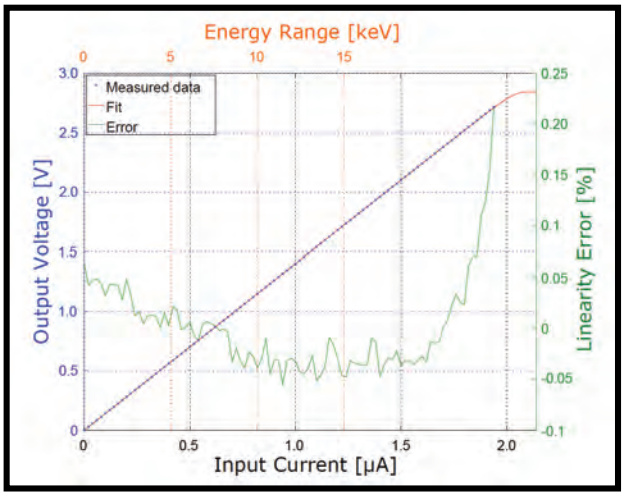

Fig. 3: Linearity Measurement of the VERITAS-2.1 in drain readout. The linearity is < ±0.1% within the dynamic range of 15keV (assuming a DEPFET gain of 300pA/el.).

Results:

- A linearity of < ±0.1% was measured for a dynamic range of 15keV with the VERITAS-2.1.
- First spectroscopic measurements of a small DEPFET device with a VERITAS-2.1 drain readout show an ENC of 3.5 el. rms.

Currently the VERITAS-2.1 is under test with DEPFET prototype devices and studies especially regarding the readout speed are performed.

References:

•Porro, M., et al. 2014, *Proc. SPIE*, 9144, 91445N
•Meidinger, N., et al. 2015, *JATIS*, 1, 1, 014006

A. Koch

Estimation of the ATHENA WFI instrument background

High energetic cosmic ray particles will pass the ATHENA WFI instrument and create secondary particles, e.g. electrons and photons in interactions with material surrounding the detectors. These secondary particles might mimic the expected x-ray signal and reduce therefore the confidence level with which a signal can be detected. In order to allow for a good confidence level also for the detection of faint signals, this background needs to be reduced as far as possible and its level needs to be known with small uncertainty. Detailed GEANT4 simulations are applied to understand the background and different roads for background reduction are being followed.

Some of the data analysis projects foreseen at the ATHENA WFI depend on a low background level for observations made with the large WFI DEPFETS. The ATHENA scientific requirement on the instrumental background is $5 \cdot 10^{-3}$ cts/(cm^2 s keV). Monte Carlo simulations, employing the GEANT4 (2003)-based GRAS tool (2005), are used to estimate the expected instrumental background. Contributions due to cosmic ray protons, electrons and He ions are taken into account.

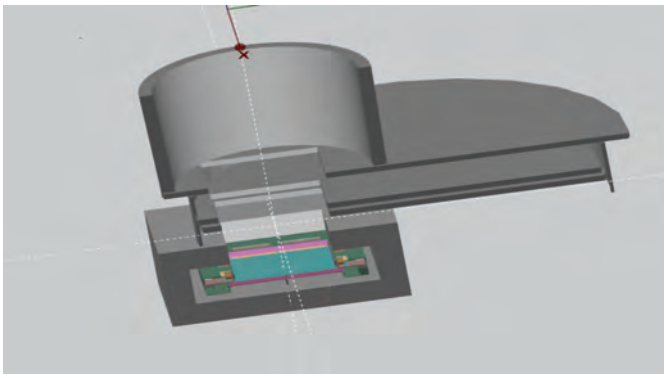

Fig. 1: Cut through the simplified WFI model used to simulate the presented instrumental background spectra.

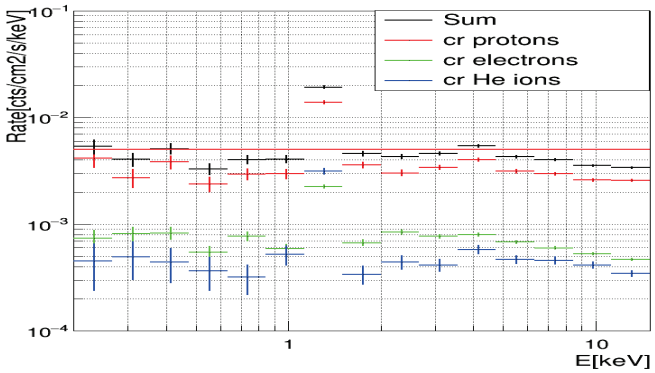

Fig. 2: Instrumental background spectra, for the simplified WFI model. Frames in which at least one pixel is in overflow are discarded. The red line marks a background level of $5 \cdot 10^{-3}$ cts/(cm^2 s keV), which corresponds to the scientific requirement.

The WFI mass model used in these simulations will be updated whenever major modifications in the WFI camera head development appear. The mass model presented in Fig.1 is a simplified version of the latest stage of the WFI development. These simplifications help to keep the computing time under control. In the resulting instrumental background spectra, presented in Fig. 2, event selection criteria have been applied to reduce the overall background level, leading to a background which is apart from fluorescence lines below the scientific requirement of $5 \cdot 10^{-3}$ cts/(cm^2 s keV). Hit pixels which touch the detector border are discarded, as well as readout frames in which in at least one pixel more energy is deposited than possible by an X-ray photon. Assuming a readout time of the large area DEPFETS of 1.3ms, these selection criteria lead to a signal loss of ~18% and a background reduction of ~39%. This event selection could be applied on ground. Possible improvements to this event selection are being studied.

References:

• Agostinelli, S., et al. 2003, NIM, 506,3, pp 250-303
• Santin, G., et. al. 2005, IEEE Trans. Nucl. Sci., 52,6, pp2294-2299

T. Eraerds

Offline Data Analysis for Developing the ATHENA WFI Detectors

The ATHENA WFI detectors will use DEPFET pixel arrays as key elements. The currently available designs need to be tested and optimized in several ways to fulfill the needs of the WFI in terms of energy and time resolution. A lot of parameters need to be quantified from each measurement such as offset values, noise, charge clear, pixel-individual gains, and finally energy resolution and peak-to-valley ratio. This task is accomplished by the Offline analysis software tools originating from the tools of eROSITA and MIXS (BepiColombo). Improving and enhancing the set of algorithms is an ongoing work as done recently for better quantization of incompletely cleared charges or improving the robustness of pixel-individual gains at low statistics. One major issue for the near future will be a major speed up of the whole analysis by parallelizing the calculations in view of the upcoming larger devices.

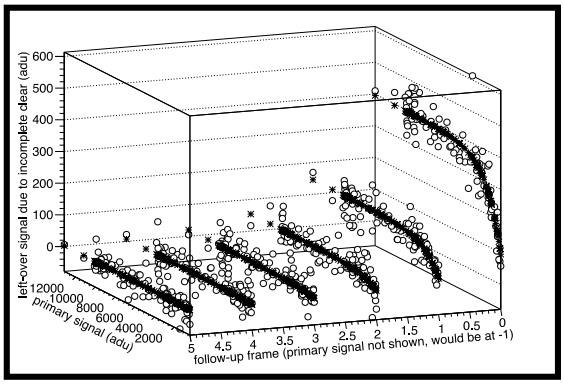

One parameter for judging between different DEPFET designs describes the quality of the charge clear process. It quantifies if and how many charges are left over after clearing the pixel. A new algorithm including a model for the incomplete clear has been developed. The left figure shows for illustration the data (circles) of a pixel with a pronounced incomplete clear and the fitted model (asterisks). The model assumes a potential pocket which releases charges by diffusion. The left-over charges increase with larger primary signals until the pocket is completely filled and then saturate as seen in the first follow-up frame (=0 in fig. left).

In the successive frames the signal decreases exponentially due to diffusion of electrons out of the potential pocket. This effect has been confirmed by device simulations and optimizations of the design are already implemented on the current WFI prototype sensor production.

A critical step in evaluating the detector performance is the determination of the gain for an energy calibration. Each DEPFET pixel has its individual gain since it is an amplifier, and this gain depends on several parameters. That means that it is necessary to determine the peak position of a X-ray line for each pixel (4096 for small prototype devices and up to ~10^6 for the full WFI) in each measurement. Principally a fit of a simple gaussian is sufficient. In practice this is not very robust. Especially in the case of the Mn-Kα and β lines of the widely used ^{55}Fe lab source, the algorithm may mix up α and β peaks or in case of a measurement with bad energy resolution both peaks may not be separated well. Some pixels may show a pronounced background of incompletely measured events. This is the case for example at corner and edge pixels when charges are split over at the edge(s) of the sensitive area (partial events). A model of two gaussians and a constant background gives more reliable results. In the figure (right) the spectrum of an edge pixel and the corresponding fit is shown. This example is an uncritical case selected for illustration. There are measurements with lower statistics, a significantly pronounced background, or lower energy resolution. Then the peak often cannot be separated well enough from the other components so that a fit of a simple gaussian fails.

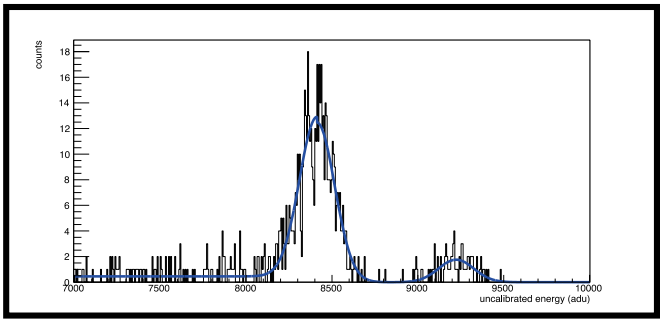

References:

• R. Andritschke et al., “Data Analysis for Characterizing pnCCDs”, 2008 IEEE NSS Conf. Rec., 2166 ff.

• T. Lauf, R. Andritschke, “ROOT based Offline and Online Analysis (ROAn)”, NIM A 762, 142-148

R. Andritschke

Screening and validation of EXTraS data products

MPE is participating in the EU-funded EXTraS project (Exploring the X-ray Transient and variable Sky) which is aimed at fully exploring the serendipitous content of the XMM-Newton EPIC database in the time domain. The teams are in charge in characterising aperiodic variability for all 3XMM sources, searching for short-term periodic variability on hundreds of thousands sources, detecting new transient sources that are missed by standard source detection, searching for long term variability by measuring fluxes or upper limits for both pointed and slew observations, and finally performing multiwavelength characterisation and classification. MPE is in charge of the screening and validation of the different products.

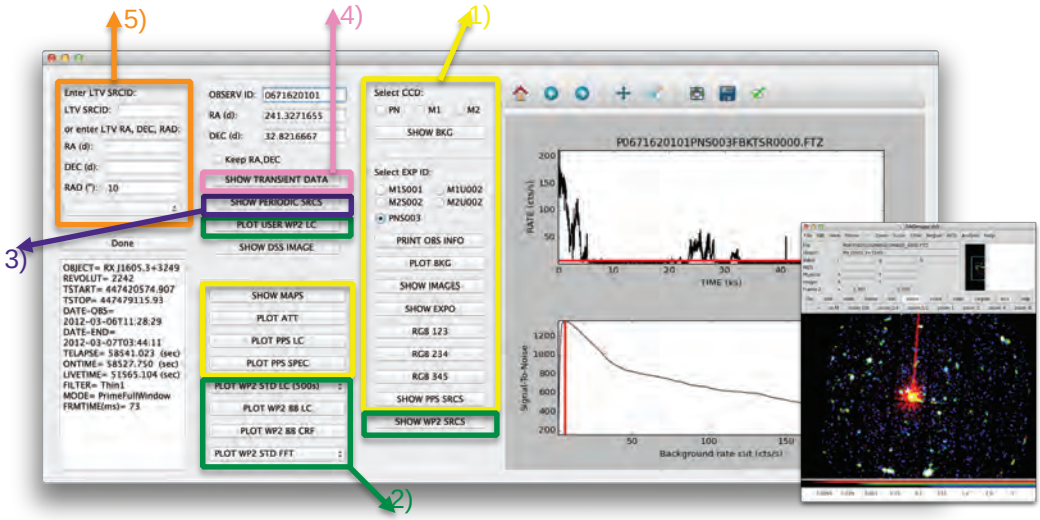

Fig. 1: A Graphical User Interface has been developed to allow a quick visualisation of the XMM-Newton PPS files, EXTraS data products and optical dss image of the FOV. Written in Python, it has a plot/graphic window and an interface to ds9 for image display.

1) PPS products: the GUI displays images like background, exposure maps but also scientific images in one or several bands (including RGB images), plots of the background light curve, changes in the attitude, light curves and spectra of brightest sources, and prints information about the observation.
2) WP2 products (aperiodic variability): the GUI displays light curves (with different binning times), Bayesian Block light curves, Cumulative Rate Functions, Fast Fourier Transforms and Energy spectra. It also allows the user to produce its own light curves using different settings.
3) WP3 products (periodic variability): the GUI displays graphs of the Discrete Period Search, Power Spectra Density, folded light curve and Epoch Folding search around period. The user can also perform its own period search via Lomb Scargle Periodograms, using different settings.
4) WP4 products (transient sources): the GUI displays images of the transient candidates in the relevant time interval, with exposure and background maps, prints the detection parameters and allows the user to produce its own light curve using different settings.
5) WP5 products (long term variability): the GUI displays long term light curves using the WP5 catalogue which contains fluxes and upper limits from pointed observations and slew surveys. It prints variability parameters and shows images of the sources in the different observations.

Besides a case-by-case screening, we are also planning to perform some systematic analysis from part of or from the entire catalogues, eventually that will not require visual inspection.

EXTraS webpage: http://www.extras-fp7.eu/

S. Carpano, F. Haberl

The 4MOST Operations System

The 4MOST multi-object spectroscopic instrument, to be mounted on the ESO/VISTA telescope, will be used to conduct an ambitious multi-year wide area sky survey. A disparate set of science goals, requiring observation of tens of millions of galactic and extragalactic targets, must be satisfied by a unified program of observations. The 4MOST Operations System is designed to facilitate this complex task by i) providing sophisticated simulation tools that allow the science team to plan and optimize the 4MOST survey; ii) carrying out optimized medium-term scheduling, using survey forecasting tools and feedback from previous observations, and iii) producing sets of observation blocks ready for execution at the telescope. We present an overview of the Operations System, highlighting the advanced facility simulator tool and the novel strategies that will enable 4MOST to achieve its challenging science goals.

Operations of the 4MOST facility imply managing a system with many moving parts (positioners) and many science cases (parallel survey mode) over a 5 years time frame in an effective and efficient manner. The **OpSys**, for Operation System, is the main interface through which the 4MOST users will drive the 4MOST activities, and will be used to:

- Ingest catalogues, success metrics, survey strategy parameters, instrument descriptions, and manage them over time.
- Faithfully simulate and optimize scheduled observations, then create and validate Observing Blocks (OBs).
- Monitor and report survey progress.

The Facility simulator (4FS) part of the OpSys offers the following features:

4FS_OpSim: An *Operation Simulator* that simulates the running of a full, 5 years, 4MOST sky survey. It takes as input a set of real or mock target catalogues, with estimated required exposure times for a limited set of observing conditions. 4FS_OpSim uses a detailed model of the 4MOST facility, the observing conditions at Paranal, and observational constraints, it models the various survey strategy algorithms (sky tiling, OB scheduling, fibre assignment, progress monitoring) that will be used by the real 4MOST survey to deliver the maximum science impact possible, as measured by numerical *Figures of Merit* for each reference survey.

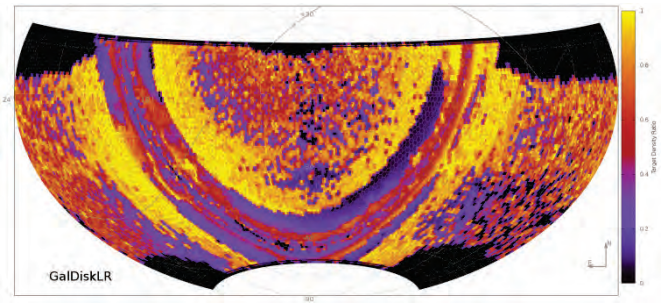

Output sky density fraction of observed galactic targets

4FS_ETC: The *Exposure Time Calculator*, is used to fold model spectral templates through the 4MOST system response (Throughput Simulator module), and to make quality judgements from the resultant spectral realisations (Data Quality Control Tools module). 4FS_ETC is typically used to estimate the minimum exposure time required under a set of observational conditions to "successfully" observe a target, where success is defined by a set of machine-readable metrics that can be calculated from a folded spectrum. The 4FS_ETC can also generate 1D folded spectra for external analysis.

4FS_RST: The Reference Star and Tiling optimisation tool, takes a list of tiling, mocking a whole survey and, using a reference star catalogue, a set of rules for success, and a few optional optimisation options, checks whether each of these tiles is observable. A tile is observable if the system can find enough reference stars in the guiding areas, for the guiding, rotation, monitoring of the optical conditions and calibration of the guide spine. The tool returns the list of feasible tiling and a list of the ones which can't be observed, and plots them on the sky.

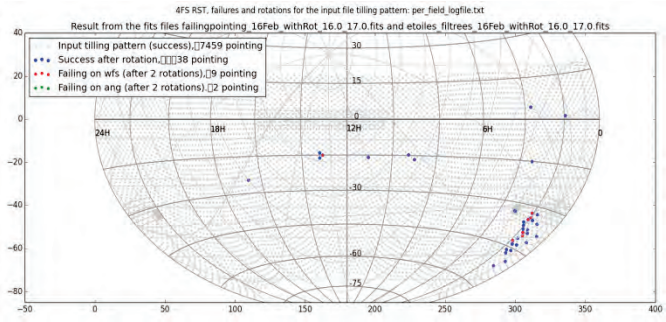

References:

• Boller & Dwelly, 2012, SPIE, 'The 4MOST facility simulator: instrument and science optimisation' http://arxiv.org/abs/1208.4733
• De Jong et al., 2014, SPIE, '4MOST: 4-metre Multi-Object Spectroscopic Telescope' http://adsabs.harvard.edu/abs/2014SPIE.9147E..0MD

A. Gueguen for the 4MOST Team

Next generation X-ray Mirrors: The slumping of thin glass foils

Next generation X-ray observatories require light-weight mirrors of large collecting area combined with very good angular resolution. For their manufacturing, MPE is developing a technique known as ‘indirect slumping’: This replication process enables the production of thousands of Wolter I mirror segments by shaping thin glass foils in an oven over suitable concave moulds. After the forming step hereafter reported, the mirror segments are coated with an X-ray reflective layer before being integrated in optical modules, a number of which are finally aligned in a supporting structure to form the complete X-ray telescope assembly.

Thin glass foils are shaped on Porouse Ceramic, Silicon Carbide (CeSiC) and Fused Silica moulds. The use of different materials allow to explore the several aspects of the technology and the influence of process parameters on the final results. A thermal cycle lasts typically 24h, and the maximum temperature depends on the specific glass, being around 600°C for D263 and 800°C for AF32 glass.

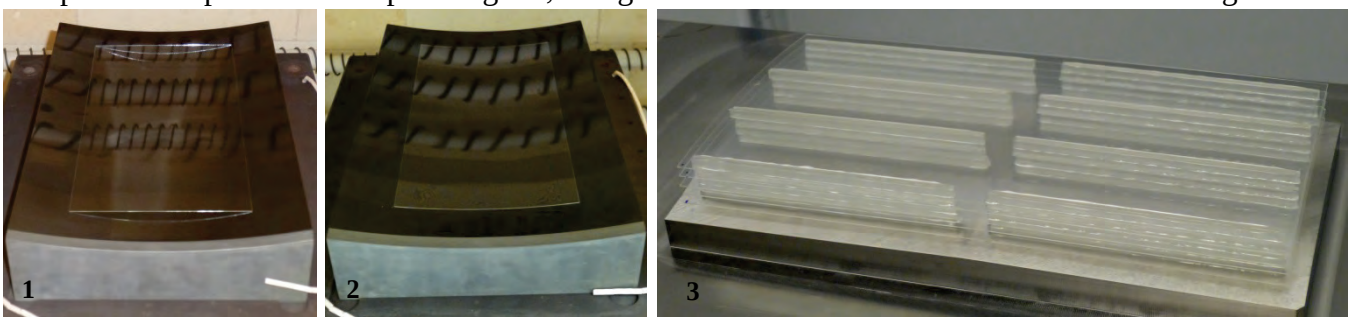

(1): D263 glass over CeSiC Wolter-I mould before slumping. The mould’s radius of curvature is 375 mm and the sagittas of few mm. (2): After the thermal cycle, the glass is bended and has replicated the shape of the mould, as clearly shown by the reflection of the heating elements. (3): Glasses of standard dimension are 200mm x 100mm, with a thickness of only 0.4 mm or even less. (4): Glasses integrated into a prototype X-ray optical module in collaboration with a research institute in Italy.

The slumped segments are characterized with an optical sensor on high-precision 3D measuring table: The comparison of their shape with the one of the mould shows the quality of the slumping process itself and where improvements can be added. A selection of glasses are afterwards integrated in prototype modules and characterized directly in X-ray at the MPE-PANTER testing facility allowing the assessment of the optical performance predictions and the validation of mechanical simulations.

Present results show a quite good replication of the mould shape, with residuals errors within few μm: Further investigations are ongoing to reach sub-μm level. The latest studies involve the innovative use of vacuum oven to explore a different thermal environment during slumping and prevent oxidation, opening the way for new materials consideration.

More than 100 glass segments have been slumped in the period 2013-2015, letting to deepen the institute worldwide recognized expertise in the field. They have been employed for integration tests both at MPE and in collaboration with INAF-OAB research institute in Italy. Vibration tests have also been performed at MPE to check the survival at launch. Recently, a new investigation on the application of Ir reflective layer has started in collaboration with Aschaffenburg University.

References:

• L. Proserpio et al.,: “JIM: a Joint Integrated Module of glass X-ray optics for astronomical telescopes”, 2015, Proc. SPIE, 9603, p. 960311
• A. Winter et al.: “Progress on indirect glass slumping for future x-ray telescope optics”, 2014, Proc. SPIE, 9144, p. 914451C

L. Proserpio, E. Breunig, P. Friedrich, M. Wen, A. Winter

Alignment and integration of slumped glass modular X-ray mirrors at MPE

MPE is studying modular X-ray telescopes based on slumped glass mirrors for future missions. An alignment and integration facility has been build and commissioned that is able to assemble representative mirror modules. With the use of numerical simulation and validation by deflectometry measurement, different concepts for mirror bonding and mirror module interface design have been studied and characterized.

The capability to assemble large X-ray mirrors from multiple smaller modules and individual optical segments is an enabling technology for the next generation of X-ray observatories (e.g. ATHENA). We study the requirements, problems and potential solutions for a number of different aspects of the alignment and integration process.

The major contributions to mirror performance degradation during alignment and integration come from the shrinkage of the epoxy adhesives that are used to bond the individual mirror segments to the module structure and from thermo-elastic distortion which is also affecting the mirror assembly in space. Both effects can be mitigated by proper design of the mirror segments interfaces and optimization of the bond geometry. Any such solution has however also a feedback to the mirror assembly overall design and can influence the modularization scheme and mirror geometry.

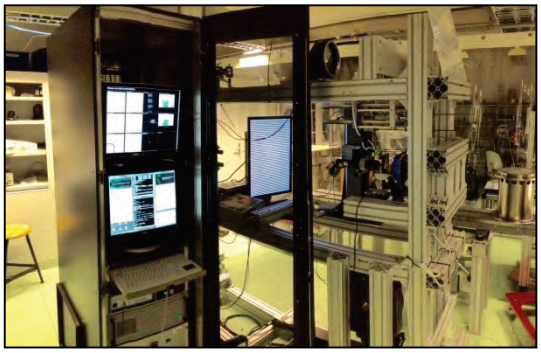

Figure 1: Panoramic view of the alignment and integration facility in the MPE laboratories. Note the deflectometer reference screen in the middle of the image

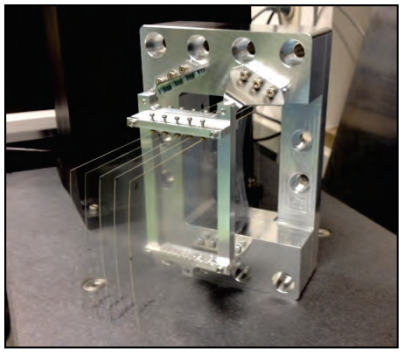

Figure 2: A recently assembled mirror module demonstrator connected to a shaker adapter. Five mirror segments are integrated (foreground).

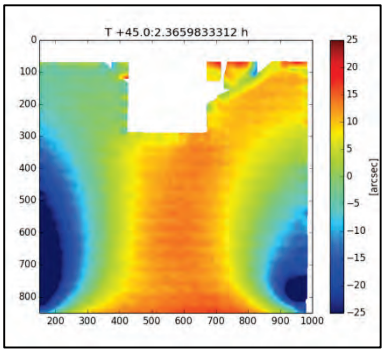

Figure 3: Slope error data obtained with the deflectometer showing shrinkage effects during integration on the parabolic surface.

FEM simulation can be used to predict and optimize most steps of the alignment and integration process. Nevertheless it is essential to obtain experimental data to validate the numerical results and check the practical feasibility of our concepts. To do so, an alignment and integration facility is available in the MPE laboratories that can be used to study the different effects and the evolution of the mirror‘s optical performance with a number of different metrology systems. These include a 15cm diameter collimated laser beam and a deflectometry system. The deflectometer, which uses the reflected image of a sinusoidal reference pattern to infer surface slope variations, allows us to precisely track variations in the mirror segment shape during the integration and is considered a novelty with respect to X-ray mirror development.

The current activities focus on the detailed mechanical design of the mirror segment interface and environmental tests of a mirror module demonstrator for launch survivability.

References:

• E. Breunig, P. Friedrich, L. Proserpio, et al., "Characterising x-ray mirror deformations with a phase measuring deflectometry system", Proceedings of SPIE Vol. 9144, 914449 (2014)
• E. Breunig, P. Friedrich, L. Proserpio, et al., "Alignment and integration of slumped glass x-ray mirrors at MPE", Proceedings of SPIE Vol. 9144, 91444B (2014)

E. Breunig, P. Friedrich, L. Proserpio, M. Wen

The application of low-stress iridium coatings on thin glass mirrors

Light-weight grazing incidence mirrors with high angular resolution and covered with high density coatings are required for the next generation X-ray. Among the high density materials, iridium (Ir) is preferred due to its high reflectivity and large critical angle for the photon energy up to ~10 keV. Despite the superior optical performance, the iridium coatings exhibit high stress in the order of gigapascal, large enough to deform the thin mirrors whose thickness is of only few hundred microns. A series of samples with Ir single layer coatings is being studied w.r.t. different deposition parameters in order to optimize for both low-stress and low-roughness Ir coatings.

We investigated the effect of several different sputtering parameters on the stress of the Ir coatings deposited via the radio frequency magnetron sputtering technology at the Aschaffenburg University on flat glass and slumped glass samples. The metrology of the glasses was carried out with an optical sensor on high-precision 3D measuring table in MPE before and after the layer deposition. The stress of the coatings can be calculated from the shape deformation according to the Stoney equation.

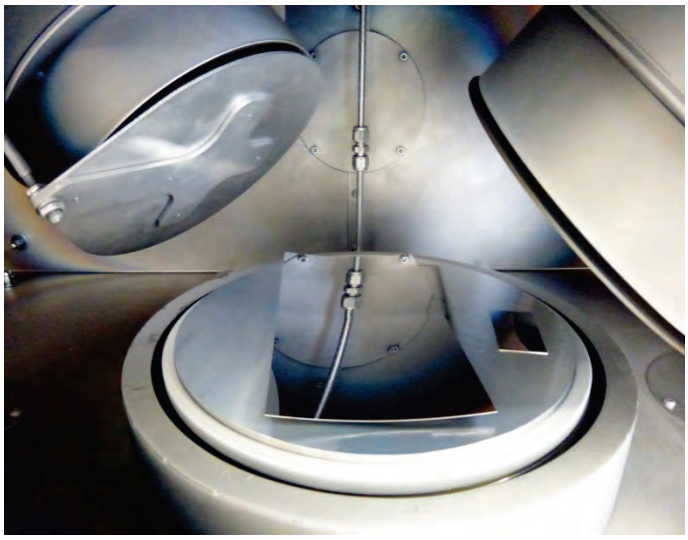

Fig. 1 Radio-frequency magnetron sputtering chamber used for coating. The big glass in the center is one slumped D263 sample, while the smaller one on the right is a flat glass used as a reference to measure the thickness of the coating.

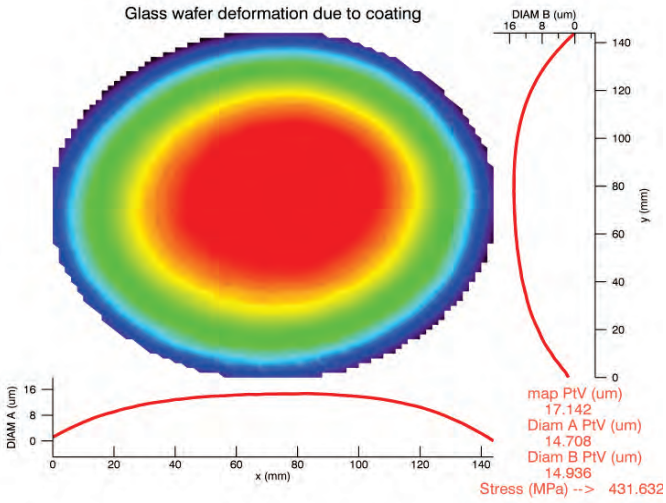

Fig. 2 The shape deformation of a circular flat glass sample as evaluated by its shape difference before and after the application of coating: The stress can be calculated from the variation of the radius of curvature by applying the Stoney equation.

We found that the argon pressure is one of the most critical parameter to control the film stress. The stress of the Ir coating (100 nm thick) deposited with the argon pressure of 5 mTorr was approximately 432 MPa while the one deposited with 50 mTorr argon pressure exhibited a low stress of less than 100 MPa. This work was done via the corporation between MPE and Aschaffenburg University. The investigations are ongoing to further reduce this value and to explore the effect of different deposition parameters on the surface roughness of the coatings.

References:

• A. Winter et al., “Indirect glass slumping for future x-ray missions: overview, status and progress,” 2015, Proc. SPIE, 9603, p. 96030S.
• T. Döhring et al., “The challenge of developing thin mirror shells for future X-ray telescopes”, 2015, Proc. SPIE 9826, p. 962809

M. Wen, L. Proserpio

A large area X-ray collimator

One question of particular interest in the measurement of X-ray imaging optics for space telescopes concerns the characteristics of the point spread function (PSF) in orbit and the focal length for an infinite source distance. In order to measure such a PSF, a parallel X-ray beam with a diameter of several centimeters to meters is required. For this purpose a large area transmission X-ray zone plate (ZP) for collimating X-ray beams has been designed, built, and tested. From X-ray measurements we obtain an upper limit for the angular resolution of 0.2" and a first order diffraction efficiency of 13%. These results show that it is possible to use a ZP as a collimator for the PANTER X-ray test facility and thus can contribute to a better understanding of optics developed for ATHENA.

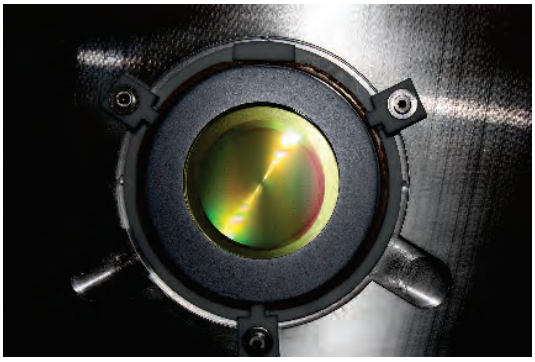

Fig. 1: Large area ZP (20 cm²) mounted in the PANTER X-ray test facility.

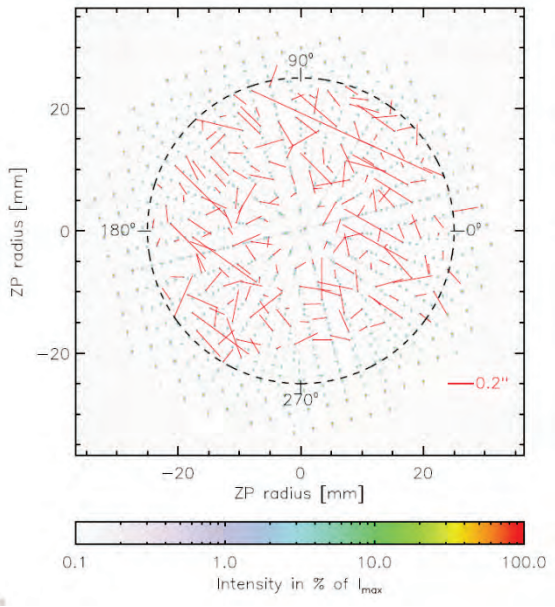

Fig. 2: The measurement to determine the excellent angular resolution (0.03 ± 0.13)" of the ZP. The red aberration vectors show the magnitude and the direction of angular aberrations.

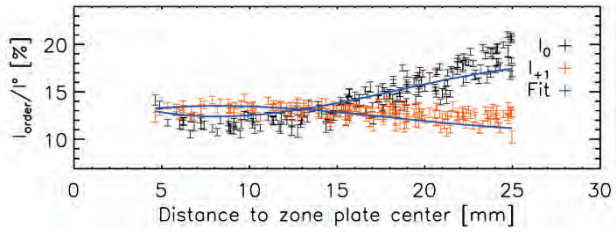

Fig. 3: The measured and modelled (blue) diffraction efficiency depending on ZP radius. The ZP has a high first order diffracted efficiency (red points) of 13 %.

We designed, fabricated, and measured a phase zone plate (ZP) optimized for the energy of the Al-K emission line 1.49 keV. The ZP, shown in Fig. 1, has a diameter of 5 cm and thus an aperture of 20 cm², which is similar to the aperture of ATHENA type SPOs.

Fig. 2 shows a measurement to determine the ZP's angular resolution. The red aberration vectors especially visualize the magnitude and the direction of angular aberrations. We measured that the angular resolution is on average 0.03 ± 0.13 arc second, which is good compared to the angular resolution required for ATHENA type optics (5 arc second).

The results for the diffraction efficiency are shown in Fig. 3. We measured a first diffraction order efficiency (red) of 13 % and explained a radial trend by fabrication effects (blue).

Summarizing, the ZP has a high efficiency and an excellent resolution and is thus an ideal collimator optic.

Reference: Menz, B., et al. 2015, *Apl. Opt.* , 54, 7851

B. Menz, V. Burwitz, G. Hartner, et. al.

IV) Center for Astrochemical Studies

Chemical differentiation in L1544

L1544, a prototypical prestellar core located in the Taurus-Auriga molecular complex, shows a strong chemical differentiation. Understanding its chemical structure is important because it helps constraining physical properties of the core, as well as its chemical evolution. Here we present new observations of several emission lines in L1544. The observations have been performed with the IRAM 30m telescope. In particular, the maps of methanol and cyclopropenylidene in L1544 show a complementary distribution and trace different regions. The different observed spatial distribution observed for *c*-C_3H_2 and methanol may be the result of large-scale environmental effects. The implications on the formation of methanol in prestellar cores, and its desorption from dust grains are investigated.

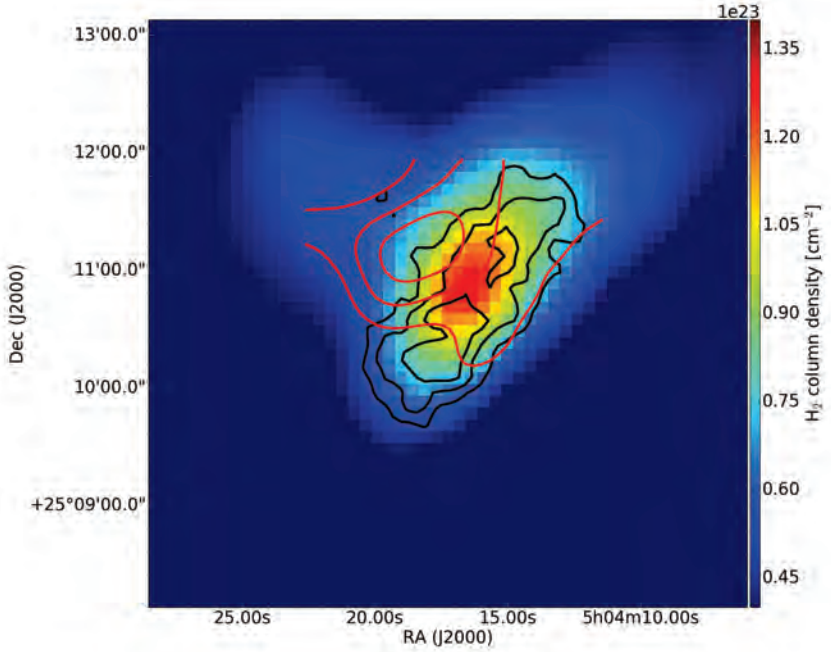

The 2_{12}-1_{11} transition of methanol (red line), already mapped by Bizzocchi et al. (2014), and 3_{22}-3_{13} cyclopropenylidene (black line) are plotted on the H_2 column density map derived from far-infrared images observed by Herschel with the SPIRE instrument. The contours indicate a 10, 15 and 20σ detection for CH_3OH and a 5 and 10σ detection for *c*-C_3H_2 (Spezzano et al., in prep.).

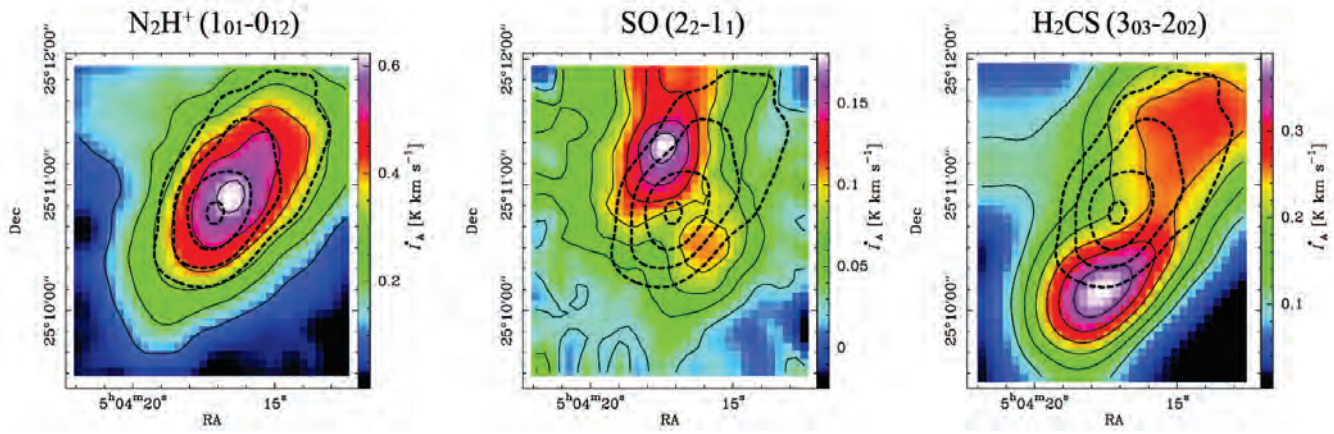

Integrated intensity maps of N_2H^+, SO and H_2CS showing the chemical differentiation within the central 4 arcmin^2 in L1544 (Spezzano et al., in prep.). The black dashed line indicates the 1.3 mm continuum emission (Ward-Thompson et al., 1999).

References:

• Bizzocchi, L., Caselli, P., Spezzano, S., & Leonardo, E. 2014, A&A, 569, A27
• Ward-Thompson, D., Motte, F., & Andre, P. 1999, MNRAS, 305, 143

S. Spezzano, L. Bizzocchi, P. Caselli

The Seeds of Star Formation in a Pre-stellar Core

Stars like our Sun form within dense molecular cloud cores, which represent the initial conditions in the star formation process. Although the physical and chemical structure of dense cores are well known at core scales (i.e. from a few thousand au to about 0.1pc), very little is known about the central 1000 au. Interferometric observations have so far failed to detect central structure in the continuum[1,2]. Here, we present the 1mm continuum map of the prototypical pre-stellar core L1544 obtained with the Atacama Large Millimeter/sub-millimeter Array. The continuum is well detected and two fragments with sizes ~200 au and masses close to a Jupiter mass are present[3]. N_2D^+(3-2) and DCO^+(3-2) maps show signs of depletion toward the central 1000 au[4].

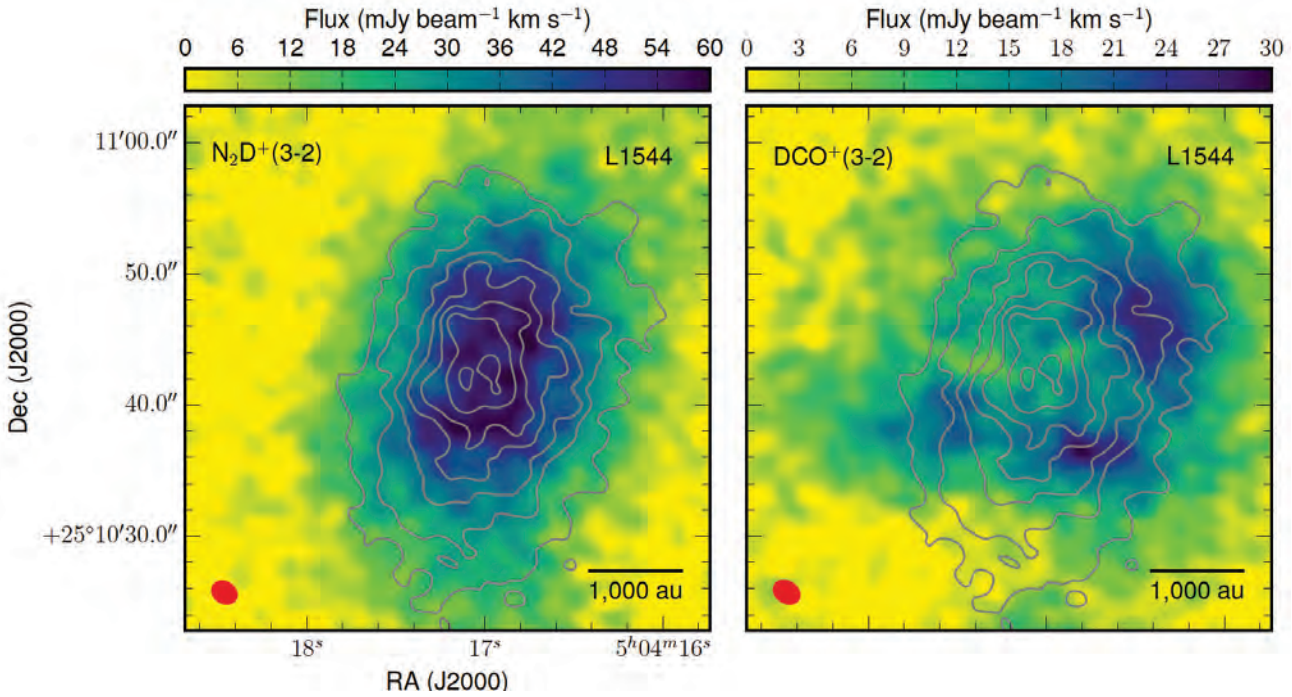

Figure 1: L1544 as seen by ALMA (Atacama Compact Array, ACA, plus 12m array) at 1mm. *Grey contours* show the dust continuum emission: the continuum levels start from 5 × rms, and with steps of 3 × rms, where the rms is 36 μJy/beam. The two 'seeds' are detected in the continuum emission map, toward the core center. Assuming a dust temperature[1] of 7 K and a dust opacity[5] $\kappa_{1.3mm}$ = 0.009 cm^2 g^{-1}, the masses of the East and West seeds are 0.9 and 1.2 Jupiter masses, respectively. The red ellipse in the bottom left corner is the synthesized beam, 2.05"x1.61" (59.53deg), with the format Major-axis × Minor-axis (PA). **Left:** N_2D^+(3-2) map (*color*) overlapped with the continuum dust map (grey contours). The emission is flat across the central 1000 au, indicating that this line is mainly tracing more extended material surrounding the seeds. **Right**: DCO^+(3-2) map (*color*) overlapped with the continuum emission. The DCO^+ map displays a broken ring of material, probably due to the well known large CO freeze-out toward the center[6], as CO is needed for DCO^+ production.

References:

(1) Crapsi, A., Caselli, P., Walmsley, C. M., Tafalla, M. 2007, A&A, 470, 221
(2) Schnee, S., Sadavoy, S., Di Francesco, J., Johnstone, D., Wei, L. 2012, ApJ, 755, 178
(3) Caselli, P., Pineda, J. E., Walmsley, C. M. et al., in preparation.
(4) Pineda, J. E., Caselli, P., Walmsley, C. M. et al., in preparation.
(5) Ossenkopf, V., Henning, Th. 1994, A&A, 291, 943
(6) Caselli, P., Walmsley, C. M., Tafalla, M. et al. 1999, ApJ, 523, L165

P. Caselli, J. Pineda, et al.

Search of grain growth towards the center of the pre-stellar core L1544

The study of dust grains in the earliest phases of star formation is crucial for understanding the chemical structure of dense cloud cores and the future evolution of solids in protoplanetary disks. It is however not clear if dust growth starts before star formation begins. Thus, we studied L1544, one of the most centrally concentrated prestellar cores on the verge of star formation, and with a well-known physical structure. We observed L1544 at 1 and 2 mm using the new NIKA bolometer at the IRAM 30-m telescope and found there is no need to increase the opacity towards the central regions of the core, which can be an indication for the absence of dust coagulation. These results will be compared with dust coagulation and chemical model predictions to gain a better understanding of the dust size distribution and initial conditions the process of star formation.

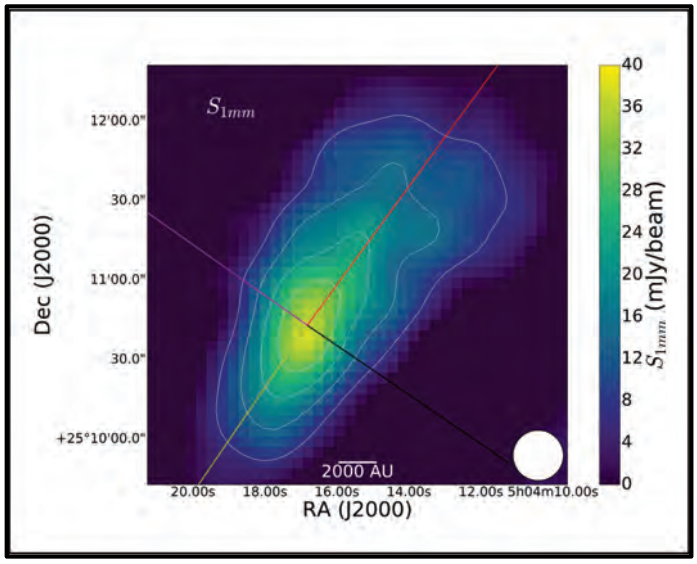

Dust continuum emission at mm-wavelengths:

$$S_\nu = \Omega B_\nu(T_d)\kappa_\nu \mu m_H N_{H_2} \qquad \kappa_\nu \sim \nu^\beta$$

From Keto et al. (2015), the temperature and density profiles of L1544 are known.

Figure 1. Emission map of L1544 at 1 mm. The map is convolved to 19" resolution. The white contours indicate the 1, 2, 3 and 4 σ-levels. The red, pink, yellow and black lines indicate the profiles shown in Figure 2.

Figure 2. Four representative profiles of the emission of L1544 from the center to the edge at 1 mm compared to the modeled emission using the temperature and density profiles from Keto & Caselli (2010) and a typical opacity value of 0.1 cm^2/g at 250 μm and a spectral index value of 1.5 (Hildebrand, 1983). As it is shown, the model can reproduce the emission only along the major axis. The shadowed green zone indicates the 1σ level.

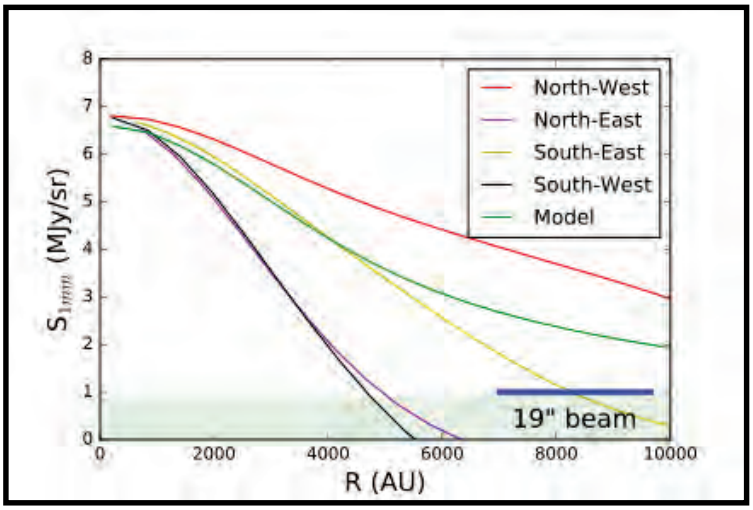

References:
• Hildebrand, R. H. 1983, QJRAS, 24, 267
• Keto, E. & Caselli, P. 2010, MNRAS, 402, 1625

A. Chacón-Tanarro, P. Caselli, L. Bizzocchi, J. E. Pineda

Deuterium fractionation in the Ophiuchus molecular cloud

Context: In cold (T < 25 K) and dense ($n_H > 10^4$ cm^{-3}) interstellar clouds, molecules such as CO are significantly frozen onto dust grain surfaces. Deuterium fractionation is known to be very efficient in these conditions as CO limits the abundance of H_3^+, which is the starting point of deuterium chemistry. In particular, N_2D^+ is an excellent tracer of dense and cold gas in star-forming regions.

Aims: We measure the deuterium fraction, R_D, and the CO depletion factor, f_d, towards a number of starless and protostellar cores in the L1688 region of the Ophiuchus molecular cloud complex and search for variations based upon environmental differences across L1688. The kinematic properties of the dense gas traced by the N_2H^+ and N_2D^+ (1-0) lines are also discussed.

Methods: Deuterium fraction has been measured via observations of the J = 1-0 transition of N_2H^+ and N_2D^+ towards 33 dense cores in different regions of L1688. We estimated the CO depletion factor using $C^{17}O$(1-0) and 850 micron dust continuum emission from the SCUBA survey. We carried out all line observations with the IRAM 30 meter antenna.

Results: The dense cores show large (~2-40%) deuterium fractions with significant variations between the sub-regions of L1688. The CO depletion factor also varies from one region to another (between ~1 and 7). Two different correlations are found between deuterium fraction and CO depletion factor: Cores in regions A, B2, and I show increasing R_D with increasing f_d, similar to previous studies of deuterium fraction in pre-stellar cores; cores in regions B1, B1B2, C, E, F, and H show a steeper R_D - f_d correlation with large deuterium fractions occurring in fairly quiescent gas with relatively low CO freeze-out factors (the group of the cores on the left part of Figure 1).

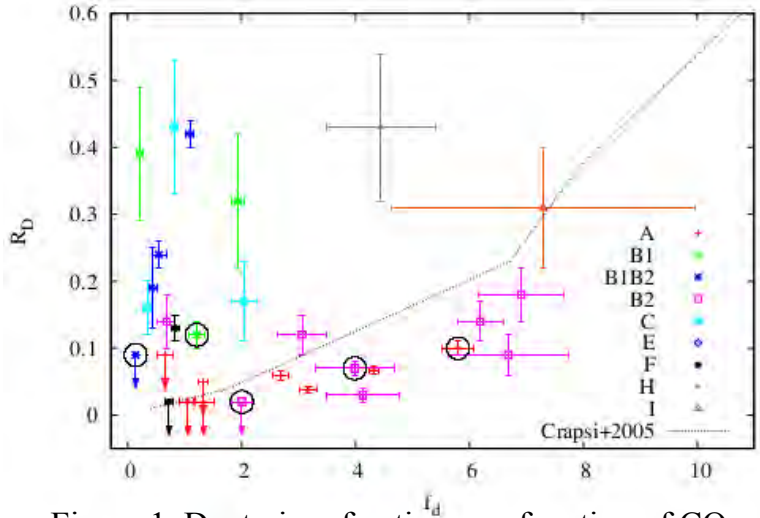

Figure 1. Deuterium fraction as a function of CO depletion factor. The protostellar cores are depicted with black open circles.

These are probably recently formed, centrally concentrated starless cores, which have not yet started the contraction phase towards protostellar formation. We also find that the deuterium fraction is affected by the amount of turbulence, dust temperature, and distance from heating sources in all regions of L1688, although no clear trend is found.

References: Punanova, A., Caselli, P., Pon, A. et al. 2016, A&A, 587, A118

A. Punanova, P. Caselli, A. Pon, et al.

Deuterium Chemistry of Interstellar Ammonia

The deuterated forms of ammonia, NH_2D, NHD_2, and ND_3, increase greatly in abundance in dense starless cores after the freeze-out of CO. They are useful probes of physical conditions in dense prestellar and star-forming cores, and enable detailed investigation into deuterium chemistry.

We combine observations of NH_3, NH_2D, NHD_2, and ND_3 with chemical modelling and radiative transfer calculations to understand how these molecules are formed, and to determine where their emission lines originate.

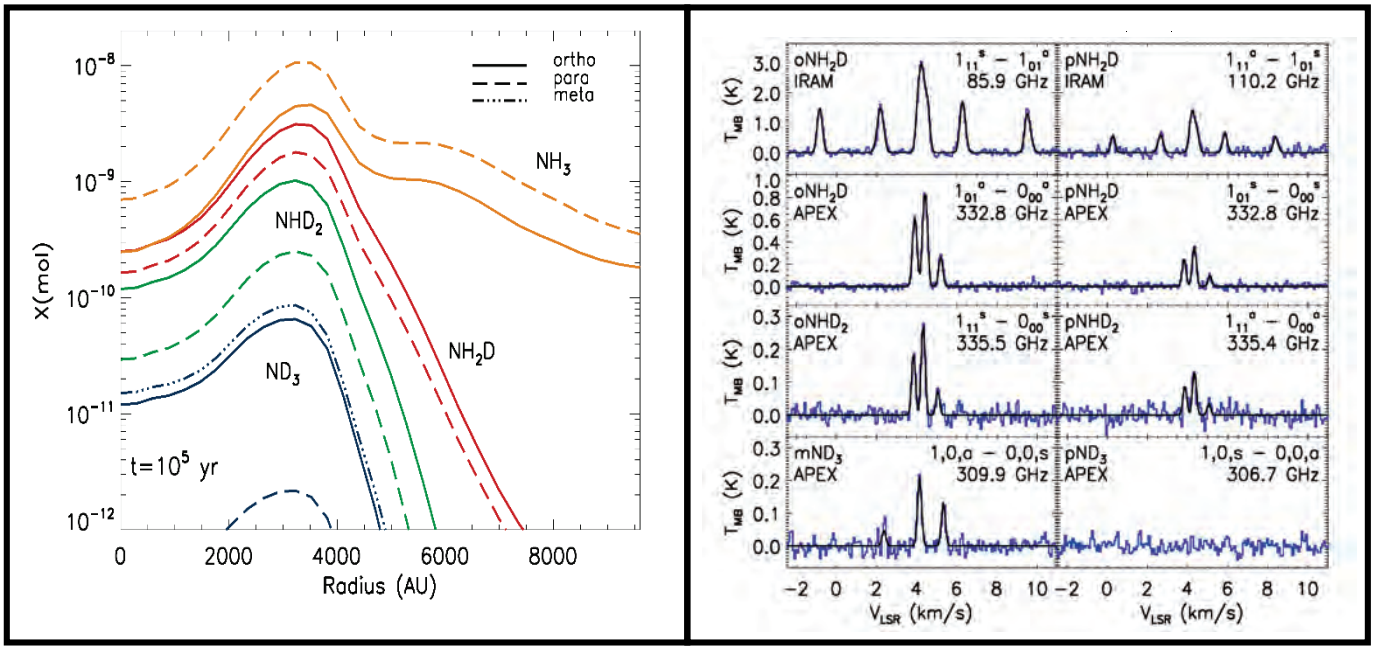

Left: Predicted fractional abundances of NH_3 and its deuterated isotopologues (relative to H_2) as functions of radial distance from the centre of a starless core. These are calculated using the chemistry model of Sipilä et al. (2015). NH_2D, NHD_2, and ND_3 are concentrated on the central parts of the core. The model distinguishes between different spin states, which is necessary for the interpretation of the observational data. **Right:** Observed lines of (ortho and para) NH_2D, (ortho and para) NHD_2, and (meta and para) ND_3 towards the starless core Ophiuchus/H-MM1. Based on the observed spin and fractionation ratios we concluded that the deuteration of ammonia occurs through gas-phase reactions which can be described as proton/deuteron hops (Harju et al., submitted). This is in constrast with the customary assumption made in chemistry models that the nuclei are completely mixed in these reactions.

We are currently preparing for a survey where the fractionation ratios and the spin ratios of ammonia molecules are determined in different physical conditions and environments. These observations, combined with chemistry modelling will be used to assess the roles of grain-surface and gas-phase chemistries in the deuteration of ammonia, and to distinguish between different gas-phase reaction schemes.

References:

• Sipilä et al. 2015, A&A 581, A122
• Harju et al. 2016, submitted to A&A

J. Harju, O. Sipilä, P. Caselli, J. Pineda, A. Punanova

From dense cores to disks: the role of specific angular momentum

The specific angular momentum in dense cores and its radial distribution are crucial to understand the formation of multiple stellar systems and protoplanetary disks. We have derived the specific angular momentum radial profile using VLA $NH_3(1,1)$ observations for 3 dense cores with young protostars (2 Class 0 and 1 first hydrostatic core candidate). We find a common profile between 10,000 au down to 750 au for all three objects. More observations are underway to expand the sample and radial coverage.

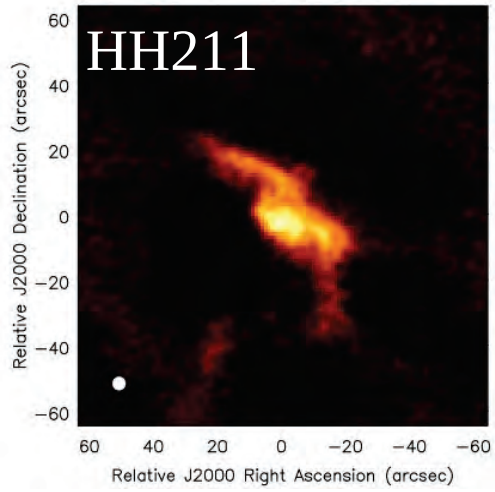

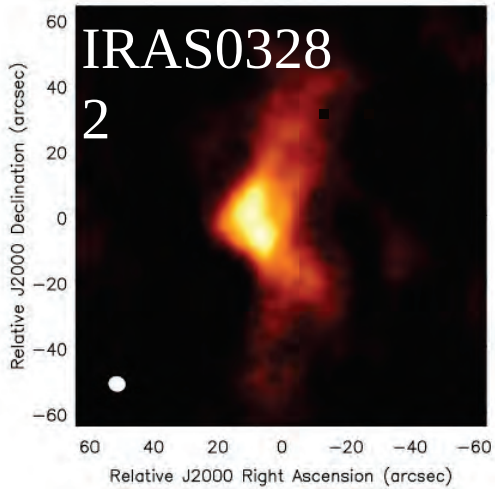

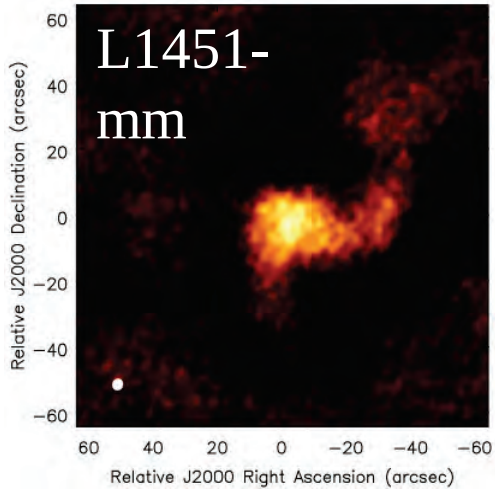

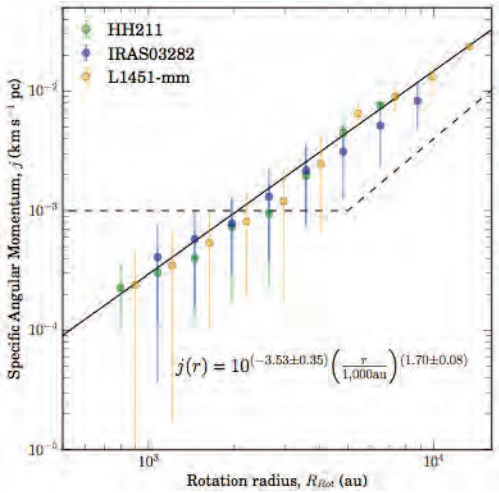

The specific angular momentum in dense cores and its radial distribution are crucial to understand the formation of multiple stellar systems and protoplanetary disks. The specific angular momentum, *j*, is directly related to the largest possible size for the Keplerian disk, $R_d = j^2/G\,M_{star}$.

We derive the specific angular momentum radial profile for 3 sources. We find a common power-law distribution from 10,000 au down to 750 au for all three objects. The power-law index, p=1.7, is substantially different than the commonly assumed for solid body rotation, p=2. We do not find a radius where specific angular momentum is conserved. We are currently carrying out non-ideal MHD simulations to reliably determine the implications on initial conditions for disk formation studies.

J. E. Pineda, B. Zhao, P. Caselli, et al.

Polarization and Kinematics in magnetized prestellar cores

Prestellar cores are objects in the early phase of star-formation, when gravity struggles against thermal pressure and magnetic fields in order to collapse and form a protostar. In this work, we perform polarization observations of a sample of prestellar cores in order to obtain the magnetic field properties in these objects. We use optical and near-infrared observations to trace the field morphology in the diffuse gas surrounding the core ($A_v \leq 5$ mag) and in more dense gas ($A_v \leq 30$ mag), respectively. Our observations are being performed with the 1.6 m telescope of the Observatório do Pico dos Dias (LNA/MCT-Brazil). Previous molecular line data of these objects exhibit kinematical variation (Crapsi et al. 2005) and our goal is to investigate if the magnetic field has a dominant role in the cores dynamics. For one of these objects, FeSt 1-457, we were able to acquire optical, near-infrared and sub-millimeter (thermal emission) observations that reveal a very ordered magnetic field across several physical scales (0.4 – 0.08 pc) and volume densities ($10^{4\text{-}6}$ cm^{-3}) (Alves et al. 2014). Previous polarization and molecular line data show that this prestellar core is embedded in a very magnetized medium and has narrow linewidths, implying a sub-Alfvénic turbulence (Alves et al. 2008, Franco et al. 2010, Frau et al. 2010). We are currently inspecting velocity fields of ions and neutral molecular species in order to find correlations with the magnetic field morphology. Our goal is to study how efficient is the coupling of matter and field lines in these magnetized environments. The data are being acquired with the IRAM 30-m, APEX, GBT and VLA telescopes. We also plan to map the molecular emission of other prestellar cores in the polarimetric survey.

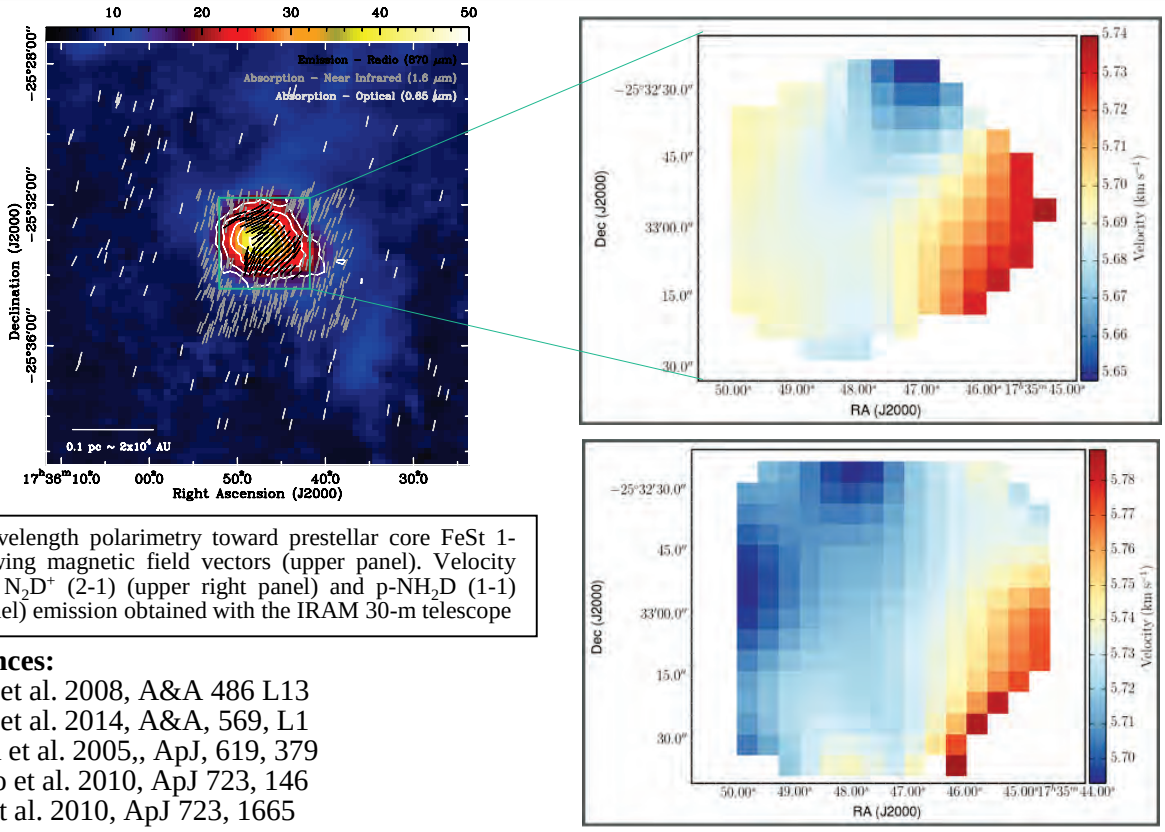

Multi-wavelength polarimetry toward prestellar core FeSt 1-457 showing magnetic field vectors (upper panel). Velocity fields of N_2D^+ (2-1) (upper right panel) and p-NH_2D (1-1) (right panel) emission obtained with the IRAM 30-m telescope

References:

- Alves et al. 2008, A&A 486 L13
- Alves et al. 2014, A&A, 569, L1
- Crapsi et al. 2005,, ApJ, 619, 379
- Franco et al. 2010, ApJ 723, 146
- Frau et al. 2010, ApJ 723, 1665

F. Alves, P. Caselli, A. Pon, et al.

The Search for Ice in the Pipe Nebula

We observed the shank region of the Pipe Nebula, a young and quiescent molecular cloud, towards several background sources with various visual extinctions. With these data, we are able to study the ice content in the Pipe Nebula as a function of visual extinction, which has direct implications on the ice composition upon formation, as well as its evolution.

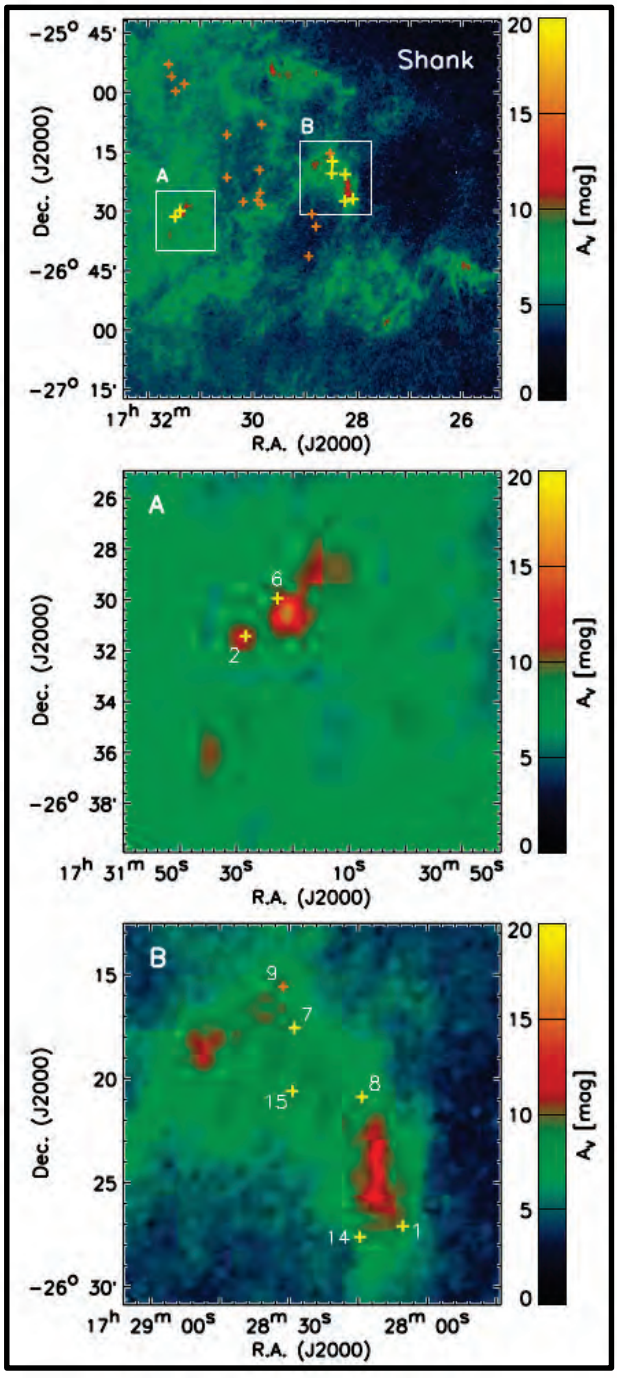

We acquired a total of 45 spectra over eight nights of observing using the SpeX instrument on the Infrared Telescope Facility (IRTF) 3-m telescope located at Mauna Kea (Rayner et al. 2003). The spectra were obtained using the cross-dispersed mode with the 0.8“ slit, having a wavelength coverage of 1.9 to 5.3 microns and a spectral resolution of about R ~ 937.

The left figure is the extinction map for the shank region of the Pipe Nebula. The top panel shows the location of all the observed sources. Panels A and B highlight the sources for which we obtained positive detections of water ice at 3.0 microns.

For each target, continua were fitted by using an appropriate template for the background star from the IRTF spectral library. The right figure offers examples of the 3.0 micron water ice feature for the two targets in panel A of the extinction map. The observed spectra are in black and in the red we overplot spectra of laboratory water ice at a temperature of 10 K (Hudgins et al. 1993). These results will be compared with gas-grain chemical models to place constraints on the chemistry of water in molecular clouds.

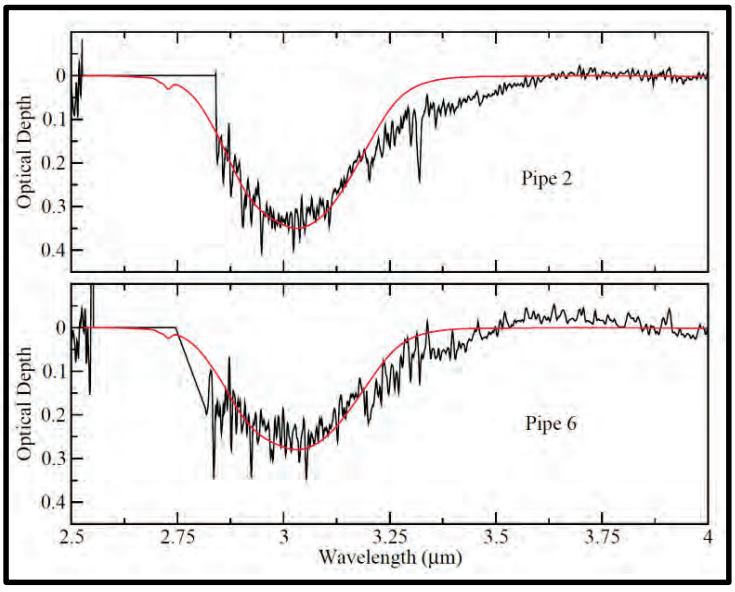

References:

• Rayner, J. T., Toomey, D. W., Onaka, P. M., et al. 2003, PASP, 115, 362

• Hudgins, D. M., Sandford, S. A., Allamandola, L. J., Tielens, A. G. G. M. 1993, ApJS, 86, 713

J. D. Bailey, M. Goto, P. Caselli

Observations of Turbulent Dissipation in GMCs

Giant molecular clouds (GMCs) contain supersonic turbulent motion, which are expected to dissipate rapidly. Mid-J CO lines should be effective tracers of this dissipated turbulent energy. We have used the *Herschel Space Observatory* to observe both a low-mass star-forming region (Perseus B1–E5) and high-mass star-forming regions (IRDC C, F, and G). We have detected mid-J CO emission from these sources consistent with turbulent dissipation occuring in low velocity shocks (~3 km / s) in roughly a turbulent crossing time.

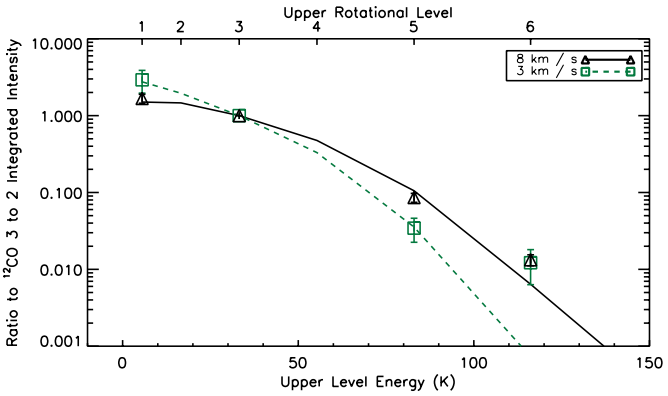

Figure 1: The points show the observed integrated intensity ratios with respect to the (3-2) line. The lines are the best fitting Kosma-**τ** PDR models. The colors are for the two different velocity components. Note how there is excess emission in the (6-5) line, consistent with shock heating.

High Mass: IRDCs C, F, and G

IRDCs C, F, and G were observed in the CO (8-7), (9-8), and (10-9) lines with *Herschel* (Pon et al. 2015) and in the ^{12}CO, ^{13}CO, and C^{18}O (3-2) lines with the James Clerk Maxwell Telescope (JCMT; Pon et al. 2016). **PDR fits to the SLEDs show that there is excess (8-7) and (9-8) emission (the 10-9 line is not detected) requiring a secondary hot gas component**. Much of this hot gas component is likely due to feedback from protostellar sources, but some of the hot gas could be due to turbulence decaying in low velocity shocks. The emission is consistent with turbulence decaying in 3 times the turbulent crossing time. Where detected, this mid-J CO emission requires hot gas to fill 0.3% of the volume of the line of sight.

References:
• Pon, A. et al. 2014, MNRAS 445, 1508
• Pon, A. et al. 2015, A&A, 577, A75
• Pon, A. et al. 2016, A&A, 587, A96

Low Mass: Perseus B1-E5

Herschel observed the CO (6-5) and (5-4) transitions towards the Perseus B1-E5 starless clump. These observations were combined with archival measurements to form a spectral line energy diagram (SLED). Photodissociation region (PDR) models fit to this SLED were able to reproduce the lines up to and including the (5-4) line, but all such models fitting the low J CO lines underpredict the (6-5) intensity (Figure 1). **The emission is consistent with turbulence decaying via low velocity shocks in 1/3 of the crossing time and filling 0.15% of the volume of the clump.** See Pon et al. (2014) for further details.

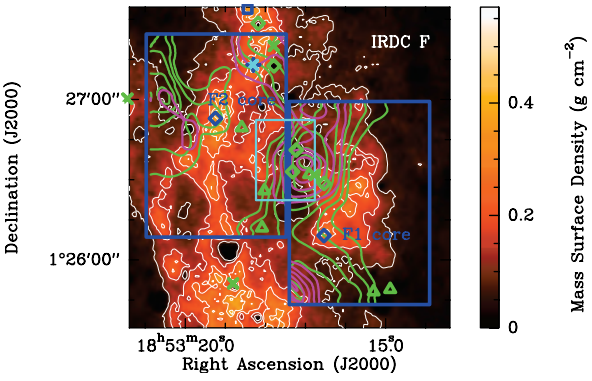

Figure 2: CO (8-7) and (9-8) integrated intensities are shown as the green and fuchsia contours. The color scale is the mass surface density. Dark blue symbols show cores, while the other coloured symbols show embedded protostellar sources. The large blue rectangles are the areas observed with *Herschel*.

A. Pon, P. Caselli, et al.

Unraveling complex kinematics of a giant stellar nursery

We present a preliminary multi-component kinematic analysis for the southern part of the IRDC G035.39-00.33, a massive infrared dark cloud harbouring a number of compact dense gas cores, some in early act of forming massive stars and protoclusters (Nguyen Luong et al. 2011). We find that while the extended gas reservoir - traced by ammonia emission - is consistent with the line centroids of compact N_2H^+ cores seen with SMA in the northern portion of the cloud, the velocities of the cores in the southern part appear to be detached from the kinematics of the extended cloud component. This velocity displacement highlights the importance of kinematical studies of different spatial scales and raises questions on the origins of the mismatch. Detailed radiative transfer calculations and simulations that connect cloud to core scales are required to fully understand the dynamics of the observed dense gas in G035.39.

Fig 1.: the velocity distribution of multiple components of multiple molecules observed within G035.39. The black stars and grey circles mark the positions of N_2H^+ line centroids observed with SMA and APEX, respectively. Additional data from APEX (CO) and GBT (NH_3) highlights the multicomponent dynamic nature of the region. The image overlay shows the mass surface density map from Butler & Tan (2012).

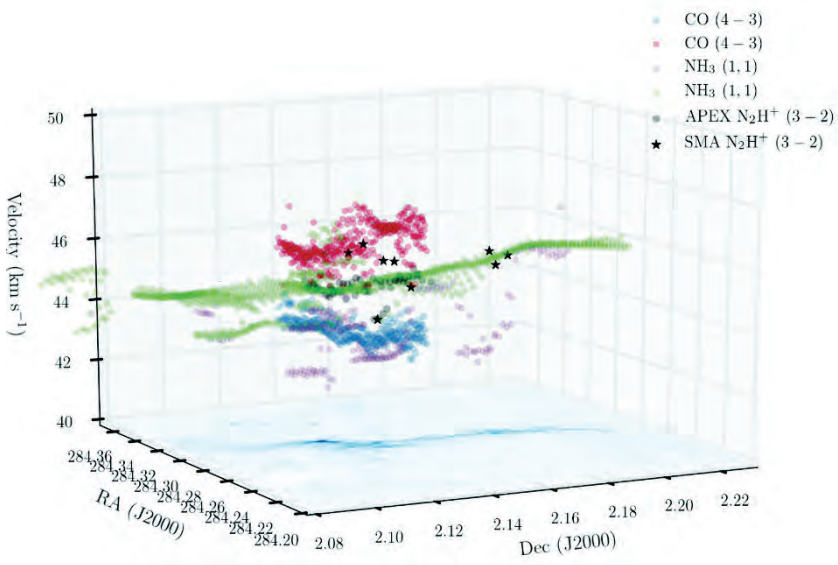

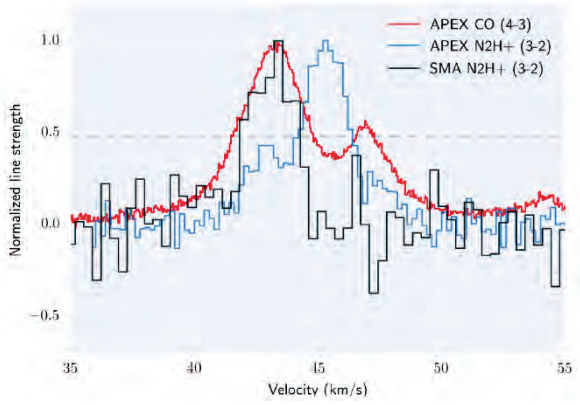

Fig 2.: an example composite spectra of a protostellar source in G035.39. The spectra were averaged around the position of the most blue-shifted SMA core (the lowest star at Fig.1). Note the large discrepancy between the APEX and SMA spectra.

References: Henshaw, J. D., et al. 2013, MNRAS, 428, 3425 • Henshaw, J. D., et al. 2014, MNRAS, 440, 2860 • Jiménez-Serra, I., et al. 2010, MNRAS, 406, 187 • Jiménez-Serra, I., et al. 2014, MNRAS, 439, 1996 • Nguyen Luong Q. et al., 2011, A&A, 535, 76 • Peretto, N., et al. 2010, A&A, 518, L98

V. Sokolov, P. Caselli, J. Pineda, A. Pon, et al.

Outflow Detection in a 70 μm Dark High-mass Core

We present 3.4 mm observations towards a high-mass (>40 $M_{\odot}$), low luminosity (<10 $L_{\odot}$) 70 μm dark molecular core G 28.34 S-A, using the *IRAM 30 m* telescope and the *NOEMA* interferometer. We report the detection of spatially resolved SiO $J = 2 \rightarrow 1$ line emission in this source at a linear resolution of ~0.1 pc. The SiO emission exhibits two lobes which are W-E oriented and centered on the continuum peak. These lobes correspond to red-shifted and blue-shifted gas with velocities up to 40 km s^{-1} relative to the quiescent cloud. This indicates the presence of a strong bipolar outflow from this 70 μm dark core. Our SiO detection is consistent with *ALMA* archival data of SiO $J = 5 \rightarrow 4$, whose high-velocity blue-shifted gas reveals a more compact lobe spatially closer to the dust center. This outflow infers that the central source may be in a transient evolutionary stage between the prestellar and the protostellar object.

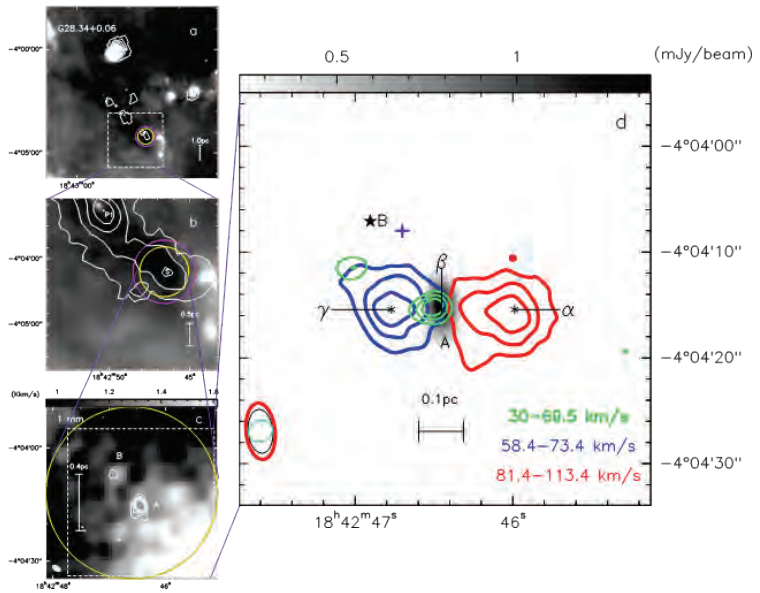

Fig.1. Compilation of the observations on G 28.34 S.
a) b) Greymap of the 70 μm dust emission observed by *Herschel*; the white contours show 870 μm continuum observed by *ATLASGAL*.
c) White contours show 1.1 mm continuum observed by *SMA*, overlaying the moment 0 greymap of highly depleted $C^{18}O$ from *IRAM 30 m* observations;
d) Greymap of the 3.4 mm continuum observed by *NOEMA*; red and blue contours show the red-/blue-shifted SiO $J = 2 \rightarrow 1$gas (Vlsr= 78.4km s^{-1}) obtained from the combination of *NOEMA-30 m*; the green contours show the blue-shifted SiO $J = 5 \rightarrow 4$ gas from *ALMA* Cycle 0 public data.

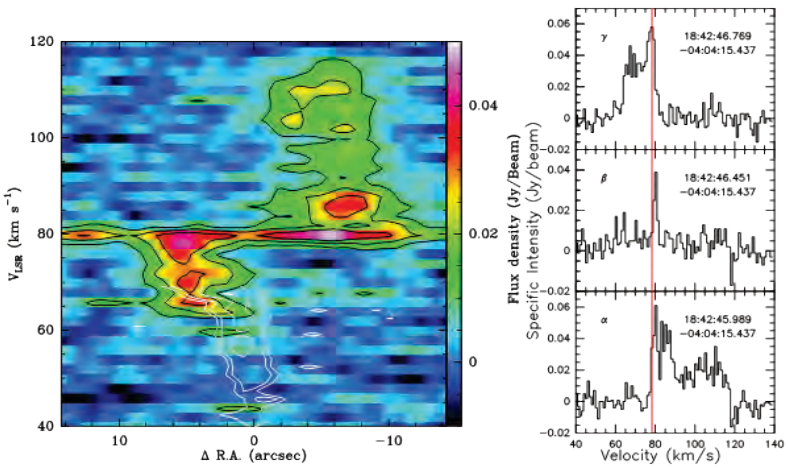

Fig.2. *Left* : position-velocity diagram along the W-E orientation with a width of 5". The color map and the black contours are from line SiO $J = 2 \rightarrow 1$, and the white contours are from the SiO $J = 5 \rightarrow 4$ line (velocity coverage up to 69.5 km s^{-1} by *ALMA*). Note that the *ALMA* data have been convolved to the same angular resolution of the *NOEMA* data for comparison;.
Right: line profiles extracted from the positions marked in Fig.1d.

References:
• Feng et al. 2016a (accepted by A&A), ***Are Infrared Dark Clouds Really Quiescent?***
• Feng et al. 2016b (submitted to ApJ), ***Outflow detection in a 70 μm dark high-mass core***

S. Feng

Absorption Line Survey of H_3^+ in the Galactic Center

H_2 is the most abundant molecule in the universe. However, H_2 neutral-neutral reaction has a barrier hard to overcome in the cold interstellar medium (ISM). Instead, H_2 participates in the chemical network in the form of H_3^+. H_3^+ plays a pivotal roles in the astrochemistry to control the abundances of larger and more complex molecules in the ISM. The formation of H_3^+ starts with the ionization of H_2 by a cosmic ray impact. As the process involved is the simplest, the molecular ion H_3^+ is the most reliable chemical probe of the low-energy comic rays.

We undertake the infrared absorption line survey of H_3^+ in the Central Molecular Zone of the Milky Way (Geballe & Oka 2010; Goto et al. 2011). The Central Molecular Zone (CMZ) is a warm region at the Galactic Center with the extent of ±1° or ±150 pc.

The equivalent widths of H_3^+ along more than 50 line of sights toward the CMZ are about an order of magnitude larger than any other line of sights outside the Galactic Center. The observation testifies that: (i) the CMZ is prevailed by the warm (T = 250 K) and diffuse (n = 100 cm^{-3}) molecular clouds, for which the heating mechanism is still unknown (Oka et al. 2005); (ii) the cosmic ray ionization rate is nearly ζ=10^{-15}s^{-1}, an order of magnitude higher than outside the Galactic Center.

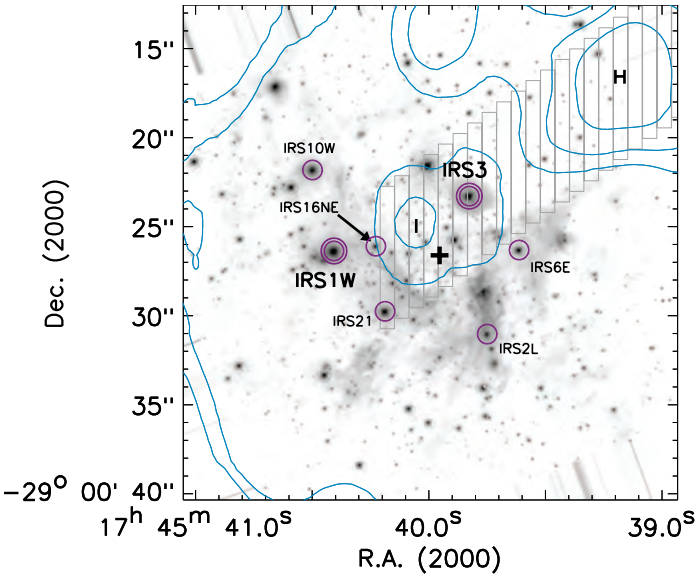

Fig. 1 : A dense clump in front of GCIRS 3. The contour is HCN 4-3 from Montero-Castaño et al. 2009, ApJ, 695, 1477.

One of a dense molecular clumps in the circumnulear disk also shows high cosmic ray ionization rate, ζ=10^{-15} s^{-1}, which is two orders of magnitude larger than dense clouds in the nearby star forming regions (Goto et al. 2013, 2014).

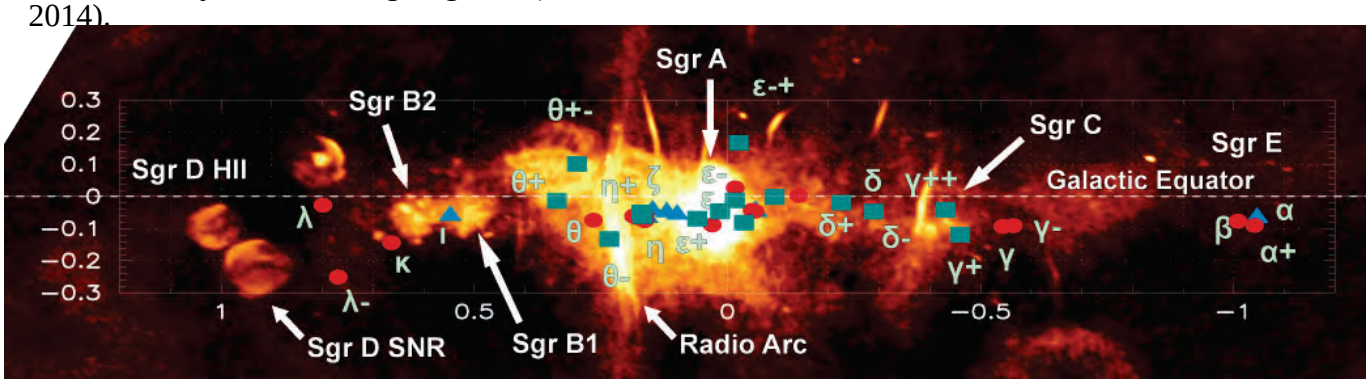

Fig. 2: The distribution of infrared point sources in the CMZ toward which spectroscopic survey of H_3^+ at 3.5−3.7 μm has been performed. The background is the VLA 90 cm image.

References:

- Geballe & Oka 2010, ApJ, 709, L70
- Goto, Geballe, Indriolo, Yusef-Zadeh, Usuda, Henning, Oka, 2014, ApJ, 786, 96
- Goto, Indrioo, Geballe, Usuda, 2013, Journal of Physical Chemistry A, 117, 9919
- Goto, Usuda, Geballe, Indrioo, McCall, Henning, Oka, 2011, PASJ, 63, L13
- Oka, Geballe, Goto, Usuda, McCall, 2005, ApJ, 632, 882

M. Goto

A multi-wavelength study of proto-brown dwarfs

The origins of very low-mass stars (VLMs) and brown dwarfs (BDs) have been subject to much debate, in order to understand if their formation and evolutionary stages are similar to those observed in solar-type pre-main sequence stars. We are conducting a multi-wavelength study to characterize Class 0/I VLMs and BDs in young, nearby star-forming regions. Our multi-wavelength observations include near-infrared to millimeter continuum and molecular line observations. By combining these observations with modeling, we have constrained the physical and chemical structure of these sources, and have also distinguished the definitive Class 0/I sources from misclassified cases of Class II edge-on disk systems. Overall, this study will highlight the similarities in the physical and chemical properties and accretion and outflow activity in VLM/BDs with low-mass protostars, and provide important insight into their possible formation mechanisms.

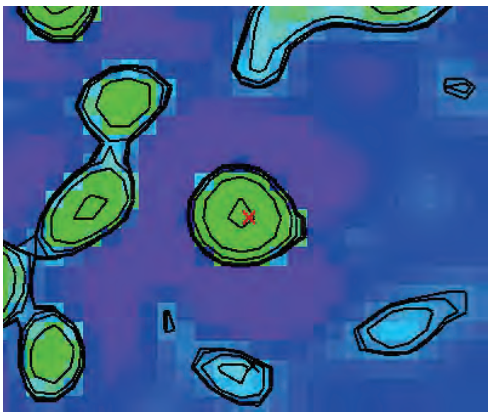

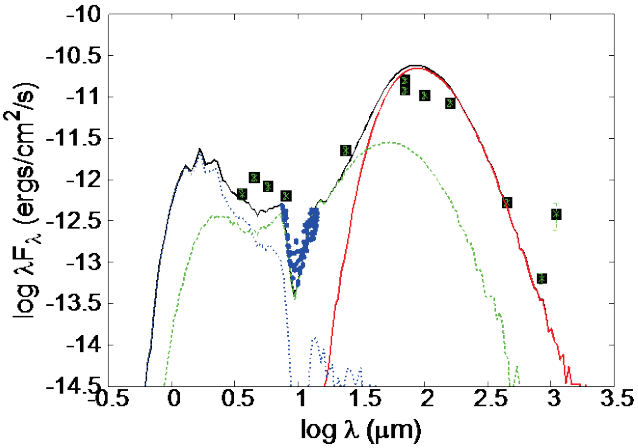

Top panel: Sub-millimeter JCMT/SCUBA-2 850mu map (left); target location is marked by a red cross. The SED with model fit (right). Bottom panel: The HCO+ 3-2 molecular line (left) associated with an infalling envelope, and the H_2 and Br-ϒ lines (right) indicating accretion and outflow activity.

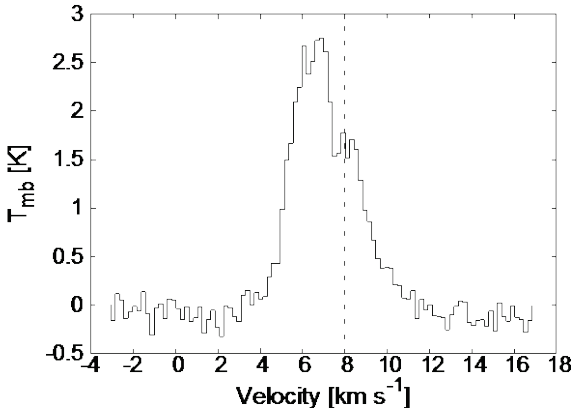

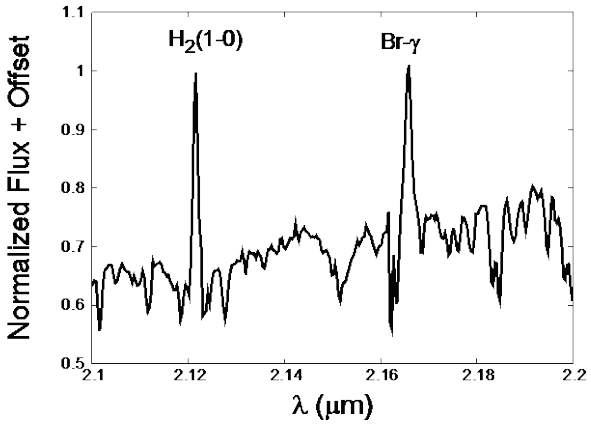

B. Riaz, et al.

Rotational spectroscopy of $^{36}ArH^+$

The recent detections of $^{36}ArH^+$ and $^{38}ArH^+$ (Barlow et al. 2013) in the interstellar medium has triggered the interest on argonium. This molecular cation has proved to be widespread in our Galaxy in the diffuse medium and may serve as a very specific tracer of atomic gas and as a proxy for cosmic ray ionisation rate (Schilke et al. 2014). Pure rotational transitions of the two isotopologues detected in the ISM have never been recorded in laboratory prior to this work. We have generated $^{36}ArH^+$ and $^{38}ArH^+$ in in a low-pressure glow discharge, and we have recorded their $J = 1 - 0$ transition for the first time. All the rotational and ro-vibrational transition frequencies available have been analysed in a global multi-isotopologue fit to give a comprehensive set of isotopic independent spectroscopic parameters. These data allow to compute an improved set of rotational and ro-vibrational rest-frequencies to assist astronomical searches of ArH^+.

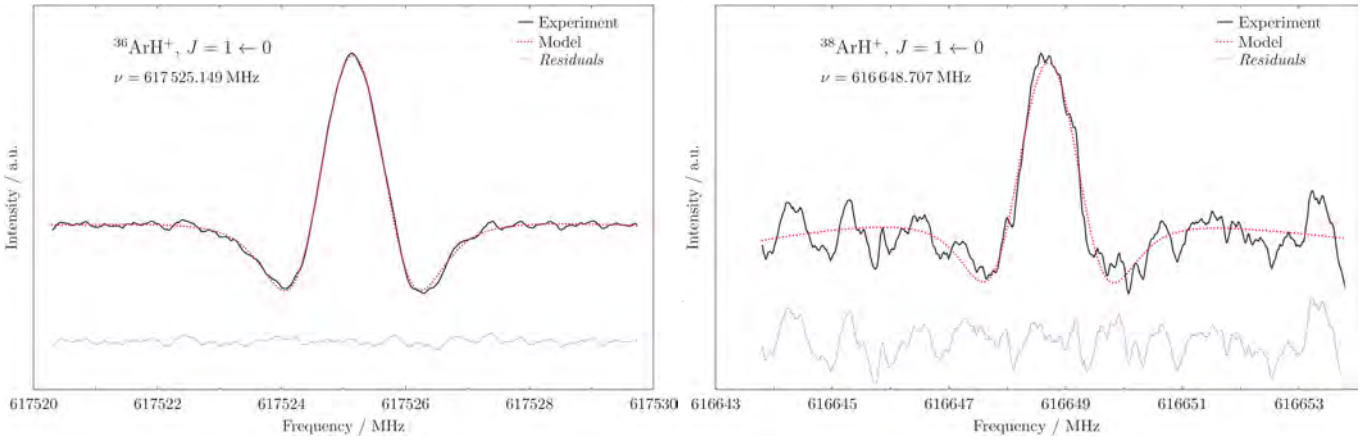

The recordings show the $J = 1 - 0$ transition of $^{36}ArH^+$ and $^{38}ArH^+$ obtained with an averaging time of 2250 and 3600 s, respectively. The central frequencies of the two lines have been derived by analysing the spectral profiles with the proFFiT code (Dore 2003) and using a frequency modulated Voigt profile function. We obtained accurate measurements of the corresponding rest-frequencies for the first time, they are: $\nu_{1-0}(^{36}ArH^+) = 617\,525.149 \pm 0.020$MHz and $\nu_{1-0}(^{38}ArH^+) = 616\,648.707 \pm 0.020$ MHz.

These novel data were added to the existing spectroscopic data set of argonium, that includes rotational and vibrational frequencies for all the available isotopologues. A global least-squares fit procedure yielded an extended set of improved Dunham coefficients, as well as a number of Born-Oppenheimer breakdown (BOB) constants (Watson 1980).

This revised set of spectroscopic constants makes it possible to compute spectral prediction for any isotopic variant of ArH^+ at a high level of accuracy. For the astrophysically relevant $^{36}ArH^+$ and $^{38}ArH^+$ species, we performed a comprehensive calculation including pure rotational transition up to $J = 10$ and ro-vibrational transitions up to $P(20)$ and $R(19)$ for the fundamental $v = 1$ infrared band. The calculated 1σ uncertainties are lower than 0.03 kms^{-1} up to 50 μm for the pure rotational lines, while they range in the 0.06–0.15 kms^{-1} for the ro-vibrational transitions in the 4 μm region.

References:

- Barlow M.J., et al., 2013, Science, 342, 1343.
- Dore L., 2003, J. Mol. Spectrosc., 221, 93.
- Schilke P., et al., 2014, A&A, 566, A29
- Watson J.K.G, 1980, 80, 411.

L. Bizzocchi, et al.

Chirped-Pulse FTMW spectroscopy in a cryogenically cooled waveguide

A chirped-pulse Fourier transform microwave (CP-FTMW) spectrometer is currently being built in the CAS laboratories at MPE. The ability to polarize a molecular sample and study its free induction decay on microsecond timescales with large instantaneous bandwidth does not only allow to measure its rotational spectra, but also to monitor time-depended processes. In preparation of a buffer gas cooling cell for the CP-FTMW, which will be used to study molecules at astrophysically relevant temperatures, a cryogenically cooled waveguide has been set up at the University of Cologne. Temperature programmed desorption experiments with pure ammonia ice have been performed in order to benchmark the system and to guide further development.

Chirped-Pulse Fourier Transform Spectrometer

The molecular sample is polarized with a short chirped microwave pulse (~1 µs) and the subsequent free induction decay (FID) is recorded with an instantaneous bandwidth of about 1 GHz. The pulse is generated by a 5 GHz arbitrary waveform generator, upconverted in frequency (8-26 GHz), amplified (~1W) and fed into the waveguide containing the molecular sample. The FID is recorded with a 25 GHz scope after amplification and frequency down-conversion.

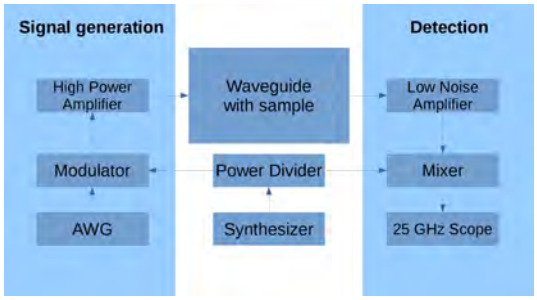

Fig. 1: Scheme of the CP-FTMW spectrometer

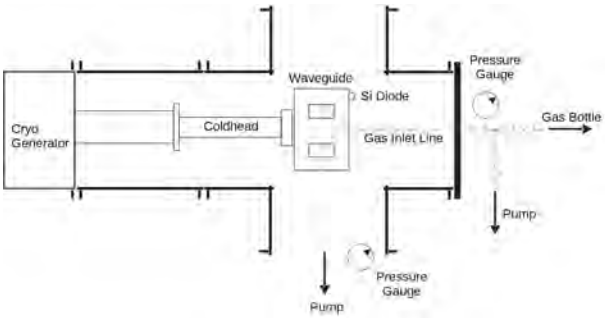

Fig.2: Scheme of the cooled waveguide setup

Experimental setup of the main chamber

A U-shaped Ku-band waveguide (V ~ 19 cm^3) is placed inside a vacuum chamber and mounted to the second stage of a cold head. The temperature of the waveguide is measured with a silicon diode on the outer part of the waveguide. Pressure gauges are connected to the gas inlet line and the main chamber. A temperature of 20 K is reached. The waveguide is connected via SMA cables and feedthroughs to the spectrometer.

Temperature programmed desorption

The setup is benchmarked by recording the inversion spectrum of desorbing ammonia ice. Pure ammonia is injected in the 20K cold waveguide and frozen on the inner surface of the waveguide. The temperature is linearly ramped (0.4 K/min) and a spectrum of the desorbing molecules is acquired as a function of temperature. The desorption energy for NH3 derived from the TPD curves (Fig.3) is E_{DES} = 31.6 ± 0.1 kJ/mol. The detection limit for ammonia has been determined to be about $3 \cdot 10^{12}$ molecules after 2s of integration time.

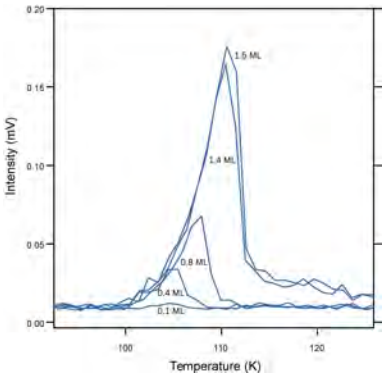

Fig.3: Temperature programmed desorption curves for NH_3 ices with approx. 0.1, 0.4, 0.8, 1.4 and 1.5 monolayer (ML) thickness. The intensity of the *J,K = 3,3* inversion transition is plotted as a function of temperature

References:

- P. Theulé et al., A&A, submitted

C. P. Endres, et al.

Laboratory study of water ice mixtures

We present an investigation on the far-infrared spectra of binary ice mixtures relevant in various astrophysical environments. The foremost goal is to compare the spectroscopic features of the ice mixtures to those of the pure ices, and to search for changes in the peak frequencies, intensities, and band strengths of the main bands.

Since its first identification in 1979 by Léger et al., water ice has been observed in the insterstellar medium along several lines of sight and in different sources, mainly in dense molecular clouds. Water is the most abundant component of ice observed in space. However, other molecular species have been identified as minor ice components by their spectroscopic features in the infrared (IR) region.

New spectroscopic observations in the far-IR range are expected from future planned missions, requiring laboratory characterization of the corresponding spectra.

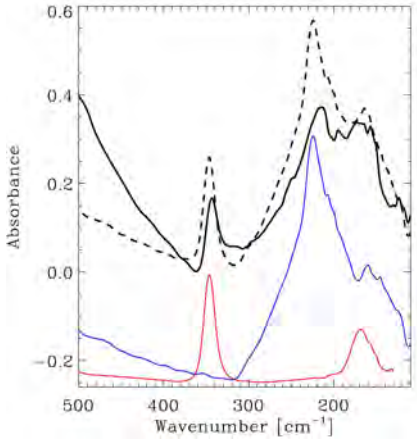

IR spectra of an H_2O:CH_3OH 1:1 ice mixture in the far-IR region at 130 K (black solid line) along with the spectra of pure water (blue solid line) and methanol (red solid line) ices of the same thickness than that of each species in the ice mixture. Dashed line is the sum of the two pure ice spectra.

In Giuliano et al. (2014), the infrared band strengths in the 25-500 μm region were measured for pure ices of H_2O, CO_2, CH_3OH, and NH_3, at a temperature of 8 K followed by warm-up. In the present work, the same analysis has been extended to binary ice mixtures of water with methanol and ammonia in different proportions.

We have measured the spectra in the near- and mid-IR regions to derive ice column densities that were subsequently used to calculate the band strengths in the far-IR region. Theoretical models have also been designed to study these mixtures and to predict their spectra.

Band strengths in the far-IR are missing in the astrophysics literature for ice mixtures. The results presented here can be valuable to detect the presence and composition of such mixtures from future space observations in this spectral region.

References:

- Léger, A., Klein, J., de Cheveigne, S., Guinet, C., Defourneau, D., Belin, M. 1979, A&A, 79, 256L
- Giuliano, B. M., Escribano, R. M., Martín-Doménech, R., Dartois, E., & Muñoz Caro, G. M. 2014, A&A, 565, A108

B. M. Giuliano, et al.

An updated line catalog for the interstellar search of the methoxy radical

The methoxy radical has been a molecule of great interest to the astrochemical community since its initial interstellar detection a few years ago toward a prestellar core. Its interstellar detection was unexpected because it was found in the gas-phase at an extremely low temperature, thus raising questions about its formation and its possible connection to methanol. Methanol itself can be found across an large variety of interstellar environments, yet its formation and related chemistries are still not yet well understood. As a molecular radical, methoxy contains an unpaired electron, which makes it highly-reactive and hard to prepare for study in the laboratory. We have collected data from previous literature, as well as new observations in the laboratory of its rotational spectrum in the frequency range of 240-310 GHz. Using specialized spectral analysis software, we have analyzed its millimeter/ submillimeter wave rotational spectrum so that we may provide an updated line catalog so that astronomers have a greater opportunity of detecting methoxy in interstellar environments and unravel the mysteries of its unexplained chemistries.

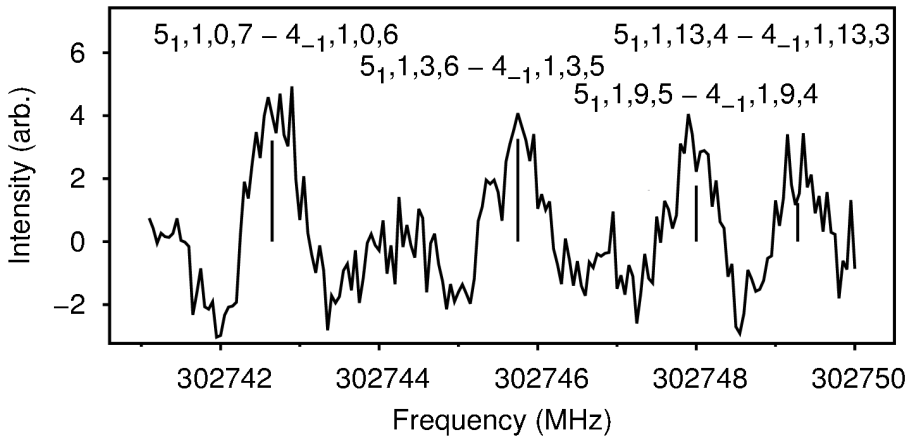

(**left**) Shown here is an exemplary spectrum of jet-cooled ($T_{rot} \approx 7$ K) methoxy obtained in the laboratory. The labeled quanta are N_K, Λ, t, F for the upper and lower states for each rotational transition, where t corresponds to a look-up table in the catalog for additional quantum numbers describing the hyperfine structure.

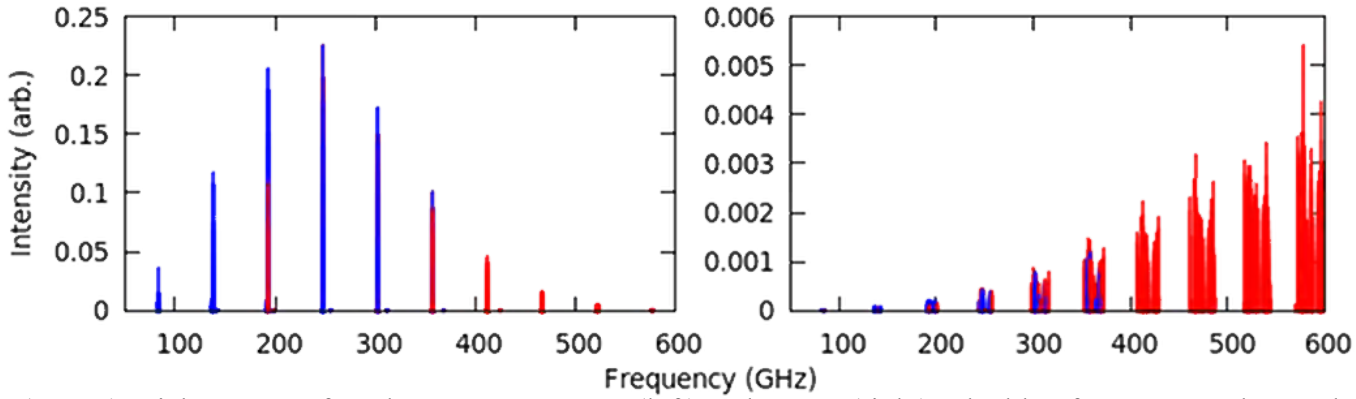

(**above**) Stick spectra of methoxy at $T_{rot} = 15$ K (left) and 300 K (right). The blue features are observed lines and the red features remain to be observed/assigned. At low temperatures, the compact rotational spectrum clearly characterizes that of a symmetric top, with energy levels of a given rotational level being closely spaced together. At higher temperatures, complexities arise from its hyperfine structure due to both symmetry-breaking and additional spin interactions involving its unpaired electron.

References:

- Cernicharo et al. 2012, ApJ Lett., 759, L43
- Laas & Widicus Weaver 2016, ApJ Supp. Series, *in preparation*

J. Laas, et al.

Terahertz Spectroscopy of Sulfur Species

Many S-bearing species have been detected in different astronomical environments and have allowed to derive important information about the chemical and physical composition of interstellar regions. Rotational spectroscopy has been used to characterize and extend molecular data well into the THz region for two important sulfur radical systems, SO and HSO.

Sulfur-bearing species are known to be important astrochemical tracers of hot-core environment time evolution. Among the most prominent sulphur-bearing molecules, SO, sulphur monoxide radical, is one of the more ubiquitous and abundant, observed also in its isotopic substituted species such as ^{34}SO and S^{18}O. Due to the importance of this simple diatomic system and to face the challenge of modern radioastronomical facilities, an extension to THz range of the rare isotopologues of sulphur monoxide has been performed. High-resolution rotational molecular absorption spectroscopy has been employed to extend the available dataset of four isotopic species, SO, ^{34}SO, S^{17}O, and S^{18}O up to the 1.5 THz region. On the other hand, although the HSO radical has not been detected in the interstellar gas yet, the large abundances in space of triatomic species harbouring sulfur, oxygen, and hydrogen such as H_2O, H_2S, OCS, SO_2, HCS^+ is very well known, specially in high-mass star forming regions (and also in cold dark clouds). Therefore, a triatomic species containing these three atoms, such as the HSO radical, could be expected towards these astronomical objects.

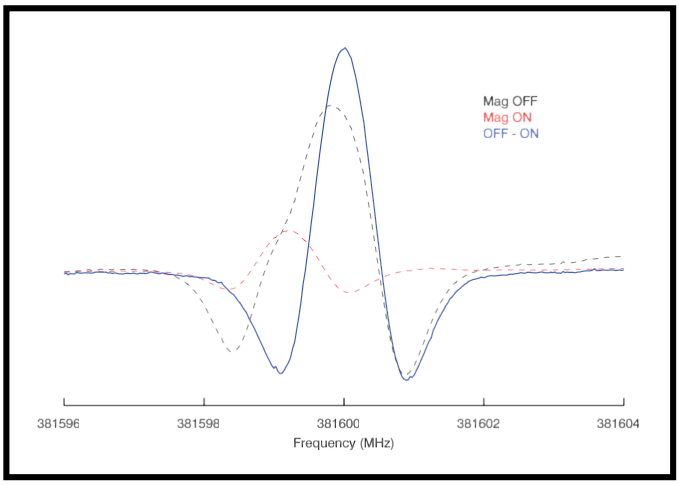

The N, J = 9,10 - 8,9 rotational transition of ^{34}SO. The black-dashed shows the first acquired spectrum, in which a contaminant species transition is on the left edge of the ^{34}SO rotational transition. The effect of applying a magnetic field is to cancel the radical transition, isolating the non-magnetic contaminant transition (in red), whose contribution can then be easily subtracted to derive a precise information on the radical of interest (in blue). Owing to the modulation and detection scheme employed, the instrumental lineshape is approximately the second derivative of a Lorentzian.

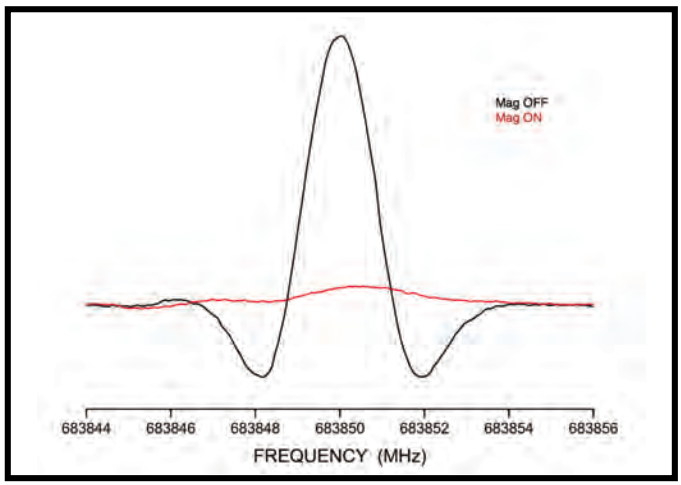

The N = $17_{1,16}$ - $16_{1,15}$ transition of HSO at ~ 683.8 GHz. In black the signal produced by discharging (current = 55 mA) 43 mTorr of pure H_2O into the absorption cell where previous sulfur experiments took place. When to the previous conditions a magnetic field of 126 G is applied, the Zeeman effect causes the splitting of the rotational transition in multiple components, resulting also in a dilution of the overall intensity (in red).

References:

• V. Lattanzi, G. Cazzoli, C. Puzzarini, Ap.J, 813, 4 (2015)
• G. Cazzoli, V. Lattanzi, et al. A&A, submitted

V. Lattanzi, et al.

Ionization and dust charging in molecular clouds and protoplanetary disks

We have developed an exact analytical model for protoplanetary disks (PDs) and very dense molecular clouds, which enables self-consistent calculations of densities of the charged species (Ivlev et al. 2016). In particular, this allows us to obtain dust charges for arbitrary grain size distributions. This analytical model can be easily included in available numerical codes simulating the formation of PDs and following the dust evolution.

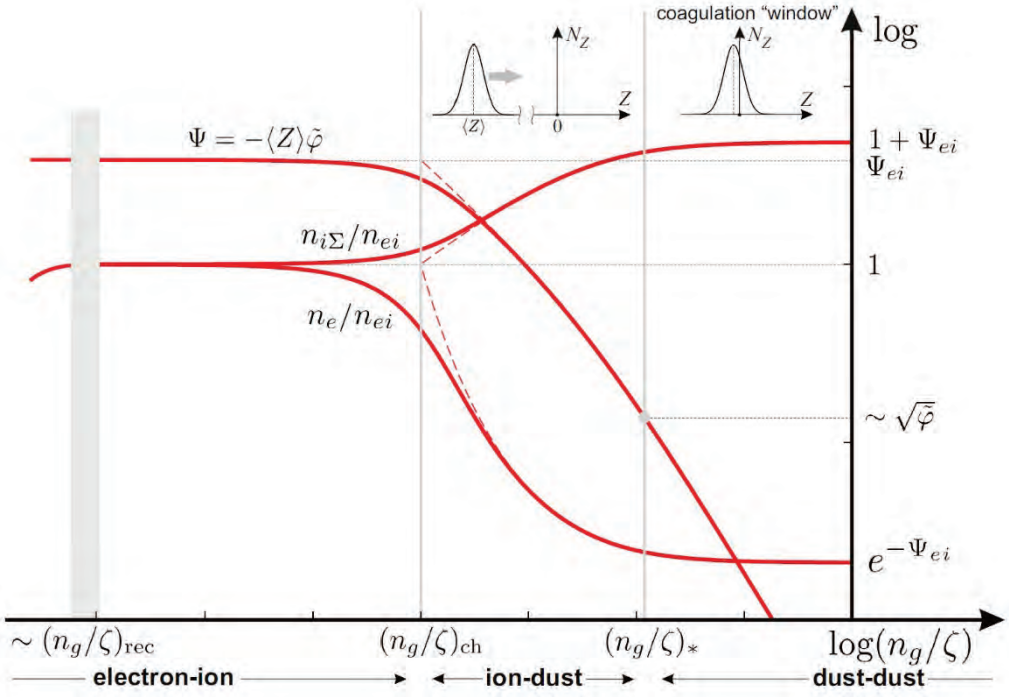

Universal behavior of charged species at gas densities $n_g \geq n_{g\,\mathrm{rec}}$, where the electron-ion accretion on grains is the main mechanism of recombination. All normalized parameters have a universal dependence on $n_g/\zeta(n_g)$, where $\zeta(n_g)$ is the local ionization rate. We identify three characteristic ranges of density, representing a "conventional" **electron-ion plasma**, $n_g \leq n_{g\,\mathrm{ch}}$, an "intermediate" **ion-dust plasma**, $n_{g\,\mathrm{ch}} \leq n_g \leq n_{g\,*}$, and a "high-density" **dust-dust plasma**, $n_g \geq n_{g\,*}$ (typically, $n_{g\,\mathrm{rec}} \sim 10^6$–$10^8$ cm^{-3}, $n_{g\,\mathrm{ch}} \sim 10^9$–$10^{11}$ cm^{-3}, and $n_{g\,*} \sim 10^{11}$–10^{13} cm^{-3}). The red solid lines depict the normalized potential of a grain Ψ, proportional to the average dust charge $\langle Z \rangle$ (Draine 2009), as well as the electron density n_e and the total ion density $n_{i\Sigma}$, both normalized by the electron-ion plasma density $n_{ei}(n_g)$. For $n_g \leq n_{g\,\mathrm{ch}}$, electrons and ions have the same densities equal to $n_{ei}(n_g)$, the potential $\Psi = \Psi_{ei}$ does not depend on n_g. A gradual crossover to an ion-dust plasma occurs at $n_g \geq n_{g\,\mathrm{ch}}$, where the charge neutrality is regulated by (positive) ions and (negative) grains, while the peak of the grain charge distribution N_Z moves toward $Z = 0$. At $n_g \sim n_{g*}$, the magnitude of $\langle Z \rangle$ becomes comparable to the width of N_Z, which indicates a crossover to a dust-dust plasma. Asymptotically, the charge neutrality is regulated by positively and negatively charged grains, the normalized $n_{i\Sigma}(n_g)$ slightly increases, the normalized $n_e(n_g)$ approaches a small constant, while $\Psi(n_g)$ tends to zero as $\sim \zeta(n_g)/n_g$. In a dust-dust plasma, the repulsion between charged grains virtually disappears and a coagulation "window" opens up, promoting a rapid grain growth and planetesimal formation in dense (inner) regions of PDs.

References:

• Ivlev, A. V. et al. 2016 (in preparation)
• Draine, B. T. 2011, Physics of the Interstellar and Intergalactic Medium (Princeton Univ. Press)

A. Ivlev, P. Caselli, et al.

Ionisation in Turbulent Magnetic Molecular Clouds

Structure formation in the early stages of star formation is a delicate balance between several physical processes. We perform thin-disk non-ideal magnetohydrodynamic (MHD) simulations of ionised turbulent molecular clouds to investigate the effect of magnetic fields, turbulence and ionisation profile on the structures formed and the underlying kinematics within the region.

Linear analysis of non-ideal MHD equations shows that the length scale for structure formation depends on the strength of the magnetic field and degree of ionisation (Bailey & Basu, 2012). Microturbulent simulations (Bailey & Basu, 2014) show that clumps form at the intersection of two colliding flows with cores forming along the edges of the low velocity regions (see Figure 1).

Kinematic analysis via synthetic spectra (Bailey, Basu & Caselli, 2015) shows that low density gas regions ($2 < A_V < 7$) with a step-like (SL) density dependent ionisation profile (i.e., high ionisation at low density and low ionisation at high density with a step like transition between) tend to exhibit larger non-thermal contributions than regions with only low ionisation via cosmic rays (see Figure 2). Conversely, synthetic spectra within core regions ($A_V > 7$) show little difference between the SL and CR models.

Our current turbulent simulations of ionised magnetised molecular clouds show that above Mach 2 there is no difference between the resulting structures formed in SL vs. CR models (Bailey, Basu & Caselli, 2016a). Analysis of filamentary structures shows a decreasing trend in filament width with respect to turbulent velocity. Our simulations of highly magnetised regions tend to suggest that fertile and sterile fibres likely form in trans-/supercritical and subcritical regions, respectively.

Future analysis of synthetic spectra within our turbulent simulations will focus on whether kinematic signatures exist which can delineate between ionisation profiles in highly turbulent regions (Bailey, Basu & Caselli, 2016b).

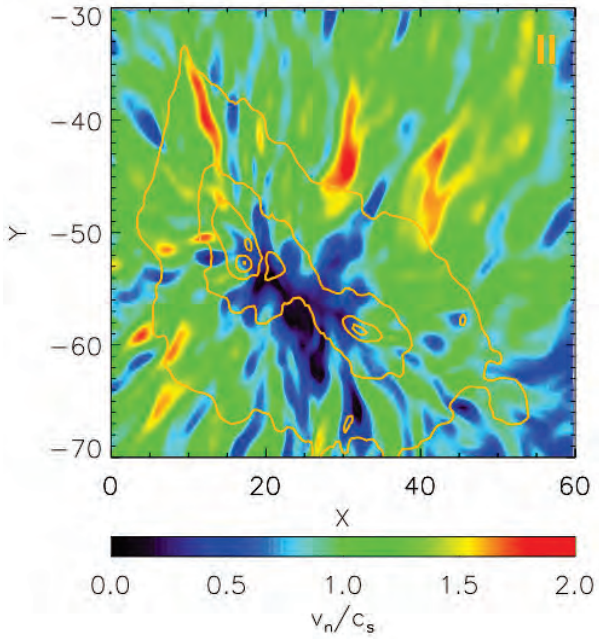

Figure 1: Sample velocity magnitude map for a microturbulent region with a step-like ionisation profile. Orange contours show the column density enhancement in 2 magnitude steps starting at $A_V = 2$ mag.

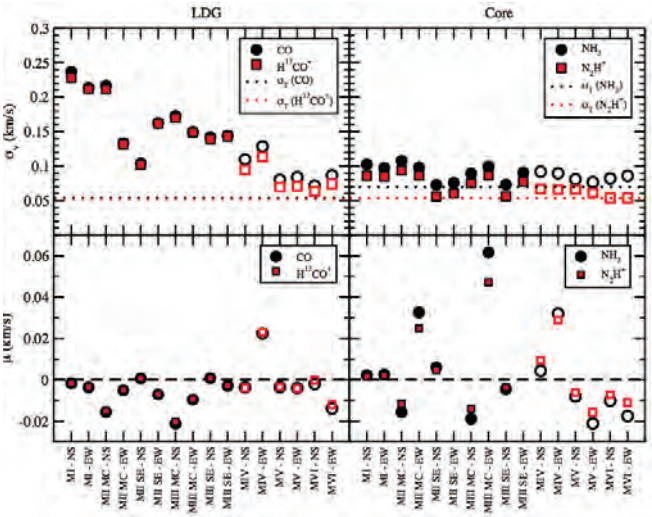

Figure 2: Gaussian parameters for neutral particles and ions for all fits. Symbols depict the molecular tracers as indicated in the legends. Dotted lines depict the respective thermal variances (σ_T) assuming 10 K. Dashed line shows $\mu = 0$ for visual convenience.

References:
Bailey, N. D., & Basu, S., 2012, ApJ, 761, 67
Bailey, N. D., & Basu, S., 2014, ApJ, 780, 40
Bailey, N. D., Basu, S., & Caselli, P., 2015, ApJ, 798, 75
Bailey, N. D., Basu, S., & Caselli, P., 2016a, submitted
Bailey, N. D., Basu, S., & Caselli, P., 2016b, in prep.

N. D. Bailey, P. Caselli, et al.

Protostellar Disk Formation Enabled by Removal of Small Dust Grains

It has been shown that a realistic level of magnetization of dense molecular cloud cores can suppress the formation of a rotationally supported disk (RSD) through catastrophic magnetic braking in the ideal MHD limit. We present conditions for the formation of RSDs through non-ideal MHD simulations including an equilibrium chemical network computed self-consistently. We find that removing from the standard MRN distribution the large population of very small grains (VSGs) of ~10 Å to few 100 Å that dominate the coupling of the bulk neutral matter to the magnetic field increases the ambipolar diffusivity by ~1-2 orders of magnitude at densities below 10^{10} cm^{-3}. The enhanced ambipolar diffusion (AD) in the envelope reduces the amount of magnetic flux dragged by the collapse into the circumstellar disk-forming region. Therefore, RSDs and self-gravitating rings of tens of AU are able to form, survive, and even grow in size.

Non-ideal MHD effects are determined by chemistry and microscopic physical processes:

$$-cE = -v_n \times B + \eta_{Ohmic} J + \eta_{Hall} J \times \hat{B} - \eta_{AD} (J \times \hat{B}) \times \hat{B}$$

$$\eta_{AD} = \frac{c^2}{4\pi}\left(\frac{\sigma_P}{\sigma_P^2+\sigma_H^2} - \frac{1}{\sigma_\parallel}\right) \qquad \sigma_\parallel = \frac{ecn(H_2)}{B}\sum_i Z_i x_i \beta_{i,H_2}$$

$$\eta_{Hall} = \frac{c^2}{4\pi}\left(\frac{\sigma_H}{\sigma_P^2+\sigma_H^2}\right) \qquad \sigma_P = \frac{ecn(H_2)}{B}\sum_i \frac{Z_i x_i \beta_{i,H_2}}{1+\beta_{i,H_2}^2}$$

$$\eta_{Ohmic} = \frac{c^2}{4\pi\sigma_\parallel} \qquad \sigma_H = \frac{ecn(H_2)}{B}\sum_i \frac{Z_i x_i}{1+\beta_{i,H_2}^2}$$

Hall parameter $\beta_{i,H_2} = \left(\frac{Z_i eB}{m_i c}\right)\frac{m_i + m_{H_2}}{\mu m_H n(H_2) < \sigma v >_{i,H_2}}$

VSGs have Hall parameter ~1, they are both well-coupled to the magnetic field and able to exert strong drag to neutral molecules. VSGs hence dominates the fluid conductivity at low densities.

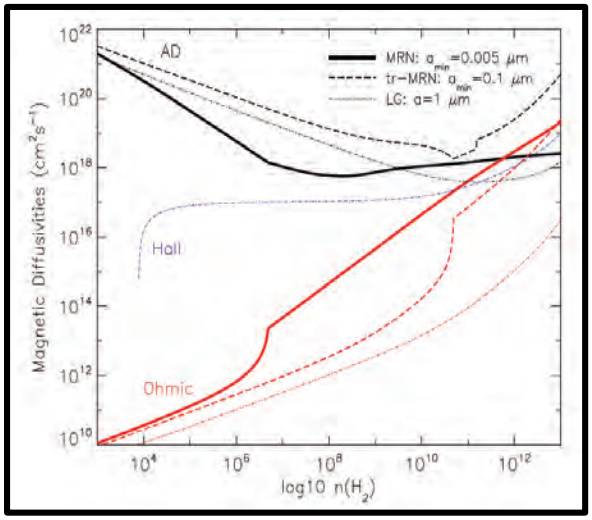

Truncating the full MRN size distribution at a_{min}=0.1 μm yields the optimal enhancement on ambipolar diffusivity η_{AD} at low densities.

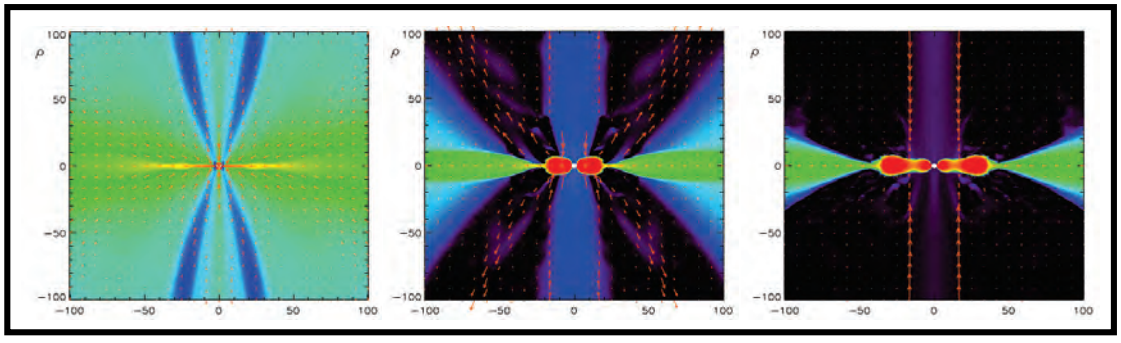

Logarithmic distribution of mass density ρ for models with standard MRN grain size distribution (left panel), and with truncated MRN distribution (middle and right panels). Left and middle panels are slow rotating models, and the right panel is a fast rotating model. All models are for strongly magnetized cores (mass-to-flux ratio of 2.4).

References

• Zhao, B., Caselli, P., Li, Z.-Y., Krasnopolsky, R., Shang, H., & Nakamura, F. 2016, arXiv:1602.02729

CAS

B. Zhao, P. Caselli, et al.

Spin states as probes of the ages of molecular clouds

Chemical species with multiple protons and/or deuterons can exist in different spin states, which can be treated as distinct species since rotational transitions between the spin states are forbidden by selection rules. One important example of this is the H_2D^+ ion which can exist in two spin states, labeled ortho and para. The abundance ratio of the ortho and para states changes as a function of time, and can be used to determine the chemical age of a molecular cloud.

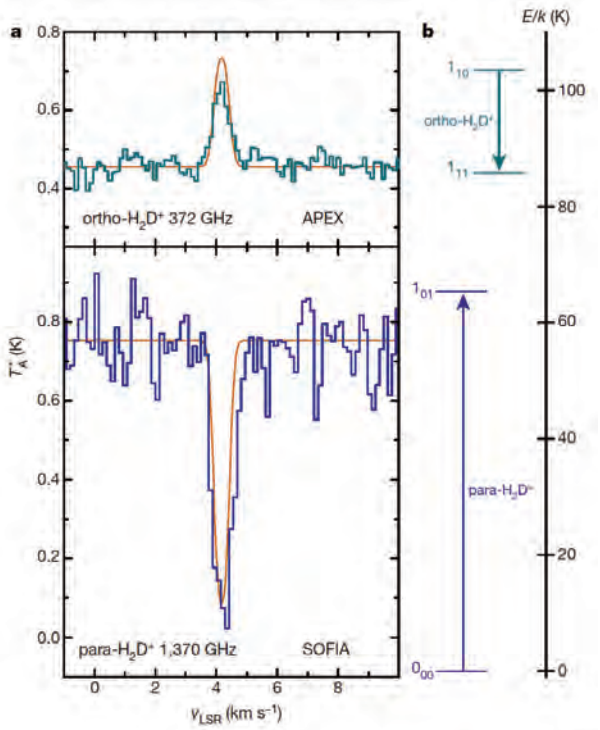

On the right, we show the H_2D^+ ortho/para ratio as a function of temperature at different times as given by our detailed chemical model. The shaded regions show the temperature range applicable in the region where most of the emission/absorption originates, and the observed H_2D^+ ortho/para ratio. Our modeling indicates that the chemical age of the envelope surrounding the protostar, which is the remnant of the natal cloud in which the protostar formed, is around 10^6 years.

The H_2 and H_2D^+ ortho/para ratios are closely connected. The H_2 ortho/para ratio decreases as a function of time, and low values of the ratio are expected in chemically old gas. The H_2D^+ ortho/para ratio follows the decrease of the H_2 ratio. Thus, observations of both the ortho and para states of H_2D^+ can yield information on the chemical age of the observed object. In Brünken et al. (2014), we presented the first confirmed detection of para-H_2D^+ in space, achieved with the airborne SOFIA observatory toward the protostar IRAS 16392A. We also detected ortho-H_2D^+ toward the same source with APEX. On the left, we show the observed lines (histograms) along with fits from our chemical model (solid lines).

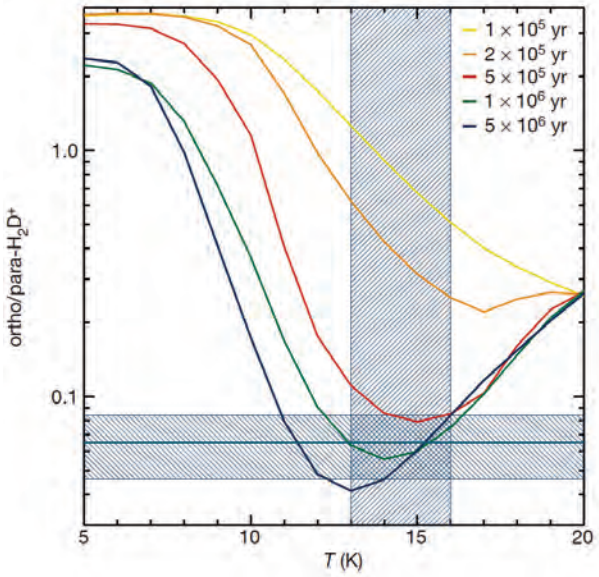

References:

• Brünken, S., Sipilä, O., Chambers, E.T., et al. 2014, Nature, 516, 219

O. Sipilä, J. Harju, P. Caselli

Complex organic molecules in L1544

We present the results of chemical modeling of the formation of terrestrial-type complex organic molecules (COMs) under conditions typical for prestellar cores. We utilized an advanced gas-grain astrochemical model based on Vasyunin&Herbst (2013) with added multilayer approach to ice-surface chemistry and up-to-date treatment of reactive desorption based on recent experiments of Minissale et al. (2016). We found that terrestrial-type COMs can be formed efficiently in L1544 up to the fractional abundances of 10(-10) wrt. to H. Abundances of many COMs such as CH_3OCH_3, $HCOOCH_3$, HCOOH and others peak at similar radial distance of ~4000 AU, which is consistent with recent observations.

The formation of recently discovered complex organic molecules (COMs) in cold clouds is not yet fully understood. Here, we present the results of the modeling of the formation of COMs in a well studied pre-stellar core L1544.

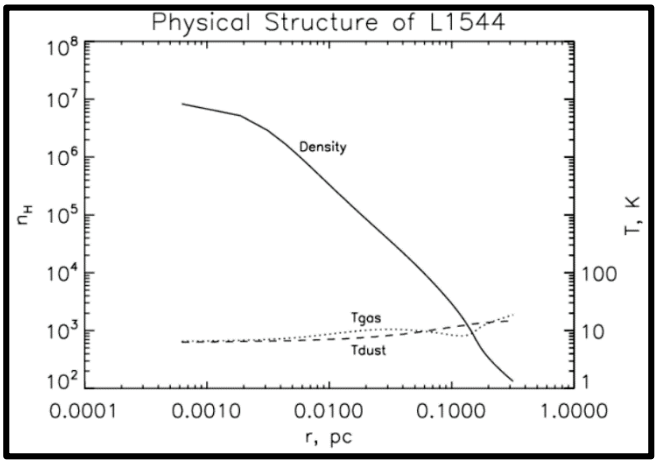

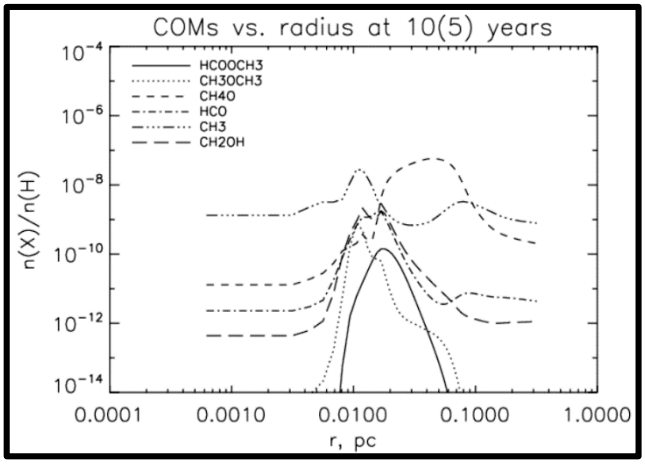

To model the radial profiles of COMs in L1544, we utilized the results from a 1D physical model of the prestellar core developed by Keto&Caselli (2012) (see left figure). In the core, one can single out the very dense and dark central part, an intermediate shell with moderate density, and the outer part with low density and penetrating UV field.

Using the developed three-phase chemical code and updated chemical network, we studied the formation of complex organic molecules in the pre-stellar core L1544. Radial profiles of molecules including COMs were calculated for the case of prototypical prestellar core L1544 at the moment of time when modeled depletion factor of CO became equal to that observed (see right figure). The terrestrial-type COMs are formed efficiently in L1544 up to the fractional abundances of 10(-10) wrt. to H. Abundances of many COMs such as CH_3OCH_3, $HCOOCH_3$, HCOOH and others peak near the radial distance of ~4000 AU. Gas-phase abundances of COMs depend on the efficiency of reactive desorption, which is in turn depends on the composition of outer monolayers of icy mantles. In prestellar cores, outer monolayers of mantles are likely include large fraction of CO, which may increase the efficiency of reactive desorption according to Minissale et al. (2016), and makes formation of COMs under conditions typical for prestellar cores efficient.

References:

A.I. Vasyunin, E. Herbst, ApJ, 769, 34 (2013)
P. Caselli, E. Keto, E. Bergin et al., ApJ, 759L, 37C (2012)
A.I. Vasyunin, E. Herbst, ApJ, 762, 86 (2013)
A. Bacmann, V. Taquet, A.Faure et al., A&A, 541, L12 (2012)
M. Minissale, F. Dulieu, S. Cazaux, S. Hocuk, A&A, 585A, 24M (2016)

A. Vasyunin, P. Caselli, et al.

Chemical evolution in quiescent clumps

Massive pre-stellar clumps are the earliest phases of high mass star formation. Recent Galaxy wide surveys have started to explore the physical conditions of these clumps, however, our understanding of the chemical evolution in these clumps are far from complete. We investigate the evolutionary ages of these clumps using a chemical evolutionary code including the existing continuum and line survey data spanning over far infrared to (sub-)mm wavelengths.

A large number of massive pre-stellar clumps are identified using (sub-)mm dust emission in the ATLASGAL surveys. Column density and dust temperature maps of these clumps are derived using multi-band far-infrared Hi-GAL observations. These clumps are followed up in MALT90 survey that mapped each of these clumps in 16 different molecular transitions among which only seven transitions are detected towards these clumps. Molecular column densities of the observed transitions were calculated assuming local thermodynamic equilibrium.

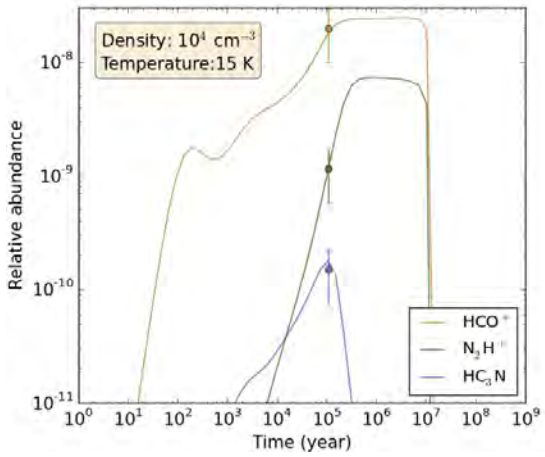

Fig. 1

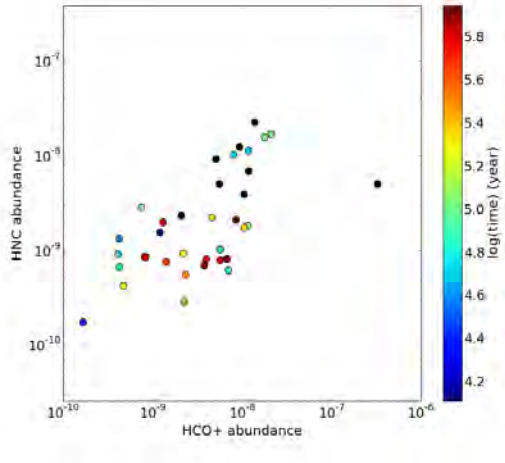

Fig. 2

The existing continuum observations are useful to estimate the physical conditions but our aim is also to constrain the ages of these clumps. It is well-known that chemical evolution strongly depends on both time and physical conditions, therefore, we investigated the time-dependent chemical evolution in these clumps to estimate the evolutionary ages. We constructed a grid of physio-chemical conditions guided by the estimated physical conditions and molecular abundances of these massive pre-stellar clumps and then calculated the temporal evolution of molecular abundances using the chemical evolutionary code *Saptarsy*[1]. Observed molecular abundances of a particular clump were then compared against the grid of chemical models and the best fit model was identified. The particular time at which a satisfactory match was obtained between observed and the best-fit model abundances, indicated the evolutionary age of that particular clump. (Fig. 1). The goodness of fit was estimated using the complementary error function. For further verification, we also checked various abundance vs. abundance plots for both observed and best-fit model abundances and find satisfactory matches (Fig. 2) which also demonstrates the robustness of the modelling process. In summary, we estimated the median ages of massive pre-stellar clumps as 2×10^5 years[2] using chemical modelling.

References:

1. Choudhury, R., Schilke, P., Stéphan, G., et al. A&A, 2015, 575, A68
2. Choudhury, R., Caselli, P., Contreras, Y., Rathborne, J. et al., 2016, in prep.

R. Choudhury, P. Caselli, et al.

The chemical factor in star formation

In the earliest phases of star-forming clouds, stable molecular species, such as CO, are important coolants in the gas phase. Depletion of these molecules on dust surfaces affects the thermal balance of molecular clouds and with that their whole evolution. For the first time, we studied the effect of grain surface chemistry (GSC) on star formation and its impact on the initial mass function (IMF). We performed 3D hydrodynamical simulations with detailed surface chemistry, focusing on the processes freeze-out and chemical desorption. While our results show that doing proper surface chemistry is crucial in obtaining correct abundances, our findings on star formation should excite the non-chemists among astronomers.

The impact of freeze-out is significant.
The equation of state (EOS) of the gas becomes softer, but this balanced by the non-thermal processes: chemical and photodesorption. This is important for gas thermodynamics and chemical abundances.

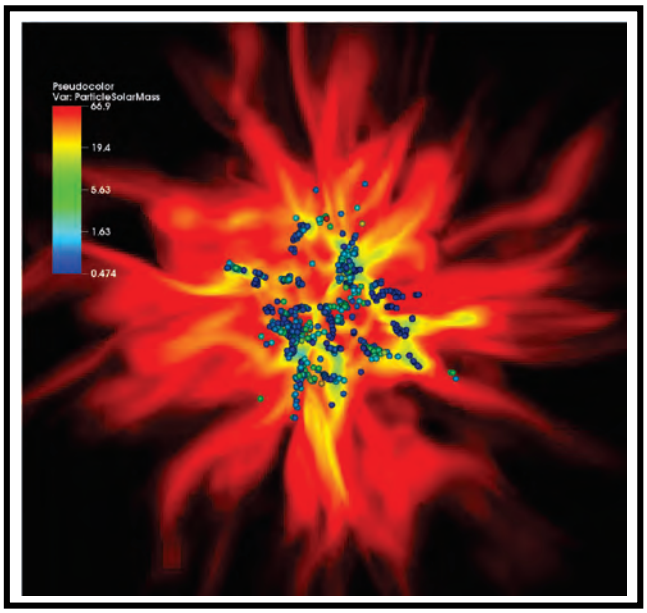

The impact on the IMF is modest
When considering all the competing processes on small scales (i.e., chemistry) and on large scales (e.g., gravity, turbulence), the discovery is that star formation is robust against chemical changes during the early stages of cloud evolution.

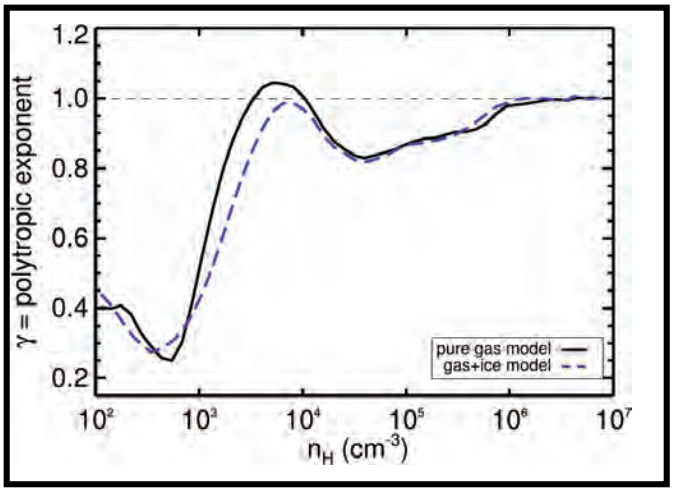

A giant molecular cloud collapsing under his own gravity and forming stars.
The number of formed stars differ by 7% if the chemistry is treated properly or not, that is, if, for solid-state chemistry, only the process of freeze-out is applied or the full chemisrty is performed instead.

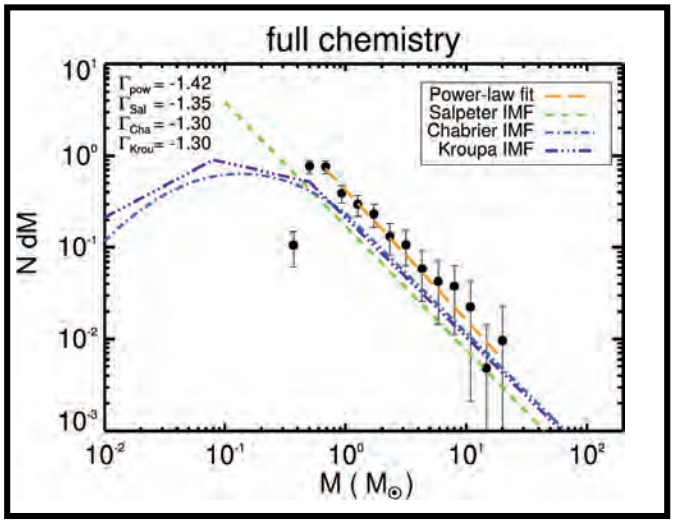

References:
• Hocuk et al. 2016, MNRAS, 456, L56

S. Hocuk, P. Caselli, et al.

Do the carbon and nitrogen chemistry reach equilibrium in dynamically evolving molecular clouds?

We model the chemical evolution of parcels of gas (SPH particles) as they are accreted to a protostellar core. The variations in density, irradiation and temperature are taken into account. The abundances are compared to the steady state abundances of the same physical conditions. We find good agreement when photochemical reactions dominate the chemistry (i.e. low A_v). At high density and A_v, the difference can be multiple orders of magnitude. Here, grain surface reactions dominate, with time scales much longer then the accretion time of the gas parcels.

The chemical models of molecular clouds and cores often assume steady state physical conditions and evolve the chemical abundances for millions of years. In reality, however, the abundances are also expected to depend on the dynamic history of the gas (Glover et al., 2010). We post-process hydro-dynamic simulations of molecular cloud evolution (Szűcs et al., 2014; submitted), using a complete chemical network (Albertsson et al., 2013), to estimate the difference between stead state abundances and those which take the dynamic history into account (Szűcs et al., in prep). The figures below show the physical and chemical evolution of a typical accreted SPH particle. We find orders of magnitude difference in the abundances, especially when grain-surface processes dominate the chemistry (see e.g. the CO abundance at late times). Generally, gas dynamics lessens and delays the freeze-out to grains.

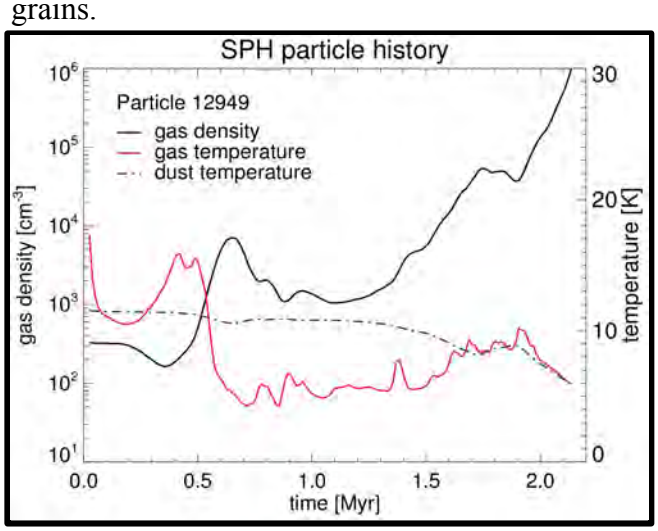

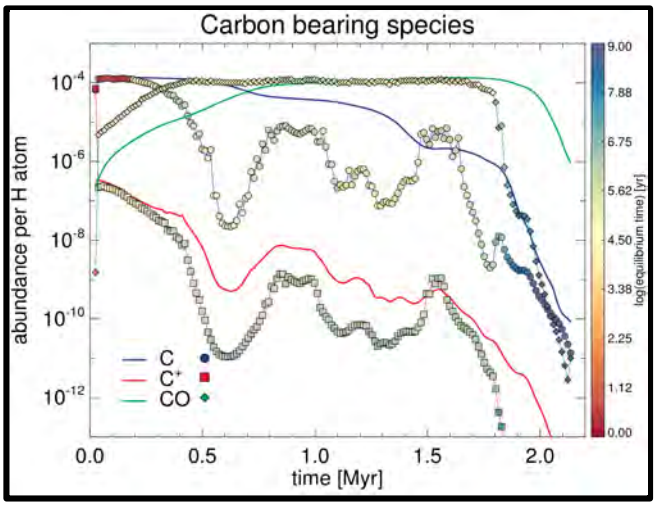

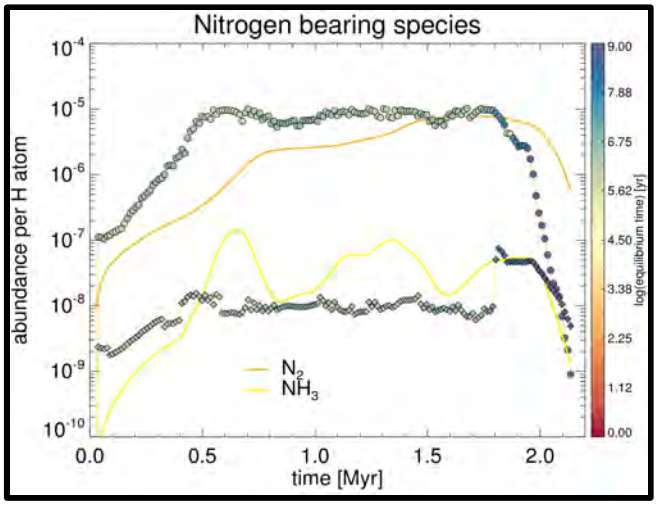

Top left: The density and temperature evolution of a typical SPH particle, that ends up in a prestellar core at the end of the simulation. Note the fluctuation in density and gas temperature. **Top right**: The evolution of the major carbon bearing species. The solid line shows the dynamic, while the symbols represent the steady state calculations. The symbol colour indicates the time required to reach steady state. **Bottom:** The same as above, but for the major nitrogen-bearing species. The N_2H^+ abundance (not shown here) is much lower than 10^{-10}.

References:

- Albertsson, T., et al., 2013, ApJS, 207, 27
- Glover, S., et al., 2010, MNRAS, 404, 2
- Szűcs, L., et al., 2014, MNRAS, 445, 4055
- Szűcs, L., Glover, S., Klessen, R., submitted
- Szűcs, L., Caselli, P., et al., in prep.

L. Szűcs, P. Caselli, et al.

Combining gas-phase, surface chemistry, dust charging physics in a protoplanetary disk model

Knowing the ionisation fraction and the charge carriers is paramount to the efficient of the efficiency of the Magneto-Rotational Instabilities (MRI), which can drive turbulent in protoplanetary disks. Dust grains and PAHs can be important charges carriers. We implemented details grain charging physics in the protoplanetary disk code ProDiMo.

Pre-main-sequence stars (TTauri and HerbigAe stars) are surrounded by planet-forming disks in keplerian rotation. The disks are massive at the early stage reaching gas masses of $10^{-2}\,M_{\odot}$ or even higher and disappear after a few million years. The disk material can evaporate, form giant planets, or fall onto the star. Gas can accrete from the inner rim of disks to the star. The most promising explanation to drive mass accretion in disks is turbulence driven by magnetorotational instability (MRI). Many non-ideal Magneto-Hydro-Dynamics resistivities can restrict the development of MRI turbulence. The resistivities (Ohmic and ambipolar diffusion) depend on the abundances of the charge carriers among other factors. On the other hand, Hall diffusion can overcome the limits on the value of α in certain conditions. The resistivites have a strong dependence on the disk ionisation fraction.

We explored the effects of a detailed treatment of the physics and chemistry of PAHs and grain charging on the disk ionization. The aim of the study was to determine the extent of the dead-zone, the area in disks where the ionization fraction is too low for the magnetic field to couple to the neutral gas, and hence for MRI to sustain turbulence. For this purpose we implemented MRI- turbulence heating and cooling in the photo-chemical disk code ProDiMo (Woitke et al. 2016 A&A 586, 103). We consider far-ultraviolet from the star and the accretion excess, X-ray, and cosmic-rays as sources of ionization. We sought possible tracers of turbulence in disks. The dust grain charges is constrained in the upper disk atmospheres mostly by the photo ejection due to the strong UV field whereas in the mid-plane electron attachment and ion recombinations onto grain surfaces control the grain charges. Knowing the chair carriers makes if possible to determine the Ohm, Ambipolar Diffusion resistivities. We can then estimate the turbulent contribution to the line width. See the right figure below. The paper is to be submitted.

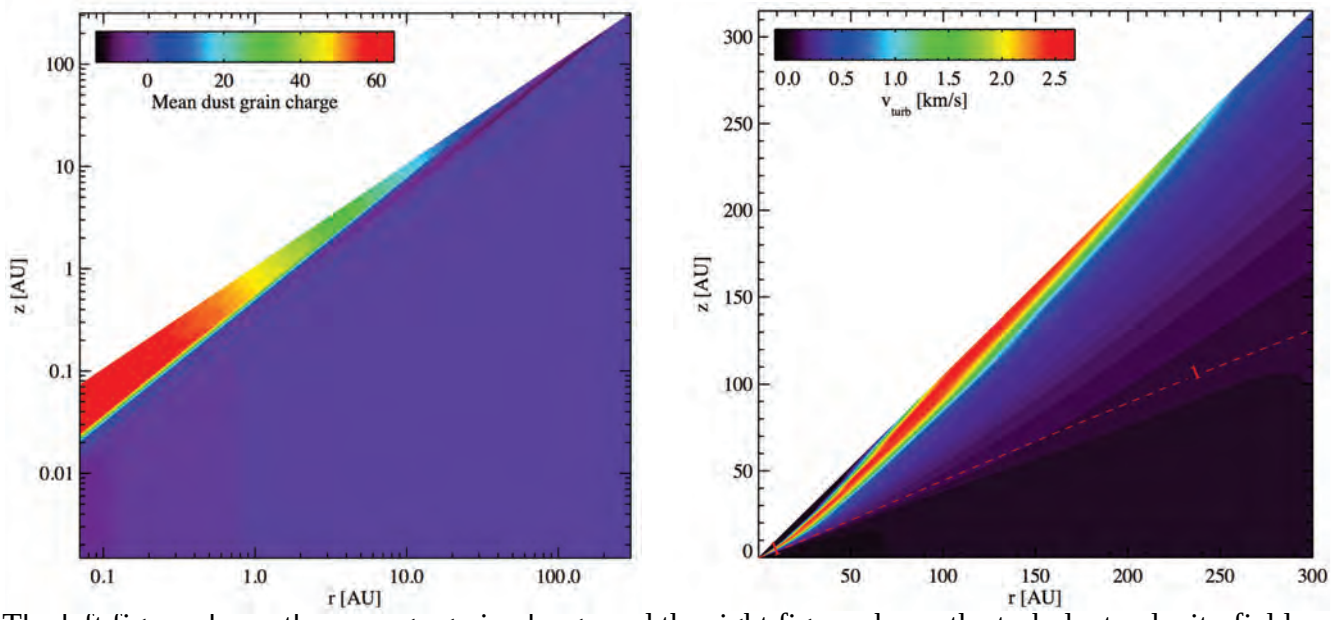

The left figure shows the average grain charge and the right figure shows the turbulent velocity field.

W.-F. Thi

Wave turbulence observed in a complex (dusty) plasma

Complex or dusty plasmas consist of micrometer-sized particles embedded in a low-temperature plasma and are ideal model systems for nanofluids, phase transitions and transport processes. As an example of complex system dynamics, these solid particles immersed into a weakly ionized plasma are the subject of many detailed studies.

We report on a complex plasma under microgravity conditions that is auto-oscillating due to a heartbeat instability. The instability triggers the low-R turbulent flow in a complex plasma cloud (see fig.1). The flow reveals a complicated and neatly structured multi-cascade turbulent process. A direct and an inverse energy cascade, influenced by friction, modulational and short-wavelength instabilities, resulting in a quasi-stationary turbulent state seems to be a promising model able to adequately address all the fine features of the observed particle and energy transport.

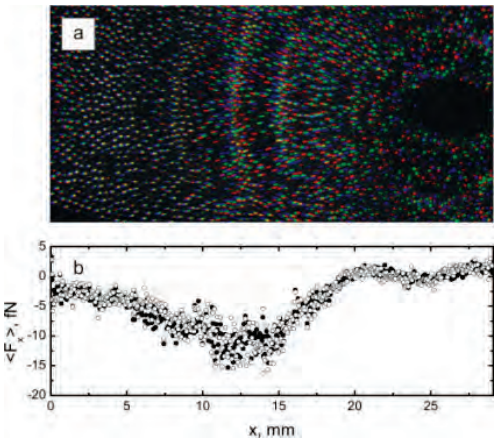

Fig.1. Positions of the particles inside the cloud and the mean force driving oscillations. (a) RGD-coded and imposed three one period–shifted images taken from three consecutive periods of particle oscillations. The field of view is 1.17 × 2.92 mm². (b) The averaged horizontal component of the driving force. Bold (open) dots: the forces computed taking into account all particles tracks longer than 5 (10) time steps.

We numerically studied two-dimensional vortices in a complex plasma. In particular, we showed that turbulence is present in the flow induced by the vortices and demonstrated that the velocity structure functions scale very close to the predictions by Kolmogorov theory (fig.2). The results obtained show that complex plasmas are a promising tool to study turbulence on the level of individual particles.

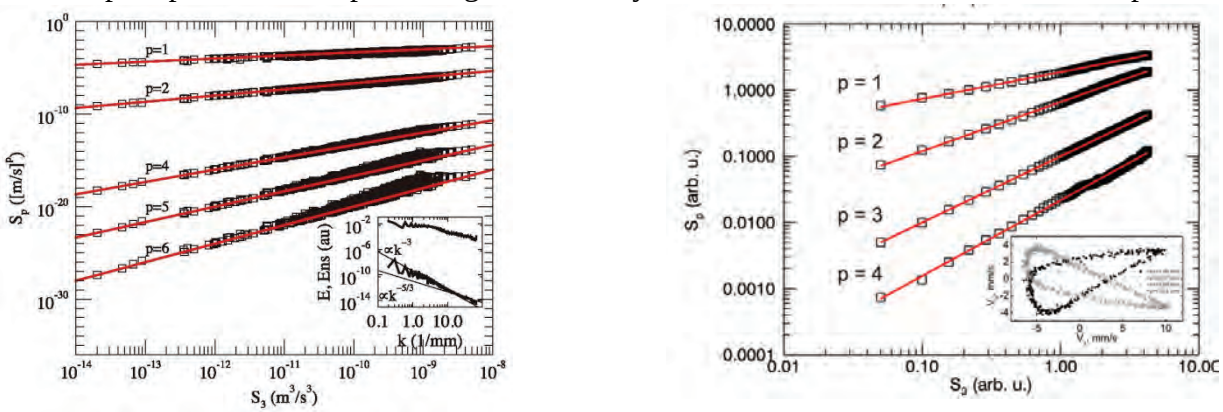

Fig.2. Structure functions S_p of wave turbulence simulated (left) and observed (right) in a complex plasma. The lines are those predicted by classical Kolmogorov theory $S_p \propto r^{p/3}$. Inset (left): energy (bottom) and enstrophy density spectrum (top). Inset (right): phase portraits of two particles located symmetrically inside the particle cloud. Note the intrinsic asymmetry of the dynamical pattern.

References:
• M. Schwabe, S. Zhdanov, Ch. Räth, D.B. Graves, H.M. Thomas, and G.E. Morfill, PRL, **112**, 115002 (2014).
• S. Zhdanov, M. Schwabe, Ch. Räth, H.M. Thomas, and G.E. Morfill, EPL, **110**, 35001 (2015).

S. Zhdanov, G. E. Morfill, et al.

V) MPE Research Groups

V.1) Group Prof. Andreas Burkert

The G2+G2t complex as an outflow?

Observations of the gas component of the cloud G2 in the Galactic Center have revealed its connection to a tail (G2t) lying on the same orbit (Pfuhl et al., 2015; see also the contributions from the IR group). We show - by means of 3D hydrodynamic simulations - that an outflow by a central source (possibly a T Tauri star) moving on G2's orbit and interacting with a hot atmosphere surrounding SgrA* can have G2 and G2t as a byproduct.

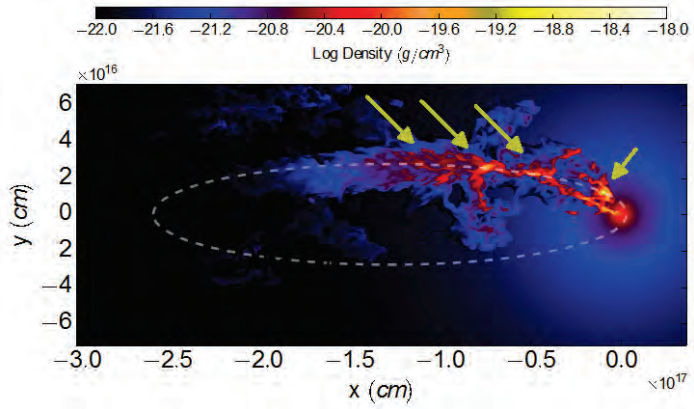

Our model consists of a spherical outflow with mass-loss rate equal to 5 x 10^{-7} $M_{\odot}$/yr and velocity equal to 400 km/s, interacting with the hot accretion flow in the inner 0.1 pc of the Galactic Center and with the strong tidal field of the central supermassive black hole. Simulated position-velocity (PV) diagrams result in a bimodal distribution (see figure below), with G2 being the bow-shock formed in the head of the source and G2t being the result of the stripping of the rest of the shocked material by the ram pressure of the surrounding hot gas and of its successive accumulation in a trailing tail. This is shown in the density cut on the left.

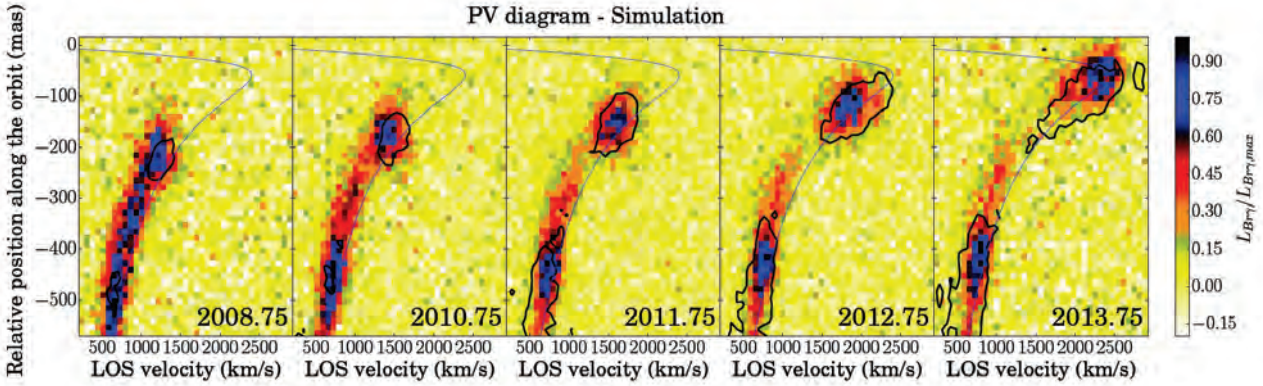

The parameters of our model are roughly comparable with those of outflows from T Tauri stars. This could naturally explain the presence of dust embedded in G2 and the more moderate MIR emissions seemingly associated to G2t (Pfuhl et al. 2015), if the material launched in the outflow is also dusty. Though some tension between the observations and the simulated model remains, we argue that this might be due to issues in the construction of observed position-velocity (PV) diagrams and/or to a poor treatment of some physical processes - like hydrodynamic mixing - in our simulation. Furthermore, the present model neglects the discovery of the cloud G1, that seems to be associated with the former objects. However, the connection between G1 and the G2+G2t complex is still speculative and only future observations will clarify this point.
Hence, such a scenario offers a valuable potential explanation for G2 and its following tail G2t.

References:

• Ballone, Schartmann, Burkert et al., accepted for publication in ApJL
• Pfuhl, Gillessen, Eisenhauer et al., 2015, ApJ, 798, 111
• Ballone, Schartmann, Burkert et al., 2013, ApJ, 776, 13

A. Ballone, M. Schartmann, A. Burkert, S. Gillessen, P. M. Plewa, R. Genzel, O. Pfuhl. F. Eisenhauer, T. Ott, E. M. George, M. Habibi

Gravitational Dynamics and Star Formation

The *gravitational energy spectrum* enables us to quantify gravity with data from observations and numerical simulations. The method provides multi-scale understandings of gravity in star-forming regions, and allows us to address fundamental questions such as the interplay between turbulence and gravity in molecular clouds. It is also useful for other astrophysical systems.

Motivation: Many previous methods are blind to the spatial organisation of the gas. We overcome this by developing a new method to quantify the structure of the gas.

Data

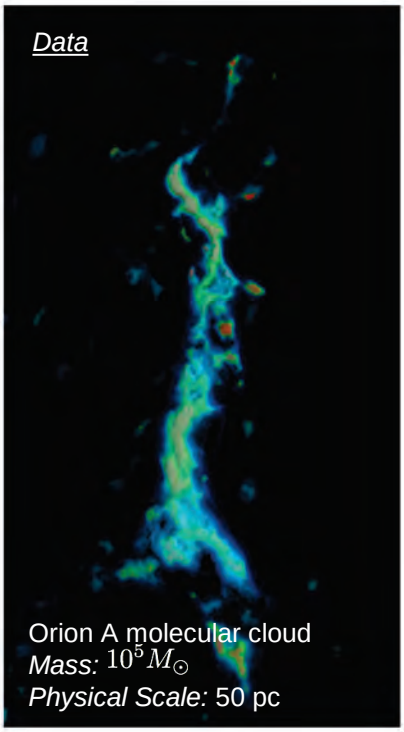

Orion A molecular cloud
Mass: $10^5 M_\odot$
Physical Scale: 50 pc

Method

Gravitational potential

$$\nabla^2\phi = 4\pi G\rho$$

Multi-scale Gravitational energy

$$\mathcal{E}_l = -\frac{1}{2}\int \phi_l \rho \mathrm{d}^3x$$

Decomposition

$$\phi = \sum_l \phi_l$$

ϕ_l

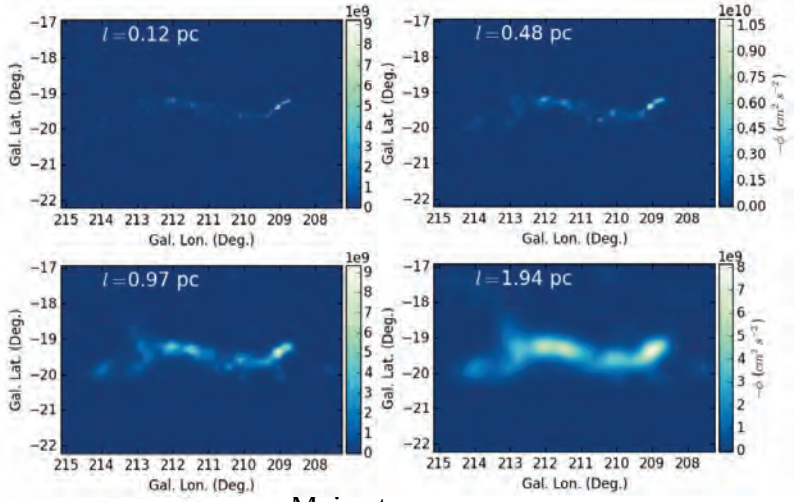

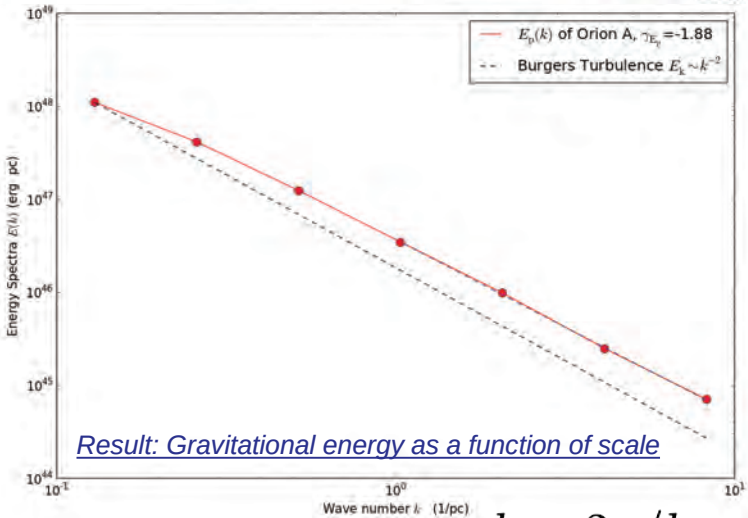

Result: Gravitational energy as a function of scale

$$k = 2\pi/l$$

Main steps:

- Constructing 3D density distributions from observations [1]
- Computing gravitational potential
- Computing the gravitational energy spectrum [2, 3]

The gravitational energy spectrum represents the distribution of gravitational energy across different scales.

Main findings (left panel):

In molecular clouds, turbulent kinetic energy and gravitational energy reach a multi-scale (0.1 -10 pc) equipartition.

$$E_{\rm grav} \sim k^{-2} \sim E_{\rm kin}$$

References:
[1] Kainulainen et al, Science, 344, 183
[2, 3] Li & Burkert 2016 (a, b), submitted

The project is connected to CAST group (LMU) and CAS group (MPE)

G.-X. Li, A. Burkert

Stellar feedback efficiencies

Stellar winds and supernova (SN) explosions of massive stars ("stellar feedback") create bubbles in the interstellar medium (ISM) and insert newly produced heavy elements and kinetic energy into their surroundings, possibly driving turbulence. Most of this energy is thermalized and immediately removed from the ISM by radiative cooling. The rest is available for driving ISM dynamics.
With one-dimensional spherically symmetric simulations we estimate the amount of feedback energy retained as kinetic energy when the bubble walls have decelerated to the sound speed of the ambient medium.
We find that taking into account the stellar wind phase drastically increases the retained kinetic energy in our model for a 60 $M_\odot$ star: The plots below show that the retained energies with and without SN differ by a factor 6. Furthermore, our models show that simulations with a SN blast without preceding stellar wind converge for all resolutions, whereas the spatial resolution of the simulations taking the stellar wind into account has an effect on the retained energy. This behavior is caused by the radiative losses at the contact discontinuity (CD) separating the swept-up medium from the stellar ejecta.
We argue that the spatial resolution of our simulation can be interpreted as the length-scale of a diffusive process at the CD. Thus, the non-converging models shown below are models for different diffusivities.

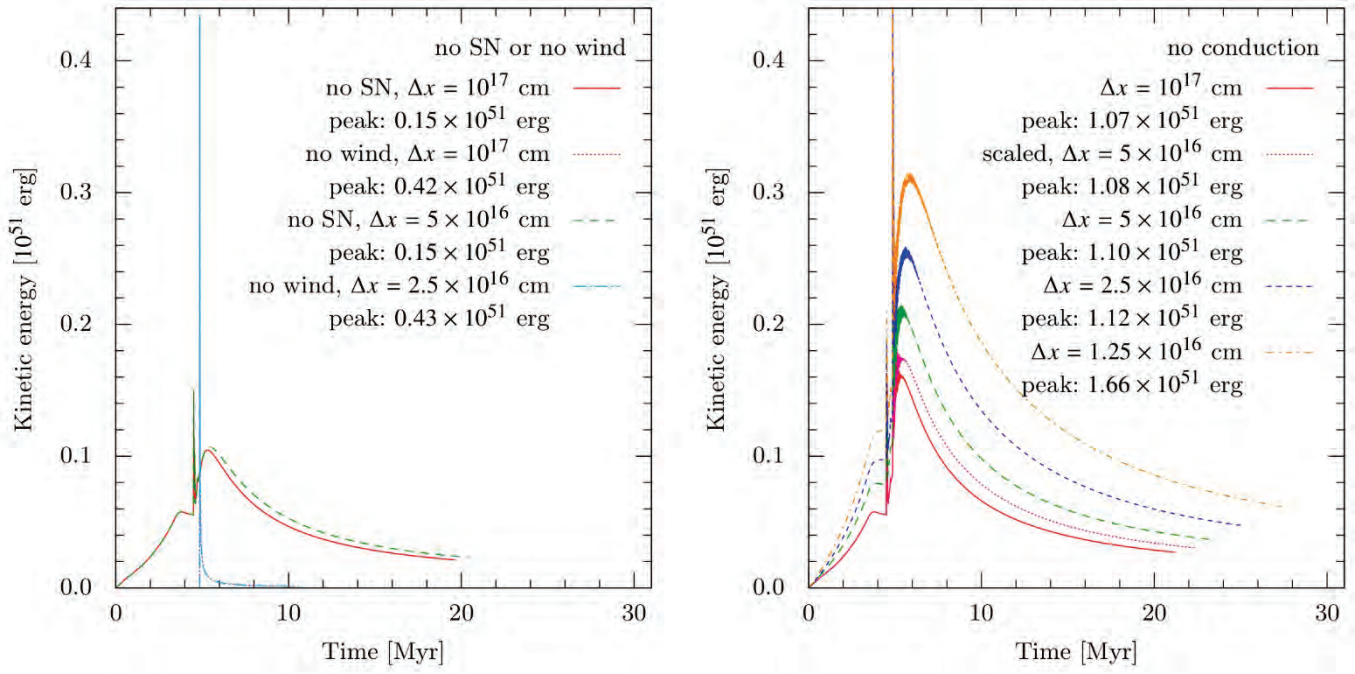

Left: Wind-only or SN-only models for a 60 $M_\odot$ star in a cold medium with a density of 100 particles/cm^3. The SN models converge for different resolutions since the radiative losses peak in the well-resolved newly swept-up medium. The retained energy in SN-only models is negligible.
Right: Models with stellar wind and SN. This figure shows the time-dependent retained feedback energy for a variety of diffusive length-scales.

References:

• Fierlinger et al, 2016 MNRAS 456, 710 (and references therein)

K. M. Fierlinger, A. Burkert, E. Ntormousi, P. Fierlinger, M. Schartmann, A. Ballone, M. G. H. Krause, R. Diehl

Origin of the giant clumps at high-z: the bottom-up scenario

Giant clumps are a characteristic feature of observed high-redshift disk galaxies. We propose that these kpc-sized clumps have a complex substructure and are the result of many smaller clumps self-organising themselves into clump clusters (CCs). This bottom-up scenario is in contrast to the common top-down view that these giant clumps form first and then sub-fragment. Using a high-resolution (~3pc) hydrodynamical simulation of an isolated, fragmenting massive gas disk and mimicking the observations from Genzel et al. at z~2, we find remarkable agreement in many details.

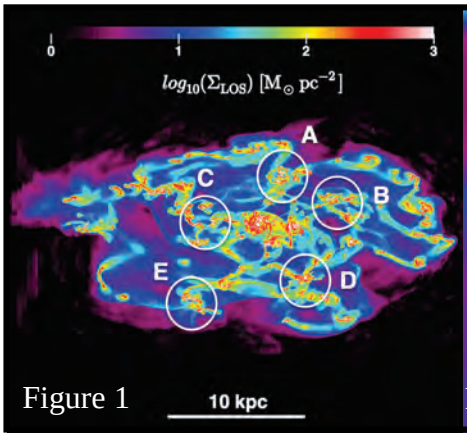

Figure 1

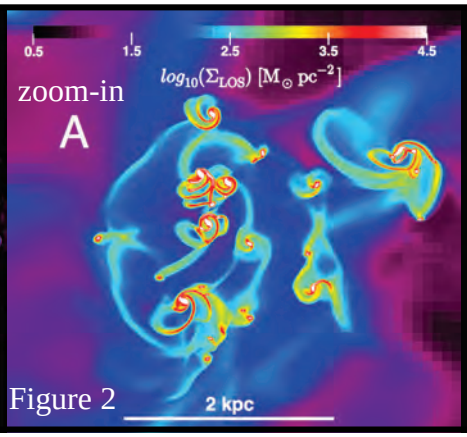

Figure 2

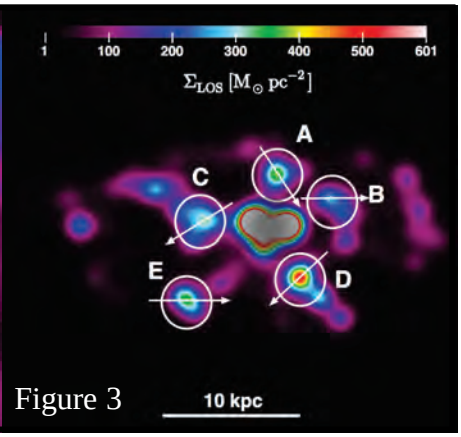

Figure 3

Revised picture of the disk fragmentation

In a 'Toomre unstable' disk, linear perturbation theory indeed predicts a dominant wavelength on kpc scales. However, this wavelength determines the initial sizes of a few axisymmetric rings growing from inside-out instead of a few kpc-sized clumps if initially the densities in the mid-plane are sufficiently resolved (Behrendt et al. 2015). These rings break-up into many clumps after they collapsed onto parsec-scales. The typical clump ensemble in a simulation of a massive disk with several 10^{10} $M_\odot$ is initially dominated by clumps with average masses of several 10^7 $M_\odot$. Later on most of the mass resides in a population of clumps with several 10^8 $M_\odot$ and ~120 pc in diameter (M. Behrendt et al. 2016a, in preparation). They self-regulate into the mass-radius relation $M \propto R^2$ (similar to the Milky Way), which persists over several hundred Myrs.

'Small' clumps self-organise into clusters

The 'small' clumps subsequently self-organize into a few 100 pc to kpc-sized CCs (Figure 1, 2) and appear as single kpc-sized objects at the observed resolution of FWHM~1.6 kpc (Figure 3), Behrendt et al. 2016. CCs also have an interesting and complex evolution. For example they are exchanging their substructure, or even disperse and reform (M. Behrendt et al. 2016b, in preparation). In a parameter study of different dark matter halos and 'Toomre unstable' disks we found no evidence for the common top-down view that these giant clumps form first and then sub-fragment.

Kinematic properties

By mimicking the SINFONI instrument of the VLT, we find high velocity dispersion in the disk and in the giant clumps, typical for high-z observations. The intrinsic velocity dispersion of the giant clumps is caused by their sub clump's high irregular motions. No additional energy input e.g., via stellar feedback, is necessary. Small velocity gradients along the CCs correspond mainly to the rotation around their center of mass.

References:

• Genzel et al. 2011, ApJ, 733, 101
• Behrendt et al. 2015, MNRAS, 448, 1007
• Behrendt et al. 2016, ApJ, 819, L2
• Behrendt et al. 2016 (a,b), in preparation

M. Behrendt, A. Burkert, M. Schartmann

Dynamical friction and scratches of orbiting satellite galaxies on host systems

We study the dynamical response of extended systems, hosts, to smaller systems, satellites, orbiting around the hosts using extremely high-resolution *N*-body simulations with up to one billion particles. This situation corresponds to minor mergers which are ubiquitous in the scenario of hierarchical structure formation in the universe. According to Chandrasekhar, satellites create density wakes along the orbit and the wakes cause a deceleration force on satellites, i.e. dynamical friction. This study proposes an analytical model to predict the dynamical response of hosts as reflected in their density distribution and finds not only traditional wakes but also mirror images of over- and underdensities centred on the host. Our controlled *N*-body simulations verify the predictions of the analytical model.

[Right] Distribution of enhancement and reduction in the column density of the host system derived from the simulation performed with a code designed and optimized for GPU clusters (Ogiya et al. 2013). The colour bar represents enhancement and reduction in the column density, $(\Sigma - \Sigma_0)/\Sigma_0$, where Σ_0 is the initial column density at given position in the host frame. Spatial coordinates are scaled by the scalelength of the host system, r_s. The black line shows the satellite orbit.

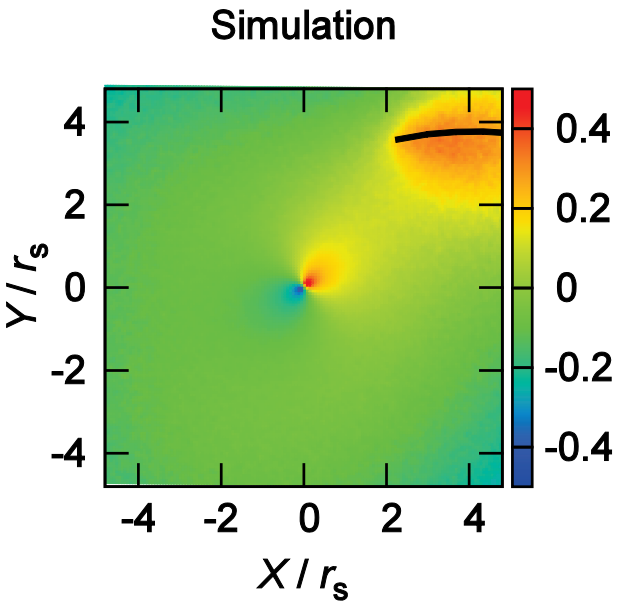

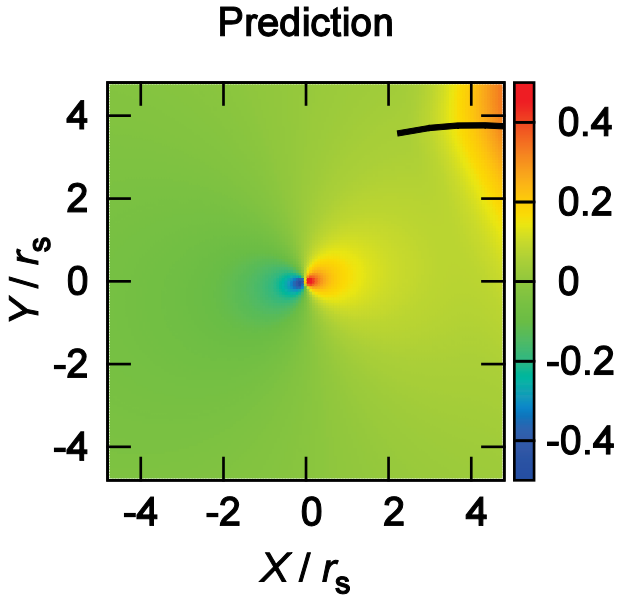

[Left] Distribution of enhancement and reduction in the column density derived by the analytical model based on the formulation of dynamical friction. The position, velocity and mass of the satellite are taken from the simulation. The analytical model reproduces the simulation result well.

The scratches are classified into two types: the first one is the gravitational wake along the orbit of satellites as discussed in Chandrasekhar (1943). The second type is a mirror image of the over- and underdensities which become more evident in the centre of the hosts. The tidal force of the satellite perturbs the position of the highest density point in the host. This causes the central overdensity and a corresponding underdensity on the opposite side because of mass conservation (Ogiya & Burkert 2016).

References:

• Chandrasekhar S., 1943, ApJ, 97, 255
• Ogiya G., Burkert A., 2016, MNRAS, 457, 2164
• Ogiya G., Mori M., Miki Y., Boku T., Nakasato N., 2013, J. Phys. Conf. Ser., 454, 012014

G. Ogiya, A. Burkert

V.2) Group Prof. Joseph Mohr

Finding galaxy clusters in RASS using DES

The RASS is the deepest and highest quality all-sky X-ray survey up to date. It is therefore naturally a good test field to prepare techniques and catalogs for the upcoming X-ray survey performed by the eROSITA satellite. In order to archive the goals of the eROSITA project in the field of cluster cosmology, clusters have to be identified and their redshift has to be measured. For the majority of the clusters this can only be done with additional optical data, such as those provided by the Dark Energy Survey (DES).

We identify clusters in the second ROSAT all-sky survey source catalog (2RXS) [1] using a multi-filter red sequence technique which incorporates X-ray information such as count rate and position of a source. By simultaneous usage of several colours beyond that one including the prominent 4000 Ångstrom break allows us to further suppress contamination and improve redshift and richness estimates.

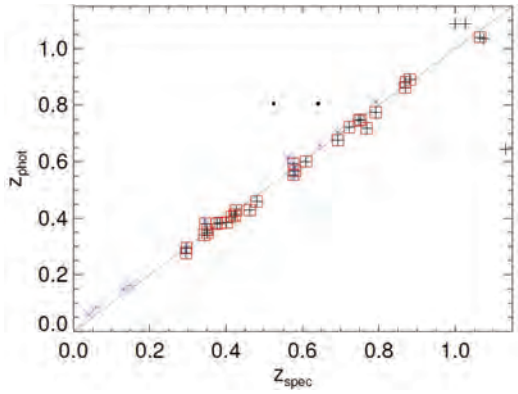

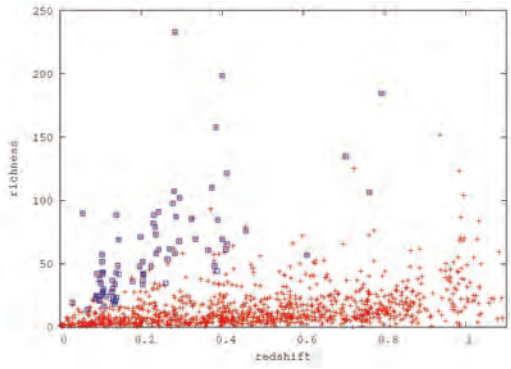

By applying the method on random pointings excluding the regions around 2RXS sources allow us to estimate the optical detection probability at low redshifts and the X-ray selection at higher redshifts.
Estimators based on this random pointing together with center offsets between X-ray and optical center allow a well defined selection of galaxy clusters.

We find about 80 clusters within our 200 square degree test area of the DES since verification data set. Extrapolating these numbers to the full DES area results in a catalog of about 1500 to 2000 clusters over the 5000 square degree of the survey. The number of clusters is of the same order as the combined, REFLEX II [2] and NORAS II cluster catalog that cover the full extra galactic sky.

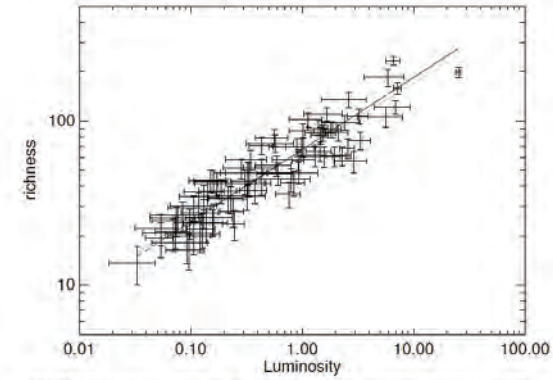

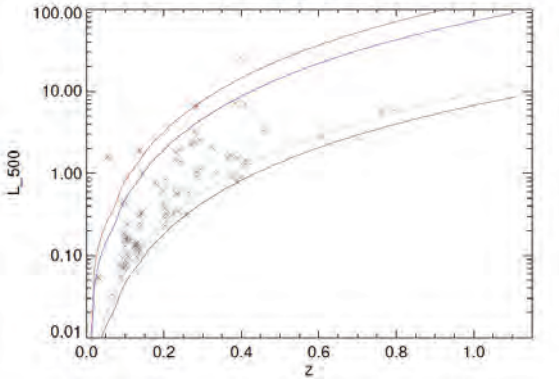

Figures:
top-right: Photo-z performance, red special tiles, blue cluster in survey area
mid-left: Redshift-Richness distribution of all 2RXS sources (red) and selected clusters (blue).
mid-right: Luminosity-Richness relation of the selected clusters
bottom-right: Luminosity-Redshift relation, flux limits of REFLEX and REFLEX II are indicated in red and blue

References:
[1] Boller et al. 2016
[2] Böhringer et al. 2013, A&A, 555, 15
Images, Methods: M. Klein et al. 2016 (in prep.)

M. Klein, J. Mohr, et al.

High Frequency Cluster Radio Galaxies and Sunyaev-Zel'dovich Effect Selected Cluster Samples

We study the overdensity of high frequency cluster radio galaxies toward X-ray selected clusters with the goal of measuring the cluster radio galaxy luminosity function (LF) at 95, 150 and 220 GHz. We correct for flux biases due to the galaxy cluster Sunyaev-Zel'dovich effect (SZE) at 95 and 150 GHz using a model for the SZE signature of galaxy clusters. We find that the radio galaxies at high frequencies are approximately an order of magnitude rarer than those at 843 MHz. Producing South Pole Telescope survey like cluster samples, we show that the radio galaxies introduce incompleteness in these samples at the 1.7+/-0.8 percent level, which is too small to be relevant for the cosmological analysis of the SPT SZE selected cluster sample.

We identify cluster radio galaxies by examining the excess of systems in the SPT maps that are in the direction of galaxy clusters in the MCXC X-ray selected cluster sample. At 95 and 150 GHz, the fluxes of these systems are biased low by the SZE flux from the cluster itself. We correct for this bias by using a model of the cluster SZE that depends on the cluster mass and redshift.

To the right is a plot of the LF (number per unit cluster mass versus radio power) of the 150 GHz cluster radio galaxy population extracted from 139 MCXC clusters both with and without SZE flux bias corrections. The flux bias corrections boost the LF relative to the uncorrected case.

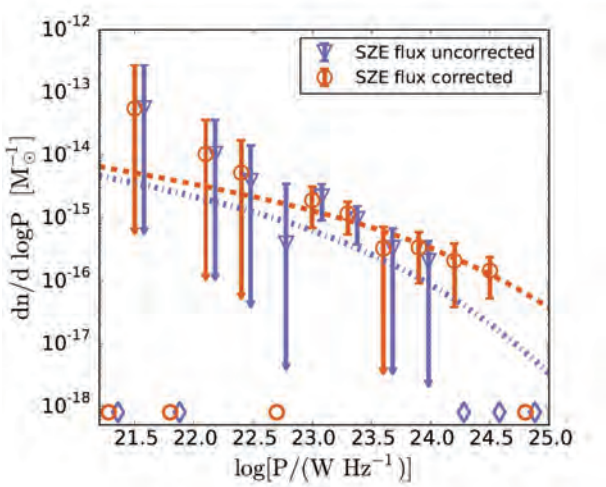

The figure below shows the best fit 843 MHz and 95, 150 and 220 GHz cluster radio galaxy LFs. It is clear that the high frequency radio galaxies are rarer by an order of magnitude in comparison to the low frequency SUMSS 843 MHz radio AGN. Given the small sample sizes it is difficult to quantify differences between the 95, 150 and 220 GHz LFs.

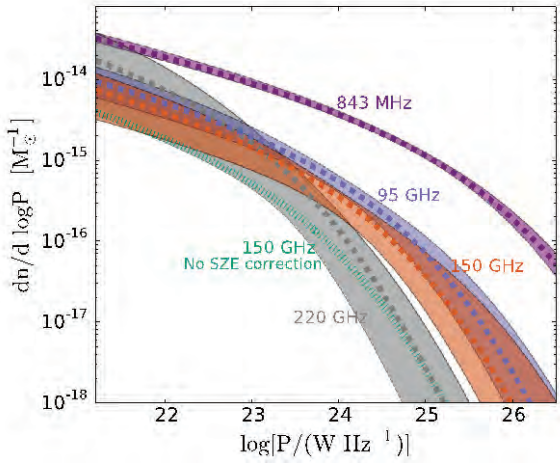

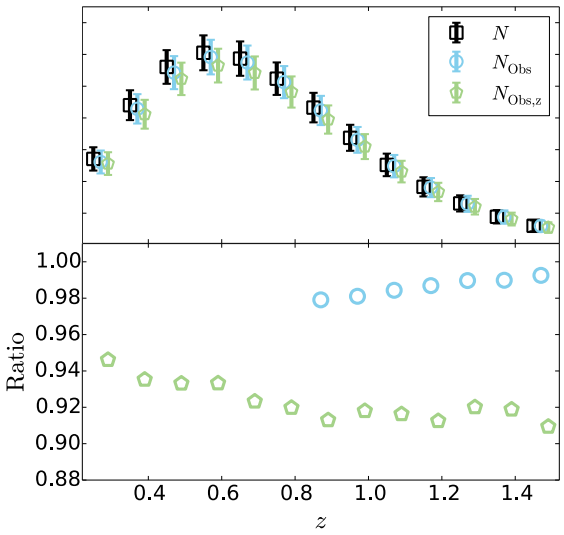

To the left is a prediction of the incompleteness of SZE selected cluster samples from SPT for two LF evolution models: (1) no evolution (blue) and (2) strong evolution (green). In the case of no evolution we find that 1.8+/-0.7 percent of the clusters are lost, and in the strong evolution case we find the fraction of lost clusters is 5.6+/-1.0 percent. In both cases the impact is too small to be relevant for the current cosmological analyses.

N. Gupta, J. Mohr, et al.